J. Astrophys. Astr. (1986) **7,** 1–6

The Neutrino Hypothesis for Dark Matter in Dwarf Spheroidals

Ramnath Cowsik *Tata Institute of Fundamental Research, Homi Bhabha Road, Colaba, Bombay 400005*

Received 1985 April 4; accepted 1985 October 4

Abstract. The theoretical expectation of the high mass of $\gtrsim$ 400 eV for the particles constituting the dark matter in dwarf-spheroidals as an artifact of the implicit assumption that the density of particles vanishes at the visible edge. On the contrary if our Galaxy and the dwarf-spheroidals are embedded in a neutrino condensation of the dimensions of the cluster then $m_\nu \simeq 10$ eV can accommodate all the observations.

Key words: galaxies, dark matter — galaxies, dwarf-spheroidals—neutrino, mass

1. Statement of the problem and its resolution

The measurement of a finite mass for the electron-neutrino by the ITEP group using the β-spectrum in ^{3}He decay (Boris *et al.* 1983 quoted by V. A. Lubimov at the *Int. Conf. on High Energy Phys.*, Brighton; see also Lubimov *et a1.*1980 and references therein) has led to a number of very interesting studies (Tremaine & Gunn 1979; Bond, Efstathiou & Silk 1980; Schramm & Steigman 1980; Klinkhamer & Norman 1981; Sato & Takahara 1981; Wasserman 1981; Davis *et al.* 1981; Doroshkevich *et al.* 1981; Melott 1983; Peebles 1984 and references therein) of the basic idea that 'if neutrinos have a rest mass of a few eV/c^2 then they would dominate the gravitational dynamics of large clusters of galaxies and of the universe, and through their mutual gravitational interactions, neutrinos may have triggered the initial condensations that led to the formation of clusters of galaxies' (Cowsik & McClelland 1973). Also, observationally, evidence for the extent and the distribution of nonluminous matter on various scales has been accumulated by systematic observations on clusters of galaxies (Bahcall 1977; Peebles 1979), binary galaxies, rotation curves of spirals (Faber & Gallagher 1979) and recently in a sequence of papers on dwarf spheroidals (Aaronson 1983; Faber & Lin 1983; Lin & Faber 1983). These observations, particularly those mentioned last, have exacerbated the apparent conflict (Bludman 1977) between the neutrino hypothesis and the observed amount of dark matter in various systems. In this paper, we first present the arguments that have lead to the apparent conflict and then point out that the observations are indeed in conformity with the idea that on length-scales comparable to or greater than that of cluster of galaxies ‘neutrinos dominate the gravitational dynamics of the Universe’ (Cowsik & McClelland 1973).

The nature of the disagreement can be understood as follows: the density contributed

by neutrinos at any point can be written as

$$\rho_\nu = g m_\nu \int_0^{p_{\max}} f(p) \mathrm{d}^3 p. \tag{1}$$

Here, g represents the total number of degrees of freedom for the neutrinos, counting one for each helicity state, each flavour and one for each particle or antiparticle; $f(p)$ is the phase-space density. Davis *et al.* (1981), following the ideas of Tremaine & Gunn (1979), estimate

$$\rho_\nu \lesssim \frac{4\pi g m_\nu}{3} \left(\frac{m_\nu v}{h} \right)^3 \tag{2}$$

where $v = p/m$ is a suitably defined average velocity of the neutrino. Lin & Faber (1983) assume that the neutrino distribution terminates at R, the visible edge of the dwarf spheroidal so that

$$\frac{p_{\max}^2}{2m_\nu} = \frac{GMm_\nu}{R}; \qquad \text{or} \qquad v^2 \simeq \frac{2GM}{R}. \tag{3}$$

Substituting this in Equation (2), and assuming $\rho_\nu \simeq M/(4\pi/3)R^3$ consistent with the idea of neutrino domination, one finds

$$m_\nu^8 \gtrsim \frac{3^4 \pi^2}{2^5 g^2} \frac{\hbar^6}{G^3 R^3 M} \tag{4}$$

which matches exactly the formula derived with the assumption of a square-well potential and ν_e, $\bar{\nu}_e$, ν_μ, $\bar{\nu}_\mu$, giving $g = 8$ by Cowsik & McClelland (1973). Lin & Faber, adopting $R \sim 1$–3 kpc and $M = 10^7\ M_\odot$, note that Equation (4) yields $m_\nu \gtrsim 400$ eV which exceeds substantially the bounds on neutrino masses (Boris *et al.* 1983 quoted by V. A. Lubimov at the *Int. Conf. on High Energy Phys.*, Brighton; see also Lubimov *et al.* 1980; Dolgov & Zeldovich 1981; Particle data group 1982 and references cited therein).

This contradiction detailed here stems from the implicit assumption that the neutrino distribution terminates at the visible edge of the baryonic matter used in interpreting Equation (4). On the contrary, the formula should merely be interpreted as the typical R and M over which neutrinos of a given mass m_ν can form self-gravitating systems, and all the work on the condensation of neutrinos indicate that the typical scales are that of clusters of galaxies with $M \sim 10^{15}\ M_\odot$ and $R \sim 1$ Mpc. If this is so, then the distribution of galaxies in a cluster essentially traces out the cluster's gravitational potential generated predominently by the neutrino condensations, and our Galaxy, the dwarf spheroidals *etc. are* embedded in such a neutrino cloud. Strictly speaking, this does perturb the neutrino density by a small amount (Cowsik 1983; Gilbert 1970; Marochnik 1968), as shown schematically in Fig. 1. What is important here to note is that contributions to the density comes not merely from neutrinos with $v_\nu < 10$ km s^{-1} and orbits confined by the visible edge of the dwarf spheroidals but more importantly from neutrinos with velocities up to ~ 1000 km s^{-1} and with orbits extending up to the visible edge of the cluster. With such high velocities, Equation (2) yields a possible maximum density of neutrinos $\sim 10^{-24}$ g cm^{-3} for an acceptable $m_\nu \sim 10$ eV/c^2. The actual density at the location of any specific dwarf spheroidal would depend upon its proximity to the centre of the neutrino cloud; closer it is to the centre, higher is the density of the background neutrinos. To see that such a density is more than adequate to explain the observations on dwarf spheroidals let us focus attention

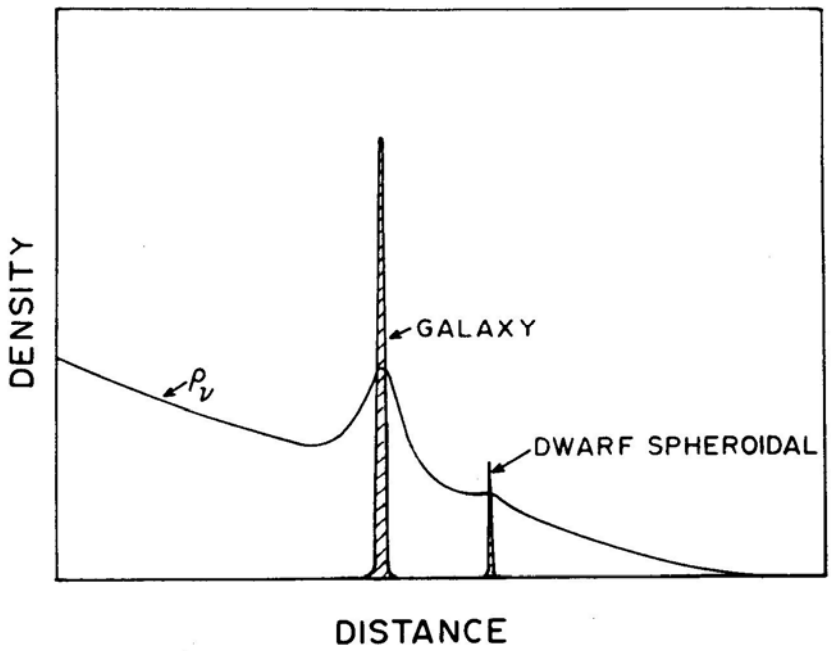

Figure 1. Schematic representation of density perturbations induced by the Galaxy and the dwarf spheroidals in a neutrino cloud of cluster dimensions.

on Leo I which has a central density of visible matter $\rho_*(0) \simeq 6 \times 10^{-3}\, M_\odot\ \mathrm{pc}^{-3} \simeq 4 \times 10^{-25}$ g cm^{-3} and requires for tidal stability a mass $M_t \sim 4 \times 10^7\, M_\odot$ within a radius $R \sim 0.88$ kpc. This latter requirement implies a neutrino density $\rho_\nu \simeq 1.3 \times 10^{-25}$ g cm^{-3} quite consistent with the possible maximum density. Also it is interesting to note that the rms velocity of stars needed to yield the observed core radius, r_c 0.53 kpc, is

$$\langle V^2 \rangle^{1/2} = \tfrac{1}{3} r_c [4\pi G(\rho_*(0) + \rho_\nu)]^{1/2} \simeq \tfrac{1}{3} r_c [4\pi G \rho_*(0)]^{1/2} \simeq 5.6\ \mathrm{km\,s^{-1}} \quad (5)$$

since the central density is dominated by stars. The Keplerian velocity of the stars at the tidal radius r_t 0.88 kpc is given by

$$V_K = (GM_t/r_t)^{1/2} \simeq (\tfrac{4}{3}\pi G \rho_\nu r_t^2)^{1/2} \simeq 15\ \mathrm{km\,s^{-1}} \quad (6)$$

since the mean density up to the limiting radius is dominated by the neutrinos. These numbers are consistent with observations.

The point that is made here is that the neutrinos inside the visible edge of the spheroidal exert gravitational force on the stars, irrespective of whether the neutrino orbit takes them later beyond the edge or not. Indeed, in Equation (1), the upper limit $P_{\max}$ should pertain to the cluster in which the various galaxies, dwarf spheroidals, *etc. are* embedded. In such an embedding the dwarf spheroidals are stable against tidal

disruption if they are situated in the central regions of the neutrino cloud. The exact criterion for tidal stability is derived in Appendix. Thus we might conclude that the new observations on the dwarf spheroidals indeed support the idea of neutrino domination and that the baryonic condensates like the stars and galaxies serve merely to light up the potential wells generated by the neutrinos. This idea is a viable alternative to the one in which weakly interacting particles of different masses hypothesized in the context of GUT are invoked to explain the invisible matter on different scales (Peebles 1983; Rees 1983; D. W. Sciama 1984, personal communication). The basic point that by increasing the effective radius of the distribution of dark matter one can reduce the mass of particles needed to explain the observations of dwarf spheroidals has been noted independently (Norman & Silk 1984).

2. Discussion

The hypothesis that dwarf spheroidals are embedded in extended clouds of neutrinos, typically of the dimensions of rich clusters of galaxies, immediately leads to several questions and consequences: 1. Would the dwarf spheroidals be stable against tidal disruption when they are so embedded? 2. How is the dynamics of their constituent stars affected, and could one model their profiles of luminosity on such a dynamical basis? 3. If the clouds of neutrinos are extended they would encompass other galaxies, galactic groups and galactic clusters as well; what are the predictions for such embedding? 4. Would the dynamical friction play an important rote? 5. Finally, in the expanding universe how are such clouds formed and how does the formation of such clouds affect the formation of galaxies?

All these questions cannot be answered immediately and we have listed them here merely to indicate that they should be considered carefully. In the appendix to this paper the criterion for the tidal stability of dwarf spheroidals is derived assuming that they are moving in orbits within the cloud of neutrinos; the dwarf spheroidals are stable in the central regions of the neutrino clouds. The dynamical equations for the self-consistent distribution of stars in galaxies embedded in a cloud of neutrinos have been developed; their solutions and their applicability to the luminosity profiles and rotation curves of galaxies will be discussed in forthcoming papers. We have also studied systematically how the dynamical masses of astronomical systems vary with their radii. These studies also support the embedding hypothesis.

The last question listed above as to the detailed dynamics of the formation of structures and growth of fluctuations in the universe is indeed the most difficult one and has been the focus of extensive work by many workers over the last five years. The reader may refer to the recent papers by Bond *et al.* (1984), White, Frank & Davis (1984), Shappiro, Marcell & Melott (1983) and references therein, for the various ideas that are being investigated. It is safe to say that the field is a very complex one and that as yet no consensual view has emerged as to the dynamical evolution of the condensates in the universe. It is for this reason that our first attempts will be primarily focussed on characterizing the state of the various astronomical systems today. Once a dynamically self-consistent and a sufficiently detailed picture of the astronomical system is obtained, the problem of the formation of such systems in an expanding universe may become tractable.

Appendix

Criterion for Tidal Disruption of a Stellar Cluster Embedded in a Cloud of Neutrinos

The equations of motion of a test particle around a star cluster is best studied in a frame of reference rotating about the centre of the cloud with an angular frequency ω which is constant over a circular orbit assumed here for simplicity. The rotating frame is spanned by three Cartesian co-ordinates ζ,η,ζ, along the radius vector from the centre of the cloud, along the tangent to the assumed circular path and along the normal to the orbital plane. respectively. The Hamiltonian for the system is given by

$$H = \{\omega(\eta p_\xi - \xi p_\eta) + (1/2m)(p_\xi^2 + p_\eta^2 + p_\zeta^2)\} + U \tag{A1}$$

with

$$p_\xi = m(\dot{\xi} - \omega\eta), \quad p_\eta = m(\dot{\eta} + \omega\xi) \quad \text{and} \quad p_\zeta = m\dot{\zeta}. \tag{A2}$$

The relevent equations of motion are

$$\dot{\xi} = \omega\eta + \frac{p_\xi}{m}, \quad \dot{\eta} = -\omega\xi + \frac{p_\eta}{m}, \quad \dot{\zeta} = \frac{p_\zeta}{m} \tag{A3}$$

and

$$\dot{p}_\xi = -\left\{-\omega m(\dot{\eta} + \omega\xi) + \frac{\partial U}{\partial \xi}\right\}, \quad \dot{p}_\eta = -\left\{-\omega m(\dot{\xi} - \omega\eta) + \frac{\partial U}{\partial \eta}\right\},$$

$$\dot{p}_\zeta = -\frac{\partial U}{\partial \zeta}. \tag{A4}$$

Assuming now that the size of the star cluster r is small compared to the distance ξ_c to the cloud centre, Equation (A4) for the radial acceleration of a test particle reads

$$\ddot{r} = -\left\{-\omega(\dot{\eta} + \omega r + \omega\xi_c) + \frac{GM_v(\xi_c + r)}{(\xi_c + r)^2} + \frac{GM_*}{r^2}\right\}. \tag{A5}$$

Note that $M_v = (4\pi/3)\,\xi^3\bar{\rho}_v$, $dM_v/d\xi = 4\pi\xi^2\,\rho_v$ and $M_* = (4\pi/3)r^3\,\bar{\rho}_*$ with $\bar{\rho}_v$ being the mean density internal to ξ ,ρ_v the density at and $\bar{\rho}_*$ the mean density of the stellar cluster. The most favourably bound orbit obtains for $\eta = -a\omega_c$, its maximum negative value; here the Coriolis force is directed inward. Expanding Equation (A5) about ξ_c and substituting $\omega = [(4\pi G/3)\,\bar{\rho}_v]^{1/2}$ and $\omega_c = (4\pi G/3)(\bar{\rho}_v + \bar{\rho}_*)^{1/2}$, we get the condition for tidal stability by demanding r be negative

$$\bar{\rho}_* + \{(\bar{\rho}_* + \rho_v)\bar{\rho}_v\}^{1/2} - 3(\bar{\rho}_v - \rho_v) > 0. \tag{A6}$$

Now, specializing to the case of dwarf spheroidals embedded in an Emden-sphere of isothermal neutrinos we find that this condition for stability is satisfied up to 5 times its core radius even for very small $\bar{\rho}_*$ The forces along η and ζ are compressive and so do not impose any restrictions. Now, for radial orbits the condition for tidal stability can be shown similarly to be

$$\bar{\rho}_* + 3\rho_v - 2\bar{\rho}_v > 0. \tag{A7}$$

Acknowledgements

I am indebted to Drs P, Ghosh, T, Padmanabhan and M. Vasanthi for many fruitful

discussions. We thank Dr S. Tremaine for prompting improvement of our discussion of the tidal stability.

References

Aaronson, M. 1983, *Astrophys. J.,* **266,** L11.
Bahcall, N. A. 1977, *A. Rev. Astr. Astrophys.,* **15,** 505.
Bisnovatyi-Kogan, G. S., Lukash, V. N., Novikov, 1. D. 1983, in *IAU Symp.* 104: *Early Evolution of the Universe and its Present Structure,* Eds G. **0.** Abell & G. Chincarini, D. Reidel, Dordrecht, p. 327.
Bludman, S. A. 1977, *Ann. N.Y. Acad. Sci.,* **262,** 181.
Bond, J. R., Centrella, J., Szalay, A. S., Wilson, J. R. 1984, *Mon. Not. R. astr. Soc.,* **210,** 515.
Bond, J. R., Efstathiou, G., Silk, J. 1980, *Phys. Rev. Lett.,* **45,** 1980.
Cowsik, R. 1983, *Current Science,* **52,** 1104.
Cowsik, R., McClelland, J. 1973, *Astrophys. J.,* **180,** 7.
Davis, M., Lecar, M., Pryor, C., Witten, E. 1981, *Astrophys. J.,* **250,** 423.
Dolgov, A. D., Zeldovich, Ya. B. 1981, *Rev. Mod. Phys.,* **53,** 1.
Doroshkevich, A. G., Khlopov, M. Yu, Sunyaev, R. A., Szalay, A. S., Zeldovich, Ya. B. 1981, *Ann. N.Y. Acad. Sci.,* **375,** 32.
Gilbert, **1.** H. 1970, *Astrophys. J.,* **159,** 239.
Faber, S. M., Gallagher, J. S. 1979, *A. Rev. Astr. Astrophys.,* **17,** 135.
Faber, S. M., Lin, D. N. C. 1983, *Astrophys. J.,* **266,** L17.
Klinkhamer, F. R., Norman, C. A. 1981, *Astrophys. J.,* **243,** Ll.
Lin, D. N. C., Faber, S. M. 1983, *Astrophys. J.,* **266,** L21.
Lubimov, V. A., Novikov, E. G., Nozik, V. Z., Tretyakov, E. F., Kosik, V. S. 1980, *Phys. Lett.,* **94B,** 266.
Marochnik, L. S. 1968, *Sov. Astr.,* **11,** 873.
Melott, A. L. 1983, *Astrophys. J.,* **264,** 59.
Norman, C., Silk, J. 1984, in *Formation and Evolution of Galaxies and Large Structures in the Universe,* Eds J. Audouze & J. Tran Thanh Van, D. Reidel, Dordrecht, p. 215.
Particle Data Group, 1982, *Phys. Lett.,* **111B,** 104.
Peebles, P. J. E. 1979, in *Physical Cosmology,* Eds R. Balian, J. Audouze & D. N. Schramm, North-Holland, Amsterdam, p. 213.
Peebles, P. **J.** E. 1984, *Astrophys. J.,* **277,** 470.
Rees, M. J. 1983, in *IAU Symp.* 104: *Early Evolution of the Universe and its Present Structure,* Eds, G. **0.** Abell & G. Chincarini, D. Reidel, Dordrecht, p. 299.
Sato, H., Takahara, R. 1981, *Prog. Theor. Phys.,* **66,** 508.
Schramm, D. N., Steigman, G. 1981, *Astrophys. J.,* **243,** 1.
Shappiro, P. P., Marcell, C. S., Melott, A. L. 1983, *Astrophys. J.,* **275,** 415.
Tremaine, S., Gunn, J. L. 1979, *Phys. Rev. Lett.,* **42,** 407.
Wasserman, I., 1981, *Astrophys. J.,* **248,** 1.
White, S. D. M., Frank, C. S., Davis, M. 1984, *Mon. R. astr. Soc.,* **209,** 27.

J. Astrophys. Astr. (1986) **7,** 7–15

Dynamical Effects of an Extended Cloud of Dark Matter on Dwarf Spheroidals

Ramanath Cowsik & Pranab Ghosh *Tata Institute of Fundamental Research, Homi Bhabha Road, Colaba, Bombay 400005*

Received 1985 April 4; accepted 1985 October 4

Abstract. If the dwarf spheroidals are embedded in an extended cloud of dark matter then their density profiles can be reproduced by assuming a Maxwellian distribution of velocities for the constituent stars. The observed luminosity profiles of dwarf spheroidals imply densities for the dark matter in the range 10^{-26} to 10^{-25} g cm^{-3}, and mass-to-luminosity ratios which are typically an order of magnitude greater than those of globular clusters. Neutrinos of mass ~ 10 eV and $\langle v \rangle$ ~ 1000 km s^{-1} can provide this requisite density for the background.

Key words: galaxies, dark matter—galaxies, dwarf spheroidal—neutrino, mass

1. Introduction

The observation of high velocity dispersion of carbon stars in one dwarf spheroidal galaxy (Aaronson 1983) and considerations of the *M/L* ratios of dwarf spheroidals of the Local Group, based on tidal cut-off arguments (Faber & Lin 1983; Lin & Faber 1983) have indicated the presence of dark matter in these systems. In an earlier paper (Cowsik 1986) we have argued that the theoretical expectation of a high mass $\gtrsim$400 eV/c^2 for the particles constituting this dark matter is an artifact of the assumption that the density distribution of the dark matter follows that of the visible matter and that if our Galaxy and the dwarf spheroidals are embedded in a neutrino condensation ~0.1 Mpc in size, then m_ν, ~10 eV can accommodate these observations. In this paper we investigate further this idea that the dwarf spheroidals are embedded in an extended cloud of dark matter and show that this model also predicts correctly the observed radial luminosity profiles (Hodge 1966 and references therein; Hodge & Michie 1969). The quality of the fit is so good as to lend strong support to the idea that neutrinos with a rest mass ~10 eV/c^2 generated copiously in the big bang triggered the initial condensations that led to the formation of the clusters of galaxies. In our picture, the visible matter in the form of spiral and elliptical galaxies, and dwarf spheroidals are embedded in these neutrino condensations, and through their gravitational dynamics delineate the distribution of the dark matter.

2. Calculation of self-consistent luminosity profiles

We assume that the velocity distribution of stars in a dwarf spheroidal is Maxwellian with typical velocity dispersion ~ 1–10 km s^{-1} Making use of a theorem due to Jeans

(Lynden-Bell 1962), the distribution function of the stars can be expressed as any function of their total energy $E = \frac{1}{2} m_* v^2 + m_* \psi$. Here $\psi = \psi_\nu + \psi_*$ is the total gravitational potential due to the background neutrino gas and the stars. Thus

$$f(v) \sim \exp\left[-\frac{m_*}{kT_*} (\tfrac{1}{2} v^2 + \psi_* + \psi_\nu) \right] \tag{1}$$

so that

$$\rho_* = \int f \, \mathrm{d}^3 v = \rho_0 \exp\left[-\frac{m_*}{kT_*} (\psi_* + \psi_\nu) \right]. \tag{2}$$

The potentials satisfy the Poisson equation

$$\nabla^2 \psi = 4\pi G(\rho_* + \rho_\nu),$$

or

$$\nabla^2 \psi_* = 4\pi G \rho_* \qquad \text{and} \qquad \nabla^2 \psi_\nu = 4\pi G \rho_\nu, \tag{3}$$

with obvious notation. Now note that the typical length-scales for the spatial variations of the stars and neutrinos are given by

$$l_* \sim \left(\frac{kT_*}{4\pi G \rho_0 m_*} \right)^{1/2} \qquad \text{and} \qquad l_\nu \sim \left(\frac{kT_\nu}{4\pi G \rho_0 m_\nu} \right)^{1/2} \tag{4}$$

where ρ_0 is the net central density. In the context of dwarf spheroidals embedded in an extended cloud of neutrinos we have $\langle v_*^2 \rangle^{1/2} \simeq (3kT_*/m_*)^{1/2} \sim$ 1–10 km s^{-1} and $\langle v_\nu^2 \rangle^{1/2} \simeq (3k\ T_\nu/m_\nu)^{1/2} \sim 1000$ km s^{-1} so that $l_\nu \gg l_*$. This means that we can neglect the variation in the density of neutrinos over the extent of the dwarf spheroidals and set $\rho_\nu \simeq$ constant in Equation (3).

Now we substitute Equation (1) in Equation (3), and make the resulting equation dimensionless by expressing the radial distance r from the centre of the dwarf spheroidal in units of the structural radius $l_c = (kT_*/4\pi G \rho_c m_*)^{1/2}$, *i.e.*, $x = r/l_c$, and the potentials in units of kT_*, *i.e.*, $\phi_\nu = m_* \psi_\nu / kT_*$ and $\phi_* = m_* \psi_* / kT_*$. With these manipulations and the boundary condition on ϕ_ν that $\phi_\nu(0) = 0$, the equation for ϕ_* becomes

$$x^{-2} (\mathrm{d}/\mathrm{d}x)(x^2 \, \mathrm{d}\phi_*/\mathrm{d}x) = \exp\left[-\phi_* - \frac{1}{6} \frac{\rho_\nu}{\rho_c} x^2 \right]. \tag{5}$$

Here ρ_c is the central density of the stars. We obtain the solution of Equation (5), subject to the boundary condition $\phi_*(0) = 0 = \phi'_*(0)$, in a straightforward manner, following the method described by Emden (1907) and Chandrasekhar (1939).

Once $\phi_*(r)$ is known, the Poisson equation yields $\rho_*(r)$ and this can be projected to get the luminosity profile. We have with obvious notation,

$$\sigma(\varpi) = 2 \left\langle \frac{L_*}{m_*} \right\rangle \int_0^\infty \rho_* [(\varpi^2 + z^2)^{1/2}] \, \mathrm{d}z. \tag{6}$$

3. Results

In Figs 1(a)-(f) we show the observed luminosity profiles of the six well-studied dwarf spheroidals of the Local Group (Hodge 1961a,b, 1962, 1963, 1964a, b, 1966; Hodge &

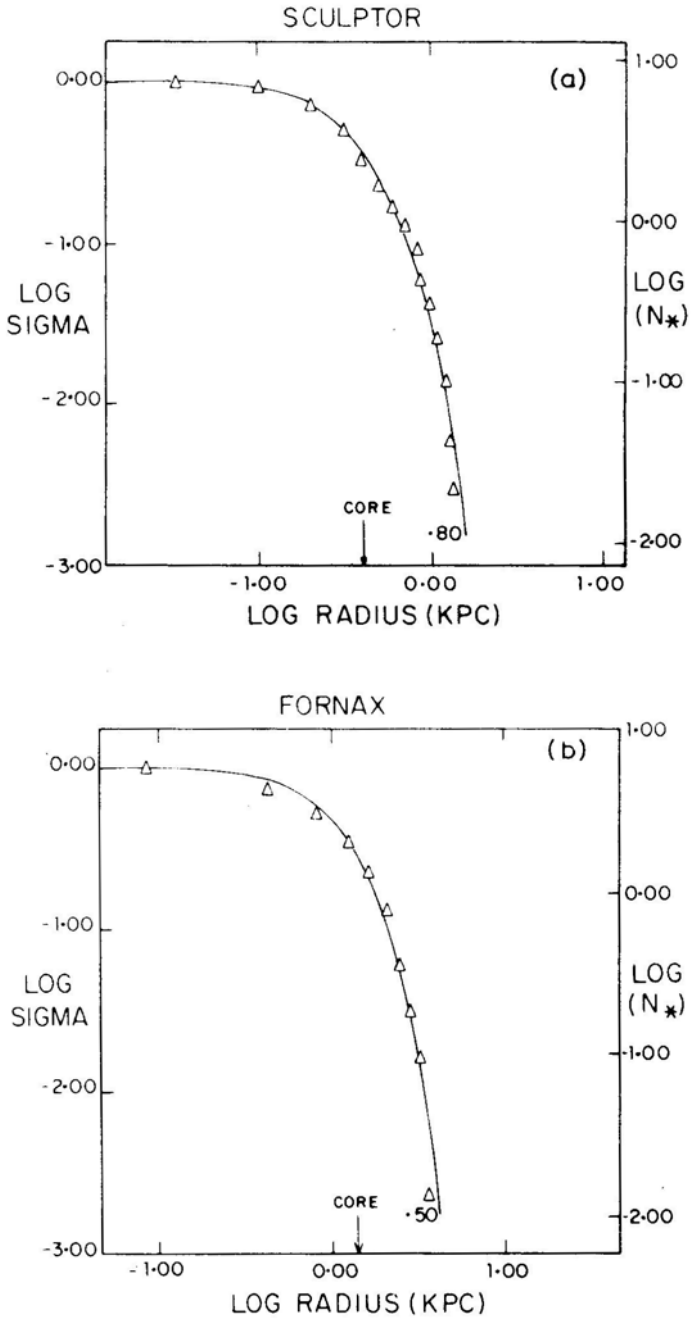

Figure 1. Surface density and star count profiles of: (a) Sculptor, (b) Fornax, (c) Leo I**,** (d) Leo II**,** (e) Draco, and (f) Ursa Minor, with the best fit model profiles, each model profile labelled by its value of log (ρ_c/ρ_v). Surface density (sigma) in units of its central value, and star count data are from Hodge (1961a, b, 1962, 1963, 1964a, b). Core radius is marked by arrow.

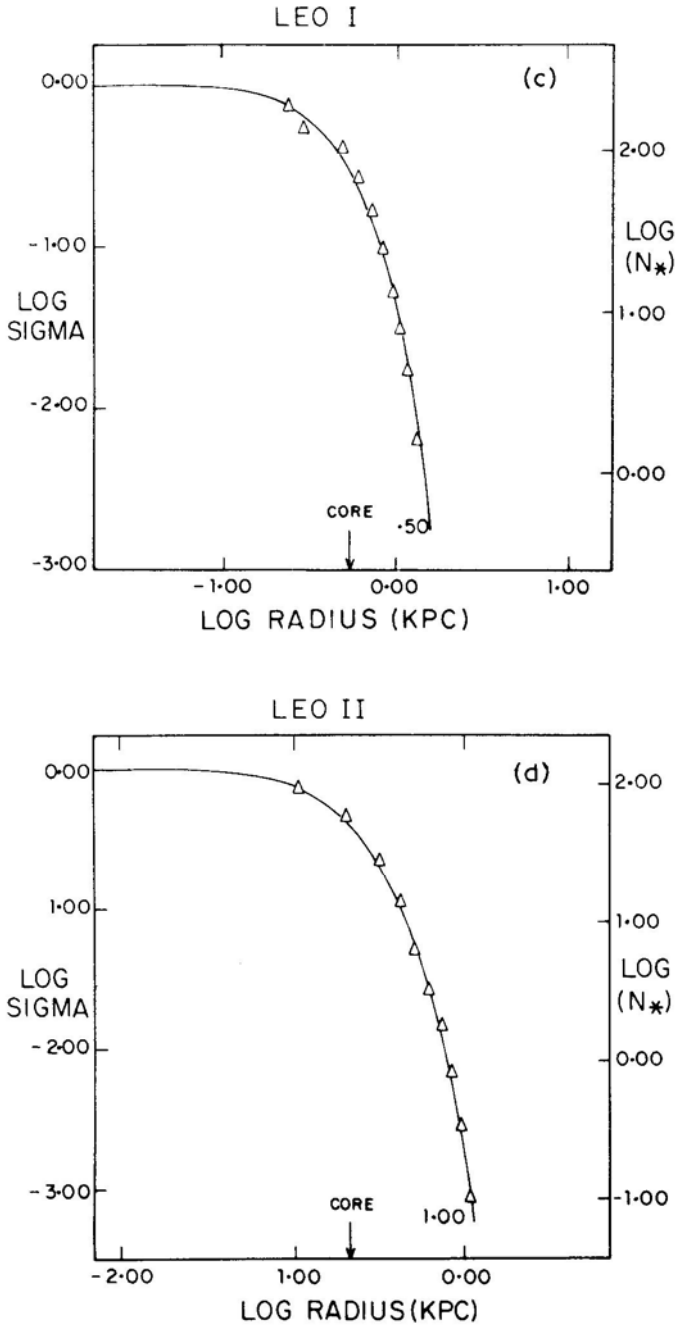

Figure 1. Continued.

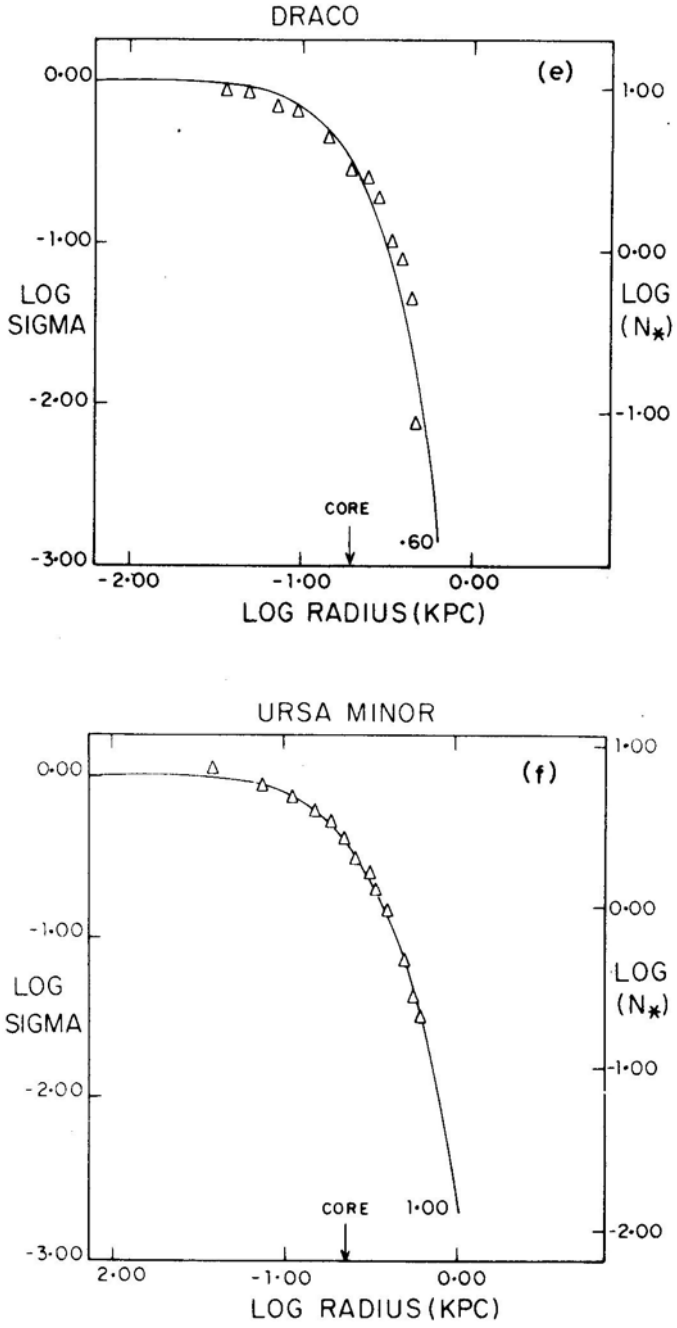

Figure 1. Continued.

Michie 1969) fitted by theoretical profiles. The fitting parameters are the core radius $r_c = \langle v_*^2 \rangle^{1/2}/(4\pi G\rho_c/3)^{1/2} = 3\ l_c$ and the density ratio (ρ_c/ρ_ν). To obtain the 3-D velocity dispersion $\langle v_*^2 \rangle^{1/2}$ and the neutrino density ρ_ν, one needs an estimate of the central density ρ_c, which can be obtained by two methods: either (a) one can integrate our model to obtain the total visible mass and normalize to Hodge's (1966) value for this mass, or (b)† one can adopt the Lin–Faber (1983) value for the central surface brightness and assume a visible $M/L = 2$. In Table 1 we display the parameters obtained by the two methods: the second one gives somewhat higher ρ_c, and therefore larger ρ_ν and $\langle v_*^2 \rangle^{1/2}$. (Note that the values of ρ_c in Table la are higher than those given by Hodge (1966) himself because there was a numerical error in his calculations. The corrected Hodge values are consistent with ours.) However, the important point is that both methods give a background density $\rho_\nu (\sim 10^{-25}\ 10^{-26}$ g cm^{-3}) which lies in the range of densities expected for the dark matter in the clusters of galaxies (Cowsik & Vasanthi 1986). In attributing this density of the background to neutrinos, we write

$$\rho_\nu \simeq \frac{8\pi g m_\nu \eta}{3}\left(\frac{m_\nu v_\nu}{h}\right)^3. \tag{7}$$

Here, v_ν is the maximum velocity of the neutrinos and η is the fraction of the phase-space filled by them. For example, with g = 1, $\eta = 0.5$, $m_\nu \simeq 10$ eV/c^2 and $v_\nu \simeq 1000$ km s^{-1}, Equation (7) yields $\rho_\nu \simeq 10^{-24}$ g cm^{-3}.

Now consider the velocity dispersion. (Note that line-of-sight dispersion = $\langle v_*^2 \rangle^{1/2}/\sqrt{3}$.) The values for Draco are somewhat lower than those reported by Aaronson (1983), while those for Fornax are in good agreement with those reported by Cohen (1983). The former discrepancy is unlikely to be significant because of the following uncertainties. On the one hand, Aaronson's measurements have insufficient statistics (3 stars measured, 2 only once), the measured stars may be in binaries, and Draco may be in the process of being disrupted (Hodge & Michie 1969). On the other, both methods of calculating ρ_c make use of the assumption that M (visible)/ L for dwarf spheroidals and globular clusters is the same ($\simeq 2$), which could be incorrect by an unknown amount.

The visible and dark components of the mass for a typical dwarf spheroidal galaxy in our model are shown in Fig. 2. The visible mass, which varies on a length-scale l_c, saturates by the limiting radius, whereas the dark mass, which varies on a much larger length scale (and is therefore nearly uniformly distributed on a scale l_c) still increases like r^3. Inside the core of a dwarf spheroidal, the visible density dominates, while at the limiting radius, the total dark mass dominates the total visible mass. Indeed, the ratio of the *total* mass to the luminosity, M_{tot}/L, is typically an order of magnitude higher than the visible (M/L) ratio (see Table 1). We emphasize two features of our model. First, the neutrino background does increase the central condensation and the velocity dispersion in DS galaxies, but this is done only indirectly by deepening the gravitational potential well in which the visibile matter resides; the density and the velocity dispersion in the core of a dwarf spheroidal are still dominated by the visible matter contributions. Second, the velocity distribution in our model is not truncated, so that there is no upper limit to the allowed random velocity.

† We thank Dr S. Tremaine for pointing out the second method to us. Method (a) is in better accord with the recent observations.

Table 1. Parameters for Dwarf Spheroidals.

	Sculptor	Fornax	Leo I	Leo II	Draco	Ursa Minor
(a) Method A: Using mass estimates.						
Core radius, R_c(kpc)	0.39	1.4	0.53	0.21	0.19	0.22
Limiting radius*, R_L(kpc)	1.2	3.1	0.91	0.65	0.51	1.2
Visible mass*, $M_{vis}(M_\odot)$	3×10^6	2×10^7	4×10^6	1×10^6	1.2×10^5	1×10^5
ρ(visible) at centre $(M_\odot/pc^3)$	7.1×10^{-3}	1.7×10^{-3}	6.0×10^{-3}	1.3×10^{-2}	3.5×10^{-3}	1.1×10^{-3}
ρ(dark) (g cm^{-3})	7.6×10^{-26}	3.6×10^{-26}	1.3×10^{-25}	8.6×10^{-26}	5.9×10^{-26}	7.5×10^{-27}
M_{dark}/M_{vis}	6.2	12.4	8.5	1.8	12.5	10.1
Total mass, $M_{tot}(M_\odot)$	2.2×10^7	2.7×10^8	3.8×10^7	2.8×10^6	1.6×10^6	1.1×10^6
M_{tot}/L ratio $(M_\odot/L_\odot)$	14	27	19	6	27	22
3-D velocity dispersion, $\langle v_*^2 \rangle^{1/2}$ (km s^{-1})	4.5	7.7	5.6	3.2	1.5	0.97
(b) Method B: Using central surface brightness estimates.						
Core radius, R_c(kpc)	0.39	1.4	0.53	0.21	0.19	0.22
Limiting radius, R_L(kpc)	1.2	3.1	0.91	0.65	0.51	1.2
Central surface brightness‡ m_v (mag arcsec^{-2})	23.9	23.3	21.5	23.9	24.6	25.0
ρ(visible) at centre $(M_\odot/pc^3)$	2.4×10^{-2}	1.2×10^{-2}	1.6×10^{-1}	4.4×10^{-2}	2.6×10^{-2}	1.6×10^{-2}
ρ(dark) (g cm^{-3})	2.6×10^{-25}	2.5×10^{-25}	3.5×10^{-24}	3.0×10^{-25}	4.5×10^{-25}	1.1×10^{-25}
M_{dark}/M_{vis}	6.2	12.4	8.5	1.8	12.5	10.1
3-D velocity dispersion, $\langle v_*^2 \rangle^{1/2}$ (km s^{-1})	8.2	20	29	6.0	4.1	3.7
M_{tot}/L ratio $(M_\odot/L_\odot)$, assuming $M_{vis}/L = 2$	14	27	19	6	27	22

* Data taken from Hodge (1966).

‡ Data taken from Lin & Faber (1983). Model (a) fits the recent observations on velocity dispersions better.

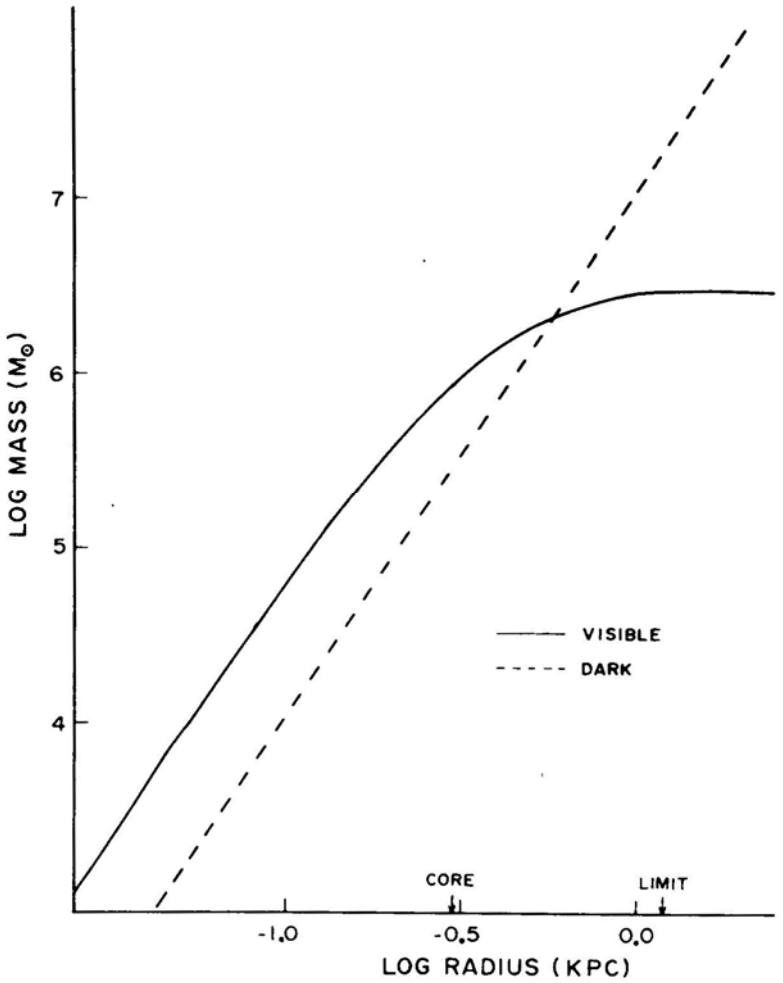

Figure 2. Visible and dark mass inside radius r for Sculptor. Visible mass dominates inside core. At limiting radius, dark mass (which goes as r^3) dominates over visible mass (which saturates).

We conclude from this study that neutrinos with a mass of ~ 10 eV/c^2 can provide the requisite binding for the stars in the dwarf spheroidals provided the neutrino distribution extends to the typical dimensions of a cluster of galaxies. Exotic particles such as photinos, gravitinos and right-handed neutrinos with masses as high as 500 eV/c^2 (Pagels & Primack 1981; Cabibbo, Farrar & Maiani 1981; Olive & Turner 1982) tend to condense on much smaller length-scales. Therefore these cannot explain in a simple way the profiles of luminosity of the spheroidals. The hypothesis that neutrinos have a mass of ~ 10 eV/c^2 naturally yields a density for the universe near closure (Gershtein & Zel'dovich 1966; Marx & Szalay 1972; Cowsik & McClelland 1972), a length- and mass-scale for condensations comparable to those of the clusters of galaxies (Cowsik & McClelland 1973; Bludman 1974; Schramm & Steigmann 1981), and also explains the dynamics of objects embedded in such condensations. Strictly speaking, any candidate for dark matter can be made to fit the observations if we adjust its density correctly and

allow it a velocity dispersion of 1000 km s^{-1}. But it is only for the neutrinos that this condition is naturally satisfied in a big-bang universe.

References

Aaronson, M. 1983, *Astrophys. J.*, **266**, L11.
Bludman, S. A. 1974, in *Proc. Neutrino* 74, **1,** 284.
Cabibbo, N., Farrar, G. R., Maiani, L. 1981, *Phys. Lett.*, **105B,** 155.
Chandrasekhar, S. 1939, in *An Introduction to the Study of Stellar Structure,* Univ. Chicago Press, p 156.
Cohen, J. G. 1983, *Astrophys. J.*, **270,** L41.
Cowsik, R. 1986, *J. Astrophys. Astr*., **7,** 1.
Cowsik, R**.,** Vasanthi, M. 1986, *J. Astrophys. Astr*., **7,** 29.
Cowsik, R., McClelland, J. 1972, *Phys. Rev. Lett*., **29,** 669.
Cowsik, R., McClelland, J. 1973, *Astrophys. J*., **180,** 7.
Emden, R. 1907, *Gaskugeln*, Leipzig, Teubner.
Faber, S. M., Lin, D. N. C. 1983, *Astrophys. J.*, **266**, L17.
Gershtein, S. S., Zel'dovich, Ya, B. 1966, *JETP Letters*, **4,** 174.
Hodge, P. W. 1961a, *Astr. J*., **66,** 249.
Hodge, P. W. 1961b, *Astr. J*., **66,** 384.
Hodge, P. W. 1962, *Astr. J*., **67,** 125.
Hodge, P. W. 1963, *Astr. J.*, **68,** 470.
Hodge, P. W. 1964a, *Astr. J*., **69,** 438.
Hodge, P. W. 1964b, *Astr. J*., **69,** 853.
Hodge, P. W. 1966, *Astrophys. J*., **144,** 869.
Hodge, P. W., Michie, R. W. 1969, *Astr. J*., **74,** 587.
Lin, D. N. C., Faber, S. M. 1983, *Astrophys. J.*, **266,** L21.
Lynden-Bell, D. 1962, *Mon. Not. R. astr. Soc.*, **124,** 95.
Marx, G., Szalay, A. S. 1972, *Proc. Neutrino* 72, Technoinform, Hungary, **1,** 123.
Olive, K. A., Turner, M. S. 1982, *Phys. Rev*., **D25,** 213.
Pagels, H., Primack, J. R. 1982, *Phys. Rev. Lett.,* **48,** 223.
Schramm, D. N., Steigman, G. 1981, *Astrophys. J*., **243,** 1.

J. Astrophys. Astr. (1986) **7,** 17–28

Towards a Physical Model for Galactic Rotation Curves

Ramanath Cowsik & Pranab Ghosh *Tata Institute of Fundamental Research, Homi Bhabha Road, Colaba, Bombay 400005*

Received 1985 April 4; accepted 1985 October 4

Abstract. Extensive and meticulous observations of the rotation curves of galaxies show that they are either flat or gently going up, but rarely decreasing, at large galactocentric distances. Here we show that the gravitational potential which would lead to such rotation curves arises naturally when the visible matter modelled as a collisionless Maxwellian gas is embedded in a dark halo of collisionless particles with a much higher dispersion in velocities.

Key words: galaxies, rotation curve—galaxies, dark matter—neutrino, mass

1. Introduction

Important insights into the structure and dynamics of galaxies have come from systematic and extensive observations of their rotation curves (Rubin 1979; Rubin, Ford & Thonnard 1980, 1982; Bosma 1978 and references therein). Even though the rotation curves in the central regions show great diversity and individuality in different galaxies, they exhibit a remarkable universality at larger galactocentric distances. Almost all the curves observed so far are either sensibly flat or faintly rising up to the largest observed distances. Indeed Rubin (1979) remarks ' . . . it is almost impossible to identify a galaxy with a falling optical rotation curve . . . nearly constant velocities and significant mass at large r are the rule . . . '. For the bright spirals the velocities increase rapidly with the radial distance from the centre, go through a maximum, fall initially and slowly increase to values ~ 150–300 km s^{-1} at large distances. Over this general pattern, velocity undulations of amplitude $\lesssim$ 20 km s^{-1} are seen coincident with the positions of spiral arms.

These features are usually understood in terms of a three-component empirical model, the components being a disc, a nuclear bulge and a halo or corona. The density distributions of these components are adjusted to reproduce the observed rotation curve (Einasto 1970; Ostriker & Caldwell 1979; Bahcall, Schmidt & Soneira 1982), which is obtained from the condition that the centrifugal force in a circular orbit equals the galactocentric force derived from the total potential Ψ due to these distributions, *i.e.*,

$$V_r^2 = -r\frac{\partial \Psi}{\partial r}. \tag{1}$$

Here V_r. is the (circular) rotation velocity and r is the galactocentric distance. At large distances, the observations cited above demand that $\partial\Psi/\partial r \sim r^{-\alpha}$, with $\alpha \lesssim 1$. By

analyzing a sample of 21 Sc galaxies (Burstein *et al.* 1982) and 23 Sb galaxies (Rubin, Ford & Thonnard 1982), Rubin and her co-workers have shown that α = 0.7–0.8, so that $V_r \sim r^{0\,1-0\,15}$.

The purpose of this paper is to show that such a potential arises naturally when the visible matter in the galaxy is embedded in a dark halo of collisionless gas whose velocity dispersion and spatial extent are much larger than those of the visible matter. In Section 2, we model the visible matter consisting predominantly of stars as a Maxwellian gas and calculate its self-consistent density profile; the rotation curves and the profiles of luminosity thus calculated reproduce the observations remarkably well. In Section 3 we investigate the nature of the constituents of the extended cloud of dark matter and comment on the suitability of neutrinos as the dark matter (Cowsik & McClelland 1973).

2. The model

We model the visible matter in the galaxies as a Maxwellian gas embedded in an extended cloud of collisionless particles with a much larger dispersion in their velocities. Binney (1982a, b) has shown that a Maxwellian distribution describes the luminosity profiles of elliptical galaxies well. The same is true for spiral galaxies, as we show below (see Section 2.3). A basic reason for the ubiquity of such a distribution is discussed in Cowsik (1984).

The equilibrium state of such a system is described by the Poisson equation, which, because of linearity, splits into

$$\nabla^2 \Psi_b = 4\pi G \rho_b; \qquad \nabla^2 \Psi_v = 4\pi G \rho_v . \tag{2a; b}$$

Since the dominant constituents of the visible matter are stars, the frequency of collision is very small (Chandrasekhar 1942), the phase-space distribution functions of both the visible and background gases are the solutions of the respective Liouville equations. Qualitatively, the spatial variations in the densities of the two gases will be defined by the characteristic length-scales

$$l_b \sim \left(\frac{kT_b}{4\pi G \rho_b m_b}\right)^{1/2}, \quad \text{and} \quad l_v \sim \left(\frac{kT_v}{4\pi G \rho_v m_v}\right)^{1/2}, \tag{3}$$

and we assume that $l_b \gg l_v$ so that in discussing the spatial variations in ρ_v the background density ρ_b may be treated as constant.

Now, by Jeans' theorem (Jeans 1915; Lynden-Bell 1962), the distribution function for the visible gas can be expressed as any function of $E = \frac{1}{2} m_v v^2 + m_v (\Psi_v + \Psi_b)$, the total energy of a constituent particle. There is evidence that f is Maxwellian (see above):

$$f(v) \sim \exp(-E/kT_v) \sim \exp\left[-\frac{m_v}{kT_v}\left(\frac{1}{2}v^2 + \Psi_v + \Psi_b\right)\right] \tag{4}$$

and

$$\rho_v = \int f \, d^3v = \rho_0 \exp\left[-\frac{m_v}{kT_v}(\Psi_v + \Psi_b)\right]. \tag{5}$$

We substitute Equation (5) in Equation (2b) and make the resulting equation dimensionless with $\phi = m_v \Psi_v/kT_v$, $\phi_b = m_v \Psi_b/kT_v$ and $\xi = r/l_v$. Here $l_v = (kT_v/4\pi G\rho_0 m_v)^{1/2}$. With ρ_b constant, the potential due to the background gas

which satisfies the boundary conditions $\phi_b(0) = 0$ is

$$\phi_b(\xi) = \frac{1}{6}\frac{\rho_b}{\rho_0}\xi^2. \tag{6}$$

The potential generated by the visible gas is given by

$$\xi^{-2}(d/d\xi)(\xi^2\, d\phi/d\xi) = \exp\left[-\phi - \frac{1}{6}\frac{\rho_b}{\rho_0}\xi^2\right] \tag{7}$$

for a spherically symmetric configuration. It is interesting to note that an identical equation obtains even for the collisional constituents of visible matter (Chandrasekhar 1939; Cowsik 1984).

The solutions of Equation (7) are obtained by a method described by Emden (1907) and Chandrasekhar (1939). The solutions of interest have finite, nonzero densities at the centre; hence the appropriate boundary conditions at $\xi = 0$ are $\phi = 0$ and $d\phi/d\xi = 0$, which identifies the constant ρ_0 in Equation (5) as the central density of visible matter. The numerical computation assumes the starting solution near the origin as the series $\phi = a\xi^2 + b\xi^4 + c\xi^6 + \ldots$ whose coefficients are found to be $a = 1/6$, $b = -(1+\rho_b/\rho_0)/120$, and $c = (1+5\rho_b/\rho_0)(1+5\rho_b/8\rho_0)/1890$. The potential ϕ for larger values ζ of are obtained by standard numerical methods of integration o Equation (7).

The rotation curves derived from this potential are shown in Fig. 1(a), for various values of ρ/ρ_b. The curves are drawn in terms of dimensionless variables

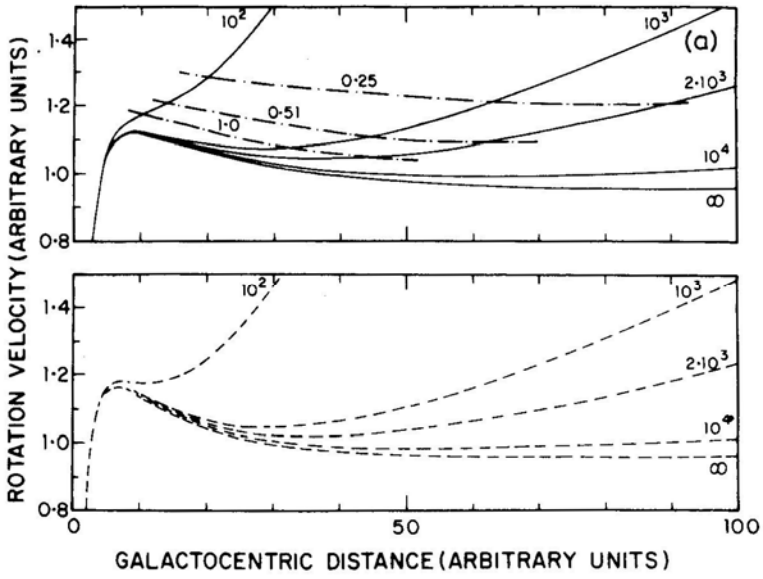

Figure 1(a). Model rotation curves in dimensionless variables (see text). Upper panel: For spherically symmetric distribution of visible gas. Solid lines are rotation curves, each labelled by its value of (ρ/ρ_b). Chain-dotted lines are isodensity contours, each labelled by its value of (ρ_v/ρ_b). The very central parts of the rotation curves are obvious and not shown. Lower panel: for disc distribution of visible gas. Dashed lines are rotation curves, each labelled by its value of (σ/σ_b).

$v = V_r/(2kT_v/m_v)^{1/2}$ and ξ Flat and gently rising rotation curves arise naturally in this model. This can be seen qualitatively by noting that when the background gas is absent the visible matter has an Emden distribution, *i.e.* $\rho_v \sim r^{-2}, \partial\Psi_v/\partial r \sim r^{-1}$ and $r(\partial\psi_v/\partial r)$ constant; *i.e.* an exactly flat rotation curve results. The effect of the background is felt through its contribution to the potential $\psi_b \sim r^2$ which cuts ρ_v off sharply for larger, so that $\partial\psi_v/\partial r$ drops faster than r^{-1}, and the visible matter no longer produces a flat rotation curve by itself. But the sum of the gradients of the two potentials, one falling faster than r^{-1} and the other rising as r^{+1}, yields the requisite gently rising behaviour for the rotation curves. The rotation curves do not rise indefinitely, of course. For $r \gtrsim l_b$, the density of dark matter falls and consequently the rotation curve begins to fall gently. For typical velocity dispersion $v_b \sim 1500$ km s^{-1} and $\rho_b \sim 10^{-25}$ g cm^{-3} (see Section 3) l_b turns out to be ~ 150 kpc.

In order to show that the basic features of the rotation curves are independent of the detailed three-dimensional shape of the visible matter distribution, we have derived rotation curves also for disc distributions which are obtained by allowing the visible matter to collapse on to a plane perpendicular to the rotation axis. The projected surface density $\sigma(\varpi)$ as a function of the radial distance ϖ on the disc is simply

$$\sigma(\varpi) = 2\int_0^\infty \rho_v\left(\sqrt{\varpi^2 + z^2}\right) dz. \tag{8}$$

The potential of such a disc can be expressed in the computationally useful form

$$\Psi_d(\varpi) = -4G\int_0^\infty \sigma(\varpi')\left(\frac{\varpi'}{\varpi_>}\right) K\left(\frac{\varpi_<}{\varpi_>}\right) d\varpi' \tag{9}$$

Here $\varpi_>$ ($\varpi_<$) is the larger (smaller) of ϖ and ϖ', and K is the complete elliptic integral of the first kind. The rotation curves due to the potential of the disc are also shown in Fig. 1(a), (for various values of σ_0/σ_b, where $\sigma_b = 6\rho_b l_v$). It is seen that these are almost identical to those for a spherical distribution of visible matter.

2.1 *Comparison with Observed Rotation Curves*

Optically observed rotation curves of spiral galaxies are usually displayed in terms of radii expressed as fractions of the isophotal radius, R_{25} (= radius where surface brightness is 25 mag arcsec^{-2}). The analogous coordinate in our model is the fraction of the isodensity radius R_{ρ_v} which can be read off from the isodensity contours in Fig. 1(a). Fig. 1(b) shows the model rotation curves in terms of $R_{0\,25}$ (radius where $\rho_v/\rho_b = 0.25$), for different values of (ρ_0/ρ_b). Figs 1(c) and (d) show the optical rotation curves for Sb and Sc galaxies respectively, for different luminosities in each class (Rubin, Ford & Thonnard 1980, 1982). Galaxies with higher ρ_0 have higher luminosities: hence we arrange the galaxies by central density in the model curves and by luminosity in the observed ones. No attempt at fitting has been made; the only scaling done was that necessary to obtain the absolute velocity scale for the model rotation curves.

The similarity between theory and observation is clear, and becomes remarkable when individual peculiarities of galaxies are averaged out. as in the 'synthetic' rotation curves given by Rubin (1983), reproduced in Fig. 1(e). The dominant correlation

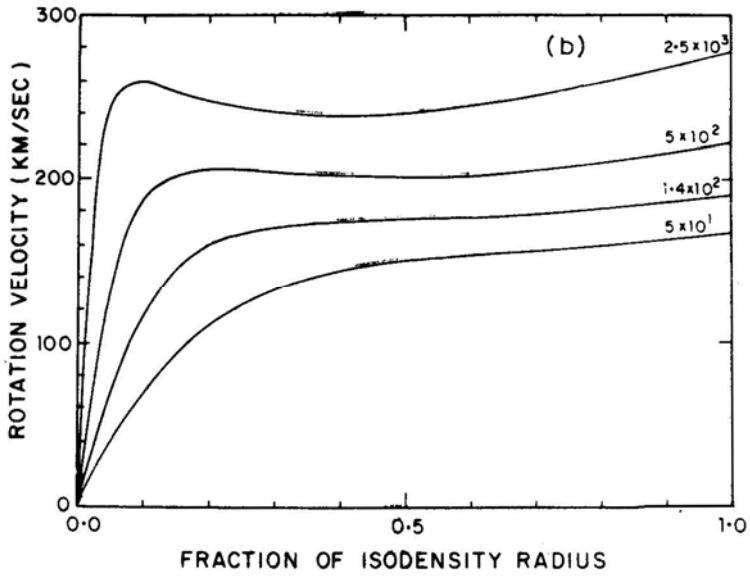

Figure 1(b). Model rotation curves in physical variables, arranged in order of increasing visible matter density. Each curve is labelled by its value of (ρ_0/ρ_b). The isodensity radius used is $R_{0\,25}$ where $(\rho_v/\rho_b)= 0.25$.

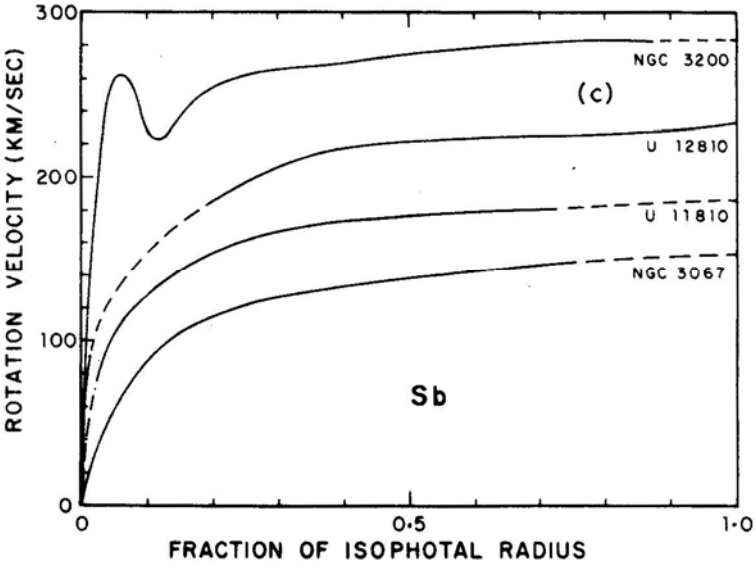

Figure 1(c). Observed rotation curves for Sb galaxies, arranged in order of increasing luminosity (after Rubin, Ford & Thonnard. 1982). The isophotal radius used is R_{25}, where the surface brightness is 25 mag arcsec^{-2}. Data not available in dashed parts of the curves.

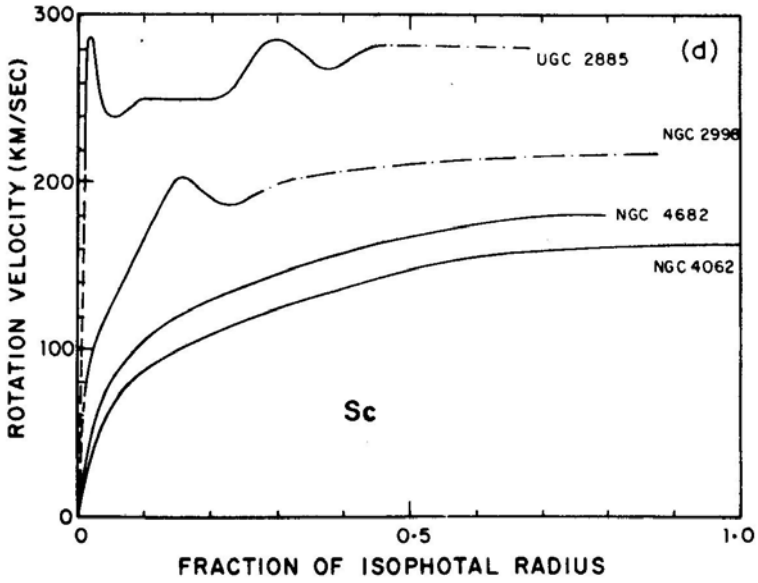

Figure 1(d). Observed rotation curves for Sc galaxies, arranged in the order of increasing luminosity (after Rubin, Ford & Thonnard 1980). Isophotal radius as before. In chain-dotted parts, wiggles containing regions of (unphysical) faster-than-Keplerian fall have been smoothed according to the prescription given by Rubin, Ford & Thonnard (1980).

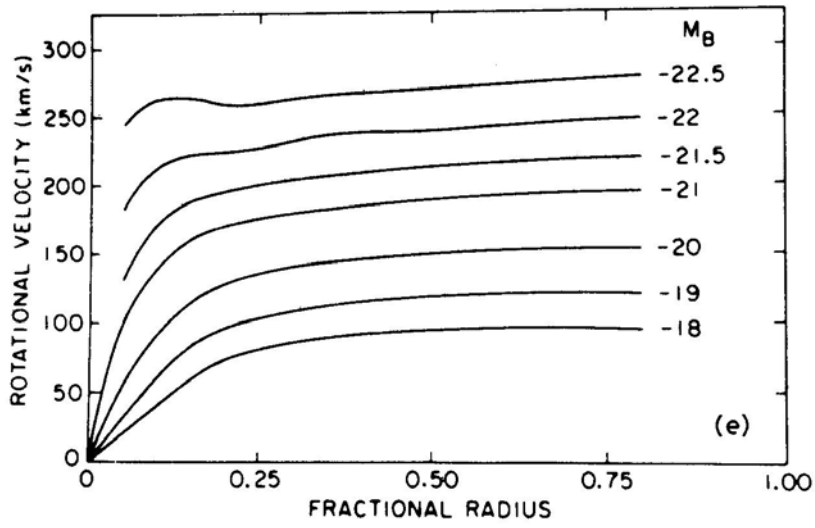

Figure 1(e). 'Synthetic' observed rotation curves for Sb galaxies, arranged in order of increasing luminosity, reproduced from Rubin (1983). The systematic progression in the form of the rotation curve with luminosity is remarkably similar to that in Fig. 1(b).

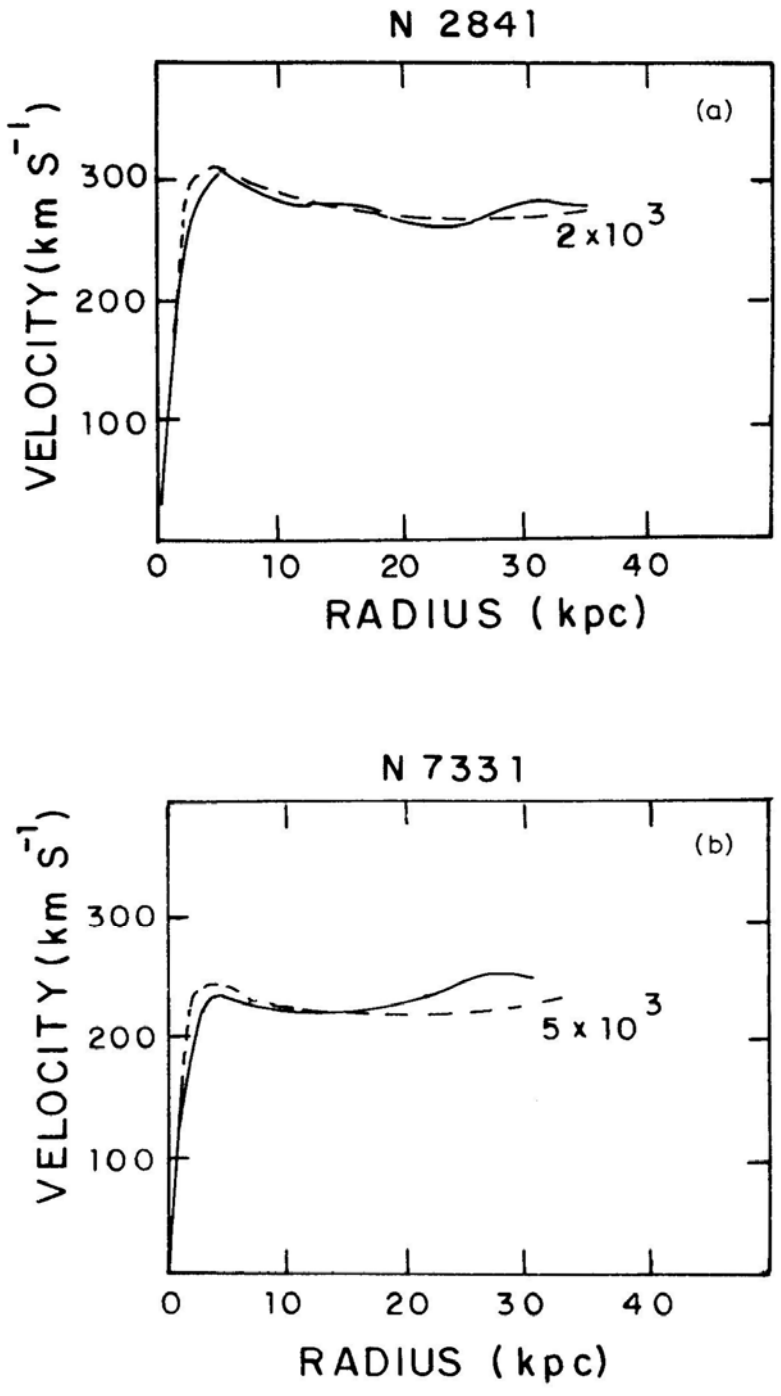

Figure 1(f). HI rotation curves for (a) NGC 2841 and (b) NGC 7331 (from Bosma 1981), compared with model rotation curves. Each model curve is labelled by its value of (ρ_0/ρ_b).

between the luminosity of the galaxy and the form of its rotation curve, so strong as to be proposed as a method of measuring luminosity (Rubin 1983), is almost identical in Figs 1(b) and (e), namely, that with *increasing* ρ_0 and luminosity, rotation velocities rise rapidly at a *smaller* fractional radius, attain *higher* maxima, and have a *longer,* nearly flat portion (Rubin, Ford & Thonnard 1982; Rubin 1983).

Hi rotation curves for spirals are often observed well beyond the optical radius, sometimes upto 2–5 times R_{25} (Bosma 1981; Wevers 1984). Our model curves agree with these observations. Two examples (NGC 2841 and 7331), using Bosma's (1981) observations, are shown in Fig. 1(f). Note that the values of the parameter (ρ_0 / ρ_b) used in these fits are exactly the same as those inferred from fitting the luminosity profiles of these two spirals (see below). This underscores the self-consistency of our model.

A preliminary study of the rotation curves of elliptical galaxies also shows agreement with our model. Detailed results will be presented elsewhere.

2.2 *Luminosity Profiles of Spirals*

A considerable body of data on the luminosity profiles of spiral galaxies has been collected (Kormendy 1977; van der Kruit 1979; Burstein 1979; Boroson 1981; van der Kruit & Searle 1981, 1982). These profiles are usually analyzed in terms of exponential

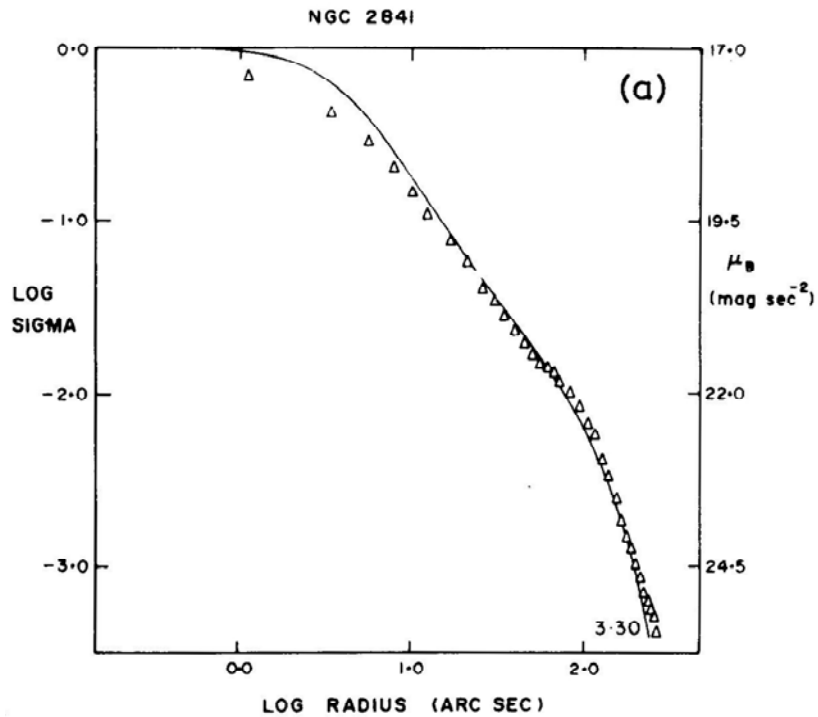

Figure 2. Observed luminosity profiles of spirals compared with model profiles. Triangles are data points for (a) NGC 2841 (from Boroson 1981), (b) NGC 7331 (from Boroson 1981), and (c) NGC 4565 (from Hama be *et al.* 1980). Solid lines are model profiles, each labelled by its value Of $\log_{10}(\rho_0/\rho_b)$.

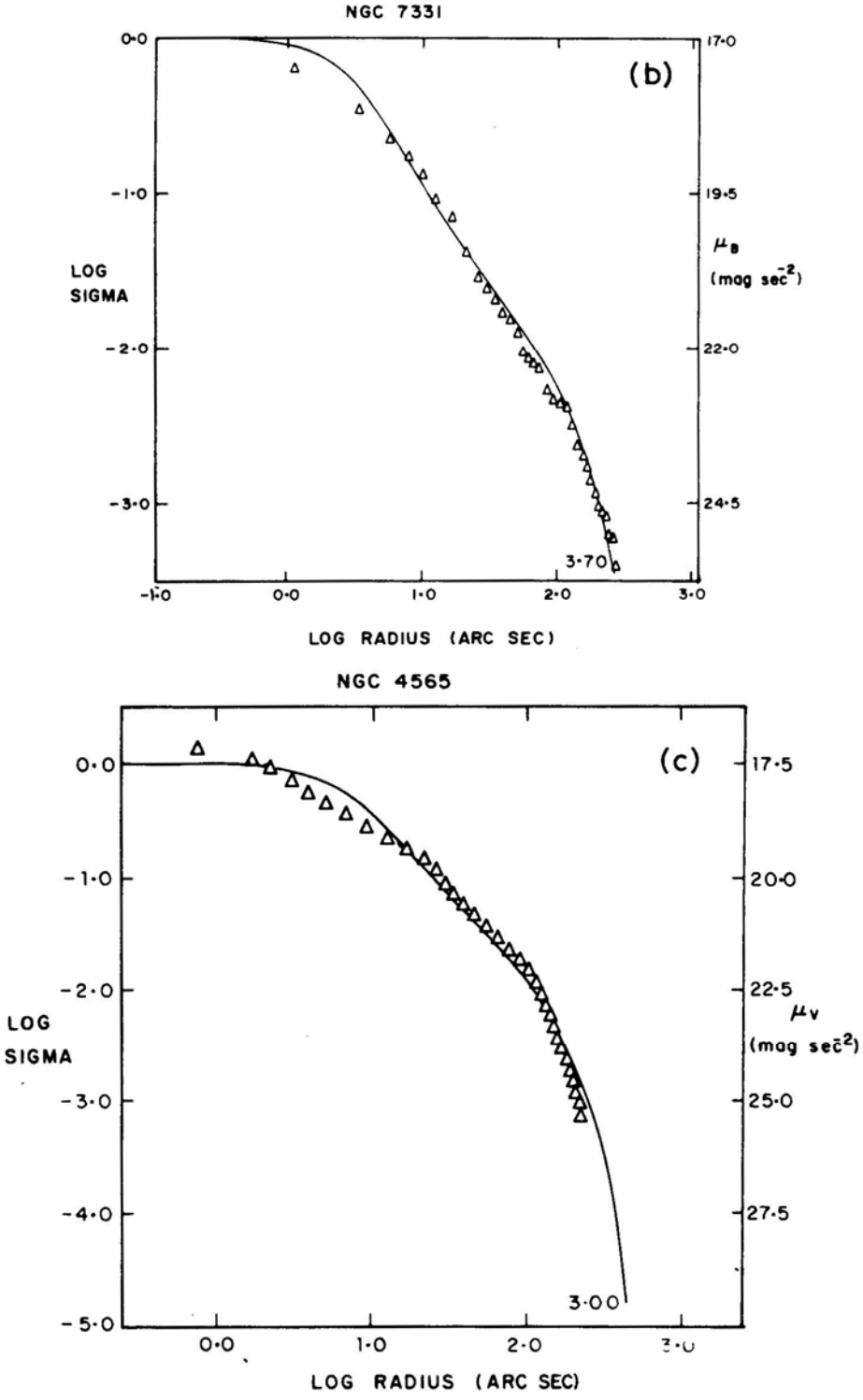

Figure 2. Continued.

discs and $r^{1/4}$ bulges, although it is known that neither functional form has a basis in physics (Boroson 1981; Seiden, Schulman & Elmegreen 1984). We find that our model gives an adequate description of these profiles. Three examples (NGC 2841, 7331 and 4565) of spirals of various sizes and bulge/disc ratios are shown in Fig. 2; more will be given elsewhere (Cowsik & Ghosh 1984). This agreement provides evidence that the distribution of visible matter in spirals is well-approximated by a Maxwellian (see above), and thus provides a physical basis for understanding the shape of luminosity profiles.

3. Discussion

This relatively simple model of a collisionless stellar distribution embedded in a background gas fits so many observations, such as the main features of the rotation curves of spirals (*e.g.* their ubiquitous flatness, gentle increase at large distances and characteristic change in shape with increasing luminosity) and ellipticals, and their luminosity profiles, that it seems worthwhile to consider the nature and composition of the invisible background gas. Quite some time ago, Ostriker & Peebles (1973) guessed at the existence of a massive halo around the Galaxy from the requirement of dynamical stability of the spirals. Many candidates, such as black holes, 'Jupiters', dust, massive neutrinos and exotic particles envisaged in GUTs and SUSYGUTs, have been suggested and their relative merits as the constituents of the 'dark matter' have been assessed (Peebles 1979). For example, the suggestion that 'Jupiters' are the constituent would come into conflict with the distribution of the masses of stars, which shows a flattening even at 0.5 $M_\odot$, so that the initial mass function will have to be bimodal. Further, if the haloes are made of baryonic matter in any form, then the average baryonic matter density in the universe would exceed 10^{-30} g cm^{-3} and the observed abundances of ^{2}D and ^{4}He would be in conflict with the expected abundances from primordial nucleosynthesis. Therefore, it is natural that the explanation for the dark matter has been sought in terms of some weakly interacting non-baryonic relic from the big bang.

The present study of the rotation curves places further constraints on the nature of the dark matter. There are two basic points: First, the density of the background needed to explain the observations is roughly equal to the density of clusters and groups estimated from dynamical considerations (Peebles 1979; Gott & Turner 1977). The large dispersion in velocities of galaxies in clusters (~ 1500 km s^{-1}) naturally fits in with the requirements of the model for the background gas. The minimum mass, m, of the particle which would condense on such a large scale can be estimated from the formula (Cowsik & McClelland 1973).

$$m^8 \gtrsim -\frac{6h^6}{G^3 R_c^3 M_c \alpha^2} . \tag{10}$$

Here, α is the fraction of the total available phase space up to the edge of the cluster that is occupied by the neutrinos. We estimate the filling fraction $\alpha \propto (3v_v/c)^{3/2} \simeq 10^{-3}$ Taking the typical mass of a cluster to be ~ 3×10^{15} $M_\odot$ and a core radius of ~ 0.1 Mpc one finds $m \gtrsim 10$ eV. Second, the systematic progression in the form of the rotation curves of the spirals with their luminosity demands that the density of background be sensibly independent of the size and mass of the spiral galaxy. It would

be difficult to accommodate this requirement in a scenario where more massive particles are involved, be they photinos or gravitinos (Cabbibo, Farrar & Maiani 1981; Pagels & Primack 1981) on the one hand, or black holes or Jupiters on the other, since these would tend to cluster on much smaller scales comparable to that of the underlying galaxies.

In summary, the systematics of the rotation curves of the galaxies can be explained on the basis of a simple model in which a Maxwellian gas is embedded in a background gas with a much larger dispersion in velocities. On the basis of these systematics, it appears that collisionless particles with $m \sim 10$ eV and $M_{J\max} \sim 3 \times 10^{15}\ M_{\odot}$ (Bond, Efstathiou & Silk 1980; Wasserman 1981; Doroshkevich *et al.* 1980; Sato & Takahara 1980), which condense typically on the dimensions of galactic clusters (Cowsik & McClelland 1973; Schramm & Steigman 1980) make up the background gas cloud needed in the model. Among the known particles, only the neutrinos could have the required mass and the weak interactions demanded of the constituents of the dark matter in the universe.

References

Bahcall, J. N., Schmidt, M., Soneira, R. M. 1982, *Astrophys. J.*, **258,** L23.
Binney, J. 1982a, *Mon. Not. R. astr. Soc.*, **200,** 951.
Binney, J. 1982b, *A. Rev. Astr. Astrophys.*, **20,** 399.
Bond, J. R., Efstathiou, G., Silk, J. 1980, *Phys. Rev. Lett.*, **45,** 1980.
Boroson, T. 1981, *Astrophys. J. Suppl.*, **46,** 177.
Bosma, A. 1978, *PhD Thesis,* Groningen Univ.
Bosma, A. 1981, *Astr. J.*, **86,** 1825.
Burstein, D. 1979, *Astrophys. J. Suppl.*, **41,** 435.
Burstein, D., Rubin, V. C., Thonnard, N., Ford W. K. Jr. 1982, *Astrophys. J.*, **253,** 70.
Cabbibo, N., Farrar, G. R., Maiani, L. 1981, *Phys. Lett.*, **105B**, 155.
Chandrasekhar, S. 1939, *An Introduction to the Study of Stellar Structure,* Univ. Chicago Press, p. . 156.
Chandrasekhar, S. 1942, *Principles of Stellar Dynamics,* Dover, pp. 48–85.
Cowsik, R. 1984, *TIFR Preprint,* TIFR-CRSP-84-16.
Cowsik, R., McClelland, J. 1973, *Astrophys. J.*, **180,** 7.
Doroshkevich, A. G. *et al.* 1980, *Ann. NY Acad. Sci.*, **375,** 32.
Einasto, J. 1970, *Teated Tartu Obs.*, **26,** 1.
Emden, R. 1907, *Gaskugeln*, Leipzig, Teubner.
Gott, J. R., Turner, E. L. 1977, *Astrophys. J.*, **213,** 309.
Hamabe, M., Kodaira, K., Okamura, S., Takase, B. 1980, *Publ. astr. Soc. Japan*, **32,** 197.
Jeans, J. H. 1915, *Mon. Not. R. astr. Soc.*, **76,** 71.
Kormendy, J. 1977, *Astrophys. J.*, **217,** 406.
Lynden-Bell, D. 1962, *Mon. Not. R. astr. Soc.*, **124,** 95.
Ostriker, J. P., Caldwell, J. A. R. 1979, in *IAU Symp.* 84: *The Large-Scale Characteristics of the Galaxy,* Ed. W. B. Burton, D. Reidel, Dordrecht, p. 441.
Ostriker, J. P., Peebles, P. J. E. 1973, *Astrophys. J.*, **186,** 467.
Pagels, H., Primack, J. R. 1981, *Phys. Rev. Lett.*, **48,** 223.
Peebles, P. J. E. 1979, in *Physical Cosmology,* Eds R. Balian, J. Audouze & D. N. Schramm, North-Holland, Amsterdam, p. 216.
Rubin, V. C. 1979, in *1 AU Symp.* 84: *The Large-Scale Characteristics of the Galaxy,* Ed. W. B. Burton, D. Reidel, Dordrecht, p. 211.
Rubin, V. C. 1983, in *Kinematics, Dynamics and Structure of the Milky Way,* Ed. W. L. Shuter, Reidel, Dordrecht, p. 379.
Rubin, V. C., Ford, W. K. Jr., Thonnard, N. 1980, *Astrophys. J.*, **238,** 471.

Rubin, V. C., Ford, W. K. Jr., Thonnard, N. 1982, *Astrophys. J.*, **261,** 439.
Sato, H., Takahara, F. 1980, *Prog. Theor. Phys.*, **64,** 2029.
Schramm, D. N., Steigman, G. 1981, *Astrophys. J.*, **243,** 1.
Seiden, P. E., Schulman, L. S., Elmegreen, B. G. 1984, *Astrophys. J.*, **282,** 95.
van der Kruit, P. C. 1979, *Astr. Astrophys. Suppl*., **38,** 15.
van der Kruit, P. C. 1982, *Astr. Astrophys*., **110,** 61.
van der Kruit, P. C., Searle, L. 1981, *Astr. Astrophys.*, **95,** 105.
Wasserman, I. 1981, *Astrophys. J.*, **248,** 1.
Wevers, B. M. H. R. 1984, *PhD Thesis*, Groningen Univ.

J. Astrophys. Astr. (1986) **7,** 29–38

Dark Matter—Systematics of its Distribution

R. Cowsik & M. Vasanthi *Tata Institute of Fundamental Research, Homi Bhabha Road, Colaba, Bombay 400005*

Received 1985 April 4; accepted 1985 October 4

Abstract. The dynamical masses of dwarf-spheroidals, spiral and elliptical galaxies, dwarf irregular binaries, groups of galaxies and clusters are shown to lie in a band about the $M \sim \rho R^3$ *line.* The value of ρ is approximately the same as that estimated for unseen matter in the solar neighbourhood. The clusters themselves lie about the $M \sim R^{-3}$ *line* derived for a self-gravitating neutrino gas; their masses are distributed around the maximum Jeans-mass, M_{Jmax}. corresponding to $m_\nu \simeq 10$ eV in an expanding universe. The present-day length scales of clusters and the dispersion in the velocities observed within them are understood in terms of a 100-fold expansion subsequent to the initial growth of the fluctuations at M_{Jmax}. These systematics on the *R-M* plane imply that the initial condensations in the expanding universe are on the scale of the rich clusters of galaxies, these condensations were triggered dominantly by the gravitation of the neutrinos and the constant density of all systems arises naturally due to the embedding of these systems in the large scale neutrino condensations. If the neutrino density falls off as r^{-2} beyond the cluster edge till the distributions from different clusters overlap, then the mean density of the neutrinos approximately equals the closure density of the universe.

Key words: galaxies, dark matter—galaxies, formation—neutrino, mass

1. Motivation

The study of the nature and distribution of dark matter which dominates the gravitational dynamics of large astronomical systems and the universe itself has received much attention of both theorists and observational astronomers in recent years. The primordial nucleosynthesis in the conventional big-bang models shows that this unseen matter, if baryonic, will yield too little deuterium (Peebles 1966; Yang *et al.* 1979; Olive & Turner 1981; Olive *et al.* 1981; however, see Stecker 1980; Rana 1982). Also high baryonic densities will cause distortions in the relic blackbody radiation to unacceptable levels (Silk 1967; Silk & Wilson 1981; Fall 1980) and pose insurmountable difficulties in theories of formation of galaxies. These considerations rule out the possibility that the unseen matter is in the form of black holes or condensates of cold matter like 'Jupiters' which might have arisen from first generation stars. The alternate hypotheses which have been considered are nonbaryonic relics of the big-bang such as massive neutrinos, gravitinos, photinos, monopoles, primordial monopoles, *etc.*

(Cowsik & McClelland 1972, 1973; Page's & Primack 1982; Olive & Turner 1982; Cabibbo, Farrar & Maiani 1981; Peebles 1982; Sikivie 1982).

Do the observations favour one or the other of these hypotheses? What is the typical scale of the initial condensations? Did the small objects typically of the size of globular clusters form first and later grew by hierarchical clustering (Peebles 1984) into the largest astronomical systems? Or did the large-scale condensations occur first and the density perturbations grew inside these to generate the smaller units? (See, Zeldovich 1970; Cowsik & McClelland 1973; Bond; Efstathiou & Silk 1980; Sato & Takahara 1980; Doroshkevich *et al.* 1980; Wasserman 1981.)

We have reviewed critically the relevant observations which are available and our analysis of their systematics suggests and supports the latter scenario. In our view the present day universe is made up of neutrino condensations typically of the dimensions of the clusters. Beyond the cluster edge the density falls off in such a way as to provide the closure density for the universe. The visible baryonic matter constituting less than 10 per cent of the mass is embedded in such a background and through its kinematic motions delineates the gravitational potential of the inhomogeneous neutrino background.

2. Dynamical masses of astronomical systems

The first evidence that there exists some form of 'invisible matter' dominating the dynamics of extended astronomical systems was obtained about half a century ago by Zwicky (1933) and Smith (1936) studying the Coma and Virgo clusters of galaxies. The point was that the dynamical mass of systems estimated from the dispersion in the velocities of the constituent elements:

$$M_d \simeq \langle v^2 \rangle r/G \tag{1}$$

exceeded substantially the mass estimated from visible luminosity. Since then enormous amount of careful observations has gone on not merely in the field of optical astronomy but in the radio (21 cm), infrared, UV and X-ray bands which has broadened the implications of the title 'Invisible Matter' and has shown that the dynamical effects of this unseen component is felt almost ubiquitously in all large astronomical systems. Detailed reviews on this subject are available in literature (Peebles 1979; Bahcall 1977; Faber & Gallagher 1979) and we summarise below the relevant information. Our studies of the systematics differ in an important way from earlier studies in that we consider the dependence of the dynamical mass on radius rather than that of mass to luminosity (M/L) ratio. Since the mass is dominated by the invisible component and the luminosity by the baryons, a one-to-one correspondence does not exist between them and taking ratios introduces large dispersion in their distribution; also the ratio is less amenable to direct interpretation.

2.1 *Clusters of Galaxies*

Peebles (1965) has reviewed the subtleties in the application of Equation (1) to astronomical systems in estimating their dynamical or virial masses.

Detailed study of the Coma cluster (Rood *et al.* 1972; Kent & Gunn 1982) and parameters of seven other Abell clusters are available (Dressler 1978). In several cases

the authors have quoted only the M/L ratios derived from the dispersion in the velocities and effective radii derived from fits to the profiles of luminosity; since the net luminosity is independently known, the dynamical masses have been calculated in a straightforward manner. These are plotted in Fig. 1 (filled circles).

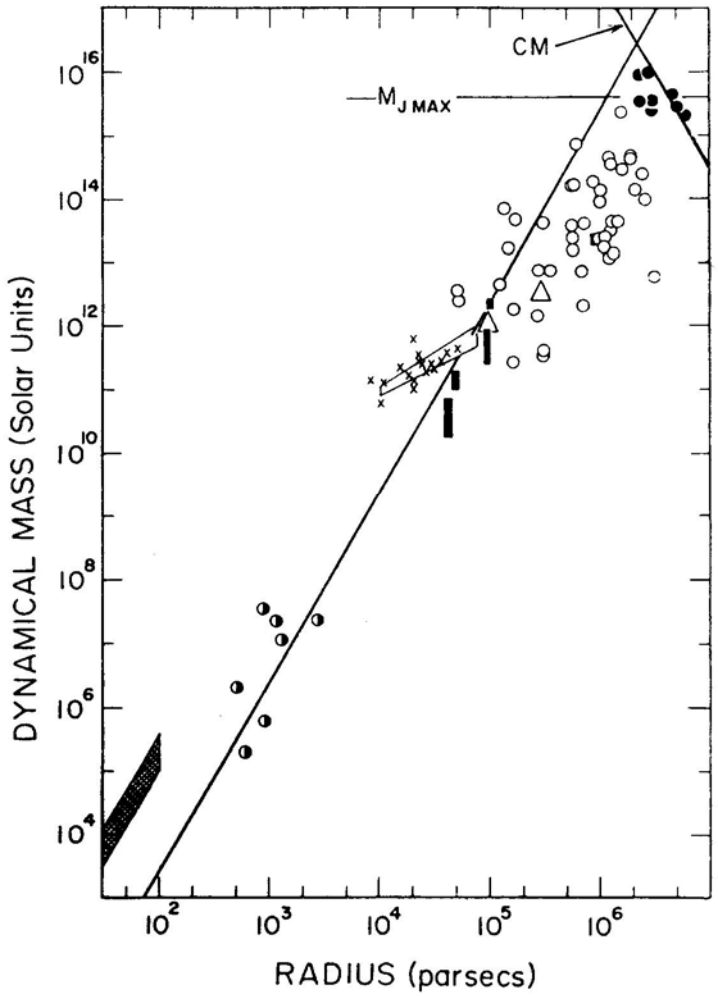

Figure 1. The dynamical masses of rich clusters of galaxies (●), groups of galaxies (○; Δ), dwarf irregular binaries (▮), spiral galaxies (×, ▱) and dwarf spheroidals (◑) are shown against the visible radius. The hatched region in the lower left hand corner is the mass of a sphere with a given radius and the density estimated from Oort-parameters in the solar neighbourhood. The dark solid line along the diagonal is the $M \sim \rho R^3$ line for $\rho \simeq 10^{-3}\ M_\odot/\mathrm{pc}^3 \simeq 6 \times 10^{-26}$ g cm^{-3}; it passes through the density estimated at the edge of our Galaxy from the rotation curve and through the M 31 group. The line marked CM is based on the dynamics of a self-gravitating neutrino cloud and is adopted from Cowsik & McClelland (1973) for $m_\nu \simeq 10\ \mathrm{eV}/c^2$. The horizontal line labelled M_{Jmax} is the maximum Jeans mass of neutrinos of mass $10\mathrm{eV}/c^2$.

2.2 *Groups of Galaxies*

A rather comprehensive and systematic study of groups of galaxies by Rood & Dickel (1978) yields data on 39 groups (Sandage & Tammann 1975; de Vaucouleurs 1975; Turner & Gott 1976) containing two to 238 members. Using Equation (1) the dynamical mass was estimated for all but two of these and the results are shown in Fig. 1 (open circles). The two which have been left out have identification numbers 40 and 91 and have 'crossing times' as long as the age of the universe. Five of these lie in the region populated by the clusters listed above but one is not shown because of overlap. We have also included data on two groups associated with M 31 and M 101 whose dynamical masses were calculated using the projected-mass method by Bahcall & Tremaine (1981).

2.3 *Binary Pairs of Dwarf Irregular Galaxies*

Lake & Schommer (1984) have studied the dynamical mass-to-light ratios of 9 binaries from the catalogues of DDO dwarfs (van den Bergh 1959; Nilson 1973) with velocities appearing in the compendium by Huchtmeier *et a!.* (1983). Out of these we select six pairs with the masses determined accurate to better than 50 per cent and with crossing times small compared to the age of the universe. The central values of the mass are uncertain typically by a factor of 2 due to projection effects and the unknown eccentricity of the orbit.

2.4 *Spiral Galaxies*

Very important insights into the structure and dynamics of the galaxies have come from systematic and meticulous observations of their rotation curves (Rubin 1979; Rubin *et al.* 1980, 1982; Rubin, Thonnard & Ford 1982; Bosma 1978). A universal feature of all rotation curves is that at large galactocentric distances they are either flat or faintly rising, and in fact there is no galaxy whose rotation curve falls. Since the rotational velocities v^2 are proportional to $GM(r)/r$, these observations imply the presence of much unseen mass up to large distances from the centre of the spirals. In Fig. 1 we have plotted a random selection of the masses of spirals measured up to the termini of the observations. For our own Galaxy we have shown how the dynamical mass increases with radius (Peebles 1979; Faber & Gallagher 1979). This progressive increase in the dynamical mass with radius is a characteristic feature of all spirals and constitutes an important clue as to the nature of the dark matter (Cowsik & Ghosh 1984a).

2.5 *Dwarf Spheroidal Galaxies*

There are seven dwarf spheroidals (DS) which have been studied recently (Aaronson 1983; Lin & Faber 1983; Faber & Lin 1983). It has been possible to measure the velocities of a few of the constituent stars in the Draco and Ursa Minor systems. These measurements as well as criteria for tidal stability have been used to estimate the dynamical masses of these objects. These are the smallest astronomical objects that bear

evidence to the presence of gravitating dark matter in them. These have typical radii of ~ 1 kpc and masses of ~ 10^7 $M_\odot$. We have discussed elsewhere in some detail the luminosity profiles of these spheroidals and the nature of dark matter in these systems (Cowsik 1986; Cowsik & Ghosh 1986a). Even now, we would like to remark that the mass determination by Lin & Faber are very tentative and are subject to change. In Fig. 1 we plot the masses as published by the authors cited here. Our own mass estimates (Cowsik & Ghosh 1986b) differ by about a factor of 2 but do not generally change the basic picture presented here.)

2.6 *Oort-Bahcall Limits on Unseen Matter near the Sun*

The very early work of Kapteyn (1922) in estimating the total matter near the Sun has been put on a much firmer footing by Oort (1932, 1960), and more recently by Bahcall (1984a, b) who solves the combined Poisson-Boltzmann equation for the gravitational potential of the Galaxy modelled in terms of several isothermal 1disc components in the presence of a massive unseen halo. Fitting the distribution of F stars and K-giants Bahcall obtains definitive constraints on the matter distribution, and estimates on the total matter density and the column density near the Sun which will be called the Oort–Bahcall limit. From this we might subtract out the observed components like the stars on the main sequence, giants, white dwarfs, interstellar gas and dust, *etc*., to obtain an estimate of the mean density for the unseen matter near the Sun; this is in the range 0.09 $M_\odot$ pc^{-3} to 0.03 $M_\odot$ pc^{-3}. In Fig. 1 we plot a mass equal to (4/3) $\pi R^3 \rho_{\rm unseen}$ (hatched region on the lower left-hand corner).

3. Discussion of the systematics

The most striking aspect of the relation between the dynamical masses of the astronomical systems and their radii shown in Fig. 1 is the strong concentration along the $M \sim R^3$ line. The solid line $M \sim 2.5 \times 10^6\ M_\odot\ (R/\mathrm{kpc})^3$ is drawn to fit the dynamical mass distribution near our Galaxy best. Notice that it passes through the dwarf spheroidals, the galactic mass up to ~ 50 kpc and the M 31 group shown as Δ. This correlation, which extends from the lightest of the dwarf spheroidals (Leo II) with a mass ~ 10^5 $M_\odot$ up to the rich clusters of galaxies with masses of ~ 10^{16} $M_\odot$, indicates that the density is roughly constant implying a common dynamical basis for all these varied systems. A systematic interpretation of this correlation is presented below.

3.1 *The Rich Clusters*

These have dynamical masses in the range 10^{15}–$10^{16} M_\odot$ and have limiting radii extending from 2 to 6 Mpc. The typical radii of cores of these clusters are in the range 0.1-0.3 Mpc, *i.e*., a factor of about twenty smaller:

$$R_{\rm L} \simeq 20\, R_{\rm c}. \tag{2}$$

For understanding their properties we start with our early analysis in terms of a self-gravitating cloud of neutrinos (Cowsik & McClelland 1973). Let us define a parameter α which represents the fraction of the available phase space filled by neutrinos on the

average across the whole cluster. Then following our earlier analysis we find

$$m_\nu^8 = \frac{91.3\hbar^6}{G^3 g^2 \alpha^2 R_c^3 M_c}. \tag{3}$$

One should not confuse the parameter α with the actual phase space density, but it represents its average taken up to a boundary defined by the dynamical constraints relevant to the system. The parameter g has the usual interpretation as the multiplicity of occupancy possible in each level, every flavour, particle-antiparticle state, and helicity contributing to it.

$$g = 2\, g_{\text{flavour}} \cdot g_{\text{helicity}}. \tag{4}$$

We can estimate a in the following way. As noted earlier, in our picture the neutrinos are the dominant constituents of the universe and the calculations of their Jeans-mass (see *e.g.* Bond, Efstathiou & Silk 1980) show that it goes through a maximum M_{Jmax} in the expanding universe when neutrinos become quasi-relativistic. In other words, at the time of formation of the initial condensations

$$V_\nu \,(\text{at } M_{\text{Jmax}}) \sim c/2. \tag{5}$$

The redshift $(1 + z_\nu)$ at which the neutrinos attain quasi-relativistic velocity is easily estimated from the fact that their momenta also scale the same way as that of the photons in an expanding universe:

$$(1 + z_\nu) \simeq 1000\, m_\nu\, (\text{eV}/c^2). \tag{6}$$

At this epoch the energy density in the thermal radiation is still comparable to that of neutrinos

$$\frac{\rho_\gamma}{\rho_\nu} \simeq \frac{(1+z_\nu)^4\, \rho_\gamma(0)}{(1+z_\nu)^3\, n_\nu(0)\, m_\nu c^2} \simeq 2. \tag{7}$$

As the universe expands, the radiation temperature drops and the radiation which is trapped in the initial condensation diffuses out of it. Thus the net gravitational binding drops and the condensate expands. The complete dynamics of the condensate is quite complicated (Gunn & Gott 1972) and is not fully understood; we fix here the nature of the expansion empirically. Now note that the present-day velocity dispersion in the cluster is 1000 km s^{-1} so that if the expansion had gone on adiabatically by a factor $s \simeq 100$ the quasi-relativistic neutrinos would now have this V_{rms}. Now, using the subscript i to designate the initial state,

$$\alpha_i = \frac{M_{\text{Jmax}}}{m_\nu g}\left(\frac{p^3_{(\text{max})i} R^3_{ci}}{h^3}\right)^{-1} \simeq \frac{1}{2}. \tag{8}$$

The value of $\alpha_i \simeq 1/2$ follows from the very definition M_J and from the assertion that the neutrinos were generated in thermal equilibrium (Tremaine & Gunn 1979). Now since the number of neutrinos in the condensate does not change during the expansion the present day value of $\alpha = \alpha_f$ is given by

$$\frac{\alpha_f}{\alpha_i} = \frac{R^3_{ci}\, v^3_{(\text{max})i}}{R^3_{cf}\, v^3_{(\text{max})f}} \simeq \frac{R^3_{ci}}{R^3_{cf}} \cdot \frac{\{G(M_{\text{Jmax}} + M_{\text{rad}})/R_{ci}\}^{3/2}}{\{G M_{\text{Jmax}}/R_{cf}\}^{3/2}}.$$

$$\simeq \left(\frac{2R_{ci}}{R_{cf}}\right)^{3/2}. \tag{9}$$

Using $s \simeq 100$ and $M_{\rm rad} \sim M_{\rm Jmax}$ as estimated in Equation (7), the present value of α turns out to be

$$\alpha_{\rm f} \sim 3 \times 10^{-3}\ \alpha_{\rm i} \simeq 1.5 \times 10^{-3}. \tag{10}$$

We adopt this value of α in Equation (3) and substitute Equation (2) in it and get

$$M_{\rm c} \simeq 1.5 \text{ x } 10^{35}\, M_{\odot}\, (R_{\rm L}/{\rm kpc})^{-3}\, (m_{\nu}({\rm eV})/c^2)^{-8}. \tag{11}$$

This relation between the mass of the cluster $M_{\rm c}$ and its limiting radius $R_{\rm L}$ is shown in Fig. 1 for $m_{\nu} \simeq 10$ eV $/c^2$, named CM. It would appear therefore that m_{ν} should be about this to fit the masses of the clusters. Even though many of the observations, and the constants that appear in the theoretical analysis, are somewhat uncertain, the eighth power on m_{ν} in Equations (3) and (11) does not allow much spread in the values of m_{ν}. Our best estimate on the allowed range of the mass of the neutrino needed to fit the cluster masses is

$$\begin{aligned} &8 \text{ eV } /c^2 < m < 25 \text{ eV } /c^2 \\ &m_{\nu} \text{ (best fit)} \simeq 10 \text{ eV } /c^2. \end{aligned} \tag{12}$$

Let us now return to the estimates of the maximum Jeans-mass (Bond, Efstathiou & Silk 1980; Sato & Takahara 1980; Klinkhamer & Norman 1981; Wasserman 1981) $M_{\rm Jmax}$ and the value of the Jeans-length $L_{\rm J}$ at that epoch

$$L_{\rm J} \simeq \frac{c}{\left[12\pi G\left(\dfrac{\rho_{\gamma}(0)}{c^2}\right)(1+z)^4\right]^{1/2}} \simeq \frac{300 \text{ kpc}}{(m_{\nu}({\rm eV})/c^2)^2}. \tag{13}$$

If we take $m_{\nu} \sim 10$ eV $/c^2$, $L_{\rm J} \sim 2$ kpc at the time of the initial condensation and the predicted size of the radius of the core today is $R_{\rm c} \sim sL_{\rm J} \sim 100$ kpc in reasonable agreement. The total mass of all the neutrinos contained in a volume of radius $L_{\rm J}$ is

$$M_{\rm Jmax} \simeq \frac{4\pi}{3} L_{\rm J}^3 m_{\nu} \left[n_{\nu}(0) + n_{\bar{\nu}}(0)\right](1+z_{\nu})^3 \simeq \frac{1.3 \times 10^{18} M_{\odot}}{(m_{\nu}({\rm eV})/c^2)^2}. \tag{14}$$

$M_{\rm Jmax}$ is shown in Fig. 1, again for $m_{\nu} \simeq 10$ eV $/c^2$, as a horizontal line. One again sees that the observed masses of the clusters are in accord with this estimate (10^{16}–$3 \times 10^{15}\, M_{\odot}$).

The typical distance between clusters today, expected from these considerations, is given by

$$D_{\nu} \sim (1+z_{\nu})\, L_{\rm J} \sim \frac{3 \times 10^5 \text{ kpc}}{(m_{\nu}({\rm eV})/c^2)}. \tag{15}$$

This gives $D \sim 30$ Mpc for $m_{\nu} \sim 10$ eV $/c^2$, in qualitative agreement with observed sizes of voids. Numerical simulations of the process of neutrino condensation supporting the analytic study have been performed by Bond, Szalay & White (1983) and Frenk, White & Davis (1983). It is interesting to note that the choice $m_{\nu} \sim 10$ eV provides the closure density for the universe. In order to obtain in this picture the requisite mean number density of neutrinos, their density should fall off roughly as r^{-2} beyond the visible edge of the clusters of galaxies, at least statistically, till the contributions from different clusters overlap at a distance of ~ 15 Mpc. This requirement of a fall in density as r^{-2} conforms exactly with that of the asymptotic behaviour of an Emden sphere.

In concluding this sub-section we have to explain why we have called the constituents of dark matter as neutrinos, when any fermion with the mass in the allowed range of

Equation (12) would do. Besides many others, we are motivated by the fact that the coupling of these particles to ordinary matter and to each other should be considerably weaker than electromagnetic, but should not be too much weaker than the Fermi-coupling, lest the decoupling from thermodynamic equilibrium be too early and their number density become too low.

3.2 *The Groups*

The fluctuations in the density of visible matter will now grow inside the neutrino condensates described in the previous section. It is to be noted that even though the scale factor of the universe changes by $(1 + z_v) \sim 10^4$ since the formation of the condensate, the neutrino cloud itself expands only by a factor of ~ 100 so that the growth in the fluctuations in the density of visible matter will proceed with greater relative rapidity resulting in the formation of galaxies. Thus most of the galaxies are expected to be embedded in the neutrino clouds and only very rarely will they find themselves in the voids in between the clouds. The dynamics of groups of galaxies, in so far as their mean density is small compared with that of the neutrino cloud, will clearly reveal the gravitating effects of the neutrinos. In other words, the dynamical masses calculated using Equation (1) will be $M_d \sim (4\pi/3)r^3\rho_v + M_v$ where M_v is the visible mass interior to r. It is clear from Fig. 1 that the mean density of groups ($\sim 2 \times 10^{-5}\ M_\odot\ \mathrm{pc}^{-3}$) is the same as that of the rich clusters but the dispersion in the densities is somewhat larger. This is to be expected since the radial density distribution of neutrinos in a condensate is not uniform but has a maximum at the centre, falls gently up to the core radius R_c, beyond which it steepens rapidly. Thus the mean density of the clusters is bound between the central density and that at large radius, but the sub-units reveal the effects of the density of neutrinos at the radius of their location.

Of special interest is the M 31 group (shown as A) with a dynamical mass of $\sim 10^{12}\ M_\odot$ and a radius of $\sim 10^5$ pc (Bahcall & Tremaine 1981) since this would give an estimate of the density in the neighbourhood of our Galaxy. This is about $10^{-3}\ M_\odot \mathrm{pc}^{-3} \sim 6 \times 10^{-26}$ g cm^{-3}**.** This value is substantiated by studying the rotation curve of our Galaxy as well as the luminosity profiles of the dwarf spheroidals as we will see in the next section. The six dwarf irregular binaries which are shown as filled oblong rectangles also yield approximately the same density.

3.3 *Spirals and Dwarf Spheroidals*

There is one essential difference between these objects and the groups we discussed in the previous section. The mass density in the central regions of these is dominated by stars rather than neutrinos. But as we move to large radii, the stellar density drops progressively and neutrinos become dominant so that mass determined only on the largest scales will bear evidence to the presence of the neutrinos. We have studied elsewhere the dynamically self-consistent distribution of the stars in these systems embedded in a large cloud of neutrinos (Cowsik & Ghosh 1986a, b). This self-consistent distribution reproduces correctly the luminosity profiles of dwarf spheroidals. Also, the flat rotation curves of the spiral galaxies arises naturally in this picture when the potentials of both the stars and neutrinos are taken into account.

4. Conclusion

From these systematics we conclude that neutrino condensates with $M \sim 10^{16}\ M_{\odot}$ were the first objects to be formed in the universe at a redshift of $\sim 10^4$. Subsequent to formation they expanded much slower than rest of the universe and fluctuations in the density of baryonic matter grew effectively with the formation of the galaxies. The dynamics of these galaxies and that of the stars within galaxies are sensitive to the background gas. Assuming that neutrinos have a rest mass of $\sim 10\ \mathrm{eV}/c^2$ the details of the dynamical motions of the galaxies and the stars can be understood quantitatively. This picture is to be contrasted with the hierarchical picture where the large clusters are built up from much smaller objects (*e.g*. Peebles 1983). An observational test of this scenario appears possible as in this picture the intensity and spatial correlations of the redshifted 21 cm line will be different from that discussed by Sunyaev & Zeldovich (1975) and by Hogan & Rees (1979). Also, further studies on the expected fluctuation spectrum of the thermal microwave background based on this picture are warranted.

Acknowledgements

We wish to thank Drs P. Ghosh and T. Padmanabhan for useful discussions and comments.

References

Aaronson, M. 1983, *Astrophys. J*., **266,** L11.
Bahcall, N. A. 1977, *A. Rev. Astr. Astrophys.*, **15,** 505.
Bahcall, J. N. 1984a, *Astrophys. J*., **276,** 169.
Bahcall, J. N. 1984b, Preprint, Princeton.
Bahcall, J. N., Tremaine, S. 1981, *Astrophys. J.*, **244,** 805.
Bond, J. R., Efstathiou, G., Silk, J. 1980, *Phys. Rev. Lett.*, **45,** 1980.
Bond, J. R., Szalay, A. S., White, S. D. M. 1983, *Nature*, **301,** 584.
Bosma, A. 1978, *PhD Thesis*, Groningen Univ.
Cabbibo, N., Farrar, G. R., Maiani, L. 1981, *Phys. Lett.*, **105B,** 155.
Cowsik, R. 1986, *J. Astrophys. Astr*., **7,** 1.
Cowsik, R., Ghosh, P. 1986a, *J. Astrophys. Astr*., **7,** 7.
Cowsik, R., Ghosh, P. 1986b, *J. Astrophys. Astr.*, **7,** 17.
Cowsik, R., McClelland, J. 1972, *Phys. Rev. Lett.*, 29, 669.
Cowsik, R., McClelland, J. 1973, *Astrophys. J*., **180,** 7.
de Vaucouleurs, G. 1975, in *Galaxies and the Universe,* Eds A. Sandage, M. Sandage & J. Kristian, Chicago Univ. Press, p. 557.
Doroshkevich, A. G., Kotok, E. V., Novikov, I. D., Polyudov, A. N., Shandarin, S. F., Sigov, Yu. S. 1980, *Mon. Not. R. astr. Soc*., **192,** 321.
Dressler, A. 1978, *Astrophys. J*., **226,** 55.
Faber, S. M., Gallagher, J. S. 1979, *A. Rev. Astr. Astrophys.*, **17,** 135.
Faber, S. M., Lin, D. N. C. 1983, *Astrophys. J.*, **266,** L17.
Fall, S. M. 1980, *Phil. Trans. R. Soc. Lond. A.*, **296,** 339.
Frenk, C. S., White, S. D. M., Davis, M. 1983, *Astrophys. J*., **271,** 471.
Gunn, J. E., Gott, J. R. 1972, *Astrophys. J.,* **176,** 15.
Hogan, C. J., Rees, M. J. 1979, *Mon. Not. R. astr. Soc*., **188,** 791.
Huchtmeier, W. K., Richter, O. G., Bohneustengel, H. D., Hauschildt, M. 1983, *ESO Preprint*, 250.
Kapteyn, J. C. 1922, *Astrophys. J*., **55,** 302.

Kent, S. M., Gunn, J. E. 1982, *Astr. J.*, **87,** 945.
Klinkhamer, F. R., Norman, C. A. 1981, *Astrophys. J.*, **243**, LI.
Lake, G., Schomer, R. A. 1984, *Astrophys. J.*, **279,** L19.
Lin, D. N. C., Faber, S. M. 1983, *Astrophys. J.*, **266,** L21.
Nilson, P. N. 1973, *Uppsala General Catalogue of Galaxies, Uppsala Astr. Dos. Ann.,* **6.**
Olive, K. A., Turner, M. S. 1981, *Phys. Rev.*, **46,** 516.
Olive, K. A., Schramm, D. N., Steigman, G., Turner, M. S., Yang, J. 1981, *Astrophys. J.*, **246,** 557.
Olive, K. A., Turner, M. S. 1982, *Phys. Rev.*, **D25,** 213.
Oort, J. H. 1932, *Bull. astr. Inst. Netherl.*, **6,** 249.
Oort, J. H. 1960, *Bull. astr. Inst. Netherl.*, **15,** 45.
Pagels, H., Primack, J. R. 1982, *Phys. Rev. Lett.*, **48,** 223.
Peebles, P. J. E. 1965, *Astrophys. J.*, **142,** 1317.
Peebles, P. J. E. 1966, *Phys. Rev. Lett.*, **16,** 410.
Peebles, P. J. E. 1979, in *Physical Cosmology*, Eds R. Balian, J. Audouze & D. N. Schramm, North-Holland, Amsterdam, p. 216.
Peebles, P. J. E. 1982, *Astrophys. J.*, **258,** 415.
Peebles, P. J. E. 1983, *Astrophys. J.*, **274,** 1.
Peebles, P. J. E. 1984, *Astrophys. J.*, **277,** 470.
Rana, N. C. 1982, *Phys. Rev. Lett.,* **48,** 209.
Rood, H. J., Page, T. L., Kintner, E. C., King, I. R. 1972, *Astrophys. J.*, **172,** 627.
Rood, H. J., Dickel, J. R. 1978, *Astrophys. J.*, **224,** 724.
Rubin, V. C. 1979, *Comments Astrophys.*, **8,** 79.
Rubin, V. C., Ford, W. K. J., Thonnard, N., Burstein, D. 1982, *Astrophys. J.*, **261,** 439.
Rubin, V. C., Thonnard, N., Ford, W. K. J. 1980, *Astrophys. J.*, **238,** 471.
Rubin, V. C., Thonnard, N., Ford, W. K. J. 1982, *Astr. J.*, **87,** 477.
Sandage, A., Tammann, G. A. 1975, *Astrophys. J.*, **196,** 313.
Sato, H., Takahara, F. 1980, *Prog. Theor. Phys.*, **64,** 2029.
Schramm, D. N., Steigman, G. 1981, *Astrophys. J.*, **243**, 1.
Sikivie, P. 1982, *Phys. Rev. Lett.*, **48,** 1156.
Silk, J. 1967, *Nature*, **215,** 1155.
Silk, J., Wilson, M. L. 1981, *Astrophys. J.*, **244,** L37.
Smith, S. 1936, *Astrophys. J.*, **83,** 23.
Stecker, F. W. 1980, *Phys. Rev. Lett.*, **44,** 1237.
Sunyaev, R. A., Zel'dovich, Ya. B. 1975, *Mon. Not. R. astr. Soc.*, **171,** 375.
Tremaine, S., Gunn, J. E. 1979, *Phys. Rev. Lett.*, **42,** 407.
Turner, E. L., Gott, J. R. 1976, *Astrophys., J. Suppl.*, **32,** 409.
van den Bergh, S. 1959, *Publ. David Dunlop Obs.*, **2,** No. 5, 147.
Wasserman, I. 1981, *Astrophys. J.*, **248,** 1.
Yang, J., Schramm, D. N., Steigman, G., Rood, R. T. 1979, *Astrophys. J.*, **227,** 697.
Zel'dovich, Ya. B. 1970, *Astr. Astrophys.*, **5,** 84.
Zwicky, F. 1933, *Helv. phys. Acta.*, **6,** 110.

J. Astrophys. Astr. (1986) **7,** 39–43

Energy Loss of Electrons in Solar Atmosphere taking Many-Body Interactions into Account

K. L. Moza, P. K. Koul, R. R. Rausaria & P. N. Khosa
Department of Physics, Regional Engineering College, Hazratbal, Srinagar, Kashmir 190006

Received 1984 April 24; revised 1985 September 12; accepted 1985 October 22

Abstract. Role of many-body interactions on the energy loss of electrons accelerated at neutral point during solar flares has been studied. Energy loss with and without many-body interactions has been computed for different electron-density models as function of height. The energy loss increases by a factor of two by inclusion of many-body interactions for incident electron energies greater than 10 keV. Role of this on the generation of hard X-rays is discussed.

Key words: Sun, flares—Sun, hard X-rays

Hard X-ray bursts ($\geqslant 20$ keV) from solar flares are believed to be generated by collisional bremsstrahlung mechanism by the interaction of nonthermal electrons with the ambient dense plasma of the chromosphere (Korchak 1967; Cline, Holt & Hones 1968). These electrons are accelerated to nonthermal energies in the current sheet near an X-type neutral point. During the downward motion of these electrons towards the photosphere they interact with regions of constantly increasing density and undergo strong deceleration resulting in the emission of hard X-ray bursts (Takakura 1969; Holt & Ramaty 1969). Most of the processes involved in the energy loss by these nonthermal electrons in flare conditions have been discussed in some detail by Brown (1971). In most of the calculations, the author considers only the short-range binary collisions and does not account for the long-range Coulomb interaction responsible for the collective behaviour of the ambient plasma. We propose, therefore, to improve upon this assumption and want to incorporate the effect of collective behaviour on the energy loss of nonthermal electrons in thick target model.

The accelerated stream of electrons moving down towards the photosphere interacts with the ambient plasma particles through electron-electron and electron-ion collisions. The electron-ion collisions result mostly in the scattering of the incident electrons and thus determine the trajectory of the precipitating electron beam. The electron-electron interactions, however, dominate the energy loss of the incident electrons. The bremsstrahlung X-ray spectrum depends on electron energy and angular distributions. The energy distribution of electrons depends on the energy loss. Therefore, the energy loss of electrons plays a role in X-ray spectrum calculations. Accounting for Coulomb interaction, the mean rate of energy loss suffered by an electron moving with a velocity v through an electron gas at a temperature T is given by

$$-\frac{1}{N_e}\frac{dE}{dx} = \left(\frac{8\sqrt{\pi}e^4}{m_e v_e v}\right) F\left(\frac{v}{v_e}\right) \ln \Lambda \qquad (1)$$

where N_e is the number density of ambient electrons, v_e is the thermal velocity of electrons and the function $F(x)$ is defined as

$$F(x) = \frac{1}{x}\int_0^x \exp(-x^2)\,dx - \exp(-x^2)$$

$$\simeq \begin{cases} -1 + \frac{5}{3}x^2 + \ldots & (x < 1) \\ \frac{\sqrt{\pi}}{2x} + \ldots & (x > 2). \end{cases} \tag{2}$$

Equation (1) is derived on the basis of binary encounter theory in which the interaction of the incident electron with the electron gas *is* looked upon as a superposition of many independent electron-electron collisions in the Coulomb field. However, the Coulomb interaction being of a long-range character, the incoming electron will interact simultaneously with the large number of ambient electrons within the Debye sphere.

The effect of many-body interactions on the rate of energy loss by an electron has quantitatively been studied in the recent past by a number of authors (Perkins 1965; Itikawa & Aono 1966; Ray 1969). In the unified theory of Kihara & Aono (1962) the rate of energy loss of an electron moving through an electron gas is given by

$$-\frac{1}{N_e}\frac{dE}{dx} = \frac{8\sqrt{\pi}e^4}{m_e v_e v}\left[F\left(\frac{v}{v_e}\right)\ln\left(\frac{2kT_e}{\gamma e^2}\lambda_D\right) + G\left(\frac{v}{v_e}\right)\right]$$

$$= \frac{8\sqrt{\pi}e^4}{m_e v_e v}\left[F\left(\frac{v}{v_e}\right)\ln\Lambda + \left\{F\left(\frac{v}{v_e}\right)\ln\frac{2}{3\gamma} + G\left(\frac{v}{v_e}\right)\right\}\right] \tag{3}$$

where $\gamma = 0.577$, is Euler's constant. The function $G(u)$ gives the dependence of the Coulomb logarithm on the velocity of the incident electron (Itikawa & Aono 1966). Analytical expression for this function has been given by Takayanagi & Itikawa (1970) in a different context. We reproduce it below for convenience.

$$\frac{2}{\sqrt{\pi}}G(u) = 4\left[\frac{1}{u}\phi(u) - \frac{d\phi(u)}{du}\right] + \left[\frac{1}{u}\tilde{\phi}(u) - 2\frac{d\tilde{\phi}(u)}{du}\right] - 2ug(u) + \frac{2}{\sqrt{\pi}}\exp(-u^2)C(u),$$

where ϕ is the error function

$$\phi(u) = \frac{2}{\sqrt{\pi}}\int_0^u \exp(-x^2)\,dx,$$

and

$$\tilde{\phi}(u) = \frac{u}{\sqrt{\pi}}\int_0^\infty dx \sinh(2ux)\ln x \exp[-(u^2 + x^2)],$$

$$g(u) = \frac{2}{\sqrt{\pi}}\frac{1}{u^2}\int_0^u dx\, x^2 \exp(-x^2)C(x),$$

$$C(x) = \frac{1}{4}\ln[\{\xi(x)\}^2 + \{\eta(x)\}^2 + \frac{\xi(x)}{2|\eta(x)|}\left[\frac{\pi}{2} - \tan^{-1}\frac{\xi(x)}{|\eta(x)|}\right].$$

The functions ξ and η in the above equation are given by

$$\xi(x) = 1 + x \text{ Re } Z(x)$$
$$\eta(x) = x \text{ Im } Z(x)$$

where Re Z and Im Z are, respectively, the real and imaginary parts of the plasma dispersion function (Fried & Conte 1961)

$$Z(x) = -2\exp(-x^2)\int_0^x \exp(t^2)\,dt + i\sqrt{\pi}\exp(-x^2)$$

which characterizes the collective interaction between the incident electron and the plasma. For $u \gg 1$, the form of the function $G(u)$ reduces to

$$\frac{2}{\sqrt{\pi}} G(u) \simeq \frac{1}{u}\ln(\sqrt{2}\,u^3).$$

Equation (3) which gives us the rate of energy loss by an electron differs from the corresponding equation obtained on the basis of binary encounter theory by the terms in the curly brackets. Corresponding to the incident electron energy of the order of a few electron volts we find that in the solar flare region $v/v_e \ll 1$. For such small values of v/v_e the values of F and G functions are approximately equal so that in this range of incident electron energies the use of the unified theory predicts the rate of electron energy loss which does not differ appreciably from that predicted on the basis of binary encounter theory. However, the electrons that are responsible for the emission of hard X-rays from flare regions have their energies of the order of 10 keV and even more. The value of v for nonthermal electrons is in the range of 4.2×10^7–1.88×10^8 m s^{-1} and the value of thermal electron velocity v_e varies from 1.23×10^6 m s^{-1} for $T = 10^5$ K to 1.23×10^7 m s^{-1} for $T = 10^7$ K. The ratio of v/v_e for $T = 10^7$ K lies between 3.41 and 15.29 for electron energies 5 keV and 100 keV respectively, and increases at lower temperatures. For electrons of such large energies ($v/v_e \gg 1$) the terms in the curly brackets assume a significant role in the rate of electron energy dissipation. For incident electron energies of the order of 10 keV or more, Equation (3) above can be rewritten as

$$\frac{1}{N_e}\frac{dE}{dx} \simeq \frac{4\pi e^4}{m_e v^2}\left[\ln\Lambda + \left\{\ln\frac{2\sqrt{2}}{3\gamma} + \ln\left(\frac{v}{v_e}\right)^3\right\}\right]. \tag{4}$$

Table 1. Electron velocities at different energies.

Energy E keV	Velocity v $5.95 \times 10^5 [E(\text{eV})]^{1/2}$ m s^{-1}	v/v_e $T(\text{K}) = 10^5$ $v_e(\text{m s}^{-1}) = 1.23 \times 10^6$	10^6 3.89×10^6	10^7 1.23×10^7
5	4.2×10^7	34.15	10.79	3.41
10	5.95×10^7	48.37	15.29	4.84
15	7.28×10^7	59.19	18.71	5.92
20	8.41×10^7	68.37	21.62	6.84
30	1.03×10^8	83.73	26.48	8.37
40	1.19×10^8	96.75	30.59	9.68
50	1.33×10^8	108.13	34.20	10.81
100	1.88×10^8	152.85	48.33	15.29

Equation (4) gives a much larger rate of electron energy dissipation and stands out in contrast to Equation (1) used previously in computing the rate of energy loss of electrons moving through the solar atmosphere.

Using Equations (1) and (4) we have computed the energy-loss rate of the incident electron as a function of its energy for different values of electron densities, the ambient temperature and Coulomb logarithm. At 10 keV, the energy loss calculated by Equations (1) and (4) differ by less than five per cent. We show the loss rate computed with and without collective effects in Fig. 1 for various values of temperature T_e, electron density N_e and corresponding Coulomb logarithm In Λ. The values of T_e and

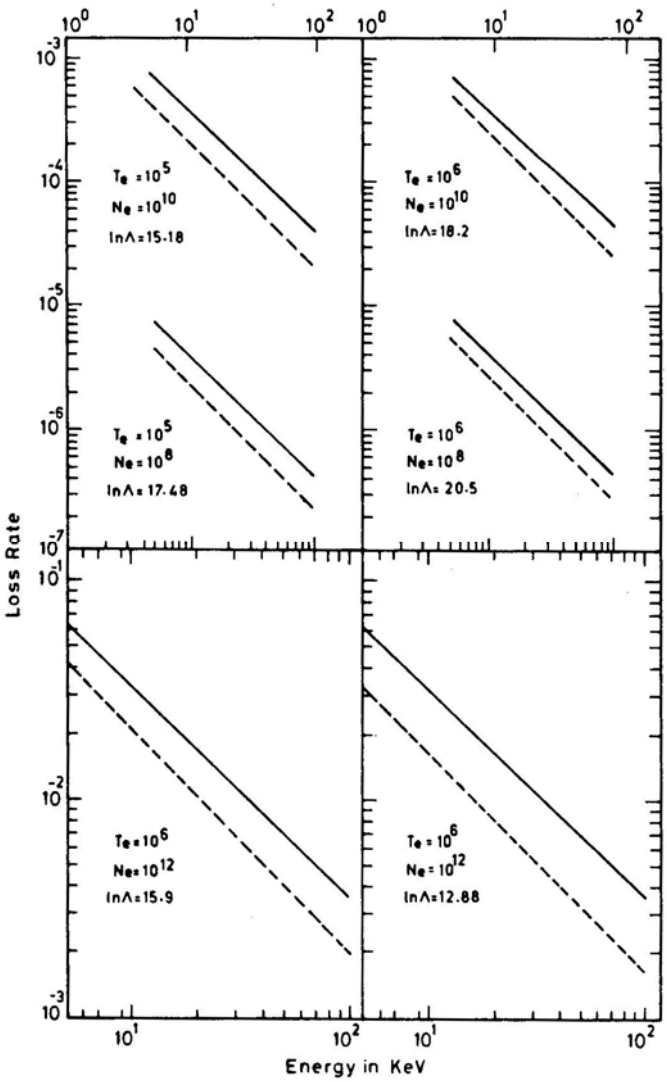

Figure 1. Variation of electron energy loss rate as a function of incident electron energies for different values of electron temperature T_e(K), electron densities N_e(cm^{-3}), and Coulomb logarithm In Λ, Solid line: with collective effect; dashed line: without collective effect.

N_e are representative of temperatures and electron densities found at different heights in solar atmosphere, at different times. A look at the figures shows that at a fixed temperature, the energy loss increases with an increase in electron number density. For a fixed electron density the energy loss becomes more at higher temperatures because the Coulomb logarithm becomes higher.

From these results we find that the rate of energy loss after the inclusion of the many-body effect is invariably larger than the corresponding one in the absence of collective effects. The enhanced energy loss must, therefore, be reflected in the polarization and energy of the bremsstrahlung X-rays generated by such electrons during their deceleration process. This role of the many-body effect would become more significant in the case of nonthermal incident electrons which travel a longer distance than the corresponding electrons of smaller energy.

Acknowledgements

We are thankful to Dr. O. N. Wakhlu, Principal, Regional Engineering College, Srinagar for his encouragement during the progress of this work. The work is supported by ISRO Grant No. 10/2/134.

References

Brown, J. C. 1971, *Solar Phys.*, **18,** 489.
Cline, T. I**.,** Holt, S. S., Hones, E. W. 1968, *J. Geophys. Res.*, **73,** 434.
Fried, B. D., Conte, S. D. 1961, *The Plasma Dispersion Function,* Academic Press, New York.
Holt, S. S., Ramaty, R. 1969, *Solar Phys.*, **8,** 119.
Itikawa, Y., Aono, O. 1966, *Phys. Fluids*, **9,** 1259.
Kihara, T., Aono, O., Itikawa, Y. 1963, *J. Phys. Soc. Japan*, **18,** 1043.
Korchak, A. A. 1967, *Soviet Phys. Dokl*., **12,** 192.
Perkins, F. 1965, *Phys. Fluids*, **9,** 1259.
Ray, R. M. 1969, *Phys. Lett*., **29A,** 577.
Spitzer, Jr., I. 1956, *Physics of Fully Ionised Gases*, lnterscience, New York.
Takakura, T. 1969, *Solar Phys*., **6,** 133.
Takayanagi, K., Itikawa, Y. 1970, *Space Sci. Rev.*, **11,** 380.

J. Astrophys. Astr. (1986) **7,** 45–51

The Identity of the Primary Component of Capella

R. & R. Griffin *The Observatories, Madingley Road, Cambridge, England CB3 0HA*

Received 1985 October 1; accepted 1985 December 1

Abstract. Ever since the discovery in 1899 that Capella is a double-lined spectroscopic binary system the sharp-lined component, which has the later spectral type, has always been regarded as the primary (more luminous) star. However, traces obtained with radial-velocity spectrometers show that the broad-lined, earlier-type component is actually the primary.

Key words: spectroscopic binaries — stars, individual

1. Historical introduction

The discovery that Capella (α Aur; HR 1708; HD 34029) is a spectroscopic binary was made by Campbell (1899, 1900) at the Lick Observatory and independently by Newall (1899, 1900) at our own observatory. Both discoverers recognized the spectrum as being double-lined, with one component much more conspicuous than the other; they considered the obvious component to be of approximately solar type. They lost no time in measuring its radial-velocity variations, and soon determined the orbit (Newall 1900; Campbell 1901; Reese 1901), which has a period of 104 days and a velocity semi-amplitude of about 26 km s^{-1}

The other component of Capella manifests itself only as a shadowy contribution to the composite spectrum, and it is much to Newall's (1900) credit that he recognized its character well enough to call it the "Procyon" component. (The spectral type of Procyon is F5.) He even estimated the amplitude of its radial-velocity changes, which led him to "think that the masses of the two components are not very different from one another." However, despite these accurate conclusions, he ended an early note on Capella (Newall 1899) with the further prescient remark, "I feel sure that Prof. Campbell will agree that there is enough work for at least two workers in deciphering the complexities of the spectrum of this new binary".

In order to avoid begging the question to which this paper is addressed, we shall follow Newall by using the terms "solar component" and "Procyon component", rather than "primary" and "secondary", to distinguish between the two stars which constitute the Capella system. As a matter of fact, both stars are evolved objects with luminosities corresponding to class III in the MK system. Their spectral types are probably late G and late F, respectively.

2. The spectrum of the Procyon component

The shadowy nature of the Procyon component's spectrum is caused by the smearing-out of its lines by rapid axial rotation. The solar component has normal line-widths.

The superposition of the two spectra makes the observed composite spectrum of Capella appear very bizarre and confusing. Indeed, at first sight it produces the strong impression that something must have gone wrong with one's eyes! The confusion created in some authors has on occasion persisted right through to publication: for example, Struve & Kung (1953), who did not attempt any quantitative spectrophotometry but depended merely upon visual examination of spectrograms, could not bring themselves to believe that the spectrum of Capella consisted solely of two more or less normal stellar spectra. They thought it necessary to invoke substantial emission components to account for the subjective impression of weakness of many of the principal absorption lines. In this they were corrected by Wright (1954), who used proper intensity tracings and showed that the subtraction of a normal G-gaint spectrum (representing that of the solar component) from the spectrum of Capella left a residuum which was entirely comparable with the spectra of late-F gaints; he pointedly remarked that "it does not seem that any abnormal features are required to explain the composite spectra". Wright's estimates of the spectral types of the two stars were G5 III and G0 III.

3. The relative luminosities

Because the Procyon component is so difficult to see in the spectrum—even Batten & Erceg (1975), working with plates having a dispersion of 2.4 Å mm^{-1} admitted that it "cannot be seen and measured directly"—no reliable assessment of the relative luminosities of the components can readily be made spectroscopically. It is of course natural that observers have assumed that the conspicuous solar component in the Capella spectrum must arise from the brighter star. However, Newall (1900) recognized the "probability that the two components do not differ much in brightness", whereas Campbell (1901) stated that "the solar-type component is estimated to be half a magnitude brighter, photographically, than the bluer component. In the visual portion of the spectrum the solar component is probably at least a whole magnitude the brighter of the two." In the only substantial quantitative work on the spectrum of Capella in the optical region, Wright (1954) found a difference of visual magnitude of 0.25 mag, the solar component being the brighter; owing to the difference in the colours of the two components, their brightnesses were found to become sensibly equal near λ4200 A, while in the ultraviolet the Procyon component seemed slightly the brighter.

Capella was directly resolved by Michelson (1920) with his interferometer, and was repeatedly measured by Anderson (1920) and Merrill (1922); and in recent years it has frequently been resolved and measured by speckle interferometry. In principle the contrast of the interference fringes, in either type of interferometer, allows the magnitude difference of the components to be determined, although the sign of the difference is less readily established. Michelson found the components to be of practically equal visual brightness, since the interference fringes disappeared entirely, rather than their visibility passing through a minimum, at the critical mirror separation. A 'visual' orbit for Capella was derived from the Michelson measurements by Merrill (1922). Owing to the 180° ambiguity in the determinations of position angles, Merrill's choice of quadrant for the ascending node may well have been arbitrary. Heintz (1975), from astrometric observations of the movement of the photocentre of the binary, considered that Merrill's choice was the wrong one, and his evidence persuaded Finsen (1975) to

reverse the quadrant in his revision of the orbit. Blazit *et al.* (1977), in early tests of a two-telescope interferometer, were able to resolve not only the Capella binary system but also the discs of the individual stars. Their belief that the cooler star is also the brighter one decisively influenced their choice when they encountered an ambiguity in the interpretation of their observations. Subsequently Koechlin, Bonneau & Vakili (1979), using the same equipment, identified the "bigger, brighter, G5 III" component* as being to the north of the other on a particular occasion. McAlister (1981) asserted that Koechlin *et al.* had 'positively shown that [the] new choice of quadrants is the correct one". However, only two years later McAlister himself, in collaboration with Bagnuolo (Bagnuolo & McAlister 1983), showed at least equally positively that the *old* choice of quadrants was the correct one.

4. Our own contribution

The purpose of the present paper is to show that the Procyon component of Capella is actually the primary in the sense of being the brighter at optical wavelengths. At first sight the various photometric assignments of the ascending node should be independent of the identification of the primary star, although obviously our proposal to invert the correspondence between the spectroscopic identities and the photometric luminosites will occasion yet another inversion of our perception of the Capella system. However, it seems likely—although we are not sufficiently familiar with the two-telescope interferometer to be certain—that Blazit *et al.* (1977), as a result of the incorrect identification of the later-type component as the photometric primary, adopted the wrong alternative from their ambiguous solutions for the diameters of the individual stellar discs; and that Koechlin *et al.*'s (1979) "positive" demonstration of the quadrant of the ascending node similarly requires revision. If that is so, the only remaining discordance among the photometric quadrant assignments is that of Heintz (1975), which in any case is not statistically secure since the size of the photocentric orbit is only half as large again as its standard deviation.

The evidence for our heretical proposal stems from traces made of Capella with photoelectric radial-velocity spectrometers. We are not appealing here to radial velocities themselves, but are simply taking advantage of another useful property of such spectrometers inasmuch as they effectively condense some of the important characteristics of a whole spectrum into a single line profile—the profile of what we (Griffin 1967) call the "dip" and what the 'Coravel' observers (Baranne, Mayor & Poncet 1979) call the "pic de correlation". The depth, or more strictly the equivalent width (area), of the dip varies in a systematic way with spectral type. In our spectrometers at Cambridge (Griffin 1967) and Palomar (Griffin & Gunn 1974), which incorporate masks based on the spectrum of the K2 III star Arcturus, the dip has a maximum intensity for late-K stars and becomes progressively shallower as one goes from there to either earlier or later types. The width of the dip reflects the widths of lines

* The phrase within the quotation marks is our rough translation of the original French. Largely owing to the perversity of the scale of stellar magnitudes in characterizing fainter stars by larger magnitudes, the actual words used by Koechlin *et al.*, "plus faible magnitude", might be held to mean either brighter or fainter, as indeed the corresponding English expression might. Our translation as "brighter" is perhaps supported by the analogous use of the same words a few lines earlier by Koechlin *et al.* where they say that "la difference de magnitude est faible ([Δ] V = 0.25)", clearly referring to numerical magnitudes.

in the stellar spectrum, and furnishes a sensitive measure of the projected rotational velocity of the star observed.

A recent paper (Shen *et al.* 1985) giving a spectroscopic orbit obtained for Capella with the Fick radial-velocity spectrometer (Beavers & Eitter 1977) includes the information that Gaussian approximations to the dips observed for the solar and Procyon components had widths represented by Gaussian constants of 10.2 ± 0.5 and 23 + 3 km s^{-1}, respectively, and that their depths were in the ratio of 1.7 ± 0.2 to 1. By taking the products of the relative widths and depths we find the areas of the two dips to be in the ratio solar: Procyon = 0.75 + 0.15 to 1. That is to say, *the dip given by the Procyon component has a decidedly larger area than that given by the solar component.* It is not clear from Shen *et al.*'s text what mask their data refer to, but it was probably one corresponding to a G-type spectrum. Almost certainly the intrinsic depth of the dips given by single stars must increase towards later spectral types throughout the relevant range of F and G giants when they are observed with the Fick spectrometer with its G mask, as it does with the spectrometers of which we have direct experience. Accordingly, the disparity in the apparent magnitudes of the components (in the blue part of the spectrum utilized by the Fick spectrometer) must be larger than the disparity in dip areas, which corresponds in magnitude terms to about 0.3 mag.

Although we have, unfortunately, not had the opportunity to make a systematic radial-velocity study of Capella with the Palomar spectrometer (Griffin & Gunn 1974), which can give traces of exemplary repeatability and signal/noise ratio, we did obtain one trace through heavy cloud on 1982 November 22. On that date the orbital phase was such that the difference in velocity between the components was not far from its maximum value, *i.e.* the two dips on the trace are nearly as well separated as they can ever be. The trace is shown in Fig. 1, where the plotted points represent the observed photon counts and the continuous curves are the model dips fitted by the least-squares procedure outlined by Griffin (1982). We must point out that our procedure is not at all similar to that used by Shen *et al.* (1985), as those authors claim. Shen *et al.* represent every dip, even one that shows substantial rotational broadening, by the best-fitting Gaussian curve, whereas we perform a proper numerical integration of the dips given by elementary parts of a rotating, limb-darkened stellar model. In practice our method gives an excellent fit even to very broad dips which are distinctly non-Gaussian, as may be seen in Fig. 1; it also provides a good estimate on the projected rotational velocity without any recourse to empirical calibrations.

We find from the Fig. 1 trace that the projected rotational velocities $v \sin i$ are 7 and 36 km s for the solar and Procyon components, respectively, and that the areas of the two dips are in the ratio solar: Procyon = 0.92:1. In the absence of other comparable traces we cannot quote external errors for any of these quantities, but we would expect the $v \sin i$ value for the solar component to be accurate to 2 or 3 km s^{-1}, that for the Procyon component to be within 1 or 2 km s^{-1}, and the relative dip areas to be within about 3 per cent. Thus we, like the Fick authors, find the Procyon component to have the larger dip and therefore, a *fortiori* since its intrinsic dip depth is smaller owing to its earlier spectral type, the brighter apparent magnitude.

It is not easy to quantify the effects of the spectral-type difference upon the dip areas. We know that there is a rapid variation of dip area with type throughout the F and G dwarf sequence and that there is an analogous variation among giant stars insofar as such stars exist. However, the Procyon component of Capella, classified by Wright (1954) as type G0 III, lies in the Hertzsprung gap, where few non-pathological objects

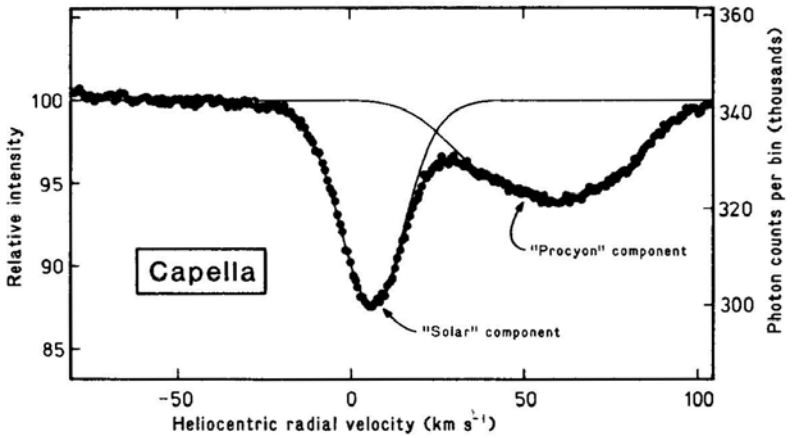

Figure 1. Photoelectric radial-velocity tracing of Capella, obtained on 1982 November 22 with the Palomar spectrometer (Griffin *&* Gunn 1974). A tracing of this sort may be viewed as the average profile of spectral lines in the object observed. In Capella the line profiles are seen to be conspicuously double: there is one relatively sharp component, which arises from the solar component of the binary star, and another broad, shallow one which arises from the Procyon-like component. The profiles are much more easily seen here than in a direct observation of the spectrum: not only is the signal/noise ratio high and the spacing of the observed points (about 10 mA) generously dense, but there is no blending with adjacent spectral lines. In the Figure, the profiles of the two dips have been fitted by a model (Griffin 1982) with seven free parameters—the position, area and width of each dip, plus the continuum height. The positions (right-to-left) of the dips give the radial-velocity information, which does not concern us here; the immediate interest lies in the shapes and sizes of the dip profiles. The widths of the dips are accurately mimicked by projected stellar rotational velocities (v sin i) of 7 km s for the solar component and 36 km s for the Procyon one. But more interesting still—and this is the principal point of the present paper—are the areas: expressed in a manner analogous to equivalent widths in conventional spectroscopy, they are 3.02 km s^{-1} for the solar component and 3.31 km s^{-1} for the Procyon component. The Procyon component therefore actually contributes more absorption to the combined spectrum than its companion; and since it is of earlier type and its intrinsic line-strength is smaller, its relative *brightness* must be even larger than the relative absorption. The reason that the Procyon component has not previously been recognized as the primary is that its lines are so broad and its spectrum therefore lacks contrast; the lines of the solar component, though weaker, have much steeper intensity gradients and are far more conspicuous both on spectrograms and on tracings of the spectrum.

are seen. Accordingly, we cannot determine directly the slope of the dip-area/spectral-type relationship in the region relevant to Capella. Moreover, there remains appreciable uncertainty as to the true spectral types of the components, so even if we knew the slope of the relationship we could not specify with much accuracy the baseline over which it operated. We offer the opinion—but without claiming that it is anything more than an educated guess—that the intrinsic dip area of the Procyon component, *i.e.* that which it would exhibit if it could be observed alone, is no more than three-quarters that of the solar component. To exhibit equal dip areas in a trace such as that shown in Fig. 1 would therefore require the Procyon component to be four-thirds as bright as, or in magnitude terms 0.3 mag brighter than, its companion. Since in fact the Procyon component gives a dip 9 per cent, or almost 0.1 mag, larger, the actual difference in magnitude—in the wavelength region utilized by the Palomar spectrometer, which is comparable with the photometric *B* band—is expected to be about 0.4 mag. Because of

the difference in colour between the two stars, the superiority of the Procyon component must decrease redwards; according to our estimate, the disparity in the *V* band will be down to about 0.15 mag (still in favour of the hotter component).

5. An attempt at reconciliation

A question that might naturally be asked is why our result should differ so appreciably from Wright's, which is the only previous objective measurement of which we are aware; and another is why, given that such a discrepancy exists, our own conclusion is to be preferred.

We could attempt to counter such implied criticisms in a number of ways. First, the amount of the late-type standard spectrum that Wright (1954) found was needed to represent the contribution of the solar component to the Capella spectrum would depend upon the line-strength in the standard star. Wright used β Dra as the standard; at type G2 Ib-IIa (Morgan & Keenan 1973; Keenan & Pitts 1980) it is probably not a particularly accurate match to the cool star in Capella, which Wright himself considered to be G5 III**.** Secondly, Wright appears to have overlooked the fact that his ratios actually refer to the relative 'continuum heights' of the components and not to the relative light intensities. Because the absorption lines are more numerous and intrinsically stronger in the cooler star, *i.e.* the line-blanketing there is greater, the contribution of that star to the combined spectrum is less when expressed in terms of light intensity than it is in terms of continuum height. Blanketing coefficients have been explicitly tabulated for Arcturus (Mäckle *et al.* 1975) and for Procyon (Griffin 1979); in the λ 4200-A region they are typically 50 per cent and 15 per cent respectively. Thus the residual light intensities, for equal continuum heights, are in the ratio of (100 – 50) : (100 – 15), *i.e.* nearly 0.6 mag when expressed in magnitudes. Certainly the disparity in spectral type between the components of Capella is not so great as that between Arcturus (K2) and Procyon (F5); but a substantial effect is clearly to be expected, and by itself would explain much of the discrepancy of about 0.4 mag between Wright's result and our own.

The above response to the first question propounded at the head of this section also goes a long way towards answering the second: by demonstrating the need for a considerable correction to Wright's relative magnitudes we bring his corrected conclusion nearly into harmony with our own. Even if we had been unable to reconcile the two results, however, the simplicity and directness of the measurement carried out on Fig. 1, together with the excellent correspondence between the model dips and the observed points, inspires some confidence in the trustworthiness of our result. It is no disparagement of Wright's work to remark that his measurements, undertaken on a very complex composite spectrum, were necessarily a great deal more difficult, and consequently more liable to accidental errors, than those we needed to make on Fig. 1.

6. Concluding remarks

In this paper we have not attempted to offer any comprehensive survey of the abundant literature on Capella, nor have we tried to summarize the present state of knowledge of the system as a whole. In the 86 years since its duplicity was discovered much has been

learnt, and more written, about Capella; and to provide a balanced and authoritative synopsis would tax not only our own powers as reviewers but also the hospitality of the Editor of this *Journal.* It would also be ulterior to the purpose of this paper. Our aim here is strictly limited to discussing matters relevant to the identity of the Capella primary; and the fact that such a fundamental matter is still open to discussion—and, as we assert, correction—reinforces the view of our predecessor Newall (1899) quoted towards the end of Section 1 above.

Acknowledgements

We are pleased to thank the Palomar Observatory for the guest-investigator privileges accorded to one of us, and to acknowledge the collaboration of Dr J. E. Gunn in observing at Palomar and his assistance in setting up the principles of the computer programme which models traces such as that shown in Fig. 1.

References

Anderson, J. A. 1920, *Astrophys. J.*, **51,** 263.
Bagnuolo, W. G., Jr., McAlister, H. A. 1983, *Publ. astr. Soc. Pacific*, **95,** 992.
Baranne, A., Mayor, M., Poncet, J. L. 1979, *Vistas Astr.*, **23,** 279.
Batten, A. H., Erceg, V. 1975, *Mon. Not. R. astr. Soc.*, **171,** 47P.
Beavers, W. I**.,** Eitter, J. J. 1977, *Publ. astr. Soc. Pacific*, **89,** 733.
Blazit, A., Bonneau, D., Josse, M., Koechlin, L., Labeyrie, A., Oneto, J. L. 1977, *Astrophys. J.*, **217,** L55.
Campbell, W. W. 1899, *Astrophys. J.*, **10,** 177.
Campbell, W. W. 1900, *Observatory*, **23,** 92.
Campbell, W. W. 1901, *Lick Obs. Bull.*, **1,** 31.
Finsen, W. S. 1975, *IAU Comm.* 26 *Circ. D'Inf.*, no. 66.
Griffin, R. F. 1967, *Astrophys. J.*, **148,** 465.
Griffin, R. & R. 1979, *A Photometric Atlas of the Spectrum of Procyon*, R. & R. Griffin, Cambridge, p. ix.
Grif[f]in, R. & R. 1982, *Observatory*, **102,** 217.
Griffin, R. F., Gunn, J. E. 1974, *Astrophys. J.*, **191,** 545.
Heintz, W. D. 1975, *Astrophys. J.*, **195,** 411.
Keenan, P. C., Pitts, R. E. 1980, *Astrophys. J. Suppl.*, **42,** 541.
Koechlin, L., Bonneau, D**.,** Vakili, F. 1979, *Astr. Astrophys.*, **80,** L13.
Mäckle, R., Griffin, R. & R**.,** Holweger, H. 1975, *Astr. Astrophys. Suppl.*, **19,** 303.
McAlister, H. A. 1981, *Astr. J.*, **86,** 795.
Merrill, P. W. 1922, *Astrophys. J.*, **56,** 40.
Michelson, A. A. 1920, *Astrophys. J.*, **51,** 257.
Morgan, W. W., Keenan, P. C. 1973, *A. Rev. Astr. Astrophys.*, **11,** 29.
Newall, H. F. 1899, *Observatory*, **22,** 436.
Newall, H. F. 1900, *Mon. Not. R. astr. Soc.*, **60,** 418.
Reese, H. M. 1901, *Lick Obs. Bull.*, **1,** 32.
Shen, L.-Z., Beavers, W. I., Eitter, J. J., Salzer, J. J. 1985, *Astr. J.*, **90,** 1503.
Struve, O., Kung, S. M. 1953, *Astrophys. J.*, **117,**1.
Wright, K. O**.** 1954, *Publ. Dom. astrophys. Obs.*, Victoria, **10,** 1.

J. Astrophys. Astr. (1986) **7,** 53–57

Thermonuclear Reaction Rates from (*p*, *n*) Reactions on Targets with *A* = 92–122

S. Kailas *Nuclear Physics Division, Bhabha Atomic Research Centre, Trombay, Bombay 400085*

Received 1985 May 8; accepted 1985 December 3

Abstract. From the experimentally measured (*p,n*) cross-sections for ^{92,94}Zr, ^{93}Nb, ^{95,96,98}Mo, ^{103}Rh, ^{107,109}Ag, ^{110}Pd, ^{115}In, ^{117,122}Sn nuclides, for proton energies below 7 MeV, thermonuclear reaction rates in the temperature range $1 \leqslant T_9 \leqslant 5$($T_9$=$10^9$ K) have been extracted. These reaction rates have been fitted to a three parameter empirical expression proposed by Fowler.

Key words: (*p,n*) reaction: *A* = 92122 targets—thermonuclear reaction rates

1. Introduction

The astrophysical calculations concerning the synthesis of elements require as input temperature-dependent expressions for thermonuclear reaction rates (TNRR). These TNRR values are obtained starting from the cross-section data of interest, measured experimentally or calculated theoretically. Recently, an excellent review on the topic of charged particle reaction cross-section and nucleosynthesis has been published (Sargood 1982,1983). Extensive tabulations of the TNRRs have been made for proton induced reactions covering the nuclei with Z up to 36. (Woosley *et al.* 1975,1978). These TNRRs have been obtained employing theoretical models for the calculation of the cross-sections. Experimentally only 5060 per cent of these cross-sections have been measured so far. For nuclei with $Z > 36$, TNRRs have been determined recently from measured (*p,n*) and (*p,y*) cross-sections (Roughton *et al.* 1979). In the present work, starting from the recently measured (*p,n*) cross-section data for nuclei with *A* = 92–122, the TNRRs have been computed. Most of the nuclei considered here have not been included in the work of Roughton *et al.* (1979). In Section 2, the procedure for the calculation of TNRR is discussed. In Section 3, the results obtained are given. General conclusions are given in Section 4.

2. Procedure

The TNRR is the rate at which a specific nuclear reaction takes place in the stellar environment. The factors contributing to this rate are the cross-section for the reaction and the temperature of the stellar environment which determines the energy

distribution of the colliding particles. Excellent reviews are available on this topic. (Burbidge *et al.* 1957; Clayton 1968). The reaction rate between two different nuclei 1 and 2 in a high temperature (T) environment depends upon the densities of 1 and 2, the temperature, and the appropriate nuclear properties of the system. It is given by the expression

$$P_{12} = n_1 n_2 \langle \sigma v \rangle \text{ reactions cm}^{-3}\text{s}^{-1}, \tag{1}$$

where n_1, n_2 are the number densities of nuclei 1 and 2. Generally, the nuclei are assumed to possess a Maxwell-Boltzmann distribution of velocities at T and hence $\langle \sigma v \rangle$ is averaged over this distribution. Converting to energy space,

$$\langle \sigma v \rangle = \left(\frac{8}{\pi\mu}\right)^{1/2} (kT)^{-3/2} \int_{|Q|}^{\infty} E\sigma(E) \exp(-E/kT)\, \mathrm{d}E \text{ cm}^3\text{s}^{-1} \tag{2}$$

where k is the Boltzmann constant, μ the reduced mass, E the centre of mass energy, Q is the Q value of the reaction. A more usual form of quoting the TNRR is as follows:

$$P_{12} = N_A \langle \sigma v \rangle \text{ cm}^3 \text{ mole}^{-1}\text{s}^{-1} \tag{3}$$

where N_A is the Avogadro number.

It is assumed that the target nucleus is in the ground state; otherwise nuclear partition functions must be included. Once the cross-section σ (E) is given as a function of E, it is easy to compute P_{12}. For the convenience of the calculation, the σ (E) values measured experimentally are fitted with an expression (Vlieks, Morgan & Blatt 1974)

$$\sigma(E) = \frac{1}{E} \sum_{i=1}^{5} a_i \exp(-b/\sqrt{E}) E^{i-1}. \tag{4}$$

This expression is introduced in Equation (3) to determine P_{12}. In the present work, we have kept the parameter $b = Z - 0.5$ where Z is the atomic number of the target. Earlier, we have reported TNRR calculation for several medium-weight nuclei using the above technique (Kailas & Mehta 1976). Starting from the experimentally measured (p,n) reaction cross-sections (Johnson *et al.* 1977; Johnson, Galonsky & Kernell 1979, Hershberger *et al.* 1980; Flynn, Hershberger & Gabbard 1979) for nuclei with A in the range 92 to 122 and for proton energies below 7 MeV, the TNRRs have now been calculated in the temperature range $1 \leqslant T_9 \leqslant 5$,where $T_9 = T/10^9$ **K.**

3. Results

The TNRRs have been calculated by the procedure discussed in Section 2. The upper limit of integration (expression 3) has been kept equal to ~7 MeV, the highest energy up to which cross-section data are available. The TNRRs are listed in Table 1. The TNRR is estimated to have an uncertainty of ±10 per cent, mainly due to error on $\sigma_{p,n}$ For comparison, we have included the values obtained by Roughton *et al.* (1979) from thick target activation measurements. They have also made measurements for ^{95,96} Mo and ^{117,122} Sn targets. For Mo targets, they have listed two sets of cross-sections, one where the final state is the ground state and the other where the low-lying isomer, is the final state. For^{95,96} Mo targets the TNRR values obtained by Roughton *et al.* (1979)—the ground state or the isomer—agree reasonably well with the present results within their respective uncertainties. Similarly, the TNRR values from both these works for

Table 1. Thermonuclear reaction rates from (p,n) reactions.

		P^{c}_{12} (cm^3 mole^{-1} s^{-1})				
Reaction	Q value (MeV) .	$T_9 =$ 1	2	3	4	5
^{92}Zr$(p,n)^{92}$Nb	−2.789	0.13(−7)	3.42(−1)	1.46(+2)	3.64(+3)	2.82(+4)
^{94}Zr$(p,n)^{94}$Nb	−1.704	0.49(−4)	3.99(+0)	4.36(+2)	6.92(+3)	4.36(+4)
^{93}Nb$(p,n)^{93}$Mo	−1.202	0.80(−4)	2.11(+0)	2.32(+2)	3.88(+3)	2.47(+4)
^{95}Mo$(p,n)^{95}$Tc	−2.441	0.74(−7)	0.36(+0)	1.13(+2)	2.76(+3)	2.20(+4)
^{95}Mo$(p,n)^{95}$Tc[a]	−2.441[a]			1.03(+2)	1.98(+3)	1.23(+4)
^{95}Mo$(p,n)^{95}$Tc[b]	Lowest isomer[b]			2.20(+2)	4.27(+3)	2.57(+4)
^{96}Mo$(p,n)^{96}$Tc	−3.717		0.70(−2)	1.74(+1)	1.03(+3)	1.27(+4)
^{96}Mo$(p,n)^{96}$Tc[a]	−3.717[a]		1.83(−2)	3.14(+1)	1.30(+3)	1.18(+4)
^{96}Mo$(p,n)^{96}$Tc[b]	Lowest isomer[b]		0.85(−2)	1.51(+1)	6.34(+2)	5.75(+3)
^{98}Mo$(p,n)^{98}$Tc	−2.372	0.72(−7)	0.32(+0)	1.20(+2)	3.36(+3)	2.88(+4)
^{103}Rh$(p,n)^{103}$Pd	−1.337	0.16(−4)	0.77(+0)	1.09(+2)	2.17(+3)	1.62(+4)
^{110}Pd$(p,n)^{110}$Ag	−1.650	0.17(−4)	0.86(+0)	9.66(+1)	1.91(+3)	1.44(+4)
^{107}Ag$(p,n)^{107}$Cd	−2.199	0.18(−6)	0.20(+0)	5.09(+1)	1.25(+3)	1.04(+4)
^{109}Ag$(p,n)^{109}$Cd	−0.951	0.99(−5)	0.44(+0)	6.69(+1)	1.43(+3)	1.11(+4)
^{115}In$(p,n)^{115}$Sn	−0.293	0.24(−5)	0.17(+0)	3.41(+1)	8.60(+2)	7.83(+3)
^{117}Sn$(p,n)^{117}$Sb	−2.603	0.33(−8)	0.39(−1)	1.92(+1)	6.37(+2)	6.34(+3)
^{117}Sn$(p,n)^{117}$Sb[a]	−2.603[a]		1.76(−1)	5.56(+1)	1.49(+3)	1.32(+4)
^{122}Sn$(p,n)^{122}$Sb	−2.405	0.24(−7)	0.93(−1)	3.22(+1)	9.02(+2)	8.29(+3)
^{122}Sn$(p,n)^{122}$Sb	−2.405[a]				9.96(+2)	9.07(+3)

[a] Roughton *et al.* 1979 'ground state'
[b] Roughton *et al.* 1979 'isomer'
[c] The number in the parenthesis is the power to which ten has to be raised *e.g.* (−1) means 10^{-1}

Table 2. Parameters fittings the TNRR data ($1 \leqslant T_9 \leqslant 5$).

Reaction	α	β	γ
$^{92}Zr(p,n)$	7.609(+5)	7.394(+5)	1.963
$^{94}Zr(p,n)$	1.402(+4)	4.120(+3)	3.914
$^{95}Mo(p,n)$	9.610(+4)	5.100(+4)	2.980
$^{98}Mo(p,n)$	4.232(+4)	2.107(+4)	3.613
$^{107}Ag(p,n)$	1.855(+4)	3.548(+3)	3.831
$^{117}Sn(p,n)$	3.377(+4)	8.949(+3)	3.518
$^{122}Sn(p,n)$	2.720(+4)	6.605(+3)	3.596

the ^{122}Sn target agree with each other. However, the results of Roughton *et al.* for the ^{117}Sn target differ considerably from that of the present work. Roughton's (1979) values are a factor of 2 to 3 higher as compared to the present results. The reason for this discrepancy is not clear and it needs to be explored. It may be noted that the TNRR rates given by Roughton *et al.* (1979) and calculated here refer to only 'laboratory' rates. Thus at high temperatures they do not include the effect of having a thermal population of accessible excited states in the target nucleus.

In order to enhance the usefulness of these TNRR values in astrophysical calculations, we have fitted them to an empirical form suggested by Fowler (1973). The TNRR is given as

$$P_{12} = (\alpha + \beta T_9^{\gamma}) \exp(-11.605\,|Q|/T_9) \tag{5}$$

where α, β and γ are constants to be found by fitting the P_{12} values at various T_9 values for each target. Even though the above functional form was tried for all the nuclides discussed in the present work, only half the number of them could be adequately fitted by expression (5) to yield α, β and γ values. The results are listed in Table 2. A careful examination of these parameters (Table 2) or the TNRR values (Table 1) does not reveal any systematic behaviour as a function of A or Z of the targets considered here.

4. Conclusion

Starting from the measured (p,n) cross-sections, we have computed the TNRR values for 13 nuclides in the mass range A = 92122. The TNRR values extracted in the present work agree with those obtained by Roughton *et al.* (1979)in the case of^{95,96}Mo and ^{122}Sn nuclei. The two results differ considerably for ^{117}Sn target. Roughton *et al.* (1979) have quoted the TNRR values with errors ranging from 15 to 50 per cent. The present results are estimated to have uncertainties of not more than 10 per cent. The compilation of the TNRR values for A = 92–122 does not seem to indicate the presence of any kind of simple systematics. It is hoped that the experimentally determined values of TNRR will be helpful in improving the theoretical models developed to compute them, so that these theoretical calculations can be extended with greater confidence to many other nuclei for which measurements do not exist.

Acknowledgement

The author thanks Professor Ramadurai for his helpful comments.

References

Burbidge, E. M., Burbidge, G. R, Fowler, W. A., Hoyle, F. 1957, *Rev. Mod. Phys.,* **29,** 547.
Clayton, D. D. 1968, *Principles of Stellar Evolution and Nucleosynthesis,* McGraw Hill, New York.
Flynn, D. S., Hershberger, R. L, Gabbard, F. 1979, *Phys. Rev.,* **C20**, 1700.
Fowler, W. A. 1973, in *Explosive Nucleosynthesis,* Eds D. N. Schramm & W. D. Arnett, Univ. Texas press, p. 297.
Hershberger, R. L., Flynn, D. S., Gabbard, F., Johnson, C. H. 1980, *Phys. Rev.,* **C21**, 896.
Johnson, C. H., Bair, J. K., Jones, C. M., Penny, S. K., Smith, D. W., 1977, *Phys. Rev.,* **C15**,196.
Johnson, C. H., Galonsky, A., Kernell. 1979, *Phys. Rev.,* **C20**, 2052.
Kailas, S., Mehta, M. K. 1976, *Pramana,* **7**, 6.
Roughton, N. A., Fritts, M. J., Peterson, R. J., Zaidins, C. S., Hansen, C. J. 1979, *Atomic Data and Nuclear Data Tables,* **23**, 177.
Sargood, D. G. 1982, *Phys. Rep.,* **93**, 61.
Sargood, D. G. 1983, *Phys. Rep.,* **98**, 396.
Vlieks, A. E., Morgan, J. F., Blatt, S. L. 1974, *Nucl. Phys.,* **A224**, 492.
Woosley, S. E., Fowler, W. A., Holmes, J. A., Zimmermann, B. A. 1975, Orange aid preprint No. 422, California Inst. Technology.
Woosley, S. E., Fowler, W. A., Holmes, J. A., Zimmermann, B. A. 1978, *Atomic Data and Nucl. Data Tables,* **22**, 371.

J. Astrophys. Astr. (1986) **7,** 59–70

Constraints on Unstable Heavy Neutrinos from Cosmology

M. M. Vasanthi & T. Padmanabhan *Tata Institute of Fundamental Research, Homi Bhabha Road, Bombay 400005*

Received 1985 September 16; accepted 1985 December 11

Abstract. Cosmological scenarios with massive unstable neutrinos are discussed. Restrictions on the mass and the lifetime of the unstable neutrino are derived from (a) age and mass density of the universe and (b) the growth of primordial fluctuations. It will not be possible to accommodate unstable neutrinos with masses above ~ 1 ke V in standard cosmology unless they have exceedingly small lifetime: $\tau < 5 \times 10^8$ s.

Key words: neutrino, unstable—cosmology

1. Introduction

It is by now quite well established that there exist three species of neutrinos. The cosmological implication of massive-ν (mass ~ 10 eV) have been analyzed in the past (Gerhstein & Zel'dovich 1966; Cowsik & McClelland 1973; Doroshkevich *et al.* 1981; Bond, Efstathiou & Silk 1980; Sato & Takahara 1981). Experimental evidence indicating a small but nonzero mass for the lightest of the neutrino species, ν_e (Lubimov *et al,* 1980) has generated further interest in the neutrino-dominated universe scenarios.Electron neutrino, if it is massive, can play two crucial roles: (i) it can provide the 'missing mass' in galaxies and clusters of galaxies and (ii) it may help the formation of galaxies and other structures. It is not yet clear as to whether massive neutrinos really achieve either (i) or (ii) in a consistent fashion (For difficulties with 'hot' dark matter scenario see *e.g.* White, Frank & Davies 1983; Hut & White 1984).

If the electron neutrino is massive, then there is every likelihood that the other two species are massive as well. However, a very massive neutrino cannot be stable over cosmological timescales. A stable neutrino with mass of a few ke V would provide the universe with density a few hundred times the closure density—which is clearly ruled out by observational bounds on decelaration parameter (see *e.g.* Sandage 1972). So massive heavy neutrino must be unstable. We discuss in this paper the bounds that can be imposed on the mass and lifetime of such an unstable heavy neutrino. (For previous and related work on this subject, see Davis *et al.* 1981; Turner, Steigman & Krauss 1984; Gelmini, Schramm & Vallee 1984; Olive, Seckel & Vishniac 1985; Fukugita & Yanagida 1984; Dicus,Kolb & Teplitz 1978; Turner 1985.)

It must be emphasized that the present paper is not an attempt at producing a viable cosmological scenario using unstable neutrinos. We are only concerned with the constraints that cosmology imposes on the parameters of unstable heavy neutrino. This approach is motivated by three different considerations. First one was a recent report

(Simpson 1985) claiming evidence for a heavy neutrino of about 17keV mass.So far this result has not been confirmed by other groups. The cosmological implications of this 17 keV neutrino (assuming it to be unstable) was discussed by the authors in a previous paper (Padmanabhan & Vasanthi 1985). It was shown that such a heavy neutrino makes the universe matter dominated (by the decay products of the heavy neutrino) at a redshift $z \lesssim 310$. Virtually no growth of perturbations occurs in the radiation dominated era. Further, the decay of the heavy neutrino is likely to disrupt and smoothen out some of the past growth. We thus found that a 17 keV neutrino would be a 'burden' to cosmology.In this paper we have extended the analysis and derived bounds on the parameters of the heavy neutrino from considerations of galaxy formation.

The second motivation is related to the interactions suggested for neutrinos. It is known that the simplest weak interaction models give too large a lifetime for massive heavy neutrinos to be cosmologically acceptable. The bounds which we derive on the lifetime and mass of the unstable heavy neutrino may help to distinguish cosmologically viable particle physics models from others.

Thirdly, the study of the parameters of muon and tau neutrino can have an indirect bearing on the lightest stable neutrino. At present, models of galaxy formation distinguish between cold and hot dark matter. Cold dark matter seems to be a current favourite even though the evidence for such a choice is far from decisive. Any clearcut experimental evidence for the mass of any of the neutrinos will upset these scenarios. It seems therefore reasonable to analyze the cosmological implications of heavy neutrino to the same extent done for the light stable neutrino in the past.

Our basic results are the following: (i) It is extremely difficult to incorporate heavy neutrinos of masses greater than about 1 ke V. In order to do that (without violating cosmological constraints), the lifetime of the neutrino has to be kept as low as about 5×10^8 s. This lifetime is much shorter than the value usually obtained ($\sim 5 \times 10^{13}$ s) in flavour-changing decays, (ii) For a given mass m_H (< 1 keV) of the heavy neutrino, the lifetime is constrained by $\tau < 6.13 \times 10^{15} (m_H / 1 \text{ keV})^{-2} \; h_0^4$ s, where $H_0 = 100 \; h_0$ km s^{-1} Mpc^{-1} . (iii) For a very narrow range of parameters, it is possible to have a radiation-dominated universe at the present epoch.

The plan of the paper is as follows: In Section 2 we discuss the basic scenario and work out the kinematical constraints. In Section 3 we look at the growth of fluctuations in the above scenario and consider various situations in which perturbations can grow effectively. The conclusions are discussed in Section 4.

2. Basic scenario and kinematical constraints

2.1 *Basic Scenario*

In a standard big-bang model, a neutrino with mass ranging from a few tens of eV up to a few MeV decouples at $t = t_{DC}$ when the temperature of the universe was about 3.4×10^{10} K (the decoupling temperature of the universe is fairly insensitive to the mass; see for *e.g.* Dicus, Kolb & Teplitz 1978). As the universe cools, the heavy neutrino—ν_H—becomes non-relativistic when the temperature is

$$T_{NR} = m_H c^2/k = 1.16 \times 10^7 \text{K}(m_H / 1 \text{ keV}) \tag{1}$$

where the mass of the heavy neutrino is scaled to 1 keV for convenience. Henceforth we

shall not display the scaling explicitly with the understanding that the heavy neutrino m_H is in units of keV. A little later, at $t = t_{eq}$, ν_H starts dominating the energy density of the universe. The temperature T_{eq} and time t_{eq} (since big bang) for this epoch is given by,

$$T_{eq} = 1.43 \times 10^6 \, m_H \, \mathrm{K}, \tag{2}$$

$$t_{eq} = 9.39 \times 10^7 \, m_H^{-2} \mathrm{s}. \tag{3}$$

This is the epoch at which the energy density of the heavy neutrino is equal to that of the rest of the (relativistic) matter. As we shall see below the decay products of ν_H are most likely to be highly relativistic. If the lifetime of ν_H is extremely small ($\tau = t_{eq}$)most of the ν_H will decay before it becomes non-relativistic and starts dominating. If this is the case, the decay products of ν_H as well as rest of the matter will merely continue to evolve as a relativistic soup. *No essential new feature due to the unstable heavy neutrino will remain.* The condition for such (an uninteresting) scenario is $t \lesssim t_{eq}$, or in other words (using Equation 3),

$$m_H^2 (\tau/10^{10} \mathrm{s}) \lesssim 9.39 \times 10^{-3}. \tag{4}$$

This also implies an extremely short lifetime for the massive neutrino and cannot be incorporated in Standard particle physics models. Nevertheless, if (4) is satisfied, no further constraints can be imposed on the unstable neutrino. We shall now proceed assuming (4) is violated. That is, we assume

$$m_H^2 (\tau/10^{10} \mathrm{s}) > 9.39 \times 10^{-3}. \tag{5}$$

Our constraints in the rest of the paper are for this particular case. In conditions (4) and (5) we have scaled the lifetime τ in units of 10^{10} s. Hereafter we shall not display the scaling in τ explicitly. It will be assumed that τ is in units of 10^{10} s unless otherwise stated. For timescales $t > \tau$ the decay of ν_H becomes important. We can take the decay to be virtually complete at a time $t = t_D$ when $p(\nu_H) < \rho$ (others). The energy density due to ν_H at t is given by

$$\rho_H(t) \simeq m_H c^2 n_H (t_{eq}) [S_{eq}/S(t)]^3 \exp[-(t - t_{eq})/\tau] \tag{6}$$

where $n_H(t_{eq})$ is the number density of ν_H at t_{eq} and S is the expansion factor. The energy density of other forms at this time will be

$$\rho_{others}(t) \simeq 2.7 \, n_\gamma(t_{eq}) k T_{eq} [S_{eq}/S(t)]^4 \tag{7}$$

where $n_\gamma (t_{eq})$is the number density of photons at t_{eq}. Comparing (6) and (7) it is easy to estimate t_D to be

$$t_D \simeq 10.34 \, \tau. \tag{8}$$

In other words, ν_H dominates the dynamics up to $t < t_D \simeq 10.34\tau$.

How does the universe behave for $t > t_D$? The decay cannot be radiative because this channel ($\nu_H \rightarrow \nu_L$ +photons) is severely constrained by the photon emissivity of the galaxy (Dicus, Kolb & Teplitz 1977; Cowsik 1977; Gunn *et al.* 1978; Silk & Stebbins, 1983). Neither can the decay be due to Standard weak interactions because the lifetime for such decays would be exceedingly large (see *e.g.* de Rujula and Glashow 1980). A remaining possibility is the decay of the heavy neutrino into a light neutrino, ν_L and another light particle, *e.g.* to a Goldstone boson, that couples weakly to a flavour-changing neutrino current (see Wilczek 1982; Gelmini, Schramm & Valle 1984;

Fukugita & Yanagida 1984). Note that the heavy neutrino cannot decay into any cosmologically stable particle of masses greater than tens of electron volts. In virtually all the particle physics models which have been proposed, the companion particle of ν_L is extremely light (< 1 eV) (see references cited above). In that case the energy m_H of the heavy neutrino is shared equally between the decay products. For the sake of definiteness we shall assume the light neutrino (ν_L) produced by the ν_H decay to carry an energy $\frac{1}{2} m_H$. Such a light neutrino would be extremely relativistic (since $\frac{1}{2} m_H \gg m_L$) at the time of decay and the universe again becomes radiation dominated.

When the universe expands further by a factor $f = (m_H/2m_L)$, these ν_L will become non-relativistic. The radiation temperature at the time of decay, $T(\tau)$ is given by (note that for $t_{eq} < t < \tau$, the universe is matter dominated with $S \sim t^{2/3}$)

$$T(\tau) = T_{eq}\,(t_{eq}/\tau)^{2/3} = (6.36 \times 10^4\ \mathrm{K})\,(m_H \tau^2)^{-1/3}. \tag{9}$$

Similarly, the radiation temperature at the time (t_{nr}) when the decay product ν_L becomes non-relativistic is given by

$$T_{nr} \simeq T(\tau)[m_L/(m_H/2)] = (1.27 \times 10^3\ \mathrm{K})\,(m_H^2 \tau)^{-2/3}\,(m_L/10\ \mathrm{eV}). \tag{10}$$

The scenario depends on whether $T_{nr} > T_0$ or $T_{nr} < T_0$ where T_0 is the present day cosmic microwave background radiation (CMBR) temperature. If $T_{nr} < T_0$ we are still in a radiation dominated era, dominated by the relativistic decay products of ν_H. On the other hand, if $T_{nr} > T_0$, the decay products would have become non-relativistic by now. In this case we are in the familiar matter dominated universe. We shall consider these two cases separately.

Case (a): $T_{nr} > T_0$, *matter domination today*:
We shall first compute the age of the universe (t_u) in the scenario. In the radiation phase, $\tau < t < t_{nr}$ $S \sim t^{1/2}$ so that

$$T(\tau)/T_{nr} = S_{nr}/S(\tau) = (t_{nr}/\tau)^{1/2}, \tag{11}$$

while for $t_{nr} < t < t_u$, $S \sim t^{2/3}$, giving

$$T_{nr}/T_0 = S_0/S_{nr} = (t_u/t_{nr})^{2/3}. \tag{12}$$

Together,

$$t_u = t_{nr}\,(T_{nr}/T_0)^{3/2} = \tau[T(\tau)/T_{nr}]^2\,[T_{nr}/T_0]^{3/2} = \tau T^2(\tau)/T_{nr}^{1/2} T_0^{-3/2}. \tag{13}$$

Using Equations (9) and (10) in (13), we get

$$t_u = (1.35 \times 10^{10}\ \mathrm{yr})(T_0/1.9\ \mathrm{K})^{-3/2}\,(m_L/10\ \mathrm{eV})^{-1/2}. \tag{14}$$

For scaling calculations it is proper to take the CMBR temperature to be 1.9 K. The enhancement of CMBR temperature to the observed 2.7 K is due to the $e^+ e^-$ annihilations. It is not necessary to take into account this completely extraneous effect.

If the minimum age of globular clusters is taken to be 15 billion years, then Equation (14) underestimates the age for m_L greater than 8 eV. Unfortunately, such a marginal contradiction is not of much value. Note that t_u was estimated in Equation (13) by scaling with respect to t_{eq} and by assuming an instantaneous decay of all ν_H at a fixed

time τ. Because of these assumptions one cannot entirely rule out a 50 per cent change in t_u. Equation (14) also implies that $h_0 < 0.6$.

It is also easy to verify that our overall picture is consistent in the present case. We assumed in deriving Equation (13) that $t_{nr} < t_u$ or equivalently, $T_{nr} > T_0$ Using (10) we see that this is same as demanding,

$$(1.27 \times 10^3\,\mathrm{K})\,(m_H^2\,\tau)^{-2/3}\,(m_L/10\,\mathrm{eV}) > 1.9\,(T_0/1.9\,\mathrm{K}). \tag{15}$$

In other words,

$$m_H^2\,\tau < 1.73 \times 10^4\,(m_L/10\,\mathrm{eV})^{3/2}\,(T_0/1.9\,\mathrm{K})^{-3/2}. \tag{16}$$

which, as we shall see, will be identically satisfied (see Equation 22 below)

Case (b): $T_{nr} < T_0$, radiation-domination today: This situation turns out to be somewhat more tricky. To begin with, note that the constraint $T_{nr} < T_0$ is equivalent to the reverse of case (a), *i.e.*,

$$m_H^2 > 1.73 \times 10^4\,(m_L/10\,\mathrm{eV})^{3/2}\,(T_0/1.9\,\mathrm{K})^{-3/2}. \tag{17}$$

Let us now compute the age in the scenario. Calculations similar to the one above give,

$$\begin{aligned} t_u &= \tau\,[T(\tau)/T_0]^2 \\ &= (3.6 \times 10^{11}\,\mathrm{yr})\,(T_0/1.9\,\mathrm{K})^{-2}\,(m_H^2\,\tau)^{-1/3}. \end{aligned} \tag{18}$$

The constraint $t_U \lesssim 10^{10}$ yr now implies that

$$(m_H^2\,\tau) < 4.67 \times 10^4\,(T_0/1.9\,\mathrm{K})^{-6}. \tag{19}$$

Thus this scenario can operate only if τ simultaneously satisfies the inequalities,

$$(1.73 \times 10^4/m_H^2)(m_L/10\,\mathrm{eV})^{-3/2} < \tau < (4.67 \times 10^4/m_H^2)(T_0/1.9\,\mathrm{K})^{-6}.$$

We shall continuously refer to cases (a) and (b) in what follows.

2.2 *Constraints from Energy Density of Decay Products*

In both the above cases—(a) and (b)—a further constraint on m_H and τ can be obtained based on the energy density contributed by the decay products of ν_H. This energy density is easily computed to be (see *e.g.* Dicus, Kolb & Teplitz 1978),

$$\begin{aligned} \rho &= m_H\,n_H\,(t_{DC})\,(1.9\,\mathrm{K}/T_{DC})^3 \int_{t_0}^{t_u} \mathrm{d}t/\tau\,(t/t_u)^{1/2} \exp[-(t-t_0)/\tau] \\ &\simeq n_H\,(t_{DC})\,(1.9\,\mathrm{K}/T_{DC})^3\,(\sqrt{\pi}/2)\,m_H\,(\tau/t_u)^{1/2} \\ &= (1.66 \times 10^{-28}\,\mathrm{g\,cm^{-3}})\,m_H(\tau/t_u)^{1/2}. \end{aligned} \tag{20}$$

The decay time t is not scaled in this expression; also it is assumed that $t_{DC} < T < t_u$.

Demanding $\rho < \Omega_m p_c$, where Ω_m is the maximum density parameter contributed by the decay product (if Ω_b is the baryonic contribution and W_L is the contribution from the primordial light neutrino, then $\Omega_m = [1 - (\Omega_L + \Omega_b)]$, we get (with $H_0 = 100\,h_0$ kms $^{-1}$ Mpc^{-1})

$$(\tau/t_u) < 1.44 \times 10^{-2}\,\Omega_m^2\,h_0^4\,m_H^{-2}. \tag{21}$$

Translation of this constraint in terms of m_H and τ is different for the two cases (a) and (b). In case (a) t_u is given by Equation (14) and combining (14) and (21) we get

$$m_H^2 \tau \leqslant 6.13 \times 10^5 \Omega_m^2 h_0^4 (T_0/1.9\,\mathrm{K})^{-3/2} (m_L/10\,\mathrm{eV})^{-1/2}. \quad (22)$$

Similarly for case (b) we get [combining (18) and (21)],

$$m_H^2 \tau < 2.51 \times 10^5 \Omega_m^{3/2} h_0^3 (T_0/1.9\,\mathrm{K})^{-3/2}. \quad (23)$$

which is only marginally different from (19). Since (19) is anyway satisfied in case (b) we do not get any new constraint from (23).

All the kinematic constraints are summarized in Fig. 1 where lifetime is plotted against the mass m_H. The vertical line at m_H = 10 eV and the horizontal line at $\tau = 4.26 \times 10^{17}$ seconds limit the region we are considering. Physically this corresponds to assuming the ν_H to be more massive than ν_L (~ 10 eV) and unstable within the age of the universe(i.e. $\tau < t_u$). The broken line above this line ($\tau = 1.73 \times 10^4 m_H^{-2}$) separates case (a) and case(b). The region above this corresponds to universes which are radiation dominated now. In that case, Equation (19) gives the upper bound based on the age of the universe. In order for the universe to be radiation dominated today, ν_H has to decay fairly late (i.e. in the recent past). On the other hand, this would lead to a rather youngish universe. Hence only a narrow region marked in the figure is allowed for case (b).

We do not get such constraints in case (a). Energy density requirement represented by Equation (22) does not lead to any new constraint because case (a) already satisfies the stronger constraint *via* Equation (16). In other words, the constraints are fairly weak for case (a).

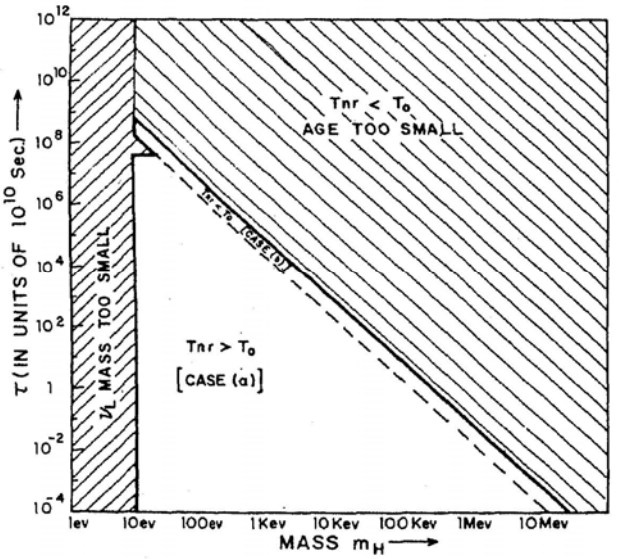

Figure 1. The lifetime τ (in units of 10^{10} s) is plotted against the mass of the heavy neutrino, m_H. The broken line separates the two cases (a) and (b) (see text). For the case (a), the regions above the horizontal line at $\tau \simeq 10_1$ s are not allowed from the constraint that τ is less than the age of the universe. For case (b) this constraint is given by the thick line just above the broken line. In both the cases the regions which are not allowed are struck out.

We shall now study the growth of fluctuations in the above scenario, which will lead to much stronger constraints.

3. Growth of fluctuations

tudies about the growth of density fluctuations in an expanding universe (Peebles 1979) have led to the following conclusions: (a) The growth is significant only when the wavelength of fluctuation is less than the size of the horizon, (b) No fluctuations can grow in a universe dominated by relativistic particles (Meszaros 1974). (c) In the matter dominated era the density contrast $\delta = (\delta\rho/\rho)$ grows as $t^{2/3}$. In other words $\delta \propto S(t)\ [T(t)]^1$.

Baryonic fluctuations cannot grow until the recombination era ($z \sim 10^3$) and hence the baryonic density perturbations cannot grow by more than a factor of 10^3 between recombination and today. This implies the existence of $\delta_B \geqslant 10^3$ at $z \sim 10^3$. For adiabatic fluctuations, $(\delta\rho/\rho)_B$ is directly related to the fluctuations in CMBR temperature. A value of $\delta_B \sim 10^3$ is entirely ruled out by the observational upper limit ($\Delta T/T < 6 \times 10^{-5}$; see Fixsen, Cheng & Wilksen 1982) on the anisotropy of CMBR. One possible solution to this dilemma is to have a scenario in which non-baryonic matter can dominate before the recombination era. Their growth of fluctuations can create a potential well into which the baryons can fall immediately after they decouple from radiation.

We have seen that the non-relativistic ν_H starts dominating the energy density from T_{eq} until they decay at the temperature $T(\tau)$. It is possible for perturbations in ν_H to grow during this epoch when the universe is matter dominated. Present day studies of galaxy-galaxy correlation functions show that the scales which are entering the nonlinear regime today (*i.e.* $\delta \lesssim 1$) have sizes $L \simeq 5h_0^{-1}$ Mpc (Davis & Peebles 1983). This length scale L would have entered the horizon in the past at $t = t_L$ when the radiation temperature was, say, T_L. We shall now estimate T_L. Two scenarios arise depending on whether this scale entered before the decay of ν_H or after (*i.e.* whether $T_L > T_t$ or $T_L < T_t$). We will consider these cases separately.

If $T_L < T_T$ then fluctuations enter the horizon in the radiation dominated era. If $d_H(t_L)$ is the horizon size at time t_L, then

$$d_H \simeq c\,t_L = c\tau T^2(\tau)/T_L^2. \tag{24}$$

The physical wavelength λ of the fluctuations scale with expansion linearly; *i.e* $\lambda(t) \propto S(t)$. Fluctuations with a wavelength L today would have a wavelength $\lambda(t_L)$ at time $t = t_L$, where

$$\lambda(t_L) = L(T_0/T_L). \tag{25}$$

Therefore the condition $d_H = \lambda$ ('fluctuations entering horizon') implies (compare (24) and (25))

$$T_L = (c\tau/L)[T^2(\tau)/T_0]. \tag{26}$$

Our condition $T_L < T(\tau)$ is equivalent to

$$\tau < 3.33\,h_0^{-3}\,m_H\,(T_0/1.9\,\mathrm{K})^3. \tag{27}$$

The fluctuations enter the horizon after the ν_H decay, in the radiation dominated universe; however *it cannot grow in this epoch.* If $T_{nr} < T_0$ (case (b) considered in the

previous section in which the universe remains radiation dominated from $t = \tau$ until today) then the *fluctuations cannot grow at all.* This completely rules out the situation corresponding to case (b) if $T_L < T(\tau)$. On the other hand if $T_{nr} > T_0$ the fluctuations can grow after (and only after) the decay products have become non-relativistic. Thus the growth occurs from $t = t_{nr}$ till today. The growth factor in this matter-dominated era is

$$\varepsilon \equiv T_{nr}/T_0 \simeq 6.68 \times 10^2 (m_H^2 \tau)^{-2/3} (m_L/10\,\text{eV}) (T_0/1.9\,\text{K})^{-1}. \quad (28)$$

It is known that the spectrum of primordial fluctuations has an amplitude $(\delta\rho/\rho) \sim 10^{-4}$ when they enter the horizon. To achieve $(\delta\rho/\rho) \sim 1$ today, the growth factor ε has to be $\geqslant 10^4$. Using (28) we get

$$m_H^2 \tau < 1.73 \times 10^{-2} (m_L/10\,\text{eV})^{3/2} (T_0/1.9\,\text{K})^{-3/2}. \quad (29)$$

While the above situation is a theoretical possibility it is of little practical importance. Note that the above condition is almost the same as Equation (4). This corresponds to a situation consisting of the following ordering of events: ν_H decays very early ($\tau \sim t_{eq}$) leaving a relativistic soup; fluctuations enter the horizon in the relativistic epoch; Decay products become non-relativistic at temperatures 10^4; fluctuations grow in the matter-dominated era. Clearly this is indistinguishable from the conventional single stable neutrino (with mass ~ 10 eV) scenario. We also note that the above constraint demands an extremely short lifetime for the unstable neutrino which is not compatible with standard particle physics.

On the other hand, if $T_L > T(\tau)$, fluctuations enter the horizon in the regime when the non-relativistic ν_H dominates the energy density. In this case, Equation (24) is replaced by

$$d_H = c\tau [T(\tau)/T_L]^{3/2} \quad (30)$$

and since

$$\lambda = L(T_0/T_L)$$

we get

$$T_L = T(\tau)(c\tau/L)^2 [T(\tau)/T_0]^2. \quad (31)$$

The assumption $T_L > T(\tau)$ now translates to the inequality,

$$\tau > 3.33 (T_0/1.9\,\text{K})^3 h_0^{-3} m_H. \quad (32)$$

The growth of fluctuation is again different for case(a) and case(b). In case(a) fluctuations can grow during two different matter-dominated epochs: (A) $t_L < t < \tau$ and (B) $t_{nr} < t < t_u$. During the (in between) radiation-dominated phase ($\tau < t < t_{nr}$) the fluctuations oscillates as an acoustic wave with negligible growth. Let ε_A be the growth factor in the ν_H dominated era (A) and ε_B be the one that arises after the decayed products become non-relativistic (B). Then

$$\varepsilon_A = T_L/T(\tau) = (c\tau/L)^2 [T(\tau)/T_0]^2 = 0.45 h_0^2 (\tau/m_H)^{2/3} (T_0/1.9\,\text{K})^{-2} \quad (33)$$

while ε_B is given by Equation (28). The total growth factor is

$$\varepsilon = \varepsilon_A \times \varepsilon_B = 2.99 \times 10^2 m_H^{-2} h_0^2 (T_0/1.9\,\text{K})^{-3} (m_L/10\,\text{eV}). \quad (34)$$

The requirement $\varepsilon > 10^4$ then implies

$$m_H < 1.73 \times 10^{-1} h_0 (T_0/1.9\,\mathrm{K})^{-3/2} (m_L/10\,\mathrm{eV})^{1/2} \tag{35}$$

i.e., mass of the heavy neutrino must be less than about 0.173 keV.

We note that ε is independent of τ while dependent on m_H^{-2}. These dependences can be understood as follows: From Equation (31) note that

$$\begin{aligned} T_L &= (\tau/L)^2 [T(\tau)/T_0]^2 T(\tau) \\ &= (t_{eq}/L)^2 (T_{eq}/T_0)^2 T_{eq} \propto 1/m_H \end{aligned} \tag{36}$$

and that T_L is independent of t (of course, for computational purpose it is convenient to scale it with respect to τ). The growth factor

$$\begin{aligned} \varepsilon &= \varepsilon_A \times \varepsilon_B = [T_L/T(\tau)] (T_{nr}/T_0) \\ &= (T_L/T_0)(2m_L/m_H) \propto m_L/m_H^2 \end{aligned} \tag{37}$$

which is independent of t (we have used (10) and (36)). Larger m_H leads to smaller T_L (delay in the entry of fluctuations into the horizon) and smaller T_{nr} (longer duration of relativistic epoch). Both the effects hinder the growth of fluctuations.

The final scenario that we have to consider corresponds to case(b) with $T_L > T(\tau)$. In this situation phase B does not exist because the universe is still radiation dominated. Thus, all the growth must take place during phase A. Using the expression for ε_A (see Equation 33) and imposing the condition $\varepsilon_A > 10^4$ we get

$$\tau > 3.33 \times 10^6 (T_0/1.9\,\mathrm{K})^3 h_0^{-3} m_H \tag{38}$$

The constraints from the growth of fluctuations are depicted in Fig. 2. Line marked (1) distinguishes case(a) from case(b), while the line marked (2) distinguishes $T_L < T(\tau)$ from $T_L > T(\tau)$. These two lines divide t-m_H plane into four regions. The region which is to the right of both (1) and (2) is completely ruled out. For case(a) with $T_L = T(\tau)$ the parameters are restricted by Equation (29). If $T_L > T(\tau)$ the only constraint is on the mass ($m_H < 173$ eV). We have also marked the vertical line at $m_H = 10$ eV. In case *B,* when $T_L > T(\tau)$ only regions above the line corresponding to Equation (38) are allowed.

Before proceeding further, it is probably worthwhile to consider various assumptions upon which Fig. 2 is based. In arriving at these constraints, we have made (rather drastic) simplifications.

(i) We have neglected all the disruptive effects of the decay of ν_H on the already formed structures. The decay can effect the structure in two ways. Firstly it can violently disrupt the condensates. Secondly, free streaming of relativistic decay products can wipe out smallscale inhomogeneities. Both these effects can change the perturbation spectrum at large scales. Hopefully this will not be important at scales of few Mpc and will manifest only at supercluster scales. This effect is under investigation.

(ii) We have assumed that there is no growth during the radiation-dominated epoch. This is not strictly true because there can be some growth due to the residual velocity field of the matter after it crosses the horizon (Primack & Blümenthai 1984). This can relax the constraints slightly.

(iii) In one particular case, we have obtained the total growth factor by multiplying the growth factors at two different epochs. If too much of structure dissipation occurs following the decay, then this calculation may not be strictly correct.

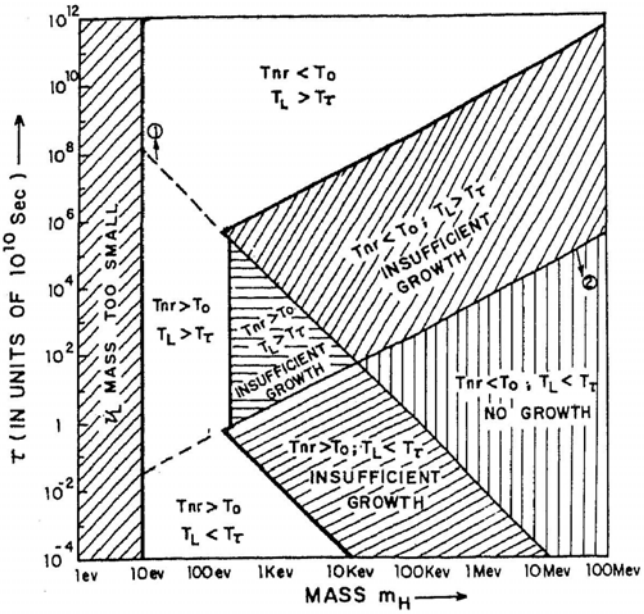

Figure 2. Lifetime τ is plotted against mass m_H. Line (1) distinguishes case (a) from case(b) while line (2) separates the region $T_L > T(\tau)$ from $T_L < T(\tau)$. The thick line separates the allowed regions (from growth of fluctuation analysis) from the 'not allowed' regions. For case (a) with $T_L > T(\tau)$ the only constraint is that $m_H < 173$ eV, while for $T_L < T(\tau)$ growth is sufficient only for regions to the left of the line given by Equation (29) (see text). For case (b), $T_L < T$ (t) has no provision for growth to occur at any time (region below line). For $T_L > T(\tau)$ growth is sufficient only for regions above the line given by Equation (38).

We plan to investigate these dynamical effects in a future publication. At this stage we may say that the effect of (i) to (iii) above makes the boundary lines drawn in Fig. 2 (and in Fig. 3) less sharp. As long as a particular (m, τ) value falls reasonably within a region one can use these constraints with confidence.

4. Conclusions

The constraints derived in Section 2 and 3 are combined into Fig. 3. The region bordered by the thick line in Fig. 3 gives the allowed domain. Clearly the top region of Fig. 2 is severely constrained by the age of the universe as shown in Fig. 1. The allowed physics with unstable neutrinos can be understood by considering three typical points in regions marked A, B and C.

Region A probably holds the least interest. Here the perturbations enter the horizon *after* the decay of unstable neutrinos, in the radiation-dominated era. The growth can take place only after the decay products have become non-relativistic. These constraints imply that the decay must occur too early ($\tau = T_{eq}$) for any interesting feature of ν_H to remain. Also note that the typical lifetime in this domain is $\sim 10^7$ s which is too small by conventional particle physics standards for ν_H.

In region B the fluctuations enter the horizon before the decay and hence can grow during the first matter-dominated era as well as after the decay products have become non-relativistic. A wide range in lifetime is available for B, but the mass of the neutrino is constrained to be less than about 173 eV.

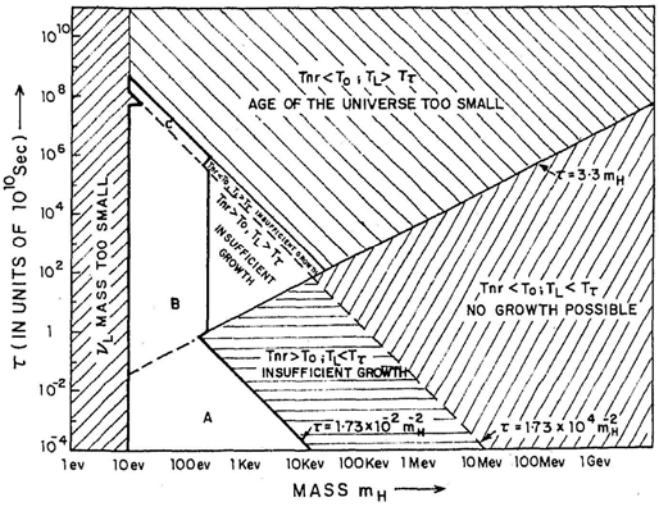

Figure 3. The constraints depicted in Figs 1 and 2 are combined in this figure. The regions allowed are within the thick lines.

Both regions A and B correspond to the situation in which the present day universe is matter dominated. In contrast, region C corresponds to a universe which is still radiation dominated. Clearly parameters in C are most severely restricted.

With no extra input from particle physics it is impossible to constrain the lower region of the figure. However, any realistic modelling of neutrino interactions will give a lower bound to the lifetime. Given such a constraint (external to cosmology) the parameter space will be restricted to a compact simply connected domain in m-τ plane. For example, if we make the conservative assumption that the lifetime is definitely greater than about 10^7 s, then the mass of the unstable neutrino cannot be greater than about 10 keV. Note that this is a reasonably powerful constraint in the modelling of neutrino interactions.

References

Bond, J. R., Efstathiou, G., Silk, J. 1980, *Phys. Rev. Lett.,* **4**5, 1980.
Cowsik, R. 1977, *Phys. Rev. Lett.,* **39, 784**.
Cowsik, R., McClelland, J. 1973, *Astrophys. J.,* **180**,
7.Davis, M., Lecar, M., Pryor, C, Witten, E. 1981, *Astrophys. J.,* **250,** 423
Davis, M., Peebles, P. J. E. 1983, *Astrophys. J.,* **267,** 465.
de Rujula, A., Glashow, S. L. 1980, *Phys. Rev. Lett.,* **45,** 942
Dicus, D. A, Kolb, E. W., Teplitz, V. L. 1977, *Phys. Rev. Lett.,* **39,** 168.
Dicus, D. A., Kolb, E. W., Teplitz, V. L. 1978, *Astrophys. J.,* **221**, 327.
Doroshkevich, A. G., Khlopov, M. Yu., Sunyaev, R. A., Szalay, A. S., Zeldovich, Ya. B. 1981, *Proc N.Y. Acad. Sci,* **375,** 32.
Fixsen, D. J., Cheng, E. S., Wilkinson, D. T. 1982, *Phys. Rev. Lett,* **50**, 620.
Fukugita, M., Yanagida, T. 1984, *Phys. Lett.,* **144B,** 386.
Gerhstein, S. S., Zeldovich, Ya. B. 1966, *JETP Lett.,* **4**, 174.
Gelmini, G, Schramm, D. N., Valle, J. W. F. 1984, *Phys. Letts.,* **146B,** 311.
Gunn, J., Lee, B. W., Lerche, L, Schramm, D. N., Steigman, G. 1978, *Astrophys. J.,* **223**, 1015.

Hut, P., White S. D. M. 1984, *Nature,* **310**, 637
Lubimov, V. A., Novikov, E. G., Nozik, V. Z., Tretyakov, E. F., Kosik, V. S. 1980, *Phys. Lett.,* **94B,** 266.
Meszaros, P. 1974, *Astr. Astrophys.,* **37**, 225.
Olive, K. A., Seckel, D., Vishniac, E. 1985, *Astrophys. J.,* **292**, 1.
Padmanabhan, T., Vasanthi, M. M. 1985, *Nature,* **317**, 335.
Primack, J. R., Blumenthal, G. R. 1984, in *Clusters and Groups of Galaxies,* Eds F. Mardirossian, G. Giuricin & M. Mezzetti, D. Reidel, Dordrecht, p. 435.
Peebles, P. J. E. 1980, *LargeScale Structure of the Universe,* Princeton Univ. Press.
Sandage, A.1972, *Astrophys. J.,* **173**, 485.
Sato, H., Takahara, P. 1981, *Prog. Theo. Phys.,* **65**, 374; **66**, 508.
Silk J., Stebbins, A. 1983, *Astrophys. J.,* **269**, 1.
Simpson, J. J. 1985, *Phys. Rev. Lett.,* **54**, 1891.
Turner, M. S. 1985, *Phys. Rev.,* **D3**1, 1212.
Turner, M. S., Steigman, G. S., Krauss, L. M. 1984, *Phys. Rev. Lett.,* **52**, 2091.
White, S. D. M., Frenk, C. S., Davis, M. 1983, *Astrophys. J.,* **274**, LI.
Wilczek, F. 1982, *Phys. Rev. Lett,* **49**, 1549.

J. Astrophys. Astr. (1986) **7,** 71–75

Relation of the Jet in M 87 to nearby Galaxies in the Virgo Cluster

Halton Arp* *Mount Wilson and Las Campanas Observatories of the Carnegie Institution of Washington, 813 Santa Barbara Street, Pasadena, CA 91101-1292, USA*

Received 1985 November 16; accepted 1986 January 8

Abstract. The massive and active galaxies in the core of the Virgo Cluster were shown in 1968 to be aligned on either side of M 87, along the direction of the jet and counter-jet. Recent observations confirm the significance of this alignment by showing that the brightest X-ray sources, including additional large galaxies, define the same line.

Detailed X-ray maps of M 86 show that this galaxy, which is part of the alignment, is probably blown by a wind from M 87 due to its close alignment with the jet. But the large radio E galaxy, M 84, which is 1.4 degrees away from M 87, and *exactly* along the line of the jet, is shown by the compression of its X-ray isophotes to be actually moving out along the line of the jet. This evidence furnishes rather spectacular support for the earlier conclusion that M 84 had originated as a proto-galaxy within M 87 and had been ejected out along the line of the jet.

Key words: galaxies, jets—radio sources—X-ray sources—Virgo Cluster

The typical giant radio galaxy consists of an elliptical (E) galaxy with radio lobes and jets extending far out in space on either side of the central galaxy. As soon as enough of these objects were mapped it became apparent that companion galaxies in the vicinity of the central E tended to be aligned along these directions of radio ejection. In 1968 all the strongest radio sources that were associated with E galaxies of bright apparent magnitude were studied (Arp 1968). The investigation revealed that ten of the thirteen radio E's turned out to be members of well marked lines of galaxies. In six cases the line of components of the radio emission was well defined. In five of these latter cases this direction of the radio components was coincident with the line of galaxies.

Since lines of galaxies cannot arise from an originally disordered cluster the galaxies must be formed along the lines. It was concluded in 1968 that the only possible explanation of these observations was that the aligned galaxies had originated as proto-galaxies within the central, large E and been ejected out along the line of the radio ejection. This strongly established observational phenomenon has subsequently gone quite unremarked however, undoubtedly because the conclusion to which it so inexorably leads is so foreign to current assumptions about galaxy formation.

It is important to realize, however, that a decade earlier Ambartsumian (1958,1961, 1965) had independently advanced the conclusion that galaxies ejected material and

* Alexander von Humboldt Senior Scientist awardee at the Max-Planck-Institut für Astrophysik, Garching, FRG.

that some of this material formed new galaxies. The observational demonstrations of this process which have accumulated in the ensuing years (see Arp 1978 for review) attest to the fundamental importance of Ambartsumian's original insight.

One of the most crucial galaxy alignments is shown below in Fig. 1. All the E galaxies in this densest region of the Virgo cluster were classified by de Vaucouleurs in 1961. They are shown by filled circles and the position angle of the jet by a dashed line. Since the mass-to-light ratio (*M/L*) is the greatest for E galaxies, and since these are generally the brightest galaxies in the vicinity, this result tells us that the most massive galaxies in the core of the Virgo Cluster are well aligned along the jet and (approximate) counter-jet direction. The arrows point to the two brightest radio sources in the region, M 87 and M 84, and so we see that the most active galaxies, in a radio sense, also fall along this line.

The reality of this line of galaxies is so important that its confirmation by recently published X-ray observations is one of the major points of this note. As Fig. 2 shows, the brightest X-ray sources in this region, which are generally different galaxies than pictured in Fig. 1, independently and very accurately *confirm this same alignment that was so striking in* 1968. The identification of these X-ray sources has been drawn from the contribution of Forman, Jones & de Faccio (1984) to the ESO Workshop on the Virgo Cluster. In their partially complete mosaic X-ray map of the Virgo Cluster the large, diffuse X-ray sources which comprise M 87 and M 86 are very conspicuous. These two galaxies almost fill in the region between them with X-rays. But the next three brightest X-ray sources in the area are moderately compact and fall almost exactly along the line previously defined by the jet in M 87. These additional X-ray sources are plotted as small crosses in Fig. 2 and identified in Table 1.

Table 1 lists all the E galaxies in the region as defined by Sandage & Tamman (1984) in the Revised Shapley-Ames Catalog. Two fainter E galaxies have been omitted from de Vaucouleurs' original listing and some classifications have been changed from E to S0 or vice versa. The 11 E galaxies listed in Table 1 give an even tighter definition of the

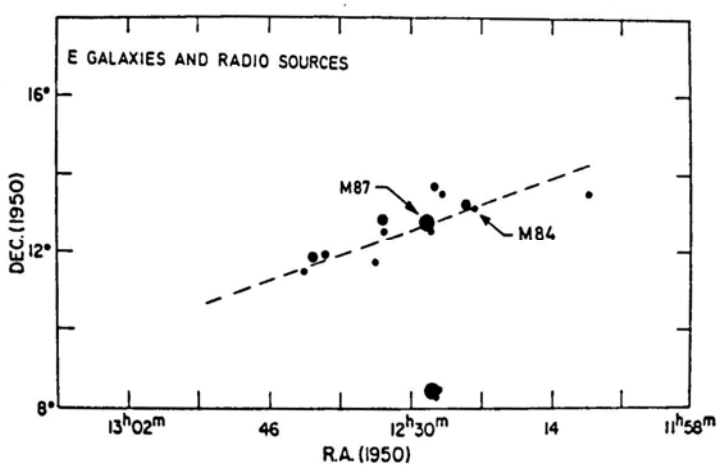

Figure 1. Filled circles represent all E galaxies in pictured region as classified by de Vaucouleurs (1961). Strongest radio sources are marked by arrows. Diagram adopted from Arp (1968).

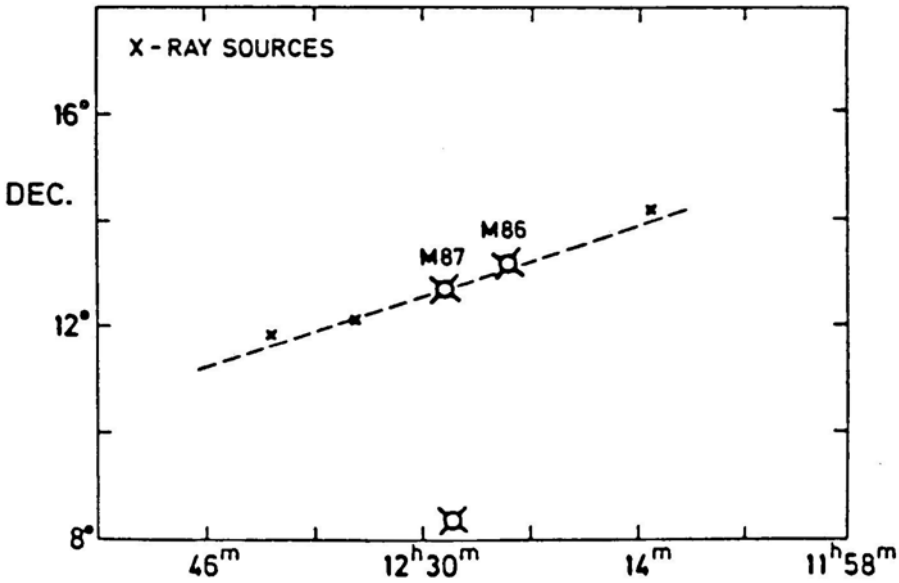

Figure 2. Symbols represent strongest X-ray source found in partially complete, mosaic X-ray map of the Virgo Cluster by Forman, Jones & de Faccio (1984). Large symbols represent extended X-ray sources, and smaller symbols the compact ones.

Table 1. Galaxies in the M 87 line*.

Galaxy NGC	$B_t^{0,i}$ (mag)	Type	Remarks
4168	12.21	E2	
4212	11.44	Sc	X-ray source
4208	—	—	
4374	10.23	E1	X-ray, radio source
4406	10.02	S0/E3	X-ray source
4473	11.07	E5	
4476	13.08	E5 pec	
4478	12.15	E2	
4486	9.62	E0	X-ray, radio source
4550	12.33	E7/S0	
4564	11.87	E6	
4579	10.01	Sab	X-ray source
4621	10.67	E5	
4647	11.66	Sc	X-ray, radio source.
4649	9.83	S0	VV object
4660	11.87	E5	

* All E galaxies in the area defined by Sandage & Tamman (1981) and strong X-ray sources from Forman, Jones & de Faccio (1984).

line through M 87 than 1961 de Vaucouleurs, classification shown in Fig. 1. Brighter X ray galaxies are also identified in Table 1.

Since this line of galaxies, radio sources and X-ray sources corresponds so closely to the line of the famous jet which originates from the centre of M 87, we could not help but examine with great interest the extended X-ray isophotes around some of the galaxies in this alignment which have also recently become available (Forman, Jones & de Faccio 1984). Fig. 3 shows the X-ray isophotes around M 86, one of the galaxies falling closely along the line to the northeast. It is evident that the outer X-ray isophotes are blowing very closely in a direction away from the line going back to M 87. The inner isophotes suggest ejection of X-ray material initially almost north-south. But as soon as the X-ray material emerges further from M 86 it clearly becomes elongated along a line almost exactly away from M 87. The position angle of M 86 from M 87 is p.a. = 296°, only about 6 degrees greater than the position angle of the jet in M 87, that is more in the direction of the 'fan jet' which comes out more broadly from M 87 (Walker 1968; Ford & Butcher 1979).

The position angle of the jet has always been taken as p.a. = 290°. For the optical jet de Vaucouleurs & Nieto (1979) measured p.a. = 290°.8 ± 0°.4. But the optical knot A is slightly north of the general line of the jet. Measures of the centre line of the radio jet, as in Fig. 4, gives p.a. = 290° ± 1°. Now the astonishing fact about the bright radio E galaxy, M 84, is that it is at p.a. = 289°.4 from M 87, that is within the accuracy of measurement, exactly along the line of the M 87 jet.

The fact that M 84 at 1.4 degrees away on the sky lies exactly along the line of the M 87 jet was first pointed out by Wade (1960). The alignment of E galaxies along this line was discussed by Arp (1968) and the exact alignment of M 84 with the M 87 jet was again emphasized by Burbidge & Burbidge (1969). But now Fig. 4 shows the most astonishing fact of all. The high resolution, HRI X-ray map of M 84 demonstrates that it is moving through the inter galactic medium of the Virgo Cluster almost exactly along this same line from M 87. The originating X-ray astronomers noted that M 84 appeared to be moving westward through the cluster medium. Fig. 4 shows that this motion is not quite west, more exactly WNW, or along the line of the jet. The inner X-ray isophotes indicate a direction about p.a. = 280° and the outer isophotes a direction about p.a. = 300°. It seems reasonable to adopt the motion of M 84 to be p.a. = 290° ±10°.

In order to estimate a rough probability of these coincidences happening by chance we take the maximum misalignment as the estimated accuracy of the angle determinations and compute

$$\text{prob} \simeq \frac{2^\circ}{360^\circ} \times \frac{20^\circ}{360^\circ} \simeq 3 \times 10^{-4}.$$

But, of course, just visual judgement of the accuracy with which the jet is defined and is pointing toward M 84 and now the direction of motion of M 84 would seem to be adequate to establish the physical significance of the configuration.

We should also remember that this observed phenomenon was predicted. In 1968 it was already stated that the observations showed: 'The only alternative . . . to be the ejection of the galaxies, or progenitors of the galaxies, from an initially large central galaxy.' It was always clear that the high surface brightness optical knots seen in the jet of M 87 represented probable examples of such protogalaxies (see review in Arp 1978).

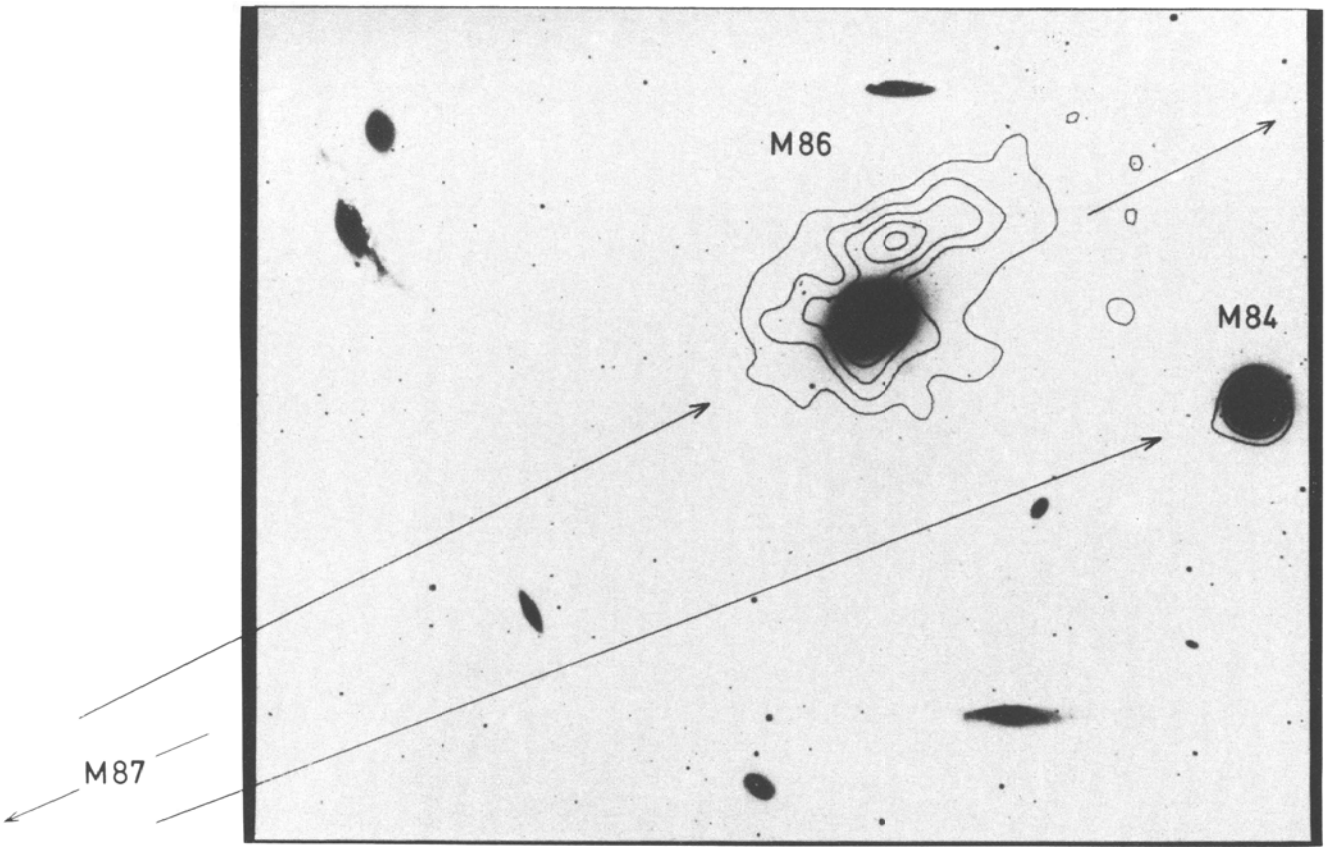

Figure 3. X-ray isophotes in region of M 86 from Forman, Jones & de Faccio (1984). Direction back toward M 87 is shown at lower left. Direction of jet in M 87 is along line toward M 84.

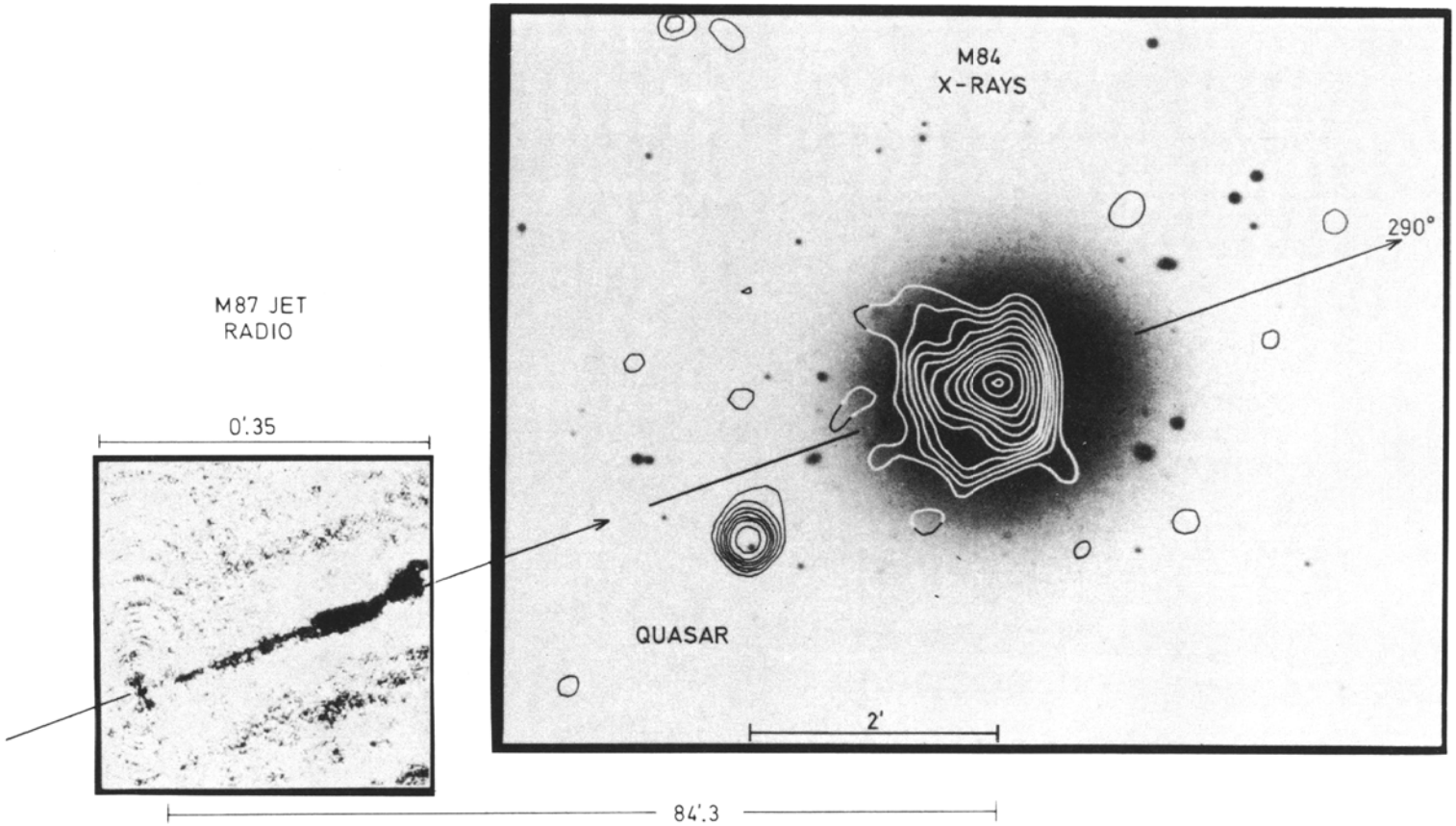

Figure 4. Highest resolution X-ray map around M 84 showing flattening of isophotes in the direction of motion (Forman, Jones & de Faccio 1984). Insert at lower left shows radio map of the M 87 jet obtained with VLA by F. N. Owen, J. A. Biretta & P. E. Hardee (The National Radio Astronomy Observatory, operated by the Associated Universities, Inc. under contract with the National Science Foundation). Radio map of M 84 by R. A. Laing (preprint) shows distension along the same line of jet.

H. ARP

Additional remarks should include the fact that the dispersion of measured redshifts of the galaxies which define the lines such as exhibited in Fig. 1, would indicate the lines cannot persist for long times. In a time about two orders of magnitude less than the usually accepted ages of the galaxies, the lines should be disrupted. Since the lines visibly exist, this may be an indication that some components of the measured galaxy redshifts are non-velocity. There is, of course, abundant other evidence now available for non-velocity redshifts in galaxies (Arp 1982, 1985, 1986).

M 86 is particularly interesting in this regard because it is one of the six galaxies in the sky with appreciably negative redshifts. All six are concentrated in this small, central region of the Virgo, cluster so there can be hardly any question of their membership. (Two are X-ay sources in the line defined in Fig. 2.) The fact that M 86 is blown by a wind from M 87, or falling toward M 87 though the medium, is additional proof of its membership in the core of Virgo Cluster despite its large negative redshift (cz_0 = -367kms $^{-1}$) . On the other hand the galaxy M 84 appears to be traveling with the jet wind and passing M 86 on the way out. M 84 may be travelling faster than the general wind in that direction. In a model where the galaxies were moving along the line, and the line is tilted away from us on the NW and towards us on the SE, the eight E's (excluding M 84 and M 86) would be moving outward from M 87 with $\simeq$ 660 km s $^{-1}$ and the four X-ray galaxies inward toward M 87 with $\Delta v \simeq 860$ km s^{-1}.

Finally there is a newly discovered quasar which falls very close to M 84 as indicated in Fig. 4. The probability of this being a chance occurrence is only $p \simeq 2 \times 10^{-3}$. Altogether there is an association of quasars with the bright E galaxies in the M87 alignment that has only about 10 ^{4} chance of being accidental (see the immediately following paper). This reinforces our conclusion that redshift values of the objects ejected from M 87, or from objects in the M 87 line, cannot be necessarily interpreted as velocity redshifts.

References

Ambartsumian, V.A.1958, *OnziemeConseilde PhysiqueSolvay,*Ed.R. Stoops,Bruxelles.

Ambartsumian, V.A.1961, *Astr.J.,* **66**, 536.

Ambartsumian, V. A.1965, in *The Structure and Evolution of Galaxies,* Interscience,New York, p. 1.

Arp,H.1968, *Publ. astr. Soc. Pacific,* **80**,129.

Arp, H. 1978, *Problems of Physics and Evolution of the Universe,* publ. Armenian. Acad. Sci.

Arp, H. 1982, *Astrophys,J.,* **263**,54.

Arp, H. 1986, *Quasars,Redshift sand Controversies,*

Arp, H.,Sulentic,J.W.1985, *Astrophys. J.,***291**, 88.

Burbidge, G. R., Burbidge, E. M. 1969, *Nature,* **224,** 21.

de Vaucouleurs, G.1961, *Astrophys. J. Suppl. Ser.,***6**,213.

de Vaucouleurs, G., Nieto, J.L. 1979.. *Astrophys. J.,* **231,** 364.

Ford,H.C,Butcher,H.1979,*Astrophys. J. Suppl. Ser.,***41**,147.

Forman, W, Jones, C,de Faccio, M.1984, in *The Virgo Cluster of Galaxies,* ESO Conference and workshop, No. 20, p. 323.

Sandage, A. R., Tamman, G. A. 1981, *A Revised Shapely-Ames Catalog of Bright Galaxies,* Carnegie Inst. Washington.

Wade, C M. 1960, *Observatory,* **80**,235.

Walker, M. F. 1968, *Astrophys. Lett.,* **2**,65.

J. Astrophys. Astr. (1986) **7,** 77–81

Quasars in the Central Region of the Virgo Cluster

Halton Arp* *Mount Wilson and Las Campanas Observatories of the Carnegie Institution of Washington, 813 Santa Barbara Street, Pasadena, CA 91101–1292, USA*

Received 1985 November 16; accepted 1986 January 8

Abstract. Quasars found from objective prism searches have been reported to show no association with galaxies in the Virgo Cluster. A simple analysis here shows significant association of the brightest of these quasars with core galaxies in the Virgo Cluster.

Key words: quasars, associations, redshift periodicities—galaxies, Virgo Cluster, alignments

1.Introduction

In 1978 three objective prism photographs were obtained of the central region of the Virgo Cluster with the United Kingdom Schmidt telescope in Australia. The plates were searched for quasar candidates by X.T. He. He reported that the quasars fell closer to the bright galaxies in the area than they did to the faint galaxies (personal communication). The analysis did not appear, however, until 1984 (He, Cannon, Peacock, Smith, & Oke, 1984). The conclusion was then put forward that there was '. . . no conclusive evidence for quasar-galaxy associations in this field. . . '. Actually within the body of the paper a different statement was made: that with the one-dimensional Kolmogorov-Smirnov test, '. .. no significant [associations] were found for any galaxy sample with the exception of the 15 galaxies brighter than $m = 12$.'

There is an obvious association in the data, however, an association of quasars and galaxies of just the kind evidenced by many previous investigations. I discuss this association in the following note.

2. The bright quasars and Virgo core galaxies

Selection of quasar candidates was limited to the central 5° × 5° area of the objective prism Schmidt plate (He *et al.* 1984). Virgo galaxies occur throughout this area but the brightest galaxies are concentrated toward the centre. When an association of the quasar candidates with the 15 galaxies brighter than $m = 12$ was found it is surprising that association with even brighter galaxies were not tested. It is visually obvious that the very brightest galaxies are even more centrally concentrated and of course the very brightest galaxies best define the core or apparent centre of the Virgo Cluster.

*Alexander von Humboldt Senior Scientist, awardee at the Max-Planck-Institut für Astrophysik, Garching, FRG.

But an even more obvious association is present in the data in just the sense which has been predicted by previous quasar-galaxy associations. The observations have shown (Arp 1970; Burbidge, O'Dell & Strittmatter 1972; Sulentic 1981; Arp 1983) that galaxies closer to the observer have quasars closer to the observer also, and therefore, in general, brighter galaxies are associated with brighter quasars. If we were to concentrate our attention instead on just the galaxies at the exact distance of the Virgo Cluster, of course the brightest galaxies would be generally the largest and most massive. If these more massive galaxies produced more massive, luminous quasars or gravitationally bound such quasars, then these galaxies would be expected to have the strongest association of quasars. So on either grounds the brightest quasars would be expected to be associated with the brightest galaxies.

Fig. l(a) shows the quasar candidates which He *et al.* tested for association with the galaxies in the region. Directly below, Fig. l(b) shows just the brightest quasars ($m \lesssim 18.5$ mag). The different distribution of these bright quasars is very striking. In addition, the location of the four brightest E galaxies in this region is shown. The general association of these bright galaxies and these bright quasars is so evident that it scarcely requires statistical testing although a simple test will be applied below.

2.1 *The Virgo Core*

It is well known that the stellar populations of which E galaxies are composed have the largest mass-to-light (M/L) ratios, more than an order of magnitude higher than for spiral galaxies. Therefore E galaxies are vastly more massive than spirals of comparable brightness. It was shown many years ago (Arp 1968) that the E galaxies in the Virgo Cluster defined a line coincident with the jet and counterjet which emerges from the dominant galaxy, M 87. This line is shown dashed in Fig. l(b). (The alignment is also discussed in the immediately preceding paper.) Since the E galaxies which define this line are among the brightest in the Virgo Cluster they are by far the most massive. This line therefore defines the core mass of the Virgo Cluster. It is an extremely interesting result that it is the most massive galaxies in Virgo with which the brighter quasars are associated.

2.2 *Statistical Association with the Core of the Virgo Cluster*

The simplest statistical test of association we can perform involves these core galaxies. Of all the galaxies classified in 1961 by de Vaucouleurs in this region, only 13 were designated E galaxies. In 1968 Arp showed that these were the galaxies which formed the core of the Virgo Cluster, aligned across M 87 as discussed above and indicated in Fig. l(b). The most recent classification of all E galaxies in the region is by Sandage & Tamman (1981) in the Revised Shapley-Ames Catalog. The 11 E galaxies they list give an even tighter definition of the line through M87 than the 1961 de Vaucouleurs' classification.

Now we see from the work of He *et αï* that two of the galaxies in this alignment of 11 have bright quasars which fall astonishingly close by. For all quasars on the sky, a conservatively large density would be 0.4 deg $^{-2}$ brighter than continuum magnitude m =18.5 mag (Arp 1981,1983), Quasars selected by objective prism searches show less than half such densities.The eight quasars pictured in Fig. 1(b),computing for an area

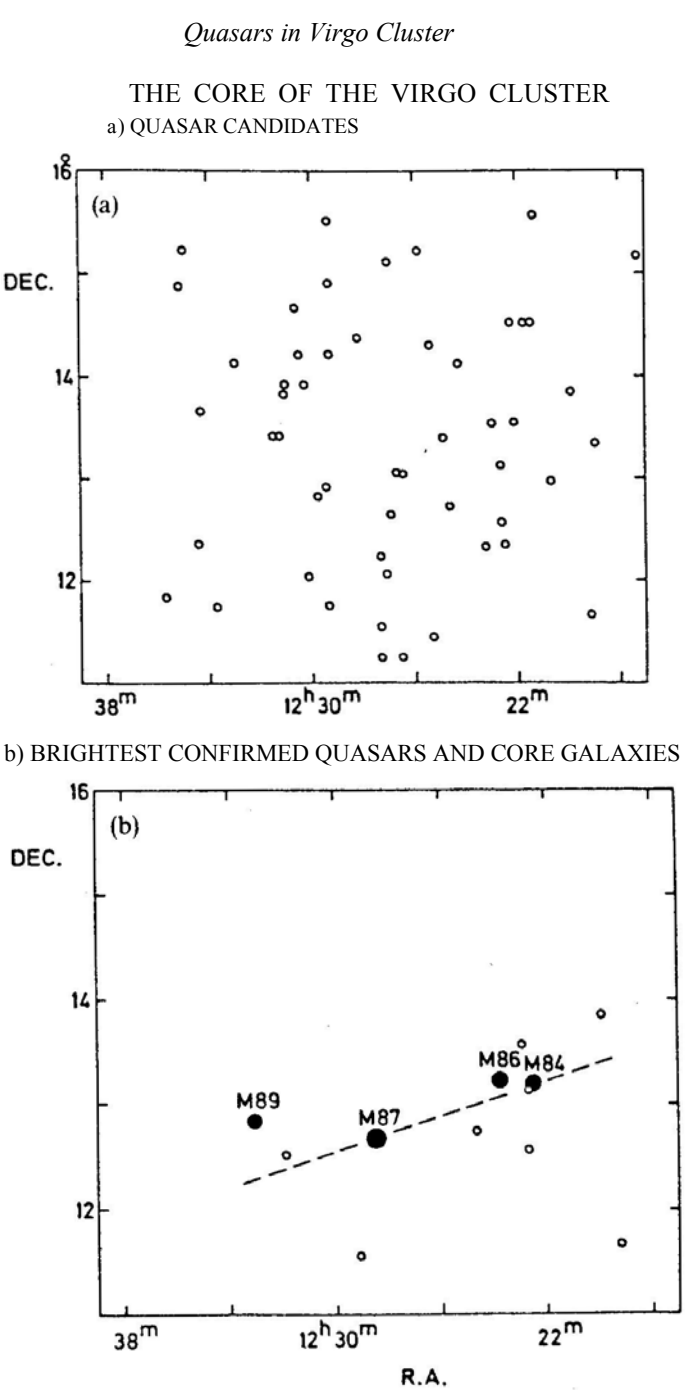

Figure 1. (a) Plot of all objective quasar candidates from He *et al.* (1984) in region near the centre of the Virgo Clustei. Note that Fig. 5 in He *et al.* (1984) is plotted with incorrect direction of right ascension, (b) Plot of all confirmed quasars with continuum magnitude $m \lesssim 18.5$ mag. Filled circles represent the four brightest E galaxies in the field. The dashed line represents the alignment of all E galaxies in the field along the M 87 jet and counterjet as defined in 1968. One object of $z = 0.235$ has been omitted and one quasar found from ultraviolet excess has been included. There are no further quasar candidates brighter than the present, 18.5 mag limit in Tables 2 and 3 (a) of He *et al.*

of $\frac{1}{2} \times 25$ deg^{-2}, give a local density of about 0.64 deg^{-2}. This is already beginning to be an excess density in an absolute sense. We adopt an average expected density for computational purposes of 0.5 deg^{-2}. This yields individual probabilities for the two quasars very near galaxies as:

$P \simeq 2 \times 10^{-3}$ for quasar at 2.3 projected distance from m84.
$P \simeq 3 \times 10^{-4}$ for quasar at 0.8 arcmin projected distance from NGC 4550.

We can ask the simple question of how likely it is, in a sample of 11 objects to find two events with probability of $\simeq 2 \times 10^{-3}$. The answer from the binomial distribution function is 2×10^{-4}. But, of course, this is an overestimate of the probability because one of the associations has a probability of much less than 2×10^{-3}.

A more simple and straightforward calculation is that the chance of finding the closest quasar to one of the 11 E galaxies is $11 \times 3 \times 10^{-4} \simeq 3 \times 10^{-3}$. The chance of finding the next closest is $11 \times 2 \times 10^{-3} \simeq 2 \times 10^{-2}$. The chance of finding both in one sample is $\lesssim 10^{-4}$. In other words the chance of finding two of the brightest quasars on this plate within the observed distance to members of the M 87 chain as defined in 1968, is less than one in ten thousand!

3. Discussion

Quasars have heretofore been shown to be associated with galaxies much closer than in the Virgo Cluster. For example M 33, NGC55, and NGC300 (Arp 1984b) and with spirals predominantly of redshift considerably less than $z \lesssim 1500$ km^{-1} (Arp 1983, Figs 14 and 15). The quasars associated with Virgo galaxies discussed above must therefore be among the most intrinsically luminous yet identified It is interesting to see whether there are any differences between these quasars and the kinds of quasars most commonly observed.

The first parameter we would examine is their redshifts. The quasars falling close to the Virgo core line have unusual redshifts. The most commonly observed redshift over the rest of the sky is near $z \simeq 2.0$.Quasarsofthisredshift are conspicuously absent from the centre of the Virgo Cluster. Redshifts in the sample of all quasars known over the sky fit peaks governed by a law $\Delta \log(1 + z) = 0.089$ (the peaks are z = 0.30,0.60,0.96, 1.41, 1.96 as shown by Depaquit, Pecker & Vigier 1984). Objective prism quasars, dominated by the surveys over the region of the Sculptor group of galaxies, obey the same periodicity with a slightly larger constant, $\Delta \log (1 + z) = 0.096$ (Box & Roeder 1984). But a set of the quasars falling close to the Virgo line obey a periodicity with an even slightly larger constant. This is shown in Table 1.

Table 1. Quasar redshifts near the centre of Virgo Cluster.

Observed	$\Delta \log (1 + z) = 0.098$
0.42	0.42
0.72 (near NGC 4550)	0.78
1.25 (near M84)	1.23
1.79	1.79
2.50, 2.46 (fainter)	2.50
(5 others near $z \simeq 2.2$)	

This redshift periodicity of 0.098 represents the highest interval constant encountered in any group so far. It is implied that this is a consequence of the relatively high luminosity of the quasars. (There are 5 other quasars in the vicinity, all with redshifts near $z \simeq 2.2$. It is not clear whether they are foreground or background quasars, or represent dispersion or exceptions from the relation, or belong to other kinds of galaxies in the Virgo Cluster.

Finally the equivalent widths of the quasar emission lines in Virgo should be measured. The Baldwin effect as measured by Baldwin *et al.* (1978), Wampler *et al.* (1984), and Arp (1984a) would predict that the high luminosity quasars should tend to have emission lines of relatively small equivalent width.

In summary, just a simple examination of the quasars reported by He *et al.* reveals that the brightest quasars are significantly associated with the most massive galaxies in the core of the Virgo Cluster. This evidence is consistent with, and expected from, all the previous evidence for the association of quasars with galaxies. More accurate and complete measurements of quasars in this region and in various comparison regions in the sky would represent an opportunity to study the detailed properties of quasars as a function of their luminosity and possibly also as a function of the types of galaxies with which they are associated.

References

Arp, H. 1968, *Publ. astr. Soc. Pacific,* **80**, 129.
Arp, H. 1970, *Astr. J.,* **75**, 1.
Arp, H. 1981, *Astrophys. J.,* **250**, 31
Arp, H. 1983, *Astrophys. J.,* **271,** 479
Arp, H. 1984a, *Astrophys. J.,* **285,** 555.
Arp, H. 1984b, *J. Astrophys. Astr.,* **5,** 31.
Baldwin, J. A., Burke, W. L., Gaskell, C. M., Wampler, E. J. 1978, *Nature,* **273,** 431.
Box, T. C, Roeder, R. C. 1984, *Astr. Astrophys.,* **134,** 234.
Burbidge, G. R., O'Dell, S. L., Strittmatter, P. A. 1972, *Astrophys. J.,* **175,** 601
Depaquit, S., Pecker, J. C, Vigier, J. P. 1984, *Astr. Nach.,* **305,** 339.
He. X. T., Cannon, R. D., Peacock, J. A., Smith, M. G., Oke, J. B. 1984, *Mon. Not. R. Astr. Soc.,* **211**, 443.
Sandage, A. R., Tamman, G. A. 1981, *A Revised Shapley-Ames Catalog of Bright Galaxies,* Carnegie Inst. Washington.
Sulentic, J. W. 1981, *Astrophys. J.,* **244**, L53.
de Vaucouleurs, G. 1961, *Astrophys. J. Suppl. Ser.,* **6**, 213.
Wampler, E. J., Gaskell, C. M., Burke, W. L., Baldwin, J. A. 1984, *Astrophys. J.,* **276,** 403.

J. Astrophys. Astr. (1986) **7,** 83–98

Classical Cepheids and the Local Chemical Inhomogeneities in the Galactic Disc

Sunetra Giridhar *Indian Institute of Astrophysics, Bangalore 560034*

Received 1985 March 14; revised 1985 December 20; accepted 1986 January 15

Abstract. Places of formation have been derived for a sample of 23 Cepheids with well-determined atmospheric abundances in an attempt to study the chemical inhomogeneities in the local interstellar medium. The abundance data available for the sample Cepheids is compiled and critically reviewed to adopt the most reliable esimates. We find that the most conspicuous irregularity in the metallicity is exhibited by stars that are born in the local arm or in the interarm region. We propose a scenario to explain these local variations in terms of supernova-induced star formation in interstellar gas enriched by massive stars formed in the density wave.

Key words: classical Cepheids, abundances — Galaxy, chemical inhomogeneities—density-wave theory—self-propagating star formation

1. Introduction

Places of formation have been derived in the past for samples of classical Cepheids (Wielen 1973; Joshi 1982; Grivnev 1983), early-type stars (Strömgren 1967; Grosbøl 1977), and young galactic clusters (Palous *et al.* 1977) with a view to comparing the predictions of the density-wave theory with the observed spiral structure and for estimating the pattern velocity (ω_p) of the density wave. In the present investigation, however, we have used birthsites of the classical Cepheids to study the local variation of metallicity in the galactic disc.

The presence of a largescale radial abundance gradient in the disc of our Galaxy is fairly well established from the observations of H II regions, planetary nebulae and stellar atmospheres. In addition to this global variation, abundance variations across individual spiral features are also observed. Talent & Dufour (1979) have claimed steeper variations of O/H and N/H across Sagittarius, local and Perseus features compared to the global radial abundance gradient.

Giridhar (1983), while studying the radial abundance gradient in the disc of our Galaxy (using classical Cepheids as probes), found smallscale chemical inhomogeneities superposed on the large scale abundance gradient. In the present investigation, the sample is enlarged by compiling good abundance estimates, and birthsites are derived for the Cepheids of the sample to eliminate the effect of the migration of stars. The chemical inhomogeneities prevalent in various locations of the galactic disc are estimated.

The observed chemical inhomogeneities could be caused by a higher rate of star formation in certain locations of the disc. Massive stars formed there would evolve at very short timescales and enrich the interstellar medium (ISM) by the processed material very close to their birth sites. Thus, the degree of chemical enrichment of ISM depends upon the star-formation rate and on the efficiency per star-forming event to produce massive stars. We will discuss later the implications of the observed chemical inhomogeneities on various models of star formation.

In the present investigation, we have derived the places of formation for a sample of 23 Cepheids for which accurate iron abundances are known. The choice of classical Cepheids was based on their high intrinsic luminosity, young age, and the existence of good period-age and period-luminosity-colour relationships which enable one to determine their ages and distances with sufficient degree of accuracy (*cf.* Giridhar 1983). The accuracy of these parameters determine the accuracy of the derived birthsites. Also, the young age of classical Cepheids with periods longer than ten days imply that the variations of [Fe/H] observed in the sample is due to the spatial variation of ISM at the current epoch.

Our compilation of spectroscopically derived [Fe/H] abundances of Cepheids is described in Section 2, together with distances and ages. The birthsites are derived in Section 3. The radial abundance gradient and the local chemical inhomogeneities across the spiral arms are estimated in Section 4 and discussed in Section 5.

2. The basic data

2.1 *Spectroscopically Derived* [*Fe/H*] *Abundances in Cepheids*

We summarize in Table 1 the compilation of [Fe/H] abundances for different Cepheids, derived by different investigators. The table also contains the basic data for these Cepheids, like the galactic coordinates, the visual magnitudes, periods, distances from the Sun and from the centre of the Galaxy. The abundance estimates used in this compilation are critically discussed below.

Rodgers & Bell (1963) determined the atmospheric abundances of β Dor employing a differential curve of growth with respect ,to the Sun. The choice of the Sun for differential analysis is not justified due to the difference in gravities. No other abundance determination exists for this star. Bappu *&* Raghavan (1969) derived atmospheric abundances of RT Aur using the same technique. The standard error of the [Fe/H] determined by them is ± 0.15 dex. Unfortunately, the *gf* values available in the 1960s were later found to be very uncertain, in many cases differences being of several orders of magnitude. As a result we were obliged to exclude from our investigation the [Fe/H] derived prior to 1970.

Van Paradijs & Ruiter (1973) determined [Fe/H] for δ Cep using curve-of-growth and model-atmosphere method, and derived almost a solar value. This is in good agreement with the recent estimates of Luck & Lambert (1981, hereinafter LL) using the spectrum synthesis method.

Schmidt (1971) derived [Fe/H] for four southern Cepheids— η Aql, S Nor, Y Oph and U Sgr— using the curve-of-growth and model-atmosphere method. The effective temperature and surface gravity were determined by matching the observed continuous energy distribution with theoretical fluxes calculated using the model atmosphere. The

Table 1. Compilation of spectroscopic [Fe/H] for Cepheids.

Star	Galactic coordinates l	b	Mag.	Period (days)	Present position $R_\odot$	R_{gc}	[Fe/H]	Source
UZ Sct	19.16	−01.49	12.4	14.744	3.3	6.96	+0.25	8
WZ Sgr	12.10	−01.30	9.0	21.849	2.16	7.89	+0.15	7
CK Sct	26.30	−00.46	10.54	7.40	2.20	8.06	+0.13	8†
S Nor	327.75	−05.39	6.11	9.755	1.00	9.16	+0.10	3
SV Vul	63.94	+00.30	6.73	45.035	2.34	9.20	+0.28	6
Y Oph	20.60	+10.38	7.15	17.123	0.76	9.29	+0.18	3
U Sgr	13.70	−04.45	6.35	6.745	0.68	9.33	+0.10	3
W Sgr	1.60	−04.00	4.70	7.595	0.48	9.52	+0.27	6
X Sgr	1.16	+00.20	4.79	7.012	0.42	9.58	+0.02	6
							+0.07	7
η Aql	40.93	−13.07	4.08	7.176	0.30	9.77	+0.06	6
							+0.08	4
X Cyg	76.87	−04.26	6.65	16.384	1.16	9.80	+0.08	4
							+0.15	6
							+0.33	8
T Vul	72.13	−10.15	5.43	4.435	0.61	9.83	−0.05	6
DT Cyg	76.54	−10.78	6.06	2.499	0.45	9.90	+0.12	6†
β Dor	271.74	−32.78	4.03	9.842	0.36	9.99	+0.01	2*
TX Cyg	84.35	−02.30	10.34	14.708	1.3	10.01	+0.39	8
αU Mi	1.49	89.03	2.0	3.97	0.1	10.05	−0.07	9
δ Cep	105.20	+00.53	4.94	5.336	0.29	10.08	+0.06	6
							−0.06	5
SU Cas	133.47	+08.51	6.38	1.949	0.31	10.21	−0.12	6†
ζ Gem	195.74	+11.89	3.68	10.151	0.39	10.37	+0.34	6
							+0.20	7
RT Aur	183.14	+8.90	5.48	3.728	0.49	10.48	−0.20	1*
							+0.06	6
TU Cas	118.92	−11.40	7.38	2.139	0.93	10.48	−0.13	6†
RS Pup	252.40	−00.20	7.59	41.387	2.08	10.81	−0.07	6
DL Cas	120.26	−02.55	9.72	8.000	1.67	10.94	−0.13	8
T Mon	203.63	−02.56	5.59	27.020	1.42	11.31	+0.12	6
							+0.03	7
							+0.14	4
RX Aur	165.80	−01.30	7.67	11.622	1.98	11.93	−0.37	4
SV Mon	203.63	−03.7	8.30	15.232	2.87	12.68	−0.10	7
BM Per	155.60	−00.09	11.40	22.952	3.0	12.79	−0.10	8
TV Cam	145.00	+06.14	11.76	5.3	5.1	13.63	−0.11	8†
YZ Aur	167.30	+00.93	11.08	18.193	4.5	14.42	−0.26	8

Sources:
1. Bappu & Raghavan (1969)
2. Rodgers & Bell (1963)
3. Schmidt (1971)
4. Schmidt, Rosendhal & Jewsbury (1974)
5. van Paradijs & Ruiter (1973)
6. Luck & Lambert (1981)
7. Giridhar (1983)
8. Harris & Pilachowski (1984)
9. Giridhar (1985)

* Rejected because of uncertain abundances.
† Rejected because of large age and unknown space velocity.

standard error of the abundance estimate is around ±0.1 dex. The Cepheid η Aql has also been investigated by LLand there is a satisfactory agreement between the two estimates.

Schmidt, Rosendhal & Jewsbury (1974, hereinafter SRJ) derived atmospheric abundances of X Cyg, T Mon and RX Aur using curve-of-growth and model-atmosphere method. The temperature scale for Cepheids was derived from a study of the Hα profile (Schmidt 1972a) and continuum photometry (Schmidt 1972b). For T Mon and X Cyg, the temperatures and gravities determined by SRJ are systematically higher than those derived by Parsons (1970) from six-colour photometry, by Pel (1978) from narrow band *VBLU W* photometry, and also the spectroscopic estimates of LL. The differences are of the order of $\Delta T_{\rm eff} \sim$ 500 K and $\Delta \log g \sim 1.6$, and therefore would lead to systematic differences of 0.1 to 0.2 dex in the derived abundances. It is therefore surprising that Fe/H derived by SRJ for T Mon and X Cyg agree with those of LL within 0.15 dex. Yet, we will use with caution the low value of [Fe/H] = –0.37 derived by SRJ for RX Aur.

LL derived atmospheric abundances for 14 Cepheids using the method of spectrum synthesis. The method involves detailed computation of the spectral region of interest using a suitable model atmosphere and atomic parameters of concerned lines. They have employed a large number of iron lines observed with high resolution. The internal error in the determination is 0.06 dex. These estimates are perhaps among the more accurate ones.

Giridhar (1983) derived atmospheric abundances of five Cepheids SV Mon, T Mon, ζGem, X Sgr and WZ Sgr. The method employed is similar to LL and there is a good agreement between the two estimates for the stars in common (T Mon, ζ Gem and X Sgr).

Harris & Pilachowski (1984 hereinafter HP) derived [Fe/H] for YZ Aur, TV Cam, DL Cas, BM Per, TX Cyg, X Cyg, CK Sct and UZ Sct using high-dispersion spectra and fine analysis. However, for X Cyg the estimate of HP is higher than the one derived by LL by 0.18 dex which is surprising. The differences in phases can partly account for the discrepancy. The observations of HP were made at a phase at which the assumption of hydrostatic equilibrium holds better than at the phase observed by LL. Since the internal errors in the abundance estimate of X Cyg and TX Cyg are higher than for other stars of the sample of HP, we have given equal weight to the estimates [Fe/H] derived by LL, HP and SRJ.

2.2 *Distances to the Cepheids*

The most commonly used relationships for determination of distances to Cepheids are the period-luminosity-colour (*P-L-C*) relationships of Sandage & Tammann (1969) and Tammann (1970). With this method, the accuracy of the derived distance depends upon the accuracy with which the colour excess is determined. Early determination of the colour excesses using *UBV* photometry showed large systematic differences between various estimates that depended on the periods and also on the amount of reddening. We now know that the broadband photometric systems like *UBV* are not suitable for the colour-excess determination because the derived colour excess depends upon the stellar energy distribution. In the case of Cepheids the situation is further complicated by the variation of spectral type over the pulsation cycle.

Recent determination of colour excesses of a large number of Cepheids by Pel (1978) using narrowband *VBLUW* photometry, by Parsons, & Bell (1975) using six-colour *UVBGRI* photometry, and by Dean, Warren & Cousins (1978) using *BVI* photometry, show a satisfactory agreement between themselves. Not only are the systematic

differences very small, but also they are independent of period. However, all these colour excess estimates differ systematically from the older estimates (*e.g.*Kraft 1961) that used broad band photometry, in the sense that the former indicate a smaller value of colour excess. The calibration of *P-L-C* relation of Sandage & Tammann (1969) was done using the colour excesses derived by Kraft (1961) and therefore requires recalibration.

Another recent attempt to determine accurate distances to Cepheids is made by Barnes, Evans & Parsons (1977). These authors used the surface brightness inferred from the (*V—R*) colour index to determine the variation in the angular dimension of Cepheids. By combining the data with linear displacements derived from the radial velocity curves, the distances and the linear radii are determined. The distances derived by Barnes *et al.* are systematically larger by about 18 per cent compared to those derived by Tammann (1970).

We have used the *P-L-C* relationship of Caldwell (1983) to derive the distances of Cepheids. Caldwell considered 22 Cepheids that are members of galactic clusters and used for reddening correction the colour excesses derived by Pel (1978), Parsons & Bell (1975) and Dean, Warren & Cousins (1978). The attractive feature of this relationship is a better agreement with the methods that do not employ estimates of cluster distances (*e.g.* Barnes, Evans & Parsons 1977).

We have taken the mean magnitudes $\langle B \rangle$ and $\langle V \rangle$ for the sample Cepheids from Schaltenbrand & Tammann (1970). The heliocentric distances derived using the *P-L-C* relation of Caldwell are given in Table 1. The standard error in distances derived are ± 10 per cent.

2.3 *Ages of the Cepheids*

If the age of a star is known, one can compute its galactic orbit backwards in time and derive its birthsite. The age of a Cepheid can be inferred from its period-age relationship (Hodge 1961; Efremov 1964). A theoretical period-age relationship for classical Cepheids was derived by Kippenhahn & Smith (1969) from stellar evolutionary calculations. Tammann (1970) gave an analytical representation to the results of Kippenhahn & Smith for a stellar model with a composition of X= 0.602 and Z = 0.044 as

$$\log\ \tau_7 = 1.16 - 0.651 \log P,$$

where τ_7 is the age in 10^7 yr and P is the period in days. Efremov (1978) derived a composite period-age relationship from the data on a large number of Cepheids belonging to clusters and associations in Magellanic Clouds, the Galaxy and M 31 as

$$\log \tau_7 = 1.157 - 0.677 \log P$$
$$\pm 0.37\ \pm 0.47$$

for 2d $< P <$ 50d. This relation agrees closely with the theoretical relation. We have listed in Table 2 the ages calculated using the semi-empirical relationship of Efremov (1978), for cepheids with P > 3d. These ages are systematically smaller by 0.25×10^7 yr compared to the ages calculated by Wielen (1973) using the theoretical relationship of Kippenhahn & Smith. After considering the spread in chemical composition for the sample Cepheids, the random errors in the derived ages of Cepheids are estimated to be less than ± 30 per cent.

Table 2. Ages, present positions, and birthsites for the sample Cephieds.

S. No.	Star	Age 10^7 yr	[Fe/H]	Present position ξ	η	ζ	birthsite in ω_p system ξ_p	η_p	R_{gc}	spiral feature Th	obs
1	UZ Sct	2.33	+0.25	3.11	1.08	−0.08	3.48	−2.52	6.99	—	C
2	WZ Sgr	1.78	+0.15	2.12	0.05	−0.04	2.19	−0.88	7.85	S	S
3	S Nor	3.07	+0.10	0.84	−0.53	−0.09	2.47	−3.88	8.47	S	S
4	SV Vul	1.09	+0.28	1.03	2.09	+0.01	0.45	+0.75	9.58	—	L
5	Y Oph	2.09	+0.18	0.70	0.26	+0.14	0.88	−2.11	9.36	—	S
6	U Sgr	3.94	+0.10	0.66	0.16	−0.05	1.60	−4.40	9.48	S	S
7	W Sgr	3.63	+0.27	0.47	0.01	−0.03	2.12	−5.34	9.52	S	S
8	X Sgr	3.80	+0.05	0.42	0.01	+0.00	1.90	−4.68	9.35	S	S
9	η Aql	3.78	+0.07	0.22	0.19	−0.07	1.54	−4.30	9.49	S	S
10	X Cyg	2.16	+0.19	0.26	1.13	−0.08	−0.62	−1.52	10.73	—	L
11	T Vul	5.23	−0.05	0.18	0.57	−0.11	1.18	−5.34	10.31	—	S
12	α UMi	5.90	−0.07	0.10	−0.05	0.08	3.37	−6.04	8.67	—	S
13	TX Cyg	2.33	+0.39	0.13	1.29	−0.05	−0.26	−1.19	10.33	—	L
14	δ Cep	4.62	+0.00	−0.07	0.29	−0.01	1.51	−4.55	9.63	—	S
15	ζ Gem	2.99	+0.27	−0.38	−0.01	0.08	−0.11	−3.77	10.81	—	—
16	RT Aur	5.90	+0.06	−0.48	−0.03	0.07	+3.19	−5.77	8.92	S	S
17	RS Pup	1.15	−0.07	−0.63	−1.98	−0.01	2.20	−4.28	8.89	S	S
18	DL Cas	3.51	−0.13	−0.84	1.44	−0.07	−0.91	−1.94	11.08	P	L
19	T Mon	1.54	+0.10	−1.29	−0.56	−0.06	−0.90	−1.54	11.01	P	L
20	RX Aur	2.73	−0.37	−1.92	+0.49	−0.04	−0.57	+1.49	10.67	P	—
21	SV Mon	2.27	−0.10	−2.62	−1.15	−0.18	−1.97	+1.72	12.09	P	P
22	BM Per	1.72	−0.10	−2.73	1.24	−0.00	−2.74	+0.26	12.73	P	P
23	YZ Aur	2.01	−0.26	−4.39	0.99	+0.07	−4.38	+0.57	14.40	—	—

3· Places of formation of Cepheids

3.1 *Computation of Galactic Orbits*

The birthsites of the Cepheids were derived by computing their galactic orbits backwards in time until the time of their birth. For axisymmetric gravitational field we have used the recent expression of Contopoulos as given by Palous *et al.* (1977):

$$\Psi_0 = \text{constant} + \frac{3000}{R} - 10120.2\ R + 13.9073R^3, \qquad R < 9.732175$$

$$\Psi_0 = -402667.526\left[-\frac{(R^2-94.4784)^{1/2}}{2R^2} + 0.0514403\ \cos^{-1}\frac{9.72}{R}\right]$$

$$-\frac{97970.75}{R^2} + \frac{30000}{R} + 15.029[R^3 - (R^2-94.4784)^{3/2}]$$

$$-10625.75R + 8522.87619[(R^2-94.4784)^{1/2} - 9.72\ \cos^{-1}\frac{9.72}{R}],$$

$$R > 9.732175,$$

where R is in kpc. For stars close to the Sun (R ~ 10 kpc) the birthsites derived using the expression of Contopoulos & Stromgren (1965) for Ψ_0 and the recent expression mentioned above do not differ significantly. However, in our sample we have stars up to galactocentric distance R = 14.4, and hence the use of the new expression of Contopoulos was considered necessary.

For the potential of spiral field the analytical approximation of density wave by a logarithmic spiral and the set of parameters derived by Yuan (1969) were adopted. The equation of motion in (ξ , n, ζ) coordinate system is given by

$$\ddot{\xi} + 2\,\omega_0\dot{\eta} + \omega_0^2(R-\xi) = \frac{d\Psi}{d\xi},$$

$$\ddot{\eta} - 2\,\omega\dot{\xi} - \omega_0^2\eta = \frac{d\Psi}{d\eta},$$

$$\ddot{\zeta} = \frac{d\Psi}{d\zeta}.$$

The origin of this system rotates around the galactic centre with an angular velocity ω_0 = 25km s^{-1} kpc $^{-1}$ at a distance R = 10 kpc from the galactic centre, the ξ axis reckoned positive towards the galactic centre, the η axis in the direction of galactic rotation, and the ζ axis towards the galactic pole. These equations were numerically integrated using the Runge-Kutta method. A time step of 0.5 × 10^6 yr was employed.

This coordinate system of reference does not give any insight into the influence of density wave on star formation. The birthsites are hence transformed into ω_p reference system which corotates with density wave and hence gives the location of the birthsites with respect to the density wave. We have listed in Table 2 the birthsites (ξ_p, η_p) in the ω_p system.

The space velocities used in the present investigation are derived by Giridhar (1986) using the proper motion data of Karimova & Pavlovskaya (1981). These proper

motions are calculated using a number of new position catalogues and some new observations obtained with Repsoid meridian circle at the observatory of Moscowand are more accurate (0.0005 s yr $^{-1}$ in μ_α and 0.005 arcsec yr $^{-1}$ in μ_δ) compared to the ones used by Wielen (1974) to derive the space velocity components. Owing to the large uncertainty in the proper motions, the space velocity components were not derived by Wielen (1974) for the cepheids farther than 1 kpc. For distant Cepheids like RS Pup, WZ Sgr, T Mon, X Cyg *etc.* which are young, the birthsites were calculated by Wielen (1973) assuming the space velocity components to be zero. However, the space velocity components are calculated by Giridhar (1986) for these distant Cepheids using the current proper motion estimates of Karimova & Pavlovskaya (1981). As a result, we have used the space velocity components in the birth site calculations for the majority of the Cepheids in our sample. Only for three Cepheids (UZ Sct, BM Per, and YZ Aur) the proper motions, and therefore the space velocity components, were not available. Since all the three Cepheids are younger than 2.3 × 10^7 yr and could not have moved considerably from their birthsites, we felt justified in calculating their birthsites with the assumption of zero space velocities. We have omitted CK Sct and TV Cam of Table 1 from our sample because the space velocity components were not available for them and their ages are too large to validate the assumption of zero space velocity.

3.2 *Error Analysis*

The observed parameters that are used in birthsite determinations are the distances, the space velocity components, and ages. Amongst these, the distances are known to an accuracy of ± 10 per cent. As a typical example if we consider ζ Gem, then a random error of 10 per cent in the distance corresponds to an uncertainty of ~0.05 kpc in ξ_p and 0.015 kpc in η_p, in ω_p system. The random errors in ages of the Cepheids are estimated to be ~ 20 to 30 per cent. For ζ Gem a random error of 25 per cent in age led to an uncertainty of 0.07 kpc in ξ_p and 0.56 kpc in η_p. The errors in space velocities do not affect the birthsites significantly. An error of 5.0 km s^{-1} in U and V space velocity components only caused an error of 0.25 kpc over the time span of 3.0 × 10^7yr. It is due to the fact that the differences between the circular velocity of stars (250 km s $^{-1}$ in solar neighbourhood) and density-wave velocity (~ 135 km s^{-1}) which is around 115 km s $^{-1}$ is much larger than the peculiar velocities of the stars.

Since the birthsites are found to depend more strongly on the ages than on other parameters, we have limited our sample to the age range 1.2-5.5 × 10^7 yr. The Cepheids DT cyg, SU Cas and TU Cas were dropped from the sample because their ages (8–9 × 10^7 yr) were outside this range.

4. Local chemical inhomogeneities

We plot in Fig. 1 [Fe/H] as a function of present galactocentric distance for the Cepheids of Table 1. Some of the stars of Table 1 were rejected from the sample either due to very uncertain abundance estimates or due to the larger ages and absence of space velocity components for them. The rejected stars are marked in the table. Though we intended to keep the sample age to 5.5 × 10^7 yr we have retained slightly older α UMi and RT Aur in this study, since precise proper motion and hence space velocity

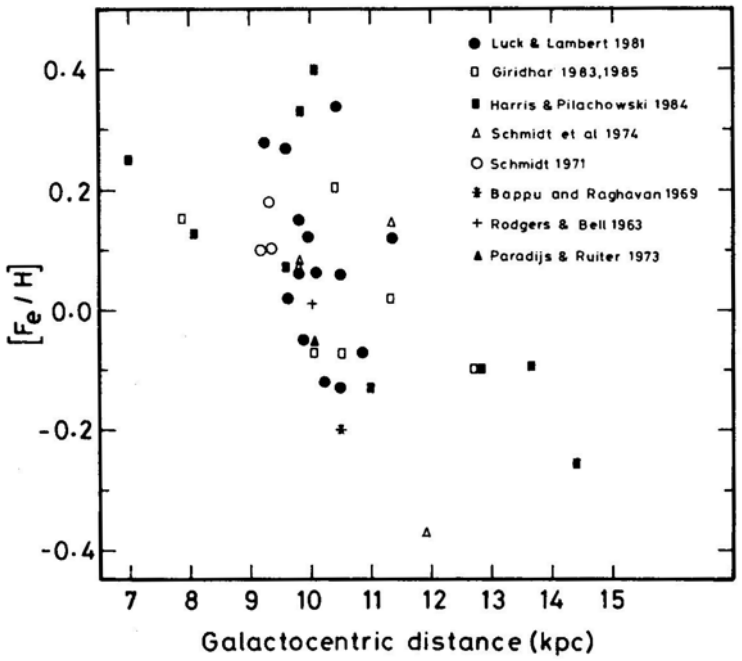

Figure 1. A plot of [Fe/H] as a function present galactocentric distances for the Cepheids of Table 1.

components are available for them (due to their small distances from the Sun). A straightline fit to the accepted data points of Table 1 gives

$$[\mathrm{Fe/H}] = 0.83 - 0.074 R_{\mathrm{gc}} \quad (n = 31,\ r = 0.61)$$
$$\pm 0.24 \pm 0.018$$

The gradient agrees reasonably well with the earlier values derived by Luck (1982), Giridhar (1983), Harris & Pilachowski (1984) and others. The stars TXCyg, RX Aur and ζ Gem lie beyond 2σ of this line and provide the first hint that there are smallscale variations superposed on global radial abundance gradient.

We have shown in Fig. 2 the places of formation in ω_{p} system for the stars in Table 2. The spiral arms are shown as bands corresponding to a positive excess of density in the model of Yuan (1971). The figure shows the Sagittarius arm (S) and the Perseus arm (P). We have divided the observed metallicities of Cepheids into four groups:

(1) metal poor	$[\mathrm{Fe/H}] < -0.10$,
(2) solar	$-0.10 < [\mathrm{Fe/H}] < +0.10$,
(3) Marginally rich	$0.10 < [\mathrm{Fe/H}] < +0.20$,
(4) Metal rich	$[\mathrm{Fe/H}] > 0.20$.

Different symbols are used for stars belonging to different groups. The stars are identified in the figure by the serial numbers in Table 2.

The tightly wound theoretical spiral pattern (pitch angle 6°) of Yuan, which was derived with an aim to explain the grand design of whole disc, fitted very well with major spiral arms like the Sagittarius and Perseus arms, but not with the Orion feature.

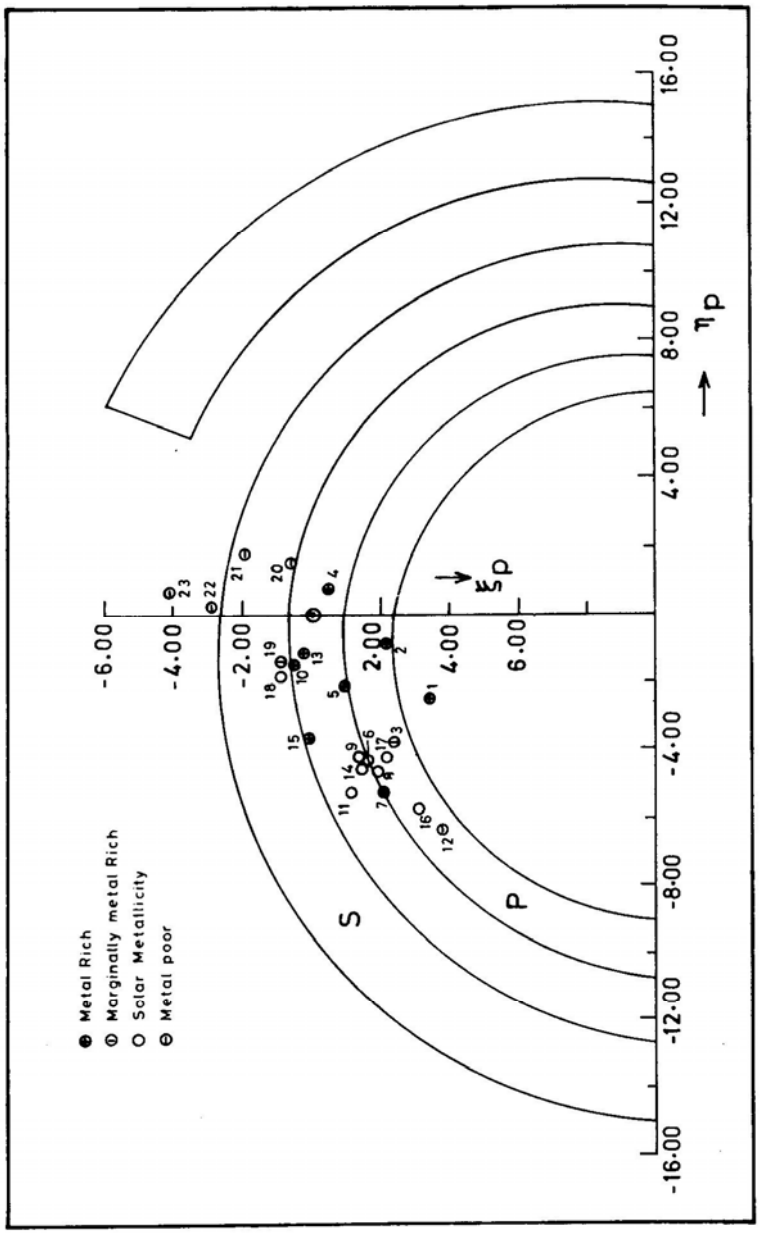

Figure 2. The distribution of the birthsites in ω_p system. The spiral arms are from the density-wave model of Yuan (1971). Sun's position is shown by ⊙ symbol.

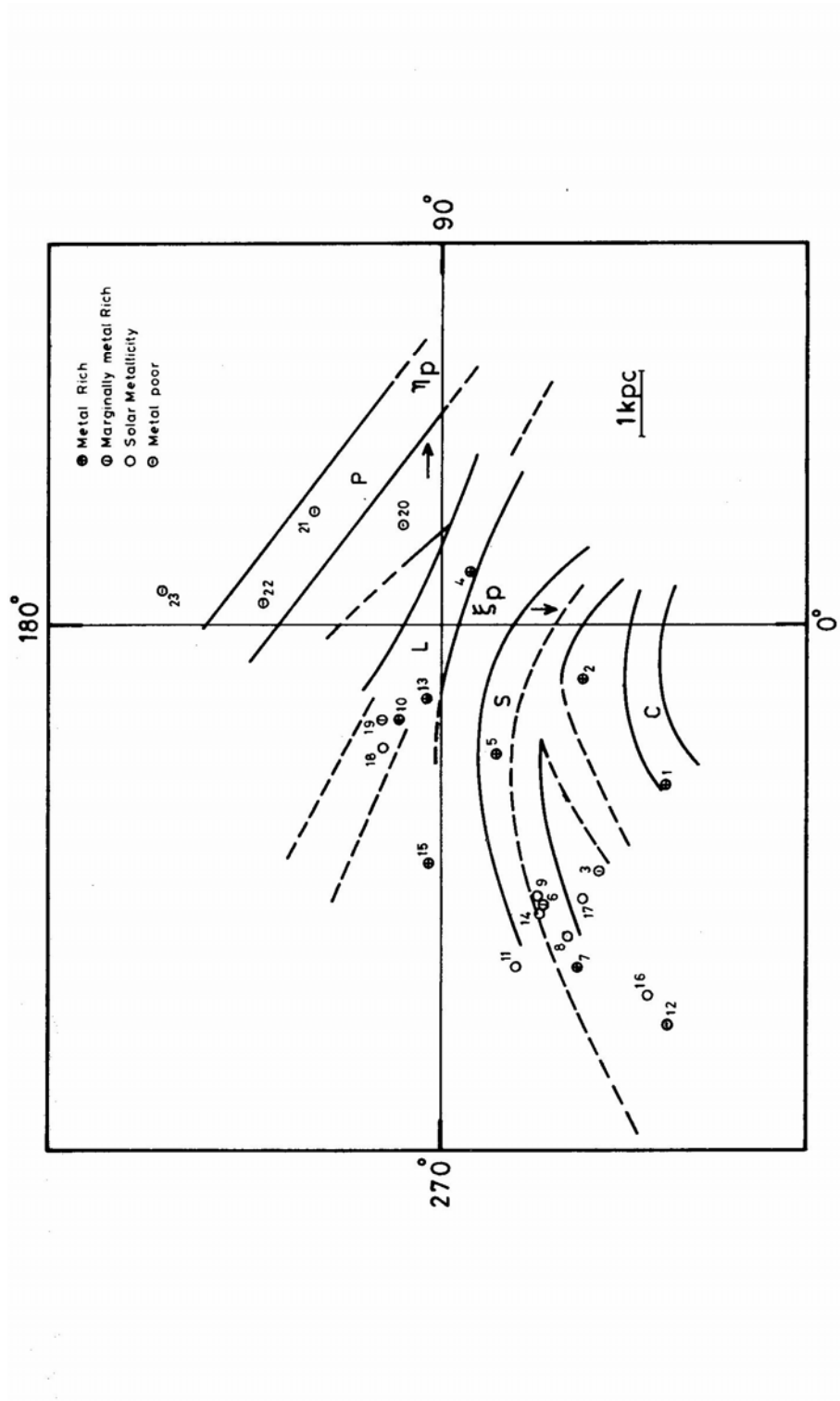

Figure 3. The distribution of the places of formation of the sample stars in the galactic plane. The outline of the optical spiral feature are taken from Humphreys (1979).

It is of interest to consider the observed spiral features traced by HII regions and young, active stellar associations. We now plot in Fig. 3 the birthsites superposed on the observed spiral features given by Humphreys (1979). The figure shows four main spiral features, the Carina arm (C), the Sagittarius arm (S), the Local arm (L) and Perseus arm (P).

We have indicated in the last column of Table 2 the assignment of Cepheids to different spiral arms. The spiral arms shown in Figs 2 and 3 are treated separately. We plot in Fig.4 (a)and (b)the [Fe/H]values of Cepheids from Table 2 as a function of the galactocentric distances of their birthsites. The Cepheids belonging to the Sagittarius and Perseus arms are shown by different symbols, and the ones that belong to neither, by a third symbol. The lone Cepheid belonging to the 'observational' Carina feature is pooled with the Sagittarius Cepheids. The local feature is treated as the interarm region.

A least-squares fit to the entire data in Fig. 4 gives

$$[\mathrm{Fe/H}] = 0.59 - 0.054\, R_{gc} \qquad (n = 23,\ r = 0.48)$$
$$\pm 0.29 + 0.022$$

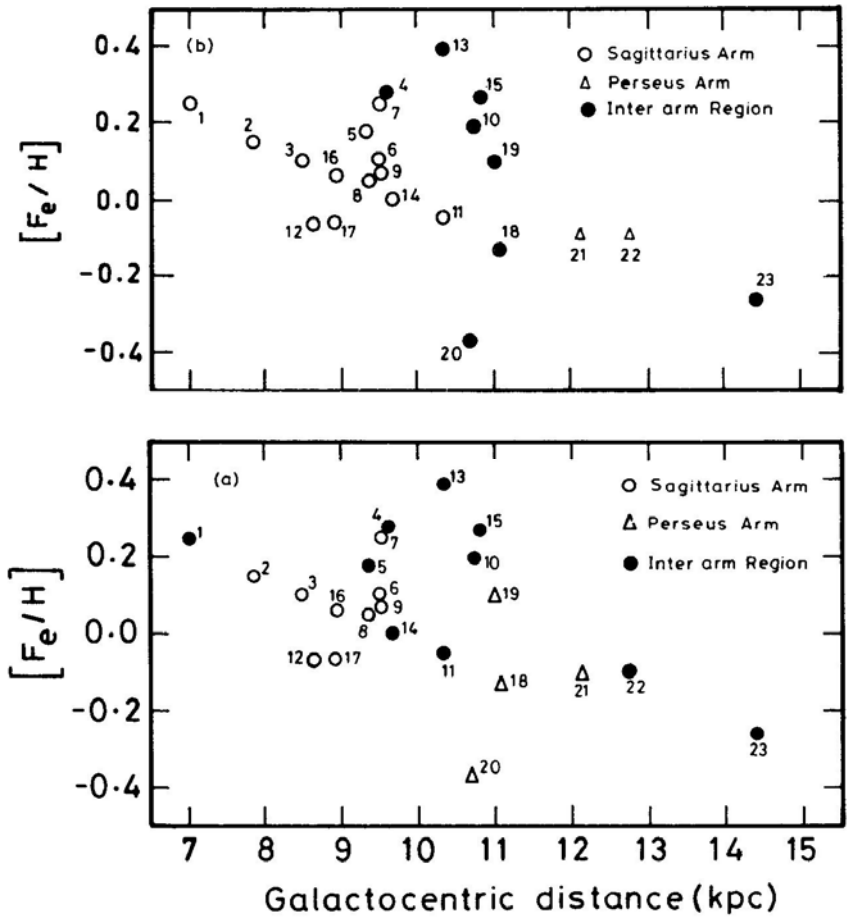

Figure 4. A plot of [Fe/H] for the stars of Table 2 as a function of galactocentric distances of their birthsites: (a) spiral-arm assignment based on Fig. 2; (b) spiral-arm assignment based on Fig. 3.

However, there is a large scatter in the region 9-11 kpc where several metal-rich interarm/local-feature Cepheids exist. Considering only the Sagittarius and Perseus Cepheids, one obtains for Fig. 4 (a)

$$[\mathrm{Fe/H}] = 0.58 - 0.059\, R_{gc} \qquad (n = 12,\ r = 0.45)$$
$$\pm 0.79 \quad \pm 0.035$$

and for Fig. 4(b)

$$[\mathrm{Fe/H}] = 0.55 - 0.052\, R_{gc} \qquad (n = 15,\ r = 0.62).$$
$$\pm 0.3.0 \quad \pm 0.018$$

The scatter in metallicities of the major-arm Cepheids corresponds to standard deviations of 0.15 and 0.09 for the theoretical and observational spiral features. On the other hand, the scatter in the metallicities of the remaining Cepheids about the line defined by the major-arm Cepheids is much higher, 0.20 and 0.26, respectively. An *F*-test shows that the two sample standard deviations differ with a probability of 85 per cent and 99 per cent respectively, for the theoretical and observational spiral features. Furthermore, the local arm and the interärm Cepheids are overabundant by 0.15 (0.09) dex, a value, though not statistically significant, yet highly suggestive.

We had remarked in Section 2 that the abundance estimate of RX Aur needs to be used with caution. This star falls in the Perseus arm in Fig. 2 and in the interarm region in Fig. 3. Its exclusion changes the gradient based on the major arm stars of Fig. 2 to a somewhat shallower value. Though its exclusion reduces the scatter, the significance levels of *F*-test do not change appreciably. On the other hand, the mean abundance of interarm and local feature Cepheids (based on Fig. 3) now increases to 0.15 dex, in agreement with the value based on Fig. 2.

Ascribing the spread in the abundances of the Cepheids in Sagittarius and Perseus arms to the errors of determination, we obtain an intrinsic spread of 0.14-0.24 dex for the interarm Cepheids, depending on whether one considers the spiral arms in Fig. 2 or Fig. 3.

5. Discussion

The observations of local chemical inhomogeneities have important implications for the models of star formation as well as galactic chemical evolution. The models of these two aspects of galactic evolution have been made in the past fairly independently, and under simplifying assumptions.

One of the popular star formation models is based on the density wave in which star formation is triggered only when the disc gas encounters the density-wave pattern and is compressed in a shock region near the wave-crest (Roberts 1969). Jensen, Strom & Strom (1976) were able to explain the radial abundance gradients observed in several galaxies using the density-wave model.

The simple models of galactic evolution which predict a smooth radial abundance gradient (in agreement with observations) assume that the star formation takes place in isolated well-mixed zones, *i.e.,* there is no variation of metallicity in these zones. A detailed study of the efficiency of various mixing processes in the disc of our Galaxy is made by Edmunds (1975). He demonstrated that over the timescale of 2×10^8 yr, which is the time interval between two successive passages of density wave, the chemical

inhomogeneities in ISM, produced by processed gas ejected by massive stars would get mixed with ISM. Over this timescale, the turbulent velocities in ISM will cause a mixed length of ~ 300 pc. The shear due to differential rotation (at solar distance) will cause the mixing to spread over a volume of 1.1×10^{11} pc^3. All these effects will dilute the inhomogeneity to $\Delta Z = 9 \times 10^{-5}$ by the time star formation due to density wave recurs in the same place.

Stochastic self-propagating star-formation model is an alternative which suits late-type galaxies with less well-defined spiral arms (Gerola & Seiden 1978). SPSF models assume the expanding shells of supernova remnants or HII regions to furnish the necessary compression at their edges where the stars would consequently form. Stars are formed in the expanding shell after the expansion velocity of the shell becomes comparable to the turbulent velocities in ISM. The massive stars among the newly born produce more such shells and thus the process propagates. The propagation of star formation process is controlled by the refractory period τ_r which is the minimum time before a given cell can undergo star formation again. The refractory period is the length of time it takes for the gas density at a given location to build up after the location has experienced a supernova. In the case of pure SPSF models the refractory period (1.6×10^8 yr) for a given region is again too large for the chemical inhomogeneities to survive before the star formation resumes. Mueller & Arnett (1976) introduced density waves in their SPSF models and found the regeneration time to decrease by a factor of 2-3. This provides for the possibility of forming second-generation stars before the chemical inhomogeneity is fully diluted.

A gas-dynamical model of ISM in the Galaxy is developed by Roberts (1982) with an aim to arrive at a better understanding of global (such as density-wave induced) as well as local processes of star formation active in the Galaxy, and their relationship with each other. Roberts employs a time delay rT_D before an active stellar association forms from colliding clouds and a time delay of $r'_D T'_D$ before the clouds could interact with associations to produce stars. Here T_D and T'_D represent the maximum probabilistically-selected delay times, and r and r' are the random numbers selected between zero and unity for each association. Roberts found that $T_D = T'_D = 0$ resulted in welldelineated spiral arms whereas $T_D = T'_D = 2 \times 10^7$ yr yielded arms with spurs.

The spread in metallicity of galactic stars of a given age, observed by Dixon (1966) and Hearnshaw (1972), indicates that the ISM is not well-mixed throughout the galactic disc and spatial variation of metallicity exists. The local chemical inhomogeneity reported by Talent & Dufour (1979) and also the one observed in the present work strengthens the view that the mixing of ISM in different zones of galactic disc is not complete. On the other hand, the shell of cold H_I, dust and molecules around supernova remnants detected by Sancisi (1974) and Knapp & Kerr (1974), and young stellar associations on the edge of supernova shells observed by Berkhuijsen (1974) and Herbst & Assoussa (1978), indicate the existence of a secondary process of star formation.

We now attempt to link these two observations in the light of what we have learnt from the models of star formation. The two observations, taken together, require that the time delay between two star-formation events is neither too large as implied by the density-wave model, nor too small as the zero-time-delay model of Roberts (1982). A time delay of $4–5 \times 10^7$ yr appears consistent with the model of Roberts (1982) as well as Mueller & Arnett (1976). Over this timescale, the gas enriched by Supernovae in Sagittarius arm would move over to the region corresponding to the local feature.

As Edmunds (1975) points out, a value of $\Delta Z \sim 4 \times 10^{-3}$ may be expected between

the inside and out side of a composite supernova shell around atypical OB association of 60 pc size containing 15 O-B2 stars. It is conceivable that this gas stays undiluted due to snowplough effect when the shell encounters high density gas. Radio observations of Perseus gas cloud by Sancisi (1974) indicate the presence of an expanding shell of H_I. Sancisi (1974) estimated the radius and thickness of the shell to be 20 pc and 5 pc respectively, and suggested that it contains $10^4 M_\odot$ of gas. If it contains the 90 $M_\odot$ of metals injected by 15 SN of a typical OB association, one would expect an enrichment of $\Delta Z \sim 9 \times 10^{-3}$. Over the time interval of 5×10^7 yr the mixing-length resulting due to turbulent eddies is 130 pc (*cf.* Edmunds 1975). This will lead to a mixed gas of mass $6 \times 10^4\ M_\odot$, if we adopt for the density near the galactic plane a value of $0.018\ M\ \text{pc}^{-1}$ (Allen 1973). Consequently, the metallicity will be diluted to $\Delta Z \sim 1.3 \times 10^{-3}$. This corresponds to an enrichment of 0.1 dex in Fe/H considering its contribution to be 0.014 to the total metallicity. It is possible that there would be more than one generation of star-formation in the spiral arm itself ($rT_D \simeq rT'_D \simeq 0$). Also, the enhancement of metals may be retained with less dilution when SN shell interacts with neighbouring shells rather than the unenriched ISM. Consequently, even higher chemical enrichment is possible. Thus it would appear that enhanced star formation in the major spiral arms, and secondary star-formation in the minor interarm features such as the local arm—when the fossil SN shell fragments to form stars—may explain the observed metallicity variations adequately.

Acknowledgements

I wish to thank Dr T. P. Prabhu for many useful discussions and two anonymous referees for comments.

References

Allen, C. W. 1973, *Astrophysical Quantities,* 3 edn, Univ. London, Athlone Press.
Bappu, M. K. V., Raghavan, N. 1969, *Mon. Not. R. astr. Soc,* **142,** 295
Barnes, T. G., Evans, D. S., Parsons, S. B. 1976, *Mon. Not. R. astr. Soc,* **174**, 503
Berkhuijsen, E. M. 1974, *Astr. Astrophys.,* **35**, 429
Caldwell, J. A. R. 1983, SAAO Preprint No. 336.
Contopoulos, G., Strömgren, B. 1965, *Tables of Plane Galactic Orbits,* Institute of Space Studies, New York.
Dean, J. F., Warren, P. R., Cousins A. W. J. 1978, *Mon. Not. R. astr. Soc,* **183**, 569.
Dixon, M. E.1966, *Mon. Not. R. astr. Soc,* **131**, 325.
Edmunds, M. G. 1975, *Astrophys. Space Sci.,* **32,** 483.
Efremov, Yu, N. 1964, *Perem. Zvezdy,* **15**, 242.
Efremov, Yu, N. 1978, *Sov. Astr.,* **22***,* 161.
Gerola, H., Seiden, P. E 1978, *Astrophys. J.,* **223,** 129.
Giridhar, S. 1983, *J. Astrophys. Astr,* **4**, 75.
Giridhar, S. 1985, in *1AU Coll* 82: *Cepheids: Theory and Observation,* Eds B. F. Madore, Cambridge Univ. Press, p. 100.
Giridhar, S. 1986, In preparation.
Grivnev, E. M. 1983, *Sov. Astr. Lett.* **9**, 287.
Grosbol, P. J. 1977 in *IAU Coll.* 45: *Chemical and Dynamical Evolution of our Galaxy,* Eds E. Basinska-Grzesik & M. Mayer, Geneva Obs., p. 279.
Harris, H. C, Pilachowski, C. A. 1984, *Astrophys. J.,* **282,** 655 (HP).
Herbst, W., Assousa, G. E. 1978, in *Proto Stars and Planets,* Ed. T. Gehreis, Univ. Arizona Press, Tucson, p. 368.

Hearnshaw, J. B. 1972, *Mem. R. astr. Soc,* **77,** 55
Hodge, P. W. 1961, *Astrophys. J.*, **133**, 64
Humphreys, R. M. 1979 in *IAU Symp.* 84: *The Large-Scale Characteristics of the Galaxy,* Ed. W. B. Burton, D. Reidel, Dordrecht, p. 93.
Joshi, U. C. 1982, *Bull. astr. Soc. India,* **10,** 271.
Jensen, E. B., Strom, K. M., Strom, S. E. 1976, *Astrophys. J.,* **209,** 748.
Kippenhahn, R., Smith, L. 1969, *Astr. Astrophys.,* **1**, 142.
Karimova, D. K., Pavlovskaya, E. D. 1981, *Sov. Astr. Lett.,* **7**, 61.
Knapp, G. R., Kerr, F. J. 1974, *Astr. Astrsophys.,* **33,** 463.
Kraft, R. P. 1961, *Astrophys. J.,* **134,** 616.
Luck, R. E. 1982, *Astrophys. J.,* **256,** 177.
Luck, R. E., Lambert, D. L. 1981, *Astrophys. J.,* **245**, 1018 (LL).
Mueller, M. W., Arnett, W. D. 1976, *Astrophys. J.,* **210**, 670.
Palous, J., Ruprecht, J., Dluzhnevskaya, O. B., Pikunov, T. 1977, *Astr. Astrophys.,* **61,** 27.
Parsons, S. B. 1970, *Bull. Am. astr. Soc,* **2**, 334.
Parsons, S. B., Bell, R. A. 1975, *Dudley Obs. Rep. No.* 9.
Pel, J. W. 1978, *Astr. Astrophys.,* **62,** 75.
Roberts, W. W. 1969, *Astrophys. J.,* **158,**123.
Roberts, W. W. 1982, in *Kinematics, Dynamics, and Structure of the Milky Way,* Ed. W. L. H. Shutter, D. Riedel, Dordrecht, p. 265,
Rodgers, A. W., Bell, R. A. 1963, *Mon. Not. R. astr. Soc,* **125,** 487.
Sancisi, R. 1974, in *IAU Symp. 60: Galactic Radio Astronomy,* Eds F. J. Kerr & S. C. Simonson, III, D. Reidel, Dordrecht, p. 115.
Sandage A., Tammann, T. A. 1969, *Astrophys. J.,* **157,** 683.
Schaltenbrand, R., Tammann, G. A. 1971, *Astr. Astrophys. Suppl. Ser.,* **4,** 265.
Schmidt, E. G. 1971, *Astrophys. J.,* **170,** 109.
Schmidt, E. G. 1972a, *Astrophys. J.,* **174,** 595.
Schmidt, E. G. 1972b, *Astrophys.* J., **174,** 605.
Schmidt, E. G, Rosendhal, J. D., Jewsbury, C. P. 1974, *Astrophys. J.,* **189**, 293.
Strömgren, B. 1967, in *IAU Symp.* 31: *Radio Astronomy and the Galactic System,* Ed. H. van Woerden, Academic Press, London, p. 323.
Talent, D. L, Dufour, R. J. 1979, *Astrophys. J.,* **233,** 888.
Tammann, G. A. 1970, in *IAU Symp.* 38: *The Spiral Structure of Galaxy,* Eds W. Beckers & G. Contopoulos, D. Reidel, Dordrecht, p. 236.
van Paradijs, T. A. 1971, *Astr. Astrophys.,* **11,** 299.
Wielen, R. 1973, *Astr. Astrophys.,* **25,** 285.
Wielen, R. 1974, *Astr. Astrophys. Suppl. Ser.,* **15,** 1.
Yuan, C. 1969, *Astrophys. J.,* **158,** 889.
Yuan, C. 1971, *Astrophys. J.,* **76,** 664.

J. Astrophys. Astr. (1986) **7,** 99–103

The Luminosity–Volume Test and the Local Hypothesis of Quasars

F. Hoyle *Department of Applied Mathematics and Astronomy, University College, Cardiff CF1 1XL, UK*

J. V. Narlikar *Tata Institute of Fundamental Research, Homi Bhabha Road, Colaba, Bombay 400005*

Received 1985 September 9; accepted 1986 January 28

Abstract. It is shown that the luminosity-volume test for optically selected objects has an in-built bias towards increasing the average value of V/V_m above the Euclidean value of 1/2. A more satisfactory bias-free statistic is suggested in the form of In (V/V_m), The result of applying the test to a sample from the Bright Quasar Survey (BQS) shows that the local hypothesis of quasars is consistent with the data.

Key words: quasars, statistics– quasars, local hypothesis

1. Introduction

In spite of the discovery of nearly 3000 quasars the question of their distance remains a controversial one. The majority of astronomers believe in the cosmological hypothesis that the quasar redshifts are due solely to the expansion of the universe. This hypothesis implies that quasars of large redshifts are considerably farther than those with small redshifts. There are, however, several examples wherein quasars of very different redshifts are found too close to one another, and sometimes in very special linear configurations. There are also cases of quasars of high redshifts near galaxies of very small redshifts. For a review of such examples see Narlikar (1983). Statistics of quasar distributions on the sky suggest that the probability of obtaining such configurations by chance is extremely small (Burbidge, Narlikar & Hewitt 1985; Narlikar & Subramanian 1985). Perhaps the most striking case of a quasar-galaxy association with highly discrepant redshifts is that reported recently by Huchra *et al.* (1985). Even with gravitational lensing thrown in, it is hard to reconcile this case with a chance juxtaposition.

These examples make one wonder whether the cosmological hypothesis is correct. Certainly one cannot rule out the possibility that quasars are considerably nearer than implied by their redshifts. To test whether a group of quasars is in fact local rather than distant, other methods may therefore be used. For example, if quasars are distant then probes of their large-scale distributions should show some effects of the non-Euclidean geometry that describes the expanding universe.

The luminosity-volume test applied to a complete magnitude limited sample is one such probe. If the quasars are very nearby (say within 30–100 Mpc), then their distribution should follow Euclidean geometry. It is then easy to verify that a quasar of

magnitude B observed in a survey of limiting magnitude B_m has the V/V_m ratio given by

$$\frac{V}{V_m} = \text{dex}\{0.6(B - B_m)\}. \tag{1.1}$$

Here V = observed volume of space up to the quasar and V_m = the maximum volume of space within which the quasar could be found within the prescribed magnitude limit. In a uniform distribution the average value of V/V_m is 1/2 when the geometry is Euclidean.

This test had earlier been applied to radio quasars by Wills & Lynds (1978) who concluded that the results were consistent with the local hypothesis. If, however, the test is applied to verify the cosmological hypothesis on the same sample, evolutionary effects have to be invoked.

This circumstance, that evolution (in number density or luminosity or both) needs to be invoked, has so far prevented any clear-cut demonstration of the hypothesis that quasars are at cosmological distances. The effects of non-Euclidean geometry implied by Hubble's law are masked by the evolutionary effects invoked to fit the data.

Schmidt & Green (1983), for example, have applied the V/V_m test to the quasars from the Bright Quasar Survey (BQS), a sample of quasars brighter than an average magnitude B = 16.16. On the basis of a comparison of their sample with other fainter quasar samples, these authors have to invoke strong evolutionary effects in a typical Friedmann model. This conclusion has, however, been challenged by Wampler & Ponz (1985, 1986) who find no evidence for evolution between the BQS quasars (mean redshift $z \simeq$ 1.8) and the CTIO sample of quasars (mean redshift $z \simeq 2.8$) of Osmer & Smith (1979).

By contrast, in a local hypothesis the evolutionary parameters cannot be invoked and it is consequently more vulnerable to observational disproof. Indeed, Schmidt & Green (1983) have already argued that the application of the V/V_m test to the BQS sample disproves the local hypothesis.

In this paper we suggest a variant of the standard V/V_m test as applied to optical samples. We do so because the standard test has an inbuilt theoretical bias that overestimates the average value of V/V_m We then apply the modified test to the BQS sample to test the validity of the local hypothesis.

2. The Modified V/V_m Test for Optical Quasars

Consider the theoretical expression for V/V_m given by Equation (1.1) in the following form

$$\frac{V}{V_m} = \exp\{0.6(\ln 10).(B - B_m)\} \simeq \exp\{1.38(B - B_m)\}. \tag{2.1}$$

Suppose that owing to errors in magnitude determinations the true magnitude in fact lies in the range $(B - \Delta B, B + \Delta B)$. Although the average value of the magnitude in this range is B, the corresponding errors in V/V_m do not average out to zero. In fact the average of V/V_m for $(B - \Delta B)$ and $(B + \Delta B)$ is

$$\left(\frac{\bar{V}}{V_m}\right) = \cosh(1.38\Delta B) \cdot \exp\{1.38(B - B_m)\}. \tag{2.2}$$

In other words, on an average the observer tends to overestimate V/V_m by a factor cosh (1.38 ΔB) that exceeds unity. A similar effect arises from errors in the estimation of plate limits B_m

Bearing in mind that both ΔB and ΔB_m are larger at fainter magnitudes where more sources are expected to lie, the above bias could lead to an average $\langle V/V_m \rangle$ significantly higher than the Euclidean value when in fact the true value may well be Euclidean. For example, an uncertainty of $\Delta B = 0.27$ increases the value of $\langle V/V_m \rangle$ for a Euclidean distribution from 0.5 to 0.535 while $\Delta B = 0.5$ raises it to 0.62.

So far as an optically selected sample is concerned we therefore suggest that instead of using

$$x \equiv \frac{V}{V_m} \tag{2.3}$$

as the variable we should choose

$$y = \ln x = 1.38(B - B_m). \tag{2.4}$$

It is evident that the errors in y due to errors $\pm \Delta B$ in B or $\pm \Delta B_m$ in B_m cancel out in a random distribution.

Since x has a uniform distribution in the range [0,1],

$$\langle y \rangle = \int_0^1 \ln x \, dx = -1, \tag{2.5}$$

while

$$\sigma_y^2 = \int_0^1 (\ln x)^2 \, dx - \langle y \rangle^2 = 1. \tag{2.6}$$

Therefore, the mean value $\langle y \rangle$ computed for a sample of N members has the Standard error $1/\sqrt{N}$. For a Euclidean distribution the mean value of y is therefore expected to lie in the range $[-1 - 3/\sqrt{N}, -1 + 3/\sqrt{N}]$ with a probability of 99.7 per cent.

3. The BQS sample and local quasars

To illustrate the above test we choose the BQS sample since it is a single homogeneous optically selected sample containing a large number of quasars. Schmidt & Green (1983) quote that their magnitudes are accurate to $\Delta B = 0.27$. However, Wampler & Ponz (1985) have discussed the various observational biases in the BQS data and have given more reliable magnitudes for the samples studied by Schmidt & Green. A comparison of the Wampler–Ponz magnitudes with the Schmidt–Green magnitudes turns up many cases of magnitude differences considerably in excess of 0.27. For example, in 15 out of the 67 entries in Table 3 of Wampler & Ponz the difference exceeds 0.50 mag. To justify the greater reliability of their magnitudes, Wampler & Ponz (1986) have shown that they are in agreement with another independent estimate.

We therefore apply the above test to the BQS quasars with the revised B magnitudes as given by Wampler & Ponz (1985). There is, however, one difficulty in this procedure. In many cases (24 out of 67) the magnitudes listed by Wampler & Ponz in Table 3 of their paper exceed the corresponding limiting magnitudes B_{lim} of the BQS survey. It is therefore not possible to set $B_m = B_{lim}$ as originally given by Schmidt & Green.

Wampler & Ponz do not give the revised values of $B_{\rm lim}$, for the various plates, but for overall consistency it is obviously necessary to suppose that the revised values of $B_{\rm lim}$ must be fainter than those quoted by Schmidt & Green.

In their Table 2, Wampler & Ponz have taken the average magnitude to be 16.5 for the BQS survey. For the 67 cases of their Table 3 the average excess of their magnitudes over the Schmidt—Green magnitudes is about 0.21. Thus it is not unreasonable to set an overall average limiting magnitude for the Wampler–Ponz data at ~ 16.4 instead of the average value ~ 16.16 given by Schmidt & Green. We will therefore consider the two cases of $B_{\rm m}$ = 16.5 and 16.4.

Accordingly, we first take $B_{\rm m}$= 16.5 in Equation (2.4). In Table 3 of Wampler & Ponz there are 58 quasars brighter than this magnitude. For this sample we find

$$\langle y \rangle = -0.92 \qquad (3.1)$$

Since $1/.\sqrt{58} = 0.13$, it is clear that the observed value of $\langle y \rangle$ does not differ significantly from the Euclidean value –1, the departure being ~ 0.6 $\sigma_{\rm y}$.

A similar analysis for $B_{\rm m}$ = 16.4 gives $\langle y \rangle$ differing from the Euclidean value of –1 by $\lesssim 1.3\ \sigma_y$. This difference also cannot be considered statistically significant. It can be easily verified that if instead of the statistic y we had used for the same data the statistic $x = V/V_{\rm m}$, the σ -departures of $\langle x \rangle$ from the Euclidean value of 0.5 would have been systematically higher, thus illustrating the in-built bias of x.

4. Conclusion

From our application of the modified bias-free luminosity volume test it is clear that the BQS sample studied here is consistent with the local hypothesis of quasars. Taken in conjunction with the earlier studies of $V/V_{\rm m}$ for radio quasars we therefore find that quasar counts do not rule out the local hypothesis. This result also bears out an earlier conclusion by one of us (Hoyle 1984) that with suitable correction for the bias in favour of objects chosen too near the plate limit, $\langle V/V_{\rm m} \rangle$ for quasars is not significantly higher than 1/2.

Since the same tests applied on the basis of the cosmological hypothesis force the supporter of this hypothesis to invent various evolutionary scenarios to ensure a good fit, we feel that on the grounds of Occam's razor the local hypothesis comes out better.

Acknowledgements

We thank Joe Wampler for discussion on magnitudes. JVN is grateful to the Science and Engineering Research Council of the U.K. for a research fellowship that made this work possible.

References

Burbidge, G R., Nariikar, J. V., Hewitt, A. 1985, *Nature,* **317**, 413.
Hoyle, F. 1984, *Asti, Sp. Sci.,* **100**, 293.
Huchra, J., Gorenstein, M., Kent, S., Shapiro, 1, Smith, G., Horine, E., Perley, R. 1985, *Astr. J.*, **90**, 691.

Narlikar, J. V. 1983, *Introduction to Cosmology,* Jones & Bartlett, Boston, p. 374.
Narlikar, J. V., Subramanian, K. 1985, *Astr. Astrophys.,* **151**, 264.
Osmer, P., Smith, M. G. 1980, *Astrophys. J.* Suppl*.,* **42**, 333.
Schmidt, M., Green, R. F. 1983, *Astrophys. J.,* **269,** 352.
Wampler, E. J., Ponz, D. 1985, *Astrophys. J.,* **298**, 448.
Wampler, E. J., Ponz, D. 1986, in *IAU Symp.* 119: *Quasars,* Eds V. K. Kapahi & G.Swarup, D. Reidel, Dordrecht (in press).
Wills, D., Lynds, R. 1978, *Astrophys. J., Suppl. Ser.,* **36**, 317.

J. Astrophys. Astr. (1986) **7,** 105–112

WSRT Observations of Radio Sources in the Galactic Plane near $l = 54°$

T. Velusamy *Radio Astronomy Centre, Tata Institute of Fundamental Research, PO Box 8, Udhagamandalam 643001*

W. M. GOSS *Kapteyn Astronomical Institute, Postbus 800, 9700 AV Groningen, The Netherlands*

E. M. Arnal *Instituto Argentino de Radioastronomia, C C No. 5, 1894, Villa Elisa, Argentina*

Received 1985 October 8; accepted 1986 February 11

Abstract. A radio continuum map of a 1.°5 × 1.°5 region in the galactic plane near $l = 54°$ is presented at 49 cm with a resolution of 100 arcsec × 200 arcsec. The shell source G 54.4 – 0.3 has the characteristics of a supernova remnant while the second large ring structure G 53.9 + 0.3 is a HII ring consisting of W 52 and several small-diameter thermal sources. One of the twelve small-diameter sources (G 54.73 + 0.61) has a spectral index ~ –1.6.

Key words: supernova remnants—HII regions—interstellar medium

1. Introduction

The complex region near $l = 54°$, $b = 0°$ was first considered to be a supernova remnant (SNR) by Holden & Caswell (1969) and was designated as HC 40. However, further observations of this region at 11 cm with higher resolution (5.5 × 5.5 arcmin) showed several resolved features (Velusamy & Kundu 1974): (1) G 54.4 – 0.3 appears to be a SNR with a nearly symmetric shell structure of size ~ 40 arcmin. A linear polarization of ~ 5 per cent was observed at 11 cm confirming the nonthermal nature. (2) G 53.9 + 0.3 to the southwest also shows a ring structure of size 40 arcmin with a deep minimum near the centre. The source W 52 (Westerhout, 1958) appears to be a part of this shell. Although some polarization was detected in G 53.9 + 0.3, the nature. of this source was not clear. (3) The source of angular size ~ 2 arcmin with a flat radio spectrum near the position of 4C 18.57, is a blending of an HII region and the 4C source (Day, Caswell & Cooke 1972). In the recent Effelsberg maps of this complex region around $l = 54°$ at 6 cm (Altenhoff *et al.* 1979) and 11 cm (Reich *et al.* 1984) with resolutions of 2.6 and 4.3 arcmin, several small-diameter sources are seen in addition to the large-diameter sources G 54.4 – 0.3 and G 53.9 + 0.3. Radio recombination line and continuum data are also available for some of these small diameter sources (Downes *et al.* 1980; Wink, Altenhoff & Mezger 1982). The pulsar 1926 + 18 lies on the boundary of G 53.9 + 0.3. It is possible that some of these features are physically associated and it is

important to investigate the nature of the various sources in this region and any physical association between them. Recently, Caswell (1985) has discussed the nature of the sources in this region based on the Penticton Synthesis telescope observations at 21 cm with a resolution of 2.6 × 1.3 arcmin. In this paper we present high resolution observations of this field using the WSRT at 49 cm and discuss our results along with the recently available high-frequency continuum and line observations.

2. Observations and results

The observations at 49 cm were made in 1978 November using the Westerbork Synthesis Radio Telescope (WSRT); the relevant observational parameters are given in Table 1. The observations, data reduction, mapping and cleaning were performed using standard procedure. The full resolution of the original 49 cm map was 50 × 191 arcsec. However, the map shown in Fig. 1 has been smoothed to a resolution of 100 × 200 arcsec in order to improve the signal-to-noise ratio. Due to the shortest spacing of 36 m, structures > 20 arcmin are heavily resolved. The extended emission near the bottom left and top right corners in Fig. 1 are spurious features caused by bad data. The improved position of the pulsar PSR 1926+ 18 (Vivekanand, Mohanty & Salter 1983) is marked in Fig.1. The positions, flux densities and angular sizes of the small diameter sources in this field are listed in Table 2. The flux densities at 49 cm are corrected for the primary beam attenuation. The angular size and flux densities were obtained using the full resolution map and the unresolved sources are indicated as P. The flux densities at 21,11 and 6 cm are from Caswell (1985), Reich *et al.* (1984) and Altenhoff *et al.* (1978) respectively. The recombination line (H 110α) velocities are from Downes *et al.* (1980).

3. Discussion

In order to clarify the nature of the individual sources in this field we have compared the present map at 49 cm with those at 6 cm (Altenhoff *et al.* 1979), at 11 cm (Reich *et al.*

Table 1. Observing parameters.

Field centre (1950.0) R.A.	$19^h29^m00^s.0$
Dec.	$+18°\,35'\,00''.0$
Period of observation	1 × 12 hours
Frequency	608.5 MHz
Baselines—Shortest	36 m
increment	36 m
largest	1476 m
Primary beam FWHM	1°.4
First grating ring (RA × Dec)	47 × 147 arcmin
Largest structure present	20 arcmin
Full resolution (RA × Dec)	50 × 191 arcsec
Map resolution (RA × Dec)	100 × 200 arcsec
Conversion from flux density to brightness temperature	S(mJy/beam) = 6.0 T_b(K)
rms noise	10 mJy/beam

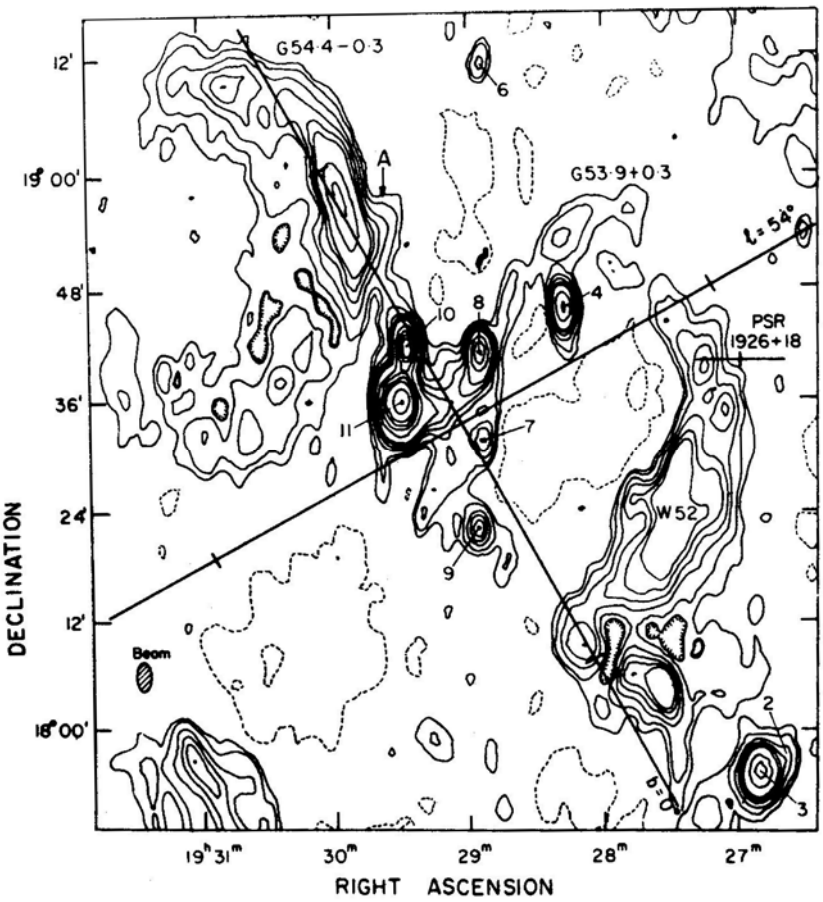

Figure 1. 49 cm continuum map of the field around $l = 54°$. The resolution is 100 × 200 arcsec (hatched ellipse). The contour levels are –20, 10, 20, 40, 60, 80, 100, 200, 300, 400, 500, 750, 1000 mJy per beam where 10 mJy per beam is 1.7K in full beam brightness. The dashed contours indicate negative values and the hatched contours indicate local minima. The map is not corrected for primary beam attenuation. The rms noise in the map is 10 mJy /beam. Small diameter sources are indicated by the WSRT source number as given in Table 1 (*i.e.* 62W1, 62W2 *etc.*). The position of pulsar 1926 +18 is indicated. Arrow 'A' indicates a distortion in the shell (see text).

1984) and at 21 cm (Caswell 1985). The spectra and nature of the small-diameter sources are summarized in Table 2.

3.1 *Small-Diameter Sources*

Twelve small-diameter sources were detected at 49 cm with flux densities greater than 50 mJy. All these sources are also present in the 21 cm map (Caswell 1985), and only one source 62W2 (Fig. 1) is not listed by Caswell probably because it is confused by 62W3. The observed parameters of these sources at 49 cm and the flux densities at 21,11 and 6 cm are listed in Table 2.

Table 2. Small-diameter sources near $l = 54°$.

WSRT No.	RA (1950) h m s s	Dec (1950) ° ′ ″ ″	Galactic coordinates	Angular size (arcsec)	Flux density (mJy) 49 cm	21 cm	11 cm	6 cm	Spectral index between 49–21 cm	Remarks
62W1	19 26 30.1 ± 0.5	18 53 04 ± 25	54.00 + 0.69	P	70 ± 15	49			− 0.42	
62W2	26 39.2 0.3	17 56 10 15	53.18 + 0.21	P	115 18					Confused by 62 W3
62W3	26 50.5 0.2	17 54 53 10	53.18 + 0.16	110	1500 100	2285	2260	2680	+ 0.50	HII. $V_{HII} \sim 8.3\,km\,s^{-1}$
62W4	28 17.3 0.2	18 45 53 10	54.09 + 0.26	40	430 30	364	580	400	− 0.20	HII?
62W5	28 18.8 0.5	19 28 40 15	54.73 + 0.61	< 40	380 80	70			− 2.00	Steep-spectrum source
62W6	28 53.7 0.5	19 11 38 14	54.54 + 0.35	P	95 15	150	290	100	+ 0.53	HII ? 21 and 11 cm fluxes include extended emission
62W7	28 52.3 0.5	18 31 50 15	53.97 + 0.02	P	45 15	105			+ 0.10	HII ?
62W8	28 54.7 0.2	18 41 10 10	54.07 + 0.10	P	390 30	170			− 1.00	Extragalactic?
62W9	28 55.1 0.3	18 22 14 15	53.82 − 0.06	P	85 15	103			+ 0.23	HII ?
62W10	29 27.3 0.2	18 41 50 10	54.17 − 0.01	P	615 40	321			− 0.76	4C 18.57—Extragalactic?
62W11	29 30.0 0.6	18 36 07 17	54.09 − 0.07	105	1300 200	2500	2650	2470	+ 0.77	HII. $V_{HII} \sim 43\,km\,s^{-1}$
62W12	32 13.4 0.2	18 13 28 10	54.07 − 0.81	P	380 20	215	200	100	− 0.67	Extragalactic?

(i) 62W8 and 10 are the most prominent nonthermal sources close to the galactic plane within $|b| < 0^{\circ}.1$ in the field shown in Fig. 1. 62W10 can be associated with the source 4C 18.57. Caswell (1985) noted this association but incorrectly listed the 4C source as 4C 18.42 due to copying error. The position at 178 MHz (Gower, Scott & Wills 1967) is within 70 arcsec of 608.5 MHz position. In the earlier low-resolution maps at centimetre wavelengths it was confused by 62W11, an HII region to the south. Both 62W8 and 10 have steep radio spectra (with $\alpha_{49-21cm} \sim -1.0$ and -0.8 respectively) and are likely to be extragalactic.

(ii) 62W3 and 11 are clearly HII regions (G53.18 + 0.16, G 54.09 – 0.07)as indicated by the radio spectrum as well as the detection of radio recombination lines (Wink, Attenhoff & Mezger 1982; Downes *et al.* 1980). Both these sources seem to have a turnover frequency around 1 GHz. 62W3 is at the far side of the galaxy at distance of ~ 11.4 kpc while 62W11 is at distance of 3.9 or 7.9 kpc from the Sun (Wink, Altenhoff & Mezger 1982).

(iii) 62W4, 7 and 9 seem to be thermal radio sources as indicated by the flat radio spectrum between 49 and 6 cm. It is interesting that 62W4, 7 and 9 and W52 lie along the ring structure centred on G 53.9 + 0.3.

(iv) 62W6 is located in the direction of the extension which appears to rise from the shell of SNR G 54.4 – 0.3(feature A in Fig. 1). This is discussed in detail in Section 3.2.

(v) 62W5 appears to be a steep spectrum source with $\alpha_{49-21\ cm} \sim -2.0$. This source is located outside the map shown in Fig. 1. It has a flux density of 380 ± 80 mJy at 49 cm and may be resolved with size $\lesssim 40$ arcsec. It may be noted that the uncertainties in the size and flux density are due to the large primary-beam correction (a factor of 3.7) as this source is about 55 arcmin away from the map centre. In Fig. 2 is shown the flux-density

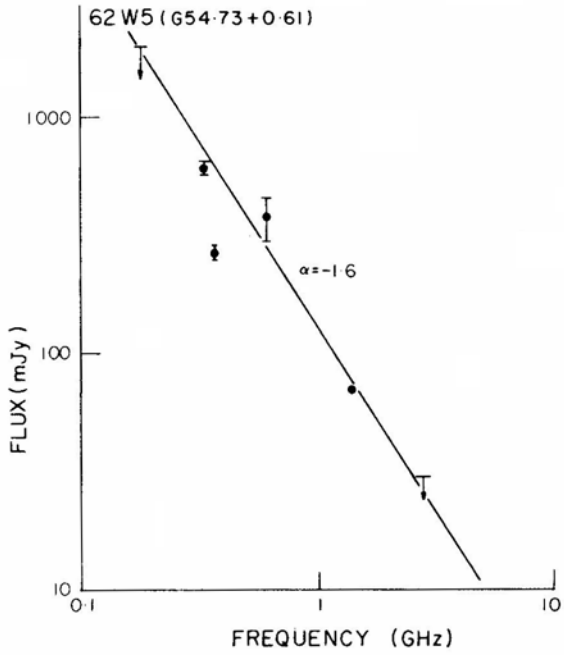

Figure 2. Flux-density spectrum of the source 62W5 (G 54.73 4 + 0.61).

Spectrum of this source. The upper limits to the flux densities at 178 MHz and 2.7 GHz are 2 Jy and 30 mJy respectively as this source was not detected in the 4C survey (Gower, Scott & Wills 1967) and in the Effelsberg map of this region (Reich *et al.* 1984). A flux density of 614 ± 30 mJy at 92 cm was obtained from the WSRT observation made in January 1984 with a resolution of 56 × 163 arcsec (Goss *et al.* in preparation). It is not clear why the flux density of 263 mJy at 365 MHz in the Texas Survey (Douglas *et al.* 1980) is not consistent with the spectrum shown in Fig. 2. In view of its close proximity to the galactic plane ($b \sim 0\overset{\circ}{.}6$) and rather steep spectrum, this source would be extremely interesting for further high-resolution observations.

3.2 *SNR G* 54.4 – 0.3

In the 49 cm WSRT map (Fig. 1) the shell structure of this source is obvious supporting its identification as a SNR. In the earlier low-resolution maps the shell structure became clear only after the substraction of a source near the 4C 18.57 position (Velusamy & Kundu 1984), and its identification as a SNR is now confirmed. In Fig. 1 this shell is nearly circular and about 60 per cent complete. However, when smoothed to lower resolution (~ 300 arcsec), we see some evidence for weaker emission extended over a nearly complete shell. The maps at 11 and 21 cm (Reich *et al.* 1984; Caswell 1985) also show a complete ring except for a small gap near the north-east boundary. The shell thickness appears to be nearly constant along the shell, with mean thickness of ~ 10 arcmin and a shell radius of ~ 20 arcmin. However, the brightness along the shell is quite irregular. The brightest emission is seen along the western part of the shell and the brightness decreases monotonically towards the east (Fig. 1). Further, the brightness along the shell is peaked near $b = 0°$ and decreases steadily away from the galactic equator. Such a brightness variation may be expected from an SNR expanding into the interstellar medium with large gradient in the density of relativistic particles and magnetic field (Caswell 1977). A detailed study of the spectral-index distribution would be very useful.

The integrated flux density of G 54.4 – 0.3 at 49 cm is only 6.6 Jy compared to the flux density of 34 Jy at 11 cm (Velusamy & Kundu 1974). However, the 11 cm flux density includes considerable background emission. The flux density at 21 cm is 18 Jy (Caswell 1985). Obviously, the flux density at 49 cm is underestimated because of missing short spacings and has severe limitations for deriving the spectral index and the physical parameters of the SNR. From the 21 cm data, Caswell (1985) has derived a distance of 5 kpc and an age of 33000 years for the SNR.

A jet-like emission (feature A in Fig. 1) emerging to the northwest is seen at $\alpha = 19^{h}29^{m}37^{s}$ $\delta = +18°55'$ along the brightest part of SNR. This feature is seen prominently also in the 21 and 11 cm maps (Caswell 1985; Reich *et al.* 1984). It is interesting to note that the source 62W6 lies 27 arcmin away from the SNR in the direction of this feature. Caswell suggests that this source and the jet-like feature are components of an extragalactic double radio source seen in projection against the SNR. Although in the 49 cm map this source is unresolved, in the 20 and 11 cm maps there are indications of extended emission around it. Further, as seen from the flux densities given in Table 2, its spectrum is rather uncertain and it is not clear whether it forms part of a double radio source. However, it would be interesting if this jet-like feature is not part of a double radio source and is associated with the SNR, particularly since such

radio jet features are not uncommon in the SNRs, for example, in the Crab Nebula (Velusamy 1984) and in G 332.4 + 0.1 (Roger *et al.* 1985). Obviously, high-resolution observations are required to investigate the nature of this interesting feature.

3.3 *HII Ring G* 53.9 + 0.3

A distinct minimum is seen near $\alpha = 19^h28^m$, $\delta = +18°35'$ in Fig. 1. This minimum is seen more prominently at high frequencies (*cf.* Velusamy & Kundu 1974; Altenhoff *et al.* 1979; Reich *et al.* 1984), indicating the presence of a ring structure with diameter about 40 arcmin. Although Velusamy & Kundu (1974) had suggested that it may be a supernova remnant, the true nature of its radio spectrum was uncertain. In Fig. 1 the radio emission in the ring is more prominent over the western part coincident with W 52. Over the eastern half, several small-diameter sources are seen superimposed on a rather faint extended emission along the ring. All the other four sources except 62W8 and 10 (Table 2) have thermal radio spectrum. Also recombination lines (V_{HII} ~ 38 km s^{-1} have been detected from the W52 region (Silverglate & Terzian 1979). Further, as shown by Caswell (1985) from a comparison of the radio brightness at 21 and 6 cm, the emission along the ring is predominantly thermal. We therefore conclude that the structure around G 53.9 + 0.3 is an HII shell at a distance of about 3.2 kpc. It is interesting to note that the close proximity of the pulsar PSR 1926 +18 to the ring structure in G 53.9 + 0.3 (Fig. 1). The distance to the pulsar derived from the dispersion measure is ~ 2.8 kpc (Manchester & Taylor 1981). A pulsar–SNR association is ruled out since G 53.9 + 0.3 appears to be an HII ring.

Recently, Sofue *et al.* (1984) have also observed HII rings with diameters ~ 50 arcmin at G 23.2 + 0.2 and G 24.6 + 0.0 in the galactic plane. These are very similar to the HII ring G 53.9 + 0.3 discussed above. The origin of such rings is not clearly understood. These HII rings or shells are perhaps the result of enhanced star formation and may be common throughout the Galaxy.

4. Conclusion

The 49 cm map confirms that G 54.4 – 0.3 is a supernova remnant with structure typical of shell-type SNRs; it has a nearly complete shell. The brightness in the shell is not uniform, with the maximum over the shell closest to the galactic plane, and decreasing steadily away from the plane. The ring-like structure centred on G 53.9 + 0.3 seems to bean HII ring consisting of several small-diameter thermal source sand W52. Of the ten small-diameter sources for which radio spectra are available, four are clearly nonthermal and probably extragalactic and the rest are compact HII regions. The source G 54.73 + 0.61 seems to be a steep spectrum source.

Acknowledgements

The Westerbork Synthesis Radio Telescope is operated by the National Foundation for Radio Astronomy (SRZM) with the financial support of the Netherlands

Organisation for the Advancement of Pure Research (ZWO). TV thanks the University of Gronigen and NFRA for support during the data reduction.

References

Altenhoff, W. J,, Downes, D., Pauls, T., Schram, J. 1979, *Astr. Astrophys. Suppl. Ser.,* **35**, 23.
Caswell, J. L. 1977, *Proc. astr. Soc. Austr.,* **31**, 30.
Caswell, J. L. 1985, *Astr. J.,* **90**, 1224.
Day, G. A., Caswell, J. L., Cooke, D. J. 1972, Austr. *J. Phys., Astrophys. Suppl. Ser.,* No. 25, 1.
Douglas, J. N., Bash, F. N., Torrence, G. W., Wolfe, C..1979, *Univ. Texas Publ. Astr.* No.17.
Downes, D., Wilson, T. L., Bieging, J., Wink, J. 1980, *Astr. Astrophys. Suppl, Ser.,* **40**, 379.
Gower, J. F. R., Scott, P. F., Wills, D. 1967, *Mem. R. Astr. Soc.,* **71**, 49.
Holden, D. J., Caswell, J. L. 1969. *Mon. Not. R. astr. Soc.,* **143**, 407.
Manchester, R. N., Taylor, J. H. 1981, *Astr. J.,* **86**, 1953.
Reich, W., Furst, E., Steffen, P., Reif, K., Haslam, C. G. T. 1984, *Astr. Astrophys. Suppl. Ser.,* **58**, 477.
Roger, R. S., Milne, D. K., Kesteven, M. J., Haynes, R. F., Wellington, K. J. 1985, *Nature,* **316**, 44.
Silverglate, P. R., Terzian, Y. 1979, *Astrophys. J. Suppl. Ser.,* **39**, 157.
Sofue, Y., Hirabayashi, H., Akabane, K., Inove, M., Handa, T., Nakai, N. 1984. *Publ. astr. Soc. Japan,* **36**, 187.
Velusamy, T. 1984, *Nature,* **308**, 251.
Velusamy, T., Kundu, M. R. 1974, *Astr. Astrophys.,* **32**, 375.
Vivekanand, M., Mohanty, D. K., Salter, C. J. 1983, *Mon, Not. R. astr. Soc.,* **204**, 81P
Westerhout, G. 1958, *Bull. astr. Inst. Netherl.,* **14**, 215.
Wink, J. E., Altenhoff, W. J., Mezger, P. G. 1982, *Astr. Astrophys.,* **108**, 227.

J. Astrophys. Astr. (1986) **7,** 113–118

On the Latitude Migration of Polar Faculae in the Solar Activity Cycle Period: 1970–1978

V. I. Makarov & V. V. Makarova *Kislovodsk Station of the Pulkovo Observatory, 357741 Kislovodsk, P.O. Box 1, USSR*

Received 1985 December 5; accepted 1986 February 11

Abstract. Coordinates of polar faculae have been measured and processed using daily photoheliograms of the Kislovodsk Station of the Pulkovo observatory with the final goal of studying their latitude distribution during the solar cycles 20–21. The results obtained are as follows:

1. The first polar faculae emerge immediately after the polarity inversion of the solar magnetic field at the latitudes from 40° to 70° with t he average $\varphi \simeq 55°$**.**
2. The zone of the emergence of polar faculae migrates poleward during the period between the neighbouring polarity inversions of the solar magnetic field. This migration is about 20° for 8 years, which corresponds to a velocity of 0.5 m s^{-1}.
3. The maximum number of polar faculae was reached at the activity minimum (1975–1976).
4. The last polar faculae were observed in the second half of 1978 at the latitudes from 70° to 80°.

Key words: Sun, faculae— Sun, activity

1. Introduction

The problem of latitude migration of solar magnetic fields is a basic one in the verification of validity of any solar cycle theory.

Twenty years ago Bumba & Howard (1965) showed that the weak magnetic fields resulted from the breakup of active regions. These fields formed largescale patterns of unipolar magnetic fields. Due to differential rotation, these fields showed up as poleward fluxes. One can detect poleward migration of weak fields in solar cycles in full detail from a plot of the dynamics of the latitude zonal structure of these fields (Makarov 1984).

At the same time the ‘butterfly diagram’ is interpreted as equatorward migration of fields of active regions (Stix 1976). However, it was known that after the minimum of the 11-year solar cycle the high latitude boundary of the ‘sunspotting’ zone first has a poleward displacement (Antalova & Gnevyshev 1983). Therefore, the maximum sunspotting latitude takes place at the maximum of the solar activity, not at the beginning of the solar cycle (Kopecky 1962). On the other hand, the equatorward drift of magnetic fields was seemingly confirmed by Howard & LaBonte (1980) on the basis

of their analysis of radial velocities for 1968–1979. They deduced that the zones of slow and fast rotation originate near the poles in the epoch of minimum, and it requires about 22 years for the zones to drift to the equator.

On the other hand, an analysis of the evolution of the largescale magnetic field on H_α charts for several solar activity cycles showed that all organized largescale field motions originate in the active region zones and are directed poleward (Makarov 1984). An analysis of direct observations (1967–1980) of the longitudinal component of the magnetic field at the Mt Wilson Observatory gives the same result.

In the recent paper by Makarov & Makarova (1984) it was inferred that polar faculae are similar to sunspot regions and are divided into unipolar and bipolar events. After the epoch of the solar magnetic field reversal the polarity of the magnetic field of faculae is opposite to that of the magnetic field in the sunspot groups of the current cycle and is the same as the polarity of the sunspot magnetic fields in the following solar cycle in each hemisphere.

The present paper reports the data on the latitude distribution of polar faculae in the period between the reversal of the magnetic field of the Sun in the 20th and 21st solar cycles (1970–1978).

2. Observations, Reductions and Results

Coordinates of 9180 polar faculae were determined on daily photoheliograms of the Kislovodsk Station of the Pulkovo observatory for the period 1970–1978. Fig. 1 gives the latitude distribution of polar faculae with time. As is seen, the first indications of the activity of polar faculae are observed immediately after the reversal of the solar magnetic field which ended in the southern hemisphere in mid-1970 and in the northern hemisphere in mid-1971 (Makarov, Fatianov & Sivaraman 1983). In the first two years polar faculae are, in fact, absent higher than 70°, scarce between 40° and 70°, the mean latitude of single faculae being 55°. Then their number grows, groups of faculae appear between 40° and 60°. The first high-latitude faculae (higher than 80°) appear two years after the field reversal. Further, the zone of emergence of the maximum number of polar faculae migrates to higher latitudes. The maximum number of faculae was observed in 1975–1976, *i.e.* during the minimum of sunspot activity. Their mean latitude at this period is about 70°. The poleward migration of the faculae-forming zone takes place in both hemispheres. The last polar faculae were observed in 1978 September at the latitudes from 70° to 80°. The mean latitude of the faculae-forming zone at this period was 75°.

The variation of the latitude of polar faculae averaged over the solar rotation in the nothern and southern hemispheres is marked by dotted lines in Fig. 2(b) and (c); a comparison of this variation with the sunspot activity (Fig. 2a, d) and dynamics of latitude zones of the background magnetic field (Fig. 2b, c) is also made. Based on Fig. 2, one may make the following conclusions:

The mean latitude of the zone where polar faculae emerge for 8 years increased from 55° (1970) to 75° (1978) in each hemisphere. It can be seen in a greater detail in Fig. 3, where the number of emerging faculae are plotted against latitude. The velocity of the variation of latitude of the facular zone is 0.5 m s^{-1}. This is an order of magnitude smaller than the mean velocity of the poleward migration of largescale magnetic field

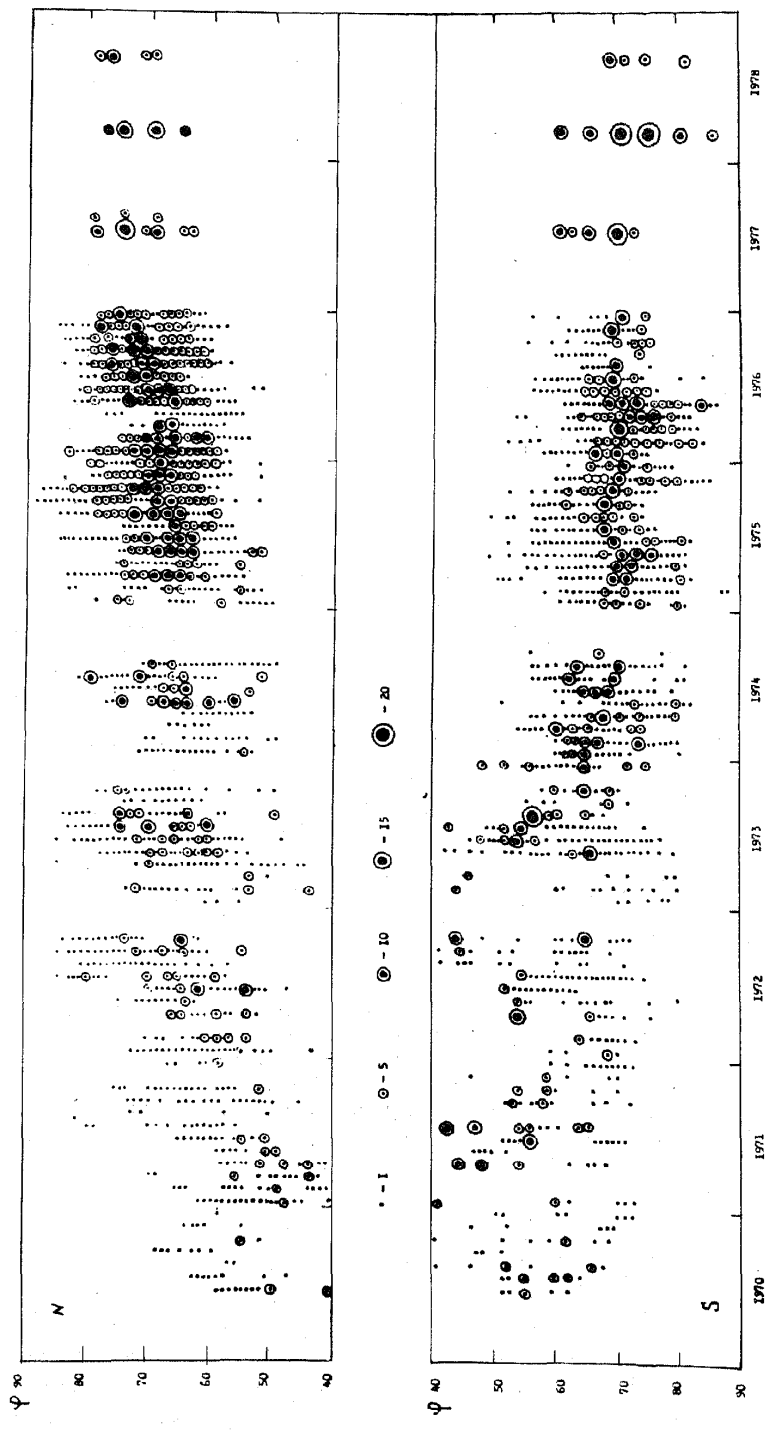

Figure 1. Latitude distribution of polar faculae in the cycle of their activity for the period 1970–1978 for the northern (N) (upper drawing) and southern (S) (lower drawing) solar hemispheres. The numbers of polar faculae are plotted at a given latitude as averaged over one solar rotation.

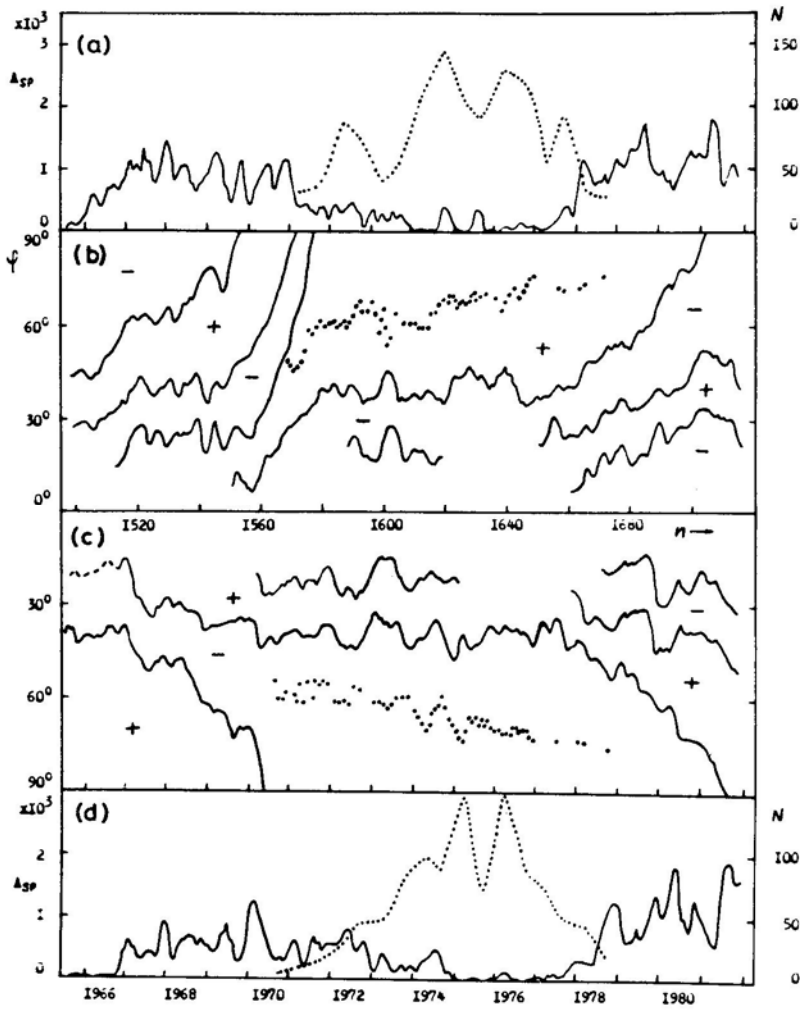

Figure 2. Curves in (b) and (c) are trajectories of the migration of the mean latitude of the neutral line of the largescale magnetic field; + and – stand for polarity sign of the magnetic field in the conventional way; *n:* number of the Carrington solar rotation; dotted lines denote the latitude of polar faculae averaged over a solar rotation; curves in (a) and (d) are mean sunspot areas *A*(sp), averaged over a solar rotation, and as smoothed using 3 points. These areas are extracted from Greenwich Photographic Results published before 1976 and Solnechnye Dannye Byulletin 1977–1981; dotted lines denote the mean number of polar faculae *N* averaged over a solar rotation.

zones during the enhancement of solar activity (Makarov & Fatianov & Sivaraman 1983).

As is seen from Fig. 2, during the period between the magnetic field reversal and the beginning of a new cycle, the latitude zones do not migrate either poleward or equatorward. The boundaries of the zones oscillate around the mean latitudes ± 40° and + 20°. Simultaneously, the polar facular zone is migrating poleward. This migration is overlapped by the irregular displacement of the facular zone latitude

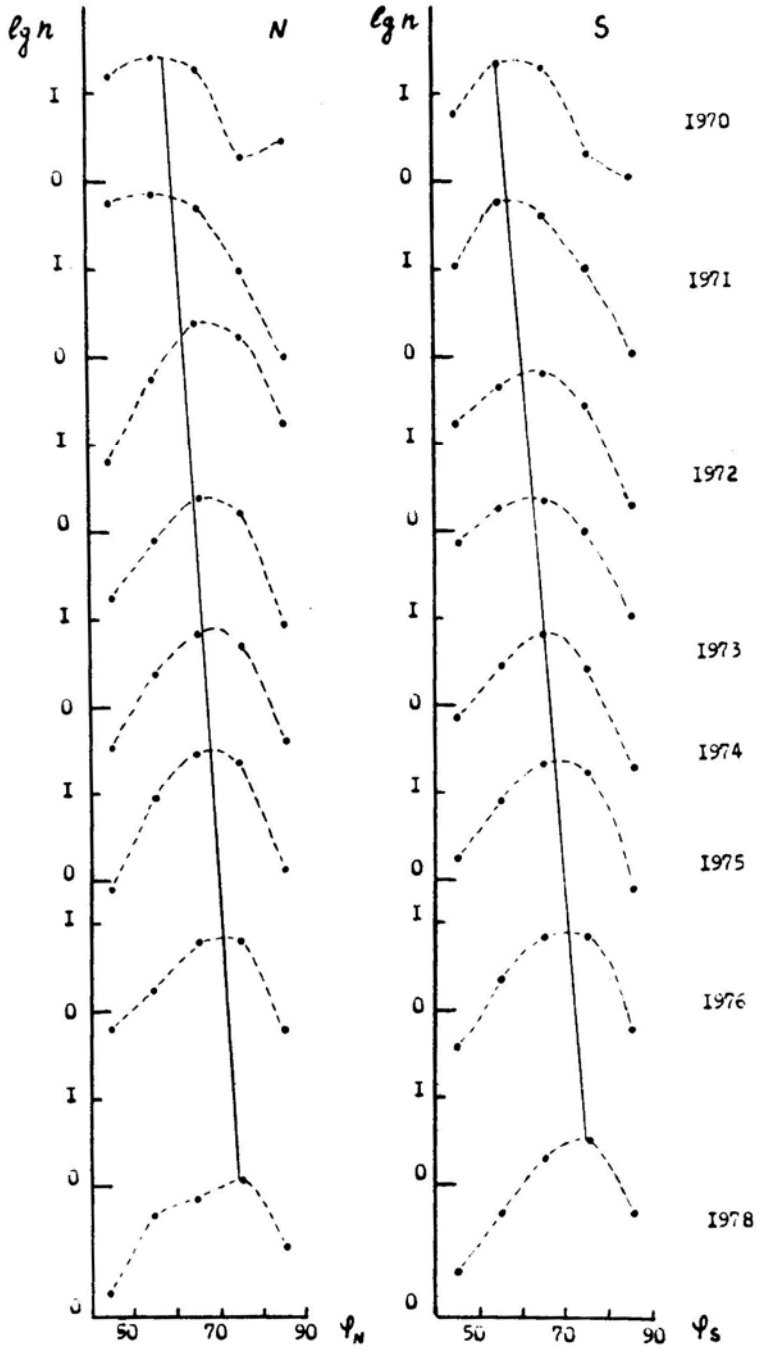

Figure 3. Yearly latitude distribution of polar faculae for the northern (N) and southern (S) hemispheres of the Sun. The solid line shows the polar migration of the zone of enhanced emergence of polar faculae.

relative to the mean level. The latter repeats most powerful fluctuations of the boundaries of latitude zones of the background magnetic field with a lag of about 3 solar rotations. Hence, the change of the latitude of the zone, where polar faculae show up, and the zone of poleward migration are unlikely to be caused by migration of largescale magnetic fields to high latitudes.

The 'latitude–time' diagram plotted for polar faculae (Fig. 1) is similar to the 'Maunder butterfly diagram' for sunspots. The difference lies in the fact that the zone of facular buildup migrates poleward, while the zone of sunspot buildup shows up first at 20°–30° of latitude, and later with the enhancement of sunspot activity the expansion takes place in both directions (to higher and lower latitudes). At the peak of activity the sunspot-forming zone is as wide as 5° to 40°. After the magnetic field reversal it is between the equator and latitudes 15°–20°.

From an analysis of the measurements of the coronal brightness in the 5303Å line and its association with the latitude zonal structure of the coronal magnetic field for the period 1944–1974 it was shown that the global process of solar activity consists of two waves of enhancement. At first the cycle shows up in the polar zone immediately after the reversal and lasts for about 11–12 years up to the next reversal of the solar magnetic field. The second and more powerful wave of enhancement of the solar activity is observed at latitudes 5° to 30° and it also lasts for about 11–12 years. Thus, a conclusion was made that the total duration of a solar activity cycle is about 17–18 years, which is in agreement with Legrand & Simon (1981). In between the reversals of the solar magnetic field, the polar zones are of the predominant polarity of the magnetic field. Polar faculae as indications of solar activity in the polar zones are regions of strengthening of this field.

Thus, the polar faculae manifest migration of the activity zone of the sub-photospheric magnetic field to high latitudes during the period between polarity reversals. This phenomenon can be explained in terms of the phenomenological model of the cycle (Makarov 1984) which suggests that a poloidal component of the field in this period exists at low and high latitudes.

References

Bumba, V., Howard, R., Smith, S. 1964, *Astr. J.*, **69**, 535.
Howard, R., La Bonte, B. J. 1980, *Astrophys. J.*, **239,** L33.
Howard, R., La Bonte, B. J. 1981, *Solar Phys.*, **74**, 131.
Kopecky, M. 1962, *Bull. astr, Inst. Czech.*, **13**, 63.
Legrand, J. P., Simon, P. A. 1981, *Solar Phys.*, **70**, 173.
Makarov, V. I., Fatianov, M. P., Sivaraman, K. R. 1983, *Solar Phys.*, **85**, 215.
Makarov, V. I., Makarova V. V. 1984, *Soln. Dann. Byull.*, No. 12, 88.
Makarov, V. I. 1984, *Soln. Dann. Byull.*, No. 9, 52.
Stix, M. 1976, *Astr. Astrophys.*, **47**, 243.

J. Astrophys. Astr. (1986) **7,** 119–129

Extragalactic Sources with Asymmetric Radio Structure II. Further Observations of the Quasar B2 1320 + 299

T. J. Cornwell *National Radio Astronomy Observatory, Post Box 0, Socorro, New Mexico 87801, USA*

D. J. Saikia *Nuffield Radio Astronomy Laboratories, Jodrell Bank, Macclesfield, Cheshire SKI1 9DL, UK** and *Radio Astronomy Centre, Tata Institute of Fundamental Research, Post Box 1234, Bangalore 560012*

P. Shastri *Radio Astronomy Centre, Tata Institute of Fundamental Research, Post Box 1234, Bangalore 560012*

L. Feretti, G. Giovannini, P. Parma *Istituto di Radioastronomia, Via Irnerio 46, I-40126, Bologna, Italy*

C. J. Salter *Institut de Radioastronomie Millimetrique, Avenida Divina Pastora 7, Nucleo Central, 18012 Granada, Spain*

Received 1985 November 21; accepted 1986 March 18

Abstract. We present VLA A-array observations at λ20, 6 and 2 cm and B-array observations at λ20 and 6 cm of the quasar B2 1320 + 299, which has a very unusual radio structure. In addition to a component, A, coincident with the quasar, there are two lobes of radio emission, B and C, on the same side of A. These are located at distances of $\simeq$ 25 and 50 arcsec respectively from A. The present observations show that A has a flat-spectrum component coincident with the quasar and a weak outer component at a distance of $\simeq$4 arcsec along PA $\simeq$ 100°. The morphology of B resembles a head-tail type of structure with its tail towards the north-east. The magnetic field lines in component B appear to follow the bend in the tail. Component C exhibits some extension towards the north-west. We discuss the possible nature of B2 1320 + 299 and suggest that while A appears to be an independent source, the relation between B and C, if they are associated at all, is unclear. Deep optical observations are essential to help clarify the situation.

Key words: extragalactic radio sources—quasars, radio structure—quasars, linear polarization

1. Introduction

The radio source B21320 + 299 (4C 29.48) is associated with a 20th magnitude quasar and has an extremely peculiar radio structure. It consists of two lobes of radio emission, B and C, located on the same side of the component, A, which is coincident with the

* Present address

quasar. B and C are at distances of $\simeq$ 25 and 50 arcsec respectively from A. This source was originally mapped by Fanti *et al.* (1977) and Fanti *et al.* (1979) with the Westerbork Synthesis Radio Telescope (WSRT) at λ6 and 21 cm as part of a programme to make 'short cuts' observations of B2 radio sources identified with quasars. Because of its unusual radio structure, Feretti, Giovannini & Parma (1982) observed this source for 12 hours with the WSRT at λ6 cm, and presented both total-intensity and linear polarization maps at this frequency. They also made linear polarization maps at λ21 cm using the earlier data. Saikia *et al.* observed this source with the VLA C-array at λ6 and 2 cm as part of a project to check the morphological classification of suspected one-sided radio sources, and make a systematic study of their properties. These observations have been described in Paper I of this series (Saikia *et al.* 1984).

Here we present VLA A-array observations at λ20, 6 and 2 cm, VLA B-array observations at λ20 and 6 cm, and discuss the possible nature of this source.

2. Observations and analyses

The A-array observations were made on 25 November 1983 at 1465 (20 cm), 4885 (6 cm) and 14965 (2 cm) MHz, all with a bandwidth of 50 MHz. The source was observed in one scan for $\simeq$ 5 to 10 minutes at each frequency. The B-array observations were made on 12 September 1982 at 1465 and 4885 MHz, for $\simeq$ 30 minutes at each frequency. The bandwidth used was 50 MHz. The primary flux-density and polarization calibrator for all the observations was 3C 286. The flux densities are on the BGPW scale (Baars *et al.* 1977). The data were edited and calibrated via standard computer programmes available at the VLA. All maps presented here have been made from self-calibrated data bases (Schwab 1980), The λ2 cm map has been made from a self-calibrated data base assuming an initial point source model. The observational parameters for the different scans are summarized in Table 1.

3. Results

In Figs 1 and 2 we show the λ20 cm maps of 1320 + 299 made from the B- and A-array data respectively, while in Fig. 3 we present the λ6 cm B-array map. The three components which we label A, B and C appear well separated in all the maps with no bridge or jet connecting any of them. In the A-array observations at the higher frequencies; we detect all the components A, B and C at λ6 cm but only A at λ2 cm. These maps are presented in Figs 4 and 5 respectively. In all figures, the linear polarization is shown by line segments superposed on the total intensity contours. The flux density and polarization properties of the three components are summarized in Table 2 which is self explanatory. The peak flux density of component A at λ2 cm is expected to be $\simeq$ 20 per cent low due to bandwidth smearing. Polarized flux density has been detected in all the three components, in agreement with previous results. It should be noted that the percentage polarization on the maps could depend considerably on the array used even at the same frequency since the components are not point sources and resolution and *uv* coverage vary with the array configuration.

Component A which appears associated with the quasar exhibits a one-sided radio morphology. It consists of a prominent radio core with a weak outer component at a

Table 1. The observational parameters.

Frequency (MHz)	1465	1465	4885	4885	14965
Array configuration	B	A	B	A	A
Bandwidth (MHz)	50	50	50	50	50
Pointing RA (1950)	$13^h\ 20^m\ 40^s.5$	$13^h\ 20^m\ 42^s.17$	$13^h\ 20^m\ 40^s.5$	$13^h\ 20^m\ 42^s.17$	$13^h\ 20^m\ 42^s.17$
Dec (1950)	29° 57′ 23″.0	29° 57′ 12″.0	29° 57′ 23″.0	29° 57′ 12″.0	29° 57′ 12″.0
Synthesized beam					
$\theta_1 \times \theta_2$ ($arcsec^2$)	3.31 × 2.95	1.24 × 1.22	1.20 × 1.15	0.37 × 0.36	0.12 × 0.11
PA (deg)	9	42	129	35	34
rms noise (mJy/beam)	0.30	0.27	0.22	0.25	0.39

Table 2. Flux density and polarization of the individual components.

		λ20 cm		λ6 cm		λ2 cm
	Comp	B-array	A-array	B-array	A-array	A-array
S_{peak}, S_{total}	A	379,427	330,385	260,270	210,260	140,160
(mJy/beam) (mJy)	B	511,669	330,645	120,229	75,250	
	C	213,247	140,225	49,73	24,80	
Polarization*, PA	A	2.6,138	5.0,130	4.1,120	5.5,132	5.5,125
(per cent) (deg)	Bw	1.5,167	~ 1,141	12.5,111	18.5,105	
	Be	3.5,61	~ 10 – 15, ~ 70	6.2,20		
	C	9.5,21	9.5,21	9.5,8	9.5,4	

* The quoted A-array values of percentage polarization represent the values at the peak of total intensity. The B-array values of percentage polarization are derived from values of the Stokes parameters Q and U integrated over the relevant component.

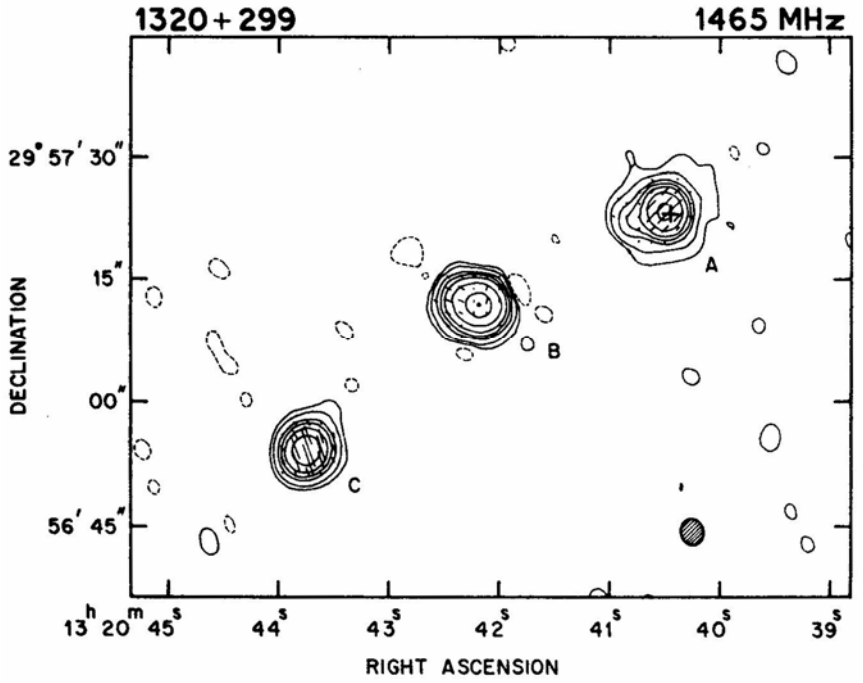

Figure 1. The B-array λ20 cm map of 1320 + 299. Beam: 3.31 × 2.95 arcsec^2 along PA 9° .Peak brightness: 511mJy/beam. Contour levels: –1, 1, 3, 10, 20, 40, 100, 300, 500 mJy/beam. Polarization: 1 arcsec = 4.5 mJy/beam. In Figs 1 to 5 the position of the optical quasar is marked by a cross while the beam is shown by a hatched ellipse. The polarization is shown by line segments superposed on the total-intensity contours.

distance $\simeq$ 4 arcsec along PA $\simeq$ 100°. These are connected by a jet-like extension. Using the peak flux densities of the λ6 cm B-array and λ20 cm A-array maps, we find a spectral index for the core of $\alpha_c \simeq 0.2$ ($S \propto \nu^{-\alpha}$). The spectral index between λ6 and 2 cm, using the A-array data is also $\simeq$ 0.2. The integrated λ2 cm flux density has been used to eliminate the effects of bandwidth smearing.

From the A-array data, component A appears to be $\simeq$ 5 per cent polarized at λ20,6 and 2 cm. Clearly there is very little depolarization. The rotation measure estimated from the similar resolution B-array λ6 cm and A-array λ20 cm data is also low, the value being $\simeq$ 5 rad m^{-2}. The *E*-vector at λ6 cm (A-array) is inclined at an angle of 30° to the jet like extension. Using VLA A-array data for a large sample of sources, Saikia & Shastri (1984) have shown that for the one-sided, core-dominated sources, there is no relation between the relative orientation of the core polarization *E*-vector at λ6 cm and the radio axis, while for the classical weak cored double-lobed sources the E-vector tends to be perpendicular to the structural elongation. Assuming that the *E*-vector is tracing the direction of the nuclear jet, the large observed misalignments in the core-dominated sources is perhaps due to amplification of small intrinsic misalignments between the nuclear and larger scale structure by projection effects.

Component B has an extremely interesting asymmetric structure which is well seen in Fig. 4b. There is a high brightness head and a tail which bends towards the north-east and extends up to a distance of $\simeq$ 3 arcsec from the peak. The magnetic field orientation

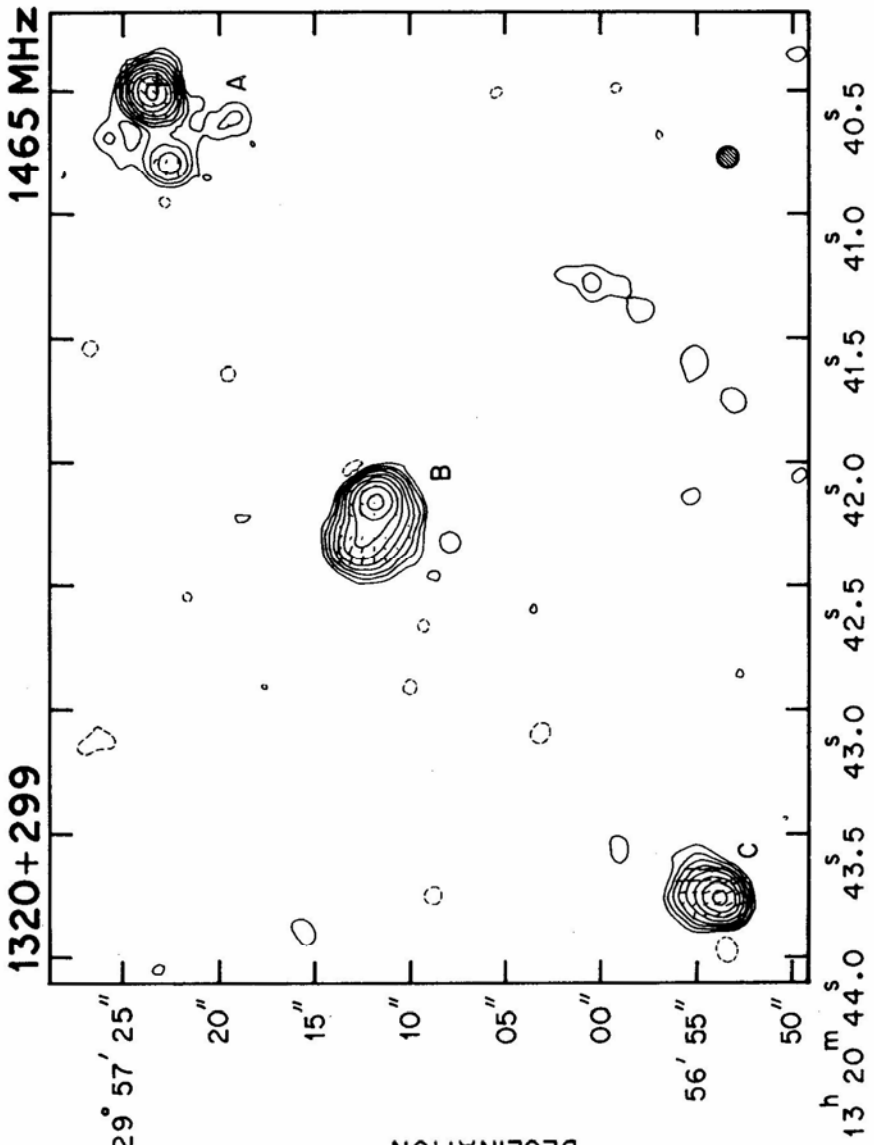

Figure 2. The A-array λ20 cm map of 1320 + 299. Beam: 1.24 × 1.22 arcsec^2 along PA 42°. Peak brightness: 329 mJy/beam. Contour levels: −4, −2, −1, 1, 2, 4, 8, 16, 32, 64, 128, 256 mJy/beam. Polarization: 1 arcsec = 26 per cent.

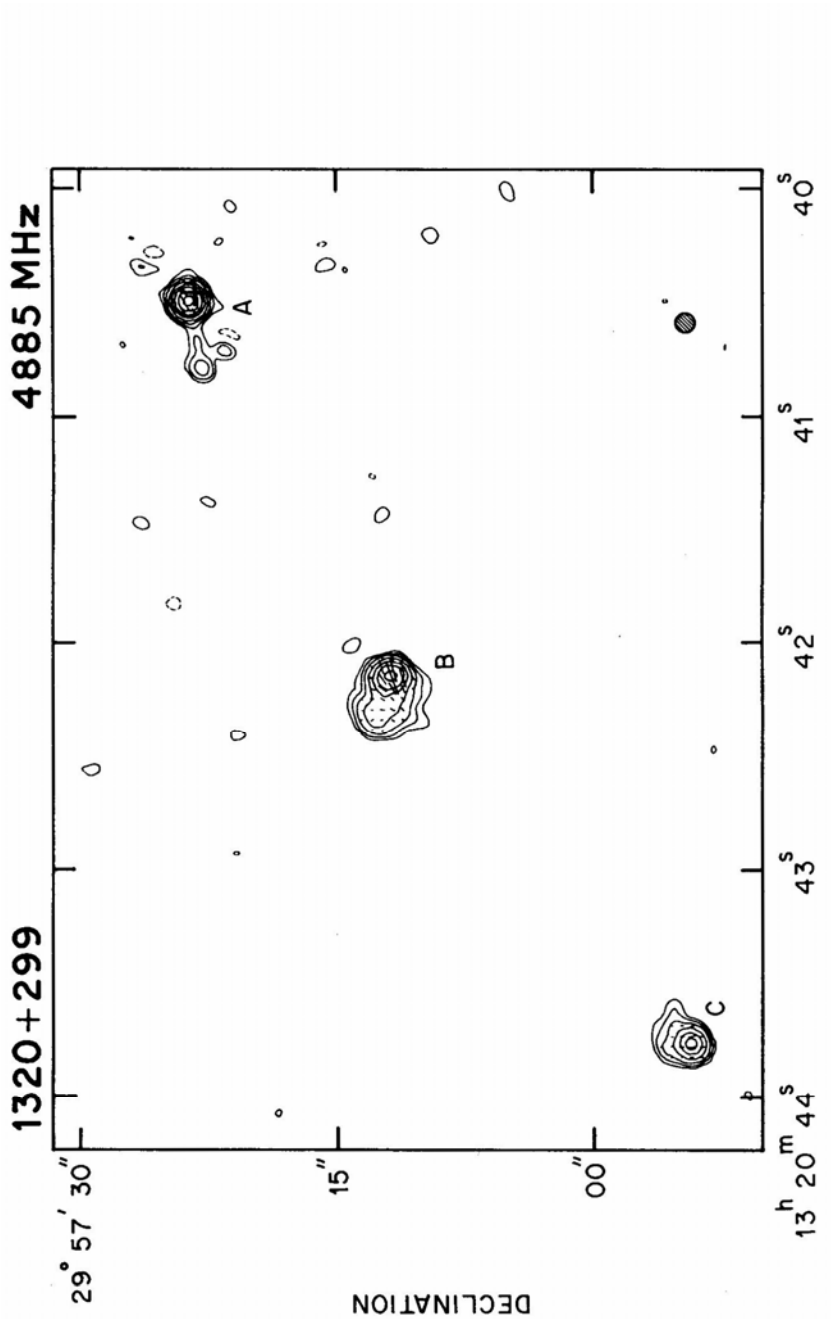

Figure 3. The B-array λ6 cm map. Beam: 1.20 × 1.15 arcsec^2 along PA 129°. Peak brightness: 251 mJy/beam. Contour levels: −0.7, 0.7, 1.4, 3, 8, 20, 40, 100, 200 mJy/beam. Polarization: 1 arcsec = 9.1 mJy/beam.

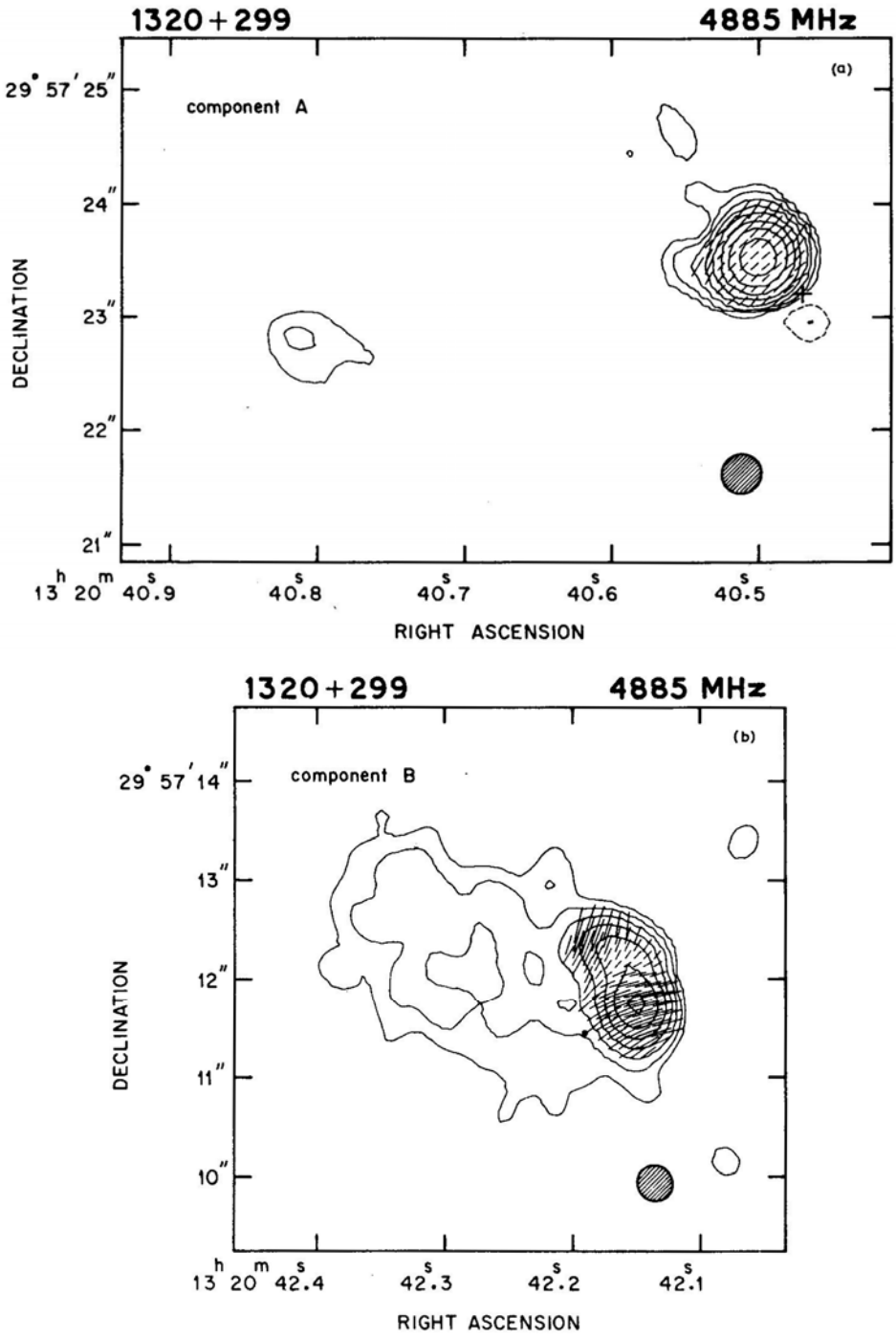

Figure 4. (a) The A-array λ6 cm map of component A. Peak brightness: 210 mJy/beam. Contour levels: –4, –2, –1, 1, 2 ,4, 8, 16, 32, 64, 128 mJy/beam. Polarization: 1 arcsec = 61 per cent. Beam: 0.37 × 0.36 arcsec^2 along PA 35° in Figs 4a, b and c. (b) The λ6 cm A-array map component B. Peak brightness: 75 mJy/beam. Contour levels, –4 , –2 , –1, 1, 2, 4, 8, 16, 32, 64 mJy/beam. Polarization: 1 arcsec = 61 per cent.

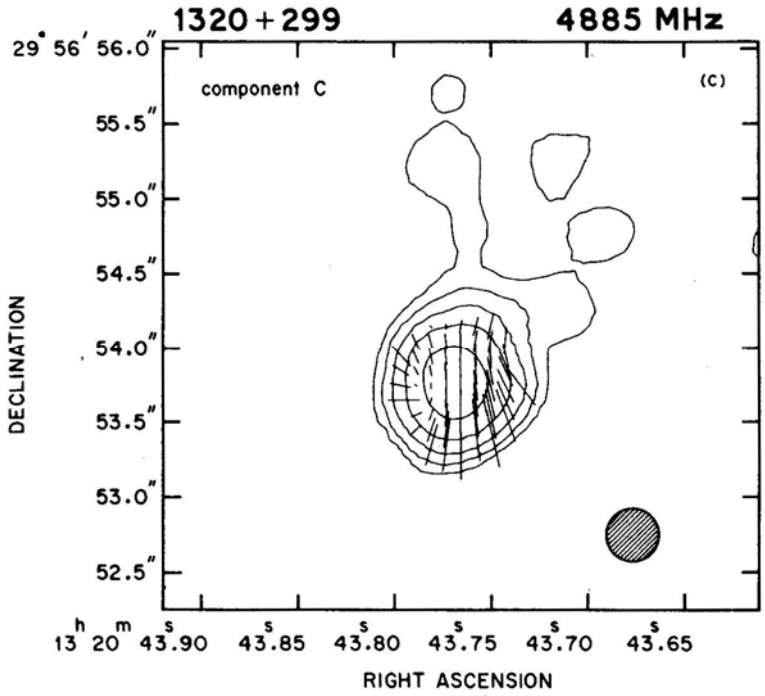

Figure 4. (c) The λ6 cm A-array map of component C. Peak brightness: 24 mJy/beam. Contour levels: –4, –2, – 1, 1, 2, 4, 8, 16 mJy/beam. Polarization: 1 arcsec = 61 per cent.

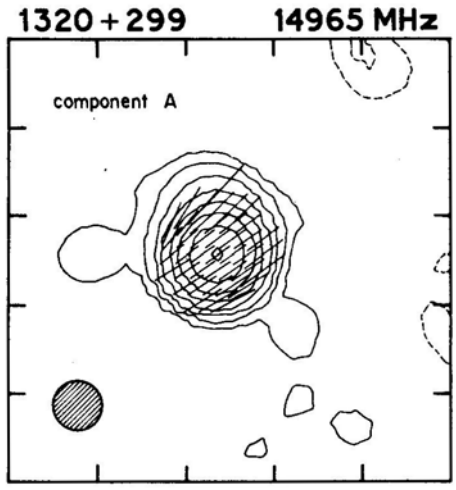

Figure 5, The λ2 cm A-array map of component A. Beam: 0.12 × 0.11 arcsec^2 along PA 34°. Peak brightness: 140 mJy/beam. Contour levels: –4, –2, –1, 1, 2, 4, 8, 16, 32, 64, 128 mJy/beam. Polarization: 1 arcsec = 80 per cent. The tick marks are 0.2 arcsec apart.

inferred from the λ6 cm data appears to follow the bend, changing by $\simeq 90°$ from west to east. The polarization parameters for the western (Bw) and eastern (Be) parts of B, *i.e* the head and tail respectively, are listed separately in Table 2. The degree of polarization at the pixel of maximum brightness at λ6 cm (A-array) is $\simeq$ 19 per cent along PA $\simeq 105°$. This value is quite high for a core: the median values of percentage polarization at $\simeq \lambda$6 cm for cores in galaxies and quasars observed with the VLA A-array are $\simeq$ 0.5 and 2 respectively (Saikia, Swarup & Kodali 1985). If the source is really a head-tail type of source, the high brightness strongly polarized feature could indicate that the core has not been adequately resolved in the λ6 cm map, and the structure of the head is more complicated.

The rotation measure for the western and eastern parts of B using again the similar resolution B-array λ6 cm and A-array λ20 cm data is $\simeq$ 15 and 25 rad m^{-2} respectively. The peak in the brightness distribution of B appears strongly polarized at λ6 cm, but depolarizes considerably at λ20 cm. The high degree of polarization seen at λ6 cm is consistent with the λ2 cm C-array observations of Saikia *et al.* (1984), who report a polarization of 16.9 per cent.

Component C shows a slightly extended feature along the NW direction, which is clearly visible in the maps made with a resolution of $\simeq$1.2 arcsec (A-array λ20 cm and B array λ6 cm). The extended feature is also seen in the A-array λ6 cm map. The degree of polarization at the pixel of maximum brightness is $\simeq$ 10 per cent at both λ6 and 20 cm indicating no significant depolarization. The rotation measure is $\simeq$ 5 rad m^{-2} using the λ 20 cm A-array and λ6 cm B-array data.

The spectra of components A, B and C are shown in Fig. 6. The integrated spectral index of the complete source is 0.64 ± 0.03 between $\simeq$ 80 MHz and 15 GHz, while the spectral indices of A, B and C are 0.42 ± 0.07, 1.12 ± 0.14 and 0.92 ± 0.02 respectively. While evaluating the spectral indices of the components, we have used the lowest resolution VLA maps at λ20, 6 and 2 cm. Component A, which is dominated by a compact core has a flat spectrum while B and C have steep spectra.

4. Discussion

The principal question regarding this source relates to an understanding of whether the three components A, B and C are physically related. Although the probability of three unrelated sources so aligned by chance is extremely low, there is no evidence from the radio data alone of any physical association. The probability of an unrelated source. with λ20 cm flux density between $\simeq$ 250 and 450 mJy lying within $\simeq$ 25 arcsec of component B is $\simeq 5 \times 10^{-5}$.

The radio morphology of component A, which is associated with the quasar, is quite similar to that of many core-dominated radio sources which have been mapped with high angular resolution at the VLA and MERLIN (Perley, Fomalont & Johnston 1982; Perley 1982; Browne *et al.* 1982). These sources are characterized by flat and complex spectra, variability of flux density and small angular size, with radio emission often being detected on only one side of the nucleus. Using the available data, it is difficult to establish convincingly that the radio core of component A is variable. However, we note that by comparing the images of the quasar in the PSS prints and in a plate taken by Braccesi in December 1967 with the Palomar Schmidt telescope, Feretti *et al.* (1982) have suggested that the quasar is optically variable.

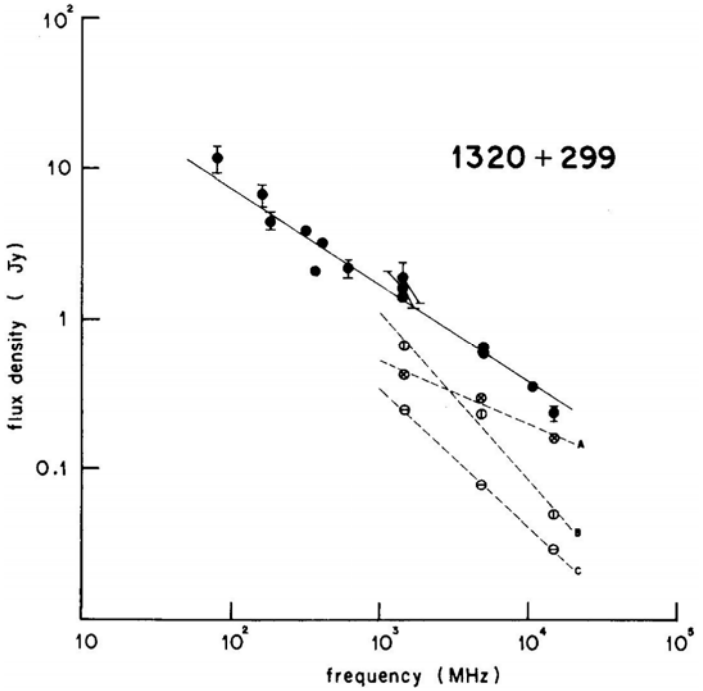

Figure 6. Spectra of the entire source and of the components A, B and C. The flux densities are on the BGPW scale (Baars *et al.* 1977). The different flux densities are represented as follows: ●: entire source,. ⊗ : component A, ⊕ : component B and ⊖: component C. Flux densities for the individual components are taken from the present data or Saikia *et al.* (1984).

Further, assuming that the redshift is $\lesssim 2$, the total linear extent of A is $\lesssim 30$ kpc in an Einstein–de-Sitter universe with $H_0 = 50$ km s^{-1} Mpc^{-1}. This is similar to the sizes of other sources in this category, and also consistent with the possibility that they are perhaps inclined at small angles to the line of sight (*cf.* Kapahi 1981; Saikia 1985 and references therein).

The radio morphology of component B is reminiscent of a head-tail source, but it could perhaps also be one of the outer components of a double-lobed source. There is no optical object visible on the PSS prints at the position of B, indicating that if B is indeed identified with a galaxy its redshift should be $\gtrsim 0.3$. Its radio luminosity at 1.4 GHz would then be $\gtrsim 2 \times 10^{25}$ W Hz^{-1} sr^{-1}, making it an extremely luminous head-tail source (*cf* O'Dea & Owen 1985). In this picture, an unresolved radio core may not have been detected in the head due to the presence of the high-brightness highly polarized feature in its vicinity.

One has now to understand whether C is an independent source or related to either A or B? Its appearance is somewhat similar to that of an edge-brightened hot-spot, and its small tail is approximately in the north-west direction. Association with A is extremely unlikely since A can be very well classified as an independent source and there is no suggestion of any physical relation. Also, its angular size, and hence the inferred linear size, would be much too large for one-sided radio sources. If B is a separate head-tail source, then A, B and C are independent sources. An exciting explanation of their mutual proximity could be that B and C are identified with faint galaxies belonging to a

very distant cluster beyond the limit of the PSS prints containing the quasar A. Another possibility is that B and C are the outer components of a double-lobed radio source whose optical identification is beyond the PSS limit. Deep optical observations should help distinguish between the different possibilities.

Acknowledgements

We thank the staff of the National Radio Astronomy Observatory for help during the observations and S. Krishnamohan for his comments on the manuscript. One of us (DJS) thanks IAU Commission 38 for travel support. The National Radio Astronomy Observatory is operated by Associated Universities Inc. under contract with the National Science Foundation.

References

Baars, J. W. M., Genzel, R., Pauliny-Toth, I. I. K., Witzel, A. 1977, *Astr. Astrophys.,* **61**, 99.

Browne, I. W. A., Orr, M. J. L., Davis, R. J., Foley, A., Muxlow, T. W. B., Thomasson, P. 1982, *Mon. Not. R. astr. Soc,* **198**, 673

Fanti, C, Fanti, R., Formiggini, L., Lari, C., Padrielli, L. 1977, *Astr. Astrophys. Suppl. Ser.,* **28**, 351.

Fanti, R., Feretti, L., Giovannini, G., Padrielli, L. 1979, *Astr. Astrophys. Suppl. Ser.,* **35**, 169.

Feretti, L., Giovannini, G., Parma, P. 1982, *Astr. Astrophys.,* **115**, 423.

Kapahi, V. K. 1981, *J. Astrophys. Astr.,* **2**, 43.

O'Dea, C P., Owen, F. N. 1985, *Astr. J.,* **90**, 954.

Perley, R. A. 1982, *Astr. J.,* **87**, 859.

Perley, R. A., Fomalont, E. B., Johnston, K. J. 1982, *Astrophys. J.,* **255**, L93.

Saikia, D. J. 1985, in *Extragalactic Energetic Sources,* Ed. V. K. Kapahi, Indian Academy of Sciences, Bangalore, p. 105.

Saikia, D. J., Shastri, P. 1984, *Mon. Not. R. astr. Soc,* **211**, 47.

Saikia, D. J. ,Shastri, P., Sinha, R. P., Kapahi, V. K., Swarup, G. 1984, *J. Astrophys. Astr.,* **5**, 429 (Paper I),

Saikia, D. J., Swarup, G., Kodali, P. D. 1985, *Mon. Not. R. astr. Soc,* **216**, 385.

Schwab, F. R. 1980, in *Proc. Int. Optical Computing Conf.,* Ed. W. T. Rhodes: *Proc. Soc. Photo-opt. Instrum. Eng.,* **231**, 18.

J. Astrophys. Astr. (1986) **7,** 131–139

On the Origin of the Galactic Ridge Recombination Lines

K. R. Anantharamaiah* *Raman Research Institute, Bangalore 560080*

Received 1986 February 14; accepted 1986 May 13

Abstract. Radio recombination lines are known to be observable at positions along the galactic ridge which are free of discrete continuum sources. Based on the results of a recent survey of H272α lines it is shown that most of the observed galactic ridge recombination lines can be explained as emission from outer low-density envelopes of normal HII regions. The distribution of low-density ionized gas and discrete HII regions as a function of the distance from the galactic centre is also derived.

Key words: Galaxy, recombination lines—galactic ridge— HII regions,low-density envelopes, distribution

1. Introduction

More than 15 years ago Gottesman & Gordon (1970) detected radio recombination lines of hydrogen from positions in the galactic plane which are free of discrete continuum sources. Since then a number of observations of similar lines have been made mainly at centimetre wavelengths (Jackson & Kerr 1971; Gordon & Cato 1972; Matthews, Pedlar & Davies 1973; Jackson & Kerr 1975; Mebold *et al.* 1976; Lockman 1976; Hart & Pedlar 1976b). There has been considerable debate in the literature about the origin of these galactic ridge recombination lines (GRRL). Initially it was argued that these lines arise in the partially ionized hot and/or cold component of the general interstellar medium itself (Gordon & Gottesman 1971; Cesarsky & Cesarsky 1971; Lockman & Gordon 1973). This interpretation, although attractive, could not explain many of the observed properties of GRRLs, for example their absence at longitudes $l > 40°$ and the correlation between line and continuum intensities. In addition such models required high interstellar ionization which conflicts with the average interstellar electron densities derived from pulsar dispersion measures.

Subsequent interpretations have all been in terms of hot ionized gas (Matthews, Pedlar & Davies 1973; Jackson & Kerr 1975; Hart & Pedlar 1976a; Shaver 1976; Lockman 1980) presumed to be in weak or evolved HII regions or the outer envelopes of normal HII regions. As most of the observations were made at high frequencies (> 1 GHz) the main difficulty so far has been in separating the contribution to the GRRLs from the normal HII regions themselves. In this context, normal HII regions are those which can be identified as discrete sources in continuum surveys of the galactic plane (for example the 5 GHz survey of Altenhoff *et al.* 1978).

* Present address: National Radio Astronomy Observatory, VLA, P O Box 0, Socorro, NM 87801, USA

2. Results from the 325 MHz Survey

We have earlier presented (Anantharamaiah 1985a–hereafter Paper I) the observational data obtained using the Ooty Radio Telescope, and a preliminary discussion of the 47 directions in the galactic plane towards which the H272α line was detected. These directions included 29 well known H II regions, 11 SNRs, the galactic centre and 6 blank regions which are devoid of any strong discrete sources within the beam used for the observations. In Anantharamaiah (1985b—hereafter Paper II) the properties of the ionized gas responsible for these lines were deduced by combining the data of Paper I with higher frequency measurements available in the literature. The main results of Papers I and II which are relevant for the present discussion are as follows. Some of the arguments are repeated here for continuity.

1. In the first quadrant of the Galaxy, for the longitude range $l < 40°$, the H272α line was detected towards every direction irrespective of whether it corresponded to an HII region, an SNR or a blank region (Paper I).

2. The line intensities are typically 0.1 per cent of the total continuum intensity and there is no marked difference in this between the directions of HII regions, SNRs and blank regions (Paper I).

3. The electron density of the ionized gas towards SNRs and blank regions is uniquely determined by combining the H272α line intensity with the measurements at higher frequencies (typically H 166α). The derived densities are in the range 0.5–6 cm^{-3} (Paper II).

4. The electron temperature and emission measure are deduced by considering high frequency continuum emission, the average interstellar electron density and the geometry of the line-emitting regions. The electron temperatures are in the range 3000–8000 K and emission measures 500–3000 pc cm^{-6}. The corresponding pathlengths are 50–200 pc (Paper II).

5. The lines observed towards SNRs and blank regions fall under the category of GRRLs. Therefore the above parameters represent the properties of the gas responsible for them.

6. The sizes of these regions are very small compared to the total pathlength through the Galaxy (filling factor < 0.005). Therefore the GRRLs cannot be considered as coming from a widely distributed component of the interstellar medium.

7. The normal HII regions studied in Papers I and II are too dense and/or too small to produce the H272α lines detected towards them because of pressure broadening, continuum optical depth and beam dilution. The lines must therefore arise in some other lower density gas present in the same direction. In other words, for the H272α lines the directions of normal HII regions are similar to those of SNRs and blank regions, in the sense that there are no known discrete continuum sources in any of these directions which can produce the observed H272α lines. Most of the observed H272α lines can therefore be identified with the GRRLs.

8. The observed velocity of the H272α line is generally in good agreement with that of the HII regions in the same direction (as determined from high frequency recombination lines like H110α). This agreement suggests a physical association between the lower-density gas seen in the H272α line and the dense HII region. The most reasonable picture is that the low density gas is in the form of an outer envelope of the normal HII regions. In other words HII regions have a core-halo structure.

9. The electron density and emission measure of the envelopes are deduced by using

the intensity of the H272α lines and the core-halo model. It is assumed that the haloes have similar temperatures as the cores. The derived densities of the envelopes are in the range 1–10 cm^{-3} and the linear sizes of 30–300 pc (Paper II).

We note from the above that the density, temperature and sizes of low-density envelopes of normal HII regions (as derived from H272α observations) are quite similar to the parameters we have deduced for the ionized gas which produces the GRRLs. It was necessary to postulate large low-density envelopes to explain the observed H272α lines at the same velocity as the normal HII regions in these directions. We wish to take this result one step further and suggest that a large part of the observed GRRLs arise in the outer envelopes of normal HII regions. In order to assess the plausibility of this hypothesis we should demonstrate;

(a) that the distribution of HII regions in the galactic disc is similar to that of the gas responsible for the GRRLs or in other words that of the gas seen in H272α

(b) that there is other observational evidence indicating large low-density envelopes to be associated with most of the normal HII regions.

(c) that there is a sufficiently large number of HII regions in the galactic plane (with $l < 40°$) to ensure that most of the lines of sight in this longitude range intersect at least one low density envelope.

3. The distribution of low-density ionized gas and HII regions

A longitude velocity (*l*-*v*) diagram is an indicator of the distribution of the gas in the galactic disc. As a sufficiently large number of H272α observations have been made (Paper I) over the longitude range $0° < l < 60°$, the *l*-*v* diagram can give a reasonable indication of the distribution of the gas. In Fig. 1 we have shown the velocity extent of the H272α line emission at different longitudes superposed on a *l*-*v* diagram for the H166α recombination lines observed by Lockman (1976). Some of the smoothness in the H166α distribution is (as noted by Lockman 1976) a result of the coarse sampling of the galactic plane in his observations. In Fig. 1 we have also marked with thick dots the location of normal HII regions observed in the H110α survey of Downes *et al.* (1980).

Most of the H110α sources are high-emission-measure (10^4–10^6 pc cm^{-6}), small-angular-diameter (few arcmin) objects and would be nearly optically thick at 325 MHz. They produce practically no detectable H272α line. On the other hand, they are easily detected in the H166α line observations such as those of Lockman (1976) and Hart & Pedlar (1976b). It is therefore remarkable that the *l*-*v* diagram for the observed H272α lines agrees so well with those for the H166α and H110α lines. This would indeed be the case if the H272α emission comes from low density gas associated with the normal HII regions, seen in the H110α surveys.

The *l*-*v* diagram of Fig. 1 is only a qualitative indicator of the gas distribution. This diagram, when combined with a model of the galactic rotation will give a quantitative picture of the distribution.

Consider an annular ring around the galactic centre extending from R to $R+\Delta R$, where R is the distance from the galactic centre. Let this ring be inside the solar circle. In any spectrum taken at a longitude $l < \sin^1 (R/R_0)$, the gas present in this ring will contribute over the velocity range V_1 to V_2. V_1 and V_2 are the radial velocities corresponding to the inner and outer edges of the ring along the line of sight and R_0 is the distance of the Sun from the galactic centre. The contribution will come, at the

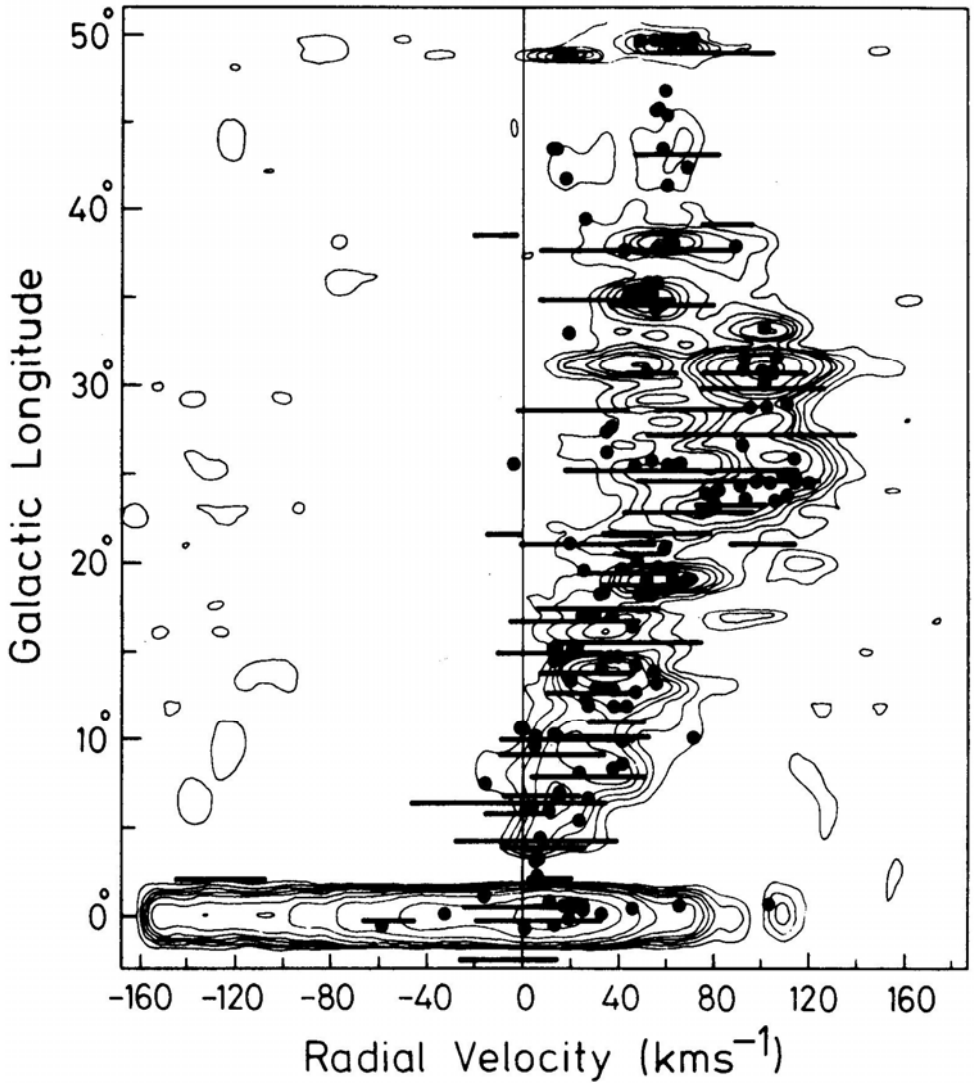

Figure 1. Longitude-velocity diagram of the recombination lines H272α (horizontal lines), H166α (contours) and H110α (dots). The horizontal lines indicate the observed half-power width of the H272α lines. The data for the three lines are taken from Paper I, Lockman (1976) and Downes *et al.* (1980) respectively.

same velocity, from the gas present at both the near and far distance of the ring from the Sun. The contribution to the power P in the observed line from the gas present in unit area of the ring is given by

$$P = \frac{\int_{V_1}^{V_2} T_L \, \mathrm{d}V}{(r_1 + r_2).\theta.\Delta r}. \qquad (1)$$

r_1 and r_2 are the near and far distances of the ring from the sun. The factor in the denominator is the area of the ring intercepted by the telescope beam of size θ parallel to the galactic plane (the size perpendicular to the galactic plane is large enough to include all the gas of interest). Δr is the extent of the ring along the line of sight and T_L is the observed line temperature. For lines of sight intersecting only the outer edges of the ring (*viz.* directions with $\sin^{-1}((R + \Delta R)/R_0) < l < \sin^{-1}(R/R_0)$), V_2 corresponds to the velocity of the tangent point. If the ring is outside the solar circle the area intercepted by the beam is $r.\theta\Delta r$, where r is the distance to the ring.

The average amount of gas present per unit area of the ring will be proportional to the quantity P. (Equation 1) averaged over all the spectra taken up to a maximum longitude of $\sin^{-1}((R + \Delta R)/R)$. This was computed as a function of the distance of the ring from the galactic centre using the data presented in Paper I. In Equation 1 we used $|\tau_L|(= T_L T_C)$ instead of T_L since the H272α lines are dominated by stimulated emission (Paper I). The velocities and distances were calculated using the Schmidt model of galactic rotation. We used the analytical approximation to the Schmidt rotation curve given by Burton (1971). For $R <$ 4kpc we used the rotation curve given by Simonson & Mader (1973). The result of the calculation is shown in Fig. 2 (continuous line).

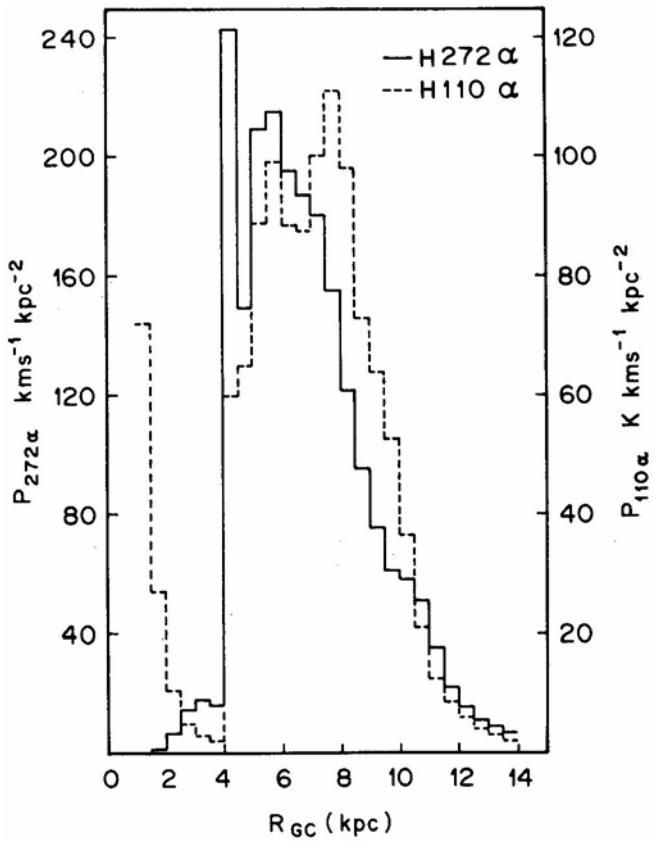

Figure 2. The distribution of low-density gas (seen in H272α) and discrete HII regions (seen in H110α) as a function of distance from the galactic centre. The data used are taken from Paper I (H272α) and Downes *et al.* (1980).

As seen in this figure, the distribution of the ionized regions responsible for the observed H272α lines is confined to galactocentric radii R < l0 kpc. The peak of the distribution occurs at $R \sim 6$ kpc and most of the gas is found between 4 kpc and 10 kpc. Inside of 4 kpc (where we have used the rotation curve of Simonson & Mader 1973), large noncircular velocities are known to be prevalent and therefore the implied distribution for this range is not reliable.

The actual distribution of the gas will in fact be narrower than suggested by Fig. 2. This is because in the above calculation we have implicitly attributed all of the observed velocity extent of the line emission to galactic rotation. The intrinsic width of the line arising from thermal motions and turbulence has not been taken into account. This will result in a smearing of the distribution.

We have also computed the distribution of normal HII regions, using the above method, from the observed line parameters in the H110α survey of Downes *et al.* (1980). This distribution is also shown in Fig. 2 (broken line).

It is clear from Fig. 2 that the sources of GRRLs and normal HII regions are distributed in a similar way in the galactic disc.

4. Sizes and number of HII regions, angular separations, scale height and galactic thermal background

The sizes derived for HII regions (Paper II) with their attendant low-density envelopes are in the range 50−300 pc. These are much larger than the sizes (1−10 pc) derived from radio continuum maps (*e.g.* Shaver & Goss 1970; Altenhoff *et al.* 1978). In the continuum, the essential contribution is from high density cores of the HII regions. The low-density envelopes are missed due to sensitivity and dynamic range limitations and also confusion with the galactic non-thermal background. All attempts to explain the observed line-to-continuum ratio as a function of frequency have always required that the HII regions have lower density gas associated with them (*e. g.* Brocklehurst & Seaton 1972; Parrish, Conklin & Pankonin 1977; Shaver 1980). Optical studies, although sensitive to low-density regions, suffer from obscuration by dust for distant objects in the galactic plane. Even so the optical data on nearby galactic HII regions (Georgelin 1971) show that more than 30 per cent of them have diameters greater than 50 pc. We also note here that the sizes of HII regions in external galaxies derived from optical studies are always greater than several tens of parsecs and extend all the way to several hundred parsecs (see for example, van den Bergh 1981; Kennicutt & Hodge 1980; Kennicutt 1984; Viallefond & Goss 1986). In fact a core-halo picture for extragalactic H II regions has been invoked by Sandage & Tammann (1974).

The total number of discrete sources in the 5 GHz survey of Altenhoff et al. (1978) over 40 square degrees of the galactic plane in the range $0° < l < 40°$ and $-0°.5 < b < +0°.5$ is . ~ 750. About 25 of these sources have been identified as galactic SNRs (see for example Green 1984). Further, from 5 GHz source counts (*e.g.* Ledden *et al.* 1980) we expect only about 25 extragalctic sources in this area with flux density > 0.1 Jy, which may have been detected in the above survey. Therefore this area of the galactic plane contains about 700 normal HII regions, strong and weak. The distances to identified HII regions range from 1 kpc to 17 kpc (see Downes *et al.* 1980). The number of HII regions at the far and near kinematic distances are about equal. Assuming an average distance of 9 kpc to these HII regions and an average size of 100 pc for their outer envelopes we

see that the latter have angular sizes of ~ 0°.6. An examination of the 5 GHz map of Altenhoff *et al.* (1978) reveals that the angular separation between prominant HII regions is on the average ~ 0°.5 up to a longitude of 40°. The separation between somewhat weaker HII regions which still appear as discrete sources at 5 GHz is much less (~ 0°.l). If, on the average, these HII regions have low-density envelopes of angular size 0°.2–0°.6 then practically every line of sight in this longitude range will intercept at least one such envelope.

Lockman (1979) has analysed the distribution of HII regions in the inner galaxy and concluded that they have a scale height ($z_{1/2}$) of 33 pc. If some of these HII regions have envelopes of 50–300 pc then the scale height of the low density gas will be a factor of 2–3 larger which is consistent with 70–80 pc scale height derived by Lockman (1976) and Hart & Pedlar (1976b) from the latitude extent of the H166α line emission.

An examination of the 5 GHz map of Altenhoff *et al.* (1978) shows that there is an extended background radiation in the galactic plane, over which the discrete sources are superposed. The outer contours of emission do not break all the way up to $l = 40°$. At this frequency more than 60 per cent of the background radiation is thermal in origin (Hirabayashi 1974). Most of this background emission must therefore be coming from the extended low-density envelopes of the HII regions which are numerous in this range. The background emission decreases and becomes more patchy and so does the number of HII regions for $l > 40°$. This again is consistent with the fact that GRRLs are seen only up to $l = 40°$.

In one attempt to resolve the question of the origin of GRRLs Mebold *et al.* (1976) observed a recombination line, using high angular resolution, at a position devoid of discrete continuum sources. They consider this line as a good candidate for emission from a partially ionized medium. They however note that an interpretation can also be given in terms of a low density extended HII region. An examination of their spectra clearly shows that the extent and velocity of this line is in good agreement with those from discrete HII regions which are within 0°.2–0°.6 of this position. This line can therefore very well come from the outer low-density parts of the same HII regions.

All the observational evidence is therefore consistent with the hypothesis that the galactic ridge recombination lines arise in low-density extended envelopes of conventional HII regions. It is no longer necessary to invoke any distributed component of the interstellar medium to account for these lines.

5. Discussion

An origin for the galactic ridge recombination lines in outer parts of HII regions is not a new idea. Based on their H166α observations of the extended gas associated with the HII region W3, Hart & Pedlar (1976a) have in fact made such a suggestion. Lockman (1980) noted the correlation between his observed H166α spectra and the composite Hl10α spectra formed by adding the H110α profiles from the survey of Downes *et al.* (1980). He used this correlation to conclude that most of the H166α line emission comes from extended outer parts of normal HII regions whose dense cores are prominent in the radio continuum. This is identical to the conclusion we have drawn from the analysis of the H272α lines.

However, Lockman (1980) distinguished the H166α emission near $l = 36°$ as coming from a more broadly distributed medium that extends over a few hundred parsecs, has a

density of 1 cm^{-3} and a temperature of few thousand degrees. His estimated parameters for this region are not unique and in his analysis this gas can have higher densities and smaller pathlengths. An increase in density to a mere 3 cm^{-3} will make this gas similar to that responsible for the observed H272α lines in the direction of SNRs, blank regions and HII regions. In other words, this gas would have properties similar to the regions responsible for GRRLs (namely the outer envelopes of normal HII regions).

The parameters derived by Shaver (1976) for the regions responsible for the GRRLs (density 5–10 cm^{-3}, pathlength 20–150 pc and temperature 5000 K) are similar to the ones obtained in Paper II. He however concluded that these are weak HII regions. Our conclusion differs from that of Shaver, in that we attribute most of this gas to extended outer envelopes of normal HII regions. To explain the smooth distribution of the H166α line emission Shaver's picture would require a large number of such weak HII regions. If these are all distinct from conventional HII regions which are prominent in the radio continuum, then it would be difficult to explain the good agreement in the velocities of the H110α, H116α and H272α lines in the direction of normal HII regions. However, the possibility that *some* of the GRRLs come from unknown low-density HII regions (as suggested by Shaver 1976 and argued further in Shaver *et al.* 1982) is not excluded by the present analysis.

Although, as shown earlier, the low density envelopes of conventional HII regions will intersect practically every line of sight having $l < 40°$ there can very well be variations in density and emission measure from one line of sight to another. HII regions are rarely symmetric, uniform density objects. There will be a radial gradient as well as fluctuations in the density both in the core and in the outer envelope. As a result, one can expect variations in the line intensity even in adjacent directions as observed by Jackson & Kerr (1975) using a beam of 6 arcmin.

In conclusion we have been able to show that most and perhaps all of the galactic ridge recombination lines can arise in extended outer envelopes of conventional HII regions. The H272α observations used here have the unique advantage that they are almost completely insensitive to emission from normal HII regions because of pressure broadening, optical depth and beam dilution. These observations have sampled practically only that gas which is responsible for GRRLs.

Acknowledgements

I thank V. Radhakrishnan and Rajaram Nityananda for discussions and a critical reading of the manuscript and W. M. Goss and P. A. Shaver for critical comments. This paper is based on a part of the doctoral thesis submitted to the Bangalore University.

References

Altenhoff, W. J., Downes, D., Pauls, T., Schraml, J. 1978, *Astr. Astrophys. Suppl. Ser.,* **35**, 23.
Anantharamaiah, K. R. 1985a, *J. Astrophys. Astr., **6,*** 177 (Paper I).
Anantharamaiah, K. R. 1985b, *J. Astrophys. Astr.,* **6**, 203 (Paper II).
Brocklehurst, M., Seaton, M. J. 1972, *Mon. Not. R. astr. Soc,* **157**, 179.
Burton, W. B. 1971, *Astr. Astrophys.,* **10**,76.
Cesarsky, C. J., Cesarsky, D. A. 1971, *Astrophys, J.,* **169**, 293.

Downes, D., Wilson, T. L, Bieging, J., Wink, J. 1980, *Astr. Astrophys. Suppl. Ser.,* **40**, 379.
Georgelin,Y.P. 1971, *Astr, Astrophys.,* **11**, 414.
Gordon, M. A., Cato, T. 1972, *Astrophys. J.,* **176**, 587.
Gordon, M. A., Gottesman, S. T. 1971, *Astrophys. J.,* **168**, 361.
Gottesman, S. T., Gordon, M. A. 1970, *Astrophys. J.,* **162**, L93.
Green, D. A. 1984, *Mon. Not. R. astr. Soc,* **209**, 449.
Hart, L., Pedlar, A. 1976a, *Mon. Not. R. astr. Soc,* **176**, 135.
Hart, L., Pedlar, A. 1976b, *Mon. Not. R. astr. Soc,* **176**, 547.
Hirabayashi, H.1974, *Publ. astr. Soc. Japan,* **26**, 263.
Jackson, P. D., Kerr, F. J. 1971, *Astrophys. J.,* **168**, 29.
Jackson, P. D., Kerr, F. J. 1975, *Astrophys. J.,* **196**, 723.
Kennicutt, R. C, Hodge, P. W. 1980, *Astrophys. J.,* **241**, 573.
Kennicutt, R. C. 1984, *Astrophys. J.,* **287**, 116.
Ledden, J. E., Broderick, J. J., Condon, J. J., Brown, R. L. 1980, *Astr. J.,* **85**, 780.
Lockman, F. J., Gordon, M. A. 1973, *Astrophys. J.,* **182**, 25.
Lockman, F. J. 1976, *Astrophys. J.,* **209**, 429.
Lockman, F. J. 1979, *Astrophys. J.,* **232**, 761.
Lockman, F. J. 1980, in *Radio Recombination Lines,* Ed. P. A. Shaver, D. Reidel, Dordrecht, p. 185.
Matthews, H. E., Pedlar, A., Davies, R. D. 1973, *Mon. Not. R. astr. Soc,* **165**, 149.
Mebold, U., Altenhoff, W. J., Churchwell, E, Walmsley, C. M. 1976, *Astr. Astrophys.,* **53**, 175.
Parrish, A., Conklin, E. K., Pankonin, V. 1977, *Astr. Astrophys.,* **58**, 319.
Sandage, A. R., Tammann, G. A. 1974, *Astrophys. J.,* **156**, 269.
Schmidt, M. 1965, in *Stars and Stellar Systems,* Eds A. Blaauw & M. Schmidt, Univ. Chicago Press, **5**, 513.
Shaver, P. A., Goss, W. M. 1970, *Austr. J. Phys. Astrophys. Suppl.* No. 14, 133.
Shaver, P. A. 1976, *Astr. Astrophys.,* **49**, 1.
Shaver, P. A. 1980, *Astr. Astrophys.,* **90**, 34.
Shaver, P. A., McGee, R. X., Newton, L. M., Danks, A. C, Pottasch, S. R. 1982, *Mon. Not. R. astr. Soc,* **204**, 53.
Simonson, S. C, Mader, G. L. 1973, *Astr. Astrophys.,* **27**, 337.
van den Bergh, S. 1981, *Astr. J.,* **86**, 1464.
Viallefond, F., Goss, W. M. 1986, *Astr. Astrophys.,* **154**, 357.

J. Astrophys. Astr. (1986) **7,** 141–153

Ionized Gas towards Galactic Centre—Constraints from Low-Frequency Recombination Lines

K. R. Anantharamaiah*[*Raman Research Institute, Bangalore 560080*]

D. Bhattacharya [*Joint Astronomy Program, Department of Physics, Indian Institute of Science, Bangalore 560012*]

Received 1986 March 7; accepted 1986 April 24

Abstract. Observations of the H272α recombination line towards the galactic centre show features near V_{LSR}= 0, –50 and + 36 kms^{-1} . We have combined the parameters of these features with the available H166α measurements to obtain the properties of the ionized gas present along the line of sight and also in the '3 kpc arm'. For the line-of-sight ionized gas we get an electron density around 7 cm^{-3} and a pathlength through it ~ 10–60 pc. The emission measure and the electron temperature are in the range 500–2900 pc cm^{-6} and 2000–6000 K respectively. The ionized gas in the 3 kpc arm has an electron density of 30 cm^{-3} and extends over 9 pc along the line of sight if we assume an electron temperature of 10^4 K.

Using the available upper limit to the intensity of the H351α recombination line, we show that the distributed ionized gas responsible for the dispersion of pulsar signals should have a temperature > 4500 K and a minimum filling factor of 20 per cent. We also show that recombination lines from the 'warm ionized' gas proposed by McKee & Ostriker (1977) should be detectable in the frequency range 100–150 MHz towards the galactic centre with the sensitivity available at present.

Key words: galactic centre, recombination lines—Galaxy, 3 kpc arm-interstellar medium, distributed ionized gas

1. Introduction

Recombination lines in the direction of the galactic centre have been detected over a wide range of frequencies from 23 GHz (Rodriguez & Chaisson 1979) to 242 MHz (Casse & Shaver 1977). The high-frequency (> 5 GHz) lines are broad (width > 200 kms^{-1}) and dominated by emission from high-density gas close to the galactic centre. At lower frequencies a narrow (~30 km s^{-1}) line near 0 kms^{-1} is dominant and is believed to originate in low-density gas along the line of sight (Pedlar *et al.* 1978).

The low-frequency (< 500 MHz) lines are particularly interesting as they have provided direct evidence for stimulated emission of recombination lines (Pedlar *et al.* 1978). The presence of a strong background continuum source, a long pathlength with no effect of differential galactic rotation, and the dominance of stimulated emission of

* Present address: National Radio Astronomy Observatory, VLA, P. O. Box 0, Socorro, New Mexico 87801, USA

recombination lines from low-density gas makes this an ideal direction to investigate the properties of any distributed ionized gas in the interstellar medium.

In this paper we make use of the recent H272α observations (Anantharamaiah1985a, Paper I) together with the H166α observations of Kesteven & Pedlar (1977) to derive the properties of the ionized gas along the line of sight to the galactic centre and in the 3 kpc arm. Further, using the upper limit for the H351α line reported by Hart & Pedlar (1980), we obtain significant constraints on the properties of the distributed ionized gas in the ISM which is responsible for the dispersion of pulsar signals.

2. Observations

The H272α data used in this paper were obtained during the recent survey of recombination lines from the galactic plane at 325 MHz (Paper I) using the Ooty radio telescope (ORT). The strongest recombination line below 500 MHz yet known is towards the galactic centre. This direction was therefore frequently observed during the survey to monitor the functioning of the system. The observing procedure is described in Paper I. A total of 34.5 hours of data were accumulated at the H271α frequency (328.5958 MHz) using the 64-channel autocorrelator with a total bandwidth of 500 kHz. Independent 62.5 hours of data were accumulated at the H272α frequency (324.9915 MHz) after the autocorrelator was expanded to 128 channels. The two resulting spectra are shown in Fig. 1. Both these spectra were taken using the full ORT which has an angular resolution of 2° in RA and 5.6 sec δ arcmin in declination. A third spectrum was taken using a part of the ORT with an angular resolution of 2° ×1° . This spectrum which has an integration of 18.6 hours is shown in Fig. 1(d). For comparison we have included in Fig. 1 the H166α spectrum observed by Kesteven & Pedlar (1977).

It is clear from Figs 1 (b) and (c) that the spectrum taken with an angular resolution of 2° × 6.4 arcmin contains at least four components. They are near velocities of – 150, −50, 0 and +36 kms^{-1}. On the other hand, in the spectrum taken with 2° × 1° resolution (Fig. 1d), it is only the component near 0 km s^{-1} which stands out. The other components have weakened below detection limit due to beam dilution.

The parameters of the four components in Fig. 1(b) and one component in Fig. 1(d) obtained from a Gaussian fit are given in Table 1. From what is known about the direction of the galactic centre (*cf.* Radhakrishnan & Sarma 1980) the feature near 0 km s^{-1} is due to gas present anywhere along the line of sight. The – 50 km s^{-1} feature corresponds to the '3-kpc arm' and the +36 kms^{-1} feature to some gas which is present within 4 kpc from the galactic centre.

The –150 km s^{-1} feature agrees in frequency with the recombination line of carbon or heavier elements, arising anywhere along the line of sight. This feature has a peak T_L of ~0.4 that of the H272α 0 kms^{-1} component in the spectrum taken with 2° × 6.4 arcmin resolution. However at lower resolution (Fig. 1d) it is not detected, the 3σ upper limit being ~ $0.25T_{L,H272\alpha}$. This suggests that the angular extent of the region producing this feature must be much smaller than that which produces the H272α line.

3. Ionized gas along the line of sight

Properties of the ionized gas along the line of sight responsible for the low-frequency recombination line near 0 km s^{-1} have been discussed by Pedlar *et al.* (1978), Casse &

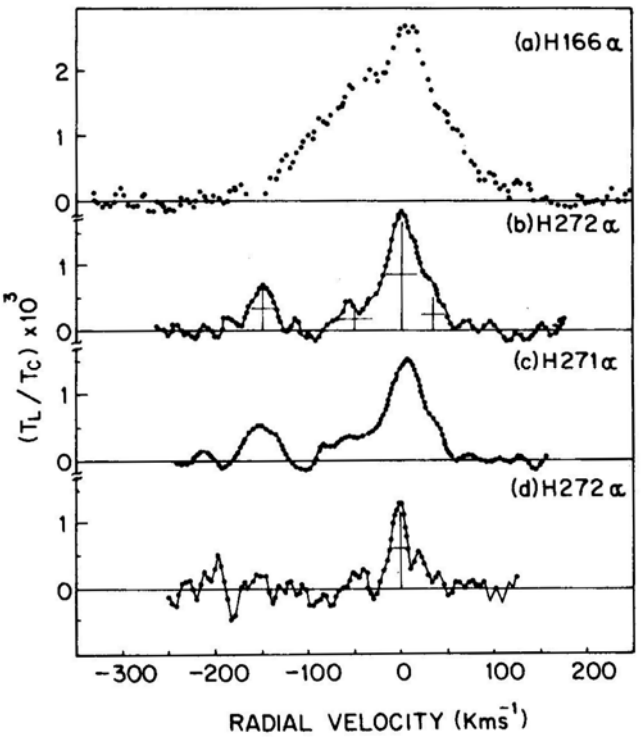

Figure 1. Recombination line spectra towards the galactic centre. The H166α spectrum is from Kesteven & Pedlar (1977). The spectra in (b) and (c) are obtained using the full Ooty radio telescope (ORT) which has an angular resolution of 2°× 6.4 arcmin. The H272α line observed using a part of the ORT (resolution 2° × 1°) is shown in (d). The crosses indicate the fitted gaussian components.

Shaver (1977) and Hart & Pedlar (1980). Although line emission near 0 kms^{-1} can accumulate over a long pathlength in this direction, it has been shown that the observed lines can be explained in terms of a single low-density, low-emission-measure, extended H II region (Pedlar *et al.* 1978) or two overlapping H II regions (Hart & Pedlar 1980) in the line of sight to the galactic centre.

Higher-frequency recombination lines at several positions around the galactic centre have been observed by Lockman & Gordon (1973), Pauls *et al.* (1976) and Kesteven &

Table 1. 272α line parameters.

Beam	Line	V_{LSR} km s^{-1}	ΔV km s^{-1}	$T_L/T_C \times 10^3$	$T_L^\dagger$(k)	$T_C^\dagger$(k)
2° × 6′.4	H272α	2.1 ± 0.5	37 ± 1	1.7 ± 0.05	4.0 ± 0.1	2330
		−49 ± 2	38 ± 5	0.4 ± 0.05	0.93 ± 0.12	
		36 ± 1	24 ± 3	0.5 ± 0.06	1.2 ± 0.1	
	C272α	−149.5 ± 1	26 ± 2	0.7 ± 0.06	1.6 ± 0.1	
2° × 1°	H272α	0.5 ± 1	15 ± 2	1.2 ± 0.1	...	...

† Beam averaged brightness temperature.
Errors quoted are 1σ values.

Pedlar (1977). As discussed by Anantharamaiah (1985b, Paper II) it is possible to derive the electron density in the gas irrespective of its temperature if both high-frequency (> 1 GHz) and low-frequency (< 500 MHz) recombination lines are observed from the same gas. This is because the intensity of recombination lines at high frequencies is dominated by spontaneous emission and at low frequencies by stimulated emission. As a result the two intensities have a very different dependence on the electron density.

The excess temperature produced at the frequency of the recombination line by a homogeneous ionized region located in front of a background continuum source is given by (Shaver 1975a)

$$T_L = T_0\left[e^{-\tau_C}\left(e^{-\tau_L}-1\right)\right] + T_e\left[\frac{b_m\tau_L^* + \tau_C}{\tau_L+\tau_C}\left(1-e^{-(\tau_L+\tau_C)}\right) - \left(1-e^{-\tau_C}\right)\right] + T_M\left[\frac{1-e^{-(\tau_L+\tau_C)}}{\tau_L+\tau_C} - \frac{1-e^{-\tau_C}}{\tau_C}\right] \quad (1)$$

where T_0 is the continuum temperature of the background source, T_e the electron temperature of the ionized region and T_M represents the nonthermal background distributed inside this region. τ_c and τ_L are the continuum and line optical depths respectively. τ_L^* is the line optical depth in LTE. The expressions for these are given in Oster (1961) and Shaver (1975a). The coefficients b_m giving the ratio of the true and LTE populations were calculated using the computer code published by Brocklehurst & Salem (1977). We have modified this code to incorporate the effect of the galactic nonthermal background on the level populations. A radiation temperature T_R = 400 K at 408 MHz and a spectral index α = – 0.7 (Intensity $\propto \nu^{\alpha}$) was used in the calculations.

The angular extent of the region which produces the emission near 0 kms^{-1} is estimated to be greater than 1° (Kesteven & Pedlar 1977) and may be as large as 2°.5 (Hart& Pedlar 1980).Therefore the H166α measurements of Kesteven & Pedlar (1977) (beam size 12 arcmin × 12 arcmin) do not suffer from beam dilution. On the other hand, the H272α measurements reported here are made with a 2°× 6.4 arcmin beam and therefore a dilution factor may have to be taken into account while using Equation (1).

The H166α line in the direction (l = 0, b = 0) can have a large contribution from stimulated emission due to the strong background source in that direction. In addition there will also be a contribution from higher-density gas present close to the galactic centre (Pauls *et al.* 1974). To minimize such complications we use the H166α measurement at (l = 0, b = +0.4) where the 1.4 GHz continuum temperature is a minimum (Kesteven & Pedlar 1977). Also there is no discrete source in this direction in the 5 GHz high-resolution map of Altenhoff *et al.* (1978), precluding the presence of a discrete dense HII region capable of making significant contribution to H166α emission. The H166α line parameters observed at this position are T_{Lmax} = 0.14 ± 0.04 K and T_C = 34 ± 5 K. The H272α parameters are given in Table 1.

The combination of emission measure and electron density required to produce the observed intensities of the H166α and the H272α lines (near 0 kms^{-1}) is shown in Fig. 2. These calculations were done using Equation (1). We assumed that the region extends l°.2 in RA based on the measurements of Kesteven & Pedlar (1977). This results in a beam dilution factor of 0.6 for the H272α line. A region with such large angular extent is most likely to be nearby and in front of the dominant source of continuum, namely the

Sagittarius A region. We therefore assumed all of the continuum radiation to originate behind the cloud. If we require that the H166α and the H272α lines arise in the same gas then the electron density in the gas is given by the intersection of the two sets of curves in Fig. 2. This gives a density of ~ 7 cm^{-3} and is practically independent of the electron temperature. If the region is larger than 2° in RA (no dilution for the H272α) then we get a density of 16 cm^{-3} which can be considered as an upper limit. Fig. 3 shows the relation between the temperature and emission measure (and therefore the pathlength) of this gas, taking the electron density to be 7 cm^{-3} . A lower limit to the pathlength through this gas can be set by considering the geometry of the region and an upper limit results from the average interstellar electron density obtained from pulsar dispersion measure (see Paper II). The angular extent of this region is at least 1°. Even if this gas is nearby, say at 2 kpc, its linear extent perpendicular to the line of sight is ~ 34 pc. Therefore to avoid peculiar geometry the line-of-sight extent of this gas is likely to be larger than, say, ~ 10 pc. This implies that EM > 500 pc cm^{-6} and T_e > 2000 K (Fig. 3). Vivekanand & Narayan (1982) have estimated the contribution to the line-of-sight

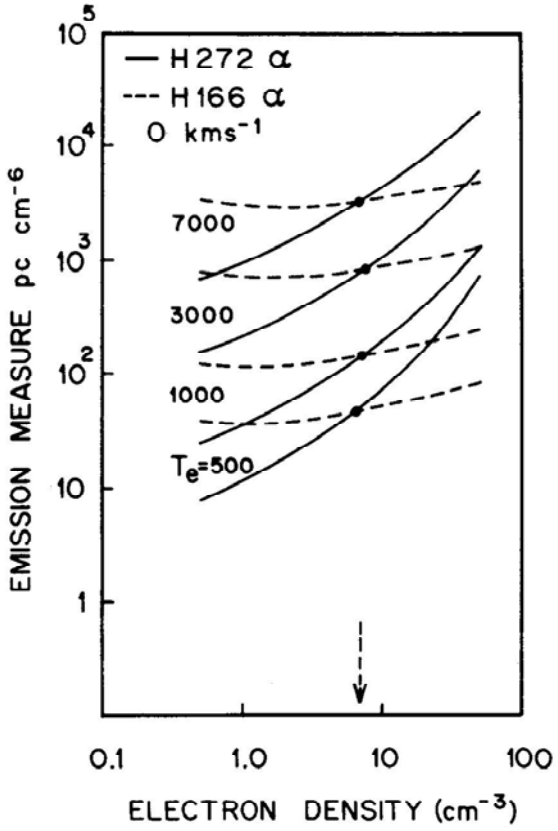

Figure 2 The relation between emission measure and electron density of the gas required to produce the observed intensity of the H16 (dashed line) and the H272α lines (full line) near 0 kms^{-1}. Curves are shown for different electron temperatures. If the two lines are produced in the same gas then the intersection points (dots) indicate the electron density, which is virtually independent of the temperature.

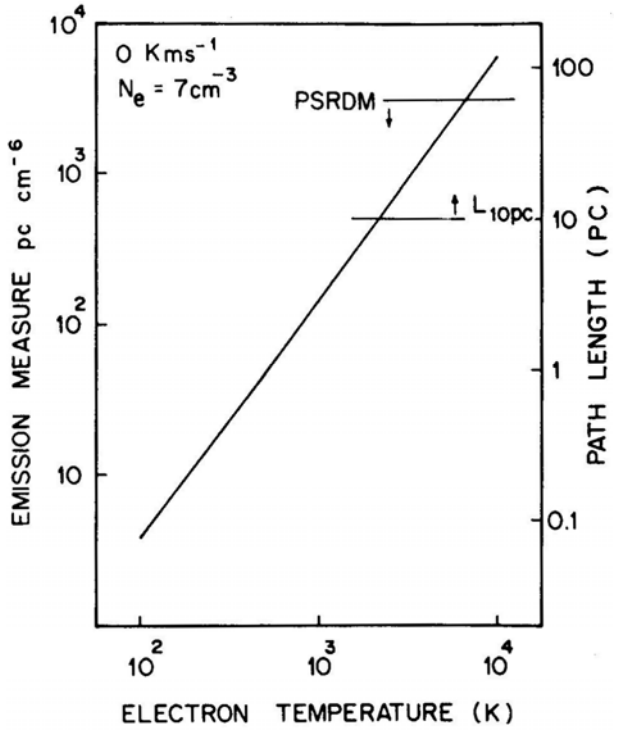

Figure 3. Constraints on the electron temperature, emission measure and pathlength through the ionized gas towards the galactic centre. Electron density derived from Fig. 2 has been used. The pathlength marked on the right follows directly from the emission measure and the electron density. The diagonal line represents the constraint based on the observed recombination lines (0 kms^{-1} components). Upper limit to the pathlength comes from consideration of the average interstellar electron density obtained from pulsar dispersion measure (PSRDM). Lower limit is obtained from the geometry of the line-emitting region (L_{10pc}). See text for arguments.

average electron densities from localized higher-density ionized regions (*e.g.* HII regions) to be $\leqslant 0.02$ cm^{-3} (see Paper II for a more detailed discussion). This would constrain the pathlength through this gas to less than ~ 60 pc, implying that EM $\leqslant 2900$ pc cm^{-6} and $T_e \leqslant 6000$ K (Fig. 3).

The properties deduced above for the line-of-sight ionized gas suggests that it may be a single large evolved HII region. Though more than one HII regions may be present along the line of sight, beam dilution will restrict the detection of line emission from the nearby ones. The parameters obtained in Paper II indicate that the low-density envelope of a single evolved HII region is quite adequate to explain the observed line strengths.

4. Ionized gas in the '3-kpc arm'

The feature near – 50 kms^{-1} in the H272α spectra (Fig. 1) can be attributed to ionized gas present in the so called '3-kpc arm' which is believed to be an expanding ring at a distance closer to 4 kpc from the galactic centre. The 3 kpc arm is a prominent feature in

both HI and CO emission from this region (see for example Cohen & Davies 1976; Bania 1980). It is also seen in HI absorption in the direction of the galactic centre (*e.g.* Schwarz, Ekers & Goss 1982).

Emission near – 50 km s^{-1} can be clearly seen in the H159α and the H166α spectra of Lockman & Gordon (1973) and Kesteven & Pedlar (1977) respectively. The H166α emission from the 3 kpc arm has been discussed by Lockman (1980).

The detection of the H272α line indicates that low-density ionized gas is present in the 3 kpc arm. As in the previous section we can determine the electron density of this gas by using both the H272α and the H166α measurements.

The measured H272α line parameters of the – 50 kms^{-1} component are given in Table 1. The angular size of the region producing this feature is about 30 arcmin from the high-resolution measurements of H166α line by Kesteven & Pedlar (1977). This corresponds to a beam dilution factor of 0.25 for the H272α line. It is interesting to note that if observations are made with higher angular resolution, the H272α line from the 3 kpc arm would be as strong as the feature near 0 km s^{-1}. We estimated the background temperature (in Equation 1) over the 30 arcmin × 6.4 arcmin of this region seen by the beam of the ORT by using (i) the measured beam brightness temperature at 325 MHz (Table 1), (ii) the 408 MHz map of the galactic centre region by Little (1974), and (iii) the 408 MHz all sky map of Haslam *et al.* (1982). We get T_0 = 5000 K. We used T_M = 0 since the maximum pathlength through this region is equal to the thickness of the 3 kpc arm (~ 700 pc, Simonson & Mader 1973).

We chose the H166α measurement at (l, b) = (0, + 0.2) instead of at (0, 0) for the reason discussed in the previous section. The measured parameters are T_L = 0.15 K and T_C = 90 K (Kesteven & Pedlar 1977).

With these parameters we get an electron density of 30 cm^{-3} using similar calculations as for Fig. 2. The relation between the electron temperature and emission measure (which also gives a pathlength since n_e is fixed) for the ionized gas in the 3 kpc arm is shown in Fig. 4.

As seen in this figure the pathlength through the gas is 9 pc for an electron temperature of 10^4 K. The thickness of the 3 kpc arm is ~ 700 pc (Simonson & Mader 1973). This gives a value of 0.01 for the filling factor along the line of sight for the ionized gas in this arm, suggesting that discrete HII regions can well account for all of this gas. The column density of electrons in the 3 kpc arm comes out to be 9.3 × 10^{19} cm^{-2}. The ratio of this to the column density of neutral hydrogen (estimated by Radhakrishnan & Sarma (1980): N(HI) = 1.2 × 10^{21} cm^{-2} for T_s = 100K) is 0.08.

5. The +36 $kins^{-1}$ feature

This feature is clearly seen in both the H272α and H271α spectra (Figs 1b, c). The presence of a positive velocity feature in the H252α spectrum towards the galactic centre has been noted by Pedlar *et al.* (1978). This feature is also seen in the H166α spectrum of Kesteven & Pedlar (1977).

The ionized gas responsible for this component must be lying inside of 4 kpc from the galactic centre where noncircular motions are known to be prevalent. We have not attempted to determine the electron density of this gas since its angular extent cannot be determined from existing observations. The observed width of the H272α line

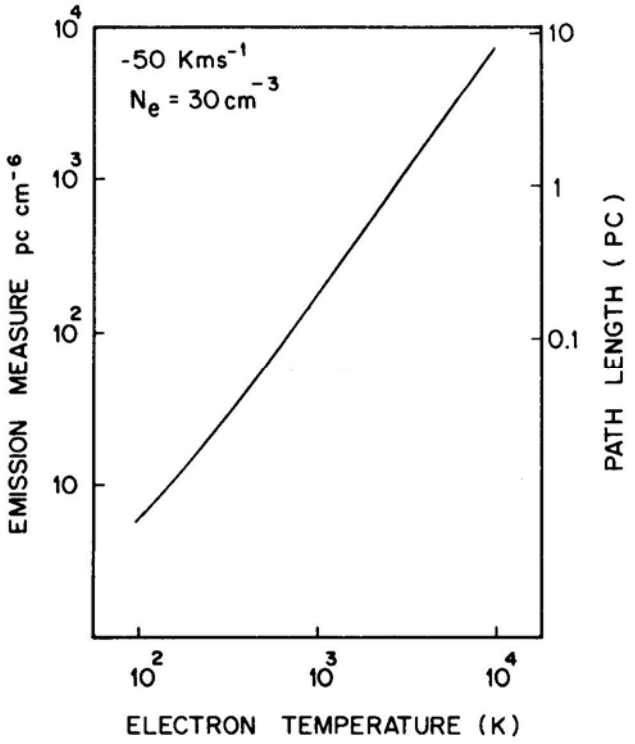

Figure 4. Constraints on the electron temperature, emission measure and pathlength through the ionized gas in the '3 kpc arm'. The electron density was obtained from calculations as in Fig. 2 based on the intensity of the H272α and the H166α lines near –50 kms $^{-1}$.

implies an upper limit to the electron density of 25 cm^{-3} from considerations of pressure broadening.

6. Constraints on the distributed ionized gas in the ISM

The sensitivity of low-frequency recombination lines to conditions in low-density ionized regions make these lines particularly suitable for the study of the distributed ionized component of the interstellar medium. Several attempts have so far been made in this direction (Shaver 1975b, 1976; Shaver, Pedlar & Davies 1976; Hart & Pedlar 1980). Existence of a distributed ionized component of the ISM has been inferred mainly from the dispersion measures of pulsars, which yield a line-of-sight average electron density $\langle n_e \rangle = 0.03$ cm^{-3} (Falgarone & Lequeux 1973; Gómez-Gonzáles & Guélin 1974; del Romero & Gómez-Gonzáles 1981; Harding & Harding 1982; Vivekanand & Narayan 1982 and many others). Other properties of this gas are rather difficult to determine and have remained uncertain to date. It was originally thought to be a uniformly distributed, partially ionized gas with filling factor close to unity (see for example Field, Goldsmith & Habing 1969). However, since then ultraviolet absorption lines of OVI have been seen in the ISM (Rogerson *et al.* 1973; Jenkins & Meloy 1974; York 1974), and the ubiquity of these lines suggest that a fair fraction of the galactic disc

must be filled with hot ($T \sim 10_6$ K), coronal gas of very low density ($n \sim 0.003$ cm^{-3}) (Spitzer 1956; see Jenkins 1984 for a recent review). It has therefore become necessary to modify the old picture of a uniform intercloud medium by introducing ionized clumps with higher density and smaller filling factor, so as to maintain the average electron density required to account for pulsar dispersion measures, as well as to accommodate the coronal gas. For example, in the model of Mckee & Ostriker (1977), this 'warm' gas has a local electron density $n_e = 0.17$ cm^{-3} and a filling factor $f_w = 0.23$. Nevertheless there is still a considerable controversy regarding these values (*e.g.* Heiles 1980; see Cowie & Songaila, 1986 for a recent review). As will be clear from the following discussion, low-frequency recombination lines are likely to provide a direct handle on the local densities and temperatures of this 'warm' ionized gas. In this section we shall attempt to obtain constraints on the parameters of this warm gas using the presently available upper limit on the H351α line emission from the direction of the galactic centre (Hart & Pedlar 1980).

The picture adopted for the line-of-sight gas towards the galactic centre is shown in Fig. 5. Clumps containing ionized gas at local density n_e contribute to the recombination-line emission. The total pathlength L in this direction is 20 kpc, of which only a fraction f_w is through the ionized region of interest. Here f_W is the filling factor defined by $f_w = \langle n_e \rangle / n_e$. The emission measure EM $= n_e^2 f_w L = n_e \langle n_e \rangle L$ Since the value of $\langle n_e \rangle$ is known from pulsar dispersion measure, the local density n_e directly determines the filling factor and the emission measure. This unique correspondence between n_e and EM allows one to obtain (using Equation 1) a relation between n_e and T_e given that this gas should produce the required line intensity. The appropriate values of T_0 and T_M are obtained as follows.

Let T_N be the contribution of the nonthermal galactic background to the total observed continuum temperature T_c. $T_{Sgr} = T_c - T_N$ can then be taken as the beam brightness temperature of the Sagittarius A region, assuming the continuum emission from other discrete sources in the line of sight to be negligible. The total amount of nonthermal background that originates within the clumps is simply $T_M = f_w T_N$. The rest of the nonthermal background originates outside the clumps contributing to the background temperature: $T_0 = T_{Sgr} + \frac{1}{2}(T_N - T_M)$. Since the stimulated emission due to T_0 is effective only over half the line of sight (due to the central location of Sgr A), we used half the total pathlength in the first term of Equation (1).

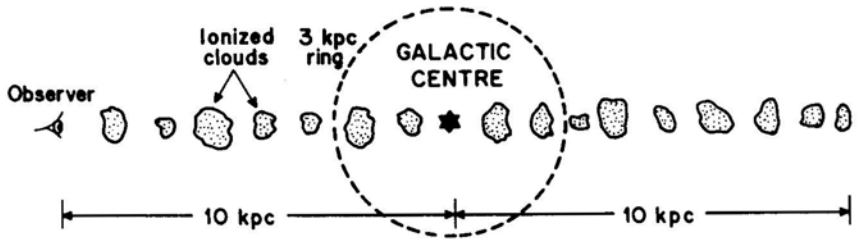

Figure 5. A schematic picture of the line of sight towards the galactic centre. The total pathlength through the galaxy is ~ 20 kpc. The distributed ionized component of the interstellar medium, which is responsible for dispersion of pulsar signals, resides in clumps represented as ionized clouds. The strong continuum source at the galactic centre causes stimulated emission of recombination lines from this gas over half the total pathlength through the Galaxy. The clumps inside the 3 kpc ring may have nonzero radial velocity due to noncircular motions.

From the 151 MHz observations reported by Hart & Pedlar (1980) we obtain T_C = (20800± 1600) K and $T_{L,351\alpha}$. < 8 K after correcting for beam efficiency factors. T_L = 8 K can then be used as an absolute upper limit to the contribution of the warm ionized gas to the H351α transition. The (n_e, T) combinations required to produce this line intensity are shown in Fig. 6 (curve b), where $\langle n_e \rangle$ = 0.03 cm^{-3} and L = 20 kpc was used. The fact that T_L = 8 K is an upper limit restricts the parameters of the gas to those above this line. The value of n_e for this gas, of course, cannot be less than 0.03 cm^{-3}, which corresponds to a filling factor f_w = 1.This sets a lower limit of 4500 K to the temperature T of this ionized component. An independent restriction on the parameters of this gas comes from the requirement of pressure equilibrium in the ISM. For an average ambient interstellar pressure P_0, the allowed values of n_e and T must be such that $n_eT \leqslant \frac{1}{2}P_0/k$, where k is Boltzmann's constant. The equality is reached only in the case of complete ionization. The implicit assumptions here are, of course, that the neutrals, ions and electrons have the same temperature and that most electrons are provided by singly ionized species. Both these assumptions seem reasonable under normal interstellar conditions. We adopt a value of P_0/k = 3200 cm^{-3} K, consistent with the value used by McKee & Ostriker (1977). The line corresponding to n_eT = 1600 cm^{-3} K is also shown in Fig. 6. The allowed region of the parameter space lies to the left of this line. The intersection of this line with curve (b) gives an upper limit to the electron density, and hence a lower limit to the filling factor of this gas: n_e < 0.2 cm^{-3}, f_W > 0.15. The filled circle in this diagram represents the parameters for the warm ionized medium (n_e = 0.17 cm^{-3}, T = 8000 K) chosen by McKee & Ostriker (1977). If the actual parameters are indeed close to this value then it is evident from the diagram that with slightly increased sensitivity one should be able to detect low-frequency recombination lines from this gas.

In the above discussion we have attributed the entire ~ 8 K line temperature to that arising from the distributed interstellar gas. However, as the analysis in Section 3 has shown, there is a relatively dense discrete ionized region in the above line of sight, which is also likely to contribute to the H351α emission. The electron density derived for this region is in the range 7–16 cm^{-3} , the higher values corresponding to smaller beam dilution for the H272α. If this region is indeed so large that the dilution in the 151 MHz beam (2°.5 × 2°.5) is small, then the corresponding high inferred densities (n^e ~ 16 cm^{-3}) will pressure broaden the H351α line to more than 80 kms^{-1} and any such contribution would have been removed in the process of baseline subtraction. On the other hand, at lower densities (n_e ~ 7 cm^{-3}) the region would produce a strong line but in this case the region will be of small angular size, and beam dilution will be appreciable. The maximum contribution to the H351α line from this dense gas is thus estimated to be ~ 3–5 K. If we attribute the remaining ~ 4 K to emission from the distributed component, then in Fig. 6 the lower boundary of the allowed region moves up somewhat, as shown by curve (d). This gives T > 6000 K, n_e < 0.16 cm^{-3}, f_w > 0.2. Interestingly, the warm ionized medium of McKee & Ostriker (1977) now falls outside the allowed region. It is clear that even a slight improvement in the H351α upper limit may require the parameters of the warm ionized medium to be modified; lower densities and correspondingly higher filling factor may be necessary.

Uncertainties in the above estimate are introduced by significant noncircular motion of gas within ~ 3 kpc of the galactic centre. This restricts the total pathlength over which line emission can accumulate at zero velocity. If we assume that this central region makes no contribution at all to the line emission, then L is reduced to 14 kpc,

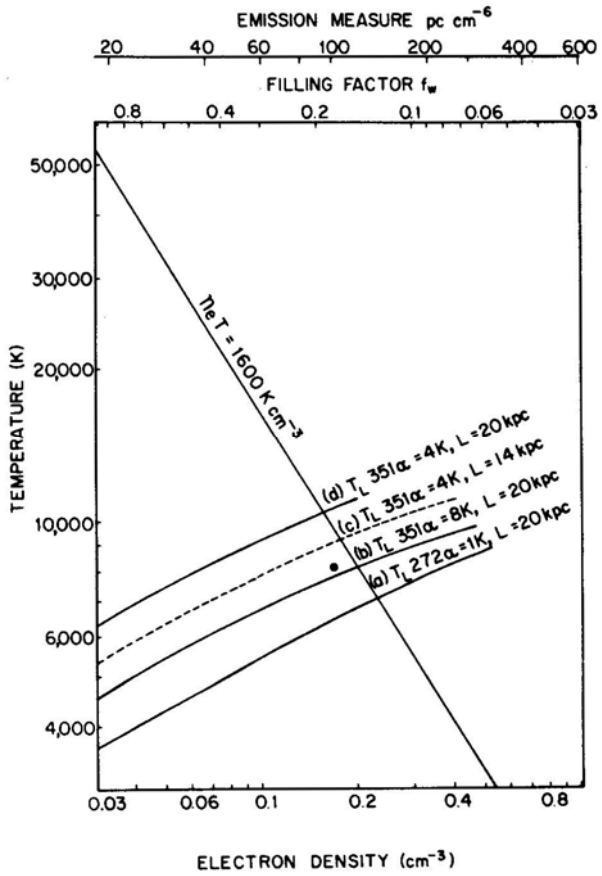

Figure 6. Constraints on the temperature (T), local electron density (n_e) and filling factor (f_w) of the distributed ionized gas which has an average electron density $\langle n_e \rangle$ = 0.03 cm^{-3}. The markings on the top are obtained using, $f_w = \langle n_e \rangle / n_e$ and EM = $n_e \langle n_e \rangle$ L, where L = 20 kpc. The constraints are obtained from pressure equilibrium in the ISM (the line marked n_eT) and the intensity of the low-frequency recombination lines in the direction of the galactic centre (lines marked a, b, c and d). The strictly allowed parameters for this ionized gas are below the line marked n_eT and above the line (b) which results from an observed upper limit of 8 K to the H351α line (Hart & Pedlar 1980). Our realistic estimate of the upper limit to the H351α line restricts the parameters to above the dashed line (c). The filled circle indicates the parameters of the warm ionized gas in the model of McKee & Ostriker (1977).

which weakens the above-mentioned limits to some extent. $T_{L351\alpha}$ = 4K line for L=14 kpc is shown in Fig. 6 (curve c). The change, however, is not more than ~ 10 per cent.

Another factor that has not been included in the above analysis is the absorption by the thermal gas around the galactic centre. This will restrict the amount of line radiation received from behind the galactic centre. We estimate the error due to this to the final result to be small ($\lesssim$10 per cent), since most of the line emission arises in front of the galactic centre, because of stimulated emission due to strong continuum radiation from the galactic centre region.

It appears that frequencies in the range 100–150 MHz are most suitable for the purpose of studying recombination-line emission from distributed ionized component of the ISM. At higher frequencies most of the line emission comes from the localized dense gas in this line of sight, as discussed in Section 3. For example, based on the H351α upper limit, we estimate the contribution of the distributed component to the H272α line intensity to be < 0.6 K, whereas the total observed H272α line intensity is ~ 4 K. We have shown in Fig. 6 (curve a), for purposes of comparison, the line corresponding to $T_{\mathrm{L},272\alpha}$ = 1 K contribution from the distributed gas. Frequencies much lower than 100 MHz, though more sensitive to the low-density component, suffer from the fact that the dense gas mentioned above becomes optically thick, thus drastically reducing the pathlength over which line emission can accumulate. It seems extremely important, therefore, to carry out new observations at 100–150 MHz with improved sensitivity to obtain a direct handle on the properties of the distributed ionized component of the interstellar medium.

7. Conclusions

The H272α recombination line in the direction of the galactic centre is seen at velocities near 0 kms^{-1}, – 50 kms^{-1} and +36 kms^{-1}. These features are also evident in the H166α observations of Kesteven & Pedlar (1977). The feature near 0 km s^{-1} is due to ionized gas along the line of sight. We attribute the –50 km s^{-1} feature to ionized gas present in the '3 kpc arm' and the +36 kms^{-1} feature to ionized gas inside of 4 kpc from the galactic centre.

The properties of the ionized gas responsible for these features are deduced using a single-component model to fit both the H272α and the H166α observations. We obtain an electron density of about 7 cm^{-3} for the ionized gas along the line of sight. From considerations of the geometry of the line-emitting region and the average interstellar electron density, we deduce that the pathlength through this gas is in the range 10–60 pc. This corresponds to a possible range in the emission measure of 500–2900 pc cm^{-6} and in the electron temperature of 2000–6000K.

The electron density derived for the ionized gas in the 3 kpc arm is about 30 cm^{-3} . For an electron temperature of 10^4K, the pathlength through this gas is 9 pc. This leads to an electron column density of 9.3×10^{19} cm^{-2} and a ratio of electron to neutral hydrogen column density of 0.08.

The upper limit on the H351α line in the direction of the galactic centre (Hart & Pedlar 1980) imposes strong constraints on the properties of the distributed ionized gas responsible for the dispersion of pulsar signals. We obtain a *lower limit* to its electron temperature (7) of 4500 K. Assuming this gas to be in pressure equilibrium with the ISM, we get an *upper limit* to its electron density (n_{e}) of 0.2cm^{-3} which corresponds to a *lower limit* to the line-of-sight filling factor (f_{w}) of 0.15. These limits are somewhat conservative. Our more realistic estimates are T > 6000K, n_{e}< 0.16cm^{-3} and f_{w} > 0.2. The parameters for the 'warm ionized' component of the ISM proposed by McKee & Ostriker (1977) are only marginally consistent with these limits. Recombination lines in the frequency range 100–150 MHz from this gas must therefore become observable with only slightly improved sensitivity.

8. Acknowledgements

We thank V. Radhakrishnan, R. Nityananda and G. Srinivasan for useful comments. DB thanks National Council of Educational Research and Training for financial support and Raman Research Institute for extending research facilities.

References

Altenhoff, W. J., Downes, D., Pauls, T., Schraml, J. 1978, *Astr. Astrophys. Suppl. Ser.,* **35**, 23.
Anantharamaiah, K. R. 1985a, *J. Astrophys. Astr.,* **6**, 177 (Paper I).
Anantharamaiah, K. R. 1985b, *J. Astrophys. Astr.,* **6**, 203 (Paper II).
Bania, T. M. 1980, *Astrophys. J.,* **242**, 95.
Brocklehurst, M., Salem, M. 1977, *Computer Phys. Commun.*, **13**, 39.
Casse, J. L., Shaver, P. A. 1977, *Astr. Astrophys.,* **61**, 805.
Cohen, R. J., Davies, R. D. 1976, *Mon. Not. R. astr. Soc,* **175**, 1.
Cowie, L. L, Songaila, A. 1986, *A. Rev. Astr. Astrophys.,* **24** (in press).
del Romero, A., Gómez-Gonzáles, J. 1981, *Astr. Astrophys.,* **104**, 83.
Falgarone, E., Lequeux, J. 1973, *Astr. Astrophys.,* **25**, 253.
Field, G. B., Goldsmith, D. W., Habing, H. J. 1969, *Astrophys. J.,* **155**, 149.
Gómez-Gonzáles, J., Guélin, M. 1974, *Astr. Astrophys.,* **32**, 441.
Harding, D. S., Harding, A. K. 1982, *Astrophys. J.,* **257**, 603.
Hart, L., Pedlar, A. 1980, *Mon. Not. R. astr. Soc,* **193**, 781.
Haslam, C.G.T., Salter, C.J.,Stoffel, H.,Wilson, W.E. 1982, *Astr. Astrophys. Suppl. Ser.,* **47**,1.
Heiles, C. 1980, *Astrophys. J.,* **235**, 833.
Jenkins, E. B. 1984, in *IAU Coll.* 81: *The Local Interstellar Medium,* Eds Y. Kondo, F. C. Bruhweiler & B. Savage, NASA CP-2345, p. 155.
Jenkins, E. B., Meloy, D. A. 1974, *Astrophys. J.,* **193**, L 121.
Kesteven, M. J., Pedlar, A. 1977, *Mon. Not. R. astr. Soc,* **180**, 731.
Little, A. G. 1974, in *Galactic Radio Astronomy,* Eds F. J. Kerr & S. C. Simonson, D. Reidel, Dordrecht, p. 491.
Lockman, F. J. 1980, *Astrophys. J.,* **241**, 200.
Lockman, F. J., Gordon, M. A. 1973, *Astrophys. J.,* **182**, 25.
McKee, C. F., Ostriker, J. P. 1977, *Astrophys. J.*, **218**, 148.
Oster, L. 1961, *Rev. mod. Phys.,* **33**, 525.
Pauls, T., Mezger, P. G., Churchwell, E. 1974, *Astr. Astrophys.,* **34**, 327.
Pauls, T., Downes, D., Mezger, P. G., Churchwell, E. 1976, *Astr. Astrophys.,* **46**, 407.
Pedlar, A., Davies, R. D., Hart, L, Shaver, P. A. 1978, *Mon. Not. R. astr. Soc,* **182**, 473.
Radhakrishnan, V., Sarma, N. V. G. 1980, *Astr. Astrophys,* **85**, 249.
Rodriguez, L. F., Chaisson, E. J. 1979, *Astrophys. J.,* **228**, 734.
Rogerson, J. B., Spitzer, L, Drake, J. F., Dressler, K., Jenkins, E. B., Morton, D. C, York, D. G. 1973, *Astrophys. J.* ,**181**, L97.
Schwarz, U. J., Ekers, R. D., Goss, W. M. 1982, *Astr. Astrophys.,* **110**, 100.
Shaver, P. A. 1975a, *Pramana,* **5**, 1.
Shaver, P. A. 1975b, *Astr. Astrophys.,* **43**, 465.
Shaver, P. A. 1976, *Astr. Astrophys.,* **49**, 149.
Shaver, P. A., Pedlar, A., Davis, R. D. 1976, *Mon. Not. R. astr, Soc,* **177**, 45.
Simonson, S. C, Mader, G. L., 1973, *Astr. Astrophys.,* **27**, 337.
Spitzer, L. 1956, *Astrophys. J.,* **124**, 20.
Vivekanand, M., Narayan, R. 1982, *J. Astrophys. Astr.,* **3**, 399.
York, D.G.1974, *Astrophys. J.,* **193**, L127.

J. Astrophys. Astr. (1986) **7,** 155–170

Is the Stephani–Krasiński Solution a Viable Model of the Universe?

D. Lorenz-Petzold *Fakultät für Physik, Universität Konstanz, D-7750 Konstanz, FRG*

Received 1985 November 20; accepted 1986 April 30

Abstract. We present a detailed study of the inhomogeneous Stephani-Krasiński solution with time-dependent curvature index. In general, the cosmological behaviour of the models depends on six arbitrary functions of time. Such models are termed 'private universes' and cannot be in accord with observation in the most general case. Two simple models with changing topology are considered as illustrating examples. In one of these models the pressure turns out to be negative and hence a violation of the weak energy condition in the singularity theorems is possible. A brief review of other inhomogeneous cosmologies is included for the sake of clarity. It is shown that the geodesic equation can be reduced to a complicated differential equation, which depends on the three arbitrary functions involved. Therefore, it is difficult to obtain explicit formulas for the various observational relations.

Key words: cosmology, inhomogeneous — general relativity

1. Introduction

In 1967, Stephani (1967a, b) constructed some new solutions of Einstein's field equations, which can be embedded in a flat five-dimensional space (see Goenner 1980; Stephani 1983, for general reviews of such imbedding classes). However, no relation to the cosmological problem was given. Recently, Krasiński (1980) has reported on his investigations of space-times with intrinsic spherical symmetry in the sense of the definition due to Collins (1979). (See also Collins & Szafron 1979 a, b; Szafron & Collins 1979.) According to Krasiński a 'new' solution was found, but remarks in an added note state that the solution was already found by Stephani (1967a) (see his solution 15). Since then this Stephani–Krasiński (SK)-solution has often been advocated by Krasiński as a viable model of the universe (Krasiński 1981, 1982, 1983a, b, 1984a, b).

One of the main differences between the SK-model and the standard Friedmann–Robertson–Walker (FRW)-models is reflected by the time-dependence of the curvature index $k = k(t)$ of three-space. By setting k=const, we rediscover the FRW-models with k=(0,1,–1) according to the various fixed topologies (flat, closed, open) the models might have. In contrast to the FRW-models, the SK-model may appear in general to have a positive curvature at one time and a negative one at another. Thus the SK-model seems to be an interesting model of the universe with changing

topology. However, some critical points must be clarified and hence a detailed study of the SK-model will be given in this paper.

Let us take a closer look at the various publications of Krasiński. The papers of Krasiński (1980,1982,1983b) are brief reports given at various conferences with only a short discussion of the SK-model. The basic paper (Krasiński 1981) can be termed a review of spacetime solutions with spherically symmetric hypersurfaces, essentially with no cosmological discussion of the SK-model. The reports of Krasiński (1984a, b) are mainly concerned with some more general cosmological models which are solely due to him, with some repetitions of the properties of the SK-model. The only discussion of the cosmological implications of the SK-model in some more detail is given by Krasiński (1983a). We make the following comments.

Solutions with $k = k(t)$ have been first discussed by Wesson (1975a, b, c) (see Section 2 here). The papers of Wesson seem to be unknown to Krasiński (1981). However, in his paper, Krasiński (1983a) is aware of the solution given by Bergmann (1981), which represents a cosmological solution with $k=k(t)$ in case of an energy-momentum tensor of heat flow. Next we observe that no relation to the original Friedmann equations is given by Krasiński. We refer to Equations (34) and (35) of Krasiński (1981) and to Equations (5) and (6) of Krasiński (1983a). Thus it is not clear how the connection with the dynamical field equations for the various cosmological functions (world radius, energy density, *etc.)* in the FRW-models is given in the limiting case, k = const. It should be noted that the evolution of the SK-model depends in general on six arbitrary functions and therefore represents actually a whole class of solutions, which according to this fact may be termed 'private universes' (see below for further justification). We believe that this point has to be clarified, since it has been claimed by Krasiński (1983a) (but not proved) that by choosing the arbitrary functions appropriately one can make the predictions of the SK-model arbitrarily close to the predictions of the FRW-models.

Another point is that Equation (31) of Krasiński (1981) is given in a representation from which it is not obvious (contrary to the statement given by the author) that Equation (33) is the desired solution, which is crucial for the main differences between the FRW-and the SK-models. Equation (31) is an identity for the FRW-models, but for the SK-model with $k=k(t)$ being not a constant we obtain a high degree of freedom in choosing the corresponding cosmological functions. For instance, the energy density of the perfect fluid matter incorporated in the SK-model turns out to be an arbitrary function of time. The same applies to the expansion parameter, which characterizes the Hubble 'constant'. Since one is free to choose any functions for these cosmological quantities we have called such models 'private universes'. It follows that one has to be cautious in considering the general SK-model as a viable model of the real universe. Assuming the energy density of matter to be a constant from the very beginning, we rediscover the de Sitter solution, being foliated in an exotic way in the given coordinate system of the SK-model (see metric 1). It is this well-known solution which has been discussed by Krasiński (1983a) (assuming the simple law $k = k(t) = - t$) and not the SK-model. The SK-model in its most general form has not been discussed by Krasiński as an alternative description of the universe. In Krasiński (1983a) the author restricts himself to an analysis of the global geometry of the SK-model on the hypersurfaces t = const, on which we have also k = const. It is therefore not too surprising that the obtained formulas (20)-(22) for the radial length are essentially the same as in the FRW-models (see, *e.g.* Weinberg 1972; Zel'dovich & Novikov (1983).

In Section 2, we present a short review of inhomogeneous cosmologies. Ellis, Maartens & Nel (1978) have discussed the viability of static, spherically-symmetric (SSS) cosmologies as an alternative description of the universe. The SK-and the SSS-models are two explicit examples of nonstandard cosmologies which are not based on 'philosophical principles' (Ellis 1984). We make some critical remarks. It is also worth comparing the analysis of the SK-model with the various studies of the so-called Tolman-Bondi (TB) solutions, which have been made over the last 50 years. The solutions of Wesson (1975a, b, c) with $k = k(t)$ are only special cases of the TB-models. In Section 3 we present a complete discussion of the SK-field equations. We believe that our representation is much more transparent than that given by Krasiński (1981). The generalized Friedmann equations are given in an explicit form. From the mathematical point of view it is not too surprising that the FRW-models with $\dot{k} = 0$ are contained as special cases in the SK-spacetimes. However, assuming $\dot{k} \neq 0$ from the very beginning, the Laplacian Dämon is free to choose the initial values of the arbitrary functions, which determine the behaviour of the general SK-models. We present a simple example, which is not in accord with observation. A more serious approach is to ask for some physical criterion to decide whether the SK-model can be made compatible with observation, at least from a given moment. We consider also the Raychaudhuri equation.

In Section 4 we turn to a discussion of some cosmological tests. The geodesic equation is derived for the first time and a search for explicit solutions is made. For the sake of completeness, we present a short derivation of the field equations in Appendix.

2. Inhomogeneous cosmologies: a brief review

The SK-model belongs to the large class of inhomogeneous solutions of Einstein's field equations (see MacCallum 1979,1984 for reviews). The corresponding metric is given by

$$ds^2 = -D^2\,dt^2 + (R/V)^2\,[dr^2 + r^2\,(d\theta^2 + \sin^2\theta\,d\phi^2)] \tag{1a}$$

where

$$D = D(r, t), \quad V = 1 + \frac{k}{4}r^2, \quad k = k(t), \quad R = R(t). \tag{1b}$$

The function D obeys the simple equation

$$D' = \frac{1}{2}\dot{k}r\,(F/V^2), \quad D = F(\ln(V/R)^{\cdot}) \tag{2}$$

where $F = F(t)$ denotes an arbitrary function, $(\,)' = \mathrm{d}/\mathrm{d}r$ and $(\,)^{\cdot} = \mathrm{d}/\mathrm{d}t$. It should be noted that metric (1) is not the most general form possible (Krasiński 1981; Martinez & Sanz 1985). However, we restrict ourselves to this 'ansatz' since it is obviously the simplest generalization of the standard FRW-metric

$$ds^2 = -dt^2 + R^2[(1 - k\bar{r}^2)^{-1}\,d\bar{r}^2 + \bar{r}^2\,(d\theta^2 + \sin^2\theta d\phi^2)] \tag{3}$$

with $k = (0,1, -1)$. By setting $k = 0$ it follows from Equation (2) that $D = 1$ (without loss of generality) and by the final transformation $r = r/V$ we obtain metric (3) as desired. No such transformation is possible in the general case $k \neq 0$.

According to Krasiński (1981), his study of the SK-model as an alternative description of the universe was motivated by the criticism of standard cosmology by

Ellis. Ellis has revised and improved his standpoint several times during the last ten years (See Ellis 1975,1978,1980,1984; Ellis, Maartens & Nel 1978; Ellis & Perry 1979; Ellis *et al.* (1985). A simple inhomogeneous model has been discussed by Ellis (1978) and Ellis, Maartens & Nel (1978) in thought-provoking articles. The metric of the corresponding static, spherically-symmetric (SSS) spacetime is given by

$$ds^2 = -D^2dt^2 + dr^2 + f^2(d\theta^2 + \sin^2\theta d\phi^2) \tag{4a}$$

where

$$D = D(r), \quad f = f(r), \tag{4b}$$

and the source of the gravitational field is assumed to be a perfect fluid as in the SK-model. Can the observations be explained by means of this simple model? By comparison of the two metrics (1) and (4) we see that the situation is much simpler in the SSS-model. The scalar quantities n, ε, p (number density of galaxies, energy density, pressure) depend only on the radial coordinate r and the basic observational relations are determined in terms of the functions D, f, and n. The corresponding redshift can be explicitly calculated and is given by the simple expression

$$1 + z = D_e^{-1}, \quad \text{with} \quad D(0) = 1, \tag{5}$$

where $D_e = D(r_e)$ is the position of the source. By using only the kinematic approach (see Ellis 1971) one can make a nonstandard cosmological model that reproduces precisely any spherically symmetric observations that are made of the universe on the basis of the standard FRW-models. However, this is true only if one does neglect the influence of matter, which must obey the corresponding field equations with some reasonable equation of state. It has been shown by Ellis, Maartens & Nel (1978) that one cannot obtain a good fit to the observed (m, z) relation if the Einstein field equations are taken into account. Thus the more optimistic statements due to Ellis (1978) have had to be revised. Moreover, it has been shown by Collins (1983) that if the equation of state is of the form $p = (\gamma - 1)\,\varepsilon$, $\gamma \neq 0,1$, the SSS-models turn out to be unphysical. The difficulty arising is due to the fact that the field equations are not regular at the centre, $r = 0$. No such critical remarks can be found in the various papers of Krasiński.

We now turn to the so-called Tolman–Bondi (TB) solutions to see whether the situation is much better in these models and if we could get some insight which may have applications to the SK-models. The TB-solutions have been discussed by many authors during the last half century. In general it is believed that the most fundamental studies are due to Tolman (1934a) and Bondi (1947). However, both authors referred to Lemaître's (1933) prior discovery so it is curious that the solutions are called the Tolman–Bondi models (see also Peebles 1984). The corresponding metric is given by

$$ds^2 = -dt^2 + S^2dr^2 + R^2(d\theta^2 + \sin^2\theta d\phi^2), \tag{6a}$$

where

$$S^2 = R'^2/f, \quad f = f(r) > 0, \quad R = R(r, t), \tag{6b}$$

with the matter content taken as dust ($p = 0$), in general, with a nonvanishing cosmological term Λ. The corresponding energy density ε is given by

$$\varepsilon = \varepsilon(r, t) = m'/R^2R', \quad m = m(r), \tag{7a}$$

and the function $R = R(r,t)$ must be a solution of

$$\dot{R}^2 = f - 1 + 2m/R + \Lambda R^2/3. \tag{7b}$$

Special solutions to Equation (7b) under restricted conditions have been given by Tolman (1934a), Datta (1938), Bondi (1947) and Omer (1949), the most general solution being due to Omer (1965). There are also some discussions of the TB-model in the books of Zel'dovich & Novikov (1971) and Landau & Lifshitz (1981).

The solution of Wesson (1975a) is given by the 'ansatz'

$$\varepsilon = \varepsilon_0(t)r^{-2}, \tag{8a}$$

and the corresponding metric may be recast in the familiar FRW-form (3):

$$ds^2 = -dt^2 + R^2[(1-kr^2)^{-1}\,dr^2 + r^2(d\theta^2 + \sin^2\theta\, d\phi^2)], \tag{8b}$$

Where

$$\begin{aligned} R^2 &= [a\varepsilon_0(t)]^{-2/3} \\ k &= k(t) = [\Lambda + 2\ddot{\varepsilon}_0/3\varepsilon_0 - (\dot{\varepsilon}_0/\varepsilon_0)^2]\, R_0^2/(a\varepsilon_0)^{2/3}, \\ \varepsilon_0 &= \varepsilon_0(t), \quad R = R_0(t), \quad a = \text{const.} \end{aligned} \tag{8c}$$

The sign of the curvature scalar k is determined by $\varepsilon_0 = \varepsilon_0(t)$. If the simplest case, $\varepsilon_0 = t^{-n}$, $\Lambda = 0$, are adopted then the dividing line between positive and negative k occurs at $n = 2$:

$$n < 2 \Rightarrow k > 0, \quad n > 2 \Rightarrow k < 0, \quad n = 0 \Rightarrow k = 0. \tag{9}$$

A similar consideration can be made in the SK-model (see our Equation (17). However, the energy density ε in the SK-model is given by $\varepsilon = \varepsilon(t) = 3C^2(t)$ and not by $\varepsilon = \varepsilon(r, t)$. Moreover, the $p = 0$ condition reduces the SK-model already to the FRW-solutions. Thus the cosmological behaviour of the SK-model is completely different from that possible for the TB-models

The observational implications of such special TB-models have been discussed by Wesson (1975b, c). However, we have some doubts that one can deduce the corresponding redshift relation (see Equation A6; Wesson 1975c) as a solution of the geodesic equation. No such deduction was given by Wesson. Further discussions of inhomogeneous cosmologies are given in the papers of Wesson (1978a, b, 1979). For the more general TB-models the discussion of the redshift relation has a long history. The first step into this direction was given by Bondi (1947). A calculation of $z = z(r, t)$ was made and a rather complex expression containing both the velocity shift and the Einstein shift was obtained. A more general discussion of the geodesic equation was given by Omer (1949) and more recently by Hellaby & Lake (1984,1985) and Ellis *et al.* (1985). The corresponding differential equation has thus far proved intractable. This is mainly due to the nonexistence of a conformal Killing vector in such spacetimes. This property is shared by the SK-model and also by the more general inhomogeneous models due to Szekeres (1975), which have no Killing vector at all (Bonnor, Sulaiman & Tomimura 1977). It has been shown by Dyer (1979) and Szekeres (1980) that infinite blueshifts can occur along radial rays in the TB-models. Thus one has to be very cautious in considering the TB-models as representing the universe in the large. Further cosmological implications of the TB-models can be found in the papers by Bonnor (1972), Korkina (1975), Mavrides (1976), Miller (1976), Silk (1977), Ellis, Maartens &

Nel (1978), Eardley & Smarr (1979), Olson & Silk (1979), Zel'dovich & Grishchuk (1984), Lake (1984) and Stein-Schabes (1985).

3. Field equations and their solutions

The SK-model is a solution of Einstein's field equations with a perfect fluid source

$$G_{\mu\nu} = T_{\mu\nu} = (\varepsilon + p)\, u_\mu u_\nu + p g_{\mu\nu}, \quad u_\mu\, u^\mu = -1, \tag{10}$$

where $G_{\mu\ \nu}$ denotes the Einstein tensor (given in the appendix), $T_{\mu\nu}$ the energy-momentum tensor of the perfect fluid matter, u_μ the velocity four-vector, and ε and p are, respectively, the density and pressure of the fluid. The corresponding metric $g_{\mu\nu}$ is given by (1a, b).

We present a complete discussion of the field equations. From (A10) we find that

$$G_{02} = G_{03} = G_{12} = G_{13} = G_{23} = 0, \quad \text{and} \quad G_{22} = G_{33}, \tag{11a}$$

where the Einstein tensor $G_{\mu\nu}$ has been computed by

$$G_\beta^{\ \delta} = \varepsilon^{\delta\rho\sigma\tau}\varepsilon_{\beta\mu\nu\tau} R^{|\mu\nu|}{}_{|\rho\sigma|}, \tag{11b}$$

where $\varepsilon_{\alpha\beta\gamma\delta}$ denotes the four-dimensional Levi–Civita pseudotensor with $\varepsilon_{0123} = 1$. (Vertical bars around the indices mean summation extends only over $\mu < \nu$, $\rho < \sigma$.) It follows that

$$u_2 = u_3 = 0. \tag{12}$$

The crucial equation is given by $G_{01} = T_{01}$. In general we could have $u_1 \neq 0$, which yield a tilted model (see Lorenz 1982, for a discussion of tilted models) and which should be a generalized SK-model (Krasiński 1981). However, the original SK-model is given by $u_1 = 0$, *i.e.*, the perfect fluid is moving along t-lines. In this case the $G_{01} = 0$ field equation may be recast into the simple form

$$(D'/D)\,(\dot{V}/V - \dot{R}/R) = (V'/V)^{\cdot} = (\dot{V}/V)' = (\dot{V}/V - \dot{R}/R)', \tag{13a}$$

from which we obtain the general solution

$$D = F\,(\dot{V}/V - \dot{R}/R), \tag{13b}$$

where $F = F\,(t)$ is an arbitrary function of t. It follows that

$$D' = F\dot{k}r/2V^2. \tag{13c}$$

By comparison, we see that our Equation (13a) is much more transparent than the one given by Krasiński (1981: Equation 31) and the general solution (13b) is obtained in an easy manner. From Equation (13c) we conclude that $\dot{k} = 0$ implies that $D = D(t)$, which, without loss of generality, may be assumed to be equal to 1 (after a simple coordinate transformation). Thus we are back to the FR-Wmodel with k = const (see Section 2).

We now show that $G_{11} = G_{22}$ (= G_{33}) is obeyed automatically (as in the FRW-model) by using Equation (13b). From the condition

$$R^{01}{}_{01} + R^{13}{}_{13} = R^{02}{}_{02} + R^{23}{}_{23}, \tag{14a}$$

it follows that

$$(V/Rr)^2 + (V/R)[(V/R)(1/r - V'/V)]'$$
$$= (D'V^2/DR^2)(1/r - V'/V) - (V/R)(D'V/DR)' - (D'V/DR)^2. \tag{14b}$$

The left-hand side of Equation (14b) vanishes by the definition of V, while the right-hand side turns out to be equal to zero as a result of Equation (13c). This completes our simple proof.

The energy density ε and the pressure p of the SK-model are now determined by the remaining field equations

$$G_{00} = T_{00} = \varepsilon g_{00}, \quad G_{11} = T_{11} = p g_{11}, \tag{15a}$$

where we have made use of the relation $u_0 = -(-g_{00})^{1/2}$, which follows from the condition $u_\mu u^\mu = -1$, $u_1 = u_2 = u_3 = 0$. The results are given by

$$\varepsilon = 3[(1/D^2)(\dot{R}/R - \dot{V}/V)^2 + k/R^2] = \varepsilon(t) \tag{15b}$$
$$p = -(3/D^2)(\dot{R}/R - \dot{V}/V)^2 - k/R^2$$
$$- (2/D)[(1/D)(\dot{R}/R - \dot{V}/V)]^{\cdot}$$
$$+ (2D'V^2/DR^2)(1/r - V'/V)$$
$$= p(t, r).$$

These are the desired generalized Friedmann equations (see our remarks given in the introduction). By setting $k = 0$, *i.e.* $D' = \dot{V} = 0$, we rediscover the original Friedmann equations of the FRW-model (see, *e.g.* Weinberg 1972) with $\varepsilon = \varepsilon(t)$ and $P = P(t)$. For the FRW-model we may postulate an equation of state

$$p = (\gamma - 1)\varepsilon, \quad 1 \leqslant \gamma \leqslant 2. \tag{16a}$$

which in conjunction with the conservation law $T^{\mu}{}_{\nu;\mu} = 0$ (where ';' denotes covariant derivation) yield

$$\varepsilon = mR^{-3\gamma}, \quad m = \text{const.} \tag{16b}$$

The dynamical field equations (15) and (16) (with $k = 0$) can be completely solved for $R = R(n)$ in conformal time $\mathrm{d}t = R\,\mathrm{d}\eta$ for each γ (Vajk 1969).

However, assuming $k \neq 0$ from the very beginning, the situation for the SK-model is totaly different from that given for the FRW-models. First of all we have $\varepsilon = \varepsilon(t)$ and $p = p(r,t)$, which is physically difficult to understand. Thus the perfect fluid matter cannot obey an equation of state (16a). Assuming an arbitrary set of functions k, R, $F = f(t)$, it follows from Equations (15b, c) and (13b) that we can give the physical quantities ε and ρ an arbitrary mathematical behaviour. It is hard to believe that we may live in such 'private' universe, even if we do not know much about the matter distribution in space-time (compare with the arguments given by Krasiński 1983a).

The FRW-models are contained as special cases in the SK-model if $k = 0$. This is a mathematical fact and does not allow for a cosmological insight into the SK-model. It is generally believed that the universe at present (and also at some earlier times) is described by a perfect fluid matter whose pressure can be neglected (see, *e.g.* Zel'dovich & Novikov 1983), *i.e.* $p = 0$. Can this case be made compatible with the SK-field equations (15b) and (15c)? In order to discuss this special case it is convenient to

introduce the new function

$$C^2 = 1/F^2 + k/R^2, \quad i.e.\ k = (C^2F^2 - 1)(R/F)^2 \gtreqless 0, \tag{17}$$

from which it follows that we may replace Equations (15b) and (15c) by

$$\varepsilon = 3C^2, \tag{18a}$$

$$p = -3C^2 + 2C\dot{C}(V/R)/(V/R)^{\cdot}, \tag{18b}$$

which are identical with the expressions given by Krasiński (1983a). By setting $3C^2 = l\Lambda$, $l^2 = 1$, *i.e.* $\dot{C} = 0$, we rediscover the de Sitter solutions (Krasiński 1981,1983a) in an unusual coordinate system as a byproduct. We have made a check that the field equations yield no restriction on the function $k = k(t)$ in the coordinate system given by Equation (1).However, we do not enter into the discussion of the de Sitter solutions in this paper (for a thorough discussion, see Krasiński 1983a). We only remark that the Equation(31b) of motion(see below) is indeterminate for such a fluid with $\varepsilon = 3C^2$ and $P = -3C^2$ (see Hawking & Ellis 1973).

From Equation (18b) one can conclude that the condition $p = 0$ implies

$$(V/R)^{\cdot} = (2/3)(\dot{C}/C)(V/R) \tag{19}$$

and thus from Equation (13b) that $D = (2/3)(C/C)F$, *i.e.,* $D = D(t)$. The field equation (13c) implies then that $\dot{k} = 0$, i.e., we are back to the FRW-model. Thus the following interpretation seems to be possible. The SK-model may be considered as a solution representing some earlier stages in the expansion of the universe, the detailed behaviour depending on the initial values of the functions *C,R* and *F*. During the course of expansion the effect of pressure would become negligible at acertain time $t = t$ ($p = 0$) and the further evolution of the universe would be the same as in the standard FRW-models with fixed topology. However, if the Laplacian Dämon is free to choose the initial values of the arbitrary functions *C, R, F* $= f(t)$ in such a way that at some moment Equation (19) is fulfilled, we cannot see any reason why he should not be free to arrange the functions in such a manner that they obey the equation

$$[(C^2F^2 - 1)(R/F)^2]^{\cdot} = 0, \tag{20}$$

i.e., that we live in a FRW-model with $\dot{k} = 0$ from the very beginning (see Equation 17). In any case he must take a sophisticated selection in the space of functions *C, F, R* if he does not want to come in conflict with observations. For instance, he could try to make the simple choice

$$R = C = F \quad \text{with} \quad R = t^m, \quad m < 0, \quad k = R^4 - 1 \tag{21}$$

from which it follows that $k \to 0$ as $t \infty$. However, this leads to the contradiction that we must live in an asymptotically 'open' ($k \to -1$) universe with vanishing radius *R*. Another possibility is given by the 'ansatz'

$$k = t^{-1} + k_{\mathrm{FRW}} \tag{22}$$

in connection with some appropriate choice of two of the arbitrary functions. However, the Laplacian Dämon is also free to choose some exotic models with $k = \sin t$, $\sinh t$, $1n t$ or something else. The same applies to the behavior of the energy density ε in such 'private' universes. Instead of choosing first the curvature scalar *k* he could also make an arbitrary choice of the energy function C^2, which could be made finite or infinite at

$t = -\infty$. Note that the pressure ρ has a singularity at the zeros of (V/R).

We now turn to the kinematical quantities to gain a deeper insight into the SK-model. According to Equation (15a) the velocity four-vector u^μ is given by

$$u^\mu = D^{-1}\,\delta^\mu_0 \tag{23a}$$

from which we obtain the acceleration vector

$$a^\mu = \dot{u}^\mu = u^\mu_{;\nu}\,u^\mu \quad \text{with} \quad \dot{u}^0 = 0 \quad \text{and} \quad \dot{u}^1 = (D'V^2/DR^2), \tag{23b}$$

and the volume expansion

$$\theta = u^\mu_{;\mu} = (3/D)\,(\dot{R}/R - \dot{V}/V) = -3/F \tag{23c}$$

as the only nonvanishing kinematic quantities. The SK-model has no shear σ and no rotation ω . It can be shown that the SK-solution is the most general conformally flat solution with an expanding perfect fluid source (Krasiński 1984a; Barnes 1984; Koch-Sen 1985). A simple proof of this theorem was given by Barnes (1984). In general the class of shear-free perfect fluid solutions is of much interest in general relativity. However, most of these studies are devoted to the $p = p\ (\varepsilon)$ case (see, *e.g.* Collins & Wainwright 1983; White & Collins 1984; Collins & White 1984; Barnes 1984; Collins 1985), which does not hold in the SK-model (besides the dust case).

According to Equation (23c) the expansion parameter Θ is an arbitrary function of t: $\theta = \theta\ (t)$, while in the FRW-model we have $\theta = 3\dot{R}/R$, where $R = R\ (t)$ is determined *via* the Friedmann equations (see Equations 15b, c with $D' = \dot{V} = 0$). For instance, the 'flat' ($k = 0$) solution is given by

$$R = R_\gamma\, t^{2/3\gamma}, \quad i.e., \quad \theta = \theta_\gamma\, t^{-1}, \tag{24}$$

where R_γ, θ_γ= const. For $\gamma = 1$ we obtain the well-known Einstein–de-Sitter model (Weinberg 1972), which is in good agreement with an estimate of the age of the universe. It can be seen at once that our special SK-model defined by Equation (21) is not in accord with such a behaviour. A more satisfactory model is given by the 'ansatz'

$$C^2 = 1/R^3, \quad F = R = t^m, \quad m > 0, \quad k = 1/R - 1, \tag{25}$$

with the asymptotic properties $k \to -1$ and $\varepsilon \to 0$ at $t\infty$. Note that at $r = 0$ we have $p = 0$ in such a case. By setting $m = 2/3$ our model is an asymptotically 'open' model with dust-like matter at the origin and negative expansion parameter. However, the pressure becomes singular at $r^2 = 4/(1 - 2/R)$. It is not our intention to list all the possible 'simple' cases and to discuss their physical interpretation. Everybody is free to choose his own 'private universe' on the basis of the SK-field equations.

For a cosmological model one requires in general that the perfect fluid matter obey certain inequalities of the kind

$$\varepsilon > 0, \quad \varepsilon + p > 0, \quad \varepsilon + 3p > 0. \tag{26}$$

(Ellis 1971; Hawking & Ellis 1973). Although the first of these inequalities may be violated in the SK-model (see Equation 15b), we have arranged the arbitrary functions in such a way that the positivity of the energy density ε is guaranteed (see Equations 17 and 18a). However, the other two inequalities can be violated by choosing the arbitrary functions in an appropriate manner. A simple example of this kind is provided by our solution defined by Equation (21). We have

$$\varepsilon + p = -2C^2, \quad \varepsilon + 3p = -12C^2, \quad p = -5C^2 \tag{27}$$

at $r = 0$. Note that our solution is 'flat' ($k = 0$) at $t = 1$ and 'open' ($k < 0$) for any later time. According to Raychaudhuri (see *e.g.* Raychaudhuri 1979) one has the general relation

$$\tfrac{1}{3}\theta^2 + \theta_{,\mu}u^\mu - \dot{u}^\mu{}_{,\mu} = -R_{\mu\nu}u^\mu u^\nu = -\tfrac{1}{2}(\varepsilon + 3p) \tag{28}$$

from which it follows that the standard arguments that a singularity of a certain kind must occur breaks down in case of our SK-model. A general discussion of the existence or nonexistence of singularities in the SK-model is impossible due to the arbitrary nature of the functions involved. Note that one can always choose the energy function $C2$ in such a way that ε remains finite at $t = 0$ or $t = -\infty$.

The equation of state in the SK-model is not of the form given by Equation (16a), but depends on the spatial position:

$$p = p(r, t) = p(\varepsilon, r, t) = \varepsilon[-1 + (1/3)(\dot{\varepsilon}/\varepsilon)(V/R)(1/(V/R)^{\cdot})]. \tag{29}$$

This property means that temperature must enter the equation of state and that the temperature varies also with spatial position. From the energy and momentum conservation equation

$$T^{\mu\nu}{}_{;\nu} = 0 \tag{30}$$

applied to Equation (10) one finds

$$\varepsilon_{;\mu}u^\mu + (\varepsilon + p)u^\mu{}_{;\mu} = 0, \tag{31a}$$

$$(\varepsilon + p)\dot{u}^\mu + h^{\mu\nu}p_{;\nu} = 0, \tag{31b}$$

where $h^{\mu\nu} = u^\mu u^\nu + g^{\mu\nu}$ denotes the projection tensor. Assuming that $C \neq 0$ ($C = 0$ is the de Sitter solution), we obtain

$$p_{;1} = -2C\dot{C}(V/R)(D'/D)(1/(V/R)^{\cdot}) = -(\varepsilon + p)(D'/D) \tag{32}$$

as the expression for the spatial pressure gradient in the SK-model.

In addition to Equation (30) we assume the conservation of the particle rest-mas density p, measured by an observer traveling with four-velocity $u_\mu = D^{-1}\delta^\mu_0$:

$$(\rho u^\mu)_{;\mu} = 0, \quad i.e., \quad \rho l^3 = m = \text{const.} \tag{33}$$

where $i/l = \theta/3$ denotes the representative length. The function l is used to define the Hubble parameter H and the deceleration parameter q:

$$H = \dot{l}/l, \quad q = -(\ddot{l}/l)(1/H^2) \tag{34}$$

(Ehlers 1961). According to our relation (23c), all these parameters are in general arbitrary functions of time. This is in contrast to the FRW-models, where we have $R = R(t) = l$ and the detailed behaviour of the world radius R is completely determined by the field equations.

4. Observational relations

In order to derive cosmological conclusions which will have relationship to the observational data, it is necessary to derive observational relations among the various observable quantities in the SK-model. A basic study of observations in inhomogeneous cosmologies was given by Kristian & Sachs (1966). Their work calculates observational quantities on the observer's past null cone near our present position by

using an approximation scheme. An application to the TB-modei has been discussed by Bonnor (1972) and the redshift versus luminosity distance was calculated. However, the model discussed by Bonnor turns out to be incompatible with the redshift observations. A generalization of the Kristian–Sachs procedure was given recently by Ellis *et al*. (1985). The aim of their study was to determine what could be done, in principle, to determine the geometry at substantial distances from our present spacetime position. For example, the TB-solution due to Bondi (1947) has been analysed in detail. However, the present authors have been unable to reproduce the redshift relation first given by Bondi. The basic problem is that, even in comoving coordinates, it is not possible to find explicitly the relation between the redshift z and the affine distance v. Further details concerning the state of the art of finding observational relations in the TB-models have already been given in Section 2. Let us see whether the situation is much better in the SK-model.

We consider the geodesic equations

$$k^\mu \nabla_\mu k^\nu = 0, \quad k^\mu k_\mu = l, \tag{35}$$

where k^μ denotes any geodesic tangent vector, null or timelike, and ∇ denotes the covariant operator. The second of the relations given by Equation (35) is the null or timelike condition, where $l = 0$ or -1, respectively. By setting $(x^0, x^1, x^2, x^3) = (t, r, \theta, \phi)$ we obtain the following equations for the SK-metric (1):

$$\begin{aligned} &k^\mu k^0{}_{,\mu} + 2(D'/D)k^0k^1 + (\dot{D}/D)(k^0)^2 + (1/2D^2)(R^2/V^2)^{\cdot}(k^1)^2 \\ &\quad + (r^2/2D^2)(R^2/V^2)^{\cdot}(k^2)^2 + (r^2/2D^2)(R^2/V^2)^{\cdot}\sin^2\theta(k^3)^2 = 0, \end{aligned} \tag{36a}$$

$$\begin{aligned} &k^\mu k^1{}_{,\mu} + (V^2/R^2)(R^2/V^2)^{\cdot}k^1k^0 + (V^2/2)(1/V^2)'(k^1)^2 \\ &\quad + DD'(V^2/R^2)(k^0)^2 - (V^2/2)(r^2/V^2)'(k^2)^2 \\ &\quad - (V^2/2)(r^2/V^2)'\sin^2\theta(k^3)^2 = 0, \end{aligned} \tag{36b}$$

$$\begin{aligned} &k^\mu k^2{}_{,\mu} + (V^2/R^2)(R^2/V^2)^{\cdot}k^2k^0 + (V^2/r^2)(r^2/V^2)'k^2k^1 \\ &\quad - \sin\theta\cos\theta(k^3)^2 = 0, \end{aligned} \tag{36c}$$

$$\begin{aligned} &k^\mu k^3{}_{,\mu} + (V^2/R^2)(R^2/V^2)^{\cdot}k^3k^0 + (V^2/r^2)(r^2/V^2)'k^3k^1 \\ &\quad + 2\cot\theta k^3k^2 = 0, \end{aligned} \tag{36d}$$

where $k^\nu_{,\mu} = \partial k^\nu/\partial x^\mu$.

If in Equation (36 c) we take $\theta = \pi/2$ and $k^2 = 0$ as initial conditions, then $k^\mu k^2{}_{,\mu} = 0$. This means that, if a geodesic initially lies within this plane, it remains within the same plane throughout its trajectory. Similarly, in Equation (36d), if the geodesic was initially a radial line with $k^3 = 0$, then $k^\mu\, k^3{}_{,\mu} = 0$ and the geodesic remains a radial line. This property is shared by the SK-model with the TB-models and the FRW-models. In general we could have $k^3 \neq 0$ with $\theta = \pi/2$. The general solution of Equation (36d) can be readily found to yield

$$k^3 = aV^2/R^2r^2, \quad V = 1 + \tfrac{1}{4}k(t)r^2, \tag{37}$$

where a denotes an effective impact parameter (see Zel'dovich & Novikov 1971; Hellaby & Lake (1984) for comparison). Thus we have an influence of the curvature index k on the equation of motion in the case of non radial trajectories. By setting $\dot{k} = 0$,

i.e. $D' = D = V = 0$, we rediscover the FRW-solution (with $l = 0$)

$$k^0 = 1/R, \quad k^1 = \pm (V/R^2)\,(1 - a^2 V^2/r^2)^{1/2}, \quad k^3 = aV^2/R^2 r^2. \tag{38}$$

By using Equation (23a) and Equation (38), the corresponding redshift relation is given by

$$1 + z = (u^\mu k_\mu)_e/(u^\mu k_\mu)_0 = R_0/R_e \tag{39}$$

which is the standard FRW result (Ellis 1971).

For the more general SK-model the geodesic equations can be decoupled to give

$$(k^0)^2 = (R^2/V^2 D^2)\,(k^1)^2 + (a^2 V^2/r^2 D^2 R^2) - l/D^2, \tag{40a}$$

and

$$\begin{aligned}[(R^2/V^2D^2)(k^1)^2 + (a^2V^2/r^2D^2R^2) - l/D^2] \times [k^1_{,0} + (V^2/R^2)(R^2/V^2)^{\cdot} k^1]^2 \\ = \{k^1 k^1{}_{,1} + (V^2/2)\,(1/V^2)'\,(k^1)^2 - (a^2V^6/2r^4R^4)\,(r^2/V^2)' \\ + (DD'V^2/R^2)\,[(R^2/V^2D^2)\,(k^1)^2 + (a^2V^2/r^2R^2D^2) - l/D^2]\}^2 .\end{aligned} \tag{40b}$$

After solving Equation (40b) for $k^1 = k^1\,(r,\ t)$, $k^0 = k^0(r,\ t)$ can be found from Equation (40a). Note that the function $D = D(r,t)$ is related to the functions R and V *via* Equation (13b). We have been unable to solve the complicated Equation (40b), even if one assumes the simple SK-models which were proposed in Section 3. Note that the situation is much more complicated than in the TB-models, where we have $D' = 0$. Thus we have no explicit information about the measure of the redshift in the SK-model. It does not help us to use a series expansion to solve Equation (40b) since we do not know the behaviour of the arbitrary functions involved. There is no cosmological principle from which we can deduce that the cosmological functions must have a power-law behaviour. Our SK-models defined by Equations (21) and (19) are only '*ad hoc*' assumptions and could be replaced by any other combination of any other functions. By using the alternative local approach given by Kristian & Sachs (1966), no further insight can be obtained for the very same reason. In a recently published paper by Partovi & Mashhoon (1984) such an application of the Kristian-Sachs procedure to a pertubed FRW-model with radial inhomogeneities was given. The corresponding curvature index k turns out to be time-dependent as a result of higher-order terms in r in the metric 'ansatz'. However, in contrast to the SK-model this approach allows for an equation of state of the form $p = p\,(\varepsilon)$. Thus the energy density and the pressure are on equal footing and a series expansion in the radial coordinate r is possible.

It follows from Equation (39) that the redshift z turns out to be a function of t and r throughout the spacetime. By setting $a = l = 0$, we have the relation

$$1 + z = (R_e/R_0)\,(V_0/V_e)\,(k^1_e/k^1_0), \tag{41}$$

from which we conjecture that the curvature scalar $k=k(t)$ may have an effect on the unction $z = z(r,t)$ due to the relation $V = 1 + (k/4)r^2$ (Note that in the FRW-model the factor V_o / V_e cancels out). By choosing the arbitrary SK-functions in an appropriate manner we also expect the occurrence of infinite blueshifts, which we regard as an additional indication that some unphysical behaviour is present in the most general case.

5. Conclusion

The Stephani-Krasiński solution in its most general form cannot be regarded as a viable model of the real universe. Two simple models with changing topology have been proposed by us in this paper. Our solution (21) is an example of an unviable SK-model. A much better model is given by Equation (25). However, all models are given by *ad hoc* assumptions. A physical criterion is given by $\rho > 0$. It can be shown (Krasiński 1983a) that a sufficient condition is given by $\dot{k}R\dot{R} > 0$ (at $r = 0$). Note that our solution (25) has been chosen in such a way to fulfill the condition — $(\dot{C}/C)\,(\dot{R}/R) \geqslant 3/2$ (see Krasiński 1983a) at $r = 0$.

The pressure becomes infinite at the singular surfaces $rf(r) = \pm\, 2{,}f^{2} = (\dot{k}R/\dot{R}) — k$. Thus the SK-model is nonregular at these surfaces, which depend on three arbitrary functions. In a recently published paper by Knutsen (1985), a study of such additional singularities was given in case of another simple solution due to Kustaanheimo & Qvist (1948). It was shown that the corresponding singular surface is always hidden by trapped surfaces. No such definite conclusion can be made in our case due to the great number of arbitrary functions involved.

It is true that the FRW-models are contained as special cases in the SK-model. This is a simple mathematical fact. Assuming $\dot{k} = 0$ from the very beginning, we can apply the whole machinery of standard cosmologies (see, *e.g.* Weinberg 1972; Zel'dovich & Novikov 1983). It is also not too surprising that the special solution obeying the condition (19) is nothing but the FRW-dust solution. (The perfect fluid matter obeys the equation of state (16a) with $\gamma = 1$.) Perhaps the condition $p = 0$ can be regarded as a cosmological condition, which must be fulfilled by any viable model of the universe at a certain time during the course of evolution. In this sense the SK-model may be regarded as representing some exotic earlier stages of the universes. This would make the discussion of the observational tests much easier (see Section 4). Due to the high symmetry, everything is simple in the FRW-models. This is in contrast to the case $\dot{k} \neq 0$. In general, the SK-spacetime has nothing in common with the FRW-spacetime. It is a trivial result that on the hypersurfaces t = const we rediscover the symmetry shared by the FRW-models. This follows from the very construction of the SK-metric (1). No explicit cosmographic analysis can be made in the whole spacetime. For instance, it is impossible to discuss the propagation of light, which is governed by the conditions $\mathrm{d}s = 0$ and $\mathrm{d}\theta = \mathrm{d}\phi = 0$ along the radius r. Only the case t = const has been discussed by Krasiński (1983a), which gives no new insight.

It is an unpleasant feature of the SK-model that no explicit observational relation can be obtained. The only way out of this dilemma would be a numerical study for some special cases. However, there is no guidance on which choice would be the best one.

Acknowledgement

The work was supported by the Deutsche Forschungsgemeinschaft, Bonn.

Appendix

In choosing a local orthonormal basis σ^{μ}, we can put the metric (1a, b) of the SK-model in the form

$$\mathrm{d}s^2 = \eta_{\mu\nu}\,\sigma^{\mu}\sigma^{\nu}, \tag{A1}$$

where $\eta_{\mu\nu}$ the Minkowski metric tensor and

$$\omega^0 = D\mathrm{d}t, \quad \omega^1 = (R/V)\mathrm{d}r, \quad \omega^2 = (Rr/V)\mathrm{d}\theta, \quad \omega^3 = (Rr\sin\theta/V)\mathrm{d}\phi, \tag{A2}$$

are the differential one-forms. The exterior derivatives are readily found:

$$\begin{aligned}
\mathrm{d}\omega^0 &= (D'V/DR)\omega^1 \wedge \omega^0 \\
\mathrm{d}\omega^1 &= (1/D)(\dot{R}/R - \dot{V}/V)\omega^0 \wedge \omega^1 \\
\mathrm{d}\omega^2 &= (1/D)(\dot{R}/R - \dot{V}/V)\omega^0 \wedge \omega^2 + (V/R)(1/r - V'/V)\omega^1 \wedge \omega^2 \\
\mathrm{d}\omega^3 &= (1/D)(\dot{R}/R - \dot{V}/V)\omega^0 \wedge \omega^3 + (V/R)(1/r - V'/V)\omega^1 \wedge \omega^3 \\
&\quad + (V\cot\theta/Rr)\omega^2 \wedge \omega^3.
\end{aligned} \tag{A3}$$

By using the relation

$$\mathrm{d}\omega^\mu = -\omega^\mu{}_\nu \wedge \omega^\nu \tag{A4}$$

we obtain the six nonvanishing components of the connection one-forms

$$\begin{aligned}
\omega^0{}_1 &= (D'V/DR)\omega^0 + (1/D)(\dot{R}/R - \dot{V}/V)\omega^1, \\
\omega^0{}_2 &= (1/D)(\dot{R}/R - \dot{V}/V)\omega^2, \\
\omega^0{}_3 &= (1/D)(\dot{R}/R - \dot{V}/V)\omega^3, \\
\omega^1{}_2 &= -(V/R)(1/r - V'/V)\omega^2, \\
\omega^1{}_3 &= -(V/R)(1/r - V'/V)\omega^3, \\
\omega^2{}_3 &= -(V\cot\theta/Rr)\omega^3.
\end{aligned} \tag{A5}$$

It is now an easy matter of calculation to find the components of the curvature two-forms

$$\Omega^\mu{}_\nu = \omega^\mu{}_\alpha \wedge \omega^\alpha{}_\nu + \mathrm{d}\omega^\mu{}_\nu, \tag{A6}$$

by using the compatibility equation

$$0 = \mathrm{d}\eta_{\mu\nu} = \omega_{\mu\nu} + \omega_{\nu\mu}. \tag{17}$$

Out of this calculation, one reads the individual components $R^{\mu\varpi}{}_{\alpha\beta}$ of the curvature tensor by using the second Gartan equation

$$\Omega^\mu{}_\nu = \tfrac{1}{2} R^{\mu\nu}{}_{\alpha\beta}\omega^\alpha \wedge \omega^\beta \tag{A8}$$

as an identification scheme. The results are

$$\begin{aligned}
R^{01}{}_{01} &= (1/D)[(1/D)(\dot{R}/R - \dot{V}/V)]^{\cdot} + (1/D^2)(\dot{R}/R - \dot{V}/V)^2 \\
&\quad - (V/R)(D'V/DR)' - (D'V/DR)^2, \\
R^{02}{}_{02} &= (1/D)[(1/D)(\dot{R}/R - \dot{V}/V)]^{\cdot} + (1/D^2)(\dot{R}/R - \dot{V}/V)^2 \\
&\quad - (D'V^2/DR^2)(1/r - V'/V) = R^{03}{}_{03}, \\
R^{12}{}_{12} &= (1/D^2)(\dot{R}/R - \dot{V}/V)^2 - (V/R)[(V/R)(1/r - V'/V)]' \\
&\quad - (V^2/R^2)(1/r - V'/V)^2 = R^{13}{}_{13}, \\
R^{23}{}_{23} &= (1/D^2)(\dot{R}/R - \dot{V}/V)^2 - (V^2/R^2)(1/r - V'/V)^2 + (V/Rr)^2, \\
R^{12}{}_{02} &= (D'V/D^2R)(\dot{R}/R - \dot{V}/V) - (1/D)[(V/R)(1/r - \dot{V}/V)]^{\cdot} \\
&\quad - (V/RD)(1/r - V'/V)(\dot{R}/R - \dot{V}/V) = R^{13}{}_{03}.
\end{aligned} \tag{A9}$$

Thus one can easily determine the nonvanishing components of the Einstein tensor $G_\mu{}^\nu$

$$
\begin{aligned}
G_0{}^0 &= -[R^{12}{}_{12} + R^{13}{}_{13} + R^{23}{}_{23}],\\
G_1{}^1 &= -[R^{02}{}_{02} + R^{03}{}_{03} + R^{23}{}_{23}],\\
G_2{}^2 &= -[R^{01}{}_{01} + R^{03}{}_{03} + R^{13}{}_{13}],\\
G_3{}^3 &= -[R^{01}{}_{01} + R^{02}{}_{02} + R^{12}{}_{12}],\\
G_0{}^1 &= -[R^{12}{}_{02} + R^{13}{}_{03}].
\end{aligned}
\tag{A10}
$$

The result is given in the text. No computer program is needed. In principle, we could also obtain the desired result by using the old computation by Dingle (1933) (see also Tolman 1934b).

References

Barnes, A. 1984 in *Classical General Relativity,* Eds W. B. Bonnor, J. N. Islam & M. A. H. MacCallum, Cambridge Univ. Press, **p**. 15.
Bergmann, O. 1981, *Phys. Lett.,* **82A**, 383.
Bondi, H. 1947, *Mon. Not. R. astr. Soc,* **107**, 410.
Bonnor, W. B. 1972, *Mon. Not. R. astr. Soc,* **159**, 261.
Bonnor, W. B., Sulaiman, A. H., Tomimura, N. 1977, *Gen. Relativ. Gravitation,* **8**, 549.
Collins, C. B. 1979, *Gen. Relativ. Gravitation,* **10**, 925.
Collins, C. B. 1983, *J. math. Phys.,* **24**, 215.
Collins, C. B. 1985, *J. math, phys.,* **26**, 2009.
Collins, C. B., Szafron, D. A. 1979a, *J. math. Phys.,* 20, 2347.
Collins, C. B., Szafron, D. A. 1979b, *J. math. Phys.,* **20**, 2362.
Collins, C. B., Wainwright, J. 1983, *Phys. Rev.,* **D27**, 1209.
Collins, C. B., White, A. J. 1984, *J. math. Phys.,* **25**, 1460.
Datta, B. 1938, *Z. Phys.,* **103**, 546.
Dingle, H. 1933, *Proc. Nat. Acad. Sci. Am.,* **19**, 559.
Dyer, C. C. 1979, *Mon. Not. R. astr. Soc,* **189**, 189.
Eardley, D. M., Smarr, L. 1979, *Phys. Rev.,* **D19**, 2239.
Ehlers, J. 1961, *Abh. Akad. Wiss. und Lit. Mainz, Math. Nat. Kl*, **11**.
Ellis, G. F. R. 1971, in *General Relativity and Cosmology,* Ed. R. K. Sachs,Academic Press, New York, p. 104.
Ellis, G. F. R. 1975, *Q. J. R. astr. Soc,* **16**, 245.
Ellis, G. F. R. 1978, *Gen. Relativ. Gravitation,* **9**, 87.
Ellis, G. F. R. 1980, *Ann. N. Y. Acad. Sci.,* **336**, 130.
Ellis, G. F. R. 1984, in *General Relativity and Gravitation,* Eds B. Bertotti, F. de Felice & A. Pascolini, D. Reidel, Dordrecht, p. 215.
Ellis, G. F. R., Perry, J. J. 1979, *Mon. Not. R: astr. Soc,* **187**, 357.
Ellis, G. F. R., Maartens, R., Nel, S. D. 1978, *Mon. Not. R. astr. Soc,* **184**, 439.
Ellis, G. F. R., Nel, S. D., Maartens, R., Stoeger, W. R., Whitman, A. P. 1985, *Phys. Rep.,* **124**,315.
Goenner, H. F. 1980, in *General Relativity and Gravitation,* Vol. 1, Ed. A. Held, Plenum, New York, p. 441.
Hawking, S. W., Ellis. G. F. R. 1973, in *The Large Scale Structure of SpaceTime,* Cambridge Univ. Press, p. 124.
Hellaby, C, Lake, K. 1984, *Astrophys. J.,* **282**, 1.
Hellaby, G, Lake, K. 1985, *Astrophys. J.,* **290**, 381.
Knutsen, H. 1985, *Physica. Scripta,* **31**, 10.
Koch-Sen, L. 1985, *J. math. Phys.,* **26,** 407.
Korkina, M. P. 1975, *Sov. Astr.* 1b9, 185.
Kramer, D., Stephani, H., MacCallum, M., Herlt, E. 1980, *Exact Solutions of Einstein's Field Equations,* VEB, Berlin.
Krasiński, A. 1980, in *GR* 9, Jena, p. 44. Krasiński, A. 1981, *Gen. Relativ. Gravitation.,* 13, 1021. Krasiński, A. 1982, in *The Birth of the Universe,* Eds J. Audouze & J. Tran Thanh Van, Editions
Frontieres, Gif Sur Yvette, p. 15.

Krasiński, A. 1983a, *Gen. Relativ. Gravitation,* **15,** 673.
Krasiński, A. 1983b, in *GR* 10, Padova, p. 841.
Krasiński, A. 1984a, in *The Big Bang and Georges Lemaitre,* Ed. A. Berger, D. Reidel, Dordrecht, p. 63.
Krasiński, A. 1984b, in *Relativistic Astrophysics and Cosmology,* Eds V. de Sabbata & T. M. Karade, World Scientific, Singapore, p. 45.
Kristian, J., Sachs, R. K. 1966, *Astrophys. J.,* **143**, 379.
Kustaanheimo, P., Qvist, B. 1948, *Comment. Phys. Math. Helsingf.,* **13**, 12.
Lake, K, 1984, *Phys. Rev.,* **D29**, 771.
Landau, L. D., Lifshitz, E. M. 1981, in *Klassische Feldtheorie,* 8 Edn, Akademie Verlag, Berlin, p. 377.
Lemaitre, G. 1933, *Ann. Soc. Scient. de Bruxelles,* **A53**, 51.
Lorenz, D. 1982, *Gen. Relativ. Gravitation.,* **13**, 795.
MacCallum, M. A. H. 1979, in *General Relativity, An Einstein Centenary Survey,* Eds S. W. Hawking & W. Israel, Cambridge Univ. Press, **b**. 533.
MacCallum, M. A. H. 1984, in *Lecture Notes in Physics,* Vol. 205, Eds C. Hoenselaers & W. Dietz, Springer Verlag, Berlin, p. 334.
Martinez, E., Sanz, J. L. 1985, *J. Math. Phys.,* **26**, 785.
Mavrides, S. 1976, *Mon. Not. R. astr. Soc,* **177**, 709.
Miller, B. D. 1976, *Astrophys. J.,* **208**, 275.
Olson, D. W., Silk, J. 1979, *Astrophys. J.,* **233**, 395.
Omer, G. G, Jr. 1949, *Astrophys. J.,* **109**, 164.
Omer, G. C, Jr. 1965, *Proc. nat. Acad. Sci. Am.,* **53**, 1.
Partovi, M. H., Mashhoon, B. M. 1984, *Astrophys. J.,* **276**, 4.
Peebles, P. J. E. 1984, in *The Big Bang and Georges Lemaitre,* Ed. A. Berger, D. Reidel, Dordrecht, p. 23.
Raychaudhuri, A. K. 1979, *Theoretical Cosmology,* Clarendon Press, Oxford.
Silk, J. 1977, *Astr. Astrophys.,* **59**, 53.
Stein-Schabes, J. A. 1985, *Phys. Rev.,* **D31**, 1838.
Stephani, H. 1967a, *Commun. math. Phys.,* **4**, 137.
Stephani, H. 1967b, *Commun. math. Phys.,* **5**, 337.
Stephani, H. 1983, in *Unified Field Theories of more than* 4 *Dimensions,* Eds V. de Sabbata & E. Schmutzer, World Scientific, Singapore, p. 229.
Szafron, D. A., Collins, C. B. 1979, *J. math. Phys.,* **20**, 2354.
Szekeres, P. 1975, *Commun. math. Phys.,* **41**, 55.
Szekeres, P. 1980, in *Lecture Notes in Phys.,* Vol. 124, Ed. E. Edwards, Springer Verlag, Berlin, p. 477.
Tolman, R. C. 1934a, *Proc. nat. Acad. Sci. Am.,* **20**, 169.
Tolman, R. C. 1934b, *Relativity, Thermodynamics and Cosmology,* Clarendon Press, Oxford.
Vajk, J. P. 1969, *J. math. Phys.,* **10**, 1145.
Weinberg, S. 1972, *Gravitation and Cosmology,* Wiley, New York.
White, A. J., Collins, C. B. 1984, *J. math. Phys.,* **25**, 332.
Wesson, P. S. 1975a, *Astrophys. Space Sci,* **32**, 273.
Wesson, P. S. 1975b, *Astrophys. Space Sci.,* **32**, 305.
Wesson, P. S. 1975c, *Astrophys. Space Sci,* **32**, 315.
Wesson, P. S. 1978a, *Astrophys. Lett.,* **19**, 121.
Wesson, P. S. 1978b, *Astr. Astrophys.,* **68**, 131.
Wesson, P. S. 1979, *Astrophys. J.,* **228**, 647.
Zel'dovich, Ya. B.; Grishchuk, L. P. 1984, *Mon. Not. R. astr. Soc,* **207**, 23P.
Zel'dovich, Ya. B., Novikov, I. D. 1971, *Relativistic Astrophysics,* Vol. 1, Univ. Chicago Press.
Zel'dovich, Ya. B., Novikov, I. D. 1983, *Relativistic Astrophysics,* Vol. 2, Univ. Chicago Press.

Note added in proof

The Stephani universes have been also discussed by C. Bona & B. Coll (1985, C. R. Acad. Sc. Paris, **301,** Série I, n° 11, 613).

J. Astrophys. Astr. (1986), **7,** 171–194

Spectrophotometric Studies of CQ Cephei

B. S. Shylaja *Indian Institute of Astrophysics, Bangalore 560034*

Received 1986 *January* 22; *accepted* 1986 *May* 12

Abstract. Spectrophotometric and spectroscopic observations of CQ Cep—the shortest-period binary with WN component—are presented. Excepting the N V λ4603, the fluxes of all other emission lines show enhancement at minima. They can be explained by the Roche surfaces that take into account the strong wind of the WN7 component. Various radial velocity curves for emission and absorption give different orbital solutions with a general positive shift of γ axes. Although N IV λ4058 represents the true motion of the WN7 component, its flux variations are influenced by geometric effects. There is no signature of the companion. The extent of the atmosphere of CQ Cephei appears larger than in V444Cyg, another eclipsing binary with a Wolf-Rayet component.

Key words: Wolf-Rayet binaries—stars, spectrophotometry—stars, individual

1. Introduction

CQ Cep is an eclipsing binary classified as (WN7 + O) (van der Hucht *et al.* 1981) with a period of 1.64 d. The light curve resembles that of the contact W UMa systems. Broadband photometry in the optical region made by various investigators (see references in Stickland *et al.* 1984) suggests variability of orbital period and of the shape of the light curve.

An interesting finding by Hiltner (1950) was the behaviour of He II λ4686, whose minima occurred at phases 0.25 and 0.75 and the intensities increased at phases 0.0 and 0.5. This behaviour was further investigated by Bappu 1951a, b, 1952) and Bappu & Sinvhal (1955, 1959) who pointed out that other emission lines like He II λ5410 and λ 4860 also followed the pattern of λ4686.

Hiltner (1950) attempted to explain the behaviour of the emission line of He II λ4686 by assuming that although the nitrogen lines are produced more or less symmetrically, the He II lines are produced throughout a common envelope surrounding both the stars. Khaliullin (1973) obtained data in four wavelength bands (two emissions and two continua) and attempted to model the variation incorporating an assumed variation of the absorption due to secondary. However, no evidence of such absorptions was found subsequently by Stickland *et al*. (1984), although Niemela (1980) found it for He I λ3888 line.

In a recent study of the variation of the radial velocities and light curves, Leung, Moffat & Seggewiss (1983) arrived at a mass ratio of 0.75 for the components though the radial velocities were disparate. The smaller amplitude of the λ4686 radial-velocity

curve has been related to the ejection of hot λ4686-emitting material with a strong radial velocity component directed towards the observer at phase 0.8.

The most recent and exhaustive study of CQ Cep is by Stickland *et al*. (1984), who analysed the IUE data, UBVJKL photometry as well as the radial-velocity measurements in the optical from Hiltner's (1950) plates. Stickland *et al.* obtained a total of 18 continuum light curves covering the wavelength range 0.13–0.3 μm. Their conclusions may be summarized: (1) The light-curve solutions indicate that half the amplitude of light variation is produced by ellipticity effects and the other half by geometric effects. (2) None of the spectral features is an indicator of the companion's presence or motion. (3) The companion does not modify the overall expected variation of excitation velocity characteristics, and in this respect the combined spectrum resembles any other single WN 7 atmosphere. (4) The luminosity ratio implied by light curves is not consistent with allowable radii and separation values unless their masses and temperatures are considerably raised.

The past investigations provide information on the variations of fluxes in the optical region, as a function of phase, only for continuum at $\lambda\lambda$3550, 5300, 4790, 6300 and the emission lines He II λ4686 and λ6562. Our main interest in observing this system was to obtain light curves in all major emission lines in the optical region systematically. Such data combined with existing spectroscopic information in *UV* and optical is likely to give a better insight and may lead us to unravel at least some of the mysteries of this system. Section 2 gives the details of observations and Section 3 the details of light curves and radial velocities. Section 4 discusses the correlation between light and velocity curves for each line studied. A possible model is discussed in Section 5 in terms of the line variations, light-curve solutions and *IR* and *UV* studies. Finally, in Section 6 the results are compared with another eclipsing system with a Wolf-Rayet component—V444 Cyg.

2. Observations

2.1 *Spectrophotometry*

CQ Cep was observed with the automated spectrum scanner (Bappu 1977) with a 600 lines mm^{-1} grating blazed at 7600 Å, at the Cassegrain focus of the 102 cm reflector of Vainu Bappu Observatory, Kavalur, during 1980–84. The blue region ($\lambda\lambda$3800–5800) was covered in the second order with a channel spacing of 5 Å. The red region ($\lambda\lambda$ 5800–6800) was covered in the first order with a channel spacing of 10 Å. The exit slit was 40 μm in width which corresponds to a resolution of 10 Å in the second order and 20 Å in the first order. The spectroscopic standards from the lists of Hayes (1970) and Breger (1976) were observed every night to derive the extinction coefficients.

2.2 *Reddening Corrections*

The affiliation of CQ Cep to the Cep OB 1 association has been confirmed by Stickland *et al*. (1984) from the observed strengths of interstellar lines in the *UV* spectrum obtained at high resolution. Thus, CQ Cep is at a distance of more than 3 kpc from us and, therefore, its energy distribution will be affected by interstellar reddening. We

determined the reddening corrections by comparing it with 10 Lac (O7 V)—whose reddening corrections are known (Hua, Woo & Nguyen 1982)—at wavelengths selected so as to be free of emission-line contaminations. Similar corrections have been derived by Kuhi (1966) and Hua, Woo & Nguyen (1982). Stickland *et al*. (1984) derived the reddening corrections from the $\lambda 2200$ depression, using Seaton's curve for reddening. The dereddened energy distributions are shown in Fig. 1, where samples at three different phases are plotted. It may be seen that our values agree well with Stickland *et al.* (1984).

2.3 *Spectroscopic Studies*

The spectrograms obtained with Mt Wilson 60 inch telescope by late Prof. Bappu in 1951–52 were used in this study. The data consist of (1) the blue spectra on baked IIa-O plates covering $\lambda\lambda 4000$–5000 at a dispersion of ~ 75 Å mm^{-1} at $\lambda 4340$, and (2) the red spectra on 103a-F plates covering $\lambda\lambda 5100$–6700 at a dispersion of ~ 160 Å mm^{-1} at $\lambda 5500$. Relative intensity values of the calibration strips were not available. However, the intensity profiles for a few lines (He II $\lambda\lambda 4686$, 4860, 5410, N V $\lambda 4058$) were provided by Bappu. Radial velocities were already available for some lines (Bappu & Viswanadham 1977; Giridhar 1978). The lines He II $\lambda 4860$, $\lambda 6562$, N III $\lambda 4640$, N V $\lambda 4603$ and He I $\lambda 5876$ and $\lambda 4471$ were measured afresh. For N v $\lambda 4603$, it was possible to measure both emission and absorption velocities, whereas for He I $\lambda 5876$, it was possible to measure only the absorption velocities.

3. Results

3.1 *Light Curves*

From the observed energy distributions at various phases, it was possible to construct the monochromatic light curves, as well as to derive the orbital variations of emission fluxes. Based on broadband photometry from various investigators, Stickland *et al*. (1984) and Walker *et al.* (1983) have analyzed the behaviour of the orbital period over the last few decades. It appears that the period has remained constant during the last 45 years. Khaliullin (1973) derived a mean period combining Hiltner's data with his own, and the ephemeris derived by him is similar to that of Semeniuk (1968). We have adopted the ephemeris

$$T_{\min} = 24432456.668 + 1.641246\, E$$

from Semeniuk (1968) for our studies.

Eight wavelengths were selected to be free of line emission and the light curves were constructed. These are shown in Fig. 2. They all generally resemble the $\lambda 5300$ light curve of Hiltner.

The photometric errors varied from season to season. In 1982, the error at quadratures and conjunctions never exceeded 0.05 mag. In 1983 and 1984 the errors were slightly higher – 0.06 mag at quadratures and 0.08 mag at conjunction. On some occasions, when the error exceeded 0.1 mag, the observations were not included in the light curve.

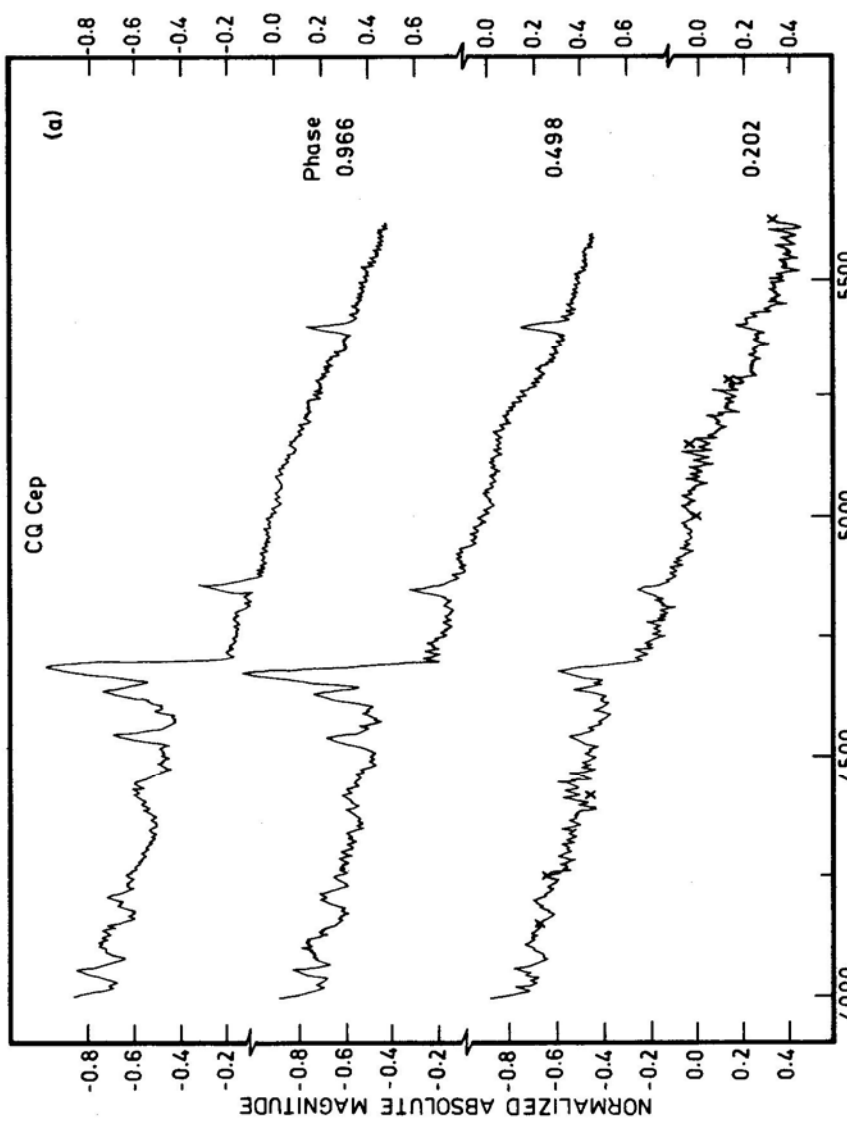

Figure 1. Sample scans of (a) blue region and (b) red region. Crosses correspond to observations of Stickland *et al.* 1984.

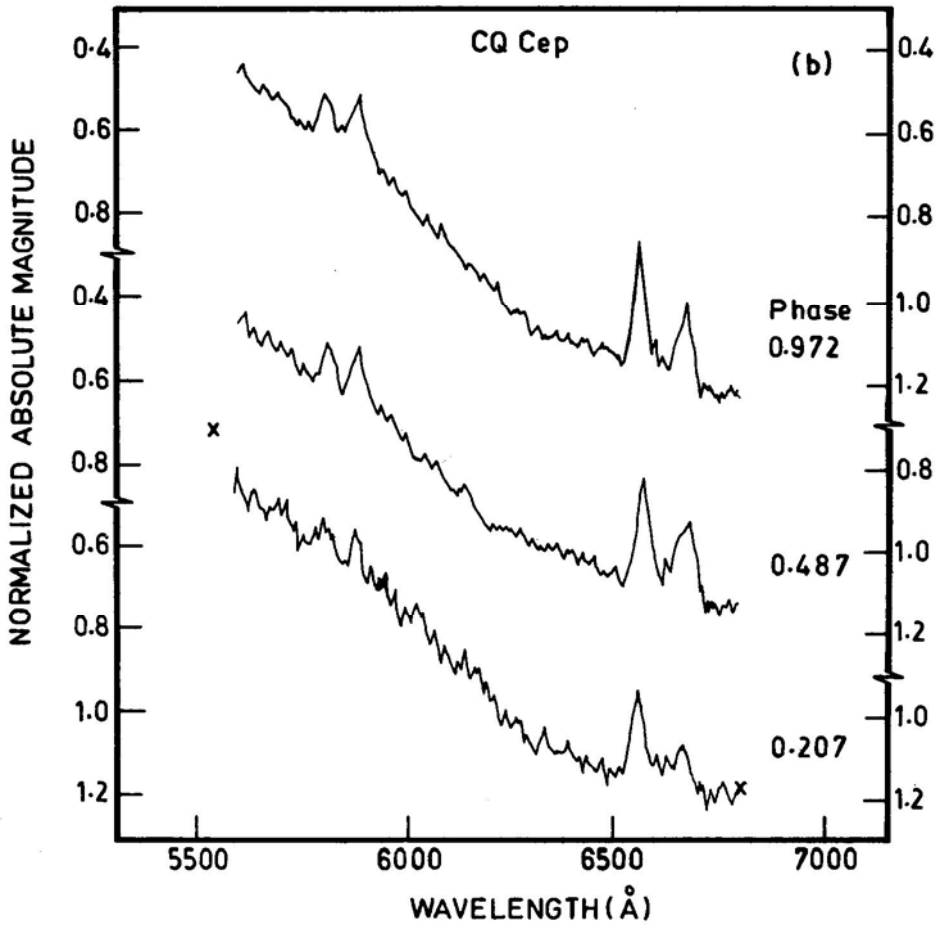

Figure 1. Continued.

3.2 *Emission Line Fluxes*

The fluxes of some lines of He I, He II, N III, N IV, N V and C IV were estimated using the spectrophotometric data. Many lines appear as blends—the most complicated region being $\lambda\lambda$4600–4700. Nv λ4603 is associated with an absorption throughout the orbit. The emissions of N III λ4640 and He II λ4686 follow immediately and are very strong. In our spectrophotometric scans it was barely possible to resolve these three emissions (at a resolution of 10 Å). The profile was decomposed by hand assuming approximately gaussian components. The continuum was fixed at $\lambda\lambda$4460 and 4790. The estimated errors indicated in the flux plots (Figs 3–7) include the errors due to the decomposition procedure as well as the photometric errors. Strong lines like the N IV λ4058 and He II λ4860 have least errors because they are unblended. Intrinsically weak emissions like C IV λ5808 show larger errors.

It was also found that the errors were larger at phases near 0.25 and 0.75. The scan in general looked more noisy probably because the line strengths also diminished at these

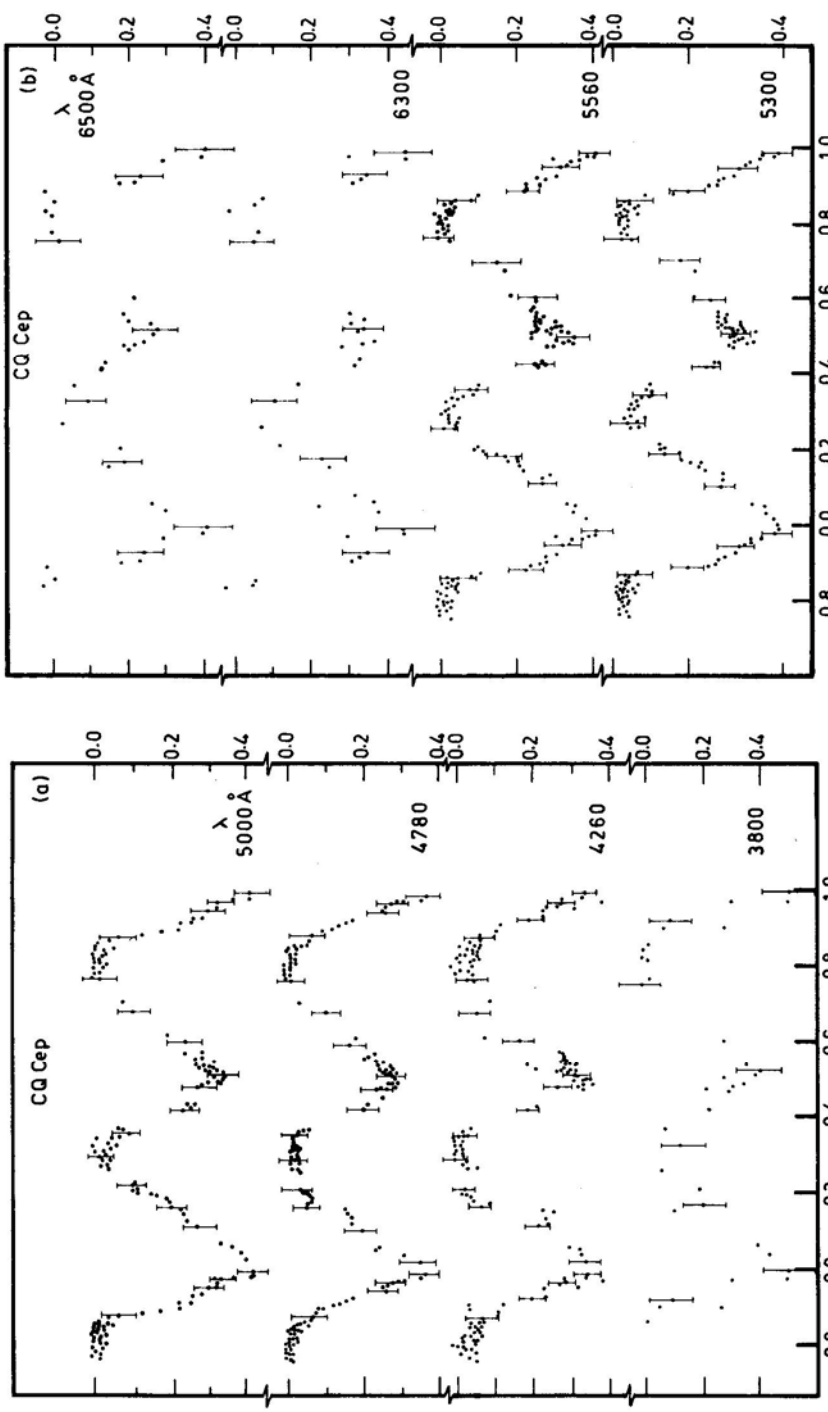

Figure 2. Monochromatic light curves at eight wavelengths free of emission line effects.

phases. At phases close to 0.75 it was not possible to measure the emission fluxes at times because the emission was buried in the continuum noise. Table 1 lists the measured fluxes at different phases.

3.2 *Radial-Velocity Curves*

The radial velocities were measured using the Abbe comparator. The central portion of the emission line was chosen for the measurement. The errors are large (40–60 km s^{-1}) since the features are broad. The radial velocity curves were solved for the orbit by Lehmann-Filhes method. All solutions (including the ones obtained by others) are listed in Table 2. The individual velocity curves appear with the flux plots (Figs 3 to 7). It appears reasonable to assume that the measures of Stickland *et al.* (1984) and Leung, Moffat & Seggewiss (1983) are more accurate by virtue of the method of measurement and solution.

4. Correlation between light and velocity curves

4.1 *Helium lines*

Among the lines of He II studied here ($\lambda\lambda$4686, 4861, 5410, 6562), λ4686 is the strongest. Fig. 3(a) shows the measured line intensities and fluxes, together with the radial velocity measurements of Bappu & Viswanadham (1977), who derived an orbital solution with eccentricity e = 0.31 and the velocity for the centre of mass as γ = 118 kms^{-1}. Bappu & Viswanadham noted that the line profiles were narrow and sharp at minima and broad and rounded at quadratures. Fig. 3(a) clearly shows the enhancement of flux and intensity near phases 0.0 and 0.5, in conformity with the earlier studies (Hiltner 1950; Khaliullin 1973; Bappu & Viswanadham 1977). The two maxima are of unequal magnitudes, the one closer to phase 0.0 being stronger. Also the maxima appear somewhat earlier than phases 0.0 and 0.5. Similar shift was also noticed by Hiltner (1950), but in the opposite direction. The continuum light curves (Fig. 2) show that the falling edges of the minima are not smooth. Similar effect is probably reflected in the flux measures, as was seen earlier by Walker *et al.* (1983).

The intensities, radial velocities and fluxes of He II λ4860 are shown in Fig. 3(b). Although the behaviour is similar to λ4686 in general, it may be seen that the fluxes at phases 0.0 and 0.5 are of almost similar magnitude and they do not show sudden increase like the latter. Also, the variation is smoother and the fluxes at 0.75 are lower compared to those at 0.25. The amplitude of the radial-velocity curve is slightly larger than that of λ4686 and the orbital solution yields e = 0.35 and γ = 196 km s^{-1}. The line profiles given by Bappu & Viswanadham (1977) show that the violet absorption cuts into the emission wing at some phases especially after the secondary minimum. To study this more clearly, all the plates were checked for the behaviour of this line. It appears that the structure of λ4860 is complex and variable, as noticed by Hiltner (1950). The effect of the absorption on the violet wing is more prominent at phases close to 0.75. There appears to be another absorption component which moves with the emission. Since this component is weak at all phases, it was not possible to measure it precisely.

Table 1. Emission fluxes of CQ Cep.

JD 2440000+	Phase	N IV 4058 $\times 10^{-9}$	N V 4603 10^{-11}	N III 4640 10^{-9}	He II 4686 10^{-9}	He II 4860 10^{-9}	He II 5410 10^{-9}	C IV 5808 10^{-10}	He I 5876 10^{-10}	He II 6562 10^{-10}	He I 6678 10^{-10}	Blend 4100 10^{-9}	Blend 4540 10^{-9}	Blend 4200 10^{-9}
4541.109	0.972	110.0	25.0	204.0	504.0	203.0	133.0	68.0	97.0	182.0	95.0	—	—	—
4542.141	0.601	108.0	72.0	103.0	384.0	103.0	114.0	102.0	180.0	140.0	90.0	—	—	—
5253.180	0.833	68.0	92.0	24.0	571.0	24.0	35.0	18.0	96.0	117.0	62.0	246.0	163.0	114.0
5253.196	0.842	165.0	102.0	58.0	410.0	58.0	—	—	—	—	—	219.0	199.0	184.0
5253.209	0.850	75.0	78.0	88.0	522.0	88.0	—	—	—	—	—	282.0	160.0	93.0
5253.219	0.857	56.0	83.0	127.0	478.0	127.0	—	—	—	—	—	163.0	184.0	59.0
5253.231	0.863	63.0	76.0	84.0	431.0	84.0	—	—	—	—	—	180.0	136.0	84.0
5253.244	0.871	72.0	72.0	87.0	484.0	87.0	—	—	—	—	—	170.0	207.0	63.0
5253.257	0.879	74.0	68.0	75.0	490.0	75.0	—	—	—	—	—	158.0	190.0	110.0
5253.272	0.888	85.0	66.0	74.0	625.0	74.0	—	—	—	—	—	167.0	177.0	148.0
5253.286	0.897	146.0	58.0	77.0	587.0	77.0	—	—	—	—	—	234.0	274.0	79.0
5253.299	0.905	175.0	44.0	147.0	480.0	147.0	92.0	65.0	132.0	190.0	72.0	196.0	153.0	98.0
5254.091	0.917	84.0	53.0	162.0	432.0	162.0	—	—	—	—	—	137.0	140.0	87.0
5254.144	0.420	160.0	78.0	87.0	375.0	87.0	136.0	88.0	99.0	95.0	90.0	275.0	150.0	200.0
5254.158	0.429	208.0	84.0	97.0	470.0	97.0	104.0	102.0	147.0	189.0	119.0	257.0	109.0	158.0
5254.239	0.478	180.0	68.0	106.0	468.0	106.0	127.0	90.0	190.0	219.0	135.0	266.0	179.0	201.0
5254.254	0.487	182.0	42.0	92.0	416.0	92.0	141.0	77.0	175.0	199.0	115.0	256.0	132.0	125.0
5254.272	0.498	180.0	59.0	115.0	407.0	115.0	132.0	—	—	—	—	177.0	176.0	96.0
5256.089	0.526	132.0	75.0	83.0	440.0	83.0	—	—	—	—	—	196.0	230.0	83.0
5268.080	0.911	70.0	42.0	151.0	535.0	151.0	—	92.0	87.0	150.0	75.0	115.0	209.0	52.0
5268.106	0.926	115.0	48.0	158.0	480.0	158.0	106.0	109.0	125.0	205.0	102.0	209.0	239.0	50.0
5269.107	0.537	162.0	80.0	114.0	490.0	114.0	77.0	110.0	185.0	225.0	125.0	286.0	198.0	79.0
5314.096	0.948	124.0	42.0	162.0	428.0	162.0	—	—	—	—	—	163.0	60.0	42.0
5314.106	0.954	72.0	47.0	133.0	323.0	133.0	—	—	—	—	—	202.0	80.0	205.0
5314.116	0.960	94.0	38.0	180.0	487.0	180.0	—	—	—	—	—	192.0	224.0	220.0
5314.125	0.966	98.0	25.0	184.0	416.0	184.0	—	—	—	—	—	134.0	168.0	207.0
5314.135	0.972	140.0	22.0	196.0	402.0	196.0	—	—	—	—	—	150.0	177.0	187.0
5314.147	0.979	132.0	18.0	177.0	410.0	177.0	157.0	122.0	170.0	240.0	135.0	201.0	104.0	187.0
5314.158	0.986	149.0	22.0	170.0	412.0	170.0	147.0	110.0	191.0	235.0	140.0	165.0	94.0	137.0
5649.171	0.107	90.0	62.0	150.0	332.0	50.0	—	—	—	—	—	201.0	134.0	125.0

Table 1. Continued.

JD 2440000+	Phase	N IV 4058 $\times 10^{-9}$	N V 4603 10^{-11}	N III 4640 10^{-9}	He II 4686 10^{-9}	He II 4860 10^{-9}	He II 5410 10^{-9}	C IV 5808 10^{-10}	He I 5876 10^{-10}	He II 6562 10^{-10}	He I 6678 10^{-10}	Blend 4100 10^{-9}	Blend 4540 10^{-9}	Blend 4200 10^{-9}
5649.217	0.135	92.0	72.0	—	330.0	—	—	—	—	—	—	97.0	83.0	106.0
5649.235	0.146	72.0	106.0	—	260.0	—	—	—	—	—	—	102.0	110.0	77.0
5649.254	0.157	113.0	115.0	—	290.0	—	35.0	24.0	82.0	180.0	85.0	102.0	110.0	97.0
5651.071	0.264	70.0	78.0	139.0	320.0	39.0	17.0	37.0	51.0	81.0	52.0	75.9	99.0	62.0
5651.091	0.277	98.0	52.0	125.0	267.0	48.0	27.0	—	—	—	—	50.0	38.0	39.0
5651.100	0.283	68.0	76.0	113.0	335.0	53.0	—	—	—	—	—	68.0	55.0	49.0
5651.120	0.294	82.0	64.0	108.0	296.0	58.0	—	—	—	—	—	101.0	75.0	65.0
5651.129	0.300	92.0	78.0	92.0	252.0	62.0	—	—	—	—	—	92.0	115.0	101.0
5651.139	0.306	65.0	82.0	131.0	277.0	51.0	—	—	—	—	—	106.0	92.0	82.0
5651.149	0.312	81.0	52.0	78.0	311.0	58.0	—	—	—	—	—	76.0	65.0	66.0
5651.158	0.318	115.0	106.0	106.0	340.0	60.0	—	—	—	—	—	96.0	110.0	45.0
5651.168	0.324	65.0	78.0	85.0	357.0	65.0	—	—	—	—	—	87.0	88.0	62.0
5651.194	0.339	95.0	92.0	90.0	290.0	50.0	—	—	—	—	—	90.0	117.0	71.0
5651.203	0.345	126.0	65.0	84.0	326.0	64.0	—	—	—	—	—	128.0	95.0	101.0
5651.213	0.351	103.0	60.0	120.0	300.0	60.0	35.0	—	—	—	—	140.0	140.0	101.0
5651.222	0.357	115.0	72.0	109.0	342.0	109.0	—	—	—	—	—	—	—	—
5651.232	0.363	142.0	114.0	175.0	380.0	115.0	—	—	—	—	—	155.0	170.0	115.0
5651.242	0.369	108.0	82.0	120.0	357.0	120.0	119.0	77.0	123.0	172.0	70.0	—	—	—
5660.093	0.124	80.0	102.0	—	295.0	—	—	—	—	—	—	114.0	106.0	82.0
5660.093	0.762	87.0	91.0	55.0	365.0	55.0	18.0	40.0	85.0	70.0	45.0	69.0	75.0	97.0
5660.102	0.767	74.0	107.0	—	260.0	—	—	—	—	—	—	32.0	44.0	86.0
5660.123	0.780	50.0	88.0	64.0	297.0	64.0	—	—	—	—	—	42.0	49.0	73.0
5660.134	0.787	—	102.0	—	312.0	—	—	—	—	—	—	36.0	38.0	66.0
5660.161	0.803	—	110.0	52.0	300.0	52.0	—	—	—	—	—	—	—	—
5660.171	0.809	48.0	78.0	—	275.0	—	—	—	—	—	—	75.0	66.0	109.0
5660.181	0.815	60.0	103.0	—	372.0	—	—	—	—	—	—	86.0	69.0	85.0
5660.191	0.821	50.0	68.0	—	354.0	—	—	—	—	—	—	92.0	98.0	136.0
5660.202	0.828	55.0	97.0	32.0	302.0	32.0	—	—	—	—	—	—	—	—
5660.212	0.834	75.0	92.0	—	302.0	—	—	—	—	—	—	108.0	103.0	77.0
5660.221	0.840	96.0	75.0	—	296.0	—	—	—	—	—	—	99.0	124.0	118.0

Table 1. Continued.

JD 2440000+	Phase	N IV 4058 $\times 10^{-9}$	N V 4603 10^{-11}	N III 4640 10^{-9}	He II 4686 10^{-9}	He II 4860 10^{-9}	He II 5410 10^{-9}	C IV 5808 10^{-10}	He I 5876 10^{-10}	He II 6562 10^{-10}	He I 6678 10^{-10}	Blend 4100 10^{-9}	Blend 4540 10^{-9}	Blend 4200 10^{-9}
5660.231	0.846	88.0	106.0	28.0	365.0	28.0	22.0	28.0	62.0	68.0	60.0	115.0	110.0	185.0
5676.092	0.510	206.0	68.0	158.0	455.0	148.0	109.0	105.0	198.0	192.0	120.0	211.0	201.0	176.0
5676.104	0.517	173.0	62.0	152.0	407.0	152.0	—	—	—	—	—	—	—	—
5676.114	0.523	154.0	78.0	120.0	350.0	120.0	—	—	—	—	—	—	—	—
5676.124	0.530	192.0	51.0	135.0	422.0	105.0	—	—	—	—	—	231.0	176.0	128.0
5676.135	0.536	180.0	72.0	101.0	464.0	101.0	—	—	—	—	—	—	—	—
5676.146	0.543	193.0	69.0	102.0	401.0	102.0	—	—	—	—	—	—	—	—
5676.156	0.549	190.0	101.0	132.0	355.0	132.0	—	—	—	—	—	—	—	—
5676.166	0.555	180.0	91.0	106.0	388.0	106.0	—	—	—	—	—	210.0	162.0	86.0
5676.176	0.561	146.0	81.0	83.0	418.0	83.0	73.0	125.0	152.0	210.0	105.0	—	—	—
5676.187	0.568	161.0	84.0	94.0	382.0	94.0	—	—	—	—	—	—	—	—
5945.535	0.675	95.0	102.0	—	412.0	—	—	—	—	—	—	41.0	109.0	31.0
5945.585	0.705	122.0	83.0	—	395.0	—	—	—	—	—	—	35.0	70.0	22.0
5963.252	0.476	192.0	42.0	—	434.0	165.0	120.0	121.0	132.0	180.0	117.0	152.0	178.0	126.0
5963.257	0.478	251.0	51.0	158.0	421.0	153.0	—	—	—	—	—	210.0	207.0	185.0
5963.317	0.514	251.0	96.0	147.0	350.0	147.0	—	—	—	—	—	177.0	155.0	214.0
5963.326	0.519	176.0	115.0	52.0	380.0	122.0	—	120.0	187.0	220.0	115.0	245.0	215.0	190.0
5963.339	0.527	205.0	98.0	135.0	325.0	135.0	—	—	—	—	—	—	—	—
5963.352	0.535	193.0	90.0	110.0	360.0	110.0	—	—	—	—	—	—	—	—
5963.360	0.540	220.0	90.0	120.0	385.0	98.0	59.0	120.0	175.0	182.0	110.0	135.0	79.0	58.0
5964.144	0.018	190.0	28.0	95.0	320.0	141.0	62.0	—	—	—	—	212.0	198.0	150.0
5964.176	0.038	178.0	58.0	99.0	380.0	108.0	75.0	99.0	160.0	227.0	122.0	201.0	205.0	188.0
5964.202	0.053	162.0	52.0	102.0	360.0	122.0	102.0	—	—	—	—	—	—	—
5964.211	0.059	195.0	85.0	120.0	375.0	92.0	60.0	90.0	155.0	215.0	104.0	176.0	192.0	140.0
6037.113	0.477	—	—	—	—	—	—	101.0	120.0	207.0	99.0	—	—	—
6047.186	0.610	116.0	68.0	—	388.0	—	—	—	—	—	—	110.0	151.0	60.0
6048.092	0.167	—	—	—	—	—	—	35.0	105.0	152.0	57.0	—	—	—
6048.158	0.207	—	—	—	—	—	—	31.0	80.0	122.0	45.0	—	—	—

Table 2. Orbital solution from radial velocity curves.

Line	γ kms^{-1}	K kms^{-1}	e	ω deg	Ref.
He II 4686	117.5	148.2	0.309	323	1
	133.8	164.0	0.26	356.4	2
He II 4860	196.0 ± 11.4	221.9 ± 12.2	0.35 ± 0.02	286 ± 18	6
	198.2	235.8	0.36		2
He II 5411	176.0	230.1	0.095	335	3
He II 6562	206.0 ± 10.2	212.0 ± 12.8	0.23 ± 0.02	331 ± 18	6
N III 4640	-114.0 ± 8.2	127.8 ± 10.4	0.014 ± 0.011	316 ± 20	6
	-114.3	127.0	0.0		2
N IV 4058	-60.8	312.7	0.035	96.7	1
	-53.4	297.4	0.0		2
	-60	310			4
	-85	285			5
N V 4603 em	159.6 ± 7.2	286.0 ± 6.4	0.041 ± 0.017	295 ± 17	6
	153	280			4
N V 4603 abs	-216.1 ± 5.8	307.5 ± 7.3	0.035 ± 0.018	298 ± 18	6
	-220	299			4

References
1. Bappu & Viswanadham (1977).
2. Stickland *et al.* (1984).
3. Giridhar (1978).
4. Leung Moffat & Seggewiss (1983).
5. Niemela (1980).
6. This work.

Fig. 3(c) shows the fluxes and intensities of He II λ5410, and also radial velocities from Giridhar (1978). The orbital solution of Giridhar yields e = 0.1 and γ= 176 kms $^{-1}$. Giridhar found the line profiles to be generally symmetrical, with an indication of a violet absorption edge after the secondary minimum. The enhancement of flux close to phases 0.0 and 0.5 is smooth, as are the intensity measures.

The radial velocities and flux measurements of He II λ6562 are shown in Fig. 3(d). The orbital solution yields e = 0.23 and γ= 206 km s^{-1} . The density tracings of this region of some spectra are shown in Fig. 4(a), which clearly show the variation of the structure of the line. Like λ4860, this also shows violet absorption effects soon after the secondary minimum. Such an effect appears to be present soon after primary minimum also, but data with better resolution are needed to ascertain this.

Among the He I lines, it was possible to study λ5876 and λ6678. Fig. 4(a) includes the λ6678 region as well. It may be seen that the line profile varies throughout the cycle, making the radial velocity measurements very difficult. Sometimes it appears as though the line is split into two components. Fig. 4(b) shows the structure of λ5876 line. It may be noticed that the violet absorption edge is very strong and appears throughout the orbital cycle, whereas the emissions are not very sharp. Thus it was possible to measure only the absorption velocities. The radial velocity curve shows a large scatter making it difficult to find any orbital solution. The behaviour of flux measures is similar to the other helium lines, but with a smaller amplitude of variations.

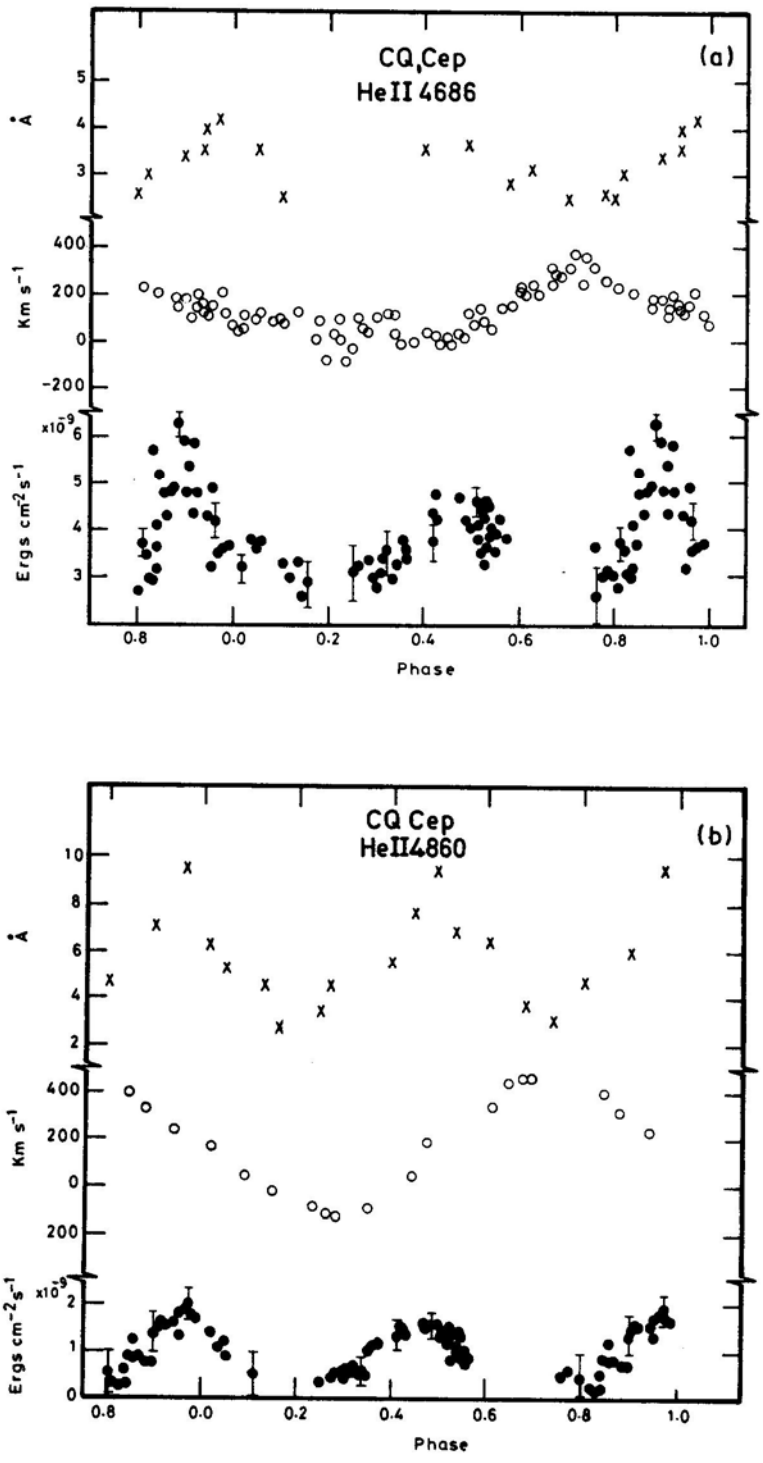

Figure 3. Measured intensities (×), radial velocities O and fluxes of He II lines: (a) λ4686, (b) λ4860, (c) λ5410, and (d) λ6562.

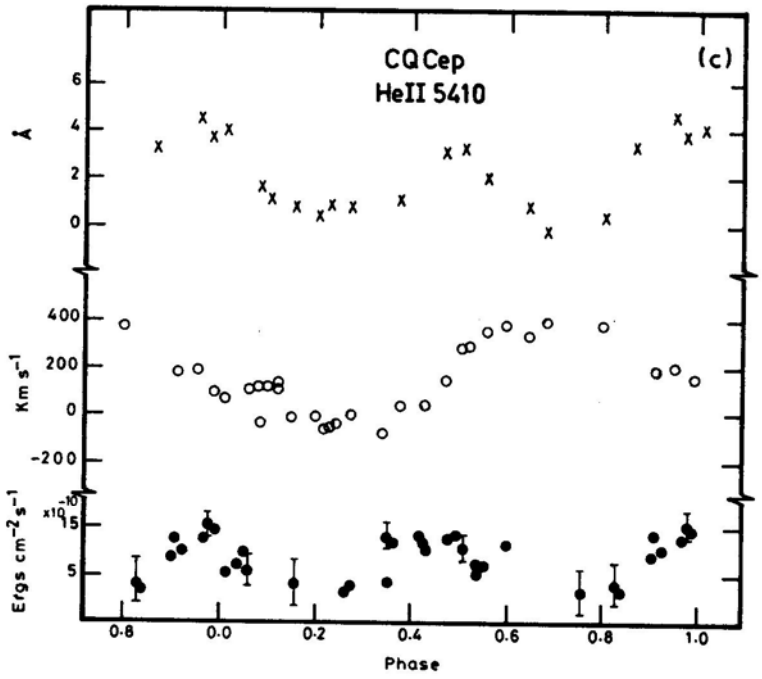

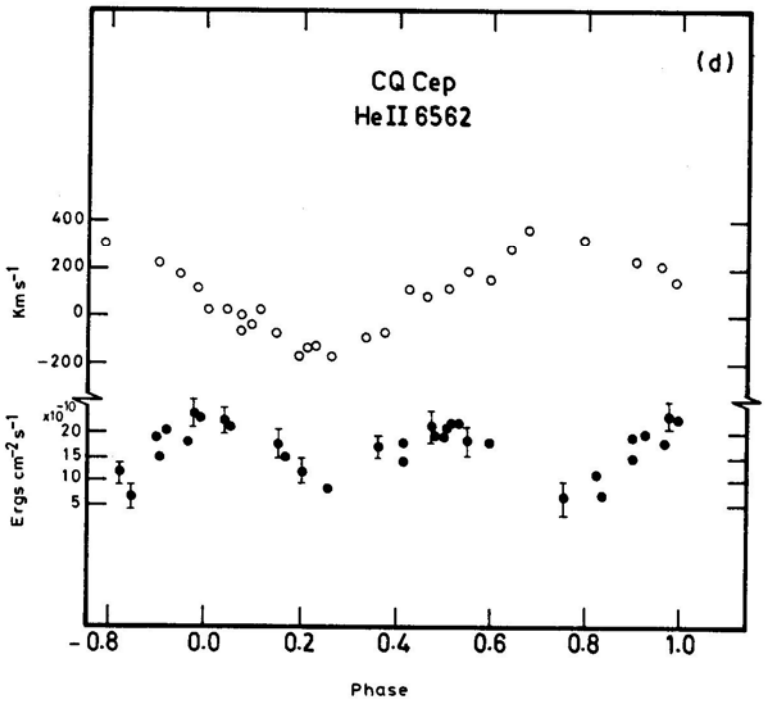

Figure 3. Continued

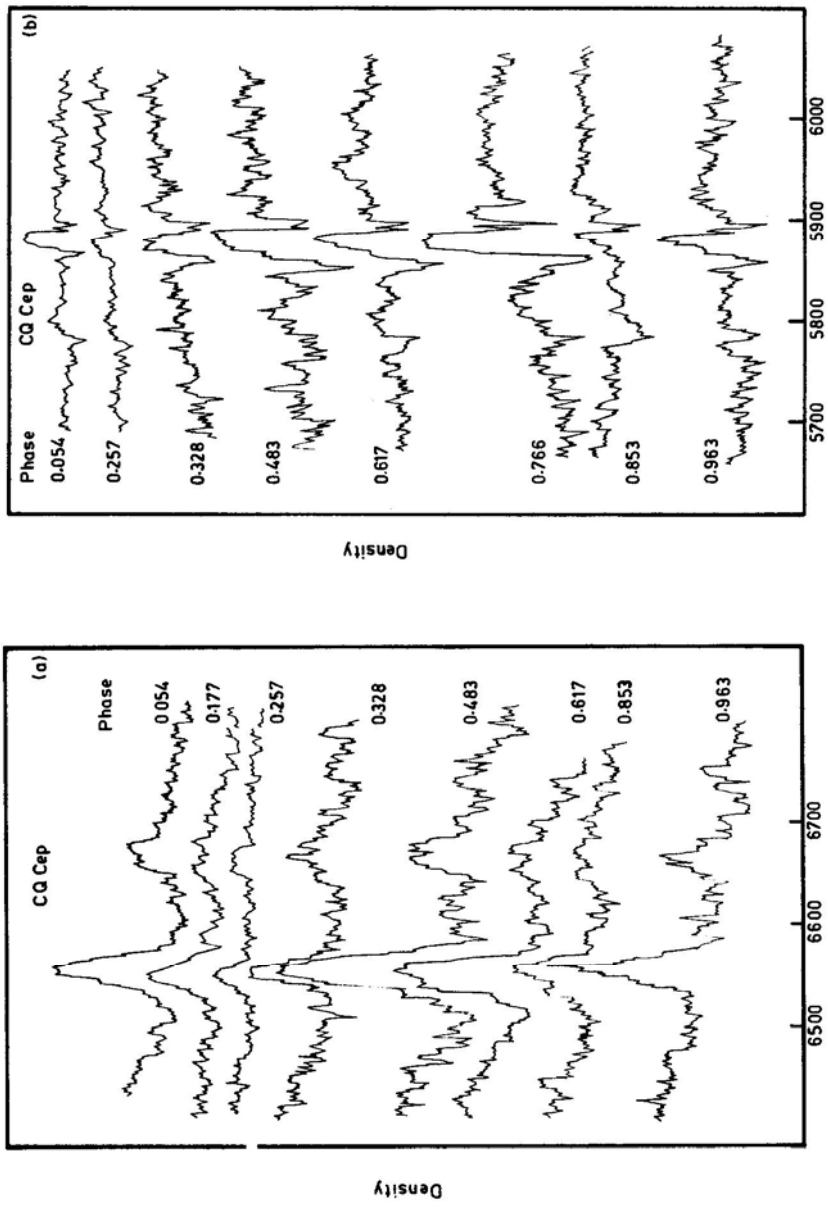

Figure 4. Density tracings at various phases showing the variation in the structure of (a) He II λ6562 and He I λ6678, and (b) He I λ5876.

4.2 *Nitrogen Lines*

The nitrogen lines that are studied are N III λ4640, N IV λ4O58, and N V λ4603. The N III line at λ4640 is affected at both the wings by He II λ4686 and N V λ4603. Thus the estimated flux is not expected to be very accurate. Allowing for these errors in flux measures, it may be seen from Fig. 5 that the flux increases at phases 0.0 and 0.5 and the total amplitude of variation is small. Bappu (1973), based on high dispersion spectral studies, has pointed out that this broad emission is probably a blend of more than 3 lines. The radial velocities shown in Fig. 5 were measured for a mean centre of the emission. It appears that the amplitude is quite small compared to radial velocity curves of other lines. An orbital solution gives almost circular orbit with e = 0.014 and γ= –114 km s^{-1}. It may be noticed that this γ value is different compared to other emission lines.

Bappu & Viswanadham (1977) emphasized that N IV λ4058 is the only line that predicts the true motion of the WN component. They derived the orbital solution with e = 0.1 and γ = – 62 km s^{-1}. They have shown that the profile is not affected by absorptions and is generally symmetrical. Fig. 6 shows the measured line fluxes and intensities, showing enhancement at minima.

Now we turn to N V λ4603, which has a stable profile and exhibits a violet absorption through the orbital phase. It was possible to derive the radial velocity curves for both emission and absorption components. These curves and the flux measures are shown in Fig. 7. The flux measures are probably affected by the violet wing of strong N III line at λ4640, but only high dispersion spectra can ascertain this. The line fluxes above the continuum only are measured, and unlike the variation of other emissions

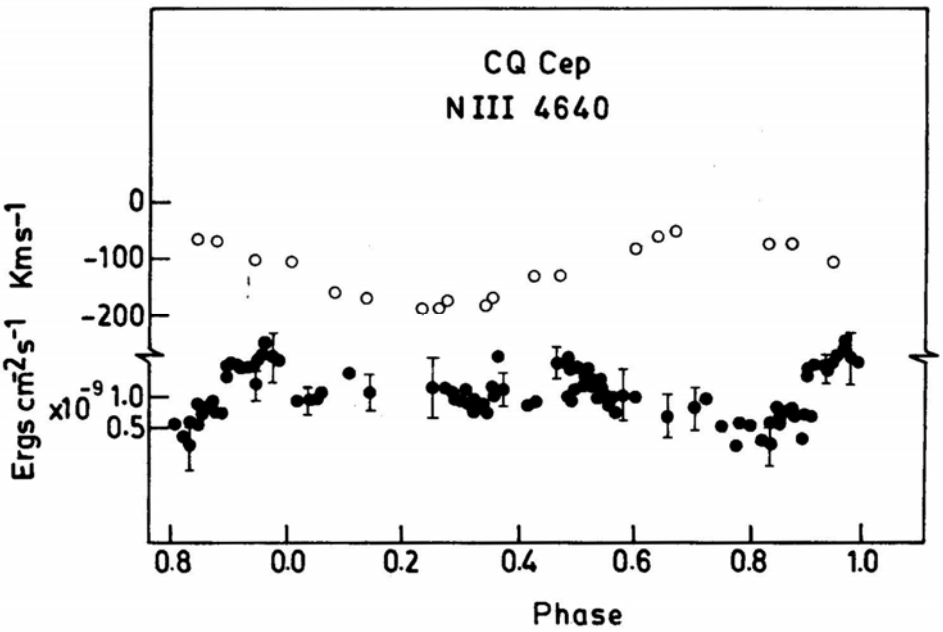

Figure 5. Radial velocity and flux measures of N III λ4640.

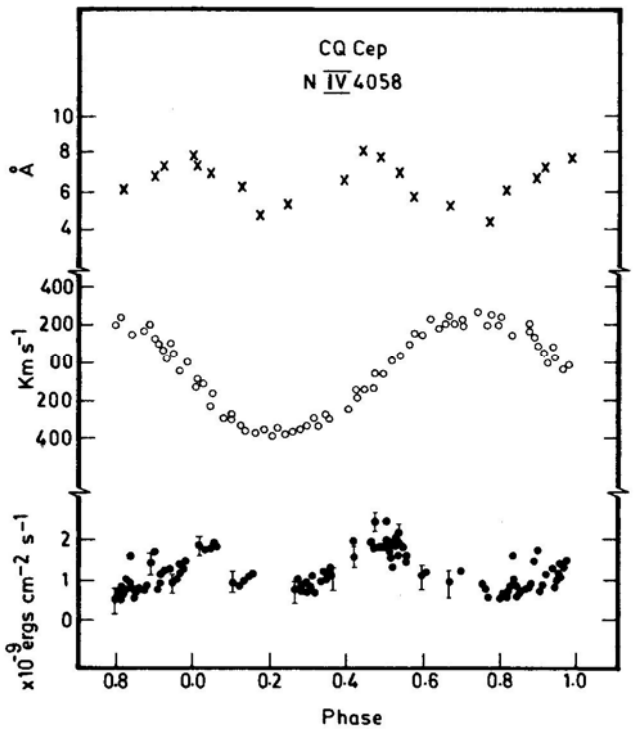

Figure 6. Intensities, radial velocities and flux measures of N IV λ4058.

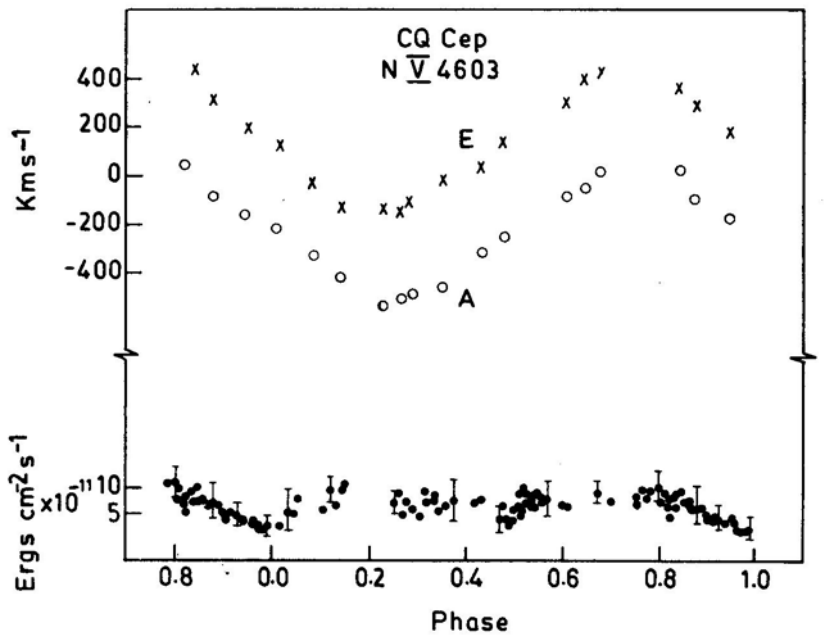

Figure 7. Radial velocity curves for both emission and absorption components, and flux measures of Nv λ4603.

discussed till now, these measures show a small dip at phase 0.0. But for this the fluxes are generally constant. Both absorption and emission components give almost circular orbit solutions with only the γ values shifted (Table 2).

4.3 *Carbon Lines*

The only carbon line that was available for measurement of fluxes in our scans is C IV λ5808. The measured fluxes clearly show the same pattern as in the remaining lines. The amplitude of variation is not very large. This region is covered in the density tracings shown in Fig. 4(b), which clearly points out the difficulty in measuring radial velocity, at any phase. Since the spectrophotometric observations made in the red region were not as frequent as in the blue region, the number of flux measures are relatively smaller. This is true also for the other lines in this region *viz.* He I $\lambda\lambda$5876, 6678, and He II λ6562.

4.4 *Line Blends*

We now look at the line blends at $\lambda\lambda$4540, 4200 and 4100. The main contributors to these emissions are known to be He II and N III. These flux measurements show a variation similar to that of other He II lines, indicating that both contributors to these blends behave in the same way. It is difficult to study the behaviour of individual contributors to these blends because of insufficient resolution.

5. Model

All the solutions from different emission-line radial-velocity curves (Table 2), together with the light curve solutions of Stickland *et al.* (1984) and Leung, Moffat & Seggewiss (1983), can be made use of in an attempt to construct a model for CQ Cep.

5.1 *Light Curve Solutions and the Nature of the Companion*

Leung, Moffat & Seggewiss (1983) solved, by Wilson-Devinney method the light curve obtained by Hiltner (1950) at λ5300. They discuss the choice of the mass ratio 0.75 in a great detail. Stickland *et al*. (1984) solved the same light curve taking into account the atmospheric eclipses, and arrived at a mass ratio of 0.6. Both the solutions necessitate a massive companion of the order of 35–38 $M_{\odot}$. The mass of WN component—46 $M_{\odot}$ from Leung, Moffat & Seggewiss (1983) and 64 $M_{\odot}$from Stickland *et al.* (1984)—appears large compared to other estimates for WN components in binaries: 10 $M_{\odot}$ for V444 Cyg (Kuhi 1968), 5–12 $M_{\odot}$for CX Cep (Massey & Conti 1981), 10–20 $M_{\odot}$ for HD 211853 (Massey 1981). Considering that the latter systems consist of WN5, WN5 and WN6 respectively, compared to the WN7 in CQ Cep, the differences in derived mass are perhaps reasonable, since it is known that WN7 subgroup behaves differently from other subgroups in many respects (Moffat & Seggewiss 1980).

However, the energy distributions obtained by us at various phases do not show any evidence of change of slope of the Paschen continuum from conjunctions to

quadratures (Figs la and b), which could have been caused by an early-type companion.

Niemela (1980), analyzing the spectra at better dispersions (15 Å mm^{-1}) found evidence for absorption arising from the companion. Leung, Moffat & Seggewiss (1983) found that He I λ3888 probably represents line splitting due to companion. Stickland *et al.* (1984) also found such line splitting but only at one epoch, the velocity of the second component being almost constant. On the plates used in this study, the region ~ λ3888 is not exposed well enough. However, He I λ4471 definitely showed two components in 1951 (Bappu & Viswanadham, 1977). The measured radial velocities of one component show a variation similar to He I λ5876, which follows the motion of the WN component; the other component has a mean value of about –900 km s^{-1} with a large scatter. Obviously, this component can not represent the motion of the companion.

From the *UV* measurements of *P* Cyg profiles, Stickland *et al.* (1984) have derived the terminal velocity, the escape velocity and the ratio $M^*/R^* = 1.2\ M_\odot/R_\odot$. Accordingly, the radius can be either 18 $R_\odot$ (for the 20 $M_\odot$WN component) or 38 $R_\odot$ (for the 46 $M_\odot$ WN component). The separation between the components in these two cases are ~ 20 $R_\odot$ and 25 $R_\odot$ respectively, which conflicts with the sizes derived for stellar radii. Further, Underhill (1969) has pointed out that atmospheres of WR systems are extended to about 5 times the core radius. In this case, even for a smaller value of 10 $M_\odot$ for WN, the extension will be ~ 45 $R_\odot$. Hence, irrespective of the method of light curve solution, the companion will be inside the stellar wind of the WN. It is also known that the WR atmospheres are generally optically thick for helium and hydrogen lines for $n < 10$ (Smith 1973). Hence these lines produced at the photosphere of the companion (which is completely embedded in the wind) will not be appreciably recognizable after passing through the thick atmosphere. To check this on spectra of medium dispersions is difficult, because the absorptions indicate the motion of WN itself. Any absorption due to the companion will move in the opposite direction, in case of helium lines, well within the 10 Å width of the emission profile. At phases close to 0.0 and 0.5, this absorption is expected to be superimposed on the emission profiles. At phase 0.25, this absorption would have moved away and at phase 0.75 it is likely to coincide with the violet wing of the emission profile. This can add to the total absorption at this phase making the effect easily recognizable, as was seen for HeII λ4860 and λ6562 and to some extent for λ5410. Whether such an effect is present for λ4686 line is hard to decide not only because of its increased strength but also because of the building up of another strong emission of N III λ4640.

The radial velocity discrepancy curves generated with reference to N IV λ4058 show more positive values at all phases, reflecting mainly the shift in γ axes. Hence, it is difficult to judge the possibility of any contribution of opposite-moving absorption. The type of absorptions shown by He II $\lambda\lambda$4860, 6562 and 5410 have not been observed by Stickland (personal communication). This may also imply that these absorptions are probably of sporadic nature, although the observed amplitude differences (and almost circular orbit for only λ5410) appear constantly at all epochs.

In the absence of evidence from spectroscopic or spectrophotometric data, other than the only one high-dispersion measurement by Niemela (1980), we may assume that the companion is of spectral type O, contributing to absorption, if recognizable, only in He II and He I lines.

5.2 *Circumstellar Matter*

The radial velocity variations and flux variations may now be studied in order to understand the structure of the envelope surrounding the star. We use N IV λ4058 to represent the motion of the WN component for the following reasons: (1) The spectra clearly show that this line is free of any blends. (2) This line does not show asymmetry in line profile due to absorptions. (3) Its radial velocity curve gives an almost circular orbit, which is anticipated in case of such close binaries. (4) Its γ velocity has a value very close to the systemic velocity of other members of the Cepheus association (Stickland *et al.* 1984).

We may start with the nitrogen lines for understanding the WN atmosphere, since they are known to be formed in the WN atmosphere only and not in the companion. The flux variation of the Nv line shows eclipse effects, implying its formation in a region closer to the WN photosphere and, therefore, an approximate size of the line-emitting region may be calculated. We may also note that no eclipse effects are seen at phase 0.5, when the WN is between the observer and the O type star. Assuming that this line originates deep in the atmosphere we can think of a configuration of an eclipse of parts of this line-emitting sphere at the primary minimum. The depth of the eclipse is about 25 per cent and the duration of the eclipse is from phase 0.85 to 0.15. Then the radius of the line-emitting region will be about 10 $R_{\odot}$.

From the variation of the line profile we see that absorption and emission are moving together so as to leave the profile unchanged. This further indicates that the decrease in flux at phase 0.0 corresponds to an eclipse effect only. The radial velocity curves of this line show an interesting phenomenon; these curves are identical but for a shift in γ axes. If we assume that this line originated in a region close to the photosphere, it should follow the characteristics of N IV λ4058, *i.e.,* γ axis should have been – 65 kms $^{-1}$. But because of the associated absorption there can be a positive shift of γ axis. It may be noticed that when we combine the effect of emission and absorption the net value of γ will be –56 km s^{-1}. This would imply that the redshift of γ axis is due to the associated absorption only. However, it is not possible to verify whether this effect exists for all other lines with absorptions or whether it is just a coincidence in case of N v λ4603.

The behaviour of helium lines has already been discussed in the previous section. Here, the shift in γ axes may be a consequence of the absorption arising in the WN itself (like N v λ4603) or because of the absorption dueto the companion. A situation like this, of two absorption features moving in opposite directions, can reduce the total flux also at phases 0.25 and 0.75. At phase 0.75 both absorptions add to the violet wing of the profile so that the measured flux will be still smaller. This is partly true, because on some occasions at phases ~ 0.75 the flux was too small to make any meaningful measurements. But this cannot totally explain the observed flux increase at phases 0.0 and 0.5.

The absence of eclipse effects for all lines other than N v λ4603 demands that their line-emitting regions will have to be larger than 10 $R_{\odot}$ (the value of the same for N v λ4603). This also sets a limit on the size of the companion at ~ 10 $R_{\odot}$. As discussed in the previous section the companion definitely sweeps through the WN stellar wind, thus partly occulting the wind during quadratures, while at minima the entire line-emitting region is visible. This geometrical effect will cause an apparent increase of flux at minima. This scenario is likely to be more plausible specially in case of CQ Cep,

because in V444 Cyg the companion is larger and all the lines show eclipse effects.

Thus it appears that in case of helium lines absorption and geometric effects cause the observed flux variation while for other lines it is mainly the geometric effect.

6. Discussion

Various models have been put forward to explain the line flux variation by the earlier investigators. The common-envelope model proposed by Bappu (1951a) explains the occultation effects, but assumes that He I lines originate deeper in the envelope compared to He II, which contradicts the velocity *versus* excitation potential (EP) relation derived from *UV* line profiles (Stickland *et al*. 1984). Sahade proposed a stream from WN towards the companion to be responsible for enhancement of HeII λ4686 (*cf.* Hack & Struve 1970). Leung, Moffat & Seggewiss (1983) provided the light-curve solutions with a mass ratio of $q = 0.75$ and explained the behaviour of some lines at phase 0.8 by assuming that the line-emitting material has a maximum velocity towards the observer at that phase. The latest model by Stickland *et al.* (1984) takes into account the difficulties encountered in fitting a simple model, and provides a hot zone between the two stars and an enhanced outflow.

6.1 *The Roche Surface*

The only emission line which shows eclipse effects is N v λ4603. If this is used for estimating the size of the line-emitting region, the size will be just equal to the inner Roche surface calculated from tables of Plavec & Kratochvil (1964). The use of these tables needs many assumptions about the components. Considering the large wind velocities of the WN component and the large extension of the atmosphere, this picture of the Roche surfaces is probably not applicable. Schuerman (1972) introduced these effects into calculations and showed that the deformation of the Roche surfaces was applicable to massive X-ray binaries. Zorec & Niemela (1980a and b) considered the radiation pressure from both components and applied to the case of V444 Cyg (*cf.* Sahade & Wood 1980). Vanbeveren (1977) considered X-ray heating, deviations from synchronous rotation and a different rate of synchronization for the two components. From all these studies, it is clear that the tables of Plavec & Kratochvil (1964) are not applicable for systems like CQ Cep. The Roche surface will extend towards the companion with lower radiation pressure, making the distribution highly asymmetric and distorting the spherical shape of the components into ellipsoids.

A sample Roche surface from Vanbeveren (1977) can be chosen for the purpose of determining asymmetries. Only hemispheres are considered for determining the ratios of line-emitting material at four phases, because it is established that generally the helium lines (considered in this work) are optically thick (Smith 1973). The ratios at phases 0.0, 0.25, 0.5 and 0.75 are 9.0:6.3:7.6:6.3 respectively. Thus at phase 0.0 the flux can be the highest, although the companion occults a small portion of the atmosphere. This kind of a flux distribution is seen for He II λ4686. For N IV λ4058 and other lines the fluxes at 0.0 and 0.5 are almost equal. This may imply that their distribution is not λ asymmetric as that of λ4686. The optical thinness of N IV lines and N III lines also may be partly responsible for this.

Kuhi (1968) suggested a hot zone between the two components of V444 Cyg because the eclipse effects were seen for all emission lines. The distribution of emitting material, in such a situation shows concentration towards the inner Lagrangian point. This will be recognizable in line profiles as is seen for HeII λ4686 in V444 Cyg as a hump moving with phase (Ganesh, Bappu & Natarajan 1967). Similar observations have been done for CIII λ5696 in case of θ Mus (Moffat & Seggewiss 1977). No such line-profile change is noticeable in CQ Cep. Therefore, either the inner Lagrangian point or Roche surface cannot explain the behaviour of emission line fluxes.

6.2 *Inferences from UV and IR Studies*

Hackwell, Gehrz & Smith (1974) were the first to detect the IR excess of CQ Cep. They also showed that for this system only a free-free emission can be fitted and not a blackbody fit, as was possible for other WR systems. Stickland *et al.* (1984) obtained the IR light curves and showed that the amplitude of the light curve decreases towards IR wavelengths. Hence the presence of a 'third source' could be recognized. The asymmetry in the distribution of a 'third source' is also similar to that of other emission lines.

The fluxes for different emission lines also have been measured by Stickland *et al.* (1984) in the *UV*. The behaviour is similar to the variation seen in this work for emission lines in the optical. The emissions in *UV* and optical thus show enhancement of flux at phases near 0.0 and 0.5. Stickland *et al.* have also shown that there is one unidentified line, whose flux variation is similar to that of N V λ4603, showing eclipse effects. The equivalent widths of some absorptions also have been measured. They have larger values at quadratures.

6.3 *Peculiarities of some Emission Lines*

We notice that the emission lines in general show enhancement at phases ~ 0.0 and 0.5. However, He II λ4686 has larger flux at ~ 0.0 and the increase is sudden. N III λ4640 does not show much variation. The radial velocity curves of these two lines have smaller values of amplitude compared to any other line. Taking N IV λ4058 as representative of the WN motion, the radial-velocity discrepancy curves for all other emission lines can be generated. These curves reflect only the differences in γ velocities and amplitudes; in general, they all show small variation through the phase, the effect being larger for lines giving eccentric orbit solutions. In these curves again the difference of λ4686 and λ4640 lines shows up: they show larger discrepancies. This may be qualitatively explained by assuming that the emitting material is distributed over a larger extent in the atmosphere. This reduces the amplitude of radial velocity curve and increases the strength of the line. The classification into WN7 itself implies the large strengths of these two lines.

In the case of V444 Cyg, Kuhi (1968) observed that λ4686 and λ4640 were brightest immediately after the secondary eclipse; The eclipse depths also were different compared to other lines of same ionization.

It is important to note that all the HeI lines have violet absorption edges produced

throughout the cycle. The velocities associated are also quite high and they follow a velocity *vs* EP relation (Stickland *et al.* 1984). This clearly confirms that they originate in the outermost regions of the extended atmosphere and are probably undisturbed by the presence of the companion although the structural changes of some lines like λ6678 may be attributed to the companion.

6.4 *Sporadic Events*

A sporadic brightening of the order of 0.03 mag was noticed by Hiltner (1950). Later Kartasheva (1976) reported variations up to 0.1 mag in 10 months. Both these observations were for the continuum only. However, in 1950, Hiltner also noticed a sudden change in the strength of He II λ4686. It is possible that we have a similar situation in 1982, when a sudden increase in flux at phase ~ 0.9 was recorded. Excepting this sporadic strengthening, the behaviour of λ4686 is similar to other lines. The peculiar behaviour of He I lines has been already discussed: λ4471 showed splitting in Hiltner's plates taken in 1943, and in Bappu's collection of 1952. Similar splitting of λ3888 was noticed in 1978 (Leung, Moffat & Seggewiss 1983). Therefore, it is likely that some transient phenomena like an enhancement of mass loss (Stickland *et al.*, 1984) were responsible for such line splitting. High dispersion spectra can reveal these aspects and the possible effect due to the companion.

7. Comparison with V444 Cyg

V444 Cyg (period 4.2 days) is the only binary with more detailed studies on the line profiles and radial velocities. Here the O-type companion is detected by its absorption spectrum and, in fact, is larger and more massive of the two. Kuhi (1968) studied the secondary eclipse so that the O-type star may be treated as an occulting disc passing in front of the WN atmosphere. He mentions the highly individualistic behaviour of lines. The difference with reference to λ4640 and λ4686 has already been mentioned. The line profiles have been studied by Ganesh, Bappu & Natarajan (1967). N IV λ4058 shows symmetric profiles, but appears to be broader at quadrature than at conjunctions. Such profile changes are present in CQ Cep also on a very small scale (Bappu & Viswanadham 1977). In the case of V444 Cyg, the profile of He II λ4686 shows a superimposed hump, as discussed in Section 6.1.

Following the stratification of CQ Cep we may try to interpret the eclipse observations of Kuhi (1968). N V lines being formed closest to the photosphere should show deepest eclipses. This is only partly true, because the deepest eclipse is that of N IV λ7112.

The Roche surface has been calculated by Niemela taking into account the stellar wind (*cf.* Sahade & Wood 1980). It may be noticed that at phase 0.5 when the O star is in front, the line-emitting region is still visible. A larger portion of the line-emitting region will be covered by the O star just before (or after, depending on i) phase 0.5. This may partly explain the shift of some eclipses from phase 0.5.

Since all the emissions are definitely showing eclipses, it appears that their line-emitting regions are of comparable size to the companion *i.e.* ~ 10 $R_{\odot}$. Thus there is a large difference in sizes of envelopes around the WN component in CQ Cep and V444

Cyg; For CQ Cep, 10 $R_{\odot}$ was the lower limit. Observing the difference in masses, absolute magnitudes, ionization structure and abundances between WN5 and WN7 (Moffat & Seggewiss 1980), this change in the size of wind and atmosphere is also probably real.

8. Conclusions

This spectrophotometric study of the shortest period Wolf-Rayet binary clearly shows the complicated structure of WN7 atmosphere. Of the many lines available in the optical region for study, only N V λ4603 shows eclipse effects. The flux variations of other emission lines appear to differ from the continuum variations. They can be explained by Roche surfaces taking into account the strong wind of the WN7 component. N IV λ4058 represents the true motion of the WN7 component and its flux variations appear to be influenced by the geometric effects of wind-dominated Roche surface.

Any signature of the companion is not detectable. The emission lines generally show a positive shift for the motion of the centre of mass (γ axis). This may be due to the strong wind characteristics and, in case of helium lines, possible absorptions from the companion. The optical thickness of this wind to the helium lines is also probably responsible for the non-detection of any line from the companion, which, according to light-curve solutions, is deeply embedded in the wind. These strong winds further prevent the application of classical, gravity-dominated Roche surfaces. Studies of high dispersion spectra may reveal weak spectral lines of companion at phases 0.25 and 0.75.

The behaviour of the strongest lines in the optical spectrum, N III λ4640 and He II λ4686 Å differs from all other emission lines in both the radial-velocity variations as well as flux variations. Sporadic events like brightening of the spectral lines, and line splitting corresponding to enhanced mass loss appear to occur occasionally.

A comparison with the only well-studied binary V444 Cyg shows a larger extent of the atmosphere, which probably is due to the inherent differences between the two subgroups WN5 and WN7.

Acknowledgements

I gratefully acknowledge late Professor M. K. V. Bappu, under whose guidance I began these studies. A critical reading of the manuscript by Drs D. J. Stickland and R. Rajamohan was immensely helpful. I acknowledge useful discussions with Professors J. C. Bhattacharyya, R. Koch, C. de Loore and K. D. Abhyankar. Valuable suggestions by Drs G. S. D. Babu, G. C. Kilambi, N. K. Rao, C. Sivaram, M. Parthasarathy and D. C. V. Mallik, were very helpful during the analysis. I thank Mr M. N. M. Rao for help in the reduction of the data onTDC 316 computer. I also thank the referees for useful suggestions.

References

Bappu, M. K. V. 1951a, PhD *Thesis*, Harvard Univ.
Bappu, M. K. V. 1951b, *Astr. J.*, **56**, 120.

Bappu, M. K. V. 1952, *Astr. J.,* **57**, 6.
Bappu, M. K. V. , Sinvhal, S. D. 1955, *Astr. J.,* **60**, 152.
Bappu, M. K. V., Sinvhal, S. D. 1959, *Observatory,* **79**, 140.
Bappu, M. K. V. 1973, in *IAU Symp.* 49: *Wolf-Rayet and High-Temperature Stars,* Eds M. K. V. Bappu & J. Sahade, D. Reidel, Dordrecht, p. 59.
Bappu, M. K. V. 1977, *Kodaikanal Obs. Bull. Ser. A,* **2**, 64.
Bappu, M. K. V., Viswanadham, P. 1977, *Kodaikanal Obs. Bull. Ser. A,* **2**, 89.
Breger, M. 1976, *Astrophys. J. Suppl. Ser.,* **32**, **1**.
Cherepashchuk, A. M., Khaliullin, Kh. F. 1976, *Soviet Astr.,* **19**, 727.
Ganesh, K. S., Bappu, M. K. V., Natarajan, V. 1967, *Kodaikanal Obs. Bull. Ser.* A, No. 184, 93.
Giridhar, S. 1978, *Kodaikanal Obs. Bull. Ser. A,* **2**, 164.
Hack, M., Struve, O. 1970, in *Stellar Spectroscopy: Peculiar Stars,* Osser. Astr. Trieste, p. 129.
Hackwell, J. A., Gehrz, R. D., Smith, J. R. 1974, *Astrophys. J.,* **192**, 383.
Hayes, D. S. 1970, *Astrophys. J.,* **159**, 165.
Hiltner, W. A. 1950, *Astrophys. J.,* **112**, 477.
Hua, C.T., Woo, J. O., Nguyen, H. D. 1982, *Astr. Astrophys. Suppl. Ser.,* **53**, 407.
Kartasheva, T. A. 1976, *Soviet Astr. Lett.,* **2**, 197.
Khaliullin, Kh. F. 1973, *Soviet Astr.,* **16**, 636.
Kuhi, L. V. 1966, *Astrophys. J.,* **143**, 753.
Kuhi, L. V. 1968, *Astrophys. J.,* **152**, 89.
Leung, K. C, Moffat, A. F. J., Seggewiss, W. 1983, *Astrophys. J.,* **265**, 961.
Massey, P. 1981, *Astrophys. J.,* **244**, 157.
Massey, P., Conti, P. S. 1981, *Astrophys. J.,* **244**, 169.
Moffat, A. F. J., Seggewiss, W. 1977, *Astr. Astrophys.,* **54**, 607.
Moffat, A. F. J., Seggewiss, W. 1980, in *IAU Symp.* 83: *Mass-loss and Evolution of O type stars,* Eds P. S. Conti & C. W. H. de Loore, D. Reidel, Dordrecht, p. 447.
Niemela, V. S. 1980, in IAU Symp. 88: *Close Binary Stars: Observations and Interpretations,* Eds M. J. Plavec, D. M. Popper & R. K. Ulrich, D. Reidel, Dordrecht, p. **177**.
Plavec, M., Kratochvil, P. 1964, *Bull. astr. Inst. Csl.,* **15**, 165.
Sahade, J., Wood, F. B. 1978, in *Interacting Binary Stars,* Pergamon Press, p. 101.
Schuerman, D. W. 1972, *Astrophys. Space Sci.,* **19**, 351.
Semeniuk, I. 1968, *Acta.Astr.,* **18**, 313.
Smith, L.F. 1973, in *IAU Symp.* 49: *Wolf-Rayet and High-Temperature Stars,* EdsM.K.V. Bappu & J. Sahade, D. Reidel, Dordrecht, p.15.
Stickland, D. J., Bromage, G. E., Budding, E., Burton, W. M., Howrath, I. D., Jameson, R., Scherrington, M. R., Willis, A. J. 1984, *Astr. Astrophys.,* **134**, 45.
Underhill, A. B., 1969, in *Mass-loss from Stars,* Ed. M. Hack, D. Reidel, Dordrecht, p. 17.
Vanbeveren, D. 1977, *Astr.Astrophys.,* **54**, 877.
van der Hucht, K. A., Conti, P. S., Lundström, I., Stenholm, B. 1981, *Space Sci. Rev.,* **28,** 227.
Walker, E.N., LIoyd, C., Pike, C. D., Stickland, D. J., Zuiderwijk, E. J. 1983, *Astr. Astrophys.,***128**, 394.
Zorec, J., Niemela, V. 1980a, *C. R. Acad. Sci. Paris,* **290, Ser. B,** 67.
Zorec, J., Niemela, V. S. 1980b, *C. R. Acad. Sci. Paris,* **290, Ser. B**, 95.

J. Astrophys. Astr. (1986) **7,** 195–223

Composite Spectra
Paper 1: HR 6902

R. & R. Griffin *The Observatories, Madingley Road, Cambridge, England CB3 0HA*;
Visiting Associates, Mount Wilson & Las Campanas Observatories, Carnegie Institution of Washington

Received 1986 February 14; accepted 1986 June 2

Abstract. Composite-spectrum binary stars generally consist of a late-type giant and a main-sequence star of type A or B. Their spectra are therefore rather confusing; but by a technique of digital subtraction of the spectra of appropriate single late-type giants, composite spectra can be split into their individual components. In favourable cases the radial velocities of both components can be measured and the mass ratio determined. The procedures are illustrated by reference to HR 6902, a fifth-magnitude composite-spectrum binary. Its components are shown to have spectral types of G9 II and B8 V, with a mass ratio of 1.31, and its orbit is determined. There is some evidence that the system shows eclipses. If it does, the masses of the components are 3.9 and 3.0 $M_{\odot}$ respectively, and HR 6902 becomes the sixth known member of the important class of ζ Aur binaries.

Key words: composite spectra—spectroscopic binaries—stellar masses—stars, individual

1. General introduction to this series of papers

1.1 *Descriptive Preamble*

1.1.1 *Composite spectra*

Binary stars exhibiting composite spectra form a particular class of double-lined spectroscopic binary systems. In the sense in which we shall use the term, a composite spectrum is one which arises from a binary or multiple stellar system whose components have a very small angular separation *and dissimilar spectral types.*

A binary star only gives a recognizably double-lined spectrum if its components have comparable luminosities. If both components are main-sequence stars they cannot have very different spectral types, otherwise the magnitude difference is so great that only the earlier spectrum can in practice be observed. Therefore a main-sequence binary cannot give a composite spectrum. However, a red giant or supergiant has an absolute magnitude quite similar to that of a main-sequence star of type A or B respectively. Thus the binary systems with which this series of papers will principally be concerned are those in which one of the members is an evolved object—a high-luminosity star of more or less late spectral type, to which we will often refer as the 'cool' or (sometimes less accurately) as the 'primary' star—and the other is an upper-main-sequence object—the 'hot' or 'secondary' star.

Inasmuch as parts of the evolutionary paths followed in the Hertzsprung-Russell diagram by fairly massive stars are nearly horizontal, it is also possible for composite spectra to arise from binaries both of whose components are evolved. Capella, for instance, would just about qualify as composite; but as an example of a composite spectrum it is a poor one, because the spectroscopic distinction between its components depends more upon the rapid rotation of one of them than it does upon a straightforward difference of spectral type.

Normally the angular separation on the sky between the components of a composite-spectrum binary is so small that there is no possibility of observing the two spectra separately. The binary system is seen on the slit-head of the spectrograph as an apparently single star, and the recorded spectrum consists of the hot and cool spectra superposed upon one another.

The appearance of the typical composite spectrum is distinctive and bizarre. Because the cool-star spectrum is full of narrow and deep absorption lines whereas the hot one is not, only the former can readily be seen in the combined spectrum. The hot star makes its presence felt mainly by its blue continuum and strong Balmer lines. The hot continuum, rapidly increasing in intensity towards shorter wavelengths in relation to the flux from the cool component, progressively veils the late-type spectrum towards the violet. Meanwhile the strong Balmer lines contribute hazy depressions which underlie the mass of sharp lines arising from the cool star, heightening the unnatural appearance of the spectrum.

In a composite spectrum, the region of the H and K lines of Ca II has a characteristic appearance. The H line, which is very strong and wide in the cool spectrum, almost coincides with the Balmer line Hε, which is of comparable strength and width in the hot spectrum, so the H-Hε blend is a particularly intense feature of the combination. The cool star's K line, on the other hand, has no comparable counterpart in the hot star, so in the composite spectrum the K line is very much filled-in. It usually has a more or less sharp core, which represents the stellar K line from the hot component and/or an interstellar feature. The sharp atomic absorptions contributed by the cool star fade out towards the centre of the feature, where owing to the extreme strength of the K-line in a late-type star the contribution of that component to the combined light is down almost to nothing.

All the above-mentioned characteristics of composite spectra are beautifully exemplified by the object we have selected for our initial study, HR 6902, whose spectrum is illustrated in Fig. 3 and is discussed in the latter part of the present paper.

1.1.2 *The desirability of objective methods for separating the constituent spectra*

Composite-spectrum binaries are by no means rare; several of them were identified in the original *Draper Catalogue* by Miss Maury (1897), and numerous examples are to be found amongst the stars of naked-eye brightness. Some of them, such as Capella and (more typically) δ Sge, are conspicuously variable in radial velocity and their orbits have long since been studied. Others, such as β Cyg, show little or no change in their radial velocities. Still others have been measured either not at all or else with conflicting results, or (like HR 6902) have simply not been well enough observed for their orbits to be

derived even in cases where radial-velocity variability has been established.

The existence of this last category illustrates a remarkable general fact about composite spectra: *they have been systematically neglected.* The reason for the neglect is, in all likelihood, that they have been perceived as being too difficult or too troublesome to be effectively investigated. It is possible, certainly, to measure a radial velocity from a composite spectrum; but that is all. The velocity that is found generally belongs largely, sometimes exclusively, to the cool component, which supplies virtually all the spectral features that can be seen or measured. Any attempt on the part of the observer to take a more substantial interest in composite objects is apt to be thwarted by their very compositeness. In particular, no useful spectrophotometry is possible for either component owing to the uncertainty as to the contribution of its companion.

Even such a fundamental parameter as spectral type is difficult to establish. It will become apparent in this series of papers that the spectral types of stars involved in composite systems may be very different from the published types, even those assigned by experts. Indeed, the whole situation concerning the classification of composite spectra has been accurately summarized by Bidelman, in a recent letter (which we were doubtless not expected to quote publicly), as “too horrible to contemplate”!

It is clear that little further general advance is likely to be made by direct measurements on composite spectra. What is needed is the objective allocation of the observed spectral flux, at any and every wavelength, to the two stellar components individually, so that each component's contribution can be studied in isolation.

1.1.3 *Principles of separation of the spectra*

In principle there are two possible means of disentangling a composite spectrum. One might try to synthesize the observed spectrum from two spectra which represent those of the respective components. Alternatively, one could attempt to isolate the spectrum of one component by subtracting from the composite a spectrum representing that of the other star. Whichever alternative is adopted, a trial-and-error approach seems inescapable: there is no way of establishing *a priori* the spectrum of either component, so the initial step in either procedure must be to make a guess at the spectrum of at least one of the stars. In the synthesis approach it is necessary to guess at both spectra and also at their mutual wavelength displacement at the outset; in the subtractive procedure only one guess is needed initially, and the estimates of the other spectrum and of the wavelength displacement are revealed as the result of the subtraction. That difference between the methods has prompted us to choose the subtractive option. The input spectra—in the honest terminology above, the “guesses”—might consist of the observed spectra of appropriate single stars, or of spectra computed from stellar models. The former choice has the disadvantages of requiring additional observing time and of being restricted to spectra related to those which exist in Nature in isolated stars; on the other hand it is rooted in reality in a manner that computed spectra may not be. For a variety of reasons we have elected to use observed spectra in our search for spectra similar to those involved in composite objects. In what follows we shall use the expression “standard” to characterize stars or spectra that serve as analogues of a single component of a composite system.

By the considerations outlined above, we have effectively narrowed our choice of procedure to one in which we adopt an observed spectrum as a trial representation of one contributor to the composite, and by subtraction we uncover the other contributor. There is, of course, nothing particularly novel about this principle, which was used by Redman (1936) at our own Observatory fifty years ago: working with equivalent widths rather than complete spectra, he subtracted the secondary components (observed while the primaries were totally eclipsed) of the Algol-type binaries U Cep and U Sge to etermine, from spectra taken during the partial phase of eclipses, the centre-to-limb variations of the strengths of absorption lines in the primary spectra. At the Dominion Astrophysical Observatory an heroic effort was made, before the days of digital computers, by Wright (1954), who isolated the shadowy early-type spectrum of Capella by subtracting from the observed spectrum of that binary system the spectrum of β Dra. In collaboration with Lee, Wright went on to derive the secondary spectra of the composite-spectrum eclipsing binaries 31 Cyg (Wright & Lee 1959) and ζ Aur (Lee & Wright 1960) by subtracting the spectra observed during eclipse from those seen at other phases. Subtraction is routinely used nowadays to remove the contribution of the sky from the spectra of objects of low surface brightness. We have ourselves used the procedure, in a less developed form than that in which we shall present it here, to demonstrate the existence and nature of the hot secondary star in the previously unrecognized composite system HD 187299 (Griffin 1979a); and Batten *et al.* (1983) employed it in an effort to measure the radial velocity of the hot secondary in the composite object 93 Leo.

Before spectra can usefully be subtracted from one another, they must be accurately registered in wavelength. Inasmuch as the only reference wavelengths available in the composite spectrum are normally the lines of the cool star, it follows that the spectrum to be subtracted must represent that component, and the spectrum which remains after subtraction is that of its hot companion. The subtraction is necessarily performed in the rest frame of the cool star. No laboratory reference source (such as an iron arc) is involved: the composite and the standard spectra are both reduced to a wavelength scale based upon selected lines identified in the stellar spectra themselves. Successful subtraction is easily monitored by eye: when the requisite proportion of a spectrum that accurately matches that of the cool primary is subtracted from the composite, the lines of the cool star completely vanish and one is left with a spectrum of (usually) a totally different character, much smoother and recognizably that of a hot star.

Such a spectrum is indeed that of the hot component of the composite; and the power of the technique lies in the fact that, once the spectrum of the hot star is thus isolated in a pureform, *it can be used for any purpose that a spectrum would normally serve,* including spectral classification and the measurement of radial velocity and equivalent widths. Of particular significance is the fact that any radial-velocity difference between the two members of the composite system will be manifested as a displacement of the spectrum that is recovered for the hot component. The wavelength scale used in the subtraction process is that in which the cool star is at rest, and naturally it applies equally to the difference-spectrum: the displacement from it of the latter therefore represents the radial-velocity difference between the components of the composite. The availability of the radial velocities of the members of a composite-spectrum binary permits us, in cases where the binary is not too widely separated and the system accordingly has an adequate radial-velocity amplitude, to determine the relative masses of the components. The use of composite spectra to determine mass ratios has already been urged by Scarfe (1970).

1.1.4 *Mass determination from composite spectra*

Mass is the most fundamental of all stellar parameters. It is also, in many cases, one of the most difficult to determine with any accuracy. The mass of a single star can in principle be obtained from a detailed spectroscopic analysis. Unfortunately the result is critically sensitive to the model employed to describe the stellar atmosphere, and small changes in the values adopted for the effective temperature and microturbulence require disproportionately large changes in log g and hence in the derived mass. The difficulty of obtaining any consensus upon a spectroscopically derived mass estimate was brought home to us some years ago by our experience concerning Arcturus: different experts, all starting from the same or similar observational premises about which there was no dissent, derived masses ranging over a factor of ten.

Mass estimates that are much less open to casuistry are obtainable from the dynamics of binary systems. There exist eclipsing binaries and visual binaries which include main-sequence stars at least from type A onwards and whose orbits and parallaxes are sufficiently accurately known to give masses that are accurate to the order of 10 per cent (Popper 1980). Unfortunately the position is far less satisfactory as regards giant stars. The masses of the components of Capella—one at least of which is a rather atypical object—are tolerably well determined (Shen *et al.* 1985) as being near 3 $M_\odot$ (Wilson 1967). There are six other binaries consisting of pairs of reasonably normal late-type giants in double-lined spectroscopic systems with known orbits: they are η And (Gordon 1946), ϕ Cyg (Rach & Herbig 1961), HR 2081 (Beavers & Griffin 1979), HR 4665 (Bopp *et al.* 1979), and HD 44780 and 65 Gem (Griffin 1986). Their minimum masses range from 0.31 to 3.2 $M_\odot$ per component, those extreme values being given by η And and HR 2081 respectively; but only in the case of ϕ Cyg are the actual values determinable (in that case 2.50 and 2.39 $M_\odot$ (McAlister 1982)) because the inclinations of the other orbits to the line of sight are unknown.

If the amplitudes of variation of the radial velocities of *both* components of a composite-spectrum binary can be measured, then the relative masses of the components follow immediately (being in inverse proportion to the amplitudes, by the principle of conservation of momentum). Inasmuch as one of the components is normally a main-sequence star, whose mass can be assigned by reference to its spectral type, the mass of the other component—the cool giant—is determined. It may seem less than satisfactory to have to assign one mass by rule of thumb in order to obtain the other; but if by so doing we have reduced the range of uncertainty of the mass of the giant from a factor of ten down to the order of ten per cent we have obviously achieved a very worth-while improvement.

Two further comments on this situation may be interjected here. The first concerns the complication which arises from the metallic-lined (Am) nature of the hot secondaries in many composite systems. One needs to decide which of the spectral types (hydrogen-line, metal-line or K-line) to use in entering the tables of main-sequence masses, *e.g.* Allen (1973), p. 209, to assign the mass. We tentatively suppose that it is the hydrogen type, which more or less corresponds to the effective temperature, which is the important quantity. The other comment is that quite a number of composite-spectrum binaries has already been resolved by speckle interferometry (McAlister & Hartkopf 1984): it is only a question of time before 'visual' orbits for many of these systems become available, and then the masses will follow directly from the observed radial-velocity amplitudes without the need for any assumptions whatsoever. An orbit based on speckle interferometry has already been published (McAlister 1982) for γ Per, a composite object for which a spectroscopic orbit was derived long ago.

1.2 *Procedural Details*

1.2.1 *General plan of the observing campaign*

Two types of observational input are needed in this investigation of composite spectra. The type to which we have alluded above is that of high-resolution spectroscopic observations, which enable us to separate the combined spectra into their two individual constituents and to determine the radial-velocity difference (if any) between those constituents. Because high-resolution spectroscopy can be quite expensive in terms of observing time, to maximize its effectiveness it is desirable first of all to investigate the radial-velocity behaviour of the composite binary. That requires the second type of input. The radial-velocity of the cool star can be measured directly with a photoelectric radial-velocity spectrometer such as ours at Cambridge (Griffin 1967) and Palomar(Griffin & Gunn 1974). Since the ho t star normally lacks the spectral lines upon which the instrument operates, the spectrometer is not sensitive to it at all: it does not confuse or invalidate the measurement, but simply dilutes the late-type spectrum and makes the 'dip' in the radial-velocity tr ace shallower and less easily measured than it would otherwise be.

In cases where the radial velocity of the cool primary in a composite-spectrum binary is constant, there is no preferred moment for obtaining high-resolution spectra, and all that one can hope to do is to identify the spectral types of the components. On the other hand, if the primary velocity proves to be variable, the next step is to determine the orbit. The orbit of the hot secondary is necessarily the inverse of that of the primary, the only unknown quantity being its amplitude of variation. Each spectroscopic observation furnishes one measurement of the relative velocity, *i.e*. the velocity difference, between the primary and secondary. When the orbit of the primary is known, only one measurement of relative velocity is needed in principle to determine the amplitude of the secondary. Obviously, the greater the relative velocity the greater the relative accuracy of its determination: if the inherent error of the determination of the velocity difference is, say, 5 km s^{-1}, then we shall be able to measure a relative velocity of 100 km s^{-1} with fair accuracy but one of 10 km s^{-1} will more or less defeat us.

Thus we use our knowledge of the orbit of the primary to select an epoch of nodal passage, when the displacements from the γ-velocity of the radial-velocities of both stars are at their maxima, for the critical spectroscopic observation. Often the velocity excursion at one node of the orbit is greater than that at the other, so one particular node is the preferred time. From spectroscopy at that time we obtain the value of the radial-velocity difference between the components. The observed difference can then be partitioned between the two components, since the departure of the primary from the γ-velocity can be computed from the orbital elements.

It will be seen that this project is quite appropriate to the authors' interests and experience, involving as it does a symbiosis of their longstanding commitments both to radial-velocity studies and to high-resolution spectroscopy.

1.2.2 *Spectroscopic data*

Among the characteristics desired in the spectra used in this work are: (a) a substantial wavelength coverage, to enable lines of different elements, and diagnostic lines in

different spectral types, to be observed simultaneously; (b) a high signal/noise ratio, particularly in view of the fact that in subtracting one spectrum from another we are subtracting the signal but adding the noise; and (c) a high density of sampling points or picture elements, to facilitate interpolation between them so that spectra to be subtracted can be placed accurately in register with one another.

Initially it was our hope and intention to use photoelectric methods to record the required spectra. Not the least of the advantages we foresaw in those methods was the possibility of having the spectra obtained for us by a 'service observing' procedure, or by a collaborator who lived near the relevant observatory, rather than by us personally: to obtain spectra at specified times (nodal passages), usually different from one another, for a lot of different objects involves a great deal of travelling when, as in our case, no suitable equipment is available at one's own observatory. It also represents a heavy imposition upon the hospitality of a host observatory when visitors are constantly wanting to come and observe at specific times.

Through the kindness of Dr H. J. Smith and the McDonald Observatory, we were enabled in 1980 to make trials of the reticon and digicon systems there. It turned out that, for our purposes, the photoelectric detectors were not altogether satisfactory. Because of the very limited numbers of their picture elements it was impossible to fulfil requirements (a) and (c) above simultaneously. Moreover, the digicon, which was the detector of choice in the important K-line region, incorporates electron optics which introduce considerable geometrical distortion, which cannot be determined and allowed for to the necessary accuracy because the small field of view simply does not contain enough unblended lines to serve as wavelength standards.

We were accordingly unexpectedly forced back on photography, which enables high-resolution spectra to be recorded over a wide wavelength region at a single exposure and moreover has quasi-continuous recording rather than the discrete elements of photoelectric detectors. (See desideratum (c) above.) We have been very fortunate in being appointed Visiting Associates of Mount Wilson Observatory, where we were given generous access to the 100-inch reflecting telescope and its coudé spectrograph; all of the spectroscopic data we have so far obtained for our work on composite spectra have come from Mount Wilson. It is, of course, a matter of serious concern (Griffin 1984, 1985a,b) that the 100-inch telescope is now closed.

As a compromise between spectroscopic detail and practical exposure times, we decided at the outset to base the composite-spectrum work on spectrograms whose reciprocal dispersion is 10 Å mm^{-1}. Such spectrograms were efficiently taken at the 100-inch telescope with the 32-inch off-axis Schmidt camera (Dunham 1955) and the '46B' grating—an original 600-line mm^{-1} grating ruled by Babcock at Mount Wilson Observatory itself. The grating is blazed in the second-order near-ultraviolet. The wavelength region we have observed is from λ 3850 to λ 4650 Å. That region can be covered with satisfactory photographic density in a single exposure for stars of spectral type earlier than about K2; the steep gradient in later types makes two exposures desirable. Above λ 4500 Å the second-order spectra are liable to be contaminated with third-order far-ultraviolet. The contamination of $\lambda\lambda$ 4500–4650 Å with the overlapping third-order $\lambda\lambda$ 30000–3100 Å is so slight that we have preferred not to use a filter to avoid it; but it needs to be borne in mind where spectra of hot stars are involved.

The photographic emulsion normally used has been Eastman Kodak IIa-O; but some hot standard stars and hot-dominated composite spectra have been photographed on IIIa-J. High signal/noise ratios have been achieved by taking very wide

spectra; in many cases we have used the maximum width permitted by the optics of the spectrograph, $2\frac{1}{2}$ mm. The entrance slit has always been set at a width of 100 μm, corresponding to 0.27 arcsec on the sky at the *f*/30 coude focus of the 100inch reflector and to approximately 15 μm or 150 mÅ projected in the spectrum.

The camera gives such good definition that the true spectral resolution is very largely set by the projected slit width. In relation to the ultimate resolution of the camera the width we have selected is rather conservative, so small differences of focus *etc.* from one observing run to another have little effect on the observed resolution. The camera also has exemplary stability, and there has been no difficulty in obtaining an extremely homogeneous series of spectra of composite and standard objects over a period of years. Spectra of the quality shown in our illustration of HR 6902 later in this paper (Fig. 3) have been obtained as a matter of routine.

Photometric calibrations have been obta ined by the methods outlined in the Introduction to our Procyon spectrophotometric atlas (Griffin 1979b), and only need brief description here. In order to make the calibration exposures as similar as possible to the stellar exposures, which are intermittent because the spectra are widened by repeated slow trials of the star image along the entrance slit, the calibration too is broken up into a series of suitable discrete instalments synchronized with the trails. A series of 12 step slits, illuminated by a tungsten source, is used to generate alongside the stellar spectrum a series of continuous spectra whose relative intensities are known from the geometry of the slits. At first we found the scale of the step-slit images to be rather small for the best photometry: the same slits served not only the 32-inch but also the 73- and 114-inch cameras where of course they were imaged at correspondingly larger scales, and their sizes were limited by the need to accommodate their images at the 114-inch camera. We found it possible to replace the step slits with a set of our own construction, with a scale better adapted to that of the 32-inch camera. As a precaution inspired by pessimism, a second calibration has normally been exposed simultaneously in a separate auxiliary spectrograph with a 24-step entrance slit (Griffin 1979b).

1.2.3 *Spectrophotometric technique*

The first step in reduction of the photographic spectra is to determine the calibration curves from microdensitometry of the step slits. The curves steepen systematically with increasing wavelength on IIa-O emulsion, and have needed to be established at 200-Å intervals. It has proved convenient, in fact, to handle the spectrophotometry throughout in four 200-Å regions centred respectively at $\lambda\lambda$ 3950, 4150, 4350 and 4550 Å, and that is how it will usually be presented in this series of papers; so those are the wavelengths at which the calibrations have been set up.

The stellar spectra are traced on our largely homemade digital microphotometer at 5-μm intervals and transferred from plate transmission to a linear scale of light intensities by means of the appropriate calibration curves. In a second step, the tracing is placed on a linear scale of wavelengths. The scale is established by the identification of a number of (almost) unblended stellar lines which are assigned their corresponding solar wavelengths (laboratory wavelengths in the cases of the hottest standard stars), the wavelength solution being computed by a trigonometrical relationship based on the geometry of the spectrograph (Griffin 1979b). Rms wavelength residuals of less than 10 mÅ, corresponding to 1 μm the plate, are the norm. The intensity values (whose

scale is already linear) are normalized so that the highest point in each 200-Å region is near the value 100; but no effort is made to level the continuum at this stage, since for our purposes it is quite useful to leave the natural gradient in the spectrum.

The final outcome of this phase of the reduction procedure is that each spectrum is reduced to four sets of numbers,4001 numbers in a set, each set representing the digital intensity values of the spectrum at precise 50-mÅ intervals for the 200-Å region starting at λ (3850 + 200n) Å where n is 0,1,2 or 3. The wavelength scale is that of the rest frame of the star (the cool star in the case of a composite spectrum). These digital data sets can then be added to, or subtracted from, the corresponding sets for other stars and represent the raw material upon which our work on composite spectra is based. From the interest shown in them by others, it is clear that the observations of standard stars are also seen as a valuable resource of spectroscopic data in their own right.

We are quite aware that photography is considered in many quarters to be an obsolete method of recording astronomical spectra, so it is perhaps worth making the points that (a) we deliberately selected it in this instance after trials of alternative methods, and (b) once one has traced a plate with a digital microphotometer the resulting data set is as modern and digital as any data can possibly be.

1.2.4 *The disentangling of composite spectra by subtraction*

The first step in attempting to disentangle a composite spectrum is to select from the library of late-type standards a spectrum to use as a surrogate for the primary star. The choice may be guided by an existing classification; but even a casual inspection of a 10-Å mm^{-1} spectrogram of the composite object often furnishes a more accurate indication of the spectral type involved. A series of trial subtractions is then made, the proportion of the late-type standard subtracted being changed by (say) 5 or 10 per cent between successive trials. We have sometimes found it useful to produce a paper plot with the trial subtractions ranged one below another so that one can follow the evolution of any given feature of the spectrum as increasing amounts of the standard are subtracted. What normally happens is that an absorption feature seen in the composite spectrum becomes progressively shallower as more of the standard is subtracted, and ultimately reverses into an emission peak when the optimum proportion has been passed.

Ideally, all the late-type absorption lines should just vanish at the same time. In practice, unless one is very lucky, some lines will disappear at one percentage subtraction of the late-type standard and others will require different percentages. A familiarity with the behaviour of the strengths of different lines as a function of spectral type and luminosity—a familiarity rapidly gained by inspection of the tracings forming the library of standard spectra—then guides one to successively better choices of standard.

Notice that it is not essential to have a dense grid of observed standard spectra. In just the same way as modest gaps in standards are readily bridged by interpolation when one is, for example, classifying spectra, so it is possible here to interpolate simply by averaging two standards—not necessarily in equal proportions. There is in fact a positive advantage in being obliged to interpolate between standards inasmuch as the averaging procedure improves the signal/noise ratio, so the interpolated spectrum is better than either of its constituents! On the other hand, one fact that the present

project has really brought home to us is the individuality of stars: if one takes the spectra of half a dozen stars all classified as (for example) K0 III they are found to be subtly different from each other. Consequently, the more standards at one's disposal the beter is the prospect of finding a good match for the star one is trying to imitate in the composite spectrum.

For the subtraction process to work effectively, very accurate registration in wavelength between the spectra concerned is essential. If one spectrum is even slightly displaced from the other, the result of subtraction is not to cancel the lines which correspond in the two spectra but to turn them into P-Cygni profiles. An analogous phenomenon occurs if there are differences in the effective resolution of the spectra, either for instrumental reasons or because of real differences in the projected rotational velocities of the stars concerned. If the lines in the spectrum being subtracted are too narrow—the light intensities rising too rapidly away from their cores—too much will be subtracted in the wings before enough is subtracted in the cores; and the resulting line profiles appear to have central emission peaks flanked on both sides by absorption. In the opposite case there is central absorption flanked by emission peaks. In practice, the differences in apparent resolution are small except in the cases of certain very luminous stars, and are readily removed through slight blurring of the 'sharper' spectrum by a digital broadening function; but the need for precise equalization of the effective resolution of the spectra does represent an additional complication in the subtraction process.

The hoped-for result of this stage of our procedure is the identification of a late-type spectrum which exactly matches the one involved in the composite binary, so subtraction of an appropriate percentage of it completely cancels all the late-type lines. The necessary percentage usually changes more or less progressively along the spectrum, as the relative fluxes from the two stars in the composite change quite rapidly with wavelength. We have routinely assessed the percentage to be subtracted separately for each 50-Å wavelength interval, and then interpolated the actual percentages applicable at every wavelength so as to avoid any discontinuity. The spectrum that is left after cancellation of the late-type lines by subtraction is evidently the spectrum of the other component of the binary: it is normally obvious that it is an early-type spectrum. It is convenient to re-scale its ordinates so that they are comparable with those that would be plotted for a directly-observed spectrum, since subtraction has reduced all the numerical intensities.

1.2.5 *The need for accurate assessment of the amount of the late-type Standard to be subtracted*

We glibly remarked in Section 1.1.3 that the spectrum that is uncovered for the hot star by subtracting away the cool contributor to a composite spectrum can be used for any purpose, including the measurement of radial velocity. That is certainly true in principle; but in actual practice much effort has had to be expended in attempts to devise procedures which lead to reliable velocities.

The difficulties that we have encountered mainly arise from the existence, in the hot stars of many composite-spectrum binaries, of many of the same spectral lines that characterize the cool components. Examples from a small region in the violet are the

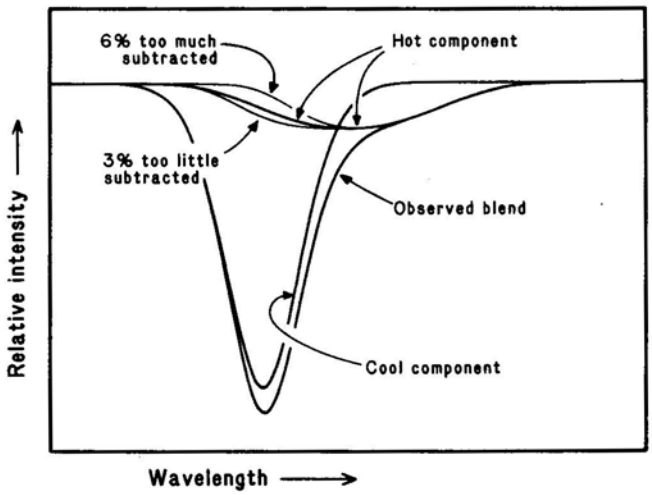

Figure 1. To illustrate the radial-velocity errors incurred through small errors in the subtraction of spectra. Two absorption lines, one deep and one broad and shallow, intended to represent corresponding lines in the spectra of the cool and hot components respectively of a composite object, are mutually displaced by a radial-velocity difference. Their blended profile is what is actually observed. In an effort to separate the components of the blend, we try to subtract the contribution of the deep component, whose strength is not known *a priori.* An appreciable range of strengths, exemplified here by 97 and 106 per cent of the true strength, leaves plausible apparent profiles for the shallow component; but it is clear that if we assign a wrong strength to the deep component we get a wrong radial velocity for the shallow one.

very strong Fe $_{I}$ lines $\lambda\lambda$ 4045, 4063 and 4071 Å, Sr $_{II}$ λ 4077 Å, and even the Mn $_{I}$ multiplet near λ 4030 Å: all are present in A-type spectra as well as in K types. In A-type spectra they are often substantially broadened by rotation, and the positions that they seem to occupy in a subtracted spectrum are then exceedingly vulnerable to small errors in the percentage of the cool star subtracted. We have tried to make the situation clear in Fig. 1, which portrays a typical absorption line appearing in both an A and a K spectrum, with a relative velocity shift between them. The illustration shows how a slight residual absorption from the K star, caused by a slight underestimate of the amount to be subtracted, draws the apparent line in the A star towards the position of that in the late-type star, *i.e.* it leads to an underestimate of the A-star's velocity shift. Conversely, slight over subtraction fills up the A-star line near the zero-velocity position and pushes the centroid of the line too far away: the velocity shift is overestimated. An accurate and objective means of assessing the amount of the late-type standard to be subtracted is essential.

1.2.6 *Methods of obtaining accuracy in subtraction*

An obvious recourse to see whether any late-type spectrum remains, either in absorption or in reversal, after subtraction is to cross-correlate the result of subtraction, *i.e.* the proposed secondary spectrum, with the late-type standard spectrum. Any

addition to spectral type, and metallicity is not even a single parameter. It is practically remaining late-type absorption should show up as a peak at zero displacement, whereas a reversed spectrum due to over-subtraction should be manifested as a 'dip' or negative peak. A complication immediately arises because, even though the absorption lines may be exactly cancelled, the secondary spectrum nevertheless contains the photographic grain noise from the late-type standard spectrum. Since that spectrum has been subtracted from the original one, its noise is present in negative form: cross-correlation with the (positive) late-type spectrum produces an autocorrelation 'noise dip' at zero displacement. At our dispersion of l0 Å mm^{-1}, the spatial frequency of the noise overlaps that of the spectrum. Therefore, if the subtraction is judged by cross-correlating the result of the subtraction with the late-type spectrum used in it, a systematic error will result, *viz.* not enough of the late-type spectrum will be subtracted, because the cross-correlation function is depressed at the all-important zero position by the autocorrelation of the grain noise. The remedy is clear: the standard spectrum used to judge the subtraction must be a different one—a spectrum of a different star, or another spectrum of the same star—from that used in the subtraction itself.

The next problem is that, because there is only a very limited number of spectral lines in each short interval of wavelength over which the proportion to be subtracted must be judged, the cross-correlation function tends to be everywhere far from level, and it is by no means clear what it should actually look like when the cool-star spectrum has been exactly annulled by subtraction. In fact, the cross-correlation of the late-type spectrum with the hot secondary spectrum itself usually has substantial features in it. A considerable improvement is obtained by reflecting the cross-correlation function about the zero-displacement position and averaging it at equal positive and negative displacements. That effectively removes the first-order gradient at the zero position. In cases where the components of a composite spectrum are sufficiently dissimilar, it may be satisfactory to judge the amount of late-type standard to be subtracted by requiring the reflected-and-averaged cross-correlation between the derived secondary spectrum and the separate, 'judging' late-type standard to be locally flat at the zero-displacement position.

Further refinement must be sought through actual modelling of the cross-correlation function. Using the procedure set up above, one obtains a fair initial estimate of the spectral type and radial-velocity shift of the secondary, and attempts to match the secondary from the library of standard stars. It is then necessary to form a cross-correlation of this standard secondary with the same 'judging' surrogate primary, over the relevant wavelength region and at the proper velocity shift; and the observed cross-correlation function is required to be locally flat at zero displacement after it has been divided by this model function. Then the procedure may need to be iterated to convergence.

1.2.7 *The radial velocity of the secondary star*

The final technical problem in this project is to determine the radial velocity from the spectrum we uncover for the hot secondary star.

The hydrogen Balmer lines are always too wide for accurate velocity measurement, and velocities derived from them are very sensitive to small errors in the wing profiles. A drawback to the use of metallic lines is that many of them are superimposed upon the

sloping wings of Balmer lines and their centroids are therefore displaced. We have sought to overcome that difficulty by normalizing the spectra of hot stars—both the one recovered from the composite spectrum and the best-matching available standard—to the *local* continuum. That is to say, for the purpose of finding the radial velocity we prepare versions of the early-type spectra in which the Balmer lines are effectively removed by normalization to their wing profiles. The deeper parts of the Balmer profiles obviously cannot be treated in this way and are omitted from consideration altogether. The radial velocity of the composite secondary is then determined by cross-correlation with the standard spectrum.

Direct cross-correlation of two early-type spectra is very inefficient, because much of each spectrum consists of continuum which contributes a lot of noise but no useful signal. By 'inverting' the spectra, so that the numerical intensity values represent depressions from the continuum, that problem is largely overcome because the cross-product terms arising from points with near-zero depressions are then very small. The noise contributed by non-significant features in the spectra is still further reduced by treating every point whose depression below the continuum is less than some specified value as having a depression that is exactly zero.

The cross-correlation function has a peak which is in general at a non-zero value of the mutual displacement of the spectra. The displacement gives the relative Doppler shift in terms of spectral elements or 'bins', which in our case are each 50 mÅ wide. Although the cross-correlation is only computed at shifts of integral numbers of bins, the function is in principle continuous and its maximum may be found by interpolation to whatever accuracy seems useful. For each 200-Å spectral region we also determine an effective mean wavelength, defined as the point at which the moments of the cross-product terms summed in the cross-correlation calculation are in balance. The effective wavelength is needed in order to convert wavelength shifts into velocity shifts. We could obviate the need to compute it if we binned the spectra in equal intervals of frequency or of log λ at the outset, so that the Doppler shift would be everywhere the same in terms of bins; our adherence to a *wavelength* scale may be seen as a manifestation of prejudice rooted in the history of astronomical spectroscopy.

1.2.8 *Intractable difficulties*

Our work on composite spectra has brought to light a number of difficulties associated with the natures of the stars involved in such systems, difficulties which we can scarcely hope to overcome.

In the first place, a surprisingly large number of primary stars proves to be Hertzsprung-gap objects with spectral types near G0 III. Good examples of such stars are almost impossible to find in isolation in the general field. Their preferential existence in composite spectra must be trying to tell us something, but we have not yet grasped what it is. In any case, it makes for difficulty in obtaining analogues for subtraction purposes.

Secondly, the hot components too are difficult to match. In their case the problem is not so much that they are of unusual types but simply that there are too many variable parameters of importance amongst A-type stars. Even if we restrict attention to stars that are on the main sequence, metallicity and rotation are continuously variable in

impossible to acquire a library of standard stars which adequately represents all the variables in such a multi-dimensional grid.

Thirdly, the high rotational velocities of certain secondary stars make for great uncertainty in the determination of their radial velocities.

Finally, too great similarity between the component spectra can create difficulties in identifying unblended lines of the primary for use in determining the wavelength scale upon which the subtraction procedure depends.

Another type of difficulty arises where the observed spectra include features which do not arise in the stars being observed. Such features can naturally vitiate the judgement of the proportions of the standard spectra to be subtracted, and the radial velocities determined for secondary stars, unless appropriate evasive action is taken. Fortunately there are not many of them: the only ones that we have come across are interstellar H and K, and emission lines near $\lambda\lambda$ 4358 and 4046 Å—mercury lines arising from artificial urban illumination scattered in the atmosphere or (worse) by cirrus cloud. One or two other mercury lines are marginally visible on the worst-affected plates. The great width of most of our spectra is achieved by the use of an entrance slit that is very long, admitting scattered light continuously from a considerable area of sky although the star image itself normally occupies only a small fraction of the slit length. Spectra of even quite bright stars thus become vulnerable to sky contamination; a practical answer to the problem would be a 'moonlight eliminator' (Bowen 1962).

1.3 *Possible Significance or Otherwise of the Results*

We have indicated in Section 1.1.3 that in cases where a composite spectrum arises from a spectroscopic binary whose orbit can be determined we shall hope to obtain the mass ratio of the binary. Even without assignment of the mass of the hot star to give an estimate of that of the other, the mass ratio itself is of great interest. According to the received theories of stellar evolution, the more massive a star is the sooner it evolves off the main sequence. Therefore in a composite-spectrum binary system, in which the two stars are presumably coeval, the more evolved component should be more massive than the one that remains near the main sequence, or at any rate it should have been so when it began its giant-branch evolution. If a case is found in which the cool giant is distinctly less massive than its main-sequence companion, it will provide evidence of substantial mass-loss during the part of its evolution that it has so far undergone.

Concern is naturally felt as to whether the masses and evolution of the members of a binary system are identical with those of corresponding single stars. Certainly there are cases in which mass-exchange is taking place, and the existence of the companion is having a profound influence on the career of the evolving star. In AR Mon and RZ Cnc (Popper 1976), which have orbital periods near 20 days, the larger star has lost most of its mass to its companion. However, disturbance of normal single-star evolution is only probable when the evolving star has at some epoch filled its Roche lobe of the Lagrangian surface. Scarfe (1970) has given reasons why, if an observed giant does not now fill its Roche lobe, it is unlikely to have done so in the past, He has also put forward a conservative criterion for non-interactive evolution in a binary system in the form of an inequality

$$\frac{P^2(1-e)^3}{R_*{}^3} > 40$$

where P is the orbital period in years, e is the orbital eccentricity and R_* is the radius of the giant star in astronomical units. Most of the binary systems that we hope to discuss seem likely to meet this criterion.

2. HR 6902

2.1 *Introduction: Existing Knowledge Concerning H R 6902*

HR 6902 is a fifth-magnitude object in the Milky Way in the eastern part of Ophiuchus, about 20° preceding Altair. It has been selected for the first paper in this series because the secondary has sharp lines and is of very different spectral type from the primary; so the disentangling of the components is relatively easy, and our procedures can perhaps be seen to work at least as convincingly as if we started with a more challenging example.

Although Miss Cannon was not the first to classify the spectrum of HR 6902, she appears to have been the first to recognize it as composite. Adams (1914) took four spectrograms of it in 1914, but simply called its type F7. Miss Cannon noted its composite nature in the *Henry Draper Catalogue* (Cannon & Pickering 1919), where she assigned it two numbers, HD 169689 and HD 169690, with spectral types G0 and A3 respectively.

During the 1920s the then new techniques of estimating stellar luminosities spectroscopically were energetically applied to a large number of stars. Adams *et al.* (1921) considered the absolute magnitude of HR 6902 to be –0.8 and the spectral type G0. Another Mount Wilson syndicate (Adams *et al.* 1935) offered a revision to M_v = +0.9 and type F9. Meanwhile Young & Harper (1924) had each independently estimated the absolute magnitude and found it to be –0.6 and +0.4 respectively; they jointly gave the spectral type of G5. In none of those investigations is there any mention that the spectrum is composite.

Much later, several further classifications of HR 6902 were made. The object appears in the *Radial Velocity Catalogue* (Wilson 1953) with type gG2. Kuhi (1963) sought to overcome the problem caused by the composite nature of the system by observing the spectrum in the red, where the contribution of the hot star is greatly reduced; he gave a type of G8 IV. Markowitz, in his doctoral dissertation(1969),found G8 III + A0 V and also supplied v sin i estimates of 60 km s^{-1} for the secondary and < 50 km s^{-1} for the primary. Most recently Hendry (1978) offered a classification of F8 V + A, but at the same time remarked that the F star is the more luminous component.

Cousins (1963) gave the photometric data V=$5^m.64$, (B–V) = $0^m.92$, (U–B) =$0^m.45$; Häggkvist & Oja (1966) obtained the identical value of V, and (B–V) =$0^m.898$. In addition, V magnitudes of 6.62 [*sic*] and 5.638 have been published by Eggen (1955) and Heck & Manfroid (1980) respectively.

The first radial velocities of HR 6902 were measured at Mount Wilson. Four plates, all taken in a three-month interval in the summer of 1914, showed a range of more than 40 km s^{-1} and prompted Adams (1914) to announce the variability of the velocity. Details of the four plates only became available in Abt's (1973) compilation. Harper (1934) reported 11 velocities obtained at the Dominion Astrophysical Observatory in the summers of 1919 and 1920; but in contrast to the experience at Mount Wilson they only showed a range of 11 km s^{-1}. This anomaly is readily understood in

retrospect, now that the orbit is known to be quite eccentric and to have a period 20 days longer than a year: there is a relatively short interval of rapid change, and it migrates around the calendar in a cycle of about 18 years. In 1914 it coincided with the season when HR 6902 was in opposition, but by 1919/1920 it did not.

Three velocities were obtained on almost consecutive nights in 1938 by Tremblot (1938). Fourteen more, measured at Perkins and Lindheimer and ranging in date from 1940 to 1976, were listed by Hendry (1978), who also published an orbit with period of 208 days and later withdrew it (Hendry 1984). Woolley *et al.* (1981) provided eight measures taken in 1966 with the 36-inch Yapp reflector at Herstmonceux.

2.2 *New Radial Velocities and Orbit*

HR 6902 was placed on the observing programme of the Cambridge photoelectric radial-velocity spectrometer (Griffin 1967) in 1981, and 42 observations have been made of it. It gives quite satisfactory radial-velocity traces, as the dilution of the light of the primary star by the secondary is fairly small in the region of the spectrum (roughly corresponding to the *B* band in *UBV* photometry) used by the radial-velocity instruments. These last few years have been a difficult time to establish the orbit of HR 6902, because the interval of rapid change in velocity, mentioned above, has occurred near the time of conjunction with the Sun. Nevertheless we have managed to cover the cycle reasonably well, and our own observations taken in isolation yield an orbit with a period of 385.7 ± 0.5 days. Their rms residual from that orbit is less than 0.7 km s^{-1}.

Armed with the preliminary orbit, we were enabled to take a critical look at the five series of radial-velocity observations found in the literature. It is likely, but not certain in all cases, that the published velocities are measured from the lines of the primary star alone; if the hydrogen lines were also measured they would be a fruitful source of confusion. The velocities published by Hendry (1978) and by Woolley *et al.* (1981) were found not to be of utility for our purposes, having residuals reaching over 20 km s^{-1}. The three measures by Tremblot (1938) are equally without value, since they cover less than one-hundredth of the period. The early velocities published by Adams (1914) and Harper (1934) seem fairly reliable, the largest residual in each series being 6 km s^{-1}. Unfortunately Harper's 11 observations span less than a fifth of the period, at a phase which is well covered by the much more accurate photoelectric measurements and at which the velocity is almost constant. The observed range of 11 km s^{-1} among Harper's velocities is to be compared with the computed variation of only 2 km s^{-1} during the interval of phase that they cover, Those velocities, therefore, cannot help us in refining the orbit.

Adams' four velocities have tolerable residuals and fall on the steep descent in the velocity curve. Taken 70 years ago, when the uncertainty in the phase derived by extrapolating the photoelectric orbit backwards in time has grown to about a month, they clearly can assist in determining the period. An orbit solution which includes them with the weight (0.05) to which their residuals entitle them has a period of 384.95 ± 0.05 days. They have an algebraic mean residual of +1.9 km s^{-1} according to that solution. However, since they all fall on the descending branch of the velocity curve, any systematic discrepancy between their zero-point and ours will cause a shift in their phases (Griffin 1981). If we apply a 'correction' of –1.9 km s^{-1} to them, the mean

residual does not become zero because the re-computed orbital period. takes the opportunity to increase again towards the photoelectric value and largely negates our correction. It requires a 'correction' of –5.6 km s^{-1} to Adams' velocities to reduce their mean residual to zero. The residuals themselves are then very small too, their values being +1.2, 0.0, –0.3 and –0.8 km s^{-1} respectively; the period is 385.10 days, with a formal standard error of 0.05 days. There is no way of deciding what, if any, correction is really warranted; and to make a change of –5.6 km s^{-1} just in order to overcome a systematic discrepancy of +1.9 km s^{-1} seems a rather extreme reaction. We consider that if we set the period at 385 days exactly we are likely to be within 0.1 day of the truth; and by holding the period at that value and using only our own velocities in the orbit solution we shall avoid any further effects of uncertain zero-point discrepancies. It is on that basis that we have performed the final orbit calculation.

Table 1 lists all the radial velocities, old and new, for the primary of HR 6902, together with the phases and residuals according to the adopted orbit, whose elements are listed in Section 2.6 below. The radial-velocity curve is illustrated in Fig. 2; the figure also includes the curve for the secondary, whose data are discussed in Section 2.5.

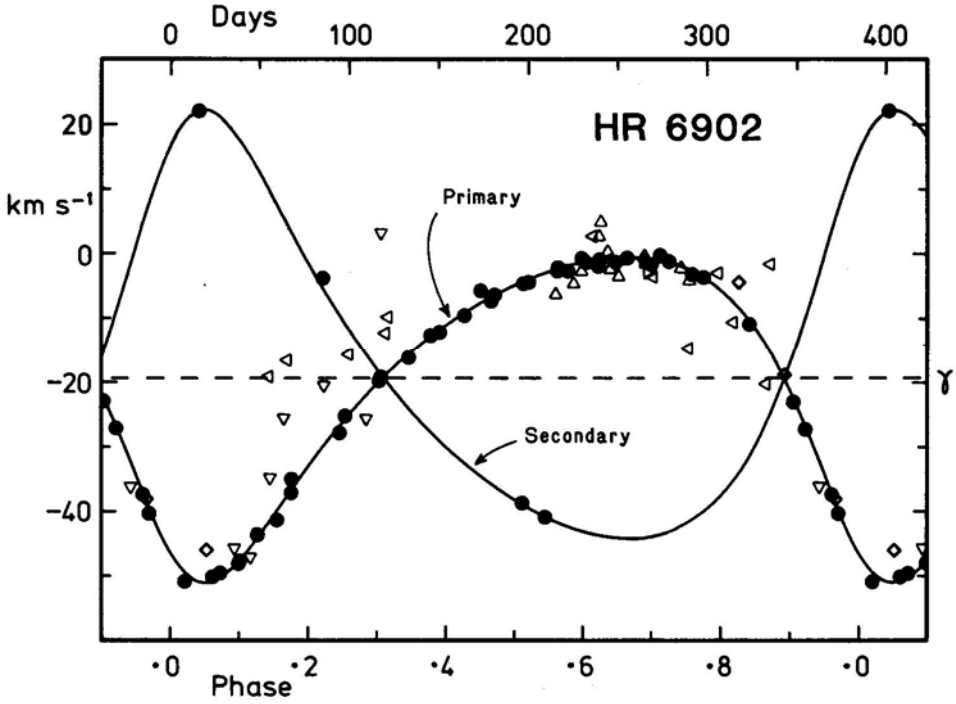

Figure 2. Radial-velocity orbit of HR 6902. The orbit is based upon our photoelectric measurements (filled circles) of the radial velocity of the primary star. Its period has been refined by appeal to the early photographic measurements of Adams (1914), represented here by open diamonds. Open triangles represent other velocities found in the literature but disregarded in the derivation of the orbit. Those with vertices up are by Harper (1934), vertices right by Tremblot (1938), vertices left by Hendry (1978) and vertices down by Woolley *et al.* (1981). The four observations of the secondary are derived from our photographic work, as described in Section 2.5 below.

Table 1. Radial-velocity measurements of the late-type primary star of HR 6902.

Date	MJD	Velocity km s^{-1}	Phase	$(O-C)$ km s^{-1}	Source*
1914 June 5.40	20288.40	−4.2	$\bar{6}\bar{4}$.826	+4.5	MtW
July 1.30	314.30	−18.6	.893	+1.6	MtW
29.24	342.24	−37.9	.966	+1.1	MtW
Aug 31.22	375.22	−45.8	$\bar{6}\bar{3}$.051	+5.3	MtW
1919 June 27.37	22136.37	+5.0	$\bar{5}\bar{9}$.626	+5.8	DAO
July 1.36	140.36	+0.4	.636	+1.1	DAO
2.38	141.38	−2.2	.639	−1.5	DAO
1920 June 21.35	22496.35	−6.1	$\bar{5}\bar{8}$.561	−3.7	DAO
July 1.38	506.38	−4.5	.587	−2.9	DAO
5.31	510.31	−2.5	.597	−1.1	DAO
15.23	520.23	+2.9	.623	+3.8	DAO
26.28	531.28	−3.3	.651	−2.7	DAO
Aug 9.27	545.27	−0.2	.688	+0.5	DAO
30.23	566.23	−2.1	.742	0.0	DAO
Sept 4.15	571.15	−3.8	.755	−1.1	DAO
1938 July 10.91	29089.91	−1.3	$\bar{4}\bar{1}$.687	−0.6	Tr
11.91	090.91	−0.7	.689	0.0	Tr
13.97	092.97	−3.0	.695	−2.2	Tr
1940 July 21.26	29831.26	+2.9	$\bar{3}\bar{9}$.612	+3.9	Hn
1947 July 23.61	32389.61	−15.5	$\bar{3}\bar{2}$.257	+9.6	Hn
1955 May 3.62	35230.62	−0.6	$\bar{2}\bar{5}$.637	+0.1	Hn
July 3.71	291.71	−2.9	.795	+2.6	Hn
1962 May 16.34	37800.34	−12.2	$\bar{1}\bar{8}$.311	+6.8	Hn
17.83	801.83	−9.6	.315	+9.0	Hn
1966 May 20.09	39265.09	−47.0	$\bar{1}\bar{4}$.116	−1.6	RGO
31.07	276.07	−34.9	.144	+6.3	RGO
June 30.00	306.00	−20.5	.222	+9.2	RGO
July 23.93	329.93	−25.6	.284	−3.7	RGO
1967 Apr 3.19	39583.19	−36.0	$\bar{1}\bar{4}$.942	−3.3	RGO
May 31.06	641.06	−45.6	$\bar{1}\bar{3}$.092	+2.8	RGO
June 28.01	669.01	−25.5	.165	+12.6	RGO
Aug 20.88	722.88	+3.1	.305	+22.7	RGO
1970 Aug 17.11	40815.11	−18.9	$\bar{1}\bar{0}$.142	+22.7	Hn
27.09	825.09	−16.5	.168	+21.1	Hn
1975 June 7.34	42570.34	−3.5	$\bar{6}$.701	−2.6	Hn
27.25	590.25	−14.6	.753	−12.0	Hn
July 22.15	615.15	−10.5	.817	−2.8	Hn
1976 Aug 28.09	43018.09	−20.1	$\bar{5}$.864	−5.7	Hn
31.13	021.13	−1.5	.872	+14.3	Hn
Sept 8.09	029.09	−18.8	.892	+1.3	Hn
1981 May 3.04	44727.04	−19.6	0.303	+0.3	C
19.44	743.44	−16.0	.345	−0.3	C
June 1.04	756.04	−12.5	.378	+0.3	C
28.98	783.98	−5.6	.451	+2.0	C

Table 1. Continued.

Date	MJD	Velocity km s^{-1}	Phase	$(O-C)$ km s^{-1}	Source*
1981 July 4.96	44789.96	−7.2	0.466	−0.5	C
26.93	811.93	−4.3	.523	−0.5	C
Aug 10.93	826.93	−2.6	.562	−0.3	C
16.88	832.88	−2.6	.578	−0.7	C
26.87	842.87	−1.1	.604	+0.1	C
Sept 3.88	850.88	−0.8	.624	0.0	C
12.86	859.86	−1.3	.648	−0.7	C
18.88	865.88	−0.5	.663	+0.1	C
Oct 2.81	879.81	−1.6	.700	−0.7	C
12.81	889.81	−1.1	.725	+0.4	C
25.19	902.19	−3.2	.758	−0.4	C
1982 Mar 5.24	45033.24	−47.9	1.098	−0.2	C
May 4.07	093.07	−25.1	.253	+0.5	C
24.02	113.02	−19.0	.305	+0.6	C
June 26.00	146.00	−12.0	.391	−0.2	C
July 9.97	159.97	−9.5	.427	−0.4	C
26.91	176.91	−6.2	.471	+0.2	C
Aug 11.92	192.92	−4.5	.513	−0.2	C
31.85	212.85	−1.8	.565	+0.5	C
Sept 13.86	225.86	−0.6	.598	+0.7	C
Oct 27.75	269.75	−0.2	.712	+0.9	C
1983 Feb 3.61	45368.61	−40.2	1.969	−0.3	V
23.24	388.24	−50.8	2.020	−1.2	C
Mar 11.17	404.17	−50.1	.061	+0.7	C
15.18	408.18	−49.6	.072	+0.6	C
Apr 16.08	440.08	−41.3	.155	−1.7	C
24.13	448.13	−34.9	.176	+1.5	C
Oct 13.19	620.19	−1.9	.623	−1.0	P
Dec 4.70	672.70	−3.1	.759	−0.2	C
10.69	678.69	−3.6	.775	+0.3	C
1984 Apr 14.16	45804.16	−47.6	3.100	−0.2	C
24.12	814.12	−43.5	.126	+0.4	C
May 13.06	833.06	−37.0	.175	−0.5	C
June 9.07	860.07	−27.7	.246	−1.1	C
1985 Jan 24.28	46089.28	−10.7	3.841	0.0	C
Feb 17.56	113.56	−23.0	.904	−0.2	V
24.20	120.20	−27.1	.921	0.0	C
Mar 11.20	135.20	−37.2	.960	+0.4	C

* Source code:

MtW	Mount Wilson (Adams 1914; Abt 1973)
DAO	Dominion Astrophysical Observatory (Harper 1934)
Tr	Tremblot (1938)
Hn	Hendry (1978)
RGO	Royal Greenwich Observatory (Woolley *et al.,* 1981)
C	Cambridge spectrometer (Griffin 1967)
V	Vctoria spectrometer (Fletcher *et al.* 1982)
P	Palomar spectrometer (Griffin & Gunn 1974)

2.3 *Spectroscopic Observations*

We have taken six 10Å mm^{-1} plates of HR 6902 at Mount Wilson, all on IIa–O emulsion. The first two were exploratory ones, taken in 1982 before we knew the orbit, with the comparatively small trailed width of 1 mm. In August of the following year, when we visited Mount Wilson principally for other purposes but knew HR 6902 to be quite near a node, we obtained a $2\frac{1}{2}$-mm-wide spectrogram. Finally, in 1984 March we took three plates on consecutive nights during a visit especially timed to enable HR 6902 to be observed at the more favourable node when the velocity difference between the components would be the maximum possible. The total width of the three spectra was $5\frac{1}{2}$ mm; on two of the nights observing conditions did not allow a spectrogram of the full $2\frac{1}{2}$ mm width permitted by the spectrograph to be obtained during the limited time that HR 6902, which is far over to the east in the morning sky in March, was accessible. Fig. 3 shows prints made from short regions of spectrograms taken at both nodes, and also of spectra whose types most nearly match those of the components of HR 6902.

In Section 1.2.1 we pointed out that in principle only one spectrogram is needed to determine the amplitude of radial-velocity variation of the secondary component of a composite-spectrum binary and thereby to find the mass ratio. That is perfectly true; but if there were a systematic—or any other—error in the measurement of velocities from our subtracted spectra, it would simply vitiate the mass ratio and would not be apparent if we relied on just a single spectrogram. In this initial paper, therefore, we have thought it wise to treat an object for which we have several spectra, including ones taken near each node. The shape of the radial-velocity curve is almost entirely defined by the spectrometer observations of the primary star; all that the velocities of the secondary are called upon to do is to fix the amplitude of variation of that component, so only one degree of freedom is thereby lost. The residuals of the secondary velocities can therefore furnish a true idea of the errors inherent in our procedures. Those velocities will be seen not to suffer from any significant nonrandom error, and their Standard deviation will be shown to be better than 1 km s^{-1}, corresponding to little more than 1 μm on our 10-Å mm^{-1} spectrograms.

2.4 *Recovery of the Secondary Spectrum*

Reduction of the spectrograms proceeded in the manner outlined in the earlier part of this paper. The digital data sets resulting from the three plates taken on consecutive nights were averaged, with weighting according to their relative widths, and were thereafter treated as a single observation. The best match to the primary spectral type from among the available standards was found to be an equally-weighted average of ε Sct (G8 II) and ε Boo A (K0 II–III), so the derived type could be said to be G9 II. The result of subtracting that hybrid cool standard from HR 6902 was a spectrum that is matched very well by that of π Cet (B7 V) and even more accurately by an equal hybrid of π Cet and ν Cap (B9.5 V). Those stars are said in the *Bright Star Catalogue* (Hoffleit 1982) to have projected rotational velocities of only 18 and 17 km s^{-1} respectively; the lines of the B star in HR 6902 are if anything sharper still. The radial velocity of π Cet has been considered variable (Moore & Albrecht 1910) but there is no hint of any secondary star in the spectrum, so for our purposes π Cet is satisfactory as a standard.

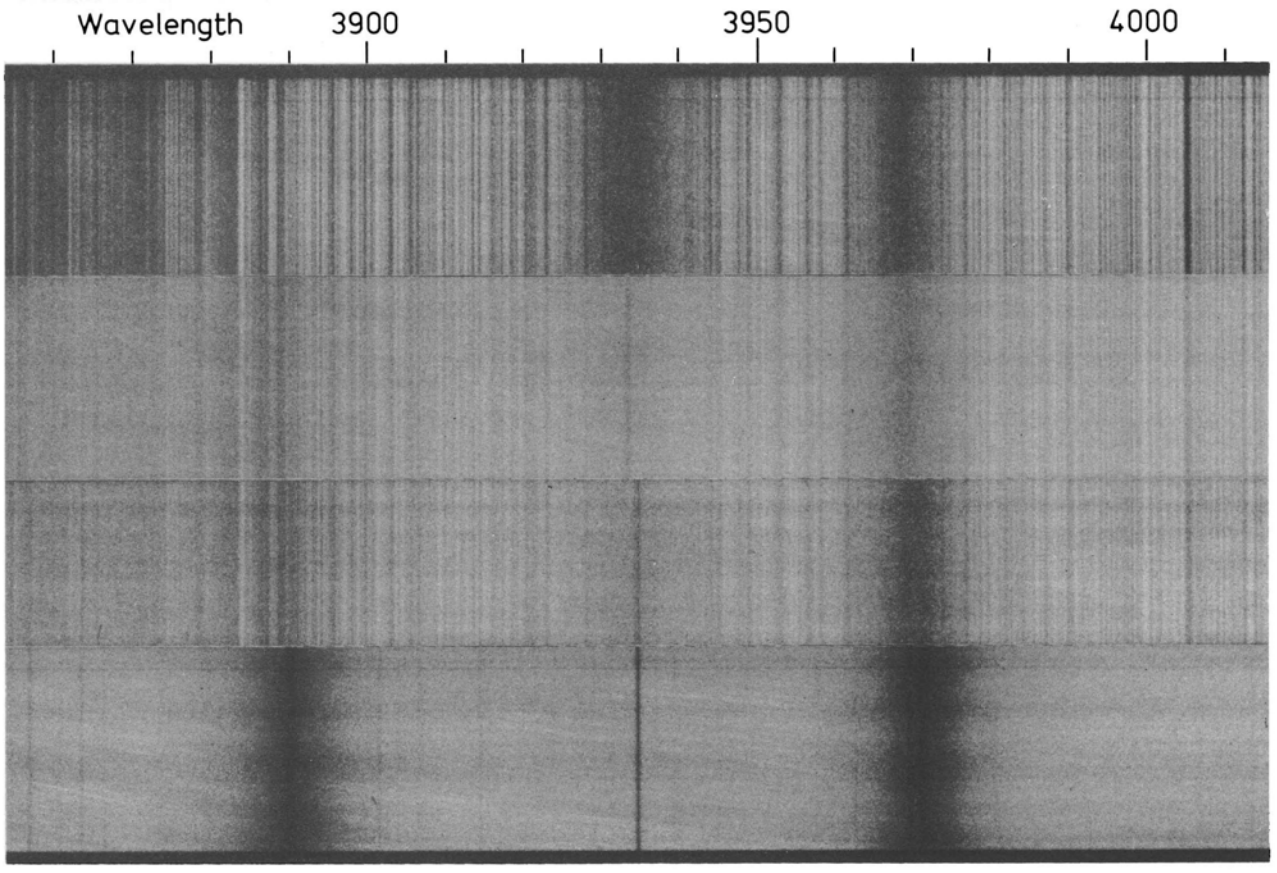

Figure 3. Small parts of some of the spectra upon which this paper is based. The middle two spectra are of HR 6902, taken near opposite nodes of the orbit on 1983 August 31 (upper) and 1984 March 24 respectively. The top spectrum is of ε Sct (G8 II) and the bottom one is of π Cet (B7 V). These spectra were taken at 10 Å mm^{-1} with the coudé spectrograph of the 100-inch Hooker reflector on Mount Wilson. R. & R. GRIFFIN

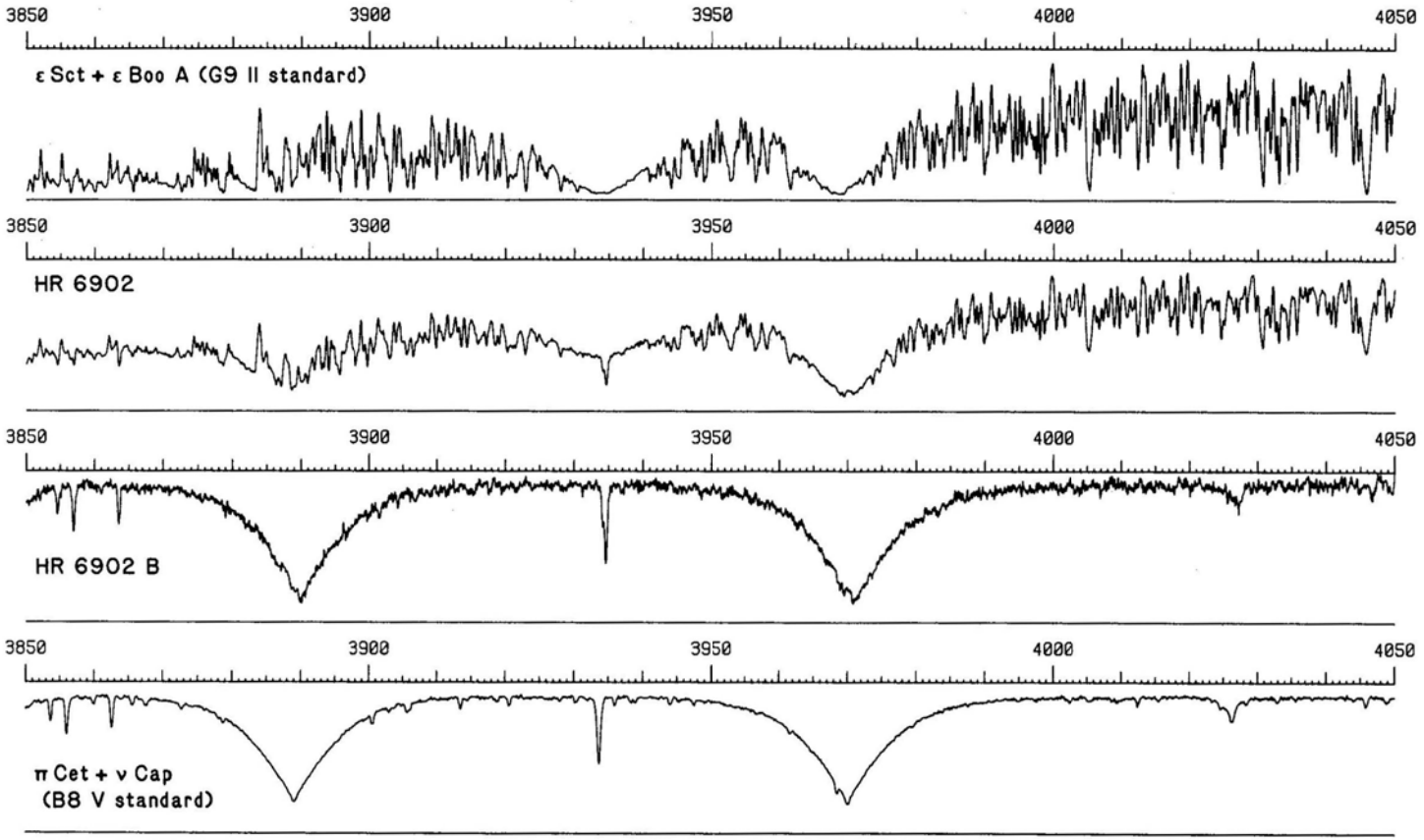

Figure 4. Subtraction of spectra. The top spectrum is adopted as the analogue of the late-type component of HR 6902. Subtraction of an optimal proportion of it from the spectrum of HR 6902 (second tracing down) isolates the early-type component (third tracing), which may be compared with the standard spectrum at the bottom. The horizontal line below each tracing is the zero-intensity level. R. & R. GRIFFIN

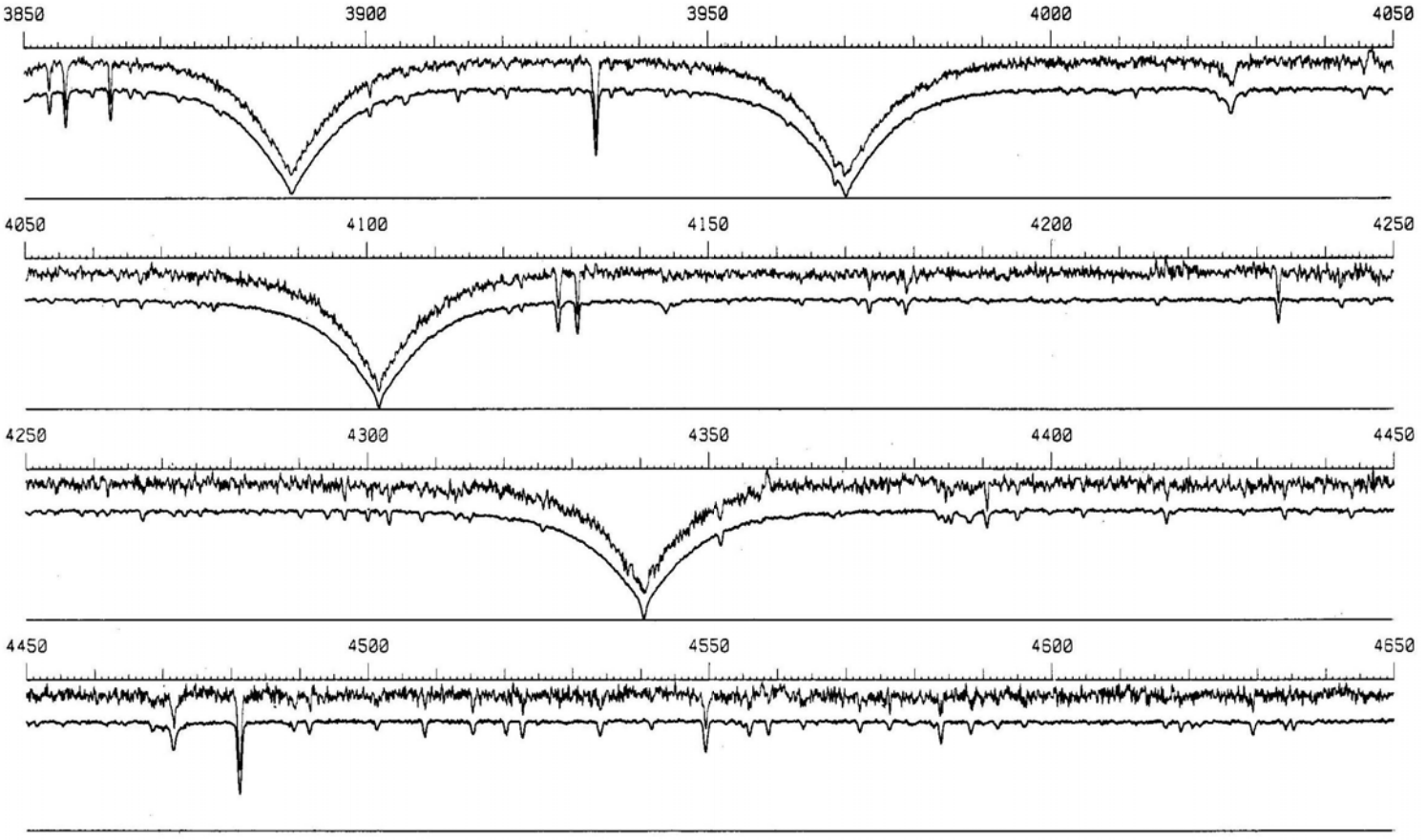

Figure 5. The spectrum of HR 6902 B (upper tracing in each panel) compared with the spectrum of the B8 V standard. The horizontal line below each tracing represents zero intensity for HR 6902 B; the B8 V spectrum has been displaced by −20 per cent of the continuum height. R. & R. GRIFFIN

The process of subtraction is well illustrated by Fig. 4, which shows just one of the four 200-Å regions into which our spectra are divided. It will be seen that the B-type spectrum, visible in the tracing of HR 6902 itself as little more than a loss of contrast of the spectrum of the cool star, emerges as a result of the subtraction with astonishing clarity and detail; and its correspondence with the B8 hybrid standard is remarkably exact. The radial-velocity displacement, of about 1Å to the red, in the spectrum uncovered for the hot component of HR 6902 is noticeable even at the small scale of Fig. 4.

An interesting feature marginally visible in Figs 3 and 4 is the duplicity of the sharp K line in HR 6902. The line contains an interstellar component as well as one arising in the B star. HR 6902 is probably some 300 pc away and has a Galactic latitude of about 9°, so the appearance of an interstellar K line is not surprising. Any effort to measure the radial velocity of the secondary star by means of the K line, such as was proposed by Hendry (1978), would be likely to give misleading results unless it were carried out on spectra of sufficiently high quality and resolution to enable a clear distinction to be drawn between the two contributors to the line. However, now that the metal lines in the secondary are known to be so sharp, a sufficiently shrewd investigator might find it possible to measure some of them directly in the composite spectrum, especially at wavelengths that are shorter than those we have illustrated and where the contribution of the primary star is smaller.

The signal/noise ratio in the spectrum of the secondary star can be maximized by averaging the results of all the available plates. The individual spectra need to be shifted back to zero displacement before they are averaged. An interesting point concerns the signal/noise requirements of the cool standard spectra: there is only one spectrogram of each of the two stars that make up the hybrid G9 II standard. Because the secondary spectra have to be shifted before they are ready to be co-added, the noise due to the G9 standard (which was used in every reduction) is out of register when the spectra are summed, so to all intents and purposes the same standard spectrum becomes different ones when it is used at sufficiently differing radial-velocity shifts. The critical shift needed to ensure independence of the noise is equal to the autocorrelation length of the noise. The noise is manifested as photographic grain, which is probably under-sampled by our 5-μm microdensitometer intervals. The limit is therefore set by our own procedures. Actual trials on featureless spectra show that the autocorrelation of the noise is down to 10 per cent at a displacement of ± 2 spectral elements (10 mÅ and is zero at ± 3 elements (15 mÅ) and beyond. Two elements correspond to about 7 km s^{-1}, so spectra whose shifts differ by more than that are effectively independent as far as the noise from the standard spectra is concerned.

Fig. 5 shows our final results on the secondary spectrum, over the complete wavelength range for which we have recovered it. The signal/noise ratio naturally tends to fall off towards longer wavelengths, where the relative brightness of the secondary star is rapidly diminishing in comparison with the primary. We repeat here the caveat given in Section 1.2.2, that the part of the spectrum above λ 4500 Å is liable to be slightly contaminated with the overlapping spectrum from the next (third) order of diffraction of the grating.

We think that the initial impression given by Fig. 5 is a generally favourable one: the spectrum that our procedure has revealed for HR 6902 B is indeed extremely similar to the genuine B-star spectrum that we have provided for the purposes of visual comparison. However, a sufficiently critical appraisal does disclose some deficiencies;

among the ones that we find most objectionable are the residual traces of the primary star's G band near λ 4310 Å, and the apparent emission lines near λ 4215 Å. These imperfections, and other lesser ones which may be detected by the discerning eye, no doubt arise because we have been unable to find an absolutely exact match for the primary star among our library of late-type standard spectra. Near the spectral type of the primary, G9 II, the G band (due to the CH radical) shows little systematic change of strength with either spectral type or luminosity, so there is no hope of finding a better match by looking for a more appropriate spectral type. What we need is another G9 II standard spectrum *with a slightly stronger G band,* no doubt reflecting a slightly greater carbon abundance or minor differences in atmospheric structure. It must be realized that the difference between the present G9 II standard and HR 6902 A is nothing like as great as the apparent defects in the spectrum of HR 6902 B; especially at the longer wavelengths, the composite spectrum is so dominated by the primary that imperfections in the match with its surrogate are magnified several-fold in the difference-spectrum that is left to represent the secondary. Just as the G band fails to match perfectly, so the CN bands, whose principal heads are at $\lambda\lambda$ 3883 and 4215 Å, are not of identical strength in HR 6902 A and in the G9 II standard. CN dominates the late-type spectrum between $\lambda\lambda$ 3850 and 3883 Å; the subtraction process (shown in detail in Fig. 4) therefore ensures that the right amount of CN is subtracted, but that is done at the slight expense of the atomic lines. Just above the head of the CN band is a 'window' where the spectrum rises nearly to the continuum; it forms an arresting feature, looking almost like an emission line, in Fig. 3. The CN band is subtracted so accurately that the spectrum attributed to HR 6902 B passes over the region of this profound disturbance with little sign of discontinuity; but then the profile of the Hζ line at λ 3888 Å is a trifle disturbed by imperfect matching of certain metal lines near its centre. Similarly, the λ4215-Å CN band has disappeared without trace in the spectrum of HR 6902 B, but only at the cost of slight mismatching of some atomic lines just beyond its head.

Except by taking spectra of more and more late-type stars of about the right spectral type in the hope that one of them might prove to be a better match to the relevant component of the composite object, there is nothing we can do to improve on Fig. 5, unless indeed HR 6902 proves to exhibit total eclipses (see Section 2.7.1) and the primary spectrum can then be observed directly free of contamination. We can only say that we are aware of the defects; that they stem in large measure from the fact that late-type spectra are not uniquely characterized by just the two parameters spectral type and luminosity alone; and that we interpret them as showing that the fundamental limitation to the accuracy with which composite spectra can be disentangled by the method we are using is set not so much by our own shortcomings as by 'cosmic scatter' in the properties of stars.

2.5 *The Radial Velocity of the Secondary*

The derivation of the radial velocity from the secondary spectrum has been partly described in Section 1.2.7. The spectra of HR 6902 B and the B-type standard are re-normalized to a 'continuum' which follows the wings of the Balmer lines, and are then inverted and cross-correlated with one another. The Balmer cores, and also the K line which we have seen to be partly interstellar, are omitted in the cross-correlation, care being taken to site the ends of the sections being correlated in featureless parts of the

Table 2. Redial velocities derived from spectra, recovered by the substraction produced, of the hot component of HR 6902.

Date	MJD	Width of spectr. mm	Wt.	Radial velocities* P km s^{-1}	$(S-P)$ km s^{-1}	S km s^{-1}	Phase	$(O-C)$ km s^{-1}
1982 Apr 22.49	45081.49	1.0	0.4	−29.5	+25.8	−3.7	1.223	+2.2
1982 Aug 24.18	45205.18	1.0	0.4	−3.0	−37.8	−40.8	1.545	−0.1
1983 Aug 31.24	45577.24	2.5	1.0	−4.4	−34.1	−38.5	2.511	+0.4
1984 Mar 23.49†	45782.49	5.5	2.2	−51.0	+73.2	+22.2	3.044	−0.1

* P is the radial velocity computed from the orbit solution for the primary at the relevant epoch; $(S - P)$ is the velocity, determined from the recovered spectrum, of the secondary in the rest frame of the primary; and S is the resulting velocity of the secondary.

† Sum of three spectrograms taken on consecutive nights.

spectrum. Each 200-Å region is considered as a whole, and the approximation is implicitly made that the Doppler shift is constant in wavelength terms throughout it, which is of course not strictly true since it is really proportional to wavelength. The error incurred by the approximation is, however, slight. The wavelength shift for each region is converted into velocity at the effective wavelength (see Section 1.2.7), and the velocities so derived independently for the four spectral intervals are averaged to give the final result.

It will be recalled that the velocities thus determined are velocity *differences* between the two components of the composite spectrum. Since the velocity of the primary can be computed for any given moment from the orbit which we have already determined, it is a straightforward matter to obtain the absolute velocities of the secondary star. The salient data are set out in Table 2.

2.6 *The Orbit Solution*

The velocity data are used, finally, in a double-lined orbit solution for HR 6902. In the expectation that the principal source of uncertainty in the relative velocities is the noise on the spectra of HR 6902, we have thought it appropriate to weight the four velocities of the secondary in direct proportion to the widths of the spectra upon which they are based. It is convenient to regard the unit of weight for the secondary velocities as being that corresponding to a spectrogram with a trailed width of $2\frac{1}{2}$ mm, because then the four measurements have a total weight of exactly 4. In the orbit solution the secondary velocities have been globally weighted by the further multiplicative factor 0.7, in order to cause their weighted mean-square errors to be equal to those of the primary velocities. The actual value of those errors is 0.53 (km s^{-1})^2, so a secondary observation of unit weight has a means-square error of 0.53/0.7, or 0.76, (km s^{-1})^2. In other words, a consideration of the external errors of the secondary velocities, as judged by the orbital residuals, leads to the conclusion that an observation of unit weight (based on a $2\frac{1}{2}$-mm spectrogram) has a standard deviation of $(0.76)^{1/2}$, *i.e.* 0.87, km s^{-1} According to our assumption that the weight of an observation is directly proportional to the width of the original spectrogram, the standard deviation of a velocity based on a spectrogram of

Table 3. Orbital elements for HR 6902.

P = 385.00 days (fixed, see text)	$(T)_2$ = MJD 45380.5 ± 1.1
γ = −19.31 ± 0.11 km s^{-1}	$a_1 \sin i$ = 127.1 ± 1.0 Gm
K_1 = 25.26 ± 0.19 km s^{-1}	$a_2 \sin i$ = 166.4 ± 3.0 Gm
K_2 = 33.1 ± 0.6 km s^{-1}	$f(m_1)$ = 0.553 ± 0.013 $M_\odot$
q = 1.310 ± 0.021 (m_1/m_2)	$f(m_2)$ = 1.24 ± 0.07 $M_\odot$
e = 0.311 ± 0.007	$m_1 \sin^3 i$ = 3.86 ± 0.13 $M_\odot$
ω_1 = 145.9 ± 1.2 degrees	$m_2 \sin^3 i$ = 2.95 ± 0.09 $M_\odot$
rms error (unit weight) = 0.73 km s^{-1}	

width W mm is $(1.9/W)^{1/2}$ km s^{-1}. Of course these numbers cannot be expected to be very accurate, in view of the fact that we are purporting to do statistics on only four observations; but they certainly should be of the right order.

The final orbit computed from the radial velocities given in Tables 1 and 2 has the elements given in Table 3. The corresponding radial-velocity curves have already been shown in Fig. 2.

2.7 *Masses, Luminosities and Rotation Periods of the Component Stars*

2.7.1 *Masses*

The mass ratio q, which is probably the most important single quantitative datum to emerge from this investigation, is seen from Table 3 to be determined to an accuracy of better than 2 per cent. The more evolved star in the system is the more massive one, as is to be expected according to stellar evolution theory; the difference of mass has a Statistical significance of 14 standard deviations.

Masses of main-sequence stars have been conveniently tabulated by Allen (1973) and in Landolt-Börnstein (Schaifers & Voigt 1982). Entering the tables at spectral type B8 V (by interpolation in the case of Allen), we find the mass to be 4.3 or 3.8 $M_\odot$ respectively. The impression is given, therefore, that the mass of the B8 component of HR 6902 might be taken as close to 4 $M_\odot$. However, the review by Popper (1980), although cited in Landolt-Börnstein as providing the most reliable data on stellar masses, presents a rather different picture. Popper's Table 2 lists the properties of main-sequence eclipsing binaries whose components are mutually detached, and includes five systems whose primaries are attributed spectral types of B8 or B9. The most massive of the five is χ^2 Hya, whose mass is given as 3.61 ± 0.08 $M_\odot$; in a (log T, log L) diagram that star is right at the upper edge of the main-sequence band, and indeed it is said by Andersen (1975)to be on the point of commencing a phase of rapid evolution. AS Cam,V451 Oph and RX Her are more or less in the middle of the main-sequence band and have masses of 3.31 ± 0.07, 2.78 ± 0.06 and 2.75 ± 0.06 $M_\odot$ respectively. AR Aur is on the zero-age main-sequence line and has a mass of only 2.48 ± 0.10 $M_\odot$ respectively.

From those data, therefore, we could conclude that the mass of a B8/B9 star is about 3.0 $M_\odot$ with an uncertainty of about 20 per cent. However, the lower part of that range is excluded, since our Table 3 shows from the spectroscopic orbit that the *minimum* mass

of HR 6902 B is 2.95 ± 0.09 $M_{\odot}$. If the actual mass is close to that lower limit there must be eclipses in the HR 6902 system. Primary eclipse would take place at phase .252, or 97 days after periastron passage, and could last up to about 13 days if central. Opportunities to watch for eclipses will occur around 1987 August 10 and then 20 days later in each succeeding year. On the first few occasions HR 6902 will be conveniently placed in the evening sky.

Table 1 shows that on 1982 May 4 a radial-velocity trace of HR 6902 was obtained at phase .253, almost exactly the time of a possible eclipse. There is no doubt that that trace shows dips that are significantly deeper than normal. The photon detection rate also suggests that the star was unusually faint on that occasion in comparison with neighbouring stars, although such evidence—acquired through a spectrometer whose entrance slit does not pass all of the star's light, and moreover through a sky which was probably far from photometric—cannot be conclusive. The trace of 1984 June 9, whose phase of .246 places it little more than two days before the computed mid-time of a possible eclipse, was unfortunately compromised by thick and variable cloud, but it does not support the idea that an eclipse was in progress then. Nevertheless we adopt as a working hypothesis, pending explicit photometric and/or spectroscopic observations at the time of a predicted eclipse, that eclipses do occur and that therefore the factor $\sin^3 i$ in the expression for the stellar masses must be almost unity. Thus the mass of the B8 V star is very close to 3.0 $M_{\odot}$ and that of the G9 II component is 3.9 $M_{\odot}$.

If eclipses do indeed take place, then HR 6902 is to be seen as an important new addition to the small class of bright ζ Aur stars, eclipsing systems consisting of a late-type supergiant and a B star. There are five presently recognized members of the class: ζ Aur itself, 31 and 32 Cyg, VV Cep and 22 Vul. Their particular significance lies in the fact that, around the times of eclipses, the line of sight to the B star passes through the outer layers of the distended atmosphere of the supergiant. Spectra taken at those times are apt to show circumstellar absorption features, and a time sequence of such spectra (e.g. Wright 1970, Plate I) can give information on the properties of the chromosphere as a function of radius from the star. Because the supergiant in HR 6902 is probably less luminous than that in any of the other ζ Aur systems, it is perhaps to be expected that the duration of any episode of circumstellar absorption will be relatively short (only a few days at most on either side of the actual eclipse). The first Mount Wilson spectrogram was exposed 11 days before a prospective eclipse date, and does not show any unusual features.

2.7.2 *Luminosities*

Appeal to the same authorities as before, this time for information on stellar luminosities, produces for types B8 V and G9 II the absolute magnitudes 0.0 and (by rather risky interpolation) – 2 respectively from Allen (1973) and – 0.25 and – 2.3 from Landolt-Bornstein (Schaifers & Voigt 1982). Popper's (1980) late-B stars are in tolerable agreement, having absolute magnitudes near zero though with a range amounting to ± 1 magnitude.

One can see immediately that a difference in luminosity of the order of two magnitudes in the V band is entirely consonant with the apparent near equality of the stars in the λ 4000 Å region. However, we ought in principle to be able to establish the luminosity difference quite accurately, using information already available in the

spectrum-subtraction process in order to obtain the true flux ratio as a function of wavelength. When we subtract the late-type spectrum from the composite one, we are in effect dividing the light in the composite spectrum between the two components in carefully defined proportions. By summing the intensities assigned to each component in every successive wavelength element within a given interval, we should be able to determine the relative luminosities of the two stars in any desired wavelength interval within the range covered by our observations.

Notice that the division of light between the components is largely independent of the photometric and spectroscopic characteristics of the standard stars employed and of such external factors as interstellar reddening and our treatment of the continuum in the various stars concerned. If, for example, we reduced the height of the continuum of the late-type standard star by a factor of two, we should simply find that we needed to subtract twice as large a proportion of it, and the result would be exactly the same. Since the proportion to be subtracted is optimized in every 50-Å band independently, effects which vary slowly with wavelength, such as reddening and the apparent slopes of the stellar continua, have negligible baselines over which to operate.

A suitable source of absolute photometry for comparison with the relative intensities derived from our spectrophotometry appears to be the tabulation by Willstrop (1965), which offers intensities in sharply-bounded 50-Å bands for stars of a number of representative spectral types. Included in the tabulation are two B8 V stars, ϕ Eri and η Aqr. For our purposes their fluxes are hardly distinguishable from one another, and we have arbitrarily selected ϕ Eri. The only late-G star of luminosity class II observed by Willstrop is ε Set (G8 II), which is one of the contributors to our hybrid analogue of the late-type primary of HR 6902, the other being ε Boo A (K0 II–III).

In Table 4 we give the flux ratios found from our splitting of the spectrum of HR 6902 into its two components. To obtain an exact correspondence with Willstrop's table, the intensities whose ratios are given have been summed in successive 50-Å bands. The ratios have been averaged from all the available plates; we ourselves were somewhat disappointed at the level of interagreement between different determinations, and the mean values shown in the Table have accuracies no better than a few per cent. The Table also lists the ratio of fluxes between ε Set and ϕ Eri, as derived from Willstrop's photometry whose errors are said to be 1 or 2 per cent. The ε Sct/ϕ Eri ratios have been multiplied throughout by the empirical factor 5.6, which represents the relative brightness we need to attribute to ε Sct relative to ϕ Eri (in the V band, to which Willstrop's data are normalized) in order to mimic the ratio observed for HR 6902. With such a factor, representing 1.9 mag in magnitude terms, there is seen to be a close correspondence between the observed flux ratios and those obtained from the absolute photometry of ε Sct and ϕ Eri. This result reassures us that the spectral types that we have assigned on purely spectroscopic grounds also provide a satisfactory photometric representation of the HR 6902 system, and it provides a rather accurate estimate of the visual luminosity difference between the components, again in close correspondence with the difference expected on the basis of the spectral types.

2.7.3 *Rotation periods*

The spectral lines of the primary star in HR 6902 are slightly but distinctly broadened by (presumably) rotation: the single Palomar radial-velocity trace furnishes an estimate

Table 4. Relative fluxes of ε Sct and ϕ Eri in 50-Å bands, compared with the ratios between the components of HR 6902. The ε Sct /ϕ Eri ratios have all been multiplied by the empirical factor 5.6, which represents the relative visual luminosities of the components of HR 6902.

λ (Å)	From Willstrop (1965) ε Sct	ϕ Eri	Ratio	HR 6902 (observed)
3850				
3900	—	—	—	0.43
3950	—	—	—	0.42
4000	—	—	—	0.80
4050	170	944	1.01	1.05
4100	170	831	1.15	1.16
4150	167	764	1.23	1.26
4200	162	843	1.08	1.01
4250	188	807	1.31	1.26
4300	184	785	1.33	1.32
4350	210	632	1.94	1.92
4400	228	711	1.78	1.80
4450	244	715	1.91	1.91
4500	270	684	2.20	2.03
4550	281	673	2.35	2.28
4600	289	651	2.49	2.47
4650	309	630	2.71	2.68

of $v \sin i \simeq 12$ km s^{-1}, so $v = 12$ km s^{-1}. The broadening is too small to be apparent in Fig. 3. If the radius of the star is estimated at 40 $R_\odot$ (28 Gm), the corresponding rotation period is about 15 Ms or 170 days. The rotation is therefore probably *not* synchronized with the 385 day orbital period: that would require $v \sin i \simeq 5$ km s^{-1} or $R_* \simeq 100\ R_\odot$ (both of which are well outside the likely range of uncertainty) or a combination of revisions (still almost unacceptable) to both $v \sin i$ and R_*.

The lines of the secondary are so sharp that we can only set an upper limit of about 15 km s^{-1} to $v \sin i$: the rotation period is longer than about 10 days.

Acknowledgements

We are very much indebted to the Mount Wilson & Las Campanas Observatories for the provision of a great deal of observing time at the 100-inch telescope, and we wish to thank the staff on Mount Wilson most warmly for their unstinted assistance. We thank the UK Science and Engineering Research Council for defraying the costs of ten visits to Mount Wilson in furtherance of our investigations of composite spectra and for the financial support of one of us. We are also very grateful to the McDonald Observatory for allowing us to make initial experiments there; to Dr C. Jaschek and the Centre de Donnees Stellaires for a printout of bibliographical data on HR 6902; and to Mrs J. Hassan and Mr R. W. Sword for assistance in the production of this paper. Finally, we are much indebted to the referees, Drs D. M. Popper and A. H. Batten for their helpful reports. In particular, Dr Popper's report, together with similar advice given by Dr P. P.

Eggleton who saw a preprint of the paper, led us to look for (and probably discover) eclipses in HR 6902; we had previously discounted the possibility of eclipses because we were misled by the exaggerated masses tabulated for late-B stars by certain reference handbooks.

References

Abt, H. A. 1973, *Astrophys. J. Suppl.,* **26**, 365.
Adams, W. S. 1914, *Publ. astr. Soc. Pacific,* **26**, 260.
Adams, W. S., Joy, A. H., Humason, M. L., Brayton, A. M. 1935, *Astrophys. J.,* **81,** 187.
Adams, W. S., Joy, A. H., Strömberg, G., Burwell, C. G. 1921, *Astrophys. J.,* **53**, 13.
Allen, C. W. 1973, *Astrophysical Quantities,* Athlone, London.
Andersen, J. 1975, *Astr. Astrophys.,* **44,** 445.
Batten, A. H., Fisher, W. A., Fletcher, J. M., Hill, G. 1983, *Publ. astr. Soc. Pacific,* 95, 768.
Beavers, W. I., Griffin, R. F. 1979, *Publ. astr. Soc. Pacific,* 91, 824.
Bopp, B. W., Fekel, F., Jr., Griffin, R. F., Beavers, W. I., Gunn, J. E., Edwards, D. 1979, *Astr. J.,* **84,** 1763.
Bowen, I. S. 1952, in *Astronomical Techniques,* Ed. W. A. Hiltner (Vol. 2 of Stars and Stellar Systems, Eds G. P. Kuiper & B. M. Middlehurst), Univ. of Chicago, p. 34. (See p. 50.)
Campbell, W. W., Albrecht, S. 1910, *Lick Obs. Bull.,* **5**, 174.
Cannon, A. J., Pickering, E. C. 1922, *Ann. Harv. Coll. Obs.,* **97**, 169 & 257.
Cousins, A. W. J. 1963, *Mon. Not. astr. Soc. Sth Africa,* **22**, 12.
Dunham, T., Jr. 1955, *Vistas Astr.,* **2**, 1223.
Eggen, O. J. 1955, *Astr. J.,* **60**, 65.
Fletcher, J. M., Harris, H. C., McClure, R. D., Scarfe, C. D. 1982, *Publ. astr. Soc. Pacific,* **94**,1017
Gordon, K. C. 1946, *Astrophys. J.,* **103**, 13.
Griffin, R. F. 1967, *Astrophys. J.,* **148**, 465.
Griffin, R. & R. 1979a, *Mon. Not. R. astr. Soc.,* **187**, 91.
Griffin, R. & R. 1979b, *A Photometric Atlas of the Spectrum of Procyon,* R. & R. Griffin, Cambridge.
Griffin, R. F. 1981, *J. Astrophys. Astr.,* **2***,* 115.
Griffin, R. & R. 1984, *Nature,* **310**, 536.
Griffin, R. & R. 1985a, *Sky Telesc.,* **70**, 100.
Griffin, R. & R. 1985b, *Nature,* **316**, 671.
Griffin, R. F. 1986, *J. R. astr. Soc. Canada,* **80**, 91.
Griffin, R. F., Gunn, J. E. 1974, *Astrophys. J.*, **191**, 545.
Häggkvist, L., Oja, T. 1966, *Ark. Astr.,* **4**, 137.
Harper, W. E. 1934, *Publ Dom. astrophys. Obs., Victoria,* **6**, 151.
Heck, A., Manfroid, J. 1980, *Astr. Astrophys. Suppl.,* **42**, 311.
Hendry, E. M. 1978, *Astr. J.,* **83**, 615.
Hendry, E. M. 1984, *Astr. J.,* **89**, 607.
Hoffleit, D. N. 1982, *Bright Star Catalogue,* Yale Univ. Obs., New Haven.
Kuhi, L.V.1963, *Publ. astr. Soc. Pacific,* **75**, 448.
Lee, E. K., Wright, K. O. 1960, *Publ. Dom. astrophys. Obs., Victoria,* **11**, 339.
Markowitz, A. H. 1969, *A Study of Stars Exhibiting Composite Spectra,* Ohio State Univ., Columbus.
Maury, A. C. 1897, *Ann. Harv. Coll. Obs.,* **28**, 1. (See p. 93.)
McAlister, H. A. 1982, *Astr. J.,* **87**, 563.
McAlister, H. A.,Hartkopf, W. I.1984, *Catalog of Interferometric Measurements of Binary Stars,* Georgia State Univ., Atlanta.
Popper, D. M. 1976, *Astrophys. J.,* **208**, 142.
Popper, D. M. 1980, *Ann. Rev. Astr. Astrophys.,* **18**, 115.
Rach, R. A., Herbig, G. H. 1961, *Astrophys. J.,* **133**, 143.
Redman, R. O. 1936, *Mon. Not. R. astr. Soc.,* **96**, 488.
Scarfe, C. D.1970, *Publ. astr. Soc. Pacific,* **82**, 1119.
Schaifers, K., Voigt, H. H. (Eds)1982, *Landolt-Börnstein*, New Series,Group 6, Vol. 2b, Springer-Verlag, Berlin.

Shen, L. Z., Beavers, W. I., Eitter, J. J., Salzer, J. J. 1985, *Astr. J.,* **90**, 1503.
Tremblot, R. 1938, *Bull. Astr.,* **11**, 377.
Trimble, V. L.,Thorne, K. S. 1969, *Astrophys. J.,* **156**, 1013.
Wilson, O. C. 1967, *Astr. J.*, **72**, 905.
Wilson, R. E. 1953, *General Catalogue of Stellar Radial Velocities,* Carnegie Institution of Washington.
Woolley, R. ,Penston, M. J., Harding, G. A., Martin, W. L., Sinclair, J. E., Haslam, C. M., Asian, S., Savage, A., Aly, K., Asaad, A. S. 1981, *R. Obs. Ann.,* No. 14.
Wright, K. O. 1954, *Publ. Dom. astrophys. Obs., Victoria,* **10**, 1.
Wright, K. O. 1970, *Vistas Astr.,* **12**, 147.
Wright, K. O., Lee, E. K. 1959, *Publ. Dom. astrophys. Obs., Victoria,* **11**, 59.
Young, R. K., Harper, W.E.1924, *Publ. Dom. astrophys. Obs., Victoria,* **3**, 1.

Note added in proof

The Dominion Astrophysical Observatory, Victoria, very kindly provided us with a generous allocation of observing time on the 48-inch reflector to monitor HR 6902 spectroscopically around the time of conjunction in 1986 July. An eclipse was seen; preliminary indications are that it was total for about 5 days. Chromospheric absorption, persisting for about 3 days after the end of totality, was also observed. Photometric observers in Arizona were alerted at short notice to the likelihood of the eclipse through the good offices of Mr R. M. Genet, but we do not yet know the outcome.

J. Astrophys. Astr. (1986) **7,** 225–236

The Jet of the Quasar 3C 273

Wolfgang Kundt *Institut für Astrophysik der Universität, Auf dem Hügel 71, D-5300 Bonn, FRG*

Gopal-Krishna *Radio Astronomy Centre, Tata Institute of Fundamental Research, Post Box 1234, Bangalore 560012*

Received 1986 January 1; accepted 1986 June 14

Abstract. New observations of the jet in 3C 273 support and refine our earlier interpretation that (i) the mapped jet is $10^{6\pm0\,3}$ yr old and grows at 0.6 to 0.75 times the speed of light, at an average angle θ of (20 ± 10)° with respect to the line of sight; (ii) its twin is not seen yet because arriving signals were emitted when it was some $10^{0\,6\pm0\,2}$ times younger; (iii) the fluid moving in the jet is an extremely relativistic $e^{\pm}$-pair plasma, of bulk Lorentz factor $\gamma \gtrsim 10^2$; (iv) the beam has swung in projection through some 10º; and (v) the small excursions (wiggles) of the jet around its average propagation direction result from a self-stabilizing interaction with the nonstatic ambient plasma. All other interpretations of which we are aware depend heavily on the ('beaming') assumption that the jet material radiates isotropically in some (comoving) Lorentz frame, an assumption which we consider unrealistic.

Key words: Jets—relativistic beaming—quasars—3C 273—lobe expansion

1. Introduction

The quasar 3C 273 is of outstanding interest because of its proximity, high luminosity, hard γ-ray spectrum and because of its one-sided radio-optical-X-ray jet without a detection of 2-sided radio lobes. Conway, *et al.* (1981) and more recently Davis, Muxlow & Conway (1985) have concluded that the jet grows almost relativistically ($\beta_{\rm head} \simeq 0.74$) and that the observed one-sidedness is intrinsic, *i.e.* that no counterjet exists. For the Lorentz factor γ of bulk motion in the jet they find a decrease from an initial value of $\gamma \simeq 6$ to a final value of $\gamma \simeq 1.5$. Roberts (1984) has argued that the jet is unlikely to consist of an $e^{\pm}$-pair plasma: Its bulk Lorentz factor would have to be high, 'hence' its inclination with respect to the line of sight is so small that its unprotected length would be excessive. Based on this conclusion and a lack of time variability of the γ-ray flux from 3C 273, Morrison, Roberts & Sadun (1984) have discussed the possibility of a hydrogen jet which produces γ-rays on collision with clumped 'warm' entrainments in the outer jet.

These models conflict with our own conclusion (drawn in 1980) that all observed jets are composed of extremely relativistic $e^{\pm}$-pair plasma moving through a thermal channel, with bulk Lorentz factor $\gamma \gtrsim 10^2$, and that one-sidedness is due to relativistic

propagation and (generalized) beaming (*cf.* Kundt & Gopal-Krishna 1981, and Section 2).

The discrepancy between our results and those mentioned above can be traced back to the canonical relativistic beaming formula which is based on the assumption of the existence of a Lorentz frame with respect to which the radiation is isotropic (reviewed by Kellermann & PaulinyToth 1981; Begelman, Blandford & Rees 1984). In Section 2 we shall argue that this assumption can be very misleading; we concur with Lind & Blandford (1985) that the observed intensity distributions 'cannot be used to derive a precise value for the flow velocity because of the uncertainty in the [beaming] models'. Section 3 is devoted to a re-discussion of the pros and cons to extreme bulk velocities. In the succeeding sections we present what we think is a consistent description of the beam head dynamics, its size, age, lobe, and fine structure, including a discussion of the unseen counterjet. The uniqueness of 3C 273 is traced back to both its youth and favourable orientation.

2. Relativistic beaming

If the material composing a jet has an isotropic velocity distribution in its (comoving) centre-of-mass frame, then its radiation will likewise be isotropic, and its radiation with respect to any other frame can be obtained by applying a boost. In particular, the bolometric luminosity in the direction θ is proportional to δ^4 where δ is the well-known Doppler factor,

$$\delta := [\gamma(1-\beta\cos\theta)]^{-1} \simeq \begin{cases} 2\gamma/(1+\gamma^2\theta^2) & \text{for } \theta, \gamma^{-1} \ll 1 \\ 1/2\gamma & \text{for } \theta \simeq \pi, \beta \simeq 1 \end{cases} \qquad (1)$$

with $\gamma := (1-\beta^2)^{-1/2}$.

If, however, the velocity (or energy) distribution in the jet satisfies a power law with suitable cutoffs (to keep all meaningful intergrals finite), then the comoving velocity distribution is far from isotropic: It contains extremely relativivstic particles in the forward hemisphere, but none in the backward hemisphere. In order to see this, insert the formula for the composite Lorentz factor (strictly valid only for parallel velocities)

$$\gamma_{\rm lab} \simeq \gamma_{\rm bulk}\cdot\gamma(1+\boldsymbol{\beta}_{\rm bulk}\cdot\boldsymbol{\beta}) \qquad (2)$$

where $c\boldsymbol{\beta}_{\rm bulk}$ is the comoving velocity and $c\boldsymbol{\beta}$ the velocity with respect to the centre of mass, into the factorized power-law distribution of the radiating charges (averaged over 3-space)

$$dN = \gamma_{\rm lab}^{-(2+g)}\, d\gamma_{\rm lab}\, d^2\omega \qquad (3)$$

in which $d^2\omega := f(\zeta)d^2\Omega$ describes the distribution over angles. The density $f(\zeta)$ should incorporate all perturbations of the beam, both by friction on the walls and by volume obstacles; it is strongly forward-peaked in the lab frame (though not as a function of the centre-of-mass quantity ζ). Using $d\gamma = \gamma^3\beta d\beta$ one gets for $\beta_{\rm bulk} \simeq 1$:

$$\gamma_{\rm bulk}^{1+g}\, dN \simeq \gamma^{-(1+g)}(1+\zeta\beta)^{-(2+g)}[\zeta+\beta\gamma^2(1+\zeta\beta)]d\beta\, d^2\omega \qquad (4)$$

with $\zeta := \cos(\beta_{\rm bulk}, \beta)$. This distribution behaves as $\gamma^{-(2+g)}\, d\gamma$ for fixed $\zeta > 0$ and large γ, and cuts off near $\gamma = 1$ for $\zeta < 0$ in order to satisfy the centre-of-mass condition $0 = \int dN\gamma\beta$. In particular, the comoving energy in relativistic particles, $\int \gamma^{-(1+g)}\, d\gamma$, converges for (realistic values) $g > 0$, hence corresponds to a small percentage of the total energy for not too-small values of g.

In other words: the comoving velocity distribution of a relativistic beam need by no means be isotropic. Rather, a few particles in forward directions can have large momenta whereas all the others are extremely soft. The beaming pattern from such an ensemble has significant intensities in all forward directions (for suitable $f(\zeta)$) but very low intensities in backward directions. Such a beaming pattern can explain the frequent occurrence of jets in spite of extremely relativistic bulk velocities: With sufficient dynamic range, we see a jet for all angles $\lesssim 90°$. We even see often both the jets (which are needed to feed the symmetrically placed outer lobes), particularly in weak sources where the flow interacts more strongly with the channel walls. For such generalized distributions, the standard estimate $\gamma_{\rm bulk} \simeq \theta^{-1}$ turns into an inequality: $\gamma_{\rm bulk} \gtrsim \theta^{-1}$. All the estimates of $\gamma_{\rm bulk}$ given in the extended literature may have to be reinterpreted in this sense.

3. Pros and cons to high γs

In this communication, we do not want to repeat all the earlier arguments against small bulk velocities (Kundt & Gopal-Krishna 1981). The strongest among them (concerning $\gamma_{\rm bulk}$) is our disbelief in the high efficiency of in-situ acceleration to the required ultrarelativistic speeds: Instead of in-situ acceleration, we prefer to think of in-situ deceleration, like for an electron beam illuminating a TV screen.

An independent argument in favour of large bulk velocities is the consideration that the jets emerge from deep inside the broad-line region where thermal emission lines indicate pressure in excess of 1 dyn cm^{-2}. At their termination points, in the heads, the inferred pressures fall mostly short of 10^{-8} dyn cm^{-2}. Consequently, the jet material is squeezed into its channels by an overpressure of more than 10^8 fold. In the absence of excessive friction–which would manifest itself by excessive surface brightness–and after expansion, the channelized plasma must acquire bulk velocities which are equal to its velocities (ordered or random) near the central engine (Landau & Lifshitz 1978). Such velocities are thought to be extremely relativistic, as inferred from the synchrotron spectra.

Now to the cons. It has been argued that extremely relativistic bulk velocities would lead to infinitesimally small scale heights h in the bends of the jets (Begelman, Blandford & Rees 1984; Phinney 1983). The argument is based on the inequality

$$\gamma_{\rm j}\beta_{\rm j}/\gamma_{\rm s}\beta_{\rm s} \lesssim (R/h)^{1/2} \tag{5}$$

where j, s stand for 'jet', 'sound' respectively, and R is the curvature radius. It assumes that the ratio of ram pressure to static pressure stays constant throughout a bend. But it is known from both theory and experiments with supersonic jets that ram pressure can be converted into static pressure via shocks, such that the cross-section of the beam in the bends does not shrink considerably (Courant & Friedrichs 1976).

Another argument against extremely relativistic bulk velocities is the concern about inverse-Compton losses in the broad-line region: Energetic electrons and positrons would lose most of their energy in collisions with the thermal photon bath (Begelman, Blandford & Rees 1984). There is, however, also the inverse reaction: Photons of energy above 10^{11} eV can produce $e_{\pm}$-pairs on collision with *UV* photons, and so can photons above 10^6 eV on collision with protons and electrons. Moreover, ordered radial flows in the inner part of the broad-line region reduce the collision rate between electrons and

photons (*cf.* Kundt 1982). More realistic calculations have to be made before this concern can be considered serious.

4. Beam propagation

Ram-pressure balance in the frame of the contact discontinuity suggests that the heads of strong young jets can advance relativistically into the ambient plasma:

$$\beta_h^2 \beta_j / (\beta_j - \beta_h)^2 = L/Ac^3\rho \tag{6}$$

can exceed unity. Here $c\,\beta_h$ is the speed of the head, $c\,\beta_j$ that of the jet, A its cross section, L is the total power flowing down the jet, and ρ is the ambient mass density, and ram pressure = $\rho_0\, c^2\, \beta^2\, \gamma^2$. Use has been made of Equations (8,10) below for the conversion from the laboratory frame to that of the contact discontinuity (= 'head').

For large β_h, only a small portion $\mathscr{L}$ of L can be dissipated so that the radiated power falls short of L. This reduction in the dissipated power is due to the fact that the needed momentum transfer for channel formation consumes almost the total infalling energy. Quantitatively, the mechanical power L_{mech} transferred to the ambient medium through the contact discontinuity exceeds the force $L\beta_j/c$ integrated over the advance rate $c\beta_h$, whence $L_{mech} \gtrsim L\beta_h\beta_j$, and

$$\mathscr{L} \leqslant L - L_{mech} \lesssim L(1-\beta_h) \tag{7}$$

holds for $\beta_j \simeq 1$. Consequently, the dissipated percentage drops to zero in the extremely relativistic limit.

We can also derive a lower bound on the dissipated portion $\mathscr{L}$ from 4-momentum conservation under the assumption of elastic particle reflections in the comoving frame of the head.This result will not be needed explicitly below, hence the reader who is only interested in 3C 273 is advised to skip the rest of this section.

In order to derive the lower bound on $\mathscr{L}$, we work in the free-particle approximation in which extremely relativistic electrons flowing down the jet (with velocity $c\beta_j$) get reflected by the swept-up ambient plasma. In the frame comoving with the head, these electrons have velocities $c\beta_c$ obtained from the relativistic composition law:

$$\beta_c = (\beta_j - \beta_h)/(1-\beta_j\beta_h) = \beta_j(1-\beta_h/\beta_j)/(1-\beta_h\beta_j). \tag{8}$$

In the laboratory frame, the reflected charges have velocities $c\beta_r$ given analogously by

$$\beta_r = (\beta_h - \beta_c)/(1-\beta_h\beta_c) = -\beta_c(1-\beta_h/\beta_c)/(1-\beta_h\beta_c). \tag{9}$$

The corresponding Lorentz factors γ follow successively from Equation (2, 8, 9):

$$\gamma_c = \gamma_j\gamma_h(1-\beta_j\beta_h) \simeq \gamma_j\gamma_h(1-\beta_h) \tag{10}$$

$$\gamma_r = \gamma_h\gamma_c(1-\beta_h\beta_c) \simeq \gamma_j(1-\beta_h\beta_c)/(1+\beta_h) \tag{11}$$

in which $\gamma_j \gg 1$ has been assumed. The Lorentz factors of the reflected charges are therefore reduced by the factor $(1-\beta_h\beta_c)/(1+\beta_h)$ compared with those in the jet.

We are now ready to calculate the maximal energy Q per particle (of rest mass m) which is available in the lab frame for dissipation. It follows from 4-momentum conservation during the collision on a heavy collective, of mass M ($\gg m$), whose velocity

changes during the collision by $\Delta\beta_h$:

$$m[(\gamma\beta)_j - (\gamma\beta)_r] = M\Delta(\gamma\beta)_h, \tag{12}$$

$$m[\gamma_j - \gamma_r] = M\Delta\gamma_h + Q/c^2 \quad . \tag{13}$$

The identity $\gamma = (1 + \beta^2\gamma^2)^{1/2}$ and equation (12) imply $\Delta y_h \simeq (m/M)\,\beta_h\,[(\gamma\beta)_j - (\gamma\beta)_r]$, whence with Equations (11), (13):

$$\begin{aligned} Q/\gamma_j mc^2 &\simeq (1-\beta_h) - (1-\beta_h\beta_c)(1+\beta_h|\beta_r|)/(1+\beta_h) \\ &\simeq 0.14\beta_h(1-\beta_h)\beta_j\gamma_j^{-2}\,10^{3.68\beta_h}, \end{aligned} \tag{14}$$

the latter for $0.1 \lesssim \beta_h \lesssim 0.8$, $10 \lesssim \gamma_j \lesssim 10^4$ (obtained *via* numerical experiments); i.e. the energy Q per incoming particle energy $\gamma_j mc^2$ which is available for dissipation in this model is smaller than 0.3 per cent for velocities $c\beta_h$ in the given range whenever $\gamma_j \gtrsim 10^2$. Expression (14) is a lower bound on the dissipated portion $\mathscr{L}/L$.

5. The jet of 3C 273

In Fig. 1 we have drawn our knowledge about the jet, both from radio (Flatters & Conway 1985; Foley & Davis 1985; Davis, Muxlow & Conway 1985), infrared (Henry & Becklin 1984), optical (Lelievre *et. al.* 1984; Röser & Meisenheimer 1986) and X-ray data (D. Harris, personal communication). For a redshift of z = 0.158 and a present Hubble parameter of H_0 = 65 km s^{-1} Mpc^{-1} = $10^{-17.7}$ s^{-1} (Bartel *et. al.* 1985), its (projected) angular size of 23 arcsec corresponds to a projected length of $r_\perp$ = 81 kpc $H_{-17.7}^{-1}$. For an inclination angle θ between 10° and 30°, its deprojected length $r = r_\perp/\sin\theta$ falls therefore between 500 and 160 kpc. We favour a value of r in the vicinity of 200 kpc because we expect the jet to be still in its near free expansion stage, yet well outside the halo of the host galaxy whose boundary may be indicated by the inner edge of the 'lobe' discovered by Davis, Muxlow & Conway (1985). For an average propagation speed $c\beta_h$ of the head, the favoured size r translates into an age $t = r/c\beta_h$ between 2×10^6 and 0.5×10^6 yr for $\beta_h \gtrsim 0.6$ (see below). β_h be better not smaller than 0.6.

On the VLBI scale, superluminal expansions have been observed with $\beta_\perp = 8\,H_{-17.7}^{-1}$ (Unwin *et. al.* 1985), suggesting relativistic motion at an angle between 10° and 20° with respect to the line of sight, depending on its bulk Lorentz factor:

$$\beta_\perp/\beta = \sin\theta/(1-\beta\cos\theta) \simeq 2/\theta, \tag{15}$$

the latter for $\gamma \gg 1$. But there is no guarantee that the inferred VLBI angle agrees with the large-scale inclination angle of the jet to within less than 10°, say. We are therefore still left with a considerable uncertainty concerning the largescale θ. Acomparatively short—and therefore young—jet implies a large θ (> 20°). Note that according to our ideas expressed in Section 2, we do not accept estimates of θ based on beaming arguments. An independent estimate, based on the width of the lobe, will be presented in the following section.

In order to assess the propagation speed $c\beta_h$ of the jet's head, we evaluate Equation (6):

$$\beta_h^2/(1-\beta_h)^2 \simeq L/Ac^3\rho = L_{45.5}/A_{43}\rho_{-29} \tag{16}$$

where we have inserted a total power of $L = 10^{45.5}$ erg s^{-1} flowing down the jet, a jet

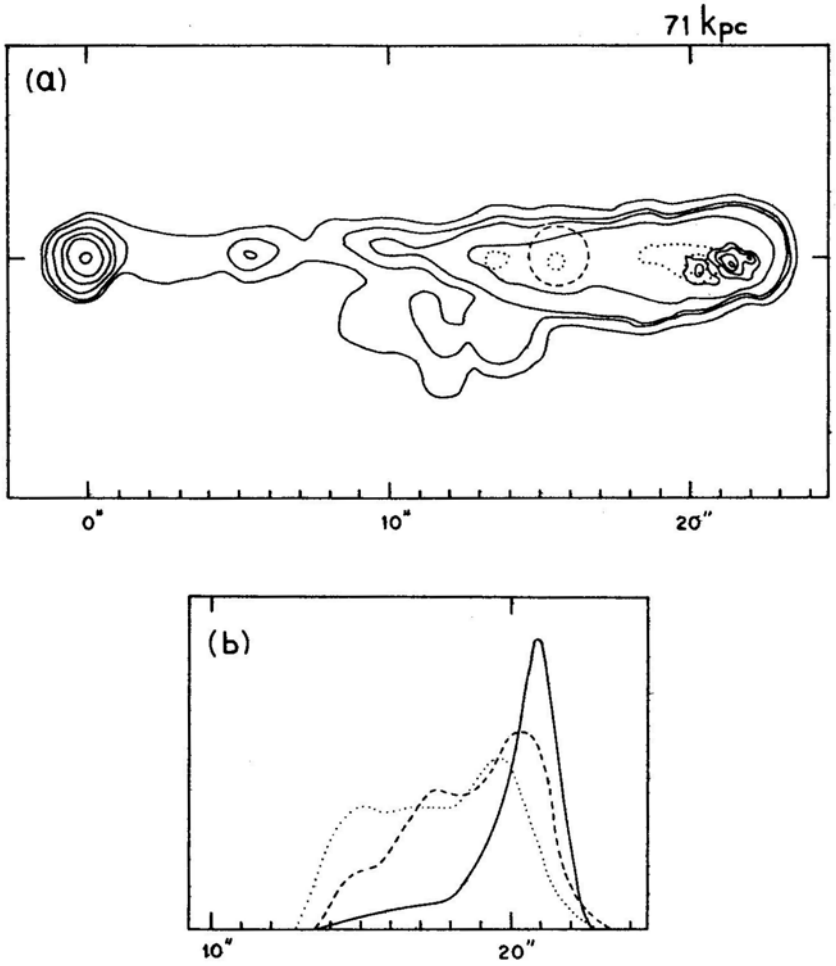

Figure 1. (a) Schematic of a radio-optical-X-ray overlay map of 3C273, rotated in position angle through 48°. Continuous lines are 4×10^8 Hz radio isophotes, reproduced from Foley & Davis (1985) and Davis, Muxlow & Conway (1985); dotted lines are optical isophotes, taken from Röser & Meisenheimer (1985); and broken lines are X-ray isophotes as communicated to the authors by D. Harris. The (upper) linear scale is based on H_0 = 65 km s^{-1} Mpc^{-1}. (b) The corresponding flux profiles along the ridge of the jet, where this time the broken curve represents the infrared profile (taken from Röser & Meisenheimer, 1985). All fluxes are plotted linearly but on different scales. The beam width for the radio profile is 1 arcsec, that for the optical-infrared profiles 2.4 arcsec.

cross-section (at termination) A of order $(kpc)^2$ and a (low) intergalactic hydrogen density of $\rho = 10^{-29}$ g cm^{-3} (*cf.* the optical map by Wyckoff, Wehinger & Gehren 1981, and Canizares, Gordon & Fabian 1983). The jet's present radiated power (if only mildly beamed) is no larger than 10^{44} erg s^{-1}. But Equations (14) and (7) tell us that the radiated fraction can be small for a near-relativistic head velocity, and most of the synchrotron radiation is expected somewhat retarded, pending on the prevailing magnetic field strengths (Equation 19 below). Also, other well-studied sources suggest that the power fed into the jets by an AGN is of order 1 per cent, corresponding to

$L \lesssim 10^{46}$ ergs^{-1} (Bezler *et al.* 1984). For $L_{45\,5}/\rho_{-29} \leqslant 3$, Equation (16) implies $\beta_h^2 \leqslant 3(1-\beta_h^2)^2$, whence $\beta_h \leqslant 0.63$. For comparison, the equations $\beta^2/(1-\beta)^2 = 1, 10$ are solved by $\beta = 0.50, 0.76$ respectively.

Lower limits on β_h follow from the fact that Davis, Muxlow & Conway (1985) have not detected the counterjet (yet). We do not believe in intrinsic one-sidedness, observationally because of the overwhelming number of extended double sources, and theoretically because the viability of models which prevent the high-pressure relativistic plasma in the broad-line region from escaping to both sides of the feeding disc is far from established. But the counter jet would have been observed unless its head has not yet reached the boundary of the host galaxy's halo (where enhanced dissipation sets in, as evidenced by the approaching jet, see Fig. 1). Its 'present' age t_+ is restricted by retarded visibility:

$$t_+/t_- = (1-\beta_h \cos\theta)/(1+\beta_h \cos\theta) \tag{17}$$

in which $t_- = r/c\beta_h$ is of order 10^6 yr. Postulating the counterjet to be shorter by at least a factor of 0.4 (*cf.* Fig. 1) means postulating t_+/t_- to be (roughly) $\leqslant 0.4$, whence $\beta_h \cos\theta \geqslant 0.43$, or $\beta_h \geqslant 0.49$ for $\theta \leqslant 30°$. This leaves us with the solid lower bound $\beta_h \gtrsim 0.5$. On the other hand, the above constraint $\beta_h \lesssim 0.75$ implies $t_+/t_- \gtrsim 0.16 = 10^{-0.8}$.

In deriving these constraints, we have tacitly assumed that β_h does not vary significantly during the lifetime of the young jet, an assumption that is suggested by Equation (16): the younger (shorter) jet has to push through an initially higher mass density ρ of the halo, yet with a smaller cross-section A ($\sim r^2$). Consequently, the 'velocity function' $L/A\rho c^3$—and hence β_h—are expected almost independent of r.

Why is the counterjet invisible? According to the canonical beaming formula, the forward-backward contrast in spectral flux $S_\nu \sim \nu^{-\alpha}$ is given by (*e.g.* Phinney 1985):

$$(\delta_-/\delta_+)^{2+\alpha} \simeq [2/(1-\beta_h \cos\theta)]^{2+\alpha} \geqslant 10^2 \tag{18}$$

for $\alpha = 0.8$, $\theta \leqslant 20°$, and $\beta_h \geqslant 0.65$. But as discussed in Section 2, the real contrast is expected much higher for a power-law distribution in energies for which hardly any relativistic charges are deflected into the backward hemisphere: charges moving with $\langle \beta_z \rangle \gtrsim 0.5$, $\gamma \gtrsim 10^2$ do not radiate into directions k with $k_z < 0$ unless the distribution is relativistically hot. A quantitative estimate would depend on the (unknown) effective temperature and turbulence of the shocked beam plasma.

A possible worry concerns the invisibility of the counterjet's cocoon whose energetic charges can be expected to have relaxed, on an average, to an almost isotropic velocity distribution. Their number per beam length is, however, small in proportion to $A\rho(1-\beta_h)$ (according to Equations 7, 14) due to the beam's slimness and fast propagation, and their radiation is further reduced by a somewhat relaxed pressure when compared with the beam head. Moreover, there are enhanced inverse-Compton losses in the galactic bulge, as well as collisional losses to neutral hydrogen atoms which can traverse the magnetized channel walls. As we do not see the inner cocoon of the approaching jet, we need not expect to see that of the receding jet.

Two further constraints on the head velocity $c\beta_h$ are worth mentioning. Within our model, the hard tail of the power-law distribution in particle energies degrades within the head, as inferred from the fact that the foremost optical hotspot lags behind the foremost radio hotspot. For an energy-density spectral index of 1.6, the share in the total energy of the degrading charges is of order 2 per cent, hence $\beta_h < 0.98$ must hold

according to Equation (7). Secondly, we compare the observed lengthscale of spectral softening in the head (Fig. 1) with the expected lengthscale for synchrotron losses. For the break frequency ν_b of synchrotron-emitting electrons in a transverse magnetic field $B_\perp$ one has:

$$\nu_b = 4\pi m_e ce/\sigma_T B_\perp^3 t^2 = 10^{14.6}\ \mathrm{Hz}\ (B_{\perp,-5})^3 t_{12}^2, \tag{19}$$

where t: $= \gamma/\dot{\gamma}$ is the e^{-1} folding timescale of particle energies. An ageing of the optical-emitting charges on the (deprojected) lengthscale of 10 kpc= 10^{12} *s.c* (which is traversed almost relativistically) therefore corresponds to an average transverse magnetic field of 10^{-5} G, a small fraction of the inferred equipartition field strength of $\lesssim 1$ mG near the front end of the jet. We shall expand on this interpretation in Section 7.

The presence and morphology of the radio lobe will impose a seventh constraint on β_h which we discuss in the following section.

6. Swinging beams and the lobe of 3C 273

The jet of 3C 273 is much narrower than the lobes of most extragalactic radio sources. We interpret this narrowness as an indication of its young age: the cocoon has not yet had time to expand into a lobe. If the cocoon consists of extremely relativistic pair plasma, this plasma wants to expand at its sound speed $c_s = c/\sqrt{3}$ as long as its pressure exceeds $\rho c_s^2 = 10^{-8\,5}$ dyn cm^{-2} ρ_{-29}. Put differently, the sideways expansion of a lobe (at speed $c\beta_l$) is expected not to a fall much behind its forward expansion:

$$\beta_l = \min\left\{\begin{matrix}\beta_h\,(p_{\mathrm{lobe}}/p_{\mathrm{hotspot}})^{1/2} \\ 1/\sqrt{3}\end{matrix}\right\} \tag{20}$$

where p_{hotspot} is the (highest) stagnation pressure and p_{lobe} is the more relaxed pressure in the extended lobe.

The half width b of the lobe must therefore fall short of the length Δr of the outer jet by β_l/β_h times the ratio t_l/t_h of their look-back ages. From $b/\Delta r \simeq \beta_l t_l/\beta_h t_h$, $\beta_h\ t_h$, cos $\theta = t_h - t_l$ (because of the finite light-travel time) and $\Delta\ r_\perp = \Delta r$ sin θ, we get for the projected length ratio:

$$b/\Delta r_\perp \lesssim \beta_l(1-\beta_h\cos\theta)/\beta_h \sin\theta \leqslant \beta_l/\beta_h \tag{21}$$

for $\beta_h \geqslant 0.7$, $\theta \leqslant 20°$. The observed ratio $b/\Delta r_\perp$ of half width to projected length in the map by Davis, Muxlow & Conway (1985) is close to 0.13. We infer that the expansion speed of the lobe satisfies $\beta_l \gtrsim 0.13\ \beta_h$ for $\beta_h \geqslant 0.7$. When compared with Equation (20), this estimate disfavours values of β_h below 0.6.

In this interpretation, we have ignored the fact that the 'lobe' mapped by Davis, Muxlow & Conway (1985) is offset from the present jet by order of 2*b.* As a transverse motion through *2b* corresponds to a speed of $\gtrsim$ 0.3 *c,* the beam must have swung sideways almost relativistically, through some 10°. Of course, the sideways speed of a beam is only a phase velocity: It is realised by a bending of its inner part in conjunction with the grinding (ramming) of a new channel. Such a bending can be achieved by the Keplerian rotation of the inner halo of the host galaxy, at $r \gtrsim 1$ kpc, which tends to freeze the channel walls. It is clearly mapped in Fig. 3b of Davis, Muxlow & Conway (1985). (Note that we discard the hard-beam model in which individual blobs perform a quasi-straight-line motion. In the soft-beam model, a precession of the central engine

could only influence the innermost part (< 1 kpc) of a jet.) When the direction of a beam is changed by almost corotation with the galactic halo, its succeeding segment is dragged across the (relativistic) lobe of the earlier channel for a long time where it finds little resistance. The resistance is resumed when it leaves the former lobe and has to ram a new channel.We interpretthis to happen atadistance of some 10 arcsec from the core.

This interpretation of the lobe offset from the jet by swinging was forced upon us by the (plausible) assumption that the jet propagates almost relativistically so that the observed sideways offset corresponds likewise to almost relativistic speed. No (intergalactic) wind can blow that fast. We would not feel confident about it had not a similar lobe offset been observed in Cyg A (for a slower propagation speed of the head, $\beta_h \simeq 0.1$; Perley, Dreher & Cowan 1985) and also in the form of 'emission bridges' in many sensitively mapped extended double sources (Leahy & Williams 1984). These emission bridges can occasionally take the shape of semi-circles, like in 3C111. In other cases they assume *Z* shape, like in 3C 52 or in the sources discussed by Ekers *et. al.* (1978).

Sources of Z shape have been often interpreted in terms of a precessing beam, based on the hard-beam model, or in terms of a deflected backflow. We prefer to interpret them as due to a swinging (soft) beam whose inner parts are dragged along by galactic rotation. This interpretation is similar to one given by Wirth, Smarr &Gallagher (1982) for the jets of close pairs of galaxies, with the distinction that we reject non-relativistic beam velocities and hence all forces on the beam other than entrainment of their channel walls by the respective galactic haloes.

Even more difficult to understand are the semi-circular sources. They have been interpreted as blown by a sideways intergalactic wind; but the required velocities are highly supersonic, comparable to or even larger than the head speed! Clearly, in all these cases the beam must have headed earlier into the directions of the 'older' lobes (as judged by their spectrum) and subsequently been swung into those of the younger lobes. A semi-circular morphology can result when the source starts out as a head-tail galaxy whose extragalactic beam segments are swept downstream by the intergalactic wind. When at some time in the past the output of the central engine strengthened, the beam got stiffer and straightened into the presently observed antipodal shape.

Why is no lobe observed inside the galactic halo of 3C 273, at projected separations $\lesssim 10$ arcsec? The electron spillover which leads to the formation of a cocoon or lobe can only be kept small by a low ambient density, so that little momentum has to be transferred. We therefore interpret the missing inner cocoon as due to a cosmic-ray halo, or sector of the halo through which the jet has propagated. The cosmic rays generated by the young stellar population(concentrated in the disc,like in Cen A) drive the galactic fountain and 'boil out' through the halo, possibly in counter-stream to infalling hot cluster gas.

7. Structure of the beam head

As already indicated in Section 5, we interpret the spectral softening in the front end of the jet as due to synchrotron losses (in-situ deceleration; The optical radiation stops before the linear polarization (E-vector) flips from transverse to parallel, *i.e.,* before the transverse magnetic field is significantly enhanced.

The brightest radio hotspot is preceded by yet another radio hotspot, at projected separation $\simeq 0.6$ arcsec, of width 0.5 arcsec (Foley & Davis 1985).Apparently, the mapped

head has an almost cylindrical geometry, with a deprojected ratio $\gtrsim 0.3$ of front width to length, where the foremost radio hotspot marks the position of the highest static pressure. This hotspot should be identified with the front end of the jet, which touches the contact discontinuity versus the ambient IGM. We infer that the conversion of ram pressure $p_{\rm ram}$ into static pressure p takes place between these two hotspots, throughout some 3 kpc. This distance is larger in proportion than the thickness of more familiar (solar-system) shock layers, yet similar to the size of hotspots in double radio sources (Miley 1980). The geometry may resemble that of the inner shock layer of the Crab nebula, for whose thickness Kundt & Krotscheck (1980) derived some 10^{17} cm based on the assumption that the optical wisps are a laser. Note that the beam plasma is extremely thin (and collisionless) and that the beam head has not had much time to relax.The bulk velocity of the jet material takes some 3 kpc for being decelerated from $\beta_{\rm j}$ to $\beta_{\rm h}$.

The question then arises of which of the two radio hotspots has the higher intrinsic luminosity. If the pair plasma near the front end had an approximately isotropic velocity distribution, then the beaming formula (1) would predict that observers at angles θ smaller than $\theta_{\rm c} = \arcsin \sqrt{2/(\gamma_{\rm h} + 1)} = 66°$ (for $\beta_{\rm h} = 0.7$) see more than average luminosity, in proportion to $\delta^{2\,5+\alpha}$ for S_ν (Equation 1). In reality, beaming will be much narrower; ordered relativistic streaming (at $\beta_{\rm j} \simeq 1$) would yield $\theta_{\rm c} = \arccos \beta_{\rm h} = 45°$ for $\beta_{\rm h} = 0.7$, because individual charges move at an average angle $\theta_{\rm c}$ with respect to the bulk flow. Beaming is expected to be even narrower for the (less decelerated) brighter radio hotspot, so that its intrinsic luminosity is still higher than that of the foremost hotspot. (Note that in this prediction we disagree with the analysis by Flatters & Conway 1985). A correct evaluation of beaming depends sensitively not only on the involved bulk Lorentz factor and inclination angle but also on the intrinsic velocity distribution.

An important observation is the presence of an X-ray hotspot in the outer jet. If it is emitted in the same electromagnetic fields as the optical radiation, the corresponding synchrotron-radiating electrons (and positrons) would have to be so energetic that they could not have survived the journey from the central engine to their present location, because of the ubiquitous 3K background radiation, see Equation (19) with $B_\perp$ (background) $= 10^{-5\,4}$ G $(1 + z)^2$. The electrons responsible for the optical jet just barely make it. (We interpret essentially the whole optical radiation from the jet as synchrotron radiation, despite its low linear polarization in the inner part: linear polarization can be wiped out by superposition of the radiation from various charges passing at different angles through the line of sight.) Instead, we interpret the X-ray hotspot as inverse Compton radiation on the infrared/optical photon bath, which is more strongly beamed than the emitted synchrotron radiation because it is a volume phenomenon, rather than an interaction with the walls, produced by particles of Lorentz factor $\gamma_{\rm j} \gtrsim 10^2$. We only see the radiation from those parts of the wiggling jet whose moving charges approach the line of sight within less than a degree. Note that a very similar beam-head structure—that of 3C33—has been recently mapped by Meisenheimer & Roser (1986).

8. Wiggling is self-stabilized

The jet of 3C 273 is not straight, nor is any other well-mapped extragalactic jet on any length-scale: there are wiggles throughout. We have interpreted the innermost bend of 3C273, on the scale of its galactic halo, as due to entrainment of its channel walls by the

galactic rotation. It is then clear that the front end of the young jet must curve backwards, because ram pressures on a swinging beam grow quadratically with the lever arm (in a uniform medium), hence freeze the outer parts of a channel. But why does the jet swing back again and oscillate around its initial direction, in a remarkably stable manner?

A partial answer to this question has been given by Hughes & Allen (1985) who hold small-scale clumping of the ambient plasma at the beam head responsible for small deflections. But why are the deflections stable, *i.e.* do not lead to an ever-increasing deviation? The answer is probably contained in the time-dependent, inhomogeneous manner in which the 'swept-up' ambient plasma reacts on the beam. This reaction is expected similar to the behaviour of the channel-wall material in the chimney of the Crab which appears not to thermalize the shock energy (Kundt 1983). When the propagating head pushes it at high speed, it continues to recede for some time after the head's sweeping until it is slowed down by the unperturbed medium; now the locally generated overpressure relaxes explosively. But sound speed of the IGM, of order $\gtrsim 10^8$ cm s^{-1}, is some 1 per cent of the head's speed, hence this explosive recoil sets in slowly and long after channel formation.

As a consequence of the recession of the newly swept ambient plasma, a fresh bend tends to straighten because successive generations of pushing charges arrive at increasingly larger distances from the local curvature centre. This sideways offset of the beam is always in the opposite direction to the former bend; it tends to deflect the beam head away from its swept-up buffer, initiating the next bend.

In this scenario, sideways offsets of the beam of order $d \tan \phi$ are expected after the traversal of a distance d at (small) inclination angle ϕ with respect to its former direction. When such an offset gets comparable to the beam width b, the beam head is deflected again. This naive model suggests for the typical distances d between bends

$$d = b \operatorname{ctg} (22)\, \phi, \tag{22}$$

in satisfactory agreement with the observations. In other words: each bend of a beam is likely to trigger the formation of a counter-bend because of time-dependent pressure fluctuations in the channel wall plasma.

At times long compared to the head's sweeping, the bends are in danger of sharpening *via* centrifugal forces, like the meanders of a river. Now the created overpressure of the relaxing channel-wall plasma serves as a buffer, counteracting centrifugal grinding. Only in this way can we understand the rema rkable straightness of a (soft) beam. 3-D numerical simulations of jets should therefore be careful in modelling the time-dependent back reaction of the channel-wall material on the flow.

9. Conclusions

Within our modified framework of relativistic beaming, we have explained the one-sidedness of the jet in 3C273 as due to almost relativistic propagation, with a head speed in the vicinity of 0.7 c, at some variable angle q between 10° and 30° with respect to the line of sight. The counterjet is too young to be visible: Most of its radiation is still beamed away from us. 3C273 is thereby exceptional both for its youth and orientation: An age of $\simeq 10^6$ yr is some 10^2 times less than the estimated ages of typical sources, and an inclination angle of $\lesssim 30°$ of one of the two jets corresponds to $\lesssim 10$ per cent of the

full spherical angle. Consequently, there should be no more than one source in a thousand similar to 3C 273.

How can future observations test this model? An obvious possibility is offered by a VLBI measurement of $\beta_\perp$, the transverse growth rate of the jet, which is expected marginally superluminal: $\beta_\perp = 10^{-0.2\pm0.2}$ (*cf.* Equation 15). According to Perley (1983), such a measurement might be possible in the foreseeable future. Another test would be to discover the (lobe of the) counterjet at a higher dynamic range.

Acknowledgements

W. K. wants to thank R. Cowsik, S. Falle, R. Porcas and P. Scheuer for discussions and T.I.F.R. and R.R.I. for their hospitality during his stay at Bangalore. Both authors are grateful to R. Nityananda for discussions, to Moxa H. for her enthusiastic typing and to a helpful referee for constructive criticism.

References

Bartel, N., Rogers, A. E. E., Shapiro, I. I., Gorenstein, M. V., Gwinn, C. R., Marcaide, J. M., Weiler, K. W. 1985, *Nature,* **318**, 25.
Begelman, M. C, Blandford, R. D., Rees, M. J. 1984, *Rev. Mod. Phys.,* **56**, 255.
Bezler, M., Kendziorra, E., Staubert, R., Hasinger, G., Pietsch, W., Reppin, C., Trümper, J., Voges, W. 1984, *Astr. Astrophys.,* **136,** 351.
Canizares, C. R., Stewart, C. G., Fabian, A. C. 1983, *Astrophys. J.,* **272,** 449.
Conway, R. G., Davis, R. J., Foley, A. R., Ray, T. P. 1981, *Nature,* 2**94**, 540.
Courant, R, Friedrichs, K. O. 1976, *Supersonic Flow and Shock Waves,* Springer, Berlin.
Davis, R. J., Muxlow, T. W. B., Conway, R. G. 1985, *Nature,* **318**, 343.
Ekers, R. D., Fanti, R, Lari, C., Parma, P. 1978, *Nature,* **276**, 588.
Flatters, C, Conway, R. G. 1985, *Nature,* **314**, 425.
Foley, A. R, Davis, R. J. 1985, *Mon. Not. R. astr. Soc.,* **216**, 679.
Hughes, P. A., Allen, A. J. 1985, *Mon. Not. R. astr. Soc.,* **214**, 399.
Henry, J. P., Becklin, E. E., Telesco, C. M. 1984, *Astrophys. J.,* **280**, 98.
Kellermann, K. I., PaulinyToth, I. I. K. 1981, *Ann. R. astr. Astrophys.,* **19**, 373.
Kundt, W. 1982, *Mitt astr. Ges.,* **57**, 65.
Kundt, W. 1983, *Astr. Astrophys.,* **121**, L15.
Kundt, W. 1984, *J. Astrophys. Astr.* **5**, 277.
Kundt, W., GopalKrishna 1981, *Astrophys. Space Sci.,* **75**, 257.
Kundt, W., Krotscheck, E. 1980, *Astr. Astrophys.,* **83**, 1.
Landau, L. D., Lifshitz, E. M. 1978, 6, Chapter X, Section 90.
Leahy, J. P., Williams, A. G. 1984, *Mon. Not. R. astr. Soc.,* **210**, 929.
Lelievre, G., Nieto, J.-L., Horville, D., Renard, L., Servan, B. 1984, *Astr. Astrophys.,* **138**, 49
Lind, K. R, Blandford, R. D. 1985, *Astrophys. J.* **295**, 358
Meisenheimer, K., Röser, H.-J. 1986, *Nature,* **319,** 459
Miley, G. K. 1980, *Ann. R. Astr. Astrophys.,* **18,** 165.
Morrison, P. Roberts, D., Sadun, A. 1984, *Astrophys. J.,* **280,** 483
Perley, R. A. 1983 in *IAU Symp.* 110: *VLBI and Compact Radio Sources,* Eds R. Fanti, K. Kellermann & G. Setti, D. Reidel, Dordrecht, p. 153.
Perley, R. A., Dreher, J. W., Cowan, J. 1985, *Astrophys. J.,* **285**, L35.
Phinney, E. S. 1985, in *Proc. Santa Cruz Summer Workshop,* Ed. J. S. Miller, Univ. Sci. Books.
Roberts, D. 1984, *Astrophys. J.,* **285**, 64.
Röser, H.-J., Meisenheimer, K. 1986, *Astr. Astrophys.,* **154**, 15.
Unwin, S. C., Cohen, M. H., Biretta, J. A., Pearson, T. J., Seielstad, G. A., Walker, R. C., Simon, R. S., Linfield, R. P. 1985, *Astrophys. J.,* **289**, 109.
Wirth, A., Smarr, L., Gallagher, J. S. 1982, *Astr. J.,* **87**, 602.
Wyckoff, S., Wehinger, P. A., Gehren, T. 1981, *Astrophys. J.,* **247**, 750.

J. Astrophys. Astr. (1986) **7,** 237–240

Is IRAS 03134 + 5958 a Herbig-Haro Object?

K. V. K. Iyengar & T. N. Rengarajan *Tata Institute of Fundamental Research, Homi Bhabha Road, Bombay 400005*

Received 1986 May 5; accepted 1986 June 27

Abstract. The source IRAS 03134 + 5958 identified by Iyengar & Verma (1984) on the Palomar Observatory Sky Survey (POSS) prints with a nonstellar optical object with $[P - R] \simeq 5.3 \pm 1.5$ is near the edge of Lynds dark cloud No. 1384 and is either embedded in or behind the cloud. The galactic latitude of this source ($b^{II} = 2\overset{\circ}{.}3$), its position *vis-a-vis* the Lynds dark cloud, its nonstellar appearance, high $[P - R]$ colour and its far-infrared spectrum, all suggest the possibility of its being a Herbig-Haro (HH) object. To test this possibility we undertook measurements of its proper motion and variability (two of the characteristic properties of HH objects). These yield $\mu_\alpha = (3.6 \pm 2.3)$ arcsec/century and $\mu_\delta = (-1.2 \pm 2.0)$ arcsec/century for its proper motion. The source reveals large variation in brightness between 1950 and 1954. Optical line studies of the source are required to confirm its classification as an HH object.

Key words: infrared sources—Herbig-Haro objects—stars, proper motion—stars, variability

1. Introduction

In the course of their work on the optical identification of the unidentified sources in IRAS Circulars 2–4 (Habing & Neugebauer 1983 a, b, c) using POSS prints, Iyengar & Verma (1984) identified the IRAS source 0313 + 599PO2 with an optical object at R.A. (1950) = $03^h\ 13^m\ 25\overset{s}{.}2$ and Dec (1950) = 59° 58′ 45″. Its angular separation from the optical object was 44 arcsec. The more accurate position now available for this source designated as IRAS 03134 + 5958 in the IRAS Point Source Catalog (Beichman *et al.* 1984) is within 3 arcsec of the optical position. Assuming the validity of the diameter-magnitude relations given for POSS prints by King & Raff (1977), we estimate $m_p = 13.8$ and $[P - R] \simeq 5.3 \pm 1.5$ corresponding to a large value of $[P - V] \simeq 3.3 \pm 1$. The optical counterpart of the IRAS source (hereafter referred to as the programme object) appears nonstellar in the POSS prints. Its high $[P - R]$ colour, and its location near the edge of Lynds dark cloud No. 1384 (R.A. (1950) = $03^h\ 16\overset{m}{.}0$, Dec (1950) = + 59° 50′, area = 0.068 deg^2 and opacity = 4; Lynds 1962) led us to examine the possibility of its candidacy for an HH object. HH objects are known to exhibit large proper motions, light variations of 2–3 mag on a timescale of 5–10 yr and have strong emission lines with weak continuum emission. In this note, we present results on the proper motion and variability of the object based on measurements of plates from the Harvard collection and POSS prints.

2. Data and Discussion

We obtained contact negatives of plates from Harvard plate collections covering this region of the sky in order to measure the proper motion and variability of the programme object. Plates MC 2028, MC 28535, MC 36685, and MC 36689 from the Harvard collections corresponding to the epochs 1912 October 6,1936 October 21/22, 1949 December 14/15,1949 December 15/16 and the POSS O plate corresponding to the epoch 1954 January 27/28, were used for this purpose. Figs 1 a–f show on a magnified scale the optical candidate of the IRAS source as seen on the Harvard plates and POSS blue and red prints. We measured the positions of the programme object

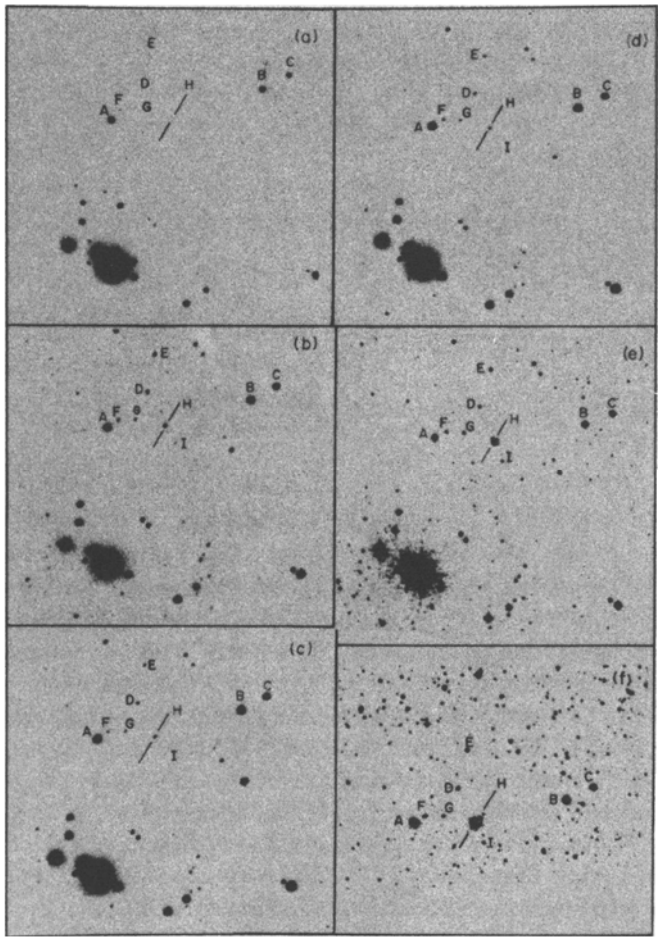

Figure 1. Enlarged prints of the Harvard plates MC 2028, MC 28535, MC 36685 and MC 36689 and the POSS blue and red prints corresponding to the epochs of (a) 1912 October 6; (b)1936 October 21/22; (c) 1949 December 14/15; (d) 1949 December 15/16; (e) blue POSS print of 1954 January 27/28; (f) red POSS print of 1954 January 27/28. In these prints east is to the right, and north is at the top. H indicates the programme object on these prints. A–I are objects around the programme object within a radius of 6 arcmin which encompass the brightness range the programme object underwent during the epoch interval 1912–1954.

Using Ascorecord, the Zeiss coordinate measuring machine. We chose as reference stars, 18 SAO starts with *P* magnitude in the range 9.5–10.2 surrounding the programme object. Also the plates were measured in direct and reverse orientations to eliminate systematic errors of a physiological nature. Corrections were made for the known proper motions of reference stars and the coordinates of the programme object were reduced to the equator and equinox of 1950.00. From a linear least-squares fit to these data we obtained μ_α = (3.6 ± 2.3) arcsec/century and μ_δ = (–1.2 ± 2.0) arcsec/century for the proper motion of the programme object. If the object is indeed an HH object, it belongs to the category of HH objects with low proper motion.

In order to measure the variability of the programme object, we need to eliminate effects arising from different exposures of plates as well as from possible difference in the effective bandwidths for the Harvard and POSS plates. For this purpose, we measured the diameter of the object with respect to several nearby objects. These objects A–I including the programme object designated as H are marked in Figs 1 a–f. From a careful study of the diameters of these objects, we conclude that the diameters of A, D and E changed by < 5 per cent. These were, therefore, used as calibration objects. Measurements on A, D, E and H were used to determine the relative diameter of H with respect to E. These relative diameters are plotted as a function of time in Fig. 2. It is seen that the programme object is variable. It has brightened considerably in 1954. The increase in diameter by a factor of 1.6 in 1954, corresponds to a brightening

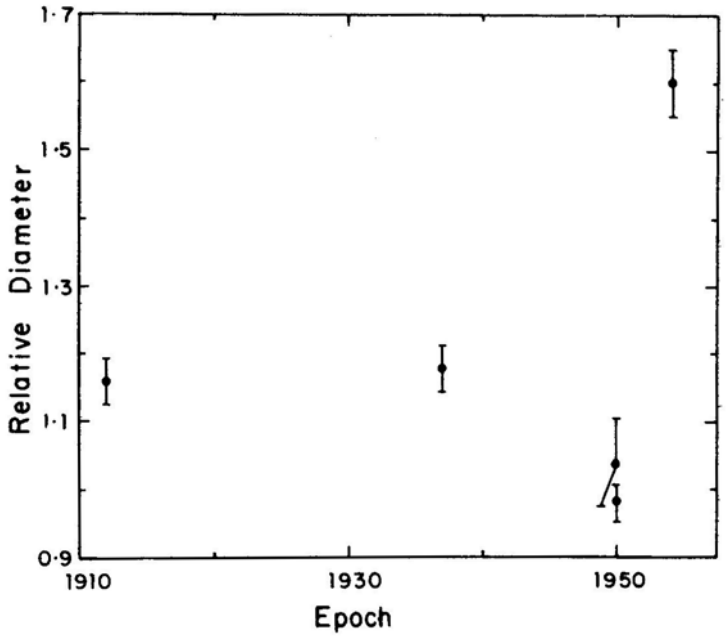

Figure 2. The relative diameter of the programme object versus the epoch of observation. The diameters of objects A, D and E changed by < 5 per cent during the epoch interval 1912–1954 and were therefore used to determine the relative diameter of the programme object on any plate with respect to the diameter of E on the same plate. The errors shown are rms deviation of measurements with respect to A, D and E.

by 2.4 magnitude in *P*. In 1950, the object seems to have reduced in brightness as compared to earlier times.

From IRAS observations the flux densities (colour corrected) of the programme object are found to be 1.78,2.09,9.19 and 35.80 Jy in the four IRAS bands of 12,25,60 and 100 μm respectively. IRAS data on other HH complexes such as HH 1, HH 11, HH 46–47, L 1551 NE and L 1551 IRS-5 (Beichman *et al.* 1984; Emerson *et al*. 1984) also indicate flux densities increasing with wavelength. However, there is a large spread in their [12–25] and [25–60] colours, which seem to depend strongly on their environments. The 100 μm flux densities being subject to cirrus contamination cannot be very effectively used. Thus, the far-infrared spectrum of the programme object, though a strong supportive indicator, cannot uniquely identify it as an HH object.

The object is not listed by Coyne & MacConell (1983) suggesting that it does not have the strong Hα emission characteristic of an H-H object. On the other hand, low dispersion deep objective prism spectrum of the core of the nebula taken at the Warner and Swasey observatory's Schmidt telescope shows (a) no evidence of strong hydrogen or nebular emission lines in the $\lambda\lambda$ 4550–5050 range, (b) no evidence of TiO or other strong absorption bands in the $\lambda\lambda$ 6800–8000 range indicating that it is not a late M or carbon star (N. Sanduleak, personal communication). Higher dispersion spectra of the object are required to resolve the conflicting evidence on its possible classification in the Herbig-Haro category.

Acknowledgements

We thank Dr Martha Hazen for access to Harvard plate collection and Dr G. Melnick for help in copying the plates.

References

Beichman, C. A., Neugebauer, G., Habing, H. J., Clegg, P. E., Chester, T. J. 1985, *Explanatory Supplement to the IRAS Catalogs and Atlases,* U.S. Government Printing Office.

Coyne, G. V., MacConnell, D. J. 1983, *Vatican Obs. Publ.,* **2***,* No. 6,73.

Emerson, J. P., Harris, S., Jennings, R. E., Beichman, C.A., Baud, B., Beintema, D. A., Marsden, P. L., Wesselius, P. R. 1984, *Astrophys. J.,* **278**, L49.

Habing, H., Neugebauer, G.1983a, *IRAS Circ., Nature,* **304**, 218.

Habing, H., Neugebauer, G.1983b, *IRAS Circ., Nature,* **305**, 578.

Habing, H., Neugebauer, G.1983c, *IRAS Circ., Nature,* **306**,646.

Iyengar, K.V. K.,Verma, R.P.1984, *Astr. Astrophys.,* **139**, 64.

King, I. R., Raff, M. I. 1977, *Publ. astr. Soc. Pacific,* **89**, 120.

Lynds, B. T. 1962, *Astrophys. J. Suppl. Ser.,* **7**, 1.

J. Astrophys. Astr. (1986) **7,** 241–257

Does Sunspot Activity Originate in Slow Global Oscillations of the Sun?

M. H. Gokhale *Indian Institute of Astrophysics, Bangalore 560034*

Received 1986 April 25; accepted 1986 July 22

Abstract. We present preliminary results of a spherical-harmonic-Fourier analysis of sunspot activity during the twenty-two years 1933–1954. The results indicate that the sunspot activity might be originating in global solar oscillations with periods of years and decades. However, except for the axisymmetric mode of degree 6, the set of other axisymmetric modes showing ~ 11 yr periodicities are different from one sunspot cycle to another. A more detailed analysis, preferably with larger data series, will be needed to arrive at a more definite conclusion.

Key words: Sun, global oscillations—sunspots—solar activity cycle

1. Introduction

It has often been suggested that the solar magnetic and activity cycles might be originating in some global oscillations of the Sun rather than in turbulent hydromagnetic processes in the convection zone (*e.g.* Walen 1947; Layzer, Rosner & Doyle 1979; Labonte & Howard 1982). The twenty-two and the eleven year periodicities of the magnetic and activity cycles could be related either to the periods of sufficiently slow global oscillations (*e.g.* Plumpton & Ferraro 1955) or to the timescales of modulation of fast global oscillations (*e.g.* Gokhale 1977, 1984). Theoretically, slow MHD modes of global oscillations could have periods in years and decades depending upon the effective depth and intensity of the magnetic field in the solar interior. In this paper we present preliminary results of a spherical-harmonic-Fourier (SHF) analysis of sunspot activity during the twenty-two years 1933–54, which was undertaken to determine whether some specific modes of global oscillations with ~ 11 yr or ~ 22 yr periods contribute predominently to the sunspot activity, assuming such oscillations to exist. Meanwhile, from SHF analysis of Mount-Wilson and Kitt-Peak magnetogram data (1959–1984), Stenflo & Vogel (1986) have shown that global oscillations with specific periods (~ 22 yr and smaller) do contribute predominently to the evolution of the largescale photospheric field. The present analysis of the sunspot data extends over first ten degrees (l = 0 to 9) and all azimuthal orders (m = 0 to l) of the spherical harmonics and over frequencies ν = 0 to 9 in units of 1/11 or 1/22 yr^{-1} depending on the length of the data used.

The Fourier amplitudes or powers, (or both), of several harmonics show peaks in their variation with ν. Some of the peaks, though not all, seem to be statistically significant according to a crude preliminary test. Peaks in the amplitudes and powers of the axisymmetric harmonics show that if sunspot activity originates in global solar

oscillations, then different sets of harmonic modes show ~ 11 yr periodicity during different sunspot cycles.

2. The data used and the method of analysis

We have used the data from Ledgers I and II of the Greenwich photoheliographic results. Since the transfer of data from the published volumes to magnetic tapes and its checking is extremely laborious, the data from only two sunspot cycles (1933–1954) could be analyzed so far.

The date and location of the first appearance of each sunspot group is noted as the nearest approximation to the time and location when and where the associated strong magnetic structure is produced inside the Sun. Spot groups born on the invisible side of the Sun and brought into view by solar rotation are omitted from the analysis in view of the large uncertainty in the date of their first appearance on the Sun's surface. This gives us a data set of 2670 spot groups during the twenty-two year period. The epochs t_i (in days, and fractions, from the zero-hour of 1933 January 1), and the heliographic colatitudes and longitudes θ_i and ϕ_i, of the 2670 spotgroups as indexed by i are noted. The maximum observed area $A_{\max}$ (i), corrected for foreshortening, during the entire life of the spotgroup (including the recurrent appearance, if any) is also noted as a measure of the magnetic flux in the structure producing the spot group i. The uncertainties in θ_i, ϕ_i and t_i are ~ 1°, 1° and 1 day respectively.

The following two functions are subjected to the spherical-harmonic-Fourier analysis:

$$A(\theta, \phi, t) = A_{\max}(i)\delta(\theta - \theta_i, \phi - \phi_i, t - t_i),$$

and

$p(\theta, \phi, \mathrm{t})$ = probability distribution of 'sunspot occurrence',
over the solar surface, with weights $A_{\max}(i)$ at $\theta = \theta_i$, $\phi = \phi_i$, $t = t_i$

where $\delta(\theta - \theta_i, \phi - \phi_i, t - t_i)$ is the three-dimensional delta function in the space (θ, ϕ, t). The harmonic amplitudes $H_\alpha(l, m, \nu)$ in the SHF analysis of a function $f(\theta, \phi, t)$, over a time-span T, are given by:

$$H_\alpha(l, m, \nu) = C_l^m \int_0^T \mathrm{d}t \int_S f(\theta, \phi, t)\, P_l^m(\cos\theta) \begin{matrix}\cos\\ \sin\end{matrix} (m\phi) \begin{matrix}\cos\\ \sin\end{matrix} (2\pi\nu t)\, \mathrm{d}S, \tag{1}$$

where l and m are respectively the degree and the azimuthal order of the spherical harmonic, ν is the frequency in units of $\Delta\nu = 1/T$, α is a *symbolic suffix* with values 'cc', 'cs', 'sc' or 'ss', depending upon the combination of cosines or sines of $m\phi$ and $2\pi\nu t$, $\mathrm{d}S$ is an element of area for integration over the surface S of a unit sphere and C_l^m are normalizing factors given by

$$C_l^m = \frac{1}{\sqrt{2\pi}} \left(\frac{2l+1}{2\pi}\right) \frac{(l-m)!}{(l+m)!} \qquad \text{for } m \neq 0 \tag{2}$$

and

$$C_l^o = \frac{1}{\sqrt{2\pi}} \left(\frac{2l+1}{4\pi}\right).$$

For the functions $A(\theta, \phi, t)$ and $p(\theta, \phi, t)$ defined above, expression (1) reduces to

$$H_\alpha(l,m,\nu) = C_l^m \sum_i A_{\max}(i) P_l^m(\cos\theta_i)^{\cos}_{\sin}(m\phi_i)^{\cos}_{\sin}(2\pi\nu t_i)\sin\theta_i \tag{3}$$

and

$$H_\alpha(l,m,\nu) = C_l^m \sum_i A_{\max}(i) P_l^m(\cos\theta_i)^{\cos}_{\sin}(m\phi_i)^{\cos}_{\sin}(2\pi\nu t_i) \tag{4}$$

respectively. The powers P_c and P_s in the harmonics involving $\cos(m\phi)$ and $\sin(m\phi)$ are calculated using

$$P_c(l,m,\nu) = \sqrt{[H_{cc}^2(l,m,\nu) + H_{cs}^2(l,m,\nu)]}$$

and

$$P_s(l,m,\nu) = \sqrt{[H_{sc}^2(l,m,\nu) + H_{ss}^2(l,m,\nu)]}. \tag{5}$$

However, since the results for $A(\theta, \phi, t)$ and $p(\theta, \phi, t)$ are qualitatively similar, we present the results for $A(\theta, \phi, t)$ only. In these, the relative uncertainty in each value of H_α, P_c, P_s, is estimated to be < 10 per cent.

3. Results and conclusions

Fig. 1 illustrates the plots of H_{cc}, H_{cs}, H_{sc}, H_{ss}, P_c and P_s as functions of frequency ν given by SHF analysis of $A(\theta, \phi, t)$ for the first twelve harmonics ($l = 0$ to 3 and $m = 0$ to l; $l = 4$, $m = 1$ and 2) obtained from the data of 1281 sunspot groups during the sunspot cycle 1933–43. The abscissa is the frequency ν in units of $\Delta\nu = 0.00025\text{d}^{-1}$ ($\sim 1/11\ \text{yr}^{-1}$). The ordinate in each plot is scaled to the range of values of one of the functions represented in the plot. It can be seen that for some modes there are one or more significant peaks at certain frequencies.

Similar peaks are also present in Fig. 2 which shows a sample of the SHF analysis of an 'imaginary' data set produced by taking for θ_i, ϕ_i and t_i, three independent series, each of 1281 random values within the same limits as those for the real data. Hence merely from the presence of the peaks in the results for the real data, one cannot conclude that sunspot activity originates in long-period global oscillations of the Sun. Fig. 3 shows results for the cycle 1944–54.

In Fig. 4 we illustrate the results obtained from the combined data for all the 2670 spot groups during the entire period of the twenty-two years 1933–1954. Here the unit of frequency is $\Delta\nu = 0.000125\text{d}^{-1}$ (*i.e.* $1/22\ \text{yr}^{-1}$).

For many modes (especially the axisymmetric modes $m = 0$) in the results from the real data as well as those from the imaginary data it is possible to estimate the noise level, though crudely, by visual inspection. Among these there are several modes for which the results obtained from the real data show significant peaks at frequencies where the imaginary data yields either no peaks or only insignificant peaks. This fact gives an indication that the sunspot activity might be physically related to, (and perhaps originating in), global oscillations represented by the peaks. However a more detailed analysis, preferably with longer data series, will be needed to arrive at a more definite conclusion.

Here we discuss only the peaks at ~ 11 yr and ~ 22 yr periodicities in the Fourier amplitudes $|H_{cc}|$, $|H_{cs}|$, and in the power P_c of the axisymmetric modes (listed in Table 1). These peaks are considered more significant since none of the results from the imaginary data shows any peaks at these periodicities. The amplitudes as well as the

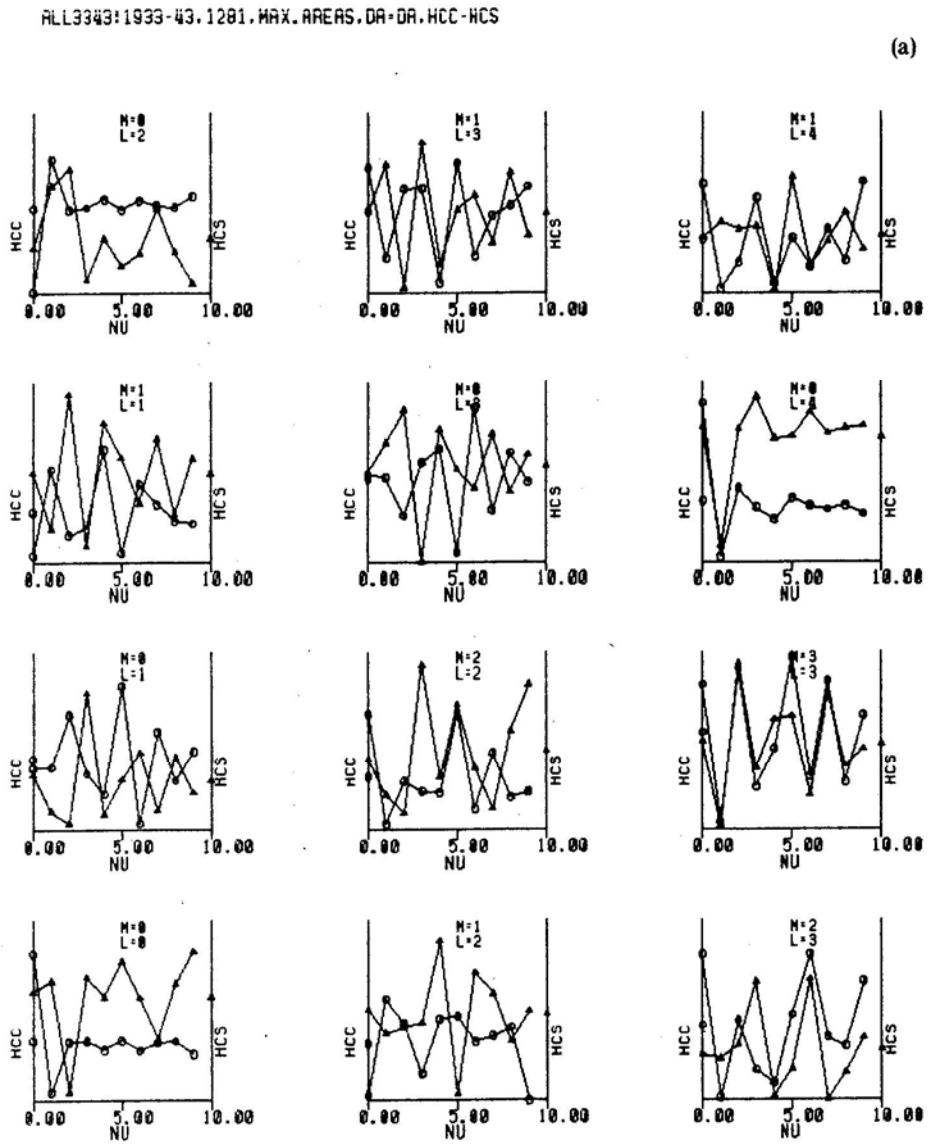

Figure 1. Plots of (a): H_{cc} (denoted by circle) and H_{cs} (denoted by triangle), (b): H_{sc} (circle) and H_{ss} (triangle), (c): P_c (circle) and P_s (triangle), as functions of frequency ν obtained from data for the 1281 spotgroups during 1933–1943. The scale on the ordinate is arbitrary in each plot and differs from one plot to another. The average values of the functions plotted are shown by the symbols circle and triangle on the ordinate. In (a) and (b) these also indicate approximate positions of the zeroes on the respective scales. For axisymmetric ($m = 0$) modes, H_{sc} , H_{ss} and P_s vanish identically. Hence the corresponding plots are blank.

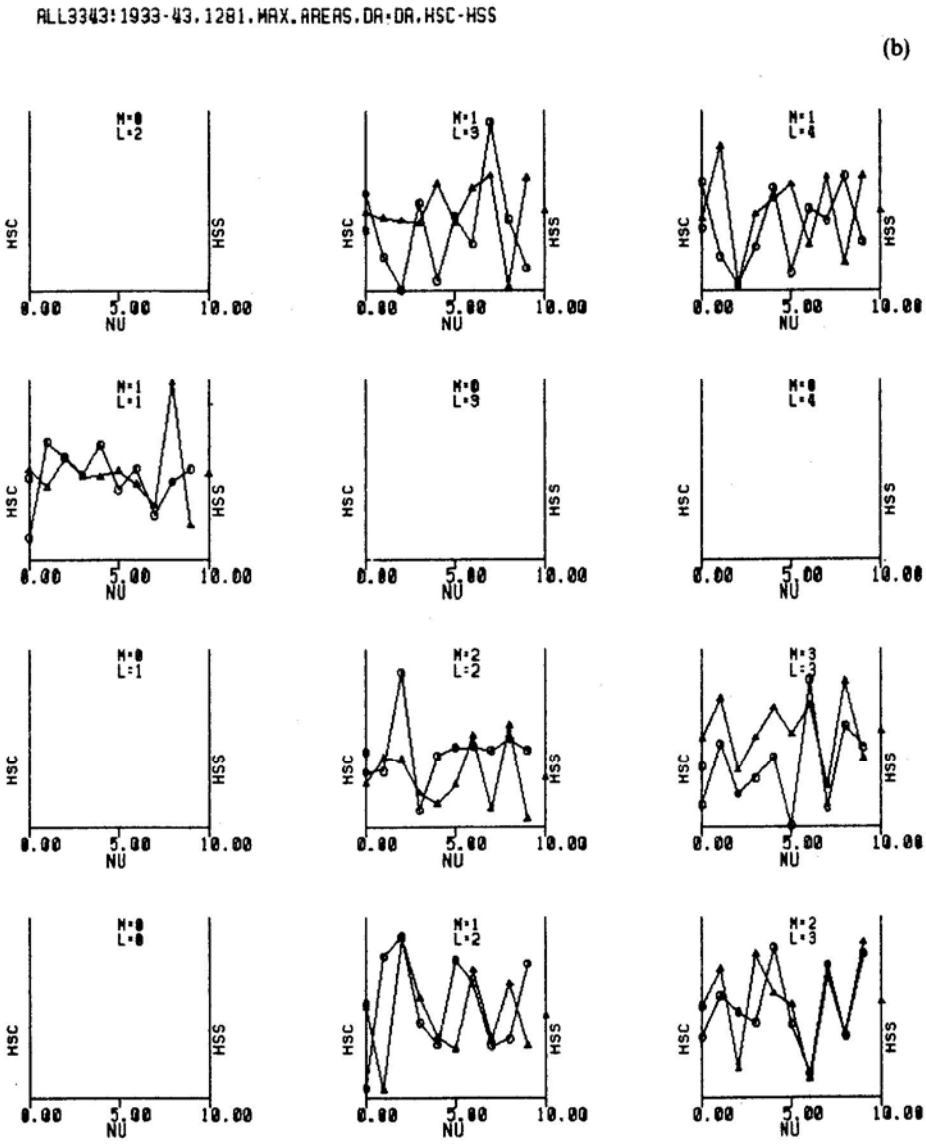

Figure 1. Continued.

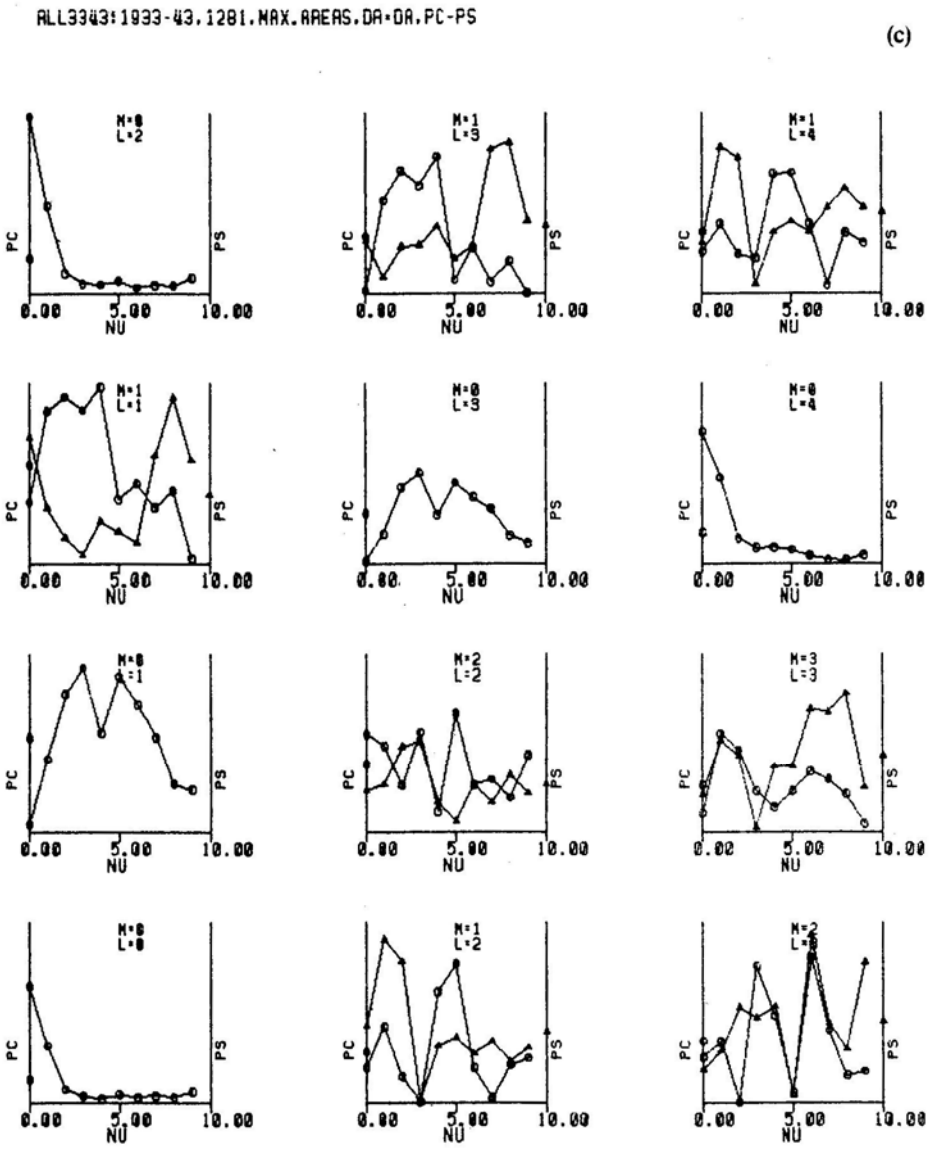

Figure 1. Continued

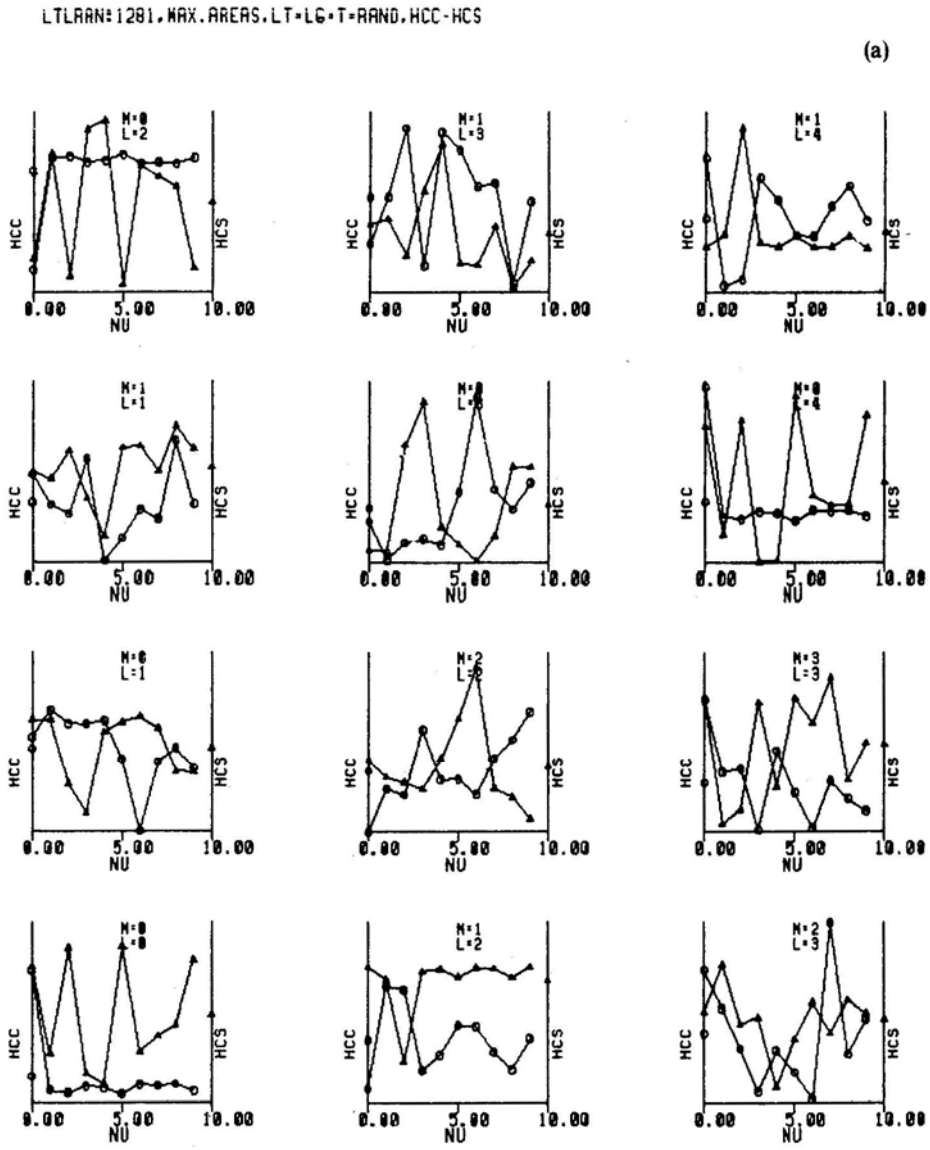

Figure 2. Results of analysis of 'imaginary' data as generated from independent random series, within appropriate limits, for θ_i, ϕ_i and t_i. Compare with the real data in Fig. 1.

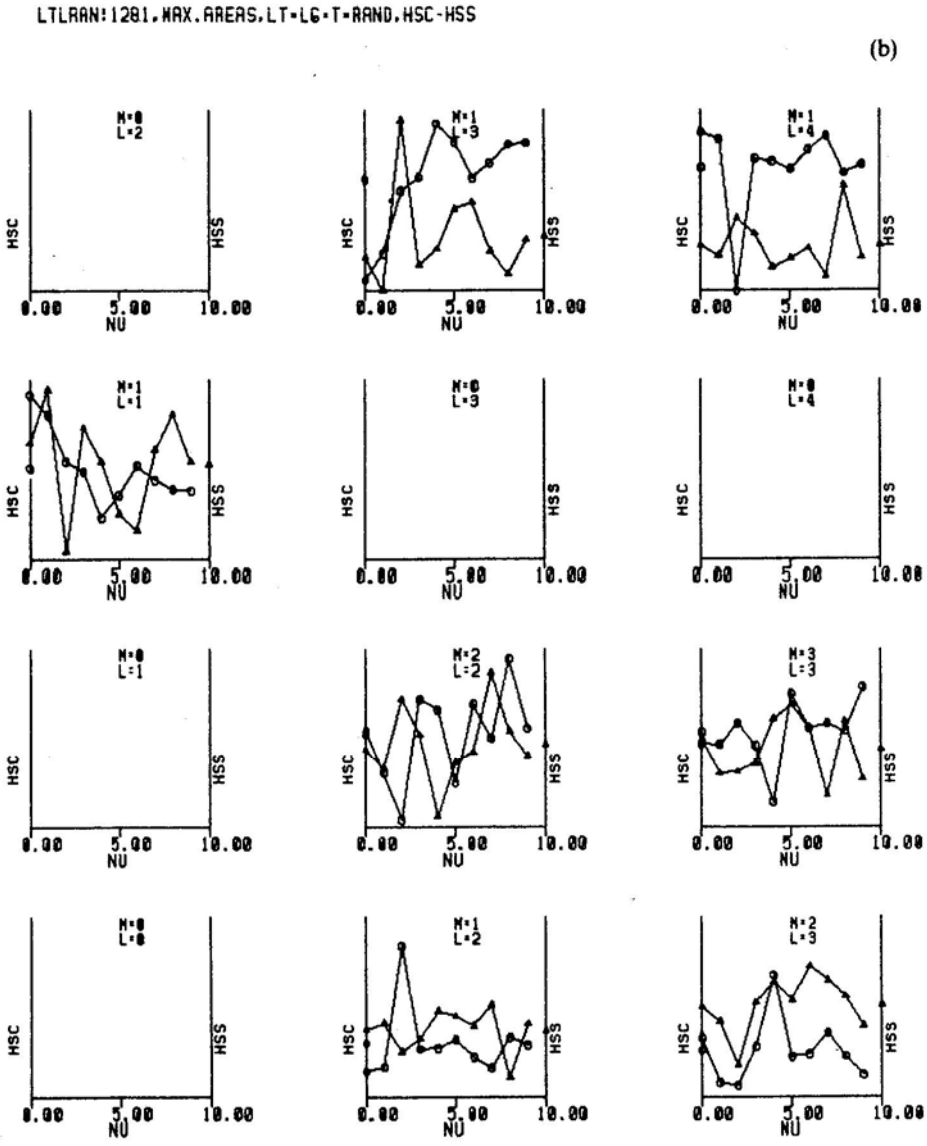

Figure 2. Continued.

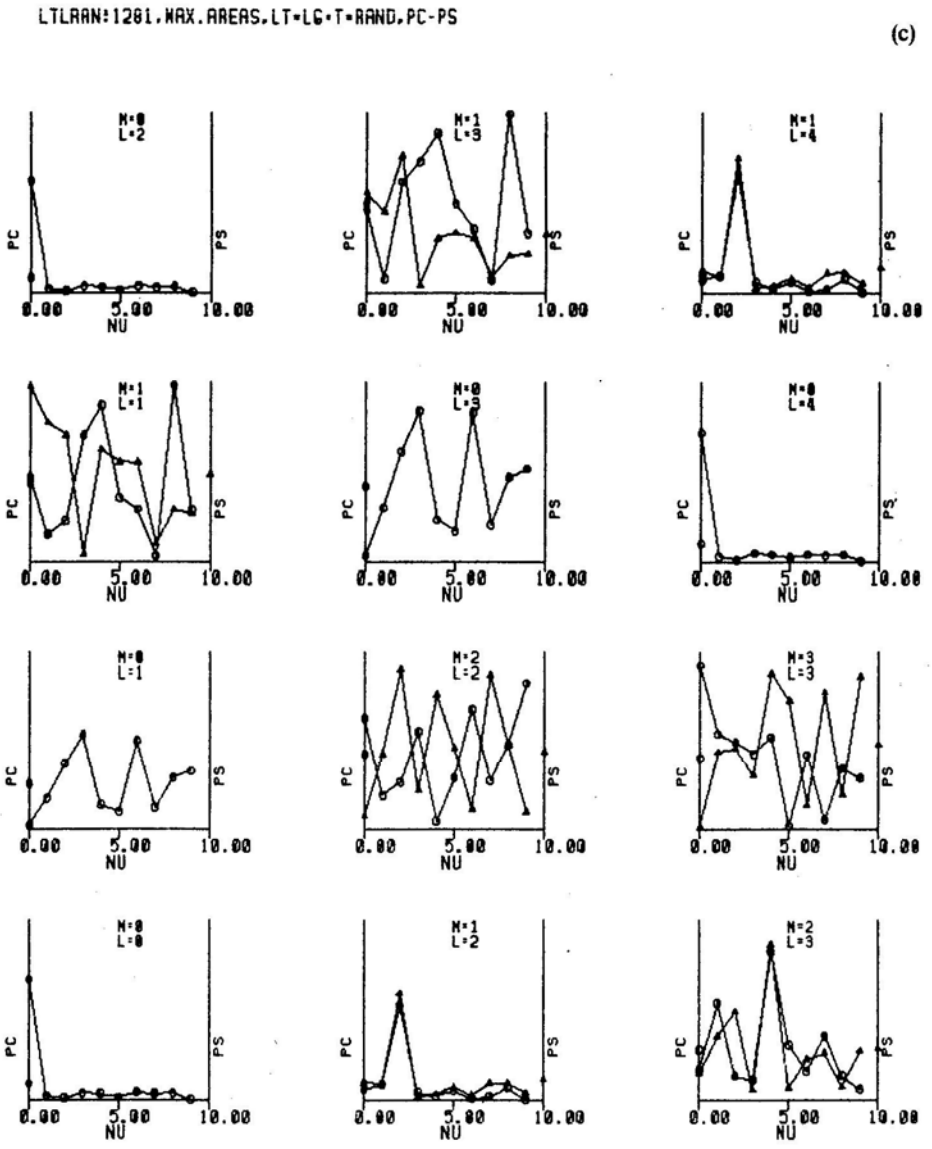

Figure 2. Continued.

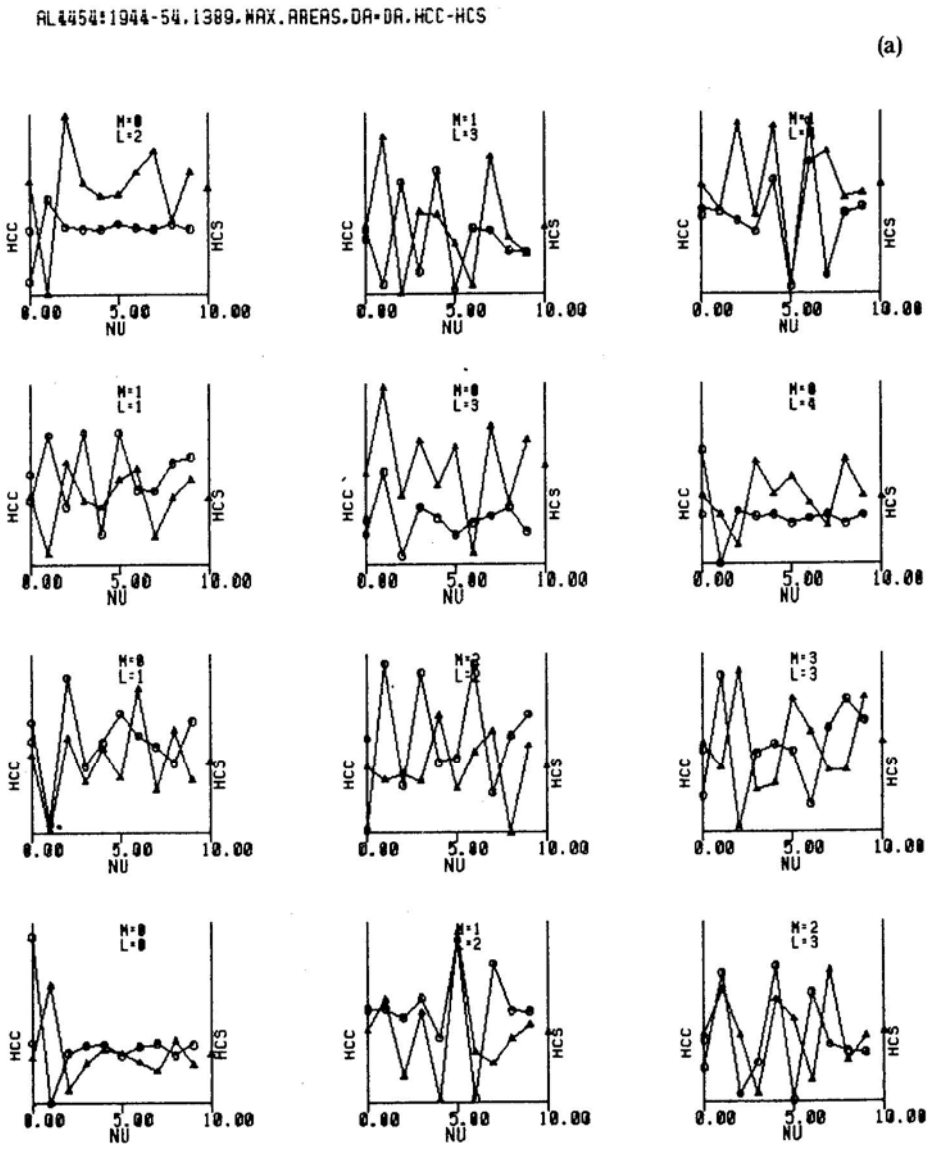

Figure 3. Results of analysis for the data on 1389 spot groups during 1944–1954. See Fig. 1 for explanations.

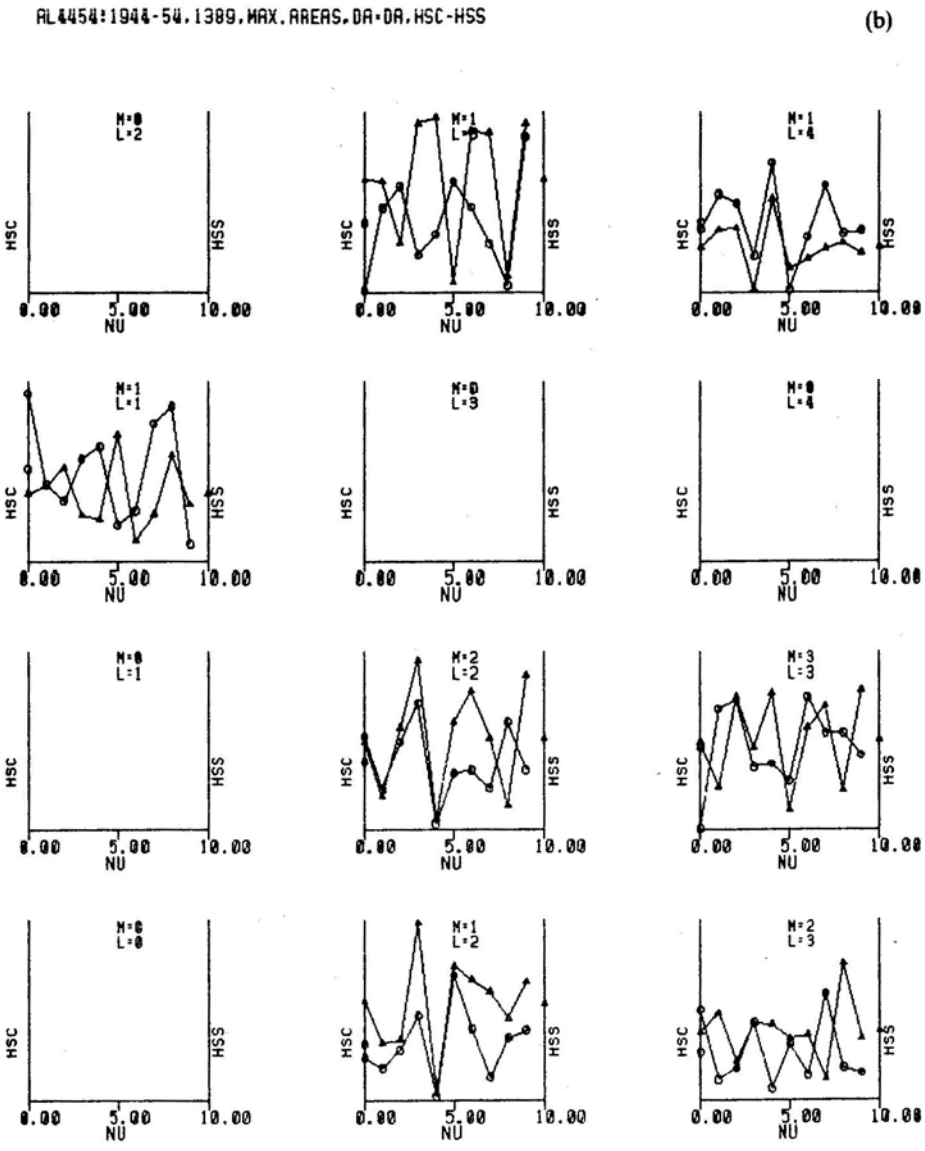

Figure 3. Continued.

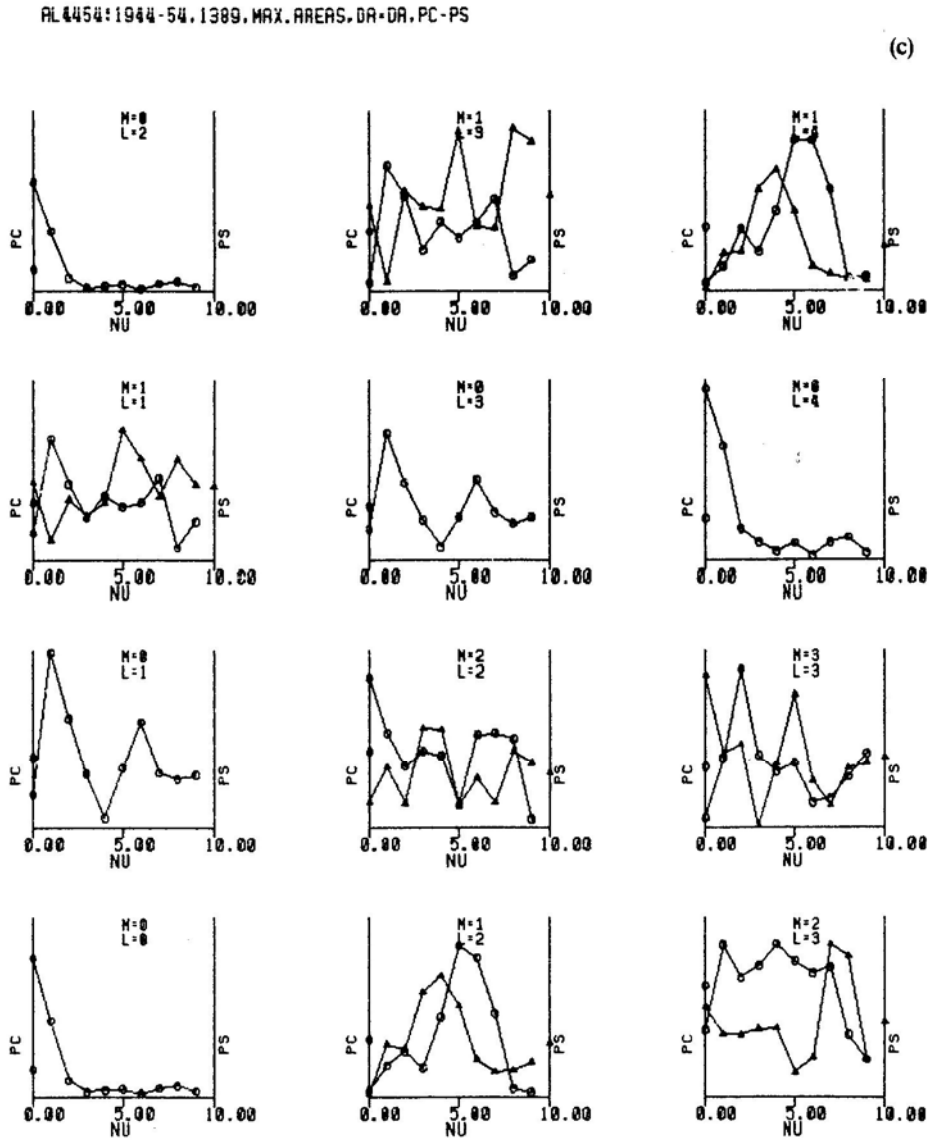

Figure 3. Continued.

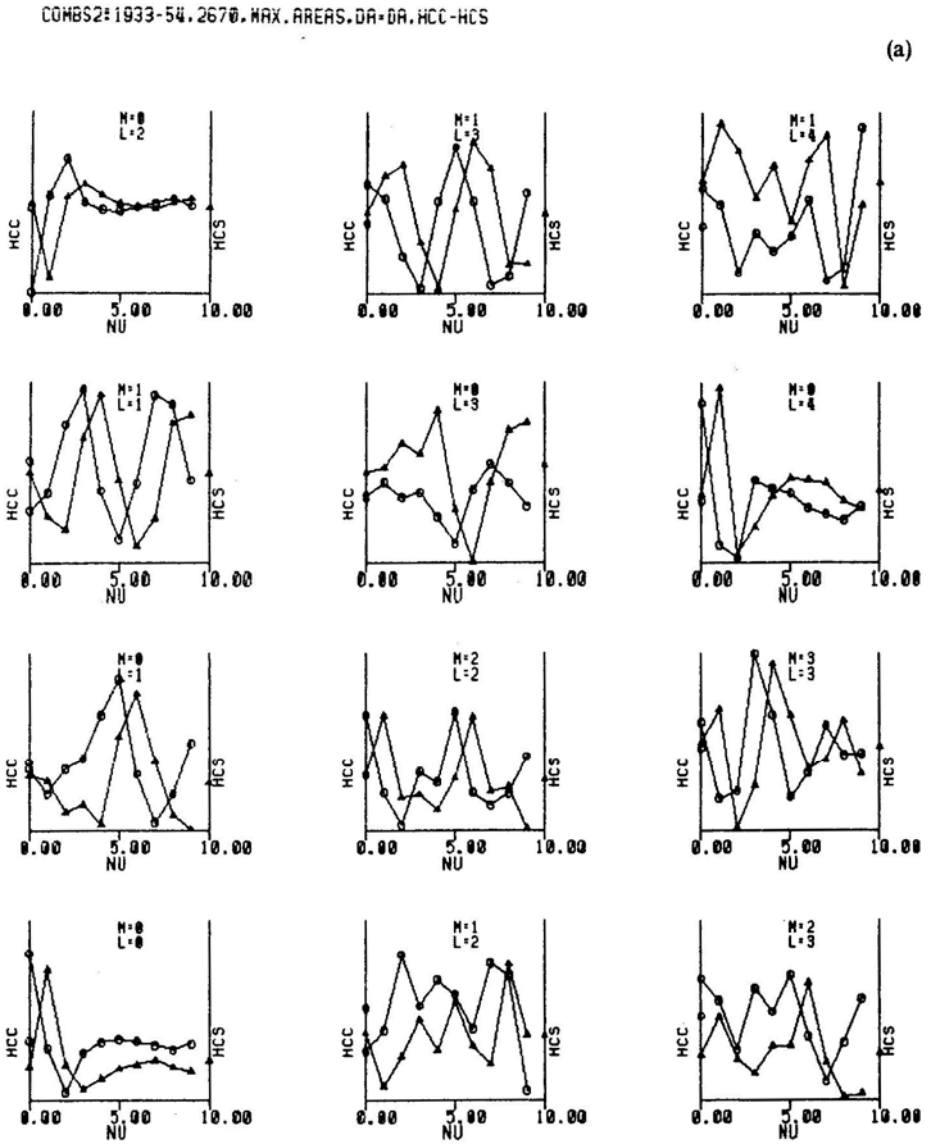

Figure 4. Results for the data on the 2670 spot groups during 1933–1954, the frequency unit being $0.000125 d^{-1}$, *i.e.* ~ $1/22\ yr^{-1}$. Explanations are similar to Fig. 1.

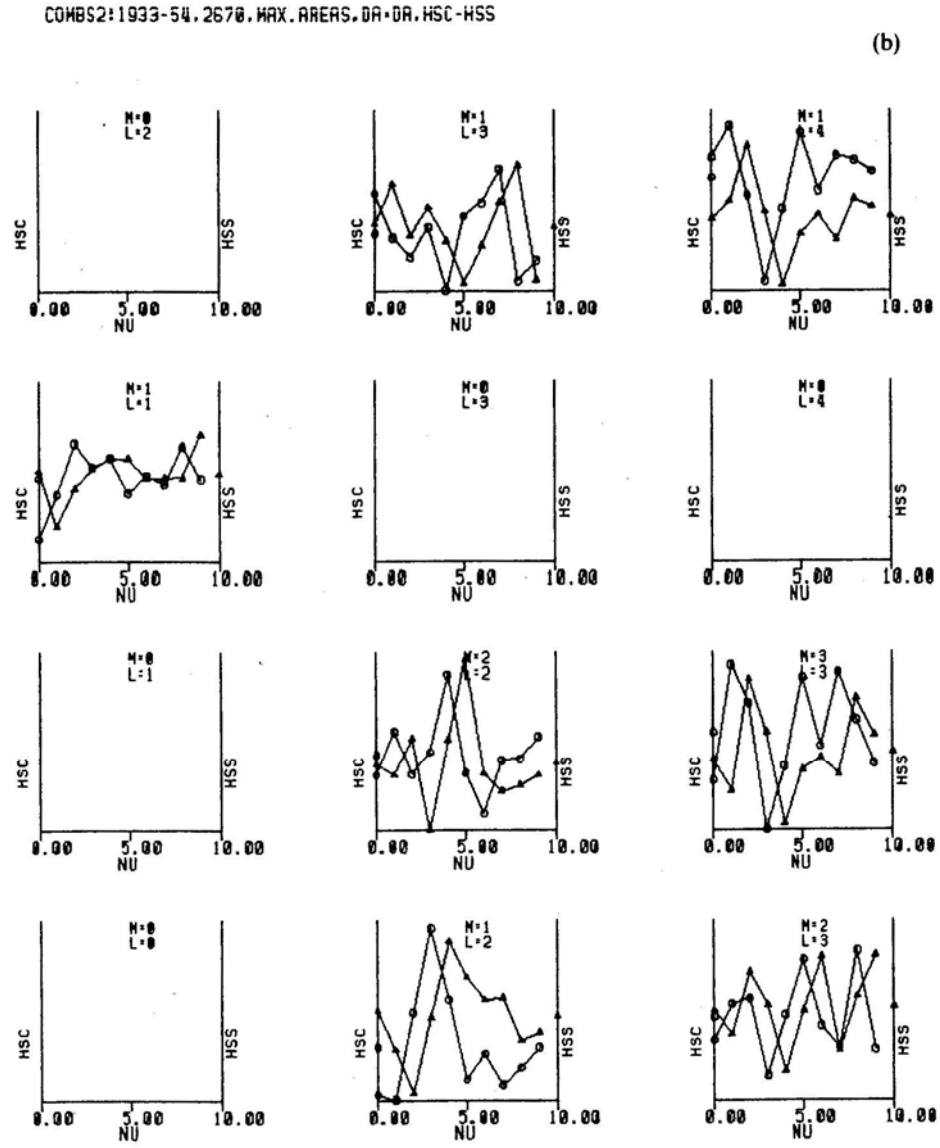

Figure 4. Continued.

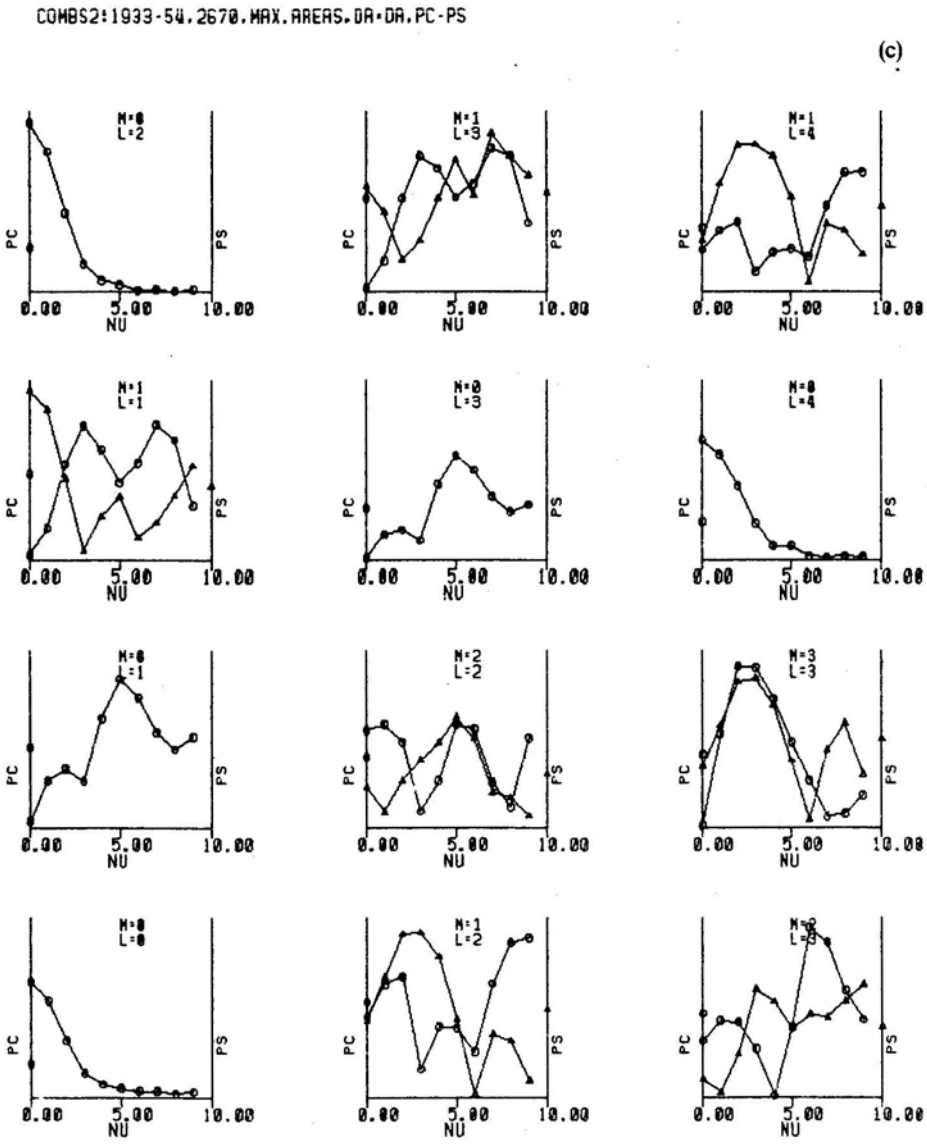

Figure 4. Continued.

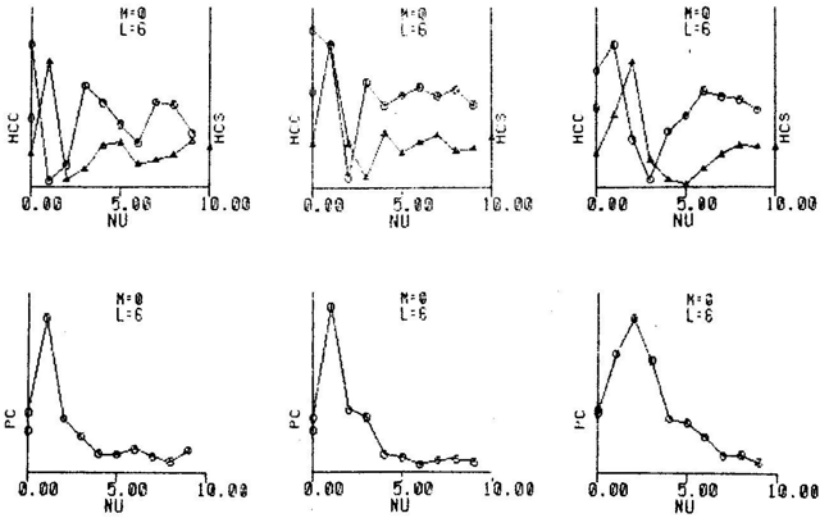

Figure 5. Plots of H_{cc}, H_{cs} (circle and triangle, respectively, in the upper panels) and P_c (circle in the lower panels) for the mode (6,0), obtained from the data during (a) 1933–43, (b) 1944–54, and (c) 1933–54.

Table 1. List of axisymmetric (m = 0) modes showing significant peaks at ~ 11 yr or ~ 22 yr periodicity in the Fourier amplitudes $|H_{cc}|$, $|H_{cs}|$ and/or in Fourier power P_c.

Data length	Fig.	Periodicity yr	$\|H_{cc}\|$	$\|H_{cs}\|$	$\|P_c\|$
1933–43 (cycle 17)	1	~11	(0,0)		—
			(2,0)		—
			(4,0)	(4,0)	—
			(6,0)	(6,0)	(6,0)
			(8,0)	(8,0)	—
1944–54 (cycle 18)	3	~11	(0,0)	(0,0)	—
			—	—	(1,0)
			(2,0)	(2,0)	—
			(3,0)	(3,0)?	(3,0)
			(4,0)	—	—
			(5,0)	(5,0)?	(5,0)
			(6,0)	(6,0)	(6,0)
			(7,0)	—	(7,0)
			(8,0)	(8,0)	—
			(9,0)	—	—
1933–54 (combined)	4	~11	(0,0)	—	—
			(2,0)?	—	—
			(4,0)	(4,0)	—
			—	(6,0)	(6,0)
			(8,0)	—	—
1933–54 (combined)	4	~22	(2,0)	(0,0)	—
			—	(1,0)	—
			—	(4,0)	—
			(6,0)	—	—
			—	(8,0)	—

power of the mode $l = 6$, $m = 0$ show a significant peak at ~11 yr periodicity during each of the cycles 1933–43 and 1944–54. In the analysis of the combined data, this mode shows ~11 yr peaks in $|H_{cs}|$ and P_c, and a ~22 yr peak in $|H_{cc}|$ (Fig. 5).

From Table 1 it is clear that significant peaks are present at the 11 yr periodicity in both the Fourier amplitudes of all the axisymmetric modes of *even* parity up to (8,0) during 1933–43. On the contrary, during 1944–54 the ~11 yr peak is present in a few of the *even* parity modes and most of the *odd* parity modes. During this sunspot cycle the power P_c shows ~11 yr periodicity in *all odd parity* modes up to $l = 7$ and in only *one even parity* mode *viz.* $l = 6$. During the *whole* 22 yr period 1933–54, the ~ 22 yr and the ~11 yr periodicity peaks are present in the amplitudes of all *even* parity modes up to (8,0) and the power P_c shows a peak at ~11 yr only in the (6, 0) mode.

Thus if the sunspot cycle really originates in global modes of ~11 yr periodicity then the set of such modes responsible for sunspot activity is different from one sunspot cycle to another. On the contrary, as found by Stenflo & Vogel (1986), axisymmetric modes of only *odd* parity exhibit 22 yr periodicity in the evolution of the largescale photospheric field. Whether the difference between the results obtained from the sunspot activity and those from the evolution of the largescale photospheric field is due to the difference in the time intervals analyzed or due to an independence of the two phenomena remains to be seen.

Acknowledgements

Mr J. Javaraiah took a major share in the actual work of computations. The author wishes to thank him and staff of the Institute's computing centres for their patience and help. Discussions with several colleagues were quite useful.

References

Gokhale, M. H. 1977, *Kodaikanal Obs. Bull.,* **A2**, 19.
Gokhale, M. H. 1984, *Kodaikanal Obs. Bull.,* **A4**, 25.
Labonte, B. J., Howard, R. 1982, *Solar Physics,* **75**, 161.
Layzer, D., Rosner, R., Doyle, H. T. 1979, *Astrophys.* ***J.,*** **229**, 1126.
Plumpton, C., Ferraro, V. C. A. 1955, *Astrophys****. J.,*** **121**, 168.
Stenflo, J. O., Vogel, M. 1986, *Nature,* **319**, 285.
Walen, C. 1947, *Ark. Mat. Astr. fys.,* **33A**, No. 18.

J. Astrophys. Astr. (1986) **7,** 259–273

Shear-Free Homogeneous Cosmological Model with Heat Flux

Gangabrata Mukherjee *Physics Department, Presidency College, Calcutta 700073*

Received 1986 March 18; accepted 1986 July 23

Abstract. We present the condition of vanishing shear in a spatially homogeneous spacetime in terms of the Ricci rotation co-efficients corresponding to an orthonormal tetrad (v^α, ${}_A\eta^\alpha$) (where v^α is the unit vector along the time axis and ${}_A\eta^\alpha$ are the three independent reciprocal group vectors). Assuming that the velocity vector can be expanded in the direction of v^α and any one of the ${}_A\eta^\alpha$'s it is shown that shear-free motion is possible only in case of some special Bianchi types, and these cases are studied assuming the velocity vector to be geodetic and that there may be a nonvanishing heat flux term.

Key words: cosmology, shear-free velocity field, Bianchi-type

1. Introduction

While spatial isotropy is usually introduced as a basic assumption in standard cosmological model, there is obviously an appeal in examining the effect of weakening this assumption. It is perhaps from this motivation that an extensive study of spatially homogeneous models has been made in which the velocity of the cosmic matter (taken as perfect fluid) is assumed to be shear-free, but the stronger assumption of spatial isotropy is left out. Even with this weaker assumption, Collins & Wainwright (1983) found that besides the Friedmann metric there exists only one solution for irrotational motion of a perfect fluid with $(\rho + p) \neq 0$, satisfying equations of state $p = p(\rho)$, given by the metric

$$ds^2 = \frac{L^2}{f^2}\left[\frac{f'^2}{m^2}dt^2 - dx^2 - e^{-2x}(dy^2 + dz^2)\right] \tag{1.1}$$

where L and m are constants, and

$$f = f(t + x) = f(b) \quad \text{and} \quad f'' + f' = -f^2. \tag{1.2}$$

The prime denotes differentiation with respect to b. However, even the above solution is physically unacceptable since at a finite x-coordinate a singular hypersurface is reached at which both the density and pressure diverge (Mashhoon & Partovi 1984).

The assumption of spatial isotropy leading to the FLRW metric automatically excludes the possibility of fluids with shear viscosity and/or heat flux (as with the FLRW metric $R_1^1 = R_2^2 = R_3^3$ and $R_0^i = 0$, where the subscript 0 indicates the time coordinate and the roman index i (= 1 – 3) stands for the three space-coordinates), unless one makes a very artificial tuning between shear and heat flux so that the non-

diagonal components of T^l_k continue to vanish (Coley & Tupper 1984). With the weaker assumption of shear-free motion for spatial homogeneous universes this is not so. Nevertheless, as we are assuming a shear-free motion, the shear-viscosity is eliminated and we can contemplate the existence of only an energy flux. We investigate whether that can be accommodated in a spatially homogeneous universe with shear-free motion.

For the Bianchi Type-I metric the study has already been made by us in a previous paper (Mukherjee 1983). In the present paper we first derive a general relation involving the Killing vectors ${}_A\xi^\alpha$ (the greek index α runs from 0 to 3, A numbers the Killing vectors and runs from 1 to 3) of the isometry group and the velocity vector u^α, for shear-free motion. Finally we express these in terms of the structure constants of the isometry group and take up the case for different Bianchi types.

2. Mathematical preliminaries

In a spatially homogeneous spacetime with the metric

$$ds^2 = dt^2 + g_{ik}\, dx^i\, dx^k, \tag{2.1}$$

three spacelike Killing vectors satisfy the following relations

$${}_A\xi^0 = {}_A\xi_0 = 0, \tag{2.2a}$$

$${}_A\xi_{(\alpha;\beta)} = 0. \tag{2.2b}$$

From (2.2b) one gets

$${}_A\xi^i_{,0} = 0. \tag{2.2c}$$

The three linearly independent reciprocal group vectors ${}_A\eta^\alpha$ are defined by (Eisenhart 1964)

$${}_A\eta^0 = {}_A\eta_0 = 0, \tag{2.3a}$$

$${}_A\eta^i_{,k} + \Gamma^i_{lk}\,{}_A\eta^l = 0, \tag{2.3b}$$

where

$$\Gamma^i_{lk} \equiv -\,{}_A\xi^i_{,k}\,{}^A\zeta_l, \tag{2.3c}$$

${}^A\zeta_l$ being the inverse matrix of ${}_A\xi^i$.

Equations (2.3b) are completely integrable and ${}_A\eta^i$ satisfy the following relations

$$(g_{ik}\,{}_A\eta^i\,{}_B\eta^k)_{,l} = 0. \tag{2.4}$$

We can choose the solutions of (2.3b) in the following form

$${}_A\eta^i = T_A\,{}_A\bar{\eta}^i \qquad \text{(no summation on rhs)} \tag{2.5a}$$

and

$$g_{ik}\,{}_A\eta^i\,{}_B\eta^k = -\,\delta_{AB} \tag{2.5b}$$

where T_A's are functions of t alone and ${}_A\bar{\eta}^i$'s are function of spatial coordinates only.

The vanishing of Lie derivative of Einstein's tensor G^α_β with respect to each Killing vector requires that the Lie derivative of T^α_β with respect to each Killing vector must vanish. Thus taking the matter energy tensor T^α_β of the form

$$T^\alpha_\beta = (\rho + p)u^\alpha u_\beta - p\delta^\alpha{}_\beta + q^\alpha u_\beta + q_\beta u^\alpha, \tag{2.6}$$

(where ρ, p, u^α, q^α are the matter density, pressure, velocity vector and heat flux vector respectively) we notice that corresponding to each Killing vector we shall have ten linear homogeneous equations in the Lie derivative of ten variables ρ, p, u^α and q^α. (Of course they are not independent as $u^\alpha u_\alpha = 1$ and $u^\alpha q_\alpha = 0$). Hence in general, Lie derivatives of ρ, p, u^α, q^α with respect to each Killing vector vanish and we get,

$$\rho_{,i} = p_{,i} = u^0{}_{,i} = q^0_{,i} = 0, \tag{2.7a}$$

$$u^i_{,k} + \Gamma^i_{lk} u^l = 0, \tag{2.7b}$$

$$q^i_{,k} + \Gamma^i_{lk} q^l = 0. \tag{2.7c}$$

From Equations (2.7b) and (2.7c) we get (*cf.* deduction of (2.4) from (2.3b))

$$(g_{ik} u^i{}_A \eta^k)_{,l} = 0, \tag{2.8a}$$

$$(g_{ik} q^i{}_A \eta^k)_{,l} = 0. \tag{2.8b}$$

Hence from Equations (2.3b), (2.8a), (2.8b) we get

$$u^\alpha = P\delta^\alpha_0 + \sum_{A=1}^{3} Q_A \, {}_A\eta^\alpha, \tag{2.9a}$$

$$q^\alpha = M\delta^\alpha_0 + \sum_{A=1}^{3} N_A \, {}_A\eta^\alpha, \tag{2.9b}$$

With

$$P^2 - \sum_{A=1}^{3} Q_A{}^2 = 1 \quad \text{as} \quad u^\alpha u_\alpha = 1, \tag{2.9c}$$

and

$$PM - \sum_{A=1}^{3} Q_A N_A = 0 \quad \text{as} \quad u^\alpha q_\alpha = 0, \tag{2.9d}$$

where P, M, Q_A, N_A are functions of t alone.

From (2.3a) and (2.3b), δ^α_0 and ${}_A\eta^\alpha$ constitute an orthonormal tetrad .In the following sections we base our analysis on this tetrad.

3. Shear-free velocity field

From the definition of the shear tensor

$$\sigma_{\alpha\beta} = u_{(\alpha;\beta)} - \frac{\theta}{3}(g_{\alpha\beta} - u_\alpha u_\beta) - \dot{u}_{(\alpha} u_{\beta)}, \tag{3.1}$$

we have $\sigma^\alpha_\alpha = 0$ and $\sigma_{\alpha\beta} u^\beta = 0$. Hence the vanishing of the six components σ_{ik} lead to the vanishing of all the ten independent components of $\sigma_{\alpha\beta}$.

With $\sigma_{ik} = 0$ one gets $\sigma_{ik} \, {}_A\xi^i \, {}_B\xi^k = 0$, *i.e.*,

$$\left[u_{(i;k)} - \frac{\theta}{3}(g_{ik} - u_i u_k) - \dot{u}_{(i} u_{k)} \right] {}_A\xi^i \, {}_B\xi^k = 0. \tag{3.2}$$

Using

$$\mathcal{L}_\xi u = 0, \text{ i.e., } {}_A\xi^\alpha_{;\beta} u^\beta = u^\alpha_{;\beta} \, {}_A\xi^\beta \text{ one gets from (3.2)}$$

$$[\sqrt{-g}(M_{AB} - L_A L_B)^{-2/3} u^\alpha]_{,\alpha} = 0 \tag{3.3a}$$

where

$$M_{AB} = g_{ik\,A}\xi^i{}_B\xi^k \quad \text{and} \quad L_A = {}_A\xi^i u_i. \tag{3.3b}$$

Although equation (3.3a) looks quite simple it is not very useful, since a group is characterized uniquely by the constants of structure rather than by the Killing vectors (which may be replaced by any independent linear combination). We therefore express the vanishing of shear in terms of the Ricci rotation coefficients which are linearly related with the structure constants.

The vanishing of all the six independent tetrad components of the shear tensor written explicitly give

$$\sigma_{\hat{1}\hat{1}} = 0 \Rightarrow P\gamma_{011} + Q_2\gamma_{211} + Q_3\gamma_{311} + \frac{\theta}{3}(1 + Q_1^2) + Q_1 A_1 = 0, \tag{3.4a}$$

$$\sigma_{\hat{2}\hat{2}} = 0 \Rightarrow P\gamma_{022} + Q_1\gamma_{122} + Q_3\gamma_{322} + \frac{\theta}{3}(1 + Q_2^2) + Q_2 A_2 = 0, \tag{3.4b}$$

$$\sigma_{\hat{3}\hat{3}} = 0 \Rightarrow P\gamma_{033} + Q_1\gamma_{133} + Q_2\gamma_{233} + \frac{\theta}{3}(1 + Q_3^2) + Q_3 A_3 = 0, \tag{3.4c}$$

$$\sigma_{\hat{1}\hat{2}} = 0 \Rightarrow Q_3(\gamma_{312} + \gamma_{321}) + Q_1\gamma_{121} + Q_2\gamma_{212} + \frac{2}{3}\theta Q_1 Q_2 + Q_1 A_2 + Q_2 A_1 = 0, \tag{3.4d}$$

$$\sigma_{\hat{3}\hat{1}} = 0 \Rightarrow Q_2(\gamma_{213} + \gamma_{231}) + Q_3\gamma_{313} + Q_1\gamma_{131} + \frac{2}{3}\theta Q_3 Q_1 + Q_3 A_1 + Q_1 A_3 = 0, \tag{3.4e}$$

$$\sigma_{\hat{2}\hat{3}} = 0 \Rightarrow Q_1(\gamma_{123} + \gamma_{132}) + Q_2\gamma_{232} + Q_3\gamma_{323} + \frac{2}{3}\theta Q_2 Q_3 + Q_2 A_3 + Q_3 A_2 = 0, \tag{3.4f}$$

where,

$$A_1 = {}_1\eta^i u_i = -P\dot{Q}_1 + PQ_1\gamma_{011} + Q_1(Q_2\gamma_{211} + Q_3\gamma_{311}) + Q_2^2\gamma_{212} + Q_3^2\gamma_{313} + Q_2 Q_3(\gamma_{312} + \gamma_{213}),$$

$$A_2 = {}_2\eta^i u_i = -P\dot{Q}_2 + PQ_2\gamma_{022} + Q_2(Q_3\gamma_{322} + Q_1\gamma_{122}) + Q_3^2\gamma_{323} + Q_1^2\gamma_{121} + Q_3 Q_1(\gamma_{123} + \gamma_{321}),$$

$$A_3 = {}_3\eta^i u_i = -P\dot{Q}_3 + PQ_3\gamma_{033} + Q_3(Q_1\gamma_{133} + Q_2\gamma_{233}) + Q_1^2\gamma_{131} + Q_2^2\gamma_{232} + Q_1 Q_2(\gamma_{132} + \gamma_{231}).$$

The γ-symbols are the Ricci rotation coefficients. (Zero numbers the vector δ_0^α with $\gamma_{0AB} = 0$ (for $A \neq B$) and $\gamma_{ABo} = 0$.)

The Equations (3.4a) to (3.4f) are extremely complicated essentially due to the fact that we have taken the vectors u^α and q^α to have components along all the four tetrad vectors. In case of Bianchi type-I metric we have found previously (Mukherjee 1983) that one can get a solution of u^α and q^α having components along the time axis and only along one reciprocal group vector. We take this result to hold quite generally for all the Bianchi types. This may be looked upon as a simplifying assumption although we

believe that it is generally true. Thus we get in place of (2.9)

$$U^\alpha = P\delta_0^\alpha + Q_1\eta^\alpha (\text{with } P^2 - Q^2 = 1), \tag{3.5a}$$

$$q^\alpha = M\delta_0^\alpha + N_1\eta^\alpha (\text{with } PM - NQ = 0), \tag{3.5b}$$

and the condition of shear-free motion reduces to

$$\sigma_{\hat{1}\hat{1}} = 0 \Rightarrow P\gamma_{011} - \dot{P} + \frac{\theta}{3} = 0, \tag{3.6a}$$

$$\sigma_{\hat{2}\hat{2}} = 0 \Rightarrow P\gamma_{022} + Q\gamma_{122} + \frac{\theta}{3} = 0, \tag{3.6b}$$

$$\sigma_{\hat{3}\hat{3}} = 0 \Rightarrow P\gamma_{033} + Q\gamma_{133} + \frac{\theta}{3} = 0, \tag{3.6c}$$

$$\sigma_{\hat{1}\hat{2}} = 0 \Rightarrow PQ^2\gamma_{121} = 0, \tag{3.6d}$$

$$\sigma_{\hat{3}\hat{1}} = 0 \Rightarrow PQ^2\gamma_{131} = 0, \tag{3.6e}$$

$$\sigma_{\hat{2}\hat{3}} = 0 \Rightarrow Q(\gamma_{123} + \gamma_{132}) = 0. \tag{3.6f}$$

The last three of the above set of equations give

$$\gamma_{121} = \gamma_{131} = 0, \tag{3.7a}$$

$$\gamma_{123} + \gamma_{132} = 0. \tag{3.7b}$$

Now γ_{ABC}'s are related to the structure constants by the relation (Heckmann & Schüking 1962).

$$\gamma_{ABC} = -\frac{1}{2}(\delta_{AD}\bar{D}^D_{BC} + \delta_{BD}\bar{D}^D_{CA} - \delta_{CD}\bar{D}^D_{AB}) \tag{3.8}$$

where $\bar{D}^A_{BC}$'s are the constants of structure of the reciprocal group given by

$$[{}_A\eta, {}_B\eta] = \bar{D}^C_{AB}\eta_C, \tag{3.9}$$

and they are negative of those of the original group (Taub 1951). So, translating the conditions (3.7a), (3.7b) in terms of the structure constants we have

$$D^1_{12} = D^1_{13} = 0, \tag{3.10a}$$

$$D^2_{31} - D^3_{12} = 0. \tag{3.10b}$$

These D^A_{BC}'s are functions of t in contrast to the usual structure constants C^A_{BC} (which are purely constant) because of our special choice of the orthonormal tetrad. In fact D^A_{BC} and T^A_{BC} are related by

$$D^A_{BC} = \frac{T_B T_C}{T_A} C^A_{BC} \quad \text{(no summation on rhs).} \tag{3.11}$$

Hence (3.10a, b) can be written as,

$$C^1_{12} = C^1_{13} = 0, \tag{3.12a}$$

$$C^2_{31} - \frac{T_2^2}{T_3^2} C^3_{12} = 0. \tag{3.12b}$$

As the C^{A}_{BC}'s are time-independent constants, Equation (3.12b) shows that either $C^{2}_{31} = C^{3}_{12} = 0$ or $T_2 / T_3 = 1$ (as usually C^{A}_{BC} are taken as ± 1). Hence the last three conditions of (3.6) reduce to
either

$$C^{1}_{12} = C^{1}_{13} = 0, \tag{3.13a}$$
$$C^{2}_{31} = C^{3}_{12} = 0;$$

or

$$C^{1}_{12} = C^{1}_{13} = 0,$$
$$C^{2}_{31} = C^{3}_{12}, \tag{3.13b}$$
$$T_2 = T_3.$$

Noticing that

$$\gamma_{0AA} = \frac{\dot{T}_A}{T_A}, \tag{3.14a}$$

and

$$\theta = \dot{P} - P \sum_{A=1}^{3} \frac{\dot{T}_A}{T_A} - QD^{A}_{A1} = \dot{P} - P \sum_{A=1}^{3} \frac{\dot{T}_A}{T_A} - QT_1 C^{A}_{A1}, \tag{3.14b}$$

the first three Equations of (3.6) can be written as,

$$\frac{\mathrm{d}}{\mathrm{d}t} \ln\left(\frac{T_1}{P\sqrt{T_2 T_3}} \right) - \frac{QT_1}{2P} C^{A}_{A1} = 0, \tag{3.15a}$$

$$\frac{\mathrm{d}}{\mathrm{d}t} \ln\left(\frac{T_2\sqrt{P}}{\sqrt{T_1 T_3}} \right) - \frac{QT_1}{2P} (C^{A}_{A1} - 3C^{2}_{21}) = 0, \tag{3.15b}$$

$$\frac{\mathrm{d}}{\mathrm{d}t} \ln\left(\frac{T_3\sqrt{P}}{\sqrt{T_1 T_2}} \right) - \frac{QT_1}{2P} (C^{A}_{A1} - 3C^{3}_{31}) = 0. \tag{3.15c}$$

The expressions for the tetrad components of the vorticity tensor are

$$\omega_{0\hat{1}} = 0, \tag{3.16a}$$

$$\omega_{0\hat{2}} = \frac{PQ^2}{2} T_2 C^{1}_{21}, \tag{3.16b}$$

$$\omega_{0\hat{3}} = \frac{PQ^2}{2} T_3 C^{1}_{31}, \tag{3.16c}$$

$$\omega_{\hat{2}\hat{3}} = \frac{\theta}{2} \frac{T_2 T_3}{T_1} C^{1}_{23}, \tag{3.16d}$$

$$\omega_{\hat{1}\hat{2}} = -\frac{QP^2}{2} T_2 C^{1}_{21}, \tag{3.16e}$$

$$\omega_{\hat{1}\hat{3}} = -\frac{QP^2}{2} T_3 C^{1}_{31}. \tag{3.16f}$$

Comparing (3.16) with (3.13) we find that in our case the vorticity is nonvanishing if

$$C^{1}_{23} \neq 0. \tag{3.17}$$

Now we are in a position to investigate the possible shear-free model for different Bianchi types. For convenience we put the results in Table 1. So far no restriction is imposed on the energy-stress tensor.

4. Solutions with heat flux

From Table 1 it is seen that Bianchi Types III, IV and VI do not allow a shear-free velocity field irrespective of the choice of the matter-energy tensor. Moreover, of the possible shear-free models, Bianchi Types II, VIII and IX have the vorticity nonvanishing. It is interesting to note that perfect fluid solution cannot be accommodated to any of these types (*i.e.* for the Types II, VIII and IX), since with the velocity vector (3.5) $T_{0\hat{1}} = T_{oi\ 1}\eta^{i} \neq 0$ if $(\rho + p) \neq 0$, while $G_{0\hat{1}} = G_{0i\ 1}\eta^{i} = 0$ identically for these types. Hence for a homogeneous universe with shear-free perfect fluid, $\omega\theta = 0$ (for $(\rho + p) \neq 0$) automatically satisfied.

For the irrotational shear-free universe, Bianchi Types V and VII can apparently accommodate perfect fluid solution. However, with the shear-free restrictions (3.13), Bianchi Types V and VII behave identically and the set of equations are found to be that due to Collins & Wainwright (details omitted here).

For the discussion of heat flux we classify the solutions into two distinct types (I) $\omega = 0$ (II) $\omega \neq 0$. In either case the equations are complicated but are under-determined. Hence we may adjoin some simplifying assumption. The assumption which we have adopted here is that the velocity vector is geodetic, although under the circumstances this assumption appears rather artificial.

Now, with the velocity vector (3.5) the acceleration vector can be written

$$\dot{u}^{\alpha} = \left(Q\dot{Q} - Q^{2}\frac{\dot{T}_1}{T_1} \right)\delta^{\alpha}_{0} + \left(\dot{Q}P - PQ\frac{\dot{T}_1}{T_1} \right)_{1}\eta^{\alpha} + Q^{2}\sum_{A=1}^{3} T_A C^{1}_{A1\,A}\eta^{\alpha}, \qquad (4.1)$$

where the last term has no contribution due to the constraints imposed on the structure constants by the shear-free velocity field. So the condition that the velocity vector is geodetic is given by

$$Q = T_1 \quad \text{(after a trivial scale transformation).} \qquad (4.2)$$

Now we proceed to investigate the different Bianchi types separately.

4.1 *Category I. Shear-free Irrotational Universe* ($\sigma = \omega = 0$)

4.1.1 *Type I*

A special solution of this type has been obtained by us (Mukherjee 1983). Here we present a solution with the assumption of geodesicity of the velocity vector. $T_{0\hat{1}} = 0$ requires

$$M = q^{0} = -(\rho + p)\left(\frac{T_1^{2} - T_2^{2}}{2T_1^{2} - T_2^{2}} \right)\left(\frac{T_1}{T_2} \right), \qquad (4.3a)$$

$$N = \frac{PM}{Q} = -(\rho + p)\left(\frac{\sqrt{T_1^{2} - T_2^{2}}}{2T_1^{2} - T_2^{2}} \right)\left(\frac{T_1^{2}}{T_2^{2}} \right). \qquad (4.3b)$$

Table 1. Results regarding the shear-free model for different Bianchi types with the velocity vector (3.5a).

Bianchi type	Nonvanishing independent structure constants	Possibility of shear-free model	Value of verticity if the shear-free motion is possible	Remarks
1	2	3	4	5
I	none	possible	$\omega = 0$	Equations (3.15a, b, c) give $T_2 = T_3$ and $P = T_1/T_2$.
II	$C^1_{23} = 1$	possible	$\omega \neq 0$	Equations (3.15a, b, c) give $T_2 = T_3$ and $P = T_1/T_2$.
III	$C^2_{21} = C^3_{31} = 1$ $C^2_{31} = C^3_{21} = 1$	not possible		Any exchange of the numbers 1, 2, 3 in the nonzero structure constants does not satisfy (3.13a, b).
IV	$C^2_{21} = C^3_{31} = 1$ $C^3_{12} = 1$	not possible		Same as Type III.
V	$C^2_{21} = C^3_{31} = 1$	possible	$\omega = 0$	Equations (3.15a, b, c) give $T_2 = T_3$ and $\frac{\dot{T}_1}{T_1} - \frac{\dot{T}_2}{T_2} - \frac{\dot{P}}{P} = \frac{QT_1}{P}$.
VI	$C^2_{21} = C^3_{31} = \sqrt{-h}\,(h < 0)$ $C^2_{31} = C^3_{21} = 1$	not possible		Same as Type III.
VII	$C^2_{21} = C^3_{31} = \sqrt{h}\,(h > 0)$ $C^2_{31} = C^3_{12} = 1$	possible	$\omega = 0$	Equations (3.15a, b, c) give $T_2 = T_3$ and $\frac{\dot{T}_1}{T_1} - \frac{\dot{T}_2}{T_2} - \frac{\dot{P}}{P} = \frac{\sqrt{h}QT_1}{P}$.
VIII	$C^1_{23} = C^2_{13} = 1$ $C^3_{21} = 1$	possible	$\omega \neq 0$	Equations (3.15a, b, c) give $T_2 = T_3$ and $P = T_1/T_2$.
IX	$C^1_{23} = C^2_{31} = C^3_{12} = 1$	possible	$\omega \neq 0$	Equations (3.15a, b, c) give $T_2 = T_3$ and $P = T_1/T_2$.

For classification of Bianchi types one can consult Landau & Lifshitz (1975) and MacCallum (1979).

The nontrivial components of the Einstein's field equations $S_{AB} = G_{AB} + 8\pi T_{AB} = 0$ are,

$$S_{\hat{1}\hat{1}} = \left(\frac{\dot{T}_1}{T_1}\right)^{\cdot} - \frac{\dot{T}_1}{T_1}\left(\frac{\dot{T}_1}{T_1} + \frac{2\dot{T}_2}{T_2}\right) + \frac{1}{2}R - 8\pi\left[(\rho + p)\frac{T_1^2 - T_2^2}{2T_1^2 - T_2^2} - p\right] = 0, \quad (4.4a)$$

$$S_{\hat{2}\hat{2}} = S_{\hat{3}\hat{3}} = \left(\frac{\dot{T}_2}{T_2}\right)^{\cdot} - \frac{\dot{T}_2}{T_2}\left(\frac{\dot{T}_1}{T_1} + \frac{2\dot{T}_2}{T_2}\right) + \frac{1}{2}R + 8\pi p = 0, \quad (4.4b)$$

$$-S_{00} = \left(\frac{\dot{T}_1}{T_1}\right)^{\cdot} + 2\left(\frac{\dot{T}_2}{T_2}\right)^{\cdot} - \frac{\dot{T}_1^2}{T_2^2} - \frac{2\dot{T}_2^2}{T_2^2} + \frac{1}{2}R - 8\pi\left[(\rho + p)\frac{T_1^2}{2T_1^2 - T_2^2} - p\right] = 0. \quad (4.4c)$$

As from Table 1, $P = T_1 / T_2$, the assumption $\dot{u}^a = 0$ gives

$$T_1^2 - T_2^2 = T_1^2 T_2^2, \quad (4.5a)$$

i.e.,

$$\frac{\dot{T}_2}{T_2} = \frac{\dot{T}_1}{T_1}\frac{1}{(1 + T_1^2)}. \quad (4.5b)$$

So, with the help of Equations (4.4a) to (4.4c) we have

$$\frac{\mathrm{d}}{\mathrm{d}t}\left(\frac{\dot{T}_1}{T_1^2 + 1}\right) = 0 \quad (4.6a)$$

so that

$$T_1 = \tan kt \quad (4.6b)$$

And

$$T_2 = \sin kt \quad (4.6c)$$

where k is the integration constant, another integration constant being absorbed by a suitable scale transformation.

The expressions for the pressure and density are given by,

$$8\pi p = -\frac{k^2}{\tan^2 kt}(4\tan^2 kt + 5), \quad (4.7a)$$

$$8\pi\rho = \frac{3k^2}{\tan^2 kt}. \quad (4.7b)$$

Though the energy density is positive, the pressure as well as $(\rho + p)$ are negative.

The heat flux vector is given by

$$8\pi M = \frac{2k^2(2\tan^2 kt + 1)\sin kt \tan kt}{2\tan^2 kt - \sin^2 kt}, \quad (4.7c)$$

$$8\pi N = \frac{2k^2(2\tan^2 kt + 1)\sec kt}{2\tan^2 kt - \sin^2 kt}. \quad (4.7d)$$

4.1.2 *Types V & VII*

In these types $S_{0\hat{1}} = G_{0\hat{1}} + 8T_{0\hat{1}}$ is the only non-diagonal nontrivial component, which exists together with the diagonal components. The components are written out explicitly below.

For Type V:

$$S_{0\hat{1}} = 2T_1\left(\frac{\dot{T}_1}{T_1} - \frac{\dot{T}_2}{T_2}\right) + 8\pi[(\rho + p)PQ + PN + QM] = 0, \tag{4.8a}$$

$$S_{\hat{1}\hat{1}} = \left(\frac{\dot{T}_1}{T_1}\right)^{\cdot} - \frac{\dot{T}_1}{T_1}\left(\frac{\dot{T}_1}{T_1} + \frac{2\dot{T}_2}{T_2}\right) + 2T_1{}^2 + \frac{1}{2}R + 8\pi[(\rho + p)Q^2 + p + 2QN] = 0, \tag{4.8b}$$

$$S_{\hat{2}\hat{2}} = S_{\hat{3}\hat{3}} = \left(\frac{\dot{T}_2}{T_2}\right)^{\cdot} - \frac{\dot{T}_2}{T_2}\left(\frac{\dot{T}_1}{T_1} + \frac{2\dot{T}_2}{T_2}\right) + 2T_1{}^2 + \frac{1}{2}R + 8\pi p = 0, \tag{4.8c}$$

$$-S_{00} = \left(\frac{\dot{T}_1}{T_1}\right)^{\cdot} + 2\left(\frac{\dot{T}_2}{T_2}\right)^{\cdot} - \frac{\dot{T}_1{}^2}{T_1{}^2} - \frac{2\dot{T}_2{}^2}{T_2{}^2} + \frac{1}{2}R - 8\pi[(\rho + p)P^2 - p + 2PM] = 0. \tag{4.8d}$$

Along with these field equations we have the shear-free condition

$$\frac{\dot{T}_1}{T_1} - \frac{\dot{T}_2}{T_2} - \frac{\dot{P}}{P} = \frac{QT_1}{P}. \tag{4.8e}$$

For Type VII:

$$S_{0\hat{1}} = 2\sqrt{h}\,T_1\left(\frac{\dot{T}_1}{T_1} - \frac{\dot{T}_2}{T_2}\right) + 8\pi[(\rho + p)PQ + PN + QM] = 0, \tag{4.9a}$$

$$S_{\hat{1}\hat{1}} = \left(\frac{\dot{T}_1}{T_1}\right)^{\cdot} - \frac{\dot{T}_1}{T_1}\left(\frac{\dot{T}_1}{T_1} + \frac{2\dot{T}_2}{T_2}\right) + 2hT_1{}^2 + \frac{1}{2}R + 8\pi[(\rho + p)Q^2 + p + 2QN] = 0, \tag{4.9b}$$

$$S_{\hat{2}\hat{2}} = S_{\hat{3}\hat{3}} = \left(\frac{\dot{T}_2}{T_2}\right)^{\cdot} - \frac{\dot{T}_2}{T_2}\left(\frac{\dot{T}_1}{T_1} + \frac{2\dot{T}_2}{T_2}\right) + 2hT_1{}^2 + \frac{1}{2}R + 8\pi p = 0, \tag{4.9c}$$

$$-S_{00} = \left(\frac{\dot{T}_1}{T_1}\right)^{\cdot} + 2\left(\frac{\dot{T}_2}{T_2}\right)^{\cdot} - \frac{\dot{T}_1{}^2}{T_1{}^2} - \frac{2\dot{T}_2{}^2}{T_2{}^2} + \frac{1}{2}R - 8\pi[(\rho + p)P^2 - p + 2PM] = 0, \tag{4.9d}$$

and

$$\frac{\dot{T}_1}{T_1} - \frac{\dot{T}_2}{T_2} - \frac{\dot{P}}{P} = \sqrt{h}\,\frac{QT_1}{P}. \tag{4.9e}$$

where h is a constant. The set of Equations (4.9) is reduced to the set (4.8) if one identifies T_1 of (4.8) with $\sqrt{h}\ T_1$ of (4.9). Now imposing the restriction of geodesicity we obtain from the set of Equations (4.8)

$$\frac{\dot{T}_1}{T_1^2+1}+\frac{T_1}{(T_1^2+1)^{1/2}}=\text{constant}=+C. \tag{4.10}$$

This can be integrated to give

$$\frac{C}{\sqrt{C^2-1}}\left(\frac{\sqrt{T_1^2+1}-1}{T_1}\right)=\frac{1}{\sqrt{C^2-1}}+\tan\frac{\sqrt{C^2-1}}{2}t. \tag{4.11}$$

An integration constant is absorbed using a scale transformation on time.

The scalars p, ρ and θ are given by

$$8\pi\rho=\frac{3\dot{T}_1^2}{T_1^2(T_1^2+1)^2}-\frac{6CT_1}{T_1^2+1}+\frac{3T_1^2}{T_1^2+1}, \tag{4.12a}$$

$$8\pi p=-\frac{(4T_1^2+5)\dot{T}_1^2}{T_1^2(T_1^2+1)^2}-\frac{2C}{T_1\sqrt{T_1^2+1}}+\frac{2+T_1^2}{T_1^2+1}, \tag{4.12b}$$

$$\theta=-\frac{3C\sqrt{T_1^2+1}}{T_1}+3, \tag{4.12c}$$

$$4\pi M=\frac{\dot{T}_1^2}{(T_1^2+1)^{3/2}}+\frac{\dot{T}_1T_1}{T_1^2+1}. \tag{4.12d}$$

From the above solution it is seen that with $C<0$ the energy density is always positive while the pressure may not. Considering the specific case $C=0$ we have

$$T_1=\frac{2e^{-t}}{1-e^{-2t}}, \tag{4.13a}$$

and the scalars are

$$8\pi p=-3, \tag{4.13b}$$

$$8\pi\rho=3, \tag{4.13c}$$

$$\theta=3, \tag{4.13d}$$

$$M=0. \tag{4.13e}$$

The heat flux vanishes and we can consider this to be a solution corresponding to false vacuum which is mathematically equivalent to a cosmological term.

4.2 *Category II. Rotating Shear-Free Model with Heat Flux* ($\sigma=0$, $\omega\neq0$)

Bianchi Types II, VIII and IX fall in this category. All these types also correspond to class A model (*i.e.* $C^A_{AB}=0$, no summation on *A)* according to the classification by Behr (1962).

Here, for all types, $P = T_1 / T_2$. Hence the components of heat flux vector, the relationship between T_1 and T_2 obey the same relationship as in Type I (Equations 4.3a, 4.3b, 4.5a, 4.5b).

The nontrivial components of Einstein's equations are listed below.

Type II:

$$S_{\hat{1}\hat{1}} = \left(\frac{\dot{T}_1}{T_1}\right)^{\cdot} - \frac{\dot{T}_1}{T_1}\left(\frac{\dot{T}_1}{T_1} + \frac{2\dot{T}_2}{T_2}\right) - \frac{{T_2}^4}{2{T_1}^2} + \frac{1}{2}R - 8\pi\left[(\rho + p)\frac{{T_1}^2 - {T_2}^2}{2{T_1}^2 - {T_2}^2} - p\right] = 0, \tag{4.14a}$$

$$S_{\hat{2}\hat{2}} = S_{\hat{3}\hat{3}} = \left(\frac{\dot{T}_2}{T_2}\right)^{\cdot} - \frac{\dot{T}_2}{T_2}\left(\frac{\dot{T}_1}{T_1} + \frac{2\dot{T}_2}{T_2}\right) + \frac{{T_2}^4}{2{T_1}^2} + \frac{1}{2}R + 8\pi p = 0, \tag{4.14b}$$

$$-S_{00} = \left(\frac{\dot{T}_1}{T_1}\right)^{\cdot} + 2\left(\frac{\dot{T}_2}{T_2}\right)^{\cdot} - \frac{\dot{T}_1{}^2}{T_1{}^2} - \frac{2\dot{T}_2{}^2}{T_2{}^2} + \frac{1}{2}R - 8\pi\left[(\rho + p)\frac{{T_1}^2}{2{T_1}^2 - {T_2}^2} - p\right] = 0. \tag{4.14c}$$

Type VIII:

$$S_{\hat{1}\hat{1}} = \left(\frac{\dot{T}_1}{T_1}\right)^{\cdot} - \frac{\dot{T}_1}{T_1}\left(\frac{\dot{T}_1}{T_1} + \frac{2\dot{T}_2}{T_2}\right) - \frac{{T_2}^4}{2{T_1}^2} + \frac{1}{2}R - 8\pi\left[(\rho + p)\frac{{T_1}^2 - {T_2}^2}{2{T_1}^2 - {T_2}^2} - p\right] = 0, \tag{4.15a}$$

$$S_{\hat{2}\hat{2}} = S_{\hat{3}\hat{3}} = \left(\frac{\dot{T}_2}{T_2}\right)^{\cdot} - \frac{\dot{T}_2}{T_2}\left(\frac{\dot{T}_1}{T_1} + \frac{2\dot{T}_2}{T_2}\right) + {T_2}^2 + \frac{{T_2}^4}{2{T_1}^2} + \frac{1}{2}R + 8\pi p = 0, \tag{4.15b}$$

$$-S_{00} = \left(\frac{\dot{T}_1}{T_1}\right)^{\cdot} + 2\left(\frac{\dot{T}_2}{T_2}\right)^{\cdot} - \frac{\dot{T}_1{}^2}{T_1{}^2} - \frac{2\dot{T}_2{}^2}{T_2{}^2} + \frac{1}{2}R - 8\pi\left[(\rho + p)\frac{{T_1}^2}{2{T_1}^2 - {T_2}^2} - p\right] = 0. \tag{4.15c}$$

Type IX:

$$S_{\hat{1}\hat{1}} = \left(\frac{\dot{T}_1}{T_1}\right)^{\cdot} - \frac{\dot{T}_1}{T_1}\left(\frac{\dot{T}_1}{T_1} + \frac{2\dot{T}_2}{T_2}\right) - \frac{{T_2}^4}{2{T_1}^2} + \frac{1}{2}R - 8\pi\left[(\rho + p)\frac{{T_1}^2 - {T_2}^2}{2{T_1}^2 - {T_2}^2} - p\right] = 0, \tag{4.16a}$$

$$S_{\hat{2}\hat{2}} = S_{\hat{3}\hat{3}} = \left(\frac{\dot{T}_2}{T_2}\right)^{\cdot} - \frac{\dot{T}_2}{T_2}\left(\frac{\dot{T}_1}{T_1} + \frac{2\dot{T}_2}{T_2}\right) + \frac{{T_2}^4}{2{T_1}^2} - {T_2}^2 + \frac{1}{2}R + 8\pi p = 0, \tag{4.16b}$$

$$-S_{00} = \left(\frac{\dot{T}_1}{T_1}\right)^{\cdot} + 2\left(\frac{\dot{T}_2}{T_2}\right)^{\cdot} - \frac{\dot{T}_1{}^2}{T_1{}^2} - \frac{2\dot{T}_2{}^2}{T_2{}^2} + \frac{1}{2}R - 8\pi\left[(\rho + p)\frac{{T_1}^2}{2{T_1}^2 - {T_2}^2} - p\right] = 0. \tag{4.16c}$$

With the assumption of geodesicity we can have a differential equation for T_1 for each type:

$$T_1 \frac{d}{dt}\left(\frac{\dot{T}_1}{T_1^2+1}\right) = -\frac{T_1^2(T_1^2+2)}{2(T_1^2+1)^2} \quad \text{(Type II)}, \tag{4.17a}$$

$$T_1 \frac{d}{dt}\left(\frac{\dot{T}_1}{T_1^2+1}\right) = -\frac{T_1^2(3T_1^2+4)}{2(T_1^2+1)^2} \quad \text{(Type VIII)}, \tag{4.17b}$$

$$T_1 \frac{d}{dt}\left(\frac{\dot{T}_1}{T_1^2+1}\right) = \frac{T_1^4}{2(T_1^2+1)^2} \quad \text{(Type IX)}. \tag{4.17c}$$

These equations can be integrated once, and the results are

$$\frac{\dot{T}_1^2}{(T_1^2+1)^2} = -\frac{T_1^4-2}{4(T_1^2+1)^2} + \text{constant} \quad \text{(Type II)}, \tag{4.18a}$$

$$\frac{\dot{T}_1^2}{(T_1^2+1)^2} = -\frac{3T_1^4-4}{4(T_1^2+1)^2} + \text{constant} \quad \text{(Type III)}, \tag{4.18b}$$

$$\frac{\dot{T}_1^2}{(T_1^2+1)^2} = \frac{T_1^4}{4(T_1^2+1)^2} + \text{constant} \quad \text{(Type IX)}. \tag{4.18c}$$

We have calculated the pressure and density in terms of T_1 in the three cases. For Types II and VIII both these scalars turn out to be negative. For Type IX, with (4.18c) the pressure and density are given by

$$8\pi p = -\frac{T_1^2}{2(T_1^2+1)} - \frac{K(4T_1^2+5)}{T_1^2}, \tag{4.19a}$$

$$8\pi\rho = \frac{T_1^2(5T_1^2+3)}{2(T_1^2+1)^2} + \frac{3K}{T_1^2}. \tag{4.19b}$$

It turns out that with the positive value of the integration constant K, the energy density is positive always whereas the pressure is not. Both the pressure and energy density are always positive if K is negative and bounded by some limits which can be found from (4.19a) and (4.19b).

The restriction condition ($p > 0$, $\rho > 0$, $\rho - 3p > 0$) lead to the following inequality:

$$\frac{T_1^4}{2(T_1^2+1)^2(4T_1^2+5)} < |K| < \frac{T_1^4(8T_1^2+6)}{6(T_1^2+1)^2(4T_1^2+6)}. \tag{4.20a}$$

But as the solution (4.18c) is possible if

$$|K| < \frac{T_1^4}{4(T_1^2+1)^2}$$

and

$$\frac{T_1^4}{4(T_1^2+1)^2} > \frac{T_1^4}{2(T_1^2+1)(4T_1^2+5)}$$

identically, the limit on $|K|$ can also be expressed as

$$\frac{T_1^4}{2(T_1^2+1)^2(4T_1^2+5)} < |K| < \frac{T_1^4}{4(T_1^2+1)^2}. \tag{4.20b}$$

The magnitude of M and N are given by

$$8\pi M = -\left(\frac{T_1^4}{(T_1^2+1)^2} - 2K\right)\sqrt{T_1^2+1}, \tag{4.21a}$$

$$8\pi N = -\frac{(T_1^2+1)}{T_1}\left[\frac{T_1^4}{(T_1^2+1)^2} - 2K\right], \tag{4.21b}$$

$$\frac{M}{\rho+p} = -\frac{T_1^2}{2T_1^2+1}\sqrt{T_1^2+1}. \tag{4.21c}$$

5. Concluding remarks

Careful investigations have revealed that both the redshift from distant galaxies and the microwave background radiation have small anisotropies which are primarily of the dipole form. It seems natural to attempt an interpretation of these dipole anisotropies in terms of a peculiar velocity of the observer's frame rather than to accept the anisotropies as intrinsic. But as the anisotropy patterns are not identical in the two cases, we arrive at two velocities in this way different both in magnitude and direction (Cheng *et al* 1979; Hart & Davies 1982; Raychaudhuri 1979; Rubin *et al.* 1976; Smoot, Gorenstein & Miller 1979).

The present paper may be looked upon as an attempt to resolve the above difficulty. The shear-free velocity field ensures an isotropy of the redshift while the anisotropy of the MBR is associated with the energy flux. However, we have made no attempt to have a quantitative comparison with observations.

Acknowledgements

The author expresses his deep gratitude to Professor A. K. Raychaudhuri for his constant inspiration and valuable guidance. The author is also thankful to an anonymous referee for constructive suggestions (which have led to an improvement in the presentation of the paper), and to the C. S. I. R., New Delhi for the award of a fellowship.

References

Behr, C. G. 1962, *Z. Astrophys.,* **54**, 268.
Cheng, E. S, Saulson, P. R., Wilkinson, D. T., Corey, B. E. 1979, *Astrophys. J.,* **232**, L 139.
Coley, A. A., Tupper, B. O. J. 1984, *Phys. Rev.*, **D29**, 2701.
Collins, C. B., Wainwright, J. 1983, *Phys. Rev.*, **D27**, 1209.
Eisenhart, L. P. 1964, *Riemannian Geometry*, Princeton Univ. Press, p. 286.
Hart, L., Davies, R. D. 1982, *Nature,* **297**, 191.

Heckmann, O., Schüking, E.1962, *Relativistic Cosmology in* '*Gravitation*', Ed. L. Witten, Wiley, New York.
Landau, L. D., Lifshitz, E. M. 1975, *Classical Theory of Fields,* Pergamon Press, p. 381.
MacCallum, M. A. H. 1979, in *General Relativity,* Eds S. W. Hawking & W. Israel, Cambridge Univ. Press, p. 533.
Mashhoon, B., Partovi, M. H. 1984 *Phys. Rev.,* **D30**, 1839.
Mukherjee, G. 1983, *J. Astrophys. Astr*., **4**, 295.
Raychaudhuri, A. K. 1979, *Theoretical Cosmology,* Clarendon Press, Oxford, p. 105.
Rubin, V. C., Thonnard, N., Ford, W. K. (Jr.), Roberts, M. S. 1976, *Astr. J.,* **81**, 719.
Smoot, G. F., Gorenstein, M. V., Muller, R. A. 1977, *Phys. Rev. Lett.*, **39**, 898.
Taub, A. H. 1951, *Ann. Math.,* **53**, 472.

J. Astrophys. Astr. (1986) **7,** 275–292

Minimum-Relative-Entropy Method—Solution to Missing Short-Baseline Problem

R. K. Shevgaonkar *Indian Institute of Astrophysics, Bangalore 560034*

Received 1986 March 7; accepted 1986 August 6

Abstract. Minimum-relative-entropy method (MREM) has been presented as a solution to the missing short-baseline problem in the synthesis observations. It is shown that a measure of distance between the prior model and the image in the plane of pixel brightness is an adequate measure of relative entropy. The method has been further extended for polarization observations and the potential of the method against the conventional MEM has been demonstrated by simulated examples.

Key words: image reconstruction—minimum-relative-entropy method—radio astronomy, reduction techniques

1. Introduction

In radio astronomy, looking at the need of large-field mapping, the maximum-entropy method (MEM) has received a new impetus over the last decade (Gull & Daniell 1978; Cornwell & Evans 1985). Application of the method to a variety of images in astronomy as well as in other fields like picture processing and medical science has clearly demonstrated the potential of the technique. However, one must accept the fact that to make the method work the problem should be well-posed. In practice one observes that it becomes difficult to obtain useful reconstruction of an image if the measurements are too noisy or too sparse. For example, we see that the extended sources are not very faithfully reconstructed if the spatial Fourier coverage (also called *uv*-coverage) is not compact (Nityananda & Narayan 1982; Narayan & Nityananda 1984). Here, by compact we mean a *uv*-coverage which is uniformly sampled with the Nyquist rate around the origin of the *uv*-plane.

In the past, the maximum-entropy-method has been presented as a general technique devised for estimating the unmeasured visibility coefficients from the knowledge of the measured ones (Nityananda & Narayan 1982; Shevgaonkar 1986b). The method does not make any assumption regarding the spatial domains of the measured and unmeasured visibilities. It is assumed that the measurements are performed over an arbitrary spatial region and we are interested in predicting the visibility coefficients over another region using entropy of the image as a measure of goodness of the image. However, if we look at the visibility function carefully, we note that the method cannot provide faithful reconstruction for any arbitrary kind of data. For an observation where the visibility coefficients are measured over a compact *uv*-coverage, all extended as well as localized sources have their respective contribution in the measured data. On the contrary, if the observations do not contain shorter baselines, the very extended

sources are completely missing in the observed data. The extended distributions, which are neither totally missing nor completely sampled, are mainly the source of degradation of the observed image. The presence of improperly sampled largescale structures is manifested in large negative bowls in the observed image. The very extended features whose visibility function lies completely within the unmeasured central region of the *uv*-plane, do not give any indication of their existence and one would never know what is actually missing from the observed data. Here we are not interested in reconstruction of these largescale structures, as their presence or absence does not make any difference in the quality of the reconstruction. In this paper we are concerned about those extended distributions whose visibility function is partly sampled and which manifest themselves in the negative bowls. The MEM, as presented in the past, due to its inherent nature of reconstructing flat background and sharp peaks, although a useful technique for improving resolution, faces serious difficulties in reconstructing extended sources observed with non-compact *uv*-coverages.

Aperture synthesis telescopes, while generally providing a uniform sampling of the visibility function, often leave an unsampled hole near the origin of the *uv*-plane. The zero-lag visibility coefficient or the integrated power of the brightness distribution can be obtained (although not very easily) from any of the synthesizing elements, but the other short spacings still remain unmeasured. A method for estimating the visibility function over short baselines is highly desired from the viewpoint of mapping largescale structures with synthesis telescopes.

Although the conventional deconvolution method CLEAN (Högbom 1974) is capable of removing the effect of sidelobes from the observed maps, it finds difficult to take away the negative bowls around the extended sources. A modified version of CLEAN called 'window CLEAN' (Schwarz 1978), by putting a CLEANing box around the positive source within the negative bowl, may relatively improve the quality of the reconstruction by forcibly discarding the presence of the extended negative features. However, practitioners of CLEAN would agree that the method does not do a very good job for reconstructing largescale structures.

In the past, few proposals have been made towards estimation of the short-baseline visibilities from synthesis data (Rots 1979; Ekers & Rots 1979; Braun & Walterbos 1985). The method suggested by Rots (1979) is a data fitting technique using the positivity constraint on the image. This technique requires a precise knowledge of the source parameters which could possibly be available only for simple distributions, and therefore the method is not quite suited for complex distributions. The method presented by Braun & Walterbos (1985) is based upon a direct nonlinear fit of the missing Fourier coefficients to the isolated map plane response. In any case, to obtain an equally good quality image of the compact sources along with the extended ones, the map ultimately has to be deconvolved with the point spread function. Therefore it appears that the most efficient way would be to obtain a proper deconvolution method which itself is capable of estimating lower as well as higher spatial frequency visibilities.

We present here a possible application of the minimum-relative-entropy method for the estimation of the visibilities over short baselines. We show that the distance between the image and the prior model in the plane of pixel brightness can provide a good measure of relative entropy *i.e.,* entropy of the image with respect to the entropy of the prior model. We further generalize this definition of relative entropy for the polarization images and by simulated examples we show that the method works very promisingly for complex extended images observed with limited information over short baselines.

2. Concept of relative entropy

The concept of relative entropy (also called 'cross entropy') was first proposed by Kullback in 1959. The concept has been subsequently promoted in various forms by others (Hobson & Cheng 1973; Johnson 1979) and has been successfully utilized by radio astronomers (Gull & Skilling 1984; Cornwell & Evans 1985) to obtain reliable deconvolution of real synthesized images. The relative entropy is a generalization of the entropy that applies in cases where a prior image B_0 that estimates the image B is known in addition to the measurements and other constraints like positivity.

Shore & Johnson (1980), using consistency arguments, have shown that in the presence of prior knowledge about the distribution one must minimize the relative entropy defined by a unique function given as

$$E_r = \iint B \ln (B/B_0)\, dx\, dy \tag{1}$$

where x, y are the image coordinates. On the other hand, Cornwell & Evans (1985) treat relative entropy as a measure of distance of reconstructed image B from an *a priori* expected image B_0. Following this concept it is possible to obtain a variety of functions which will define an equally good measure of distance between B and B_0. However, a function F (B, B_0) which defines a good measure of distance between two images B and B_0, and can be used as a relative-entropy function must possess certain basic characteristics.

(1) Firstly, since the true brightness distribution is positive definite, the entropy function should impose positivity on the reconstructed image. In other words the entropy function should explicitly be definable for positive brightness only.
(2) Secondly, as has been argued in the past (Nityananda & Narayan 1982), for any kind of extrapolation of the visibility function and for obtaining a translation-invariant reconstruction, the entropy function should provide a nonlinear image transfer function, or in other words the first derivative of the function should be a nonlinear function of the brightness.
(3) Thirdly, it is desired that the entropy function should be such that one obtains a unique reconstruction for a given measurement and a given biasing image *i.e.,* the entropy function should possess a single minimum in the acceptable range of brightness.

It is immediately clear that the scalar distance between two images defined by the sum of the squares of the pixel differences cannot be taken as a measure of relative entropy, as it obtains only a linear-image-transfer function which, as pointed out above, is not adequate for extrapolation of the visibility function. Also, the scalar distance minimization does not impose the positivity on the reconstructed image.

As a next immediate choice the scalar distance between some function of the pixel brightness of the image and the prior model as given below

$$F(B, B_0) = [f(B) - f(B_0)]^2 \tag{2}$$

can be tried for defining relative entropy. The choice of f should be such that F satisfies the three abovementioned conditions. The first two conditions can be easily achieved by choosing f as one of the simple entropy functions like $\ln B$, $-B \ln B$, or in general B^s. The third, minimality condition requires that the second derivative of F (B, B_0) with

respect to B must be greater than zero for all positive values of B giving

$$\frac{\partial^2}{\partial B^2}\{[f(B)-f(B_0)]^2\} > 0 \tag{3a}$$

or

$$\{f(B)-f(B_0)\}\frac{\partial^2 f}{\partial B^2}+\left(\frac{\partial f}{\partial B}\right)^2 > 0. \tag{3b}$$

Now since all conventional entropy functions f have $\partial^2 f/\partial B^2 < 0$ (Burg 1975; Nityananda & Narayan 1982), Equation (3b) can be rewritten as

$$f(B)+\frac{(\partial f/\partial B)^2}{\partial^2 f/\partial B^2} < f(B_0). \tag{4}$$

Therefore for a given prior model a unique reconstruction is possible only if Equation (4) is satisfied for all possible values of B.

Let us now verify which of the conventional entropy functions satisfy Equation (4)!

For entropy function $f(B) = \ln B$ the uniqueness condition (4) reduces to

$$\ln B - 1 < \ln B_0 \tag{5a}$$

or

$$B < eB_0 \tag{5b}$$

where e is the exponential constant. Equation (5b) indicates that only those points which have $B < eB_0$ in the image will be biased towards B_0 whereas the others will not. In other words this means that the *a priori* known model distribution should not be too different from the observed distribution. This is quite an undesirable requirement of the entropy function ln B. On many occasions when the prior model is not available, a choice of uniform B_0 will violate condition (5b) at many locations in the image and one will not get a good reconstruction. The relative entropy using f(B) = ln B can be made to work by choosing a prior model which satisfies Equation (5b) but has features of required B_0. The model image B_0 can then slowly be modified towards the required B_0 as the iteration progresses. One of the simplest schemes is to add a suitable constant to the image as well as to the required prior model such that Equation (5b) is satisfied at all points of the image. As the iteration progresses the value of the constant is gradually reduced and ultimately a reconstructed image is obtained which is closest to the required prior model.

So, it appears that $f = \ln B$ can be a correct choice (although with little modifications) to define the relative entropy as in Equation (2).

Other well-known function $-B \ln B$ when substituted in Equation (2) gives two solutions namely $B = e^{-1}$ and $B = B_0$. Since both solutions could very well be acceptable, the uniqueness criterion is not fulfilled and therefore $f(B) = -B \ln$ B is not a correct function to define a relative entropy of kind given by Equation (2). It should be noted that in the case of $f(B) = \ln$ B, although mathematically there are two solutions (*i*.e., at $B = B_0$ and $B = \infty$), for all practical purposes there is only one solution at $B = B_0$. Solution $B = \infty$ is automatically discarded since no observational data would support it.

Another entropy function is a power-law function of kind $f(B) = B^s$, where s is a suitable power-law index. For this function the uniqueness condition (4) can be

written as

$$B_0/B > \left(\frac{2S-1}{S-1}\right)^{1/s}. \tag{6}$$

This function also gives one solution at $B = B_0$ regardless of the choice of s. However, one may get an additional solution at $B = 0$ or $B = \infty$ depending upon the value of s. If we choose the power-law index s such that the second solution lies at $B = \infty$, for all practical purposes the function has single solution at $B = B_0$. This, in other words, puts a condition on s to be less than unity. Further, to satisfy the condition given by Equation (6) for all positive values of B, the point at which the second derivative of $F(B, B_0)$ with respect to B is zero, should be pushed to infinity giving s = 1/2. These arguments clearly indicate that the relative entropy defined by Equation (2) using $f(B) = B^{1/2}$ is always concave for any positive value of B and therefore, always biases the solution toward $B = B_0$. It appears that this form of relative entropy should be as good as the one obtained from information-theoretic arguments (Shore & Johnson 1980; Gull & Skilling 1983). This point should be verified by actually reconstructing images with two types of entropy functions.

3. Minimum relative entropy method

We are given a set of measured visibility points $\rho(u_j, v_j)$; $j = -K$ to K and an *a priori* known model distribution B_0. We want to estimate the unmeasured visibility coefficients such that the measurements are unchanged and the relative entropy integral given by Equation (2) is minimized. The measured visibility coefficients are related to the true brightness distribution $B_{\text{true}}(x, y)$ through a Fourier-transform relationship, *i.e.,*

$$\rho(u_j, v_j) = \iint_{\text{field}} B_{\text{true}}(x, y)\exp[2\pi i(u_j x + v_j y)]\,dx\,dy, \qquad j = -K \text{ to } K \tag{7}$$

and the observed image

$$B(x, y) = \sum \rho(u_j, v_j)\exp[-2\pi i(u_j x + v_j y)] \qquad j = -K \text{ to } K. \tag{8}$$

Substituting Equation (8) in (2) and differentiating with respect to the unmeasured visibility coefficients $\rho(u_j, v_j)$ we get the gradient of the entropy with respect to the unmeasured visibility coefficients as

$$g(u_j, v_j) = \frac{\partial E_r}{\partial \rho(u_j, v_j)} = \iint [f(B) - f(B_0)]\frac{\partial f}{\partial B}\exp[-2\pi i(u_j x + v_j y)]\,dx\,dy. \tag{9}$$

Knowing the gradient of the entropy through a Fourier transform, the conjugate gradient method can be implemented quite easily as has been done in the past (Shevgaonkar 1986a, b; Nityananda & Narayan 1982). However, the choice of model distribution has to be made before we proceed for gradient computation.

Simple considerations tell us that at least the integrated power of the model distribution should be equal to that of the observed image. Also, if we do not have any *a priori* knowledge about the distribution, an obvious choice would be to distribute the total power uniformly over the entire field of view (see also Cornwell & Evans 1985).

One can also use a lowresolution image of the brightness distribution as a biasing model. However, it should be mentioned that none of these choices work satisfactorily for estimating the visibilities over short baselines and one has to provide a model which is neither present in the data nor present in the built-in nature of the MEM.

In the simulations presented here it is assumed that some *a priori* information is available only for the part of the sources in the field of view. First, a model distribution is generated for the partially known sources. The integrated power in the generated distribution $\rho_0(0, 0)$ is computed. The difference between the actually measured integrated power $\rho(0, 0)$ and $\rho_0(0, 0)$ is then uniformly distributed over the field of view of the model map.

Since entropy can be defined only for positive images, during initial stages of iterations, when there are large negative bowls, the entropy of the image becomes imaginary. For computational convenience a constant intensity is temporarily added to all pixels of the image such that the image becomes positive definite. This operation is called the FLOA Ting of the image and it has been discussed and used successfully in the past (see Nityananda & Narayan 1982; Shevgaonkar 1986a, b). The value of the floating constant decides (although not very crucially) the degree of nonlinearity in the reconstruction.

It is obvious that the floating of the image in turn modifies the integrated power or the zero-lag visibility coefficient temporarily. As the integrated power of the image is modified the integrated power of the model image should also be changed accordingly. To equate the integrated power of the model image to that of the brightness distribution, the same floating constant is added to the model map also. Apart from this floating, the maps have to be further floated to satisfy the condition given by Equation (5) if ln B function is used to define the relative entropy.

As an example we have taken an extended source (Fig. 1) as the true image. If this source is observed with a *uv*-coverage as in Fig. 2 one obtains the observed image as in

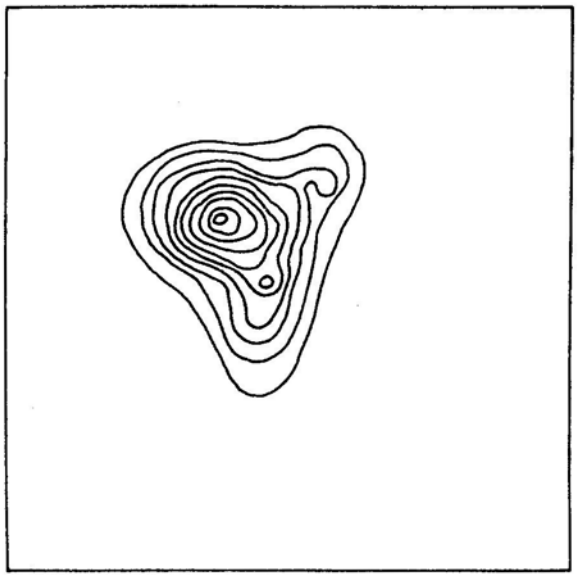

Figure 1. True image of an extended brightness distribution. Contour interval = 13.8 units.

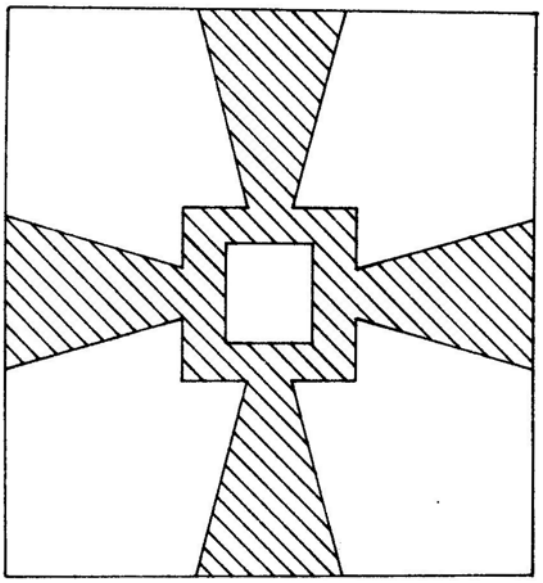

Figure 2. Simulated *uv*-coverage. Visibilities have been sampled in the hatched region. In the empty region the visibility coefficients are completely unknown. The origin of the *uv*-coverage or the integrated power of the distribution has also been measured.

Fig. 3. One should note that apart from the four missing sectors in the *uv*-plane the measurements leave a big hole around the center of the *uv*-coverage. From Fig. 3. it can be seen clearly that due to missing short baselines the map has a large negative bowl around the true position of the source. Just to emphasize the inadequacy of the existing MEM or use of relative entropy with flat model for estimating short baselines, the MEM with a uniform B_0 has been tried on the observed image. The reconstructed image has been shown in Fig. 4. It is clear that the MEM without a prior model or a flat default image could not give a faithful reconstruction.

Minimum-relative entropy method using relative entropy function $F\ (B,\ B_0) = (\ln B - \ln B_0)^2$ has been tried on the image shown in Fig. 3 and found to give quite satisfactory results. A simple circular Gaussian source (Fig. 5) is chosen as a model image. It should be noted that the model distribution does not have any direct similarity to the true source except that it tells that the source is of extended nature. The size of the gaussian is roughly decided by the expected source dimension and the height of the gaussian is decided by the equality of the total integrated powers in the model and the observed distribution. The reconstructed image as shown in Fig. 6 is a remarkable improvement over the image obtained by simple MEM (Fig. 4). The stability of the reconstruction against the choice of the model is tested by choosing model gaussian sources of different sizes and intensities located at slightly shifted locations. The reconstruction seems to be fairly stable against the choice of the initial model. However, following scheme may be useful in deciding the first-order biasing model.

As we have already mentioned in the introduction, our main objective is to reconstruct those distributions which are responsible for the large negative bowls in the

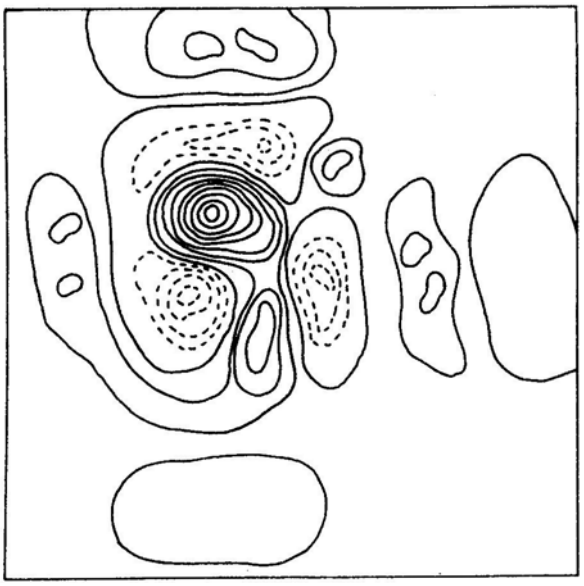

Figure 3. Image mapped by the *uv*-coverage in Fig. 2. Contour interval = 5.9 units.

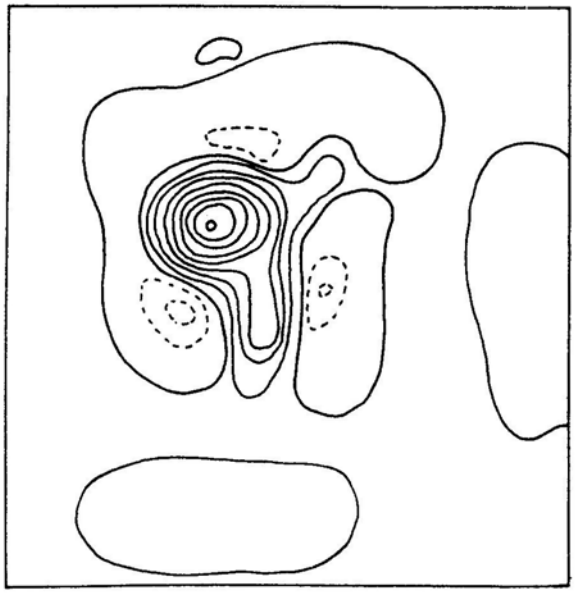

Figure 4. MEM reconstructed image after 30 iterations. Entropy function is ln *B*. Contour interval = 7.9 units.

image. It can be seen easily that the partly missing largescale structure should have a size which is larger than the inner rim and smaller than the outer rim of the negative bowl. Therefore, a first-order prior model can be taken as a gaussian distribution of width equal to the mean diameter of the negative bowl. As the reconstruction progresses and

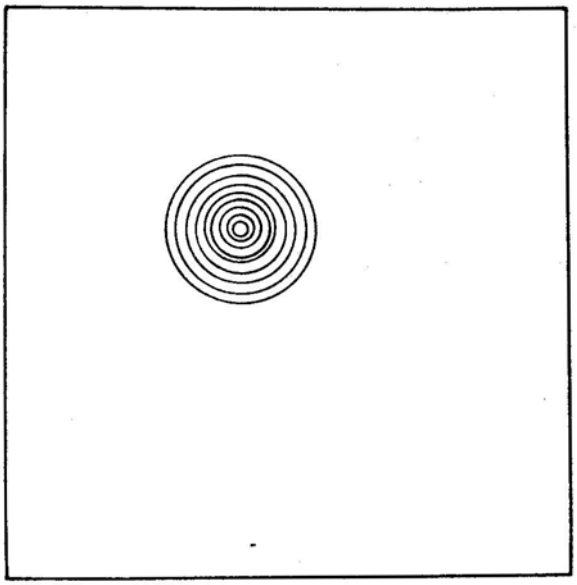

Figure 5. A circular gaussian source used as a default image to define the relative entropy. Contour interval = 16.8 units.

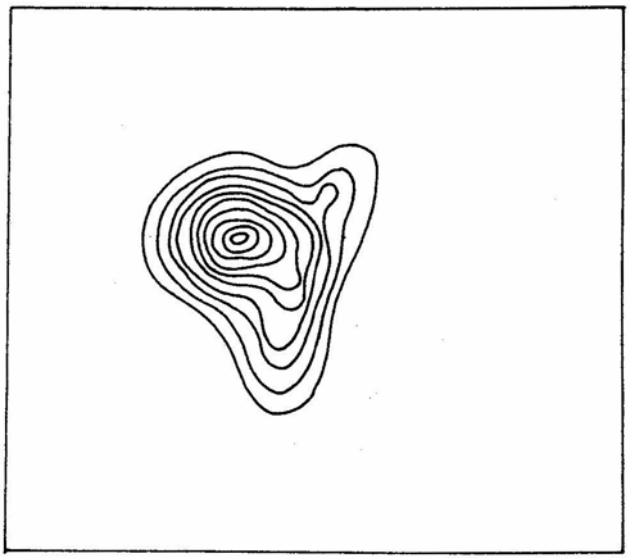

Figure 6. MREM reconstructed image after 20 iterations. Relative entropy function is $(\ln B - \ln B_0)^2$. Contour interval = 12.6 units.

the missing largescale structures are more clearly visible, the default image should subsequently be modified.

Other relative entropies $B \ln (B/B_0)$ and $(B^{1/2} - B_0^{1/2})^2$ have also been tried and found to provide reconstruction of the same quality as per our expectation. A comparison of the three relative-entropy functions is given in the next section.

4. Minimum-relative entropy method for polarized emission

The maximum entropy method has been formulated and successfully applied to the polarization images (Ponsonby 1973; Nityananda & Narayan 1983; Shevgaonkar 1986b). It has been shown that although the *a priori* positivity constraint is applied only to the total-intensity image, the polarized component images also get reconstructed remarkably well. Here we seek a possibility of successful application of the minimum-relative-entropy method to polarization images. We will confine our formulation to three relative entropy functions, namely $B \ln (B/B_0)$, $(\ln B - \ln B_0)^2$ and $(B^{1/2} - B_0^{1/2})^2$.

A partially polarized brightness distribution $\underline{B}$ can be elegantly represented by the Stokes parameters I, Q, U and V. Parameter I represents the total intensity, Q and U together represent linear polarization, and V represents the circular polarization. These Stokes parameters are related to the visibility functions ρ^I, ρ^Q, ρ^U and ρ^V through Fourier-transform relationship similar to that given by Equations (7) and (8). Following previous authors (Ponsonby 1973; Nityananda & Narayan 1983; Gull & Skilling 1984; Shevgaonkar 1986b) the entropy of an arbitrary polarized distribution is equal to the sum of the entropies of the two orthogonal polarization components λ_1 and λ_2 of the polarized image. It is shown in the past (Ponsonby 1973) that the two orthogonally polarized components λ_1 and λ_2 are equal to $I(1 + d)/2$ and $I(1 - d)/2$ respectively. Here d is the degree of polarization and is defined as

$$d = (Q^2 + U^2 + V^2)^{1/2}/I. \tag{10}$$

Now if $F(B, B_0)$ is the relative entropy function, where B is the image and B_0 is the biasing model, the relative entropy of a polarized brightness distribution $\underline{B}$ with respect to the prior model $\underline{B}_0$ can be written as

$$E_{\mathrm{rp}} = \iint F(\underline{B}, \underline{B}_0)\, \mathrm{d}x\, \mathrm{d}y = \iint [F(\lambda_1, \lambda_{10}) + F(\lambda_2, \lambda_{20}]\, \mathrm{d}x\, \mathrm{d}y. \tag{11}$$

Suffix 0 indicates the corresponding value for the model distribution. Differentiating Equation (11) with respect to the unmeasured visibility coefficients ρ^k (u_j^k, v_j^k) $(k = I, Q, U, V)$ we get the gradient of the entropy as

$$g^k(u_j^k, v_j^k) = \frac{\partial E_{\mathrm{rp}}}{\partial \rho^k(u_j^k, v_j^k)} = \mathrm{FT}\left[\frac{\partial F(\underline{B}, \underline{B}_0)}{\partial k}\right]. \tag{12}$$

Therefore, for computation of the entropy gradient we require derivatives of $F(B, B_0)$ with respect to the four Stokes parameters. The term inside the bracket in Equation (12) can be split into two parts as

$$\frac{\partial F(\underline{B}, \underline{B}_0)}{\partial k} = \frac{\partial F(\lambda_1, \lambda_{10})}{\partial k} + \frac{\partial F(\lambda_2, \lambda_{20})}{\partial k}. \tag{13}$$

Equation (13) can be re-written for different Stokes parameters as

$$\frac{\partial F(\underline{B}, \underline{B}_0)}{\partial I} = \frac{\partial F(\lambda_1, \lambda_{10})}{\partial \lambda_1} + \frac{\partial F(\lambda_2, \lambda_{20})}{\partial \lambda_2} \tag{14a}$$

and

$$\frac{\partial F(\underline{B}, \underline{B}_0)}{\partial (Q, U, V)} = \frac{(Q, U, V)}{\Sigma}\left[\frac{\partial F(\lambda_1, \lambda_{10})}{\partial \lambda_1} - \frac{\partial F(\lambda_2, \lambda_{20})}{\partial \lambda_2}\right], \tag{14b}$$

Where $\Sigma = Q^2 + U^2 + V^2)^{1/2} = Id$

Now, substituting for λ_1, λ_2, λ_{10}, λ_{20} and desired relative entropy function $F(\underline{B}, \underline{B}_0)$ in Equations (14a, b) we can obtain elegant expressions for $\delta F/\delta k$.

(i) For $F(\underline{B}, \underline{B}_0) = \underline{B} \ln (\underline{B}/\underline{B}_0)$ we get

$$\frac{\partial F}{\partial I} = 2 + \ln (D/D_0) \tag{15a}$$

and

$$\frac{\partial F}{\partial (Q, U, V)} = \frac{(Q, U, V)}{\Sigma} \ln(\chi/\chi_0) \tag{15b}$$

where $D \equiv I^2 - \Sigma^2 = I^2 - Q^2 - U^2 - V^2$ and $\chi \equiv (I + \Sigma)/(I - \Sigma)$, and suffix 0 indicates the corresponding value for the model distribution $\underline{B}_0$.

(ii) For $F(\underline{B}, \underline{B}_0) = (\ln \underline{B} - \ln \underline{B}_0)^2$ we get

$$\frac{\partial F}{\partial I} = \frac{I}{D}[\ln (D/D_0) - \mathrm{d} \ln (\chi/\chi_0)] \tag{16a}$$

and

$$\frac{\partial F}{\partial (Q, U, V)} = -\frac{(Q, U, V)}{D}\left[\ln (D/D_0) - \frac{1}{d} \ln (\chi/\chi_0)\right]. \tag{16b}$$

(iii) Finally, for $F(\underline{B}, \underline{B}_0) = (\underline{B}^{1/2} - \underline{B}_0^{1/2})^2$ we derive

$$\frac{\partial F}{\partial I} = -\frac{(I_0 - \Sigma_0)^{1/2}}{(I + \Sigma)^{1/2}} (\chi^{1/2} + \chi_0^{1/2}) \tag{17a}$$

and

$$\frac{\partial F}{\partial (Q, U, V)} = \frac{(I_0 - \Sigma_0)^{1/2}}{(I + \Sigma)^{1/2}} (\chi^{1/2} - \chi_0^{1/2}) \frac{(Q, U, V)}{\Sigma}. \tag{17b}$$

By Fourier transforming Equations (15a, b), (16a, b) or (17a, b), we can compute the entropy gradient $(g^k(u_j^k, v_j^k))$ with respect to the unmeasured visibility coefficients $\rho^k(u_j^k, v_j^k)$. Knowing the gradient of the entropy, a simple-gradient or conjugate-gradient method can be implemented easily (for details see Shevgaonkar 1986b) for minimizing the relative entropy. To test the algorithm let us take the total intensity (I) and circular polarization (V) maps of a solar active region at 6 cm wavelength (Fig. 7a, b) (Shevgaonkar & Kundu 1985) observed with the Very Large Array. To demonstrate the strength of the method we have assumed here that the measured *uv*-coverages are not identical for the two component images I and V. The total intensity map has a *uv*-coverage with four sectors and a central annular rectangle as shown in Fig. 2. We assume that the circular polarization measurement could be performed reliably only over the central annular rectangle, and for long baselines in the four sectors the polarization measurement is heavily affected by the instrumental errors and therefore it has been treated as unmeasured. It should be noted that the *uv*-coverages for both I and V have a large hole around the origin of the *uv*-plane. The synthesized beams corresponding to the two *uv*-coverages are convolved respectively with true total intensity and circular polarization maps (Fig. 7a, b) to get the observed dirty maps as shown in Fig. 8a, b.

Before we go to the minimization of relative entropy the choice of model polarized brightness distribution has to be made. A prior model for the intensity distribution could be obtained from other independent observations. However, the polarization

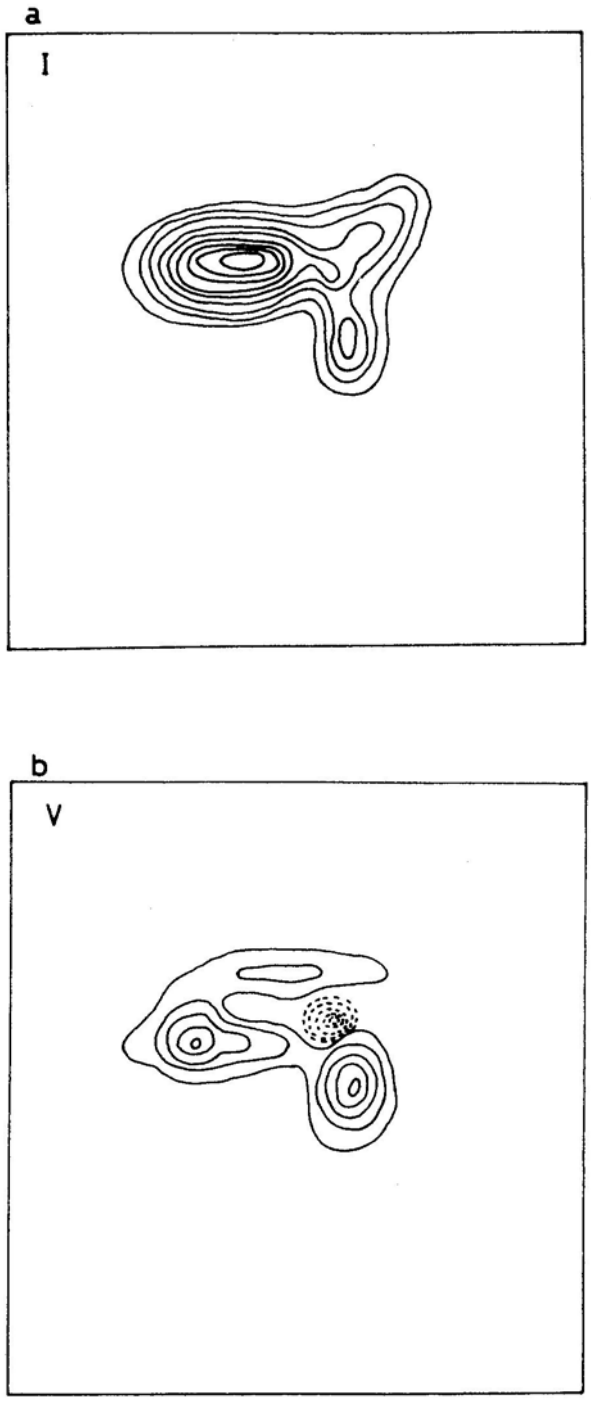

Figure 7. (a) True total intensity I and (b) circular polarization V images of a solar active region at 6 cm wavelength. Contour interval = 10.0 and 6.0 units respectively for I and V maps.

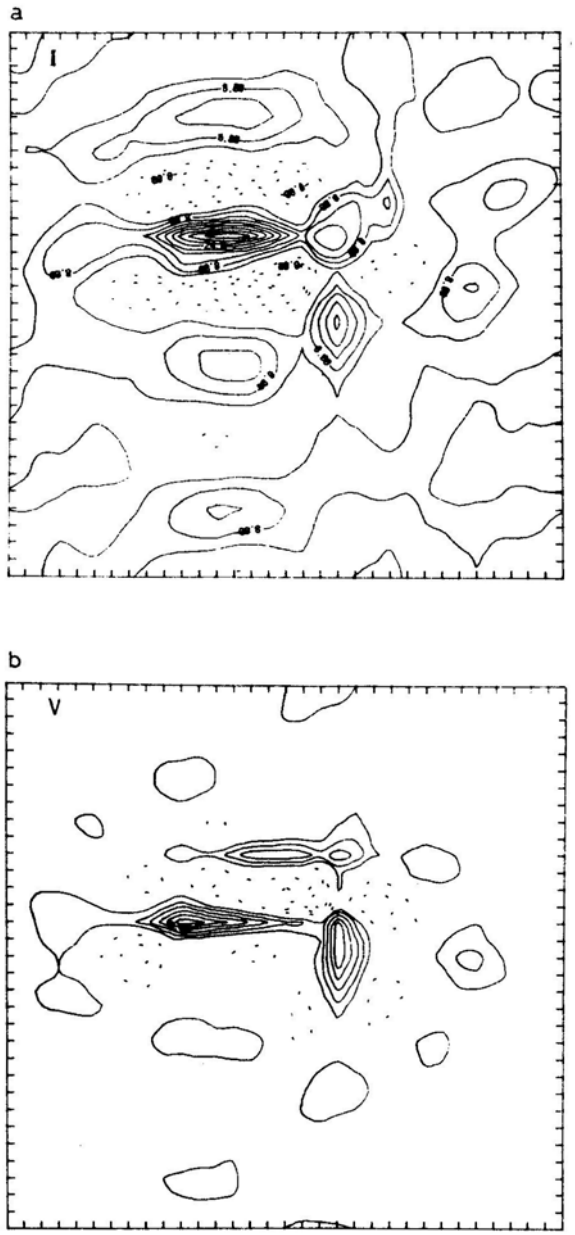

Figure 8. (a) Observed total intensity *I* and (b) circular polarization *V* maps.

model is not that readily available. To justify this statement let us take a concrete example.

Suppose we are observing a flaring event on the Sun. The event is visible over a wide range of frequencies *i.e.*, from X-rays to the radio. The radio data is capable of showing polarization whereas the optical or X-ray emission does not contain any information regarding the polarization. One can use the X-ray or optical image as a model for total

intensity image but the polarized emission is still unmodelled. If we use one of the synthesizing elements to obtain zero-lag visibility coefficient, at most we can get the integrated power in each polarization component.

As discussed in Section 3, in the absence of any prior knowledge about the image, the integrated power in each polarization component should be distributed uniformly over the entire field of view. This could be a suitable scheme provided all the four Stokes parameters are assumed to have flat default images. However, if we take a non-uniform total-intensity model and a flat polarization model, it is quite likely, especially on the edges of the source, to encounter an awkward situation of having a degree of polarization greater than unity in the model distribution. We have found that the best way is to give the polarization model as a scaled version of the total-intensity model. The scaling constant is decided by the relative integrated powers in the polarization components and the total-intensity distribution.

A distribution as in Fig. 9 has been chosen as a default model to define the relative entropy. The reconstructions for three entropy functions after 20 iterations are shown in Figs 10–12. It is clear that all the three relative entropy functions give more or less identical reconstructions. The strength of the method is quite apparent from the choice of non-identical *uv*-coverages for different polarization components and from the selection of polarization model as a scaled version of the total-intensity model. From the variety of examples given above it is convincing that the relative-entropy functions which do not have their origin in the information theory are also capable of providing good image reconstruction.

5. Conclusion

In synthesis observations one commonly encounters situations where the short baselines are inadequately sampled .As a result, the extended distributions are poorly

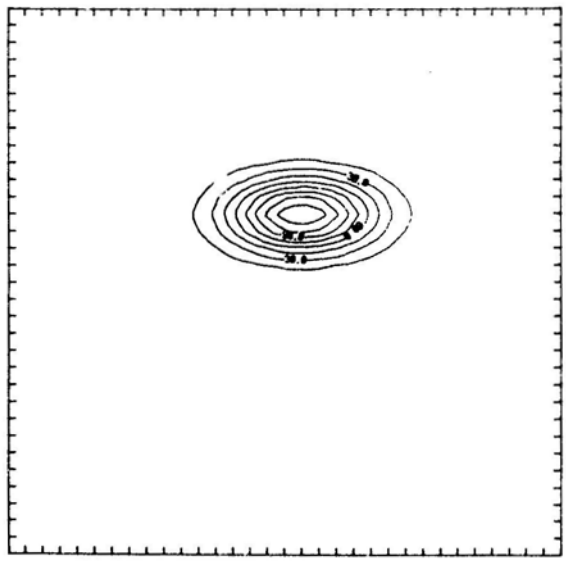

Figure 9. An elliptic gaussian source used as a default image to define the relative entropy. Contour interval =15.0 units.

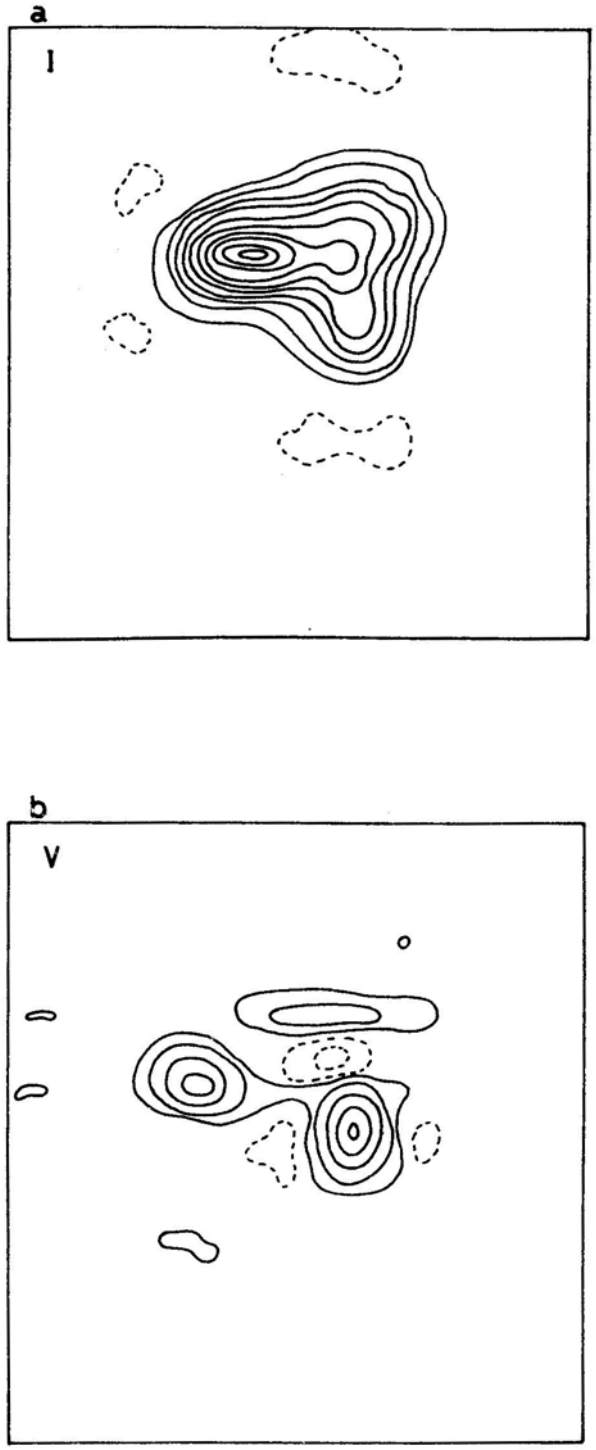

Figure 10. MREM reconstructed images after 20 iterations. Relative entropy function is $B \ln (B/B_0)$. Contour interval = 11.8 and 2.4 units for I and V maps respectively.

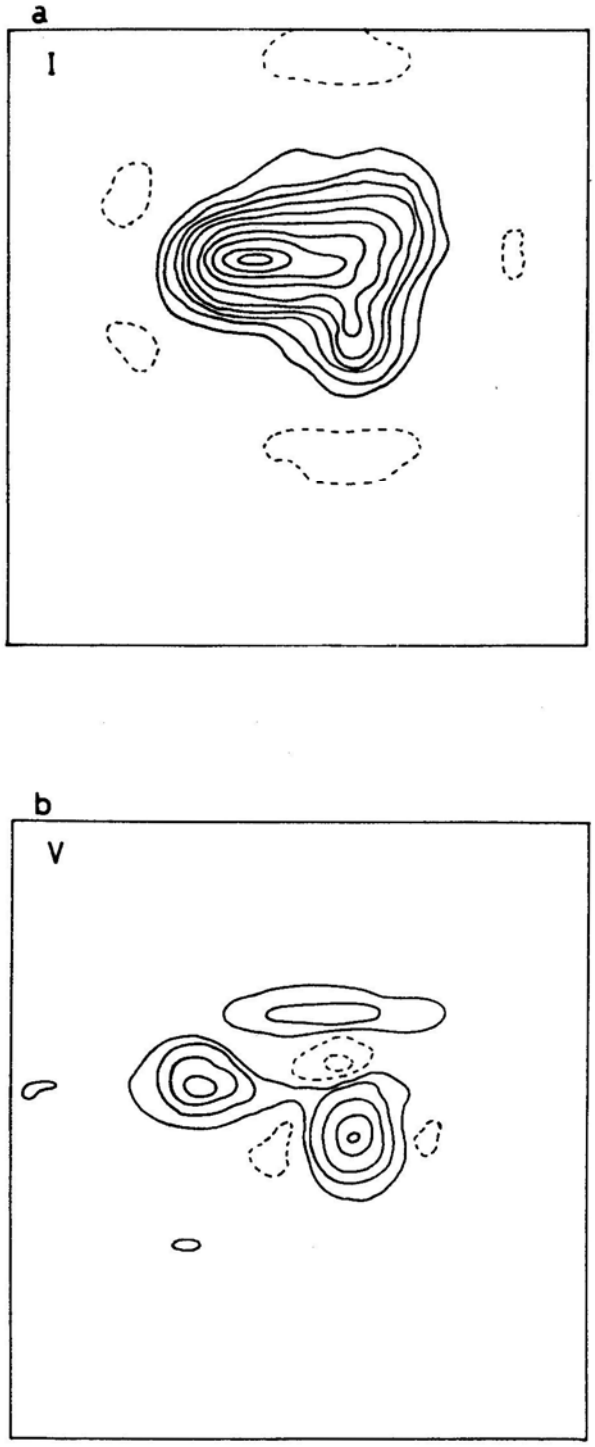

Figure 11. MREM reconstructed images after 20 iterations. Relative entropy function is $(B^{1/2} - B_0^{1/2})^2$. Contour interval = 11.8 and 2.4 units for I and V maps respectively.

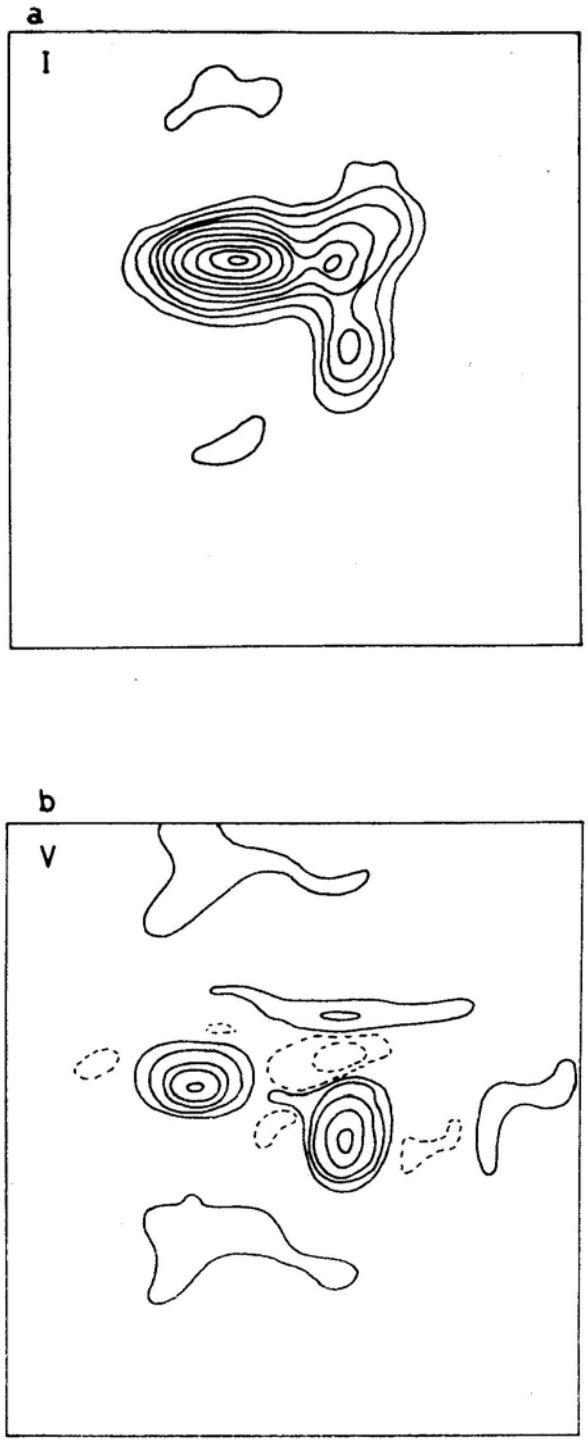

Figure 12. MREM reconstructed images after 20 iterations. Relative entropy function is $(\ln B - \ln B_0)^2$. Contour interval = 9.2 and 2.2 units for I and V maps respectively.

mapped. Minimum-relative-entropy method (MREM) has been presented as a possible scheme for reconstructing extended sources mapped with sparsely sampled short baselines. It is shown that as far as image reconstruction is concerned a measure of distance between the image and the prior model in the plane of pixel brightness is an adequate measure of relative entropy. The reconstructions obtained using this non-information-theoretic definition of the relative entropy have been compared with that obtained by minimizing the entropy B ln (B/B_0) which has a firm information-theoretic base. It has been argued that for estimation of the short baseline visibilities, a flat default image is not sufficient and one must provide a prior model which is neither present in the measurements nor in the inherent properties of the MEM.

The method has been generalized for partially polarized images. It is argued that in the absence of a prior model for the polarization components, one must choose a default image which has constant degree of polarization over the field of view. The potential of the method has been demonstrated by choosing non-identical *uv*-coverages for different polarization components.

Acknowledgements

I thank Raman Research Institute for providing excellent computing and other facilities.

References

Braun, R.,Walterbos, R.A.M. 1985, *Astr. Astrophys.,* **143**, 307.
Burg, J. P. 1975, PhD Thesis, Stanford Univ.
Cornwell, T. J., Evans, K. F.1985, *Astr. Astrophys.,* **143**, 77.
Ekers, R. D., Rots, A. H.1979, in *IAU Coll.* 49: *Image Formation from Coherence Function in Astronomy*, Ed. C. van Schooneveld, D. Reidel, Dordrecht, p. 61.
Gull, S. F., Daniell, G. J. 1978, *Nature,* **272**, 686.
Gull, S. F., Skilling, J. 1984, in *Indirect Imaging,* Ed. J. A. Roberts, Cambridge Univ. Press, p.267.
Hobson, A., Cheng, B. 1973, *J. Stat Phys.,* **7**, 301.
Högbom, J. A. 1974, *Astr. Astrophys. Suppl.,* **15**, 417.
Johnson, R. W. 1979, *IEEE Trans. Inf. Theory,* IT-25, 709.
Narayan, R., Nityananda, R.1984, in *Indirect Imaging,* Ed. J. A. Roberts, Cambridge Univ. Press p. 281.
Nityananda, R., Narayan, R. 1982, *J. Astrophys. Astr.,* **3,** 419.
Nityananda, R., Narayan, R. 1983, *Astr. Astrophys.,* **118**, 194.
Ponsonby, J. E. B. 1973, *Mon. Not. R. astr. Soc.,* **163**, 369.
Rots, A. H. 1979, in *IAU Coll.* 49: *Image Formation from Coherence Functions in Astronomy,* Ed. C. van Schooneveld, D. Reidel, Dordrecht, p. 55.
Schwarz, U. J.1978, *Astr. Astrophys.,* **65**, 345.
Shevgaonkar, R. K. 1986a, *Astr. Astrophys.*, **162**, 349.
Shevgaonkar, R. K. 1986b, *Astr. Astrophys.*, (in press).
Shevgaonkar, R. K., Kundu M. R.1985, *Astrophys. J.,* **292**, 733.
Shore, J. E., Johnson, R. W. 1980, *IEEE Trans. Inf. Theory,* IT-26, 26.

J. Astrophys.Astr. (1986) **7,** 293–298

Filamentary Structure in an Objectively-Derived Deep Galaxy Sample?

H. T. MacGillivray *Royal Observatory, Blackford Hill, Edinburgh EH9 3HJ, Scotland, UK*

R. J. Dodd *Carter Observatory, PO Box2909, Wellington, New Zealand*

Received 1986 February 25; accepted 1986 September 10

Abstract. The deep galaxy sample of MacGillivray & Dodd (1980), obtained from purely objective means, is investigated using the technique of Kuhn & Uson (1982) for the presence of structure of a filamentary nature. A variety of synthetic fields of galaxies (including both 'filament' and 'non-filament' models) generated by means of a computer simulation technique have also been studied for comparison purposes. No strong evidence for filamentary structure in the galaxy distribution is found for this deep sample.

Key words: galaxies, distribution

1. Introduction

Much controversy has surrounded, in recent years, the question of whether galaxies are distributed in space in a filamentary manner. Obviously, the outcome of such lines of enquiry holds important consequences for our understanding of physical processes present in the early Universe, and of the formation of galaxies in particular. It is now generally accepted that large scale agglomerations in the distribution of galaxies do exist (see *e.g.* Oort1984), and that there are large regions of space seemingly devoid of (or at least very deficient in) galaxies (*e.g.* Tarenghi *et al.* 1979; Kirshner *et al.* 1983; Parker *et al.* 1986). However, the picture of galaxies existing mainly in filaments or sheets (Einasto, Jõeveer & Saar 1980; Chincarini, Rood & Thompson 1981; Giovanelli & Haynes1982) is not yet secure Indeed, whilst individual instances of apparent filaments may be found to exist on the sky (Gregory, Thompson & Tifft 198.1; Parker 1986), this does not necessarily indicate that filamentary structure is a general phenomenon, nor that such filaments may not have arisen purely by accident. For example, the results of computer simulations have shown that many chance 'filaments' *do* occur (MacGillivray & Dodd 1982a, b). Clearly, the presence or absence of filamentary structure in the distribution of galaxies must be examined further to see if it *is* indeed a real, non-random phenomenon.

In an attempt to investigate the presence of filamentary structure in 2-D galaxy data, Kuhn & Uson (1982) developed a technique for searching for 'ridges' or filaments. This was applied, with apparent success, to a subset of the Lick galaxy catalogue (Shane &

Wirtanen 1967). Although it is not clear what subjective biases (if any) decided the choice of subset of the data used (which may have artificially enhanced the result), it is perfectly clear that any visual catalogue of galaxies suffers from severe subjective biases and these biases *do* have an effect on the results of statistical analyses (see ***e.g.*** Geller, de Lapparent & Kurtz 1984; de Lapparent, Kurtz & Geller1986).Ultimately, to avoid criticism due to the presence of subjective biases, analysis must be performed on catalogues obtained by purely objective means.

The COSMOS machine (MacGillivray & Stobie 1984) produces just such objective data. An objective sample of galaxies in a field of 15 square degrees of sky near the South Galactic Pole and containing galaxies done to $B \sim 22$ has already appeared in MacGillivray & Dodd (1980) and has been used for a large number of analyses (*e.g.* Hewett *et al.* 1981; MacGillivray & Dodd 1982a,b, 1984).In particular, the data have been studied by Fesenko (1982, 1984) and Guberman *et al.* (1983)in a search for evidence of filamentary or cellular structure. In the latter searches a negative result was obtained, and this was assumed by Guberman *et al.* (1983) as due to any filamentary structure present being completely swamped out by the sample containing objects over a wide range of distances. However, for consistency the technique of Kuhn & Uson (1982) ought to be carried out on the same data.

In the present paper, we present the results of applying the Kuhn and Uson technique to the MacGillivray & Dodd (1980) galaxy sample. Since the raw galaxy data are at our disposal, it is possible to reanalyse the data with different limiting magnitudes and with different spatial resolutions in order to examine the effects of such on the results. Comparison with synthetic fields of galaxies produced by means of a Monte-Carlo simulation technique will assist the interpretation of the results from the real data and also the assessment of the suitability of the Kuhn-Uson technique for detecting filamentary structure. In Section 2 we present a brief description of the procedural technique, while the results are presented in Section 3 and our conclusions discussed in Section 4.

2. The method

The Kuhn & Uson (1982) technique involves searching for 'ridges' or connected high-density points in the projected 2-D galaxy distribution, the latter being in the form of a 2-D array of galaxy density values. Full details of the procedure are given in the above paper, although a brief description is given here in. The technique involves the calculation of the quantity $\bar{\mu}$ which is the mean cosine of the direction between connected high-density array elements. One element in the array is initially chosen at random, and the 'ridge-finding' algorithm searches around this point (in the horizontal and vertical directions) until it finds the nearest element of highest density. This is then 'visited' next and the cosine of the angle of travel calculated. The procedure is repeated for the next nearest element of highest density and so on, except that elements which have already been visited are not revisited. The algorithm is allowed to continue until a suitable number of elements have been visited (in our case this was set at half the total number of non-zero elements) and the quantity μ calculated. This process is repeated 100 times (always selecting the starting array element at random) and the mean quantity $\langle\, \bar{\mu} \,\rangle$ calculated as is the standard error in the mean. In a 'random' (*i*.e. non-filament) situation, the expected value for this quantity is ~ 0.39. The presence of any detectable

linear features in the galaxy data should be observed as higher values for this quantity. A disadvantage of the method as applied by Kuhn & Uson is that since the ridge-seeking algorithm proceeds in the horizontal and vertical directions in the array, the technique will be more sensitive to filaments which are aligned in these directions. It is conceivable that, given the appropriate spatial resolution, filaments which are not thus aligned will fail to be detected. Application of the technique to include the diagonal directions results in a higher base level for the quantity $\langle \bar{\mu} \rangle$, *e.g.* $\langle \bar{\mu} \rangle \sim 0.59$ for the random situation.

3. Results

The results of applying the technique to the MacGillivray & Dodd galaxy sample are given in Table 1, where we tabulate the quantity $\langle \bar{\mu} \rangle$ and its standard error for a range of limiting magnitudes and 'bin' resolutions. One noticeable observation we can make from Table 1 is that the value $\langle \bar{\mu} \rangle$ systematically increases with decreasing resolution, being larger than 0.40 in 3 out of 4 cases of 10 arc min bins. However, the standard error is also larger, and with these standard errors the results cannot be taken as indicating an effect significantly different from the 'non-filament' situation of $\langle \bar{\mu} \rangle \sim 0.39$.

In Table 2 can be seen the results of applying the technique to various synthetic fields of galaxies. The simulation technique (based on a Monte-Carlo random-number process) for generating these synthetic fields has been described in detail elsewhere (MacGillivray & Dodd 1982a, b). Essentially, galaxies are generated in three dimensional (3-D) space according to a specified clustering description, are projected onto the plane of the sky and subsequently 'detected' by means of a process which attempts to emulate the atmosphere/telescope/photographic-plate/measuring-machine combination. The final data-set for each simulation is a catalogue of simulated galaxies. In the generation of this catalogue, all factors affecting the detection of these simulated galaxies and inclusion in the catalogue are applied in as close a manner as possible to the effects leading to the inclusion of galaxies in the catalogue of real data. Likewise, in the simulations, the angular field dimensions, limiting magnitude and total number of detected galaxies are identical to the observed data in order to make the subsequent analysis of the simulated galaxy data identical to the analysis of the real data. We used herein H_0 =75 km s^{-1} Mpc^{-1} , q_0 = + 1 and assumed no evolution of the galaxies in terms of luminosity, colour or distribution.

Table 1. The quantity $\langle \bar{\mu} \rangle$ and its standard error for the data of MacGillivray & Dodd (1980) tabulated as a function of limiting magnitude and resolution.

Limiting magnitude B	Resolution (arcmin)		
	5 × 5	7½ × 7½	10 × 10
22	0.387 ± 0.012	0.402 ± 0.016	0.414 ± 0.019
21	0.393 ± 0.012	0.393 ± 0.016	0.390 ± 0.018
20	0.380 ± 0.013	0.392 ± 0.017	0.401 ± 0.024
19.5	0.383 ± 0.015	0.401 ± 0.017	0.407 ± 0.022

Table 2. The quantity $\langle \bar{\mu} \rangle$ and its standard error tabulated as a function of limiting magnitude and resolution.

Limiting magnitude B	Resolution (arcmin) 5×5	$7\frac{1}{2} \times 7\frac{1}{2}$	10×10
(a) for a synthetic galaxy field consisting of randomly distributed clusters:			
22	0.392 ± 0.012	0.384 ± 0.015	0.408 ± 0.020
21	0.392 ± 0.010	0.381 ± 0.016	0.376 ± 0.027
20	0.389 ± 0.013	0.400 ± 0.018	0.419 ± 0.024
19.5	0.390 ± 0.013	0.381 ± 0.018	0.377 ± 0.024
(b) for a synthetic field consisting of clusters of galaxies clustered into superclusters:			
22	0.374 ± 0.011	0.375 ± 0.018	0.414 ± 0.028
21	0.390 ± 0.012	0.375 ± 0.018	0.385 ± 0.024
20	0.375 ± 0.013	0.365 ± 0.018	0.392 ± 0.023
19.5	0.387 ± 0.015	0.382 ± 0.017	0.404 ± 0.020
(c) for a synthetic field in which galaxies are distributed in long filaments:			
22	0.441 ± 0.018	0.459 ± 0.025	0.444 ± 0.034
21	0.424 ± 0.023	0.478 ± 0.036	0.461 ± 0.033
20	0.418 ± 0.021	0.474 ± 0.032	0.445 ± 0.046
19.5	0.405 ± 0.028	0.476 ± 0.050	$0.492 + 0.033$

For the purposes of the present paper, three different models were generated:

(a) clusters were generated at random in 3D space;
(b) clusters were themselves clustered into spherical 'superclusters' of size $10\ h^{-1}$ Mpc; and
(c) clusters were generated uniformly within 'filaments' (or prolate spheroids) with major axis of length $15\ h^{-1}$ Mpc and with axial ratio of 20:1. Furthermore, these filaments were allowed to have random orientations in 3D space.

The results of applying the Kuhn–Uson technique to each of the synthetic fields are shown in Table 2 for the above cases (a), (b) and (c). We see from Tables 2(a) and (b) that in both the randomly distributed cluster case and in the supercluster case, the results generally fluctuate about the value of 0.39 which is what we expect. Large values for the quantity $\langle \bar{\mu} \rangle$ are obtained for some situations of 10 arcmin resolution. However, to within their standard errors, the results are not different from the theoretically expected value, and there is no obvious correlation with limiting sample magnitude.

The results from the model involving the presence of filaments (Table 2c) *are,* however, more interesting. There are several points worthy of note in this table. Firstly, high values for the quantity $\langle \bar{\mu} \rangle$ (*i.e.* > 0.4) are consistently obtained for all sample depths (limiting magnitudes) and for all spatial resolutions. In general, the values are higher than the expected value of 0.39 by an amount which is greater than the standard error. It must be pointed out, however, that in these data the standard errors in the statistic $\langle \bar{\mu} \rangle$ are high, and the values in Table 2(c) do not represent a large deviation (in statistical terms) from the random case. We think that this is a problem of small sample size which should be improved in a study of a much larger area of sky. Secondly, the detection of the presence of filamentary structure is stronger for brighter sample limits

and for lower spatial resolutions, although nonrandom linear structure is still detected for faint sample limits and high resolution.

We conclude that the Kuhn & Uson technique is capable at least of indicating the presence of linear-type structures in the distribution of galaxies. Table 2(c) represents one particular example of a model involving filamentary structure. In actual fact, several such models were generated (each with a different amplitude for the filamentary structure) and the results studied. Obviously the detectability of filamentary structure depends upon the amplitude of that structure, the depth of the sample and the binning resolution. For example, the presence of features of low amplitude will be very difficult to detect at the best of times, and this task is made more difficult if such weak features are even further diluted by foreground and background contamination over a wide range of redshifts. Nonetheless, our extensive simulations have indicated that if filaments are a major characteristic of the distribution of galaxies (even when of a low-amplitude nature), then the Kuhn-Uson algorithm ought to reveal the presence of such. This is especially true for samples limited at bright magnitudes and with low spatial resolution for binning where, even for such low-amplitude linear features, the results generally reflect the trends shown in Table 2(c).

4. Conclusion

We have applied the technique of Kuhn & Uson (1982) to the galaxy sample of MacGillivray & Dodd (1980). The results indicate that, at least for this galaxy sample, the data do not provide strong confirmation of the presence of filamentary structure. In this respect, the results are in agreement with those of Fesenko (1982, 1984) and Guberman *et al.* (1983). Although large values for the statistic $\langle \bar{\mu} \rangle$ are obtained (especially when the resolution is low), the standard errors are large and the results are not different from the non-filament situation to within these standard errors. The results are not changed when analysis is restricted to the brighter galaxies where we might expect to investigate galaxies in a lower and more localized redshift interval, and hence wherein contamination due to galaxies in a large redshift range is reduced.

The comparison with Monte-Carlo simulations has proved valuable and has enabled an assessment to be made of the usefulness of the Kuhn-Uson technique. As expected, for non-filament models, the results revealed values for $\langle \bar{\mu} \rangle$ which were generally around the value of 0.39. Some higher values for this quantity were obtained but these were all within the associated standard errors. Simulations involving the presence of filamentary structure *do* indeed produce high values for $\langle \bar{\mu} \rangle$ æ, and these values are different from the expected 'random' value by an amount greater than the standard error. The exact values for $\langle \bar{\mu} \rangle$ for such models', and hence the detectability of filamentary structure, depends upon the amplitude of that structure, the depth of the galaxy sample and the resolution of the galaxy counts. However, the presence of even weak structures can still be detected by the technique, especially for samples limited at bright magnitudes.

In the light of the above, it is interesting to note that in the real sample of galaxies (Table 1), there is a slight tendency for high values of $\langle \bar{\mu} \rangle$ at bright magnitudes and low counting resolution. It is tempting to suggest that this is indicative of the presence of very weak linear structure. However, the results are not convincingly different from

the non-filament situation, and do not alter our conclusion concerning the lack of strong evidence for filamentary structure in these data.

Although the results herein are not encouraging for the objective verification of the existence of filamentary structure, it must be borne in mind that the sample of galaxies used is restricted to a small angle of sky and we may be looking at a region which (purely by chance) is deficient in filamentary structure. It is now necessary to repeat the analysis on a larger sample of galaxies covering a much larger area of sky, and this we intend to do on the catalogue of galaxies in the southern sky which is being carried out by the COSMOS machine (Collins *et al.* in preparation).

References

Chincarini, G., Rood, H. J., Thompson, L. A. 1981, *Astrophys. J.,* **249,** L47
de Lapparent, V., Kurtz, M. J., Geller, M. J. 1986, *Astrophys. J.,* **304,** 585
Einasto, J., Joeveer, M., Saar,E.1980, *Mon. Not. R. astr. Soc.,* **193,** 353.
Fesenko, B. I. 1982, *Pis'ma Astr. Zh.,* **8**, 458: *Soviet Astr. Lett.,* **8,** 247.
Fesenko, B. I. 1984, *Astrofizika,* **21,** 296: *Astrophys.,* **20,** 495.
Geller, M. J., de Lapparent, V., Kurtz, M. J. 1984, *Astrophys. J.,* **287,** L55.
Giovanelli, R., Haynes, M. P. 1982, *Astr. J.,* **87,** 1355.
Gregory, S. A., Thompson, L. A., Tifft, W. G. 1981, *Astrophys. J.,* **243,** 411.
Guberman, Sh. A., Doroshkevich, A. G., Kotok, E. V., Shandarin, S. F. 1983, *Astrofiz.,* **19,** 97: *Astrophys.,***19,**58.
Hewett, P. C., MacGillivray, H. T., Dodd, R. J. 1981, *Mon. Not. R. astr Soc.,* **195,** 613.
Kirshner, R. P., Oemler, A., Schechter, P. L., Schectman, S. A. 1983, *Astrophys. J.,* **248,** L57.
Kuhn, J. R., Uson, J. M. 1982, *Astrophys. J.,* **263,** L47.
MacGillivray, H. T., Dodd, R. J. 1980, *Mon. Not. R. astr. Soc.,* **193,** 1.
MacGillivray, H. T., Dodd, R. J. 1982a, in *IAU Symp.* 104: *Early Evolution of the Universe and its Present Structure,* Eds G. O. Abell & G. Chincarini, D. Reidel, Dordrecht, p. 401.
MacGillivray, H. T., Dodd, R. J. 1982b, *Astrophys. Space Sci.,* **86,** 437.
MacGillivray, H. T., Dodd, R. J. 1984, *Astrophys. Space Sci.,* **105,** 331.
MacGillivray, H. T., Stobie, R. S. 1984, *Vistas Astr.,* **27,** 433.
Oort, J. H. 1984, *A. Rev. Astr. Astrophys.,* **21,** 373.
Parker, Q. A. 1986, *PhD Thesis,* Univ. St Andrews.
Parker, Q. A., MacGillivray, H. T., Hill, P. W., Dodd, R. J. 1986, *Mon. Not. R. astr. Soc.,* in press.
Shane, C. D., Wirtanen, C. A. 1967, *Pub. Lick Obs.,* **22,** Part 1.
Tarenghi, M., Tifft, W. G., Chincarini, G., Rood, H. J., Thompson, L. A. 1979, *Astrophys. J.,* **234,** 793.

J. Astrophys. Astr. (1986) **7,** 299–304

The 59 s Periodicity of 2CG 195 + 4 (Geminga) and a Low-Mass Binary Model

D. A. Leahy *Department of Physics, The University of Calgary, Calgary, Alberta, Canada T2N 1N4*

S. V. Damle & S. Naranan *Tata Institute of Fundamental Research, Bombay 400005*

Received 1986 June 12; accepted 1986 September 10

Abstract. An examination of the existing period searches for 2CG195 + 4 leads to the conclusion that the 59 second periodicity is highly significant only for the 1981 March 17–18 detection of Bignami, Caraveo & Paul (1984). The statistical significance is increased substantially if the pulsation period is half the previously reported value. The period derivative is not well determined. Here we propose that 2CG 195 + 4 is a neutron star powered by accretion from a low ($\lesssim 1 M_{\odot}$) mass main-sequence companion. A distance of a few hundred pc would imply that the neutron star is a fast rotator and is spinning down.

Key words: accretion—gamma-ray sources—pulsation—X-ray sources

1. Introduction

The high energy γ-ray source 2CG 195 + 4 (Geminga) has recently attracted much attention. Bignami, Caraveo & Paul (1984, hereafter referred to as BCP) report an increasing 59 s period based on Einstein and Exosat soft X-ray observations. Zyskin & Mukanov (1983, hereafter referred to as ZM) give evidence for the 59 s period from observations of Cerenkov flashes from 10^{12} eV γ-rays. An optical counterpart (m_v = 21.3) has been reported (Caraveo *et al*. 1984; Sol et al. 1985). However, its association with Geminga has been questioned (Halpern, Grindlay & Tytler 1985) and two fainter (24.5 and 26 mag) candidates have been recently reported (Djorgovski & Kulkarni 1986). In this paper we discuss the 2CG 195 +4 period searches. Then we develop a low-mass binary accretion model consistent with the observations to date.

2. 2CG 195 + 4 period searches

Pulsation at high energy was first reported from SAS 2 data (Thompson *et al.* 1977), then from COS B data (Masnou *et al.* 1977). The latter was subsequently retracted (Masnou *et al.* 1981). Here we consider the recent results of ZM for photon energies greater than 10^{12} eV and of BCP for low energy X-rays (0.2 to 4 keV). The reported

detections are summarized in Table 1. The uncertainty in the period was not given by BCP. We quote for the period uncertainty, the spacing between statistically independent periods, $P^2/(2T_s)$, with T_s the timespan of the data set. The highest χ^2 value from the searches, all of which used epoch folding, is given in column 3, and the number of degrees of freedom (number of bins minus 1) in column 4. ZM used 10 degrees of freedom instead of the correct 18 (Buccheri *et al*. 1985 have previously pointed this out). P_1 is the probability using Pearson's χ^2 test, that a single trial will yield by chance (with no signal) a χ^2 value greater than the value in column 3. *N*is the number of trial periods and P_N is the probability that the χ^2 value of column 3 is exceeded by chance in N trials.

Applying the run test (Eadie *et al*. 1971) to the folded light curves yields chance probabilities of 0.51 (1981 Feb.6–8), 0.64(1981 March 17–18) and 0.41(1983 Sep. 9), for joint chance probabilities (= $p_1p_2[1 - \ln (p_1\, p_2)]$) of 0.14, 4.1×10^{-3} (4.5×10^{-2}), 0.05 (0.68) respectively, where the values in parantheses are for the 10^4 step searches Thus the confidence levels of March 17–18, 1981 detection is high, 95.5 to 99.6 per cent, whereas the confidence levels of the other four are low.

We note here that no epoch folding has been done at the statistically independent periods around 30 s (half the 60 s period) despite the appearance of a double peak separated by 5 bins in the 10-bin folded curve. A simple folding at 59.737/2 s and 60.056/2 s of the 1981 March 1718 and 1983 September 4 light curves in the 5 bins yields χ^2 values of 35.60 and 30.14; *i.e.* single-trial chance probabilities of 3.5×10^{-7} and 4.6×10^{-6} respectively. The associated increase in confidence level indicates the true period may be near 30 s.

For the light curves of ZM and BCP we find measured amplitudes $(n_{\max} - n_{\min})/(n_{\max} + n_{\min})$ of 0·36 ± 0·09 (1981 February 6–8)and 0.41 ± 0.07 (1981 March 17–18)and 0.38 ± 0.10 (1983 September 9). From the χ^2 values the expected amplitudes for a sine wave (*e.g.* see Equation (15) of Leahy *et al.* 1983) are 0.15, 0.20 and 0.21 respectively. These values are consistently less than the first set because of the large contribution of single bins to χ^2 in all the three observed light curves. One might take this to imply that the light curves cannot be dominated by a single harmonic. However, considering the high chance probabilities for all but the 1981 March detection, the high single bins are likely to be of statistical origin. The uncertainties in the period determination are less than the period changes between measurements. The SAS 2 and COS B periods give $\dot{P}/P \simeq 4 \times 10^{-11}$ s^{-1}, whereas the two ZM periods give $\dot{P}/P \simeq -5 \times 10^{-11}$ s^{-1} and the three BCP periods give $\dot{P}/P \simeq 8 \times 10^{-11}$ s^{-1}. The 1981 February 6–8 (ZM) and the 1981 March 17-18 (BCP) periods give $\dot{P}/P \simeq 3 \times 10^{-9}$ s^{-1}. One may accept at face value, a rapidly changing $\dot{P}/P$, but considering the complication of period Doppler shifts due to binary motion, one can still have a steady intrinsic $\dot{P}/P$. Furthermore, since only the March 1981 period, of all those above, has been detected with high confidence, we cannot rely on the above $\dot{P}/P$ values. So, the unknown intrinsic $\dot{P}/P$ is written as

$$\dot{P}/P = -\beta\,(5\times 10^{-11})\ \text{s}^{-1} \tag{1}$$

The alternatives of rapidly changing $\dot{P}$ or binary motion (or both) would rule out an isolated pulsar model for Geminga. This is consistent with the observed lack of radio emission and we will not consider the isolated pulsar alternative further. For a change in the observed periods due to binary motion we assume a circular orbit (radius a) and consider the 1981 February 6–8 and 1981 March 17– 18, periods. The $\Delta v \sim 2300$ km s^{-1} $< 2\ v_{\text{orb}}$ gives $a < 1.0 \times 10^{10}\ (M_1 + M_2)$ cm and $P < 540\ (M_1 + M_2)$ s with masses in solar units. However, the observation spans are approximately

Table 1. Statistical significance of detections of 59 s periodicity of 2CG 195 + 4.

Date (ref.)	Period (error)	χ^2	ν	P_1	N	P_N
1979 Jan. 29–Feb. 1 (ZM)	59.46 (.01)	33.6	18[b]	1.4×10^{-2}	200	0.94
1979 Sept. 29 (BCP)	59.466 (.05)	32.4	9	1.7×10^{-4}	400	0.066
1981 Feb. 6–8 (ZM)	59.28 (.01)	43.6	18	6.6×10^{-4}	100	0.064
1981 Mar. 17–18 (BCP)	59.737 (.064)	44.3	9	1.2×10^{-6}	600, 10^{4}[a]	7.4×10^{-4}, 1.2×10^{-2}[a]
1983 Sept. 9 (BCP)	60.056 (.05)	34.7	9	6.7×10^{-5}	300, 10^{4}[a]	2.0×10^{-2}, 0.49[a]

[a] Separate values for two searches.
[b] It is assumed $\nu = 18$ as in 1981 Feb. 6–8 (ZM). In the latter, ν is quoted erroneously by ZM as 10, the correct value being 18 (Buccheri *et al.* 1985).

10^5 s, so averaging over an orbit should occur except at long periods. Orbital periods greater than 10^5 s require $M_1 + M_2 > 200\ M_\odot$, at variance with optical observations unless one of the objects is a massive black hole. In this case the low-mass object would be the source of both the X and γ-ray radiation to give the large Doppler shifts.

3. Low-mass accretion binary model

The ratio of X-ray flux (0.2 to 4 keV) to y-ray flux (> 100 MeV), L_X / L_γ is 10^{-3}. This suggests that X-rays may be due to reprocessing of γ-rays on the surface of a companion to the γ-ray source (as suggested by BCP).Then using the best period data and ignoring $\dot{P}$ over the one month interval in 1981, we find a binary period (= beat period) of 7700 ± 1200 s. Kepler's law gives

$$a = (M_1 + M_2)^{1/3}\,(5.9 \pm 0.6) \times 10^{10}\ \mathrm{cm} \tag{2}$$

and for a circular orbit, the velocity of M_1

$$V_1 = 490\,(M_1 + M_2)^{-2/3} M_2\ \mathrm{km\,s^{-1}}. \tag{3}$$

Fig. 3b of BCP allows an upper limit to be placed on V_1 of 370 km s^{-1}. This is obtained by noting that the peak in χ^2 versus period has a width of 0.15 s which is similar to the predicted value P^2/T_s with T_s the timespan of the observation. For a γ-ray source mass (M_2) of 1.4 $M_\odot$ (*i.e.* a neutron star), we find $M_1 > 1.1\ M_\odot$ and a > 8 × 10^{10} cm. For M_2 as low as 1.0 $M_\odot$ one has $M_1 > 0.51\ M_\odot$ and a > 6.7 × 10^{10} cm.

Here we note that the binary model predicts that the values of period derivative for the neutron star γ-rays and reprocessed companion X-rays will be almost the same, differing only slightly due to orbital period derivative. Then the negative γ-ray period derivative of ZM is in conflict with the positive X-ray period derivative of BCP. The low statistical reliability of the period derivatives is the likely cause of the conflict and is the reason for writing (Equation 1) with the parameter β.

The 1 solar mass companion is consistent with the optical observations of the 21.3 mag candidate for a solar type star (G0) if the distance is 2.9 kpc. For a companion of 0.5 $M_\odot$, the distance estimate is reduced to 700 pc. The Roche lobe is > 3 × 10^{10} cm, consistent with accretion onto a neutron star from an accretion disc. The accretion disc model of Ghosh & Lamb (1979) gives

$$\dot{P}/P = -6.1 \times 10^{-11}\, n(\omega_s)\, \mu_{30}^{2/7}\, (P/60\ \mathrm{s})\, L_{37}^{6/7}. \tag{4}$$

Here $n(\omega_s)$ is the dimensionless torque, ω_3 is the fastness parameter, μ_{30} is the magnetic moment in gauss cm^3 and L_{37} is the accretion luminosity in units of 10^{37} erg s^{-1}. The accretion luminosity is related to the γ-ray luminosity L_γ by the γ-ray production efficiency α:

$$L_{37} \times 10^{37}\ \mathrm{erg\,s^{-1}} = \alpha^{-1} L_\gamma = 1.9 \times 10^{35}\, d_1^2\, \alpha^{-1}\ \mathrm{erg\,s^{-1}} \tag{5}$$

where d_1 is the distance in kpc. The fastness parameter ω_s depends on the mass, period, magnetic moment and mass accretion rate of the neutron star. Taking a 1.4 $M_\odot$ mass, 60 s period and the mass accretion rate required to produce the accretion luminosity, the fastness parameter is expressed as

$$\omega_s = 0.115\, \alpha^{3/7} d_1^{-6/7}\, \mu_{30}^{6/7}. \tag{6}$$

There are six parameters n, ω_s, μ_{30}, L_{37}, d_1 and α (assuming β is determined by the observations) but only four equations (4), (5), (6) and the n (ω_s) relation. Only limited restrictions on the parameters can be obtained in applying the model to 2CG 195 + 4. A rotating accreting neutron star is either a slow rotator ($n(\omega_s) > 0$) or a fast rotator ($n(\omega_s) < 0$), with $0 < \omega_s < 1$. Eliminatig L_{37} and μ_{30} from Equations (4), (5) and (6), we obtain for $P = 60$ s,

$$n(\omega_s) \cdot \omega_s^{1/3} = 11.7 \alpha\beta/d_1^2. \tag{7}$$

In the slow rotator case (low ω_s), $0 \leqslant n \leqslant 1.39$ and Equation (7) requires $\beta > 0$ and d_1 of the order of kpc or more. Taking $\beta = 1$ (the ZM period derivative) yields $d_1 = 5.4\ (1.39/n)^{7/12}\ \mu_{30}^{-1/6}\ \alpha^{1/2}$ kpc, with a weak dependence of distance on μ_{30}. If the values of μ_{30} and α are typical (1 and 0.1 respectively) then a distance of $\gtrsim 2$ kpc is implied in the slow rotator case. On the other hand, for the fast rotator case ($n < 0$), ω_s must be greater than 0.35 (Ghosh & Lamb 1979) which gives $d_1 < 0.27\ \alpha^{1/2}\ \mu_{30}$ kpc. For $\alpha = 0.1$, this gives an upper limit of 85 μ_{30} pc. For μ_{30} in the range 1 to 10, which is quite typical, a wide range of upper limits to distances (100–1000 pc) is allowed.

From the Einstein IPC data, Bignami, Caraveo & Lamb (1983) infer a low hydrogen column density ($N_H < 2 \times 10^{20}$ cm^{-2}) and an upper limit of 200 pc for the distance. It is well known that N_H towards the Crab nebula which is about 15° away from Geminga and at a distance of ~ 2 kpc, is 3×10^{21} cm^{-2} (Rappaport *et al*. 1969; Iyengar *et al*. 1975). However, it is interesting to observe that the contours of N_H in the solar neighbourhood, deduced from satellite ultraviolet observations (Frisch & York 1983) show a remarkable asymmetry with low neutral hydrogen densities in the quadrant $180° < l < 270°$. The contour corresponding to $N_H = 5 \times 10^{18}$ cm^{-2} corresponds to a distance > 200 pc in $180° < l < 270°$ whereas towards $l \sim 0$, it corresponds to distances < 15 pc. In the general direction of Geminga ($l = 195°$, $b = 4°$), N_H in the range of $(5–10) \times 10^{20}$ cm^{-2} is indicated up to a distance of ~ 1 kpc. Drastic change in N_H in two directions (Crab and Geminga) 15° apart is not unlikely. Further, the low N_H in the direction of Geminga is, in principle, not inconsistent with a ~ 1 kpc distance if the density of the hot component of the interstellar medium which has a filling factor of 0.7–0.8 is 0.003 cm^{-3} (McKee & Ostriker 1977). It is essential to probe the density of neutral hydrogen in the direction of the particular line of sight towards Geminga to obtain a good estimate of the distance.

If we assume however, a distance of about few hundred pc for Geminga, we can rule out the slow rotator model. Equation (7) along with the constraints $0 < \omega_s < 1$ and $n < 1.39$, for $d_1 = 0.2$ and $\alpha = 0.1$, would imply a large negative value of n. This corresponds to $\beta < 0$ (spin down) and ω_s very close to the maximum value of 1. This conclusion emerges directly from Equation (4) as follows: for low distance (few hundred pc) L_{37} is low and to account for the large $P/\dot{P}$, it is necessary to have a large $|n|$ which is possible only for $n < 0$. This makes $\omega_s \sim 1$, $\dot{P}/P > 0$ and hence $\beta < 0$ (Equation 1). It is believed that under such conditions unsteady accretion may occur (Ghosh & Lamb 1979).

Lastly, we consider the effects of having a pulse period of 30 s rather than 60 s. The binary (beat) period is then 3800 ± 600 s and the constants in Equations (2) and (3) are 2.1 (±0.2) × 10^{10} cm and 350 km s^{-1}. Since the expected width P^2/T_s of the χ^2 versus P curve is less, we may interpret the larger width of χ^2 versus P curve of BCP for the 1981 March 17–18 data as positive evidence for Doppler shifts. Then we obtain $M_1 \simeq 1 M_\odot$ for $M_2 = 1.4\ M_\odot$. The results of the accretion model are only changed slightly.

In conclusion, the period history of 2CG 195 + 4 is rather uncertain, partly due to the likely complication of binary Doppler shifts which have not been taken into account in the period analysis. Here we have pointed out the uncertainties and we have shown that a low-mass accretion binary at a distance of a few hundred pc, in which the neutron star is a fast rotator spinning down, is consistent with the current data. The separate question of the physical mechanism for generating the γ-ray emission has not been answered by any model yet. However, the high energy γ-ray source Cyg X-3 has a binary period of 4.8 hours similar to that proposed for 2CG 195 + 4.

Evidence presented here suggests the true pulse period is near 30 s. This should be further tested. The period analysis should be redone including binary motion to. determine if there is a positive or negative intrinsic P and to determine if $\dot{P}$ is changing. The determination of the period can be done more accurately by fitting the theoretical χ^2 versus P relation to the experimental data rather than picking the period with peak χ^2 (D. Leahy, in preparation). A repeat of the Čerenkov measurement would be valuable in determining the high energy behaviour. Finally, further optical observations will be valuable in verifying the nature of the companion and the distance to 2CG195 + 4.

Acknowledgment

For DL, support for this work was provided by the National Sciences and Engineering Research Council of Canada.

References

Bignami, G., Caraveo, P., Lamb, R.1983, *Astrophys. J. Lett.,* **272**, L9
Bignami, G., Caraveo, P., Paul, J. 1984, *Nature,* **310**, 464 (BCP).
Buccheri, R., D'Amico, N, Hermsen, W., Sacco, B. 1985, *Nature,* **316,** 131.
Caraveo, P., Bignami, G., Vigroux, L., Paul, J.1984, *Astrophys. J.*, **276**, L45.
Djorgovski, S., Kulkami, S. R. 1986, *Astr. J.*, **91**, 90.
Eadie, W., Drijard, D., James, F., Roos, M., Sadouet, B. 1971, *Statistical Methods* in Physics, North Holland, New York.
Frisch, P. C., York, D. G. 1983, *Astrophys. J.*, **271**, L59.
Ghosh, P., Lamb, F. 1979, *Astrophys. J.*, **234,** 296.
Halpern, J., Grindlay, J., Tytler, D. 1985, *Astrophys. J.*, **296**, 190.
Iyengar, V. S., Naranan, S., Sreekantan, B. V. 1975, *Astrophys. Space Sci.*, **32,** 431.
Leahy, D., Darbo, W., Eisner, R., Weisskopf, M., Sutherland, P., Kahn, S., Grindlay, J. 1983, *Astrophys. J.*, **266**, 160.
Masnou, J. L., Bennett, K., Bignami, G., Buccheri, R., Caraveo, P., D'Amico, N., Hermsen, W., Kanbach, G, Lichti, C. G., Mayer-Hasselwander, H. A., Paul, J. P., Swanenberg, B. N. 1977, In *Proc.* 12*th ESLAB Symp. Recent Advances in Gamma Ray Astronomy*, Ed. R. D. Wills & B. Battrick, p. 33.
Masnou, J. L., Bennett, K., Bignami, G. F., Bloemen, J. B. G. M., Buccheri, R., Caraveo, P. A., Hermsen, W., Kanbach, G, Mayer-Hasselwander, H. A., Paul, J. A., Wills, R. D. 1981, in *Proc*, 17*th Cosmic Ray Conf.* Paris, **1**, 177.
McKee, C., Ostriker, J.1977, *Astrophys. J.*, **218**, 148.
Rappaport, S., Bradt, H. V., Meyer, W. 1969, *Astrophys. J.*, **157**, L21.
Sol, H., Tarenghi, M., Vanderriest, C., Vigroux, L., Lelievre, G. 1965. *Astr. Astrophys.,* **144**,109.
Thompson, D., Fichtel, C., Hartman, R., Kniffen, D., Lamb, R. 1977, *Astrophys. J.*, **213**, 252.
Zyskin, Y., Mukanov, D.1983, *Soviet Astr. Lett.*, **9**, 117(ZM).

J. Astrophys. Astr. (1986) **7,** 305–316

A Spectrophotometric Study of the Wolf-Rayet Star HD 50896

B. S. Shylaja *Indian Institute of Astrophysics, Bangalore 560034*

Received 1986 May 9; accepted 1986 September 24

Abstract. New spectrophotometric observations of the Wolf-Rayet system HD 50896 are presented and interpreted in terms of its binary nature. The lines of N V, N IV and C IV show moderate variations, which can be explained using a binary model with a compact companion. He II λ4686 appears to arise from a larger region compared to other lines. The distortion caused by the wind can partly explain its flux variations. The emission fluxes of He I lines are generally constant indicating their non-participation in the orbit. The results are compared with other Wolf-Rayet binaries (V444 Cyg and CQ Cep) and the evolutionary status is discussed.

Key words: Stars, Wolf-Rayet—stars, binary, interacting—stars, individual

1. Introduction

HD 50896 (= EZ CMa, V = 6.94, WN5) is the sixth brightest star in the catalogue of Wolf-Rayet stars (van der Hucht *et al.* 1981). Spectral and light variability have been reported by many earlier investigators (Wilson 1948; Smith 1955; Ross 1961; Kuhi 1967). Night-to-night variations of He II λ4686 were reported by Smith (1968), Irvine & Irvine (1973) and Schmidt (1974), though none of these studies led to a positive conclusion on the binary nature. Serkowski (1970) reported strong Polarimetric variations which were confirmed by Mc Lean *et al.* (1979) and Mc Lean (1980). Small amplitude photometric variations of 3.76 d period were reported by Firmani *et al.* (1979) and confirmed by Cherepashchuk (1981), although the shapes of the light curves did not agree. The line profiles are found to vary over time scales of a few hours (Ebbets 1979; Firmani *et al.* 1980; Singh 1984). More recent precision photometry (Lamontagne, Moffat & Lamarre 1986) has revealed a complex (but stable) modulated light curve.

The most recent and detailed spectroscopic and photometric studies are due to Ebbets (1979), Firmani *et al.* (1980), Cherepashchuk (1981) and Lamontagne, Moffat & Lamarre (1986), who point to the binary nature of the system with a compact companion of mass about 1–2 $M_{\odot}$, although other mechanisms like nonradial pulsations and rotation were offered as possible but less likely explanations for the light and emission line behaviour. The binary model goes in tune with the evolutionary scheme of a WR binary in a post-X-ray-binary stage (van den Heuvel 1976; Tutukov & Yungelson 1979), and therefore makes it a particularly interesting system for study.

The study of emission lines offers an opportunity for understanding the envelope structure and its asymmetry caused by the presence of the companion. Spectrophotometric studies of CQ Cephei, a very close WN7 binary, showed that the emission-line flux variations are dependent on the stellar wind structure and Roche

surfaces modified to take into account the extended wind structure (Shylaja 1986a, Paper I). In the present analysis of HD 50896, a similar investigation is carried out with the aim of understanding the possible atmospheric stratification and the effect of the companion on it. Section 2 describes the observations and results. The flux variations and a possible model are discussed in Section 3. Section 4 compares the results with other known eclipsing binaries and discusses the evolutionary status.

2. Observations and results

The observations were obtained with the spectrum scanner (Bappu 1977) containing a 600 line mm^{-1} grating blazed at 7600 Å, at the Cassegrain focus of the 102 cm reflector of the Vainu Bappu Observatory, Kavalur, during 1983–85. A channel spacing of 5 Å, in the second order blue region ($\lambda\lambda$3800–4900) and of 10 Å in the first order green to red region (λ4800 to 7100) were employed. The entrance aperture was about 24 arcsec in diameter. An exit slot of 800 μm was used, corresponding to a resolution of 10 Å in the second order and 20 Å in the first order. The spectrophotometric standards taken from the lists of Hayes (1970) and Breger (1976) were observed every night to derive the extinction coefficients and for the determination of absolute flux.

Although HD 50896 is within the boundary of the open cluster Collinder 121, doubts have been expressed about its membership (*cf.* Firmani *et al.* 1980), because of the difference between the age of the cluster Cr 121 and of the other clusters known to contain WR stars. At the same time, the reddening of the stars in Cr 121 is small ($E(B-V) \sim 0.0$), not making it a distinctive feature of HD 50896 exclusively, for which it has been shown that the reddening corrections are small (Hillier 1984). Hence all the flux and magnitude measurements reported here, are not corrected for reddening. Fig. 1 shows sample scans at different orbital phases.

2.1 *Emission-Line Flux*

The flux of some emission lines of He I, He II, N IV, N V and C IV were measured from the scanner results. N III λ4640 flux was too weak to be measured. N V λ4603 merged with the other N v λ 4620. The type of profile variations of He II λ 4686 and N IV λ 4058 described by the previous investigators could be clearly seen on some occasions in spite of the lower resolution of only 10 Å. In the longer wavelength region, C IV λ5808–12 was generally stronger than He I λ5876, but only on some occasions was the latter stronger than the former. Some line blends at λ4200 and λ4540 were also measurable, although the individual contributors to these blends could not be resolved. The atlas of Smith & Kuhi (1981) was used as a guide to draw the line profiles. Figs 2 and 3 represent these flux variations.

Hillier (1984) discusses the influence of electron scattering on He II line profiles. Bappu (1973) had attributed the red wing of the He II (7-4) line at λ5410 to an unidentified transition, because this was not seen in the other members of the Pickering series. Hillier shows that this is due to electron scattering and the effect is apparent in other He II lines also. It was also noticed that these red wings can lead to erroneous continuum and line-flux measurements. To avoid this, only the relative line-flux ratios are compared (Table 1, Figs 2 and 3), to see the possible effect of binarity. He II λ4860

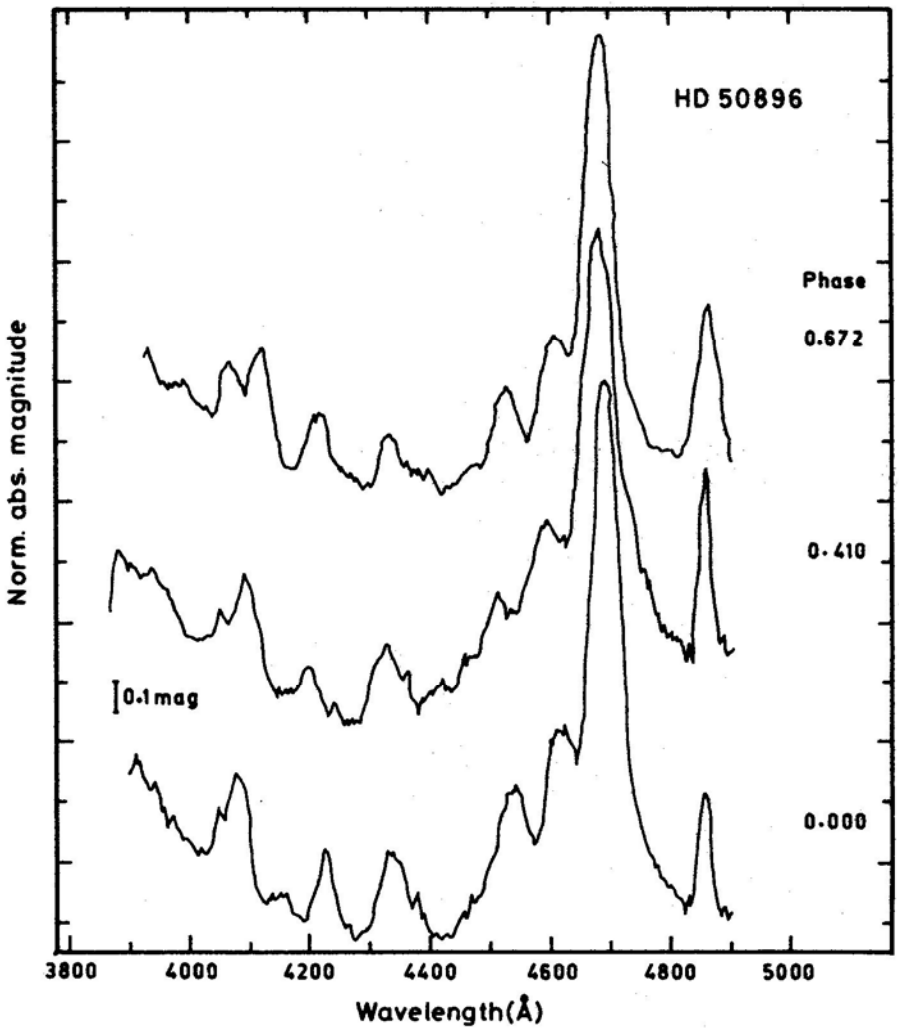

Figure 1. Sample scans of HD 50896 in the blue region. The derived absolute magnitudes are normalized to at 5000 Å.

was chosen for taking the flux ratios because it was generally covered on all occasions. The scatter of the flux of λ4860 (Fig. 2) may represent an intrinsic variation of flux for the system, which makes it difficult to isolate the variations caused by the binary nature.

3. Line flux variations and model

Many recent detailed spectroscopic investigations have established the reality of the time-dependent changes in line profiles. Although it was not possible to see the profile variations very clearly because of the low resolution in our scans, the phase dependent changes in flux are clearly seen. High dispersion spectra show the finer details of such changes (Firmani *et al*. 1980). Two peaks of the emission lines merge at

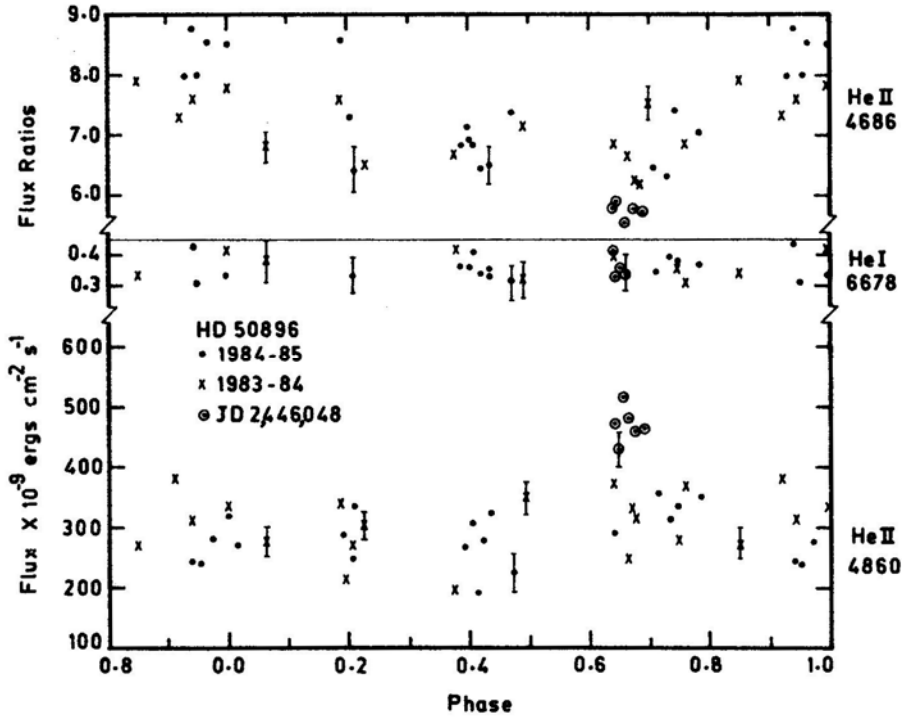

Figure 2. Flux variation of the He II lines λ4860 and the flux ratio for λ4686 and He I λ6678. Note the sudden change in flux at phase 0.68 and its absence for 4686 line. The zero phase is calculated at JD 2,445,752.279 and 2,446,072.146 separately for each season.

phase 0.5. N IV λ4058, which is considered to be very stable and deemed to represent the motion of the WN component in the narrow-lined WNL stars (Moffat & Seggewiss 1979), shows largescale profile variations in the broad lined WN5 star HD 50896 (Firmani *et al.* 1980). On the other hand, N IV λ3483 is very stable, although it is a blend of a number of multiplets. It may also be noticed that N V λ4603 does not undergo this kind of splitting and merging in profiles. The flux of this line shows a clear variation over the 3.763 d period. Hence the phase has been calculated using this as reference. The folding of the data was done separately for every season, choosing the minimum value of the λ 4603 flux to correspond to phase 0.0, similar to the definition of Firmani *et al.* (1980).

It is apparent from Fig. 2 that He II λ4860 shows a scatter around a mean value. Perhaps this scatter reflects the intrinsic variations. The other lines expressed as ratios relative to this line may be grouped into two catagories—those with no variations over the orbital period, and those with noticeable variations. He II $\lambda\lambda$5410, 6562 show insignificant changes implying variations similar to λ4860. The flux of N V λ4603 exhibits a relatively sharp dip, from which the zero phase was defined. N IV λ4058 and C IV λ5808 also show a similar dip, but of lower amplitude. It may be noticed that the flux of He II λ4686 behaves differently with a larger scatter and exhibits somewhat higher flux at phase $\sim$ 0.9. The line blends at $\lambda\lambda$4540 and 4200 have variations of flux ratio similar to the He II lines (Table 1), possibly because the main contributor is He II itself

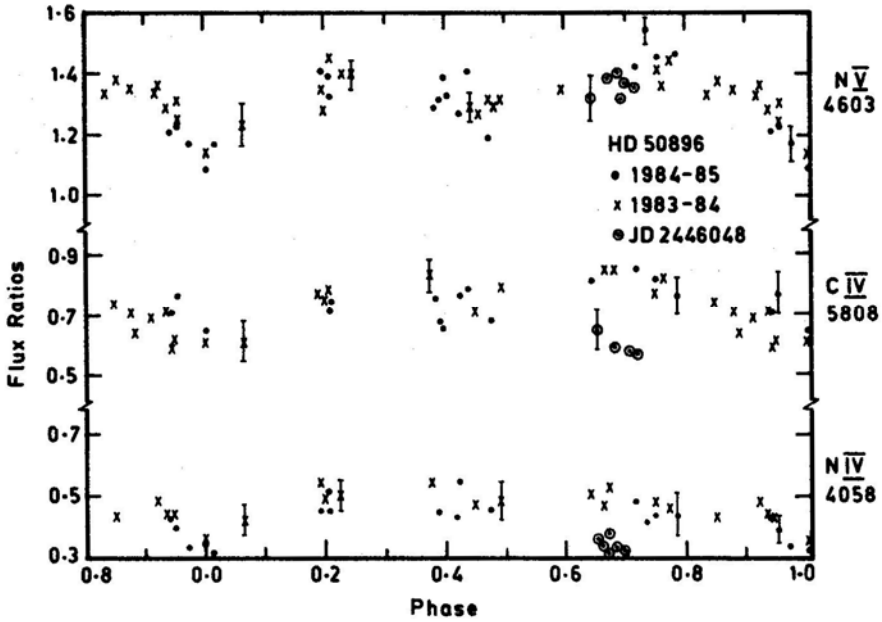

Figure 3. Flux variation of N V $\lambda\lambda$4603–20, N IV λ4058 and C IV λ5808. All are expressed as a ratio relative to 4860 line flux. Calculation of phases are same as described in Fig. 2.

As was seen in the case of CQ Cep (Paper I), if we were to assume that N V originates closest to the core, the reduction in flux at phase 0.0 can be immediately attributed to the possible eclipse effects. This requires the size of the companion to be large enough to partially cover the line-emitting region. However, the estimated mass from the mass function derived from the radial velocity curves is very small. This argument of the higher excitation lines originating closer to the photosphere holds for the line-emitting regions of the N IV and C IV also.

The observed scatter in the flux (*e.g.* λ4860) implies the presence of intrinsic variations. On the other hand, the existence of orbital effects is apparent in the variations of flux ratios, which agree with the period of 3.763 d. These facts lead to a model of asymmetric distribution of matter around the WR component exhibiting an intrinsic variation in addition to eclipse effects.

We may start with the model suggested by Firmani *et al.* (1980), which is based on precise radial velocity measurements. None of these radial velocity curves gives a circular orbit although the N V line gives a smaller value of *e.* The light curve also does not clarify this point. Therefore, we start with an eccentric orbit. The classical Roche surfaces have been found to be inapplicable in binaries with large wind velocities (Paper I). We see a single prominent minimum in λ4603 flux variation. (Firmani *et al.* (1980) have found an indication of a second minimum on one occasion, which is not very prominent in our results.) This restricts the sizes of the line emitting regions of N V, N IV and C IV closer to the WN component.

Although there is one spurious increase at phase $\sim$ 0.65 on one epoch, He II $\lambda\lambda$5410, 6562 and 4860 show no phase-dependent variation of total flux. The presence of only random variations implies that either the line-emitting regions are varying intrinsically

Table 1. Flux Ratios of HD 50896 relative to 4860A Line.

JD 2440000 +	Phase	N IV 4058	Blend 4100	Blend 4540	He II 4686	He II 5410	C IV 5810	He I 5876	He II 6562	He I 6678	N V 4620	He I 7065	He II 4860
5254.375	0.684	0.40	0.77	1.22	7.69	—	—	—	—	—	1.28	—	375.0
5254.401	0.691	—	—	—	—	1.59	0.76	1.15	1.76	0.31	—	2.31	351.0
5254.432	0.700	0.36	0.75	1.17	7.55	—	—	—	—	—	1.31	—	375.0
5330.204	0.835	0.39	0.84	1.15	6.88	—	—	—	—	—	1.33	—	345.0
5330.221	0.840	0.38	0.86	1.21	6.92	—	—	—	—	—	1.31	—	310.0
5330.234	0.843	0.40	0.75	1.31	7.12	—	—	—	—	—	1.29	—	335.0
5330.246	0.847	—	—	—	—	1.69	0.74	1.21	1.75	0.34	—	2.33	340.0
5330.259	0.850	0.43	0.78	1.10	7.92	—	—	—	—	—	1.38	—	308.0
5330.309	0.863	0.39	0.80	1.25	7.62	—	—	—	—	—	1.35	—	328.0
5330.321	0.867	0.36	0.86	1.15	7.42	—	—	—	—	—	1.40	—	345.0
5330.361	0.877	—	—	—	—	1.75	0.71	1.28	1.69	0.31	—	2.46	295.0
5330.374	0.881	0.34	0.82	1.11	7.37	—	—	—	—	—	1.35	—	309.0
5330.396	0.887	—	—	—	—	1.64	0.81	1.31	1.73	0.36	—	2.76	325.0
5370.141	0.449	—	—	—	—	1.69	0.81	1.35	1.62	0.29	—	2.65	305.0
5370.162	0.454	0.47	0.91	1.36	8.11	—	—	—	—	—	1.27	—	355.0
5370.175	0.458	0.45	0.88	1.29	8.07	—	—	—	—	—	1.25	—	347.0
5370.192	0.462	0.41	0.86	1.17	7.56	—	—	—	—	—	1.29	—	329.0
5370.236	0.474	0.44	0.85	1.22	7.92	—	—	—	—	—	1.31	—	336.0
5370.251	0.478	0.39	0.68	1.36	7.65	—	—	—	—	—	1.29	—	370.0
5370.271	0.483	0.45	0.71	1.28	7.55	—	—	—	—	—	1.31	—	365.0
5370.292	0.489	—	—	—	—	1.62	0.79	1.21	1.75	0.33	—	2.70	358.0
5370.307	0.493	0.49	0.82	1.32	7.12	—	—	—	—	—	1.33	—	349.0
5405.128	0.746	—	—	—	—	1.58	0.77	1.25	1.81	0.37	—	2.54	295.0
5405.140	0.750	0.48	0.95	1.36	7.53	—	—	—	—	—	1.41	—	289.0
5405.156	0.754	—	—	—	—	1.62	0.68	1.19	1.91	0.36	—	2.46	280.0
5405.167	0.757	0.47	0.87	1.22	7.89	1.81	0.59	1.06	—	—	1.36	—	265.0
5405.183	0.761	0.44	0.91	1.31	6.82	1.75	0.72	1.12	—	—	1.31	—	315.0
5405.197	0.765	—	—	—	—	1.66	0.75	1.20	1.88	0.31	—	2.59	368.0
5405.210	0.768	0.40	0.86	1.28	6.95	—	—	—	—	—	1.23	—	320.0
5405.223	0.772	0.46	0.92	1.29	7.51	—	—	—	—	—	1.26	—	350.0
5452.092	0.227	0.51	0.88	1.35	6.51	—	—	—	—	—	1.40	—	304.0

5602.462	0.187	0.54	0.54	0.86	7.58	1.41	0.77	1.08	—	—	1.38	—	340.0
5649.421	0.665	0.47	0.82	1.36	6.63	1.58	0.85	1.17	—	—	1.32	—	246.0
5649.439	0.671	0.43	0.87	1.28	6.17	1.62	0.89	1.23	—	—	1.29	—	330.0
5649.464	0.677	—	—	—	—	1.54	0.86	1.21	1.81	0.44	—	2.69	317.0
5650.373	0.919	0.41	0.61	1.07	7.17	1.71	0.79	1.19	—	—	1.34	—	370.0
5650.376	0.920	0.48	0.59	1.13	7.32	1.68	0.77	1.06	—	—	1.36	—	382.0
5650.380	0.921	—	—	—	—	1.53	0.69	1.13	1.79	0.41	—	2.56	360.0
5650.386	0.922	0.43	0.71	1.08	7.33	1.62	0.62	1.16	—	—	1.26	—	375.0
5650.390	0.923	0.44	0.68	1.18	7.28	1.77	0.68	0.97	—	—	1.31	—	368.0
5650.437	0.936	0.43	0.63	0.97	7.53	1.59	0.73	1.03	—	—	1.29	—	382.0
5650.441	0.937	—	—	—	—	1.63	0.71	0.89	1.76	0.43	—	2.63	340.0
5650.445	0.938	0.46	0.57	1.16	7.33	1.68	0.66	0.95	—	—	1.29	—	362.0
5650.458	0.942	—	—	—	—	1.75	0.59	0.91	1.78	0.44	—	2.68	310.0
5650.468	0.944	—	—	—	—	1.80	0.61	1.11	1.76	0.41	—	2.72	355.0
5650.467	0.943	0.43	0.64	1.15	7.54	1.65	0.65	1.08	—	—	1.31	—	355.0
5650.472	0.945	0.42	7.54	0.96	7.35	1.78	0.68	1.02	—	—	1.24	—	338.0
5651.412	0.195	—	—	—	—	1.58	0.75	0.93	1.66	0.39	—	2.68	330.0
5651.419	0.197	0.39	0.64	0.86	7.41	1.49	—	—	—	—	1.28	—	275.0
5651.439	0.202	0.33	0.64	0.97	7.38	1.62	—	—	—	—	1.26	—	305.0
5651.443	0.203	0.36	0.49	0.88	7.22	1.67	—	—	—	—	1.29	—	315.0
5651.451	0.205	—	—	—	—	1.65	0.78	0.97	1.59	0.44	—	2.66	320.0
5752.279	0.000	0.36	0.58	1.03	7.81	1.51	0.61	1.05	1.91	0.41	1.14	—	278.0
5790.158	0.066	0.42	0.62	0.83	7.97	1.56	0.61	0.89	1.88	0.38	1.23	—	295.0
5810.147	0.378	0.45	0.63	1.21	6.69	1.71	0.83	1.12	1.85	0.42	1.29	—	372.0
5811.139	0.641	0.51	0.89	1.06	6.83	1.55	0.79	1.08	1.76	0.41	1.44	—	375.0
6037.475	0.786	0.44	0.85	1.17	7.06	1.56	0.76	0.98	1.98	0.37	1.47	—	355.0
6047.260	0.387	0.46	0.55	0.99	5.95	1.46	0.76	0.96	—	—	1.22	—	285.0
6047.268	0.389	—	—	1.19	6.13	1.49	0.68	1.08	1.83	0.41	1.39	2.61	276.0
6047.277	0.391	0.49	0.53	0.96	6.22	1.48	0.77	1.07	—	—	1.33	—	210.0
6047.284	0.393	—	—	—	—	1.53	0.66	1.16	1.85	0.36	—	—	255.0
6047.317	0.402	0.43	0.69	1.11	7.13	1.65	0.75	1.03	—	—	1.41	—	190.0
6047.325	0.404	0.47	0.68	1.16	6.90	1.71	0.73	1.13	—	—	1.33	—	310.0
6047.349	0.410	0.45	0.68	1.23	6.85	1.68	0.74	0.87	—	—	1.38	—	240.0
6047.393	0.422	0.51	0.74	1.08	6.45	1.49	0.69	0.95	—	—	1.27	—	255.0
6047.400	0.424	—	—	—	—	1.59	0.77	0.92	1.91	0.34	1.36	2.54	278.0
6047.438	0.434	0.55	0.77	0.93	6.45	1.39	0.82	0.97	—	—	1.41	—	325.0

Table 1. Continued

JD 2440000+	Phase	N IV 4058	Blend 4100	Blend 4540	He II 4686	He II 5410	C IV 5810	He I 5876	He II 6562	He I 6678	N V 4620	He I 7065	He II 4860
6047.446	0.436	—	—	—	—	1.46	0.79	0.96	1.92	0.35	—	—	259.0
6048.213	0.640	0.37	0.78	1.17	5.82	1.53	0.68	0.69	—	—	1.32	—	431.0
6048.218	0.641	—	—	—	—	1.55	0.68	0.75	1.72	0.38	—	2.73	475.0
6048.224	0.643	—	—	—	—	1.58	0.59	0.73	1.68	0.33	—	2.81	520.0
6048.236	0.646	0.36	0.69	1.32	5.92	1.47	0.59	0.72	—	—	1.37	—	515.0
6048.252	0.650	—	—	—	—	1.63	0.65	0.64	1.90	0.39	—	2.79	507.0
6048.261	0.653	0.41	0.63	1.20	5.28	1.44	0.65	0.63	—	—	1.33	—	482.0
6048.300	0.663	—	—	—	—	1.47	0.56	0.69	1.65	0.34	—	2.70	475.0
6048.309	0.665	0.43	0.83	1.26	5.81	1.59	0.67	0.66	—	—	1.36	—	502.0
6048.333	0.672	0.41	0.79	1.28	5.35	—	—	—	—	—	1.39	—	486.0
6048.341	0.674	0.46	0.76	1.38	5.77	—	—	—	—	—	1.33	—	495.0
6048.359	0.679	—	—	—	—	1.46	0.59	0.81	1.93	0.42	—	2.68	506.0
6048.376	0.683	0.41	0.91	1.33	5.93	1.41	0.86	0.79	—	—	1.40	—	465.0
6048.401	0.690	0.39	0.94	1.34	5.74	1.53	0.83	0.68	—	—	1.41	—	480.0
6048 429	0.697	0.38	0.87	1.43	5.86	1.62	0.84	0.80	—	—	1.32	—	462.0
6048.445	0.702	—	—	—	—	1.58	0.78	0.82	1.55	0.39	—	2.74	481.0
6048.466	0.707	0.32	0.75	1.28	5.33	1.80	0.54	0.63	—	—	1.36	—	465.0
6048.491	0.714	—	—	1.30	5.21	1.75	0.57	0.71	1.53	0.36	1.39	2.80	335.0
6072.146	0.000	0.37	0.47	0.86	8.53	1.42	0.65	0.85	1.62	0.33	1.09	—	318.0
6083.217	0.942	0.43	0.86	0.92	8.77	—	—	—	—	—	1.21	—	358.0
6083.259	0.953	0.39	0.83	1.17	7.98	1.77	0.77	1.21	2.17	0.31	1.23	2.19	390.0
6083.337	0.974	0.33	0.81	0.85	7.97	—	—	—	—	—	1.23	—	345.0
6083.493	0.015	0.39	0.68	1.22	8.56	—	—	—	—	—	1.26	—	332.0
6148.115	0.189	0.45	0.45	0.84	8.59	0.97	0.76	0.49	—	—	1.41	—	285.0
6148.180	0.206	0.51	0.60	0.93	7.32	0.79	0.72	0.85	—	—	0.83	—	246.0
6150,094	0.714	0.48	0.91	1.05	5.89	1.49	0.86	0.71	1.81	0.34	1.43	—	358.0
6150.172	0.735	—	—	—	—	1.78	0.78	0.67	2.07	0.39	1.55	2.72	312.0
6150.218	0.747	0.44	0.88	0.94	7.40	1.81	0.84	0.60	2.12	0.38	1.46	—	335.0
6197.102	0.207	0.45	0.89	0.84	6.38	1.64	0.75	0.90	—	—	1.33	—	336.0
6198.110	0.474	0.46	0.65	0.96	7.37	1.66	0.68	1.21	1.73	0.31	1.19	—	226.0

or the asymmetry is caused by the companion. The same argument holds for the He I lines also, which show relatively constant values of flux with respect to He II λ4860. Generally (as also in CQ Cep) all the He I lines have associated violet absorption edges at high V_∞ implying their origin in the outermost parts of the envelope. The absence of orbital effects in He I lines agrees with their origin in a region surrounding both the components and not participating in the orbital motion.

The behaviour of the He II λ4686 line is different from other lines. On one occasion (JD 2,446,048 . . .) , when there was enhancement of flux at all lines, this line did not show an increase. Although He II λ4686 shows significant scatter the flux increases near phase 0.0, there is a general variation of flux from season to season as seen by Firmani *et al.* (1980) also. Two explanations are possible for this: (1) According to the model shown schematically by Firmani *et al.* (1980), the compact star will be closest to the WN star near phase 0.15. This could lead to an increase in the flux close to this phase. (2) The production of He II λ4686 is not confined to any selected zone of the atmosphere, but is produced throughout the envelope, so that at phase 0.0 we see maximum intensity of this line, by virtue of maximum line-emitting material lying completely unocculted towards the observer. The line profile also changes at this phase to one with a sharp peak and extended wings.

With the radial-velocity orbital solutions and the resulting mass function, one may derive a mass of 1–2 $M_\odot$ for the compact star assuming the mass of the WN component to be 10 $M_\odot$ and i = 70°. The separation is of the order of 20 $R_\odot$. If we adopt the measurements of V444 Cyg (WN5 + O) (Cherepashchuk, Eaton & Khaliullin 1984) for the size of the core and extent of the atmosphere of the WN5 component, the extension of the atmosphere in HD 50896 will be comparable to the separation itself. The compact star although considerably distant from the WN core in this case, cannot cause significant changes in either spectral line profiles, or in the continuum energy distribution. The accretion onto it can produce X-rays but they can become degraded to lower energies because of the dense electron envelope (Moffat & Seggewiss 1979). More recently, Vanbeveran, van Rensberger & de Loore (1982) have considered the production mechanism as well as the absorption of X-rays and discussed the different reasons for the non-detection of X-rays.

Thus we may say that the binary model proposed by Firmani *et al.* can explain the flux variation of emission lines. N V, N IV and C IV originate closer to the core in a highly ionized region (Moffat & Seggewiss 1978,1979; Sahade 1980). As noted by Firmani *et al.,* the lines of He II at $\lambda\lambda$5410, 6562 and 4860 originate in a region farther from the core. This region is distorted by the companion and therefore the flux measures of the He II lines result in a greater scatter. The region of He I line emission is outermost, probably enclosing the companion.

4. Discussion

The well-studied binary V444 Cyg has an orbital period close to that of HD 50896. Direct comparison between the two is not possible because of the differences in the type of the companion. In the case of V444 Cyg, the companion is O type, which eclipses the WN component at phase 0.5. All the emission lines show eclipse effects at both minima. The concentration of the He II emitting material is clearly shown by the line profiles (Ganesh Bappu & Natarajan 1968). In the case of HD 50896, the companion is smaller,

not producing any noticeable eclipse effects either in the continuum or in line fluxes. Its influence in the distortion of the extended atmosphere can be noticed only for N V, N IV and C IV lines. Other lines show only some scatter about the mean flux.

There are some similarities between the two systems. None of the radial velocity curves for different emission lines gives identical solutions in either case. Both the systems show variation of polarization with orbital phase; therefore, it is possible that HD 50896 has also a dense electron envelope similar to V444 Cyg. Such polarization changes are noticeable in the case of CQ Cep also (Drissen *et al.* 1986).

The peculiarity of He II λ4686 line in CQ Cep and V444 Cyg indicates its origin in a region extended through the wind (Paper I). The same is also true for N III λ4640 in those stars. In HD 50896 this line was too weak to be measured. N IV λ4058 showed stable symmetric profiles in V444 Cyg (Ganesh, Bappu & Natarajan 1968) and in CQ Cep (Bappu & Viswanadham 1977); in HD 50896, the profile was double-peaked and changed throughout the orbit (Firmani *et al.* 1980).

The wind-dominated Roche surface can explain the flux variations for CQ Cep and also partly for V444 Cyg (Paper I). In the case of HD 50896 there is a complication introduced not only by the intrinsic variation, but by the asymmetric distribution as well. The eccentricity of the orbit adds to this. The value of $e = 0.34$ is based on the radial velocity measures of N IV λ3483 emission. However, the radial velocity of absorption edge of N V λ4621 gives a still smaller value of *e,* but shows significant phase shift (Firmani *et al.* 1980), and therefore the exact value of the orbital eccentricity is difficult to specify. It is known that the λ4686 radial velocity curve usually gives an eccentric orbit solution in WN binaries (Shylaja 1986b) and therefore, other N V lines will have to be studied for establishing the true value of *e.*

Smith (1973) suggested that all Population I WR stars have masses 10 $M_\odot$ and that they all evolved from more massive stars. More recently, Massey (1981) has shown that the mean value of the mass of WR stars is $\sim 20\ M_\odot$ Since hydrogen deficiency is a general feature of all WR stars (Sahade 1981), it was also postulated that the outer hydrogen material has been lost. The evolutionary scheme of de Loore (1980) invokes two stages of WR phase in a binary. The first phase corresponds to the more widely known WR + OB phase; the second is the WR + compact phase, after a supernova explosion. In the case of a binary, it is possible that the mass from the WR star is accreted on to the companion, making it more massive and readily detectable (Paczynski 1967). However, the winds are so fast that the accretion may be negligible. When the companion is less massive and not detectable, the material is more readily lost to the surroundings and may appear like a nebula. Therefore, Wendker *et al.* (1975) attributed the presence of the nebulae in NGC 6888 to the material ejected from HD 192163, which was considered to be a single star. Recently, its binarity has been suggested (cf. van der Hucht *et al.* 1981), but remains uncertain (Vreux, Andrillat & Gosset 1985).

In the case of HD 50896, the binary nature is postulated based on radial velocity and flux variations, although intrinsically varying supposedly single stars also are known (*cf.* van der Hucht *et al.* 1981). The presence of the compact companion puts HD 50896 in the class of the second WR phase in the scenerio proposed by de Loore (1980). Another feature which would facilitate confirmation of this aspect is the space velocity. It is generally believed that the binary pulsars with high space velocities result from supernova explosions in a binary with dissimilar components. It is also derived that, depending on the mass lost, the circular orbit may change to one with high eccentricity

and a close binary may arise without being disrupted (van den Heuvel 1976; Shylaja & Kochhar 1984). The large distance of HD 50896 from the galactic plane also favours the idea. The association with the ring nebula S 308 (Chu *et al.* 1982), which indicates the nitrogen enrichment, puts its origin to the WN star itself (Kwitter 1984). Recently, a large interstellar structure has been detected in the line of sight towards HD 50896 (Heckathorn & Fesen 1984).

5. Conclusions

This spectrophotometric study of HD 50896 shows that the lines of N V, N IV and C IV display moderate variations which may be interpreted in terms of a binary model of the system. Because of the eccentric orbit and nondetection of eclipse effects in light variations, quantitative derivations of the orbital parameters are not possible. From the radial velocity determinations available, it appears that the companion is a compact star. Comparison with other eclipsing systems like V444 Cyg and CQ Cep shows that the atmospheric structures are similar. The He II lines probably arise from a region distorted by the presence of the companion. The λ4686 line of He II has a different behaviour as in other eclipsing systems. The He I lines generally have constant flux, indicating their formation outside the influence of the companion.

The association with a nebulosity and the location relatively far from the galactic plane may suggest assigning HD 50896 to the second WR binary phase as a post-SN event. Other techniques like systematic fast photometry and measurement of space velocity may yield important information on the type of companion and the accreting process.

Acknowledgements

I gratefully acknowledge the guidance of late Professor M. K. V. Bappu who initiated these observations. I thank Professor J. C. Bhattacharyya for guidance on this program. Very useful and stimulating discussions with Dr N. K. Rao are gratefully acknowledged. I also thank the referees for very valuable suggestions and for drawing my attention to some of the latest work on this subject.

References

Bappu, M. K. V. 1973, in *IAU Symp*. 49**:** *Wolf-Rayet stars and High temperatu'e stars,* Eds M. K. V. Bappu & J. Sahade, D. Reidel, Dordrecht, p. 59.
Bappu, M. K. V. 1977, *Kodaikanal Obs. Bull. Ser. A,* **2**, 64.
Bappu, M. K. V., Viswanadham, P. 1977, *Kodaikanal Obs. Bull. Ser. A,* **2**, 89.
Breger, M. 1976, *Astrophys. J. Suppl. Ser.,* **32,** 1.
Cherepashchuk, A. M. 1981, *Mon. Not. R. Astr. Soc.,* **194**, 755.
Cherepashchuk, A. M., Eaton, J. A., Khaliullin, Kh. F. 1984, *Astrophys. J.,* **281,** 774.
Chu, Y. H., Gull, T. R., Tretfers, R. R., Kwitter, K. B., Troland, T. H. 1982, *Astrophys. J.,* **254,** 562.
de Loore, C. W. H**.** 1980, *Space Sci. Rev.,* **26,** 113,
Drissen, L., Moffat, A. F. J., Bastien, P., Lamontagne, R. 1986, *Astrophys. J.,* (submitted).
Ebbets, D. 1979, *Publ. astr. Soc. Pacific,* **91,** 104.
Firmani, C. Koenigsberger, G., Bisiacc,hi, G. F. Moffat, A. F. J., Isserstedt, J**.** 1980, .4strophys. *J.,* **239,** 607.

Firmani, C., Koenigsberger, G., Bisiacchi, G. F., Ruiz, E, Solar, A. 1979, in *IAU Symp.* 83; *Mass loss and Evolution of O type stars,* Eds P. S. Conti & C. W. H. de Loore, D. Reidel,Dordrecht, p. 421.
Ganesh, K. S., Bappu, M. K. V., Natarajan, V. 1968, *Kodaikanal Obs. Bull., Ser* A, No. 184.
Hayes, D. S. 1970, *Astrophys. J.,* **159,** 165.
Heckathorn, N., Fesen, R. A. 1984, NASA CP-2349, p. 207.
Hillier, D. J. 1984, *Astrophys. J.,* **280,** 744.
Irvine, C. E., Irvine, N. J. 1973, *Publ. astr. Soc. Pacific,* **85,** 403.
Kuhi, L. V. 1967, *Publ. astr. Soc. Pacific.,* **79,** 57.
Kwitter, K. B. 1984, *Astrophys. J.,* **287,** 840.
Lamontagne, R., Moffat, A. F. J., Lamarre, A. 1986, *Astr. J.*, **91,** 925.
Landolt, A. U., Blondeau, K. L. 1972, *Publ. astr. Soc. Pacific,* **84,** 754.
Massey, P. 1981, *Astrophys. J.*, **246,** 153.
McLean, I. S. 1980, *Astrophys. J.,* **236,** L149.
McLean, I. S., Coyne, G. V., Trecker, J. E., Serkowski, K. 1979, *Astrophys. J.*, **231,** L141.
Moffat, A. F. J., Seggewiss, W. 1978, *Astr. Astrophys.* **70,** 69.
Moftat, A. F. J., Seggewiss, W. 1979, *Astr. Astrophys.* **77,** 128.
Paczynski, B. 1967, *Acta Astr.,* **17,** 355.
Ross, L. W. 1961, *Publ. astr. Soc. Pacific,* **73,** 354.
Sahade, J. 1980, *Astr. Astrophys.,* **87,** L7.
Sahade, J. 1981, *Rev. Mexicana Astr, Astrof.,* **6,** 189.
Schmidt, G. D. 1974, *Publ. astr. Soc. Pacific,* **86,** 767.
Serkowski, L. 1970, *Astrophys. J.,* **160,** 1083.
Shylaja, B. S., Bappu, M. K. V. 1983, *Kodaikanal Obs. Bull.,* **3,** 72.
Shylaja, B. S., Kochhar, R. K. 1984, *Astrophys. Space Sci.,* **97,** 121.
Shylaja, B. S., 1986a, *J. Astrophys. Astr.,* **7,** 171 (Paper 1).
Shylaja, B. S. 1986b, in *IAU Symp.* 122: Circumastellar Matter (in press).
Singh, M. 1984, *Inf. Bull. Variable Stars,* No. 2508.
Smith, H. J. 1955, *Ph.D. Thesis,* Harvard University.
Smith, L. F. 1968, in *Wolf-Rayet stars,* Eds K. G. Gebbie & R. N. Thomas, NBS SP-307, p. 21.
Smith, L. F., 1973, in *IAU Symp.* 49: *Wolf-Rayet stars and High Temperature stars,* Eds M. K. V. Bappu & J. Sahade, D. Reidel, Dordrecht, p. 15.
Smith, L F., Kuhi, L. V. 1981, *An atlas of WR line profiles,* JILA Report No. 117.
Tutukov, A. V., Yungelson, L. R. 1979, in *IAU Symp.* 83; *Mass Loss and Evolution of O type Stars,* D. Reidel, Dordrecht, p. 401.
Vanbeveren, D., van Rensberger, W., de Loore, C. 1982 *Astr. Astrophys.* **115,** 69.
Van den Heuvel, E. P. J. 1976, in *IAU Symp.* 73: *Structure and Evolution of Close Binaries,* Eds P. Eggleton, S. Mitton & J. A. J. Whelan, D. Reidel, Dordrecht, p. 35.
van der Hucht, K. A., Conti, P. S., Lundstrom, I., Stenholm, B. 1981, Space *Sci. Rev.,* **28,** 227.
Vreux, J. M., Andrillat, Y., Gosset, E. 1985, *Astr. Astrophys.,* **149,** 337.
Wendker, H. J., Smith, L. F., Isreal, F. P., Habing, H. J., Dickel, H. R. 1975, *Astr. Astrophys.,* **42,** 173.
Wilson, O. C. 1948, *Publ. astr. Soc. Pacific,* **60,** 383.